UNIVERSITÉ DE NANTES
FACULTÉ DES SCIENCES ET DES TECHNIQUES

———

ÉCOLE DOCTORALE 3MPL

Année 2012

N° attribué par la bibliothèque

Caractérisation et contrôle de l'interface électrode / électrolyte d'électrodes positives pour accumulateurs Li-ion.

———

THÈSE DE DOCTORAT
Discipline : Chimie du solide
Spécialité : Sciences des matériaux

Présentée
et soutenue publiquement par

Marine CUISINIER

Le 17 janvier 2012, devant le jury ci-dessous

Rapporteurs	D[r] Michel MÉNÉTRIER	Ingénieur de recherche au CNRS – ICMCB, Bordeaux
	Prof. Jean-Marie TARASCON	Professeur des universités – Univ. de Picardie Jules Verne
Examinateurs	Prof. Kristina EDSTRÖM	Professeur des universités – Univ. of Uppsala, Suède
	Prof. Ryoji KANNO	Professeur des universités – Tokyo Institute of Tech., Japon
	Prof. Guy OUVRARD	Professeur des universités – Univ. de Nantes
	D[r] Nicolas DUPRÉ	Chargé de recherche au CNRS – IMN, Univ. de Nantes
	D[r] Dominique GUYOMARD	Directeur de recherche au CNRS – IMN, Univ. de Nantes

Directeur de thèse : D[r] Dominique GUYOMARD
Co-encadrant : D[r] Nicolas DUPRÉ

REMERCIEMENTS

Ces quelques lignes tant attendues seront en français, tant il est plus aisé pour moi d'user de superlatifs dans ma langue maternelle.

En premier lieu, je tiens à remercier Michel Ménétrier et Jean-Marie Tarascon pour m'avoir fait l'honneur de juger, commenter, critiquer ce manuscrit. Je suis bien consciente du poids de ce « document », et donc du volume de travail que cela a du représenter pour eux. Je leur suis également reconnaissante pour leurs remarques et questions lors de la soutenance, qui m'ont notamment poussée à remettre en question les menus « détails » de mon travail expérimental. Ces *combien, comment, pourquoi,* et *pourquoi pas* sont le genre de questions qui s'oublient, après trois passés immergée dans l'électrolyte pour ainsi dire, à répéter les mêmes protocoles… - Il doit bien avoir une raison, me disais-je alors !

Je remercie tout aussi chaleureusement Kristina Edström et Ryoji Kanno pour avoir fait le déplacement pour l'occasion. J'avais rencontré Kristina Edström pour la première fois à l'ECS de Las Vegas en 2010, et ses encouragements m'avaient alors énormément touchée. Ryoji Kanno a quant à lui assisté à mes débuts de jeune thésarde (Novembre 2008), et m'a par la suite accueilli dans son laboratoire avec beaucoup de prévenance. Ses étudiants doivent probablement se souvenir avec effroi de cette toute petite Française qui ne cessait de poser des questions !

Le dernier membre « extérieur » du jury que je me dois de remercier n'est autre que Guy Ouvrard, le directeur de l'IMN. Notamment grâce à son soutien, j'ai pu bénéficier à deux reprises de bourses de l'université pour partir au soleil (Nevada en 2010, Floride en 2012). Et puis au travers de son rôle de directeur, c'est le fonctionnement même de l'institut que je souhaite mettre ici à l'honneur. J'y ai passé trois merveilleuses années, à découvrir, à apprendre, à me surprendre voir parfois à me faire peur, tant la confiance qui nous est accordée en tant qu'étudiants est également lourde en responsabilités.

Aussi j'adresse mes remerciements les plus sincères à Pierre-Emmanuel Petit et Philippe Déniard (DRX), Michel Suchaud et Philippe Léone (Mössbauer), Christophe Payen (SQUID), Jonathan Hamon et Vincent Fernandez (XPS), Michaël Paris (RMN), Philippe Moreau, Anne-Claire Gaillot, Eric Gautron, Nicolas Gautier et Luc Lajaunie (MET), Nicolas Stephant et Stéphane Grolleau (MEB), Patrick Soudan (Electrochimie), qui m'ont chacun leur tour accompagnée puis me laissée me débrouiller comme une grande. Je garderais toujours en mémoire une phrase de Philippe Moreau : « Il n'y a qu'en ne faisant rien qu'on ne fait rien de

mal ». Des boulettes j'en ai fait quelques unes, certaines plus coûteuses que d'autres, mais jamais celles-ci ne m'ont interdit l'usage ultérieur d'un appareil… Bien au contraire ! Merci à tous pour m'avoir inculqué la patience, la persévérance et l'humilité nécessaire à la recherche et pour m'avoir cédé ces pics d'adrénaline quand arrivent *sous mes propres yeux* les résultats tant attendus. Le décompte de presque mille expériences RMN témoigne du goût (de l'addiction ?) que j'y ai pris.

Après avoir tourné autour du pot, survient le moment de remercier mes encadrants, délicat puisque extrêmement émouvant. Quand j'ai reçu dans ma boite mail l'offre de thèse (merci à Hélène Terisse, ancienne de l'ENSCR !), j'ai enquêté autour de moi, pour me faire une idée de ce qui m'attendrait une fois à Nantes. Unanimement on m'a répondu « Dominique Guyomard est le parfait directeur de thèse, à la fois péniblement pointilleux et d'une extrême gentillesse ». Dans le mille ! Passées nos difficultés de communication, travailler sous la direction de Dominique a été un pur bonheur, de par l'autonomie et la confiance qu'il a bien voulu m'accorder.

Et enfin je remercie Nicolas Dupré pour avoir encadré cette thèse et pour son sourire charmant (sic). Ayant tous deux un sale caractère et un humour douteux, nous étions faits pour nous entendre. Porter la double casquette d'encadrant et d'ami n'a pas du être aisé lorsqu'il a fallu corriger la thèse, et je lui suis sincèrement reconnaissante de ne pas m'avoir tenu rigueur pour mes nombreux coups de gueule à cette époque. J'espère que nous aurons l'occasion de collaborer à nouveau ensemble, et de reprendre *quelques* Cardiff au Webb Ellis. Je remercie également tous les stagiaires que nous avons eu l'occasion d'encadrer ensemble : Romain Lavaud, Yanping Wang, Yi He et Audrey Bonzi.

Un grand merci aux occupants des différents bureaux du couloir « EO-ST2E », pour la bonne humeur, les nombreux échanges scientifiques (ou non) ; je pense aux super nanas : Audrey, Nathalie Magali, et Marika, mais aussi à Lénaic, Pierre-Emmanuel, Kalid, Yassine, Driss, Miloud, Samuel, François (pardon pour ceux que j'oublie). Je voudrais également remercier Florent Boucher, Joël Gaubicher et Philippe Moreau, avec qui j'ai pris beaucoup de plaisir à travailler sur le projet Sodium.

Enfin, j'aimerais finir en remerciant mes parents pour m'avoir soutenu tout au long de cette thèse, et d'autant plus les quatre derniers mois qu'ils ont pris à leur charge. C'était une immense fierté pour moi d'avoir toute famille réunie à l'occasion de ma soutenance, merci aux frangins d'avoir fait le voyage. Par-dessus tout, merci à Romain pour m'avoir poussée jusqu'au bout, je n'aurais probablement pas eu le courage nécessaire sans un bon coup de pied au derrière à l'occasion !

TABLE OF CONTENTS

INTRODUCTION

The demand for advanced energy storage systems has kept growing significantly each year for the past decade and will doubtlessly remain one of the major challenges of the 21st century. Laptops, cell phones, audio and/or video players, cameras, and a multitude of other portable electronic devices (PEDs) are under accelerated development and more present every day in our lives, becoming always more complex and power consuming. In the same time that we mass consume and dispose of PEDs, come almost in a schizophrenic way the awareness of natural resources finite limits and environmental pollution concerns that press us to replace gasoline cars by low emission hybrid electric vehicles (HEVs) and ultimately, zero emission electric vehicles (EVs). This transition, favored by the current economic crisis and the necessity for states to come up with innovative sources of growth, also relies on the availability of a suitable advanced energy storage system. The boom of renewable-but-intermittent energy technologies such as photovoltaics (PV) and windmills could be at last wisely exploited if only integrated into a smart-grid, coupled with large scale stationary energy storage solutions.

Thus, ever increasing expectations towards energy storage devices usually concern two important criteria, energy density (Wh/kg or Wh/L) and/or power density (W/kg or W/L), which characterize the amount of energy stored per weight/volume unit and how quickly energy can be delivered, respectively. Among the electrochemical devices able to answer these needs, we count supercapacitors, fuel cells and batteries. At present, supercapacitors exhibit the highest charge/discharge rate (i.e. the highest power density) but a rather poor energy density and an important self-discharge. On the other hand, fuel cells have the highest energy density (providing the fuel tank is large compared to the fuel cell). However, the various fuel cell technologies all suffer from poor efficiency (<60%) and other issues such as cost, lifetime and safety limit their use to niche markets. Combining a high energy density with an intermediate power capability, batteries currently stand as the most popular power source of choice.

Since Sony Corporation released the first commercial Li-ion cells in 1991, lithium-ion batteries have supplanted older rechargeable battery technologies such as lead acid, nickel cadmium and nickel metal hydride on many market segments. Surpassing their competitors in terms of both gravimetric and volumetric energy densities, Li-ion batteries also offer the

further advantages of high working voltage (~3.5V), long charge-discharge cycle life (>1000 cycles), low self-discharge rate, and no memory effect for instance [1-2]. Over the past decade, the energy of Li-ion batteries has increased by a factor of two, reaching values higher than 600 Wh/L and 250Wh/kg [3]. With recent improvements in power density, Li-ion batteries are now the best choice for high-power portable applications such as power tools. As a result, Li-ion batteries now rule the portable battery market, sharing about 75% of the worldwide sales of portable batteries. Li-ion batteries constitute a continuing strong global market, which grew up to 3.3 billion units at the end of 2008 with a 20% year-on-year growth rate so far, only slightly hindered since the economic crisis [3-4].

Regarding the transportation sector, requiring high-energy, high-power systems, Nickel metal hydride batteries dominate in current commercial HEVs through the success of the *Toyota Prius*. However, since 2010, new generation of HEVs such as the *Nissan Leaf* and *GM Chevrolet Volt* uses Li-ion batteries, demonstrating that barriers including safety, cost, life and power performance can be overcome. Actually, the market for Li-ion batteries in HEV applications is projected to grow substantially and surpass nickel metal hydride in the near future [4].

In a world producing more than a billion cell phones units, nearly 300 millions MP3 players as well as 50 millions passenger cars per year (of which 10% could be HEV/ EV in 10 years), the question is not only about how to satisfy such a high demand in terms of Li-ion cells but also about how to limit the environmental impact of these batteries, from the materials extraction to the cells production up to their disposal and recycling. Li-ion batteries will play for sure an important role in any energy future that our responsability as scientists is to make it smart and sustainable.

Among the challenges still remaining in this area of research, the need to control interfaces has become especially obvious [5]. Indeed, the solid electrolyte interphase (SEI) between the negative electrode and the electrolyte of a Li-ion battery is known to factor into the overall battery behavior in terms of irreversible capacity loss, charge transfer kinetics, and storage properties [6].

Interfacial reactions and the growth of a passivation layer at the electrode surface upon cycling have been also highlighted for different positive electrode materials and have been identified to be of paramount importance as they can lead to performance degradation of the battery upon aging and cycling [7]. The existence of surface reactions at the positive electrode/electrolyte interface has been clearly demonstrated but the experimental conditions

of formation, growth and modification, as well as its subsequent influences on the electrochemical performance, remain unclear. The chemical, physical, and structural properties of the interfacial layer at the positive electrode in particular are still not well known, and thus this more recent research area is of great interest [8, 9].

The present thesis comes within this precise scope and reports the characterization and attempts to control interfacial processes occurring on $LiNi_{1/2}Mn_{1/2}O_2$, $Li_{1.2}Ni_{0.4}Mn_{0.4}O_2$ and $LiFePO_4$ positive electrode materials during their storage and electrochemical cycling.

The first chapter is therefore dedicated to the description of battery materials, as well as basic interphasial processes hold responsible for battery failure, based on electrolyte decomposition.

Since this work proposes the extensive use of multinuclear high field NMR to extract information on the electrode / electrolyte interphase on paramagnetic active materials, the second chapter sets out to describe the development of dedicated spectroscopic tools, namely MAS NMR (^{7}Li, ^{19}F and ^{31}P) and EELS, to quantitatively describe the interphase and unravel its architecture.

The third chapter condenses the multiple studies carried out on the $LiNi_{1/2}Mn_{1/2}O_2$ / electrolyte interphase. Different types of surface modifications are envisaged and parameters such as air exposure, temperature, formulation of the composite electrode, the use of an electrolyte additive but also the overlithiation under the form of $Li[Li_{0.2}Ni_{0.4}Mn_{0.4}]O_2$ are investigated.

The fourth and last chapter covers different parameters susceptible to influence the interphasial behavior of $LiFePO_4$ such as the promotion of a particular crystalline orientation or the aging process upon exposure to atmospheric oxidative species.

In each case, this work aims at correlating the nature and evolution of the electrode / electrolyte interphase, as probed by NMR spectroscopy (but also XPS and EELS), to the material surface chemistry, and finally elucidate the overall electrochemical performance evolution.

FOREWORD

This thesis directly takes over the work carried out by Jean Frédéric Martin (thesis defended in november 2008). Some of the results obtained then are necessarily summarized here (as adverted in the section title) to ensure the continuity of the different studies. As also mentioned in the section title, the following papers were written in the frame of this thesis. Those are referred to in the text by their Roman numerals, **I-IV**.

I. Moisture driven aging mechanism of $LiFePO_4$ subjected to air exposure, M. Cuisinier, J-F. Martin, N. Dupré, A. Yamada, R. Kanno, D. Guyomard, *Electrochem. Comm*. **12** (2010) 238.

II. More on the reactivity of olivine $LiFePO_4$ nanoparticles with atmosphere at moderate temperature J.-F. Martin, M. Cuisinier, N. Dupré, A. Yamada, R. Kanno, D. Guyomard, *J. Power Sources*, **196** (2011) 2155.

III. Elucidating $LiFePO_4$ air-aging mechanism to predict its electrochemical performance. M. Cuisinier, J.-F. Martin, N. Dupré, R. Kanno, D. Guyomard, *J. Mater. Chem,*. **21** (2011) 18575.

IV. Quantitative MAS NMR Characterization of the $LiMn_{1/2}Ni_{1/2}O_2$ Electrode/Electrolyte Interphase, M. Cuisinier, J.F. Martin, P. Moreau, T. Epicier, R. Kanno, D. Guyomard, N. Dupré, *Solid State Nucl. Magn. Reson.* (2011), doi: 10.1016/j.ssnmr.2011.09.001

REFERENCES

[1] A. Guibert, Lettres des sciences chimiques / L'Actualité chimique, **65** (1998) 15.

[2] D. Linden, Handbook of Batteries, McGraw-Hill, New York (1994).

[3] “Global and China's Li-ion Battery and Its Raw Materials Market Report, 2008–2009”, Market Avenue Inc., www.marketavenue.cn;

[4] (a) “Large and Advanced Battery Technology & Markets”, (b) “Hybrid & Electric Vehicle Progress Review 2010”, BBC Research Market Forecasting, www.bccresearch.com/report/.

[5] J. M. Tarascon, M. Armand, Nature, **414** (2001) 359.

[6] D. Aurbach, B. Markovsky, I. Weissman, E. Levi, Y. Ein-Eli, Electrochim. Acta, **45** (1999) 67.

[7] D. Aurbach, M. D. Levi, E. Levi, H. Teller, B. Markovsky, G. Salitra, U. Heider, L. Heider, J. Electrochem. Soc., **145** (1998) 3024.

[8] T. Matsushita, K. Dokko, K. Kanamura, J. Electrochem. Soc., **152** (2005) A2229.

[9] K. Edström, T. Gustafsson, J. O. Thomas, Electrochim. Acta,. **50** (2004) 397.

CHAPTER 1 : CONTEXT OF THE STUDY

After a brief explanation of the functioning of a Li-ion battery and an overview of its active components, the third part of this chapter focuses on surface phenomena and their impact on the battery performance and lifetime. Degradation mechanisms are given there, in order to introduce the chemical species present at the electrode/electrolyte interface. A review of literature data concerning more specifically the interphase grown on the positive electrode then highlights the physical and/or chemical parameters influencing the interphasial chemistry. As a technique of choice to monitor interphasial processes, solid state NMR is also introduced by a state-of-the-art review on this matter. As a significant origin of the battery aging, interphases and their comprehension offer numerous prospects. Hence this chapter ends with an outlook of what still needs to be understood and/or mastered to develop the next generation of Li-ion batteries.

I- OPERATION OF A Li-ION BATTERY

A battery consists in the assembling of the cathode and anode electrodes separated by a porous layer that is both an ionic conductor and an electrical insulator. During discharge, power is generated by converting the chemical energy of the electrode active materials, via redox reactions, into electrical energy. For a rechargeable battery, the labels of anode and cathode switch when the cell changes its status from discharge to charge. To avoid confusion, the terms positive electrode and negative electrode are usually preferred, and their use will be favored in this thesis.

A conventional commercial Li-ion cell still relies on a lithium transition metal oxide such as $LiCoO_2$ for the positive electrode and a graphitic carbon as the negative electrode, exactly like the one launched by Sony in 1991. Both electrodes are immersed in a non-aqueous liquid electrolyte containing a dissolved lithium salt such as $LiPF_6$.

During discharge, oxidation at the negative electrode releases Li^+ ions which diffuse through the electrolyte towards the positive electrode, as schematically shown in **Figure I-1**. Electrons pass through the external circuit thus generating power. During charge, the reverse processes occur upon external power supply, as depicted by the half equations below.

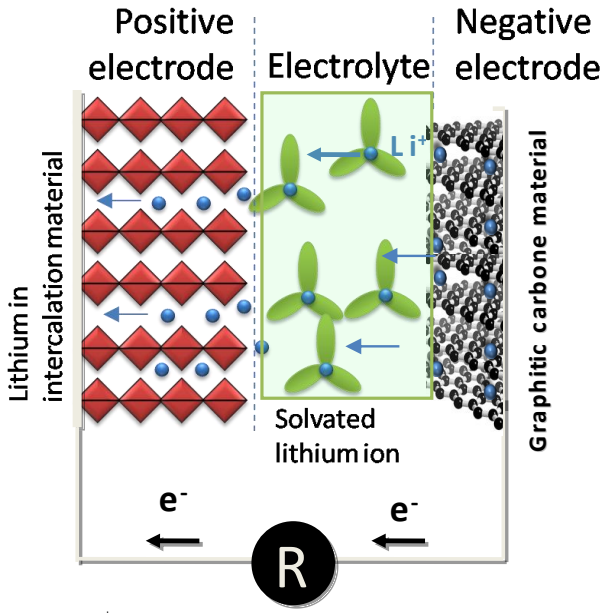

Discharge	$[HostA] + Li^+ + e^- \rightarrow [LiHostA]$	$[LiHostB] \rightarrow [HostB] + Li^+ + e^-$
Charge	$[LiHostA] \rightarrow [HostA] + Li^+ + e^-$	$[HostB] + Li^+ + e^- \rightarrow [LiHostB]$

Figure I-1. Schematic view of a Li-ion battery discharge process, followed by the redox reactions allowing the reversibility of the system.

II- BATTERY MATERIALS

The cell operation relies on the difference in the chemical potential of lithium atoms in both electrode materials. **Figure I-2** shows several electrode materials and their potentials with respect to the Li^+/Li^0 couple (–3.02 V vs. Standard Hydrogen Electrode, SHE), by convention set as the 0.00V reference. To achieve a large cell potential, positive electrode materials need to have high lithium atom binding energy (ie a high intrinsic redox potential) and the negative electrode should have a low lithium binding energy. Factors impacting intrinsic redox potential comprise the nature of the redox couple, but also of its ligands as well as structural considerations. Are discussed hereafter some of the electrode materials currently under investigation, considered relevant to our study for the variety of surface chemistries they develop and the importance of electrode/electrolyte interactions in their overall electrochemical performance.

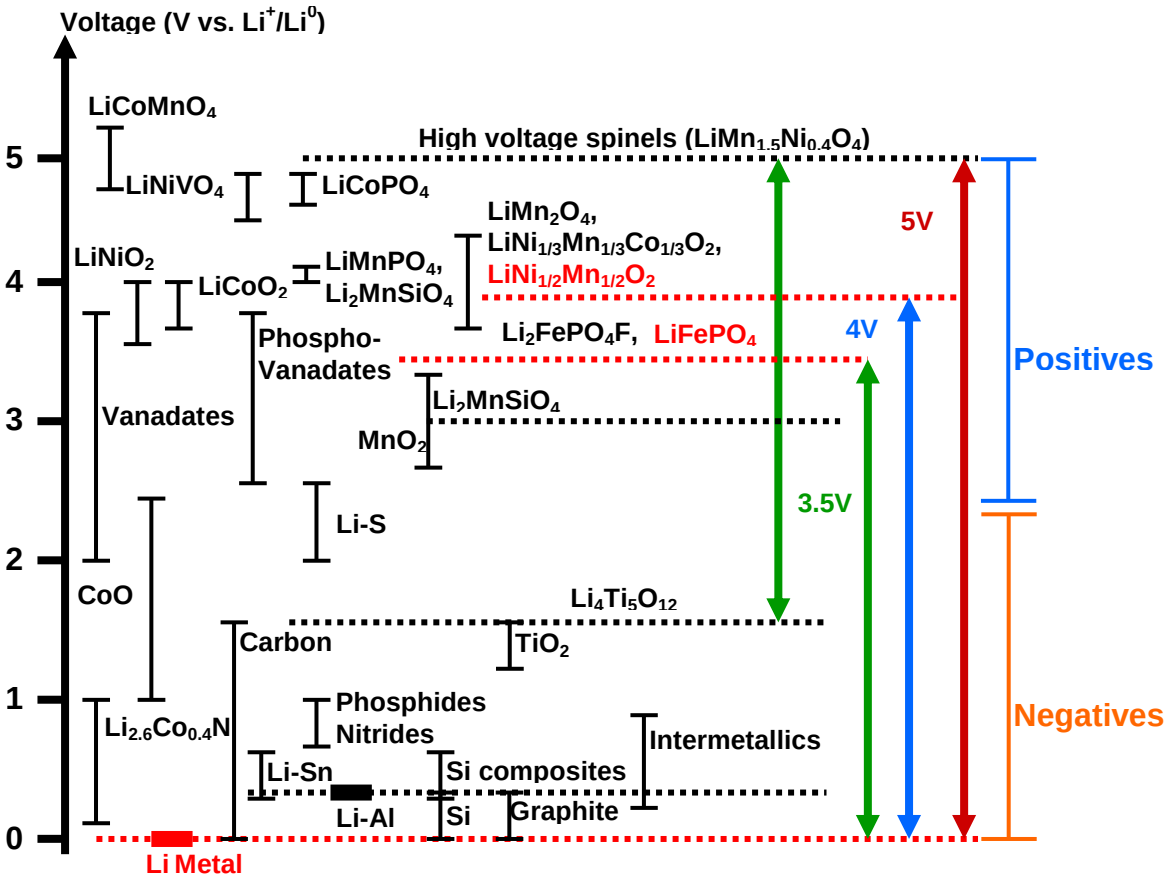

Figure I-2. Overview of various negative and positive electrode active materials currently under investigation.

II.1. Negative electrode materials

II.1.1. Lithium metal, the "Holy Grail"

By virtue of its specific position in the periodic table, Lithium metal stands as the ultimate negative electrode for battery chemistry possessing the largest theoretical capacity of 3900 $mAh.g^{-1}$. By its electronegativity and lightness, Li contributes to the highest possible cell voltage against any given positive electrode, and to the highest specific energy densities. The formation of dendrites during the repeated dissolution/deposition cycles and the subsequent propensity to shortcuts resulting in fire and explosion however, still limits the feasibility of a rechargeable battery based on lithium metal electrode and a liquid electrolyte, considered by many as the "Holy Grail" [1, 2].

II.1.2. Graphitic carbon materials

Graphitic carbon-based materials exhibit high lithium storage capacity (372 $mAh.g^{-1}$ up to the limit composition LiC_6) and small volume expansion (~10%) upon electrochemical lithium intercalation between the graphitic layers, which occurs between 0.2 and 0.05V vs. Li^+/Li^0 [3]. Their good cycling properties, together with their low cost and high availability, have made carbons the most attractive choice for commercial *Li-ion* batteries which safety is immensely improved due to the absence of metallic lithium [4].

II.1.3. Alloys materials

Still, graphite negative electrodes can be outperformed based on two important criteria: the specific capacity and the safety. The latter is related to the extremely low onset potential necessary to fully charge the material, which can result in lithium plating [5] and hence risk of shortcut similarly to Li-metal batteries. Alloy anodes exhibit good safety characteristics with onset potentials around 0.2 – 0.4 V vs. Li^+/Li^0, and theoretical specific capacities 2 – 10 times higher than that of graphite [5-7]. Most promising alloys, based on silicon and tin, incorporate lithium up to the composition $Li_{4.4}M$ (M = Si, Sn) at the cost of a dramatic volume expansion (~300%) leading to pulverization of the active alloy particles and poor cycle stability [8, 9], as further discussed in section III-5. The initial capacity loss of alloy negative electrodes is also problematically too high for practical applications and these two issues have been addressed by the use of nanosized materials [7, 10], intermetallics [6, 11] and/or dedicated electrode formulation [12, 13].

II.1.4. Transition metal pnictides

Transition metal pnictides (TMP) exhibit impressive densities of energy up to 6000 Whl^{-1} along very strong gravimetric and volumetric capacities (800Ah/l), but moderate volume changes, making it an extremely interesting alternative to negatives undergoing drastic volume changes along the electrochemical cycling [14, 15]. With the transition metal of the middle of the periodic table (M=Mn, Fe, Co, Ni), a conversion type reaction takes place transforming the MP_x pristine material into a composite electrode of metallic nano particles embedded in a Li_3P or Li_3Sb matrix ($MPn_x + 3xLi \rightarrow xLi_3Pn + M°$) [16, 17]. In this case, the redox reaction does not involve only the transition metal like in most of positive electrode materials (transition metal oxides), but also the post-transitional element (P, Sb). Although the redox mechanisms of these new materials were thoroughly investigated [18-20], the "secondary" reactions taking place at low potential (vs. Li) between the active material and electrolyte or additives, are yet totally unexplored.

II.1.5. Titanates

A state-of-the-art lithium-ion battery based on carbon or graphite negative electrode, with a lithium-insertion potential approaching 0 V (vs. $Li^+/Li^{0)}$ ensures a high cell voltage. It however, also introduces safety problem when the cell is over charged. Spinel-type $Li_4Ti_5O_{12}$ oxide has been considered as a promising alternative material to current carbon/graphite technology [21-24]. It follows a two-phase mechanism at 1.5V vs. Li^+/Li for lithium insertion and extraction as follows [25]: $Li_4Ti_5O_{12} + 3Li^+ + 3e^- \leftrightarrow Li_7Ti_5O_{12}$

Furthermore, during the lithium intercalation and de-intercalation processes there is almost no change in cell volume [26], which is beneficial for a long cycling lifetime. However $Li_4Ti_5O_{12}$ has a relatively low theoretical capacity of 175 $mAh.g^{-1}$. It also has low electronic conductivity, as a result, poor rate performance was often observed for electrode using coarse $Li_4Ti_5O_{12}$ [27]. Decreasing the particle size or surface coating with a more conductive material such as carbon and silver are the general ways to improve the rate performance of $Li_4Ti_5O_{12}$ [28, 29].

II.2. Positive electrode materials

Among the investigated materials stand two families of compounds of interest regarding their different surface chemistries, namely lamellar oxides and 3D phosphates, among which we elected our model compounds: $LiNi_{1/2}Mn_{1/2}O_2$ and $LiFePO_4$.

II.1.1. Beginnings

The reasons why $LiCoO_2$ is still the most commonly used positive electrode material in presently commercial Li-ion batteries are a high working voltage (3.9 V / Li), a fair specific capacity (140 $mAh.g^{-1}$), an excellent structural stability and a long cycle life (>1000 cycles) [5]. Nonetheless, cobalt is an expensive, toxic metal difficult to recycle and so numerous attempts have been made to come up with a cheaper alternative, which might combine low self-discharge and environmental friendliness.

II.1.2. $LiMO_2$ layered oxides and overlithiated derivatives

Among possible alternatives to $LiCoO_2$, $LiNiO_2$ (isostructural with $LiCoO_2$, **Fig. I-3 left**) has been an early promising positive electrode material, by virtue of its high specific capacity (200 $mAh.g^{-1}$), lower cost and superior elevated-temperature performance. However, a poor capacity retention upon cycling associated to an insufficient thermal stability in the delithiated state (making its use risky) explains why $LiNiO_2$ has not been commercialized successfully [30, 31].

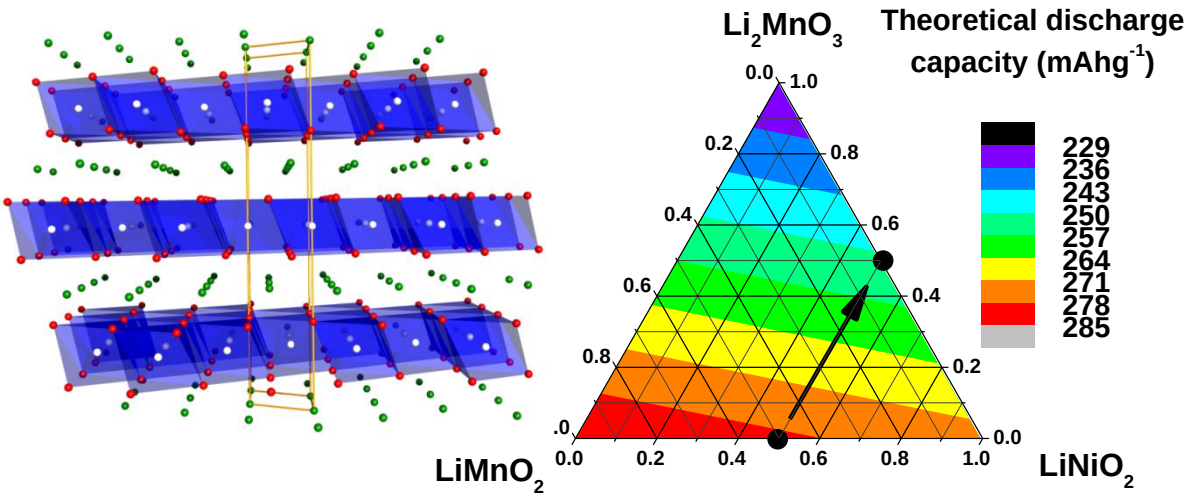

Figure I-3. (left) $NaFeO_2$-type 2D structure displayed by $LiMO_2$ positive electrode materials. (right) Theoretical discharge capacity map of the $LiNiO_2$-$LiMnO_2$-$LiMn_2O_3$ ternary system, highlighting the compositions investigated in this work.

Cationic substitution offers a way to circumvent these problems and today's most popular isostructural cathode materials are the $LiNi_{1/3}Mn_{1/3}Co_{1/3}O_2$ (NMC) [32] and the $LiNi_{0.8}Co_{0.15}Al_{0.05}O_2$ (NCA) in which electrochemically inactive Al^{3+} plays a stabilizing role in the bidimensional structure and reduces the material density [33, 34].

Cationic substitution using excess Li to fill the transition metal layers led to the discovery of higher energy density materials, formed as the single-phased composites between $LiMn_2O_3$ and $LiMO_2$ (M = Ni, Mn, Co). They are promising cathode candidates as they offer much higher practical capacity (>250 $mAh.g^{-1}$) and better safety with much reduced cost [35, 36]. The explanation for the high capacities observed lies in the particularity of this family of materials to undergo an activation process upon the first charge. During the initial charging process, the capacity originates from the oxidation of Ni^{2+} to Ni^{4+} up to 4.4 V. Above this potential, a high voltage plateau region up to 4.8V appears and the high capacities observed have been attributed to an irreversible loss of oxygen from the lattice accompanied by Li removal, referred to as an electrochemical activation step [37, 38]. As a result, the lower theoretical discharge capacity arising from the $LiMn_2O_3$ component (see **Fig I-3 right**) is compensated by a higher utilization rate of the composite material. These Li_2MnO_3-$LiMO_2$ materials usually suffer from poor rate capability [39] but increasingly clever structuration resulting in core-shell nanocomposites of the different lithium metal oxides has overcome this drawback, finally opening the door for their commercialization [40].

In this thesis, we decided to work on the Co-free $LiNiO_2$-$LiMnO_2$-$LiMn_2O_3$ ternary system (see **Fig. I-3, right**) and focused on **$LiNi_{1/2}Mn_{1/2}O_2$**, proposed by Ohzuku and Makimura [41]. They reported reversible capacities as high as 200 $mA.h.g^{-1}$ on the 2.5-4.5 V vs. Li^+/Li^0 potential with excellent capacity retention, although no one else could reproduce such performance with this material. $LiNi_{1/2}Mn_{1/2}O_2$ also exhibits lower thermal runaway, higher thermal stability than $LiCoO_2$ or $LiNiO_2$, and greater inhibition to reaction with electrolytes in the charged state [41, 42]. The study has been extended to overlithiated layered oxides, and the composition **$Li[Li_{0.2}Ni_{0.4}Mn_{0.4}]O_2$**, was selected owing to its position in the $LiNiO_2$-$LiMnO_2$-$LiMn_2O_3$ ternary system making it the Li-richest compound with a Ni/Mn ratio equal to one similarly to $LiNi_{1/2}Mn_{1/2}O_2$. Indeed, although this composition exhibits neither the highest theoretical (**Fig. I-3, right**) nor the highest practical capacity [37], the Li_2O net loss from $Li_{1.2}Ni_{0.4}Mn_{0.4}O_2$ during the initial high potential plateau would result in $Li_{0.8}Ni_{0.4}Mn_{0.4}O_{1.6}$ i.e. our model compound $LiNi_{1/2}Mn_{1/2}O_2$. The differences between the two chosen materials, in terms of interphase chemistry and electrochemical performance, therefore only lie in the initial particular charge process. This work is the subject of chapter 3.

II.1.3. LiM_2O_4 spinel-type oxides

Another early alternative to $LiCoO_2$ was the spinel $LiMn_2O_4$, offering excellent safety and high power capability owing to its 3D lattice. Besides, manganese is a cheap and environmentally benign metal in comparison with cobalt. Nonetheless, stoichiometric $LiMn_2O_4$ cathodes have been ruled out due to their capacity fade, especially at elevated temperatures (>50 °C), principally caused by Mn dissolution into the electrolyte via the disproponation of Mn^{3+} [43]. While $LiMn_2O_4$ exhibits an operating voltage of 4.1 V, its partially Ni-substituted derivatives, $LiNi_{0.5}Mn_{1.5}O_4$ and $LiNi_{0.4}Mn_{1.6}O_4$, work at about 4.7 V [44, 45]. Despite the lack of stability of conventional electrolytes, these "5V spinel" positive electrodes are already under development, usually coupled with an elevated-potential negative electrode such as the $Li_4Ti_5O_{12}$ spinel. The resulting cell voltage of about 3.5 V provides a high energy, high power system, highly promising for EV/HEV applications (see **Fig. I-2**).

II.1.4. $LiFePO_4$ olivine and the craze for polyanionic compounds

Since the pioneering works in the late 90s of Padhi et al. [46, 47] and Ravet et al. [48], $LiMPO_4$ (with M= Fe, Mn, Co, Ni) olivine-type compounds (**Fig. I-4, left**) have been the center of massive scientific attention. Literally, more than a thousand papers on this topic have been published since then.

The virtues of $LiFePO_4$ for Li-ion batteries are its excellent cycle life, the thermal structural stability of the delithiated $FePO_4$ phase and the low cost of its precursor materials. Having succeeded to overcome its low electrical conductivity (~10^{-9} $S.cm^{-1}$ at 298 K) either by carbon coating [48, 49] or by particles downsizing [50-52], the practical capacity of $LiFePO_4$ is now close to the theoretical value of 172 $mAh.g^{-1}$ and recent developments demonstrated the possibility to drastically increase power densities [53]

Driven by the tremendous performance of $LiFePO_4$, isostructural $LiMPO_4$ (with M= Mn, Co, Ni) have been synthesized and characterized in regard to their structural and electrochemical properties. Despite the higher voltage of $LiMnPO_4$ [54], $LiCoPO_4$ [55] and $LiNiPO_4$ [56] (4.1 V, 4.8 V and >5.2 V vs. Li, respectively) few studies report promising results, mainly due to their very low electrical conductivity. If breakthroughs have been recently achieved for $LiMnPO_4$ material by synthesizing carbon-coated nanopowders [57, 58], the working potentials of the cobalt and nickel counterparts represent an additional challenge.

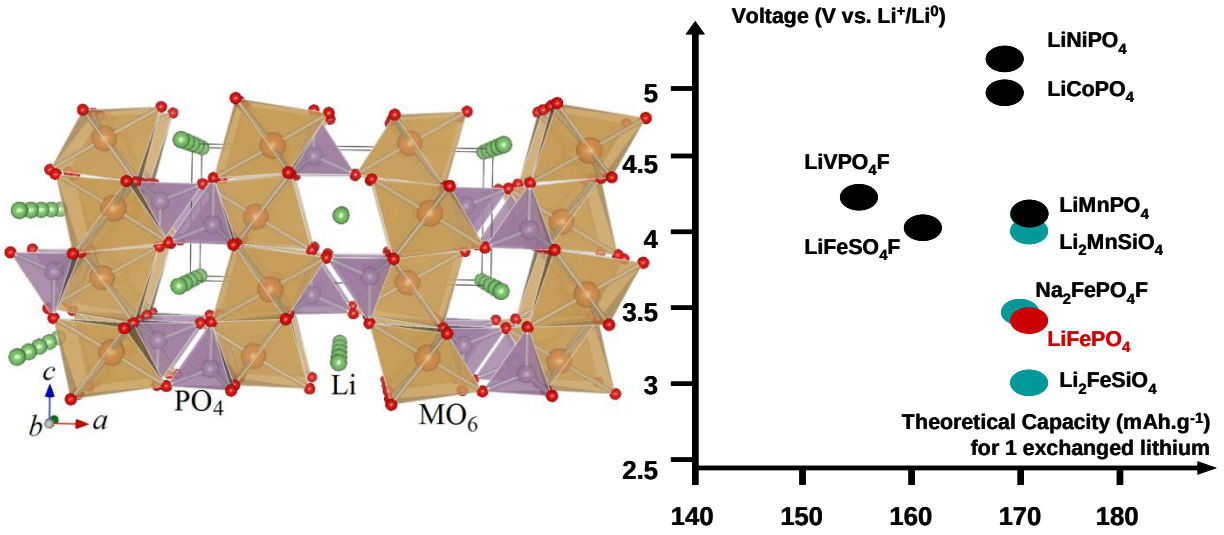

Figure I-4. (Left) $LiFePO_4$ 3D structure, in which Li^+ ions diffuse through 1D channels. (Right) Theoretical specific capacities of various polyanionic compounds. Red point corresponds to $LiFePO_4$, while blue points denote materials theoretically susceptible to exchange more than one electron per formula unit, although not accessible experimentally.

Among other polyanionic materials studied as positive electrode materials (see **Fig. I-4, right**), the most promising candidates are fluorophosphates, notably $LiVPO_4F$ [59] and the A_2MPO_4F type (A = alkali metal, M = transition metal) such as Na_2FePO_4F [60]. Although only one alkali ion can be extracted electrochemically (rather than the two expected for oxidizing M from (+II) to (+IV)), the sodium compounds have proved working well in a Li-ion cell, but could of course also be used in a Na-ion cell.

Li_2MSiO_4 silicates where M^{2+} is a transition metal are now receiving massive interest. Existing under the forms of many polymorphs, they offer a vast area of research [61-64]. However, silicates exhibit lower electronic conductivity [63] and, owing to inductive effect, a lower electrode potential compared to phosphates [65] (as for Li_2FeSiO_4 *vs.* $LiFePO_4$ for instance, see **Fig. I-4, right**). Since the extraction is limited to one Li per formula unit, those drawbacks are not balanced by a significantly higher theoretical capacity.

The low intrinsic ionic and electronic conductivity of all these compounds highlight the importance of particle downsizing and engineering to alleviate these materials drawbacks, similarly to what has been successfully done on $LiFePO_4$.

Insofar as surface reactivity towards air and/or electrolyte contact is necessarily exacerbated by small particle size and might be modified by conductive coating, we propose here to play with **$LiFePO_4$** surface chemistry. This work is the subject of chapter 4 and covers

air-aging, carbon coating, and crystalline orientation as parameters susceptible to influence interphasial and electrochemical behavior.

II.3. Non aqueous electrolytes

II.3.1. Organic solvents

The strong reducing power of lithium and hence its violent reaction with water restricts the choice of electrolytes to non-aqueous solutions. The solvent blend should be thermodynamically and kinetically stable towards electrode materials over a wide potential window, non toxic and cheap but also liquid at the operating temperature. Complete reviews dealing with electrolytes can be found in Ref. [66, 67]. Typically, solvent mixtures of alkyl-carbonates such as propylene carbonate (PC), ethylene carbonate (EC), dimethyl carbonate (DMC), diethyl carbonate (DEC) or ethylmethyl carbonate (EMC) are used. Their chemical formulae are displayed in **Figure I-5**. While PC was found responsible for graphite exfoliation thus preventing any Li^+ intercalation [68], EC-based electrolytes are frequently used for the quality of the passivation layer formed on the negative electrode [69, 70]. However, EC is a solid at room temperature and must therefore be dissolved in another solvent limiting the electrolyte viscosity hence improving conductivity.

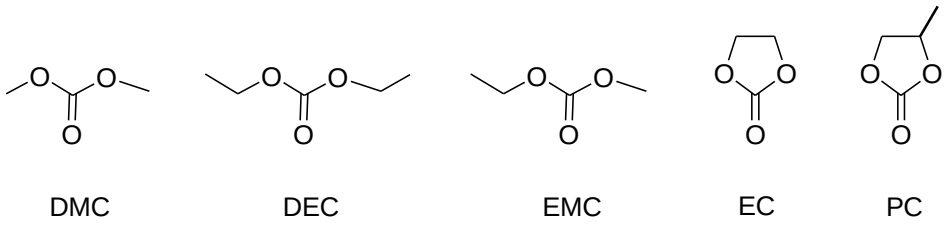

Figure I-5. Chemical formula of carbonates typically used as electrolyte solvents.

II.3.2. Lithium salts

The choice of lithium salts has been the object of numerous tryouts in the literature, the decisive criterion being their reactivity towards the electrode materials and solvents. Other selection criteria comprise their solubility, mobility, thermal stability as well as their reactivity towards passive components of the battery [67].

Lithium hexafluorophosphate ($LiPF_6$) is the commercially dominant salt used in Li-ion batteries [66]. It has good conductivity (10.7 $mS.cm^{-1}$ for a 1M concentration in EC:DMC (1 :1)) [71], and a wide electrochemical stability window. Other historical salt candidates are, for example, lithium perchlorate ($LiClO_4$) but also lithium tetrafluoroborate ($LiBF_4$) and

lithium hexafluoroarsenate ($LiAsF_6$) exhibiting a higher ionic mobility or a higher conductivity compared to $LiPF_6$, respectively. Although $LiPF_6$ decomposes easily, especially at higher temperatures [72, 73], and is moisture sensitive [74, 75], its commercial success relies on a combination of compromises, not met by any other salt.

New alternatives such as lithium trifluoromethanesulfonate ($LiCF_3SO_3$), lithium bis(trifluoromethylsulfonyl)-imide ($LiN(SO_2CF_3)_2$) and lithium bis(oxalate)borate ($LiB(C_2O_4)_2$) are also under serious investigation. $LiCF_3SO_3$ (LiTF) and $LiN(SO_2CF_3)_2$ (LiTFSI) have large anions to minimize ion-pairing and thereby offer enhanced conductivity. Their practical use is however limited due to their corroding the aluminum current collector [76, 77]. $LiB(C_2O_4)_2$ (LiBOB) exhibits a better thermal stability compared to $LiPF_6$ and allows the use of PC with graphite. Its moderate conductivity prevents LiBOB from substituting $LiPF_6$ and therefore rather favors its use as an electrolyte additive [78].

The cycle life being one of the key requirements for a lithium battery, the investigation of its aging along storage or cycling appears of paramount importance. As demonstrated in the upcoming section, electrode/electrolyte interfaces, as the only legitimate places for electrochemical reactions, also happen to host the most important alterations of electrochemical devices. A review of surface phenomena associated to the aging of each component enables to shed light on the major causes of performance degradation.

III- SURFACE PHENOMENA IN A LITHIUM-ION BATTERY: AGING OF THE DIFFERENT COMPONENTS

Since electrolyte solutions are reactive and highly sensitive to the atmospheric components and also to electrode materials, a number of parasitic reactions are susceptible to take place at the interfaces in a Li-ion battery, such as:

- Degradation of the electrolyte, resulting in electrode covering by decomposition products.
- Degradation of active materials.
- Degradation of secondary electrode components (conducting agents, binder, and current collector).

Those mostly unwanted processes significantly influence the lifetime of Li-ion batteries. Some publications are hence focused on aging of the different lithium components [79, 80] and exhaustive reviews can be found in ref [5, 81-83]. This section will therefore only briefly describe some basic interphasial processes responsible for battery failure, based on electrolyte decomposition, and electrode active materials degradation from literature data.

III.1. Electrolyte solutions and their degradation

Li-ion batteries operate in the 3.5-4.0 V vs. Li^+/Li^0 [5], and occasionally even at higher potentials [84]. However, non-aqueous electrolytes are not thermodynamically stable in this extended potential range and electrolyte reduction and oxidation will occur at the negative and positive electrode side, respectively.

III.1.1. Decomposition of carbonate-based electrolytes

The multi-step degradation mechanisms of carbonate-based electrolytes are complex but well documented [85-87]. Possible reduction mechanisms for EC are for instance shown in Eq. I-1. The one-electron reduction leads to the formation of lithium ethylene dicarbonate (LEDC), a so-called semicarbonate, believed to be the key ingredient of the SEI. Other carbonate-based solvents form similar compounds, usually abbreviated to $ROCO_2Li$. Inorganic Li_2CO_3 forms if further reduction occurs.

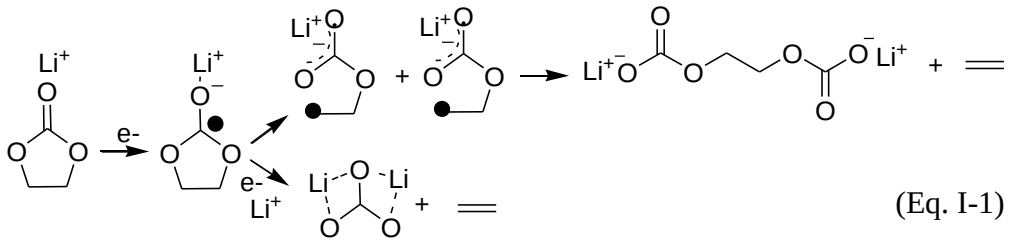

(Eq. I-1)

At room temperature, PF_5 tends to decompose carbonates via the opening of EC ring resulting in the formation of polycarbonates ($-(CH_2CH_2OCO_2)_n-$) and poly(ethylene oxide) ($-(CH_2CH_2O)_n-$), as seen from Eq. I-2 .

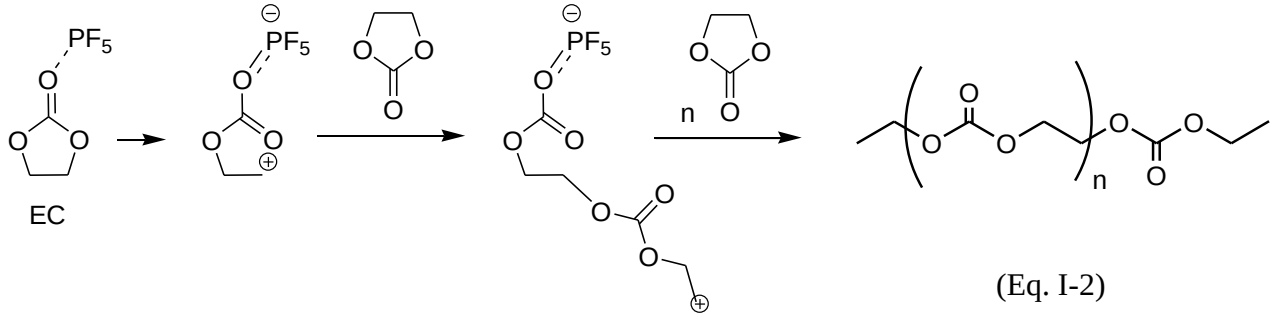

(Eq. I-2)

Regarding oxidative processes, no exhaustive study exists, but based on EC polymerization mechanism, as represented in Eq. I-3, a possible scheme could be [100]:

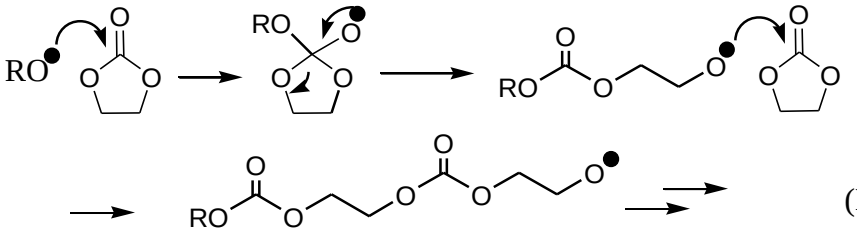

(Eq. I-3)

III.1.2. Role of contaminants

Intrinsic stability of $LiPF_6$, forming LiF and PF_5 [67], leads to several decomposition scenarii as shown here in the case of a reduction process:

$$LiPF_6 + ne^- + nLi^+ \rightarrow LiF\ (s) + Li_xPF_y\ (s) \quad \text{(Eq. I-4)}$$

Most lithium salts are highly hygroscopic. This turns to be highly damaging for the battery in the case of $LiPF_6$, which is readily hydrolyzed to form hydrofluoric acid, HF [75, 88, 89]. The multistep hydrolysis scheme of $LiPF_6$ is represented in Eq. I-5:

$$H_2O + LiPF_6 \rightarrow LiF\ (s) + POF_3 + 2HF \qquad \text{(Eq. I-5a)}$$

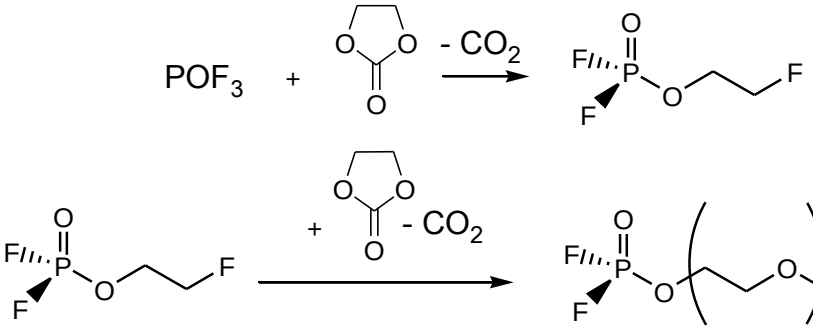

Inevitable moisture impurities can also be reduced electrochemically or, similarly to HF, attack SEI components such as carbonates. Equations displayed below (Eq. I-6) shed light on the predominance of LiF in the interphase, as the degradation product of other interphasial species.

$$H_2O + x\ Li^+ + x\ e^- \rightarrow LiOH/Li_2O\ (s) + H_2\ (g) \qquad \text{(Eq. I-6a)}$$

$$H_2O + ROCO_2Li\ (s) \rightarrow Li_2CO_3\ (s) + CO_2\ (g) + ROH \qquad \text{(Eq. I-6b)}$$

$$HF + ROCO_2Li\ (s) \rightarrow LiF\ (s) + ROCO_2H \qquad \text{(Eq. I-6c)}$$

$$2HF + Li_2CO_3\ (s) \rightarrow 2LiF\ (s) + H_2CO_3 \qquad \text{(Eq. I-6d)}$$

Eq. I- 6. Parasitic reactions driven by moisture impurities in electrolytes containing $LiPF_6$.

The decomposition of $LiPF_6$ 1M in EC :DMC (1:1) after 3 weeks at 85°C actually results in the precipitation of LiF, $Li_xPO_yF_z$,, organic fluorophosphates such as $OPF_2(OCH_2CH_2)_nF$ and OPF_2OMe, and other organic materials (ROLi, $ROCO_2Li$, polycarbonate, PEO, etc) [75].

III.2. Surface chemistry of Li and Li-C negative electrodes, concept of the S.E.I.

The reactions displayed below **Figure I-1** indicate that a Li-ion cell is assembled in the discharge state. The first charge is a crucial step seeing not only the first lithium insertion in the negative electrode but also the formation of a passivation layer on its surface, resulting from electrolyte reduction (see **Fig. I-6, left**). In the case of half-cells, similar process occurs by direct contact of the electrolyte with strongly reducing Li-metal.

The composition of this passivation layer strongly depends on the electrolyte composition, and in the case of $LiPF_6$ 1M in EC :DMC (1:1), several species are reported [90-93]. The $ROCO_2Li$-type solvents reduction products, as explained above, are $(CH_2OCO_2Li)_2$

and CH_3OCO_2Li for EC and DMC respectively [91, 92]. During storage, $LiPF_6$ hydrolysis causes their degradation and the interphasial layer hence ages into a more inorganic deposit composed of LiF, Li_xPF_y and $Li_xPO_yF_z$ detrimental to the negative electrode performance [93]. The explanation lies in the predominance of highly resistive LiF in the interphase, but also partly, in the absence of Li_2CO_3, known to have a protective role thanks to its poor affinity with water compared to the other interfacial species.

The determining role of the products formed or deposited on the negative electrode surface has given rise to the concept of Solid Electrolyte Interphase (SEI), introduced by Peled [94] and illustrated in **Figure I-6 (right)**. This layer is an ionic conductor but an electronic insulator that acts as a barrier to prevent further electrolyte decomposition in the subsequent electrochemical cycles. Although the formation of the SEI consumes lithium atoms and causes an irreversible capacity loss in the first cycle, it stabilizes the negative electrode and leads to fair charge-discharge cycle life.

This explains why the Li-ion chemistry has mostly been dedicated, for the past two decades to the understanding and control of the SEI. As a result, commercial Li-ion batteries usually undergo at least the first discharge/charge cycle, a process called "formation", before being released from the factory.

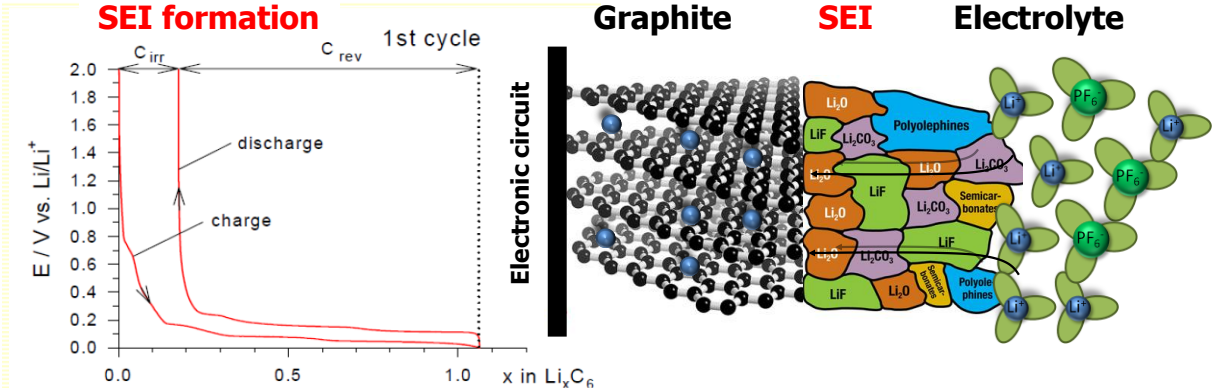

Figure I-6. (Left) Electrochemical signature of first Li insertion and extraction in graphitic carbon. C_{irr} is correlated to irreversible Li-consumption to build the SEI, schematically shown on the right side.

The definition of an efficient interface on the negative electrode side has opened the door for the investigation of positive electrode / electrolyte interface for the past decade. Considering their thickness and inhomogeneity, the term "**interphases**" was also coined to describe 3D interfaces and will here be preferred to "SEI" to describe the ensemble of species

found at the positive electrode / electrolyte interface as their nature and formation mechanism differ slightly from the interfacial layer observed on negatives.

III.3. Surface chemistry of positive electrodes and positive / electrolyte interactions

All positive electrode materials currently explored for Li-ion batteries are also subject to reaction with electrolyte solutions [81, 82, 95, 96]. Because they are the main component of the limiting electrode – in terms of cost, performance and lifetime – cathode materials deserve special attention. Essentially, aging mechanisms to be considered at the positive electrode/electrolyte comprise:

- Surface structure changes of the electrode materials, such as transition metal dissolution (especially in the case of manganates [97-99]) or oxygen release, leading to poisoning of the SEI at the negative electrode and formation of electrochemically inactive phases respectively. Significant literature results are summarized in **Table I-1**.
- Replacement within the interphase of the initial Li_2CO_3 surface layer formed by air contact on $LiMO_2$ cathodes by salt decomposition products, Li-alkyl carbonates and polycarbonates along nucleophilic or oxidative attack of solvent molecules [97, 100, 101].

Materials	**Conclusions**	**Ref.**
$LiCoO_2$	Li and Co dissolution and lattice degradation: formation of Co_3O_4, Li_2O and CoO_2.	102. 103.
$LiMn_2O_4$ $LiMn_{1.5}Ni_{0.5}O_4$	Mn and Ni dissolution and transformation to λ -MnO_2 or Mn_2O_3	83. 104. 105.
$LiNiO_2$ $LiNi_{0.8}Co_{0.2}O_2$ $LiNi_{0.8}Co_{0.15}Al_{0.05}O_2$	Pure Ni: Large and anisotropic volume jumps upon phase transitions → rapid capacity fade. Oxygen release in the electrolyte and migration of Ni and Co ions in the Li layers → disordered cubic NiO-like phase observed in the near surface → power fade	38. 106. 107.
$Li[Ni_{1/5}Li_{1/5}Mn_{3/5}]O_2$	Spinel-like solid phase formed on the surface of the electrode materials after high-voltage cycling → power fade	108.

Table I-1. Examples of structure changes observed on positives electrode materials upon contact with electrolyte or cycling.

Studies have shown that in a graphite-based battery, the interphase on the transition-metal oxide positive electrode tends to grow more quickly than the SEI on the negative upon cycling, and would eventually dominate the cell overall impedance [109, 110]. Both surface

film formation [97] and loss of conductive carbon at the positive electrode surface [111] have been pointed as possible causes of such impedance rise. The range of active materials used as positive electrodes being rather wide, and each of them possessing its own reactivity towards electrolyte, the characterization of positive electrode/electrolyte interphases is a vast area of research.

Several concepts, such the SEI+PEI (polymer electrolyte interphase) [112] or SPI (solid permeable organic/inorganic interface) [113] have been proposed (see Appendix 1, **Figure AI-3**), as well as formation mechanisms for polymeric species (polycarbonates, esters and alkyl carbonates) and inorganic decomposition products. The different parameters investigated comprise the duration of contact between positive electrode materials and electrolyte, electrochemical cycling, storage potential or state of charge (SOC), temperature and electrolyte composition. The influence of these different parameters varies with the material studied but generally induces a chemical or morphological modification of the interphase, as summarized in **Tables I-2** and **I-3**.

A number of general comments can be drawn from this literature review regarding surface phenomena on positive electrode materials. Oxides ($LiCoO_2$, $LiNiO_2$, $LiMn_2O_4$) usually exhibit a pristine interphase made of lithium carbonate which readily forms upon air exposure. While $LiFePO_4$ olivine seems to be kept intact, Li_2FeSiO_4 is also covered by Li_2CO_3. Upon contact with electrolyte, interphasial reactions remarkably depend on the material/electrolyte couple. Upon cycling in a $LiPF_6$-based electrolyte, most positive electrodes are covered by highly resistive LiF, Li_xPF_y or $Li_xPO_yF_z$ fluorophosphates but also organic and polymeric species arising from the decomposition of carbonate-based solvents above 4.5 V. Monitoring the voltage dependency of surface phenomena, several studies insist on the "dynamics" of the interphase, Li^+ "trapped" in the interphase being more or less mobile depending on the chemical species. Bulk electrochemical performance seem strongly correlated to the interphase observed, this latter being directly governed by parameters such as the temperature or presence of moisture impurities. If the deposition of electrolyte decomposition products is the major interphasial process, the dissolution of active materials ($LiFePO_4$, $LiMn_2O_4$) in electrolyte has been highlighted and certainly plays a role on the interphasial reactions. Examples making use of additives, reported in **Table I-3**, also shed light on the possibility to tailor these reactions.

Parameters	**Materials & Electrolytes**	**Conclusions**	**Ref.**
Air exposure	$LiCoO_2$, $LiNiO_2$, $LiNi_{0.8}Co_{0.2}O_2$, $LiMn_2O_4$	Pristine Li_2CO_3 formed by air contact.	95. 100. 114.
Contact with electrolyte	$LiCoO_2$, $LiMn_2O_4$, $LiMn_{1.5}Ni_{0.5}O_4$ $LiNi_{0.5}Mn_{0.5}O_2$ vs. $LiPF_6$	Film (mainly composed of LiF) is formed upon contact with electrolyte. Highly stable passivating surface film formation that protects the material from detrimental reactions with solution species. If nanosized, superficial deactivation of material due to this SEI.	115. 116. 96.
Cycling	$LiCoO_2$ vs. EC/DMC/$LiPF_6$	LiF content increases during charge and decrease during discharge (deposition/dissolution process). Formation of a several nm thick layer. Gas generation (CH_4, C_2H_6, C_2H_4, CO, CO_2, O_2) Cycling promotes the growth of the layer	95. 117. 102. 103. 115.
	$LiFePO_4$ vs. EC/DEC with $LiPF_6$	The surface film is composed of salt-based products: LiF, $LiPF_6$, Li_xPF_y and $Li_xPO_yF_z$. The film is thin or heterogeneously formed and does not limit the cell performances.	83. 118.
	$LiNi_{1-x}Co_xO_2$ vs. EC/EMC with $LiPF_6$	The film is mainly formed through two voltage regions, from OCV to 3.6 V, during which active materials and solvents react to form a highly resistive film, and between 3.6 and 3.7 V, during which a highly conductive film is developed. SEI film remains nearly invariant between 3.8 and 4.3 V, however, its conductivity falls significantly as the voltage decreases below 3.4 V.	119.
Storage potential / SOC	$LiMn_2O_4$ vs. EC/DEC with $LiPF_6$ or $LiBF_4$	Products formed on the electrodes are not governed by electrochemical cycling but they do depend on storage potential.	83. 104. 113.
	$LiCoO_2$ vs. EC/PC/DEC /$LiPF_6$	The resistance of the film on the positive electrode decreases with increasing SOC and reaches a maximum when fully discharged.	120.
	$LiNi_{0.8}Co_{0.2}O_2$ vs. EC/DEC with $LiPF_6$	No changes observed with time or SOC.	83. 101. 121.
Temperature	$LiNi_{0.8}Co_{0.2}O_2$ vs. EC/DEC with $LiPF_6$	LiF is the main product, but decomposition products as Li_xPF_y and $Li_xPF_yO_z$ can also be identified Temperature affects organic/inorganic content ratio.	83. 101. 121.
	$LiMn_2O_4$ vs. EC/DEC or DMC with $LiPF_6$ or $LiBF_4$	Insulating layer formed at room temperature: LiF, Li_xPF_y (or Li_xBF_y) and poly(oxyethylene). At 60°C: LiF, $Li_xPF_yO_z$ (or $Li_xBO_yF_z$), phosphorous oxide (or boron oxides), poly(oxyethylen) and polycarbonate. Temperature promotes film formation	83. 122. 117. 104.

Table I-2. Examples of the impact of physical parameters on the interphase observed on positives electrode materials.

Electrolytes	**Materials**	**Conclusions**	**Ref.**
PC/$LiClO_4$ and EC/DMC/$LiPF_6$	$LiNi_{0.8}Co_{0.2}O_2$	Different (Cl–O)-containing species and $ROCO_2Li$ compounds for $LiClO_4$ electrolyte and (P–O)- and (P–F)-containing species as well as $Li_xPO_yF_z$ compounds and LiF for $LiPF_6$ electrolyte.	95. 112.
EC/DEC with $LiPF_6$ or $LiBF_4$	$LiNi_{0.5}Mn_{1.5}O_4$	Interphase composed of inorganic species such as LiF and $Li_xPF_yO_z$ or $Li_xBF_yO_z$ as well as organic species such as polyethers and carbonates. At 60°C, $LiPF_6$ yields more organic species and less LiF at the surface than $LiBF_4$.	123.
EC/DMC with $LiClO_4$ or $LiPF_6$ (clean or water contaminated)	$LiFePO_4$	The acidic effect of electrolyte (presence of HF with $LiPF_6$) leads to a decreasing of the performances demonstrated by an increasing of electrode resistance upon storage. The Fe dissolution is also proven in these cases. Carbon coating promotes better stability.	124.
EC/DMC with $LiPF_6$, $LiAsF_6$ and $LiC(SO_2CF_3)$	$LiMn_2O_4$ $LiNiO_2$	The charge transfer resistance of the $LiNiO_2$ electrodes is much higher than that of the $LiMn_2O_4$ electrodes. The impact of the salt used is also more pronounced with the $LiNiO_2$ electrodes than with the $LiMn_2O_4$ electrodes. The electrode resistance is the highest in the $LiPF_6$ solution, and the lowest in the $LiAsF_6$ solution. Storage in electrolyte increases dramatically film and charge transfer resistances for $LiNiO_2$ due to massive formation of highly resistive LiF.	100. 125.
EC/DEC/DMC with $LiPF_6$ **+VC**	$LiCoO_2$ $LiFePO_4$	VC polymerization mechanism is observed at the surface of $LiCoO_2$ but not on $LiFePO_4$.	126.
EC/DEC/DMC with $LiPF_6$ **+DMAc**	$LiCoO_2$, $LiNi_{0.8}Co_{0.2}O_2$, $LiMn_2O_4$ and $LiFePO_4$	Addition of DMAc increases the thermal stability of the electrolyte and reduces both surface corrosion and deposition of electrolyte decomposition products on cathode particles.	127.
EC/DEC with $LiPF_6$ + **LiBOB**	$LiNi_{0.8}Co_{0.15}$ $-Al_{0.05}O_2$	Addition of 2 wt% of LiBOB results in better cycling stability and higher power capability than standard $LiPF_6$.	78.

Table I-3. Examples of the impact of electrolytes salts, solvents and/or additives on the interphase observed on positives electrode materials.

III.4. Electrode / Electrolyte Interface Studies in Lithium Batteries Using NMR

NMR can be used to detect hydrogen, lithium, carbon, fluorine and phosphorus amongst others. It appears as an appropriate method to study species present on the surface of electrode materials, resulting from electrolyte decomposition. This thesis making extensively use of solid state NMR, this chapter inevitably includes a review of the NMR approach developed to probe evolution of electrochemical behavior and/or failure mechanisms along

electrochemical cycling of lithium batteries. A corresponding review article has been published in *Interfaces*. It can be found at the very end of this introductive chapter. The interest of NMR lies above all in its intrinsically quantitative response, which allows the systematic investigation of the interphase evolution of a given electrode material while varying parameters impacting its surface chemistry.

III.5. Interfacial phenomena in lithium-ion batteries: challenges and perspectives

As we move to the next generation of either positive electrodes working at higher voltages (5 V) or non-insertion (e.g., Li-alloying or conversion) negative electrodes making use of nanomaterials, novel strategies to match these materials with today's electrolytes will have to be found.

Regarding alloys materials, the main issue consists in the important volume expansion (200%-300%) associated with the lithiation of Si or Sn based negative electrode materials, along which alloy surfaces are renewed at each cycle. Additional electrolyte reduction and SEI formation repeatedly take place to passivate those newly exposed surfaces. This phenomenon, together with particles decrepitation along volume variations results in the loss of active material particles. Although the interphase breakdown mechanisms on these alloy electrodes are not completely elucidated yet, it is clear that these negative electrodes interphases should be tailored to withstand major mechanical stress. Thus, one of the paths towards the successful use of Si or other alloys and conversion materials as Li ion battery negative electrode would be to develop unique surface chemistry and/or dedicated morphology so that the SEI formed thereon can accommodate such stress [128-130].

Regarding positive electrode materials, it should be reminded that carbonate-based electrolytes cannot be stabilized beyond the 4.5 V limit vs. Li^+/Li^0, constituting a severe challenge to the development of new generation of Li-ion positive electrodes like the spinel $LiMn_{1.5}Ni_{0.5}O_4$ or the layered $Li_{1+x}(Mn,Ni)_{1-x}O_2$ that aim at delivering energy at higher voltages, in the neighborhood of 5.0 V. Electrolytes with improved tolerance to higher potential of electrolytes might be achieved either with new solvents (sulfones [131, 132] or nitriles [133] seem promising alternatives to carbonates in this regard) or with additives with redox properties tailored for 5V applications [134, 135]. The trace presence (<5%) of those additives in electrolytes is expected to result in their complete consumption during the

interphases forming cycle, virtually leaving no impact on the bulk properties of the electrolytes such as cost or viscosity [136]. The use of electrolyte additives is therefore one of the most economic and effective methods for the tailoring of interphases in a Li-ion battery. According to the functions they fulfill, electrolyte additives can be divided into the following main categories: SEI forming improver, cathode protection agent, and/or $LiPF_6$ salt stabilizer. Their number being virtually infinite, listing the virtues of electrolyte additives would be beyond the scope of this introduction chapter, but a recommended review can be found in Ref [136].

With increasing knowledge about the interphasial chemistry, there were also attempts to form interphases artificially with known chemicals that are structurally close to semi-carbonates, either during electrode processing [137] or afterwards via the deposition of a surface coating [138]. The appeal of such approach consists in the minimization of irreversible capacity during the otherwise *in situ* Li-consuming SEI formation. Surface modifications such as coating of surface metal oxide cathode materials with $AlPO_4$ [139], ZnO [140], MgO, ZrO_2, Bi_2O_3 [141] or Al_2O_3 [142], have also been reported to provide a stable interface between the electrolyte and the active material and much improved electrochemical performance compared to bare positive electrodes. Those coatings should not be seen just as a resistive barrier controlling lithium diffusion; but must also govern the electrolyte degradation chemistry. The interphase thus existing between the active material and electrolyte, would consist in a multilayered composite; made of an inorganic inner part and a “SEI-like” hybrid outer ideally more stable and thinner than the original one.

Both strategies to tailor the positive electrode / electrolyte interphase chemistry, namely the use of additive and surface coating, are followed in this thesis in the case of $LiMn_{1/2}Ni_{1/2}O_2$. Their impact on electrochemical performance compared to standard electrolyte and bare positive electrodes have already been evaluated, although often solely in terms of capacity retention over extended cycling. Our aim is not to reproduce such studies, but rather to monitor the modifications induced at the interphase level with the help of dedicated analytical techniques in order to optimize these treatments more efficiently than on a trial and error basis.

IV- CONCLUSION

In the present chapter, after describing the different components of a lithium battery and their physical / chemical properties, we set out to introduce the interphasial processes occurring in a Li-ion battery and demonstrate their complexity. Indeed, the aging of electrodes and electrolyte are often interdependent and although abundant literature describe the isolated surface evolution of one of the electrode upon storage and cycling, rare are the studies correlating the electrode surface evolution to the overall electrochemical performance. However, spectroscopic results collected from these numerous reports surely provide an excellent database, which will be exploited in the following chapters.

On the contrary, studies reporting long term cyclability or the impact of storage on the performance of full cells are often suggestive of a black box, limiting the description of battery failure modes to impedance increase and/or capacity loss as a result of one physico-chemical parameter or another. Thus, the approach chosen in the present work will rather consist in trying to analyze prioritarily the impact of such external parameters on the positive electrode / electrolyte interphase in terms of quantity and chemistry of the formed species, before correlating the interphasial behavior to electrochemical performance.

Actually, surface modification constitutes a major trend in lithium batteries chemistry, and we expect here to understand more openly the impact of surface chemistry on the subsequent interphasial processes and to establish correlations with the overall battery performance, when possible.

Correlating the electrode surface evolution and the electrochemical performance is necessarily based both on an accurate knowledge of the chemistry of the battery components and the possible parasitic reactions occurring at their respective interfaces. Only such an overview allows pointing out particular interphasial behaviors and subsequently developing specific analytical tools to unravel these issues that are no less specific.

REFERENCES OF CHAPTER 1

[1] M. S. Whittingham *Chem. Rev*., **104** (2004) 4271.

[2] J.R. Dahn, A.K. Sleigh, H. Shi, B.M. Way, W.J. Weydanz, J.N. Reimers, Q. Zhong, U. von Sacken, *Lithium Batteries-New materials, developments and perspectives*, Ed. G. Pistoia, Elsevier, Amsterdam (1994).

[3] R. Yazami, P. Touzain, *J. Power Sources*, **9** (1983) 365.

[4]. J.R. Dahn, U. von Sacken, M.W. Juzkow, H. Al-Janaby, *J. Electrochem. Soc*., **138** (1991) 2207.

[5] M. Winter, J.O. Besenhard, M.E. Spahr, P. Novák, *Adv. Materials*, **10** (1998) 725.

[6] M.M. Thackeray, J.T. Vaughey, L.M.L. Fransson, *J. Met.*, **54** (2002) 20.

[7] D. Larcher, S. Beattie, M. Morcrette, K. Edström, J.C. Jumas, J.M. Tarascon, *J. Mater. Chem.*, **17** (2007) 3759.

[8] M. Winter, J.O. Besenhard, *Electrochim. Acta*, **45** (1999) 31.

[9] R. Benedek, M.M. Thackeray, *J. Power Sources*, **110** (2002) 406.

[10] J. Yang, M. Wachtler, M. Winter, J.O. Besenhard, *Electrochem. Solid-State Lett*., **2** (1999) 161.

[11] Y. Miyaki, US Patent, Patent No: US 6,908,709 B2 (2005).

[12] J. Li, R.B. Lewis, J.R. Dahn, *Electrochem. Solid-State Lett*., **10** (2007) A17.

[13] B. Lestriez, S. Bahri, I. Sandu, L. Roue, D. Guyomard, *Electrochem. Comm*., **9** (2007) 2801.

[14] J. Cabana, L. Monconduit, D. Larcher, M. R. Palacín, *Advanced Materials*, **22(35)** (2010) E170.

[15] F. Gillot, S. Boyanov, L. Dupont, M-L. Doublet, M. Morcrette, L. Monconduit , J-M. Tarascon, *Chem. Mat.*, **17(25)** (2005) 6327.

[16] F. Gillot, L. Monconduit, M. Morcrette, M-L. Doublet, J-M. Tarascon, *Chem. Mat*., **17** (2005) 3627.

[17] C. Villevieille, C.-M. Ionica-Bousquet, B. Ducourant, J-C. Jumas, L. Monconduit, *J. Power Sources*, **172(1)** (2007) 388.

[18] S. Boyanov, J. Bernardi, F. Gillot, L. Dupont, M. Womes, J-M. Tarascon, L. Monconduit, M.-L. Doublet, *Chem. Mat.*, **18** (2006) 3531.

[19] C. Villevieille, B. Fraisse, M. Womes, J-C. Jumas, L. Monconduit, *J. Power Sources*, **189** (2009) 324.

[20] S. Boyanov, J. Bernardi, E. Bekaert, M. Menetrier, M-L. Doublet, L. Monconduit, *Chem. Mater.*, **21(2)** (2009) 298.

[21] K. Zaghib, M. Armand, M. Gauthier, *J. Electrochem. Soc.*, **145** (1998) 3135.

[22] L. Kavan, M. Gratzel, *Electrochem. Solid State Lett.*, **5** (2002) A39.

[23] P.P. Prosini, R. Mancini, L. Petrucci, V. Contini, P. Villano, *Solid State Ionics*, **144** (2001) 185.

[24] C.M. Julien, M. Massot, K. Zaghib, *J. Power Sources*, **136** (2004) 72.

[25] C.M. Shen, X.G. Zhang, Y.K. Zhou, H.L. Li, *Mater. Chem. Phys.*, **78** (2002) 437.

[26] T. Ohzuku, A. Ueda, N. Yamamoto, *J. Electrochem. Soc.*, **142** (1995) 1431.

[27] C.H. Chen, J.T. Vaughey, A.N. Jansen, D.W. Dees, A.J. Kahaian, T. Goacher, M.M. Thackeray, *J. Electrochem. Soc.*, **148** (2001) A102.

[28] S.H. Huang, Z.Y. Wen, J.C. Zhang, X.L. Yang, *Electrochim. Acta*, **52** (2007) 3704.

[29] G.J. Wang, J. Gao, L.J. Fu, N.H. Zhao, Y.P. Wu, T. Takamura, *J. Power Sources*, **174** (2007) 1109.

[30] T. Ohzuku, A. Ueda, M. Ngayama, *J. Electrochem. Soc*., **140** (1993) 1862.

[31] T. Ohzuku, T. Yanagawa, M. Kougushi, A. Ueda, *J. Power Sources*, **68** (1997) 131.

[32] K. M. Shaju, G.V. Subba Rao, B.V.R. Chowdari, *Electrochim. Acta*, **48** (2002) 145.

[33] S. Madhavi, G.V. Subba Rao, B.V.R. Chowdari, S.F.Y. Li, *J. Power Sources,* **93** (2001) 156.

[34] A. M. Kannan, A. Manthiram, *J. Electrochem. Soc*., **150** (2003) A349.

[35] Z. Lu, D.D. MacNeil, J. R. Dahn, *Electrochem. Solid-State Lett.*, **4** (2001) A191.

[36] C.P. Grey, W.S. Yoon, J. Reed, G. Ceder, *Electrochem. Solid State Lett*., **7** (2004) A290.

[37] M.M. Thackeray, S-H. Kang, C. S. Johnson, J. T. Vaughey, R. Benedek, S.A. Hackney, *J. Mater. Chem.*, **17** (2007) 3112.

[38] A.R. Armstrong, M. Holzapfel, P. Novak, C.S. Johnson, S-H. Kang, M.M. Thackeray, P.G. Bruce, *J. Am. Chem. Soc.*, **128** (2006) 8694.

[39] J. Jiang, K. W. Eberman, L. J. Krause, and J. R. Dahn, *J. Electrochem. Soc.*, **152** (2005) A1879.

[40] Y. K. Sun, S. T. Myung, B. C. Park, J. Prakash, I. Belharouak, K. Amine, *Nat. Mater.*, **8** (2009) 320.

[41] T. Ohzuku and Y. Makimura, *Chem. Lett*., **30** (2001) 744.

[42] F. Zhou, X.M Zhao, Z.H. Lu, J.W. Jiang, J.R. Dahn, *Electrochem. Solid-State Lett*., **11** (2008) A155.

[43] F. Jiao, J.L. Bao, A.H. Hill, P.G. Bruce, *Angew. Chem*., *Int. Ed.*, **47** (2008) 9711.

[44] G. Amatucci, J-M. Tarascon, *J. Electrochem. Soc.*, **149** (2002) K31.

[45] J-M. Tarascon, D. Guyomard, *Electrochim. Acta*, **38** (1993) 1221.

[46] A.K. Padhi, K.S. Nanjundaswamy, J.B. Goodenough, *J. Electrochem. Soc.*, **144** (1997) 1188.

[47] J.B. Goodenough, A. Padhi, K.S. Nanjundaswamy, C. Masquelier, World Patent WO9740541 (1997).

[48] M. Armand, M. Gauthier, J-F. Magnan, N. Ravet, World Patent WO 02/27823 A1 (2002).

[49] R. Dominko, M. Gaberscek, J. Drofenik, M. Bele, S. Pejovnik, *Electrochem. Solid State Lett.*, **4** (2001) A187.

[50] A. Yamada, S.C. Chung, K.J. Hinokuna, *J. Electrochem. Soc.*, **148** (2001) A224.

[51] C. Delacourt, P. Poizot, S. Levasseur, C. Masquelier, *Electrochem. Solid State Lett.*, **9(7)** (2006) A352.

[52] N. Meetong, H. Huang, S. Speakman, W.C. Carter, Y.M. Chiang, *Adv. Funct. Mater.*, **17** (2007) 1115.

[53] B. Kang, G. Ceder, *Nature*, **458** (2009) 190.

[54] A.K. Padhi, K.S. Nanjundaswamy, J.B. Goodenough, *J. Electrochem. Soc.* **144** (1997) 1188.

[55] K. Amine, H. Yasuda, M. Yamachi, *Electrochem. Solid-State Lett.*, **3** (2000) 178.

[56] J. Wolfenstine, J. Allen, *J. Power Sources*, **142** (2005) 389.

[57] D. Wang, H. Buqa, M. Crouzet, G. Deghenghi, T. Drezen, I. Exnar, N-H. Kwon, J.H. Miners, L. Poletto, M. Gratzel, *J. Power Sources*, **189** (2009) 624.

[58] Z. Bakenov, I. Taniguchi, *Electrochem. Comm.*, **12** (2010) 75.

[59] J. Barker, M.Y .Saidi, J.L. Swoyer, *J. Electrochem. Soc.*, **150** (2003) A1394.

[60] B.L. Ellis, W.R.M. Makahnouk, Y. Makimura, K. Toghill, L.F. Nazar, *Nat. Mater.*, **6** (2007) 749.

[61] A. Nyten, S. Kamali, L. Haggstrom, T. Gustafsson, J.O. Thomas, *J. Mater. Chem.*, **16** (2006) 2266.

[62] K. Zaghib, A.A. Salah, N. Ravet, A. Mauger, F. Gendron, C.M. Julien, *J. Power Sources*, **160** (2006) 1381.

[63] A. Kokalj, R. Dominko, G. Mali, A. Meden, M. Gaberscek, J. Jamnik, *Chem. Mater.*, **19** (2007) 3633.

[64] C. Lyness, B. Delobel, A.R. Armstrong, P.G. Bruce, *Chem. Comm.*, **46** (2007) 4890.

[65] M.E. Arroyo, M. Armand, J-M. Tarascon, U. Amador, *Electrochem. Comm.*, **8** (2006) 1292.

[66] G.E. Blomgren, *J. Power Sources*, **81–82** (1999) 112.

[67] D. Aurbach, Nonaqueous Electrochemistry, Marcel Dekker, Inc., New York (1999)

[68] A.N. Dey, B.P. Sullivan, *J. Electrochem. Soc.*, **117** (1970) 222.

[69] G. Pistoia, M. de Rossi, B. Scrosati, *J. Electrochem. Soc*., **117** (1970) 500-502.

[70] J.O. Besenhard, M. Winter, J. Yang, W. Biberacher, *J. Power Sources*, **54** (1995) 228.

[71] M. Schmidt, U. Heider, A. Kuehner, R. Oesten, M. Jungnitz, N. Ignatev, P. Sartori, *J. Power Sources*, **97-98** (2001) 557.

[72] K. Nagayama, K. Kamioka, E. Iwata, H. Oka, Y. Tokunaga, T. Okada, *Electrochem. Comm.*, **69** (2001) 6.

[73] X. Zhang, P.N. Ross, R. Kostecki, F. Kong, S. Sloop, J.B. Kerr, K. Striebel, E.J. Cairns, F. McLarnon, *J. Electrochem. Soc*., **148** (2001) A463.

[74] T. Kawamura, S. Okada, J.I. Yamaki, *J. Power Sources*, **156** (2006) 547.

[75] B. Ravdel, K.M. Abraham, R. Gitzendanner, J. DiCarlo, B. Lucht, C. Campion, *J. Power Sources*, **119-121** (2003) 805.

[76] L.J. Krause, W. Lamanna, J. Summerfield, M. Engle, G. Korba, R. Loch, *J. Power Sources*, **68** (1997) 320.

[77] K. Naoi, M. Mori, Y. Narupka, W.M. Lamanna, R. Atanasoski, *J. Electrochem. Soc*., **146** (1999) 462.

[78] C. Taubert, M. Fleischhammer, M. Wohlfahrt-Mehrens, U. Wietelmann, T. Buhrmester, *J.Electrochem.Soc.*,**157** (2010) A721.

[79] P. Arora, R.E. White, M. Doyle, *J. Electrochem. Soc.*, **145** (1998) 3647.

[80] M. Broussely, S. Herreyre, P. Biensan, P. Kasztejna, K. Nechev, R.J. Staniewicz, *J. Power Sources*, **97–98** (2001) 13.

[81] B. Markovsky, A. Rodkin, Y.S. Cohen, O. Palchik, E. Levi, D. Aurbach, H.J. Kim, M. Schmidt, *J. Power Sources*, **119** (2003) 504.

[82] J. Vetter, P. Novak, M.R. Wagner, C. Veit, K-C. Möller, J.O. Besenhard , M. Winter, M. Wohlfahrt-Mehrens, C. Vogler, A. Hammouche, *J. Power Sources*, **147** (2005) 269.

[83] K. Edström, T. Gustafsson, J.O. Thomas, *Electrochim. Acta*, **50** (2004) 397.

[84] Q. Zhong, A. Bonakdarpour, M. Zhang, Y. Gao, J.R. Dahn, *J. Electrochem. Soc.*, **144** (1997) 205.

[85] S.E. Sloop, J.B. Kerr, K. Kinoshita, *J. Power Sources*, **119-121** (2003) 330.

[86] Q. Wang, J. Sun, X. Yao, C. Chen, *Thermochim. Acta*, **12** (2005) 437.

[87] G. Gachot, *J. Power Sources*, **178** (2008) 409.

[88] T. Kawamura, S. Okada, J.I. Yamaki, *J. Power Sources*, **156** (2006) 547.

[89] H. Yang, G.V. Zhuang, P.N. Ross Jr, *J. Power Sources*, **161** (2006) 573.

[90] D. Aurbach, B. Markovsky, A. Shechter, Y. Ein-Eli, H. Cohen, *J. Electrochem. Soc.*, **143** (1996) 3809.

[91] D. Aurbach, M.L. Daroux, P.W. Faguy, E. Yeager, *J. Electrochem. Soc.*, **134** (1987) 1611.

[92] D. Aurbach, Y. Ein-Ely, A. Zaban, *J. Electrochem. Soc.*, **141** (1994) L1.

[93] D. Aurbach, A. Zaban, Y. Gofer, Y. E. Ely, I. Weissman, O. Chusid, O. Abramson, *J. Power Sources,* **54** (1995) 76.

[94] E. Peled, *J. Electrochem. Soc.*, **126** (1979) 2047.

[95] D. Aurbach, B. Markovsky, M.D. Levi, E. Levi, A. Schechter, M. Moshkovich, Y. Cohen, *J. Power Sources*, **81–82** (1999) 95.

[96] D. Aurbach, B. Markovsky, G. Salitra, E. Markevich, Y. Talyossef, M. Koltypin, L. Nazar, B. Ellis, D. Kovacheva, *J. Power Sources*, **165** (2007) 491.

[97] D. Aurbach, B. Markovsky, A. Rodkin, E. Levi, Y.S. Cohen, H-J. Kim, M. Schmidt, *Electrochim. Acta*, **47** (2002) 4291.

[98] G. Pistoia, A. Antonini, R. Rosati, D. Zane, *Electrochim. Acta*, **41** (1996) 2683.

[99] D.H. Jang, Y.J. Shin, S.M. Oh, *J. Electrochem. Soc.*, **143** (1996) 2204.

[100] D. Aurbach, K. Gamolsky, B. Markovsky, G. Salitra, Y. Gofer, U. Heider, R. Oesten, M. Schmidt, *J. Electrochem. Soc.*, **147** (2000) 1322.

[101] A.M. Andersson, D.P Abraham, R. Haasch, S. MacLaren, J. Liu, K. Amine, *J. Electrochem. Soc.*, **149** (2002) A1358.

[102] N. Liu, H. Li, Z. Wang, X. Huang, L. Chen, *Electrochem. Solid-State Lett.*, **9** (2006) A328.

[103] E. Markevich, G. Salitra, D. Aurbach, *Electrochem. Comm.*, **7** (2005) 1298.

[104] T. Eriksson, A.M. Andersson, C. Gejke, T. Gustafsson, J.O. Thomas, *Langmuir*, **18** (2002) 3609.

[105] D. Aurbach , B. Markovsky, Y. Talyossef, G. Salitra, H.J. Kim, S. Choi, *J. Power Sources*, **162** (2006) 780.

[106] B.P. Abraham, R.D. Twesten, M. Balasubramanian, I. Petrov, J. McBreen, K. Amine, *Electrochem. Comm.*, **4** (2002) 620.

[107] D. Mori, H. Kobayashi, M. Shikano, H. Nitani, H. Kageyama, S. Koike, H. Sakaebe, K. Tatsumi, *J. Power Sources*, **189** (2009) 676.

[108] B. Xu, C.R. Fell, C. Miaofang, S.M. Ying, Submitted to Journal of the American Chemical Society

[109] C.H. Chen, J. Liu, K. Amine, *J. Power Sources*, **96** (2001) 321.

[110] J. Shim, K.A. Striebel, *J. Power Sources*, **119-121** (2003) 934.

[111] J. Shim, R. Kostecki, T. Richardson, X. Song, K.A. Striebel, *J. Power Sources*, **112** (2002) 3609.

[112] D. Ostrovskii, F. Ronci, B. Scrosati, P. Jacobsson, *J. Power Sources*, **103** (2001) 10.

[113] T. Eriksson, *Comprehensive Summaries **651**, Faculty of Science and Technology*, Uppsala.

[114] H. S. Liu, Z. R. Zhang, Z. L. Gong, Y. Yang, *Electrochem. Solid-State Letters*, **7(7)** (2004) A190.

[115] S. Leroy, *Etude d'interfaces électrode/électrolyte dans les batteries au lithium. Approche par XPS et AFM*, PhD thesis from the University of Pau (2006).

[116] S.S. Zhang, K. Xu, T.R. Jow, *J. Electrochem. Soc.*, **149** (2002) A1521.

[117] Z. Wang, X. Huang, L. Chen, *J. Electrochem. Soc.*, **151** (2004) A1641.

[118] M. Herstedt, M. Stjerndahl, A. Nyten, T. Gustafsson, H. Rensmo, H. Siegbahn, N. Ravet, M. Armand, J.O. Thomas, K. Edström, *Electrochem. Solid-State Lett.*, **6** (2003) A202.

[119] S.S. Zhang, K. Xu, T.R. Jow, *Electrochem. Solid-State Lett.*, **5** (2002) A92.

[120] M.S. Wu, P.C.J. Chiang, J.C. Lin, *J. Electrochem. Soc.*, **152** (2005) A47.

[121] Anna Andersson, *Comprehensive Summaries **656**, Faculty of Science and Technology*, Uppsala.

[122] J. Liu, A. Manthiram, *J. Electrochem. Soc.*, **156** (2009) A66.

[123] H. Duncan, D. Duguay, Y. Abu-Lebdeh, I.J. Davidson, *J. Electrochem. Soc.*, **158(5)** (2011) A537.

[124] M. Koltypin, D. Aurbach, L. Nazar, B. Ellis, *J. Power Sources*, **174** (2007) 1241.

[125] D. Aurbach, *J. Power Sources*, **89** (2000) 206.

[126] L. El Ouatani, R. Dedryvère, C. Siret, P. Biensan, D. Gonbeau, *J. Electrochem. Soc.*, **156(6)** (2009) A468.

[127] W. Li, B.L. Lucht, *J. Power Sources*, **168** (2007) 258.

[128] U. Kasavajjula, C. Wang, J. Appleby, *J. Power Sources*, **163** (2007) 1003.

[129] W. Zhang, *J. Power Sources*, **196** (2011) 196.

[130] N. Choi, K. Yew, K. Lee, M. Sung, H. Kim, S. Kim, *J. Power Sources*, **161** (2006) 1254.

[131] S. Song, S. Baek, *Electrochem. Solid-State Lett.*, **12** (2009) A2.

[132] S. Song, R. Reade, E. Cairns, J. Vaughey, M. Thackeray, K. Striebel, *J. Electrochem. Soc*., **151** (2004) A1012.

[133] K. Xu, C.A. Angell, *J. Electrochem. Soc*., **145** (1998) L70.

[134] A. Abouimrane, I. Belharouak, K. Amine, *Electrochem. Comm.*, **11** (2009) 1073.

[135] K. Xu, S. Ding, T.R. Jow, *J. Electrochem. Soc*., **146** (1999) 4172.

[136] S.A. Zhang, *J. Power Sources*, **162** (2006) 1379.

[137] A.V. Cresce, K. Xu, *J. Electrochem. Soc*., **158** (2011) A337.

[138] L. Yang, B. Lucht, *Electrochem. Solid-State Lett*., **12** (2009) A229.

[139] J. Liu, A. Manthiram, *Chem. Mater*., **21** (2009) 1695.

[140] R. Alcántara, M. Jaraba, P. Lavela, J.L. Tirado, *J. Electroanal. Chem*., **187** (2004) 566.

[141] T. Noguchi, I. Yamazaki, T. Numataa, M. Shirakata, *J. Power Sources*, **174** (2007) 359.

[142] J. Liu, A. Manthiram, *J. Electrochem. Soc*., **156** (2009) A66.

REVIEW ARTICLE

Electrode/Electrolyte Interface Studies in Lithium Batteries Using NMR

by Nicolas Dupré, Marine Cuisinier, and Dominique Guyomard

Easy access to portable energy sources has become necessary for the last decades and rechargeable batteries are now omnipresent in everyday tools and devices thanks to their storage capacity and relatively low weight. More recently, the possible use of lithium-ion batteries in full electric and hybrid electric vehicles has attracted considerable attention. However, great challenges still remain in this area of research and the importance of interfaces has become especially obvious in the field of electrochemistry and its applications to energy storage devices.[1,2] The solid electrolyte interphase (SEI) between the negative electrode and the electrolyte of a Li-ion battery is known to factor into the overall battery behavior in terms of irreversible capacity loss, charge transfer kinetics, and storage properties.[3-6] More than ten years of research in this field have led to excellent control and optimization of the SEI layer on carbon electrodes. Surface formulation and/or coatings of the positive electrode have been shown more recently to influence the battery performance as well.[7-11] Interfacial reactions and the growth of a passivation layer at the electrode surface upon cycling have been also highlighted for different positive electrode materials and have been identified to be of paramount importance as they can lead to performance degradation of the battery upon aging and cycling.[12,13] The existence of surface reactions at the positive electrode/electrolyte interface has been clearly demonstrated but the experimental conditions of formation, growth and modification, as well as its subsequent influences on the electrochemical performance, remain unclear. The chemical, physical, and structural properties of the interfacial layer at the positive electrode in particular are still not well known, and thus this more recent research area is of great interest.[14-18]

This article gives an overview of the NMR approach developed to extract and interpret information on the electrode/electrolyte interphase in lithium battery materials to probe evolution of electrochemical behavior and/or failure mechanisms along electrochemical cycling of lithium batteries. Such approach focuses on *ex situ* analysis of electrode materials. Recent studies have shown that *in situ/operando* NMR signals can be obtained during electrochemical processes[19-21] but these works mainly focus on the interpretation of bulk electrochemical mechanisms and therefore, are not discussed in the present article.

First are summarized the results of works dealing with the extraction and interpretation, from NMR data, of chemical information based on the chemical shift of various nuclei, and of quantitative information based on the integrated intensities of NMR signals.

The theory required to interpret NMR spectra of paramagnetic samples and to extract information on the interaction of surface layers with the electrode material bulk is then briefly described in order to make it accessible to the non-NMR audience. An earlier review article gives a more comprehensive description of the chemical and physical information that can be extracted from the presence of unpaired localized electrons.[22] This second part is then followed by illustrative examples obtained from stored or cycled electrode materials.

Use of NMR to Characterize Interface Species on Non-Paramagnetic Materials

Insofar NMR can be used to detect lithium, phosphorus, hydrogen, carbon, and fluorine among others, it appears as an appropriate method to study species present on surfaces of electrode materials, resulting from electrolyte decomposition. Among the numerous techniques to study the evolution of SEI on graphitic electrodes, Greenbaum *et al.*[23] used electrochemical impedance spectroscopy (EIS) and solid-state ^{7}Li NMR techniques to characterize the films formed on graphite anodes in low-temperature electrolytes with different mixtures of alkyl-carbonates and low-viscosity solvent additives such as aliphatic esters. A quantitative determination of SEI Li content was obtained by integrating the ^{7}Li NMR signals associated with Knight-shifted intercalated Li and unshifted Li species residing in the SEI. A compact, barrier-type, protective film is formed in alkyl-carbonate based solutions, whereas porous, and less protective films are formed with DME additives. The same group investigated the SEI on $LiNi_{0.8}Co_{0.2}O_2$[24] while Tucker *et al.*[25] showed the presence of Li-containing species on the particles surface of substituted $LiMn_2O_4$ spinel-type materials upon moisture contamination using ^{7}Li MAS NMR. The positive electrode cycled at room temperature builds up an interphase displaying similar NMR spectra with respect to that of stored positive electrodes, although in lower amount. By comparing relative integrated intensities assigned to the SEI and to lithium ions inserted in the cathode (in that case at 580 ppm), the SEI growth can be quantitatively monitored by NMR methods. More recently, ^{7}Li MAS NMR analyses of the charged silicium electrodes demonstrated that the major part of the lithium lost during the charge of batteries is not trapped in Li_xSi alloys but instead at the surface of the Si particles, likely as a degradation product of the liquid electrolyte.[26] Based on the different shifts observed for Li_xSi alloys,[21] it was demonstrated that the main cause of capacity fade of Si-based negative electrodes is the liquid electrolyte degradation in the case of nano-Si particles formulated with the carboxymethyl cellulose (CMC) binder. This degradation leads to the formation of a blocking layer on the active material, which further inhibits lithium diffusion through the electrode porosity.

Diamagnetic species containing Li, which NMR signals rise at approx. 0 ppm are frequently observed on numerous systems but not really investigated beyond a semi-quantiative analysis of the integrated intensity using ^{7}Li NMR due to the narrow chemical shift range,[27] typically between 2.8 ppm for Li_2O and -1.1 ppm for LiCl (Fig.1). The discrimination between several diamagnetic lithiated species present at the same time in the interphase might prove difficult. The interest of employing ^{19}F or ^{31}P NMR resides in the much wider chemical shift that can be used to identify fluorine or phosphorus containing products (Fig. 2), ranging in ^{19}F NMR from -72.4 ppm for PF_6^- to the products of its hydrolysis at -76.7 ppm (PO_3F^{2-}), -83.8 ppm ($PO_2F_2^-$), -153.7 (HF) and -204 ppm for LiF,[28] and ranging in ^{31}P NMR from -146 ppm for PF_6^- to -10.1 ppm (PO_3F^{2-}), -21.6 ppm ($PO_2F_2^-$). It becomes then possible to detect typical $LiPF_6$ decomposition products already observed by other techniques.[18,29-32]

First, ^{19}F NMR results drew attention to the presence of a fluorine-containing compound in the interphase, distinct from the background signal of the PVDF binder. The complementary use of ^{7}Li and ^{19}F NMR appeared indeed extremely useful to identify LiF as one of the decomposition products of $LiPF_6$ (usual salt of Li-ion battery electrolytes) despite LiF invisibility in the mid-IR (~700 to 1400 cm^{-1}) range.[33] Its formation in the solid electrolyte interphase (SEI) at both graphite and $LiCoO_2$ electrodes in lithium-ion rechargeable batteries was monitored quantitatively.[27] This study allowed establishing correlations between the amount of LiF formed on the cathode with both the number of cycles and the Li loss percentage from

(continued on next page)

the cathode while no correlation was found for LiF vs. cycle number for the anode.

In addition to this wider detection range and in order to investigate the organic components of the SEI, ^{13}C NMR provides a way to follow the decomposition reaction of organic carbonates yielding the organic part of the SEI as performed on the carbonaceous anodic electrode in C/$LiCoO_2$ batteries.[34] NMR signals assigned to lithium-based carbon derivatives showed that the Li-salt reacts with solvent, leading to accumulation of decomposition products on the electrode particles surface.[35] Furthermore, the use of ^{13}C enriched ethylene-carbonate and diethyl-carbonate solvents allowed following the decomposition pathway, indicating the presence of carbonyl groups in SEI layer, demonstrating a nucleophilic attack mechanism on the carbonyl carbon by one or more radical, alkoxy, carbanion, or fluorine-containing ionic species formed from solvent and/or salt decomposition. These results suggest a new family of electrolyte breakdown products, predominantly consisting of binary, ternary, and/or quaternary ether-type compounds (i.e., orthocarbonates and orthoesters), as well as fluorine-containing alkoxy compounds.[34]

Most of these studies, done on diamagnetic materials, rely only on the interpretation of the chemical shift to determine the chemical nature of the species formed from electrolyte decomposition, and on the monitoring of the integrated intensity to follow the progress of that reaction. In the case of transition metal compounds, NMR detection is more complicated, especially due to fast relaxation time leading to broadening of the signal caused by the presence of paramagnetic centers. However the resulting NMR spectra contain valuable additional information on the interaction between surface species and active electrode material bulk.

Use of NMR to Characterize Interface Species on Paramagnetic Materials

Magic angle spinning (MAS) NMR is generally used to characterize bulk materials. The Fermi contact interaction along with the electron-nucleus dipolar interactions and their respective effects on the $^{6,7}Li$ NMR spectra have been widely discussed in the case of lithium ions present within the host matrix of the insertion material.[22,36] The corresponding mechanisms have also recently been investigated using theoretical calculations.[37-39] Like the Chemical Shift Anisotropy (CSA), the electron-nucleus dipolar interaction scales with the field. At high field, even

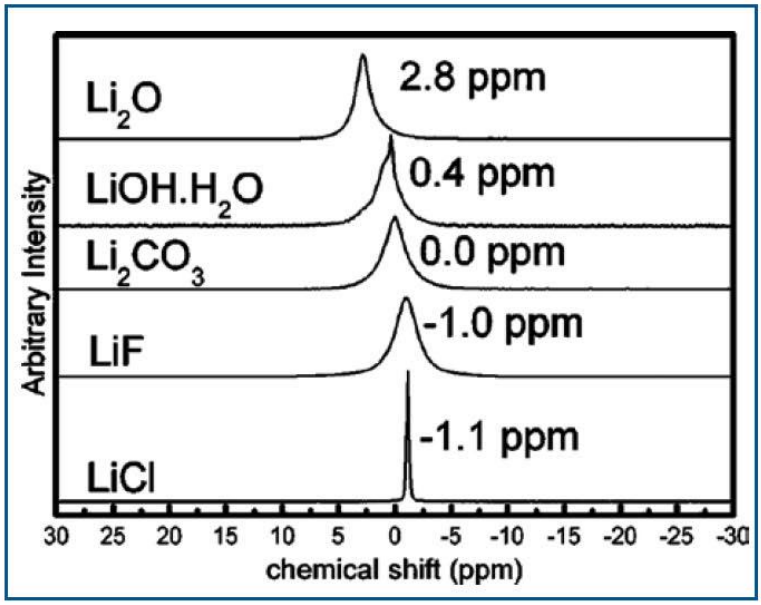

Fig. 1. *^{7}Li spectra showing chemical shift for various inorganic compounds that may be present in a SEI layer. (Reprinted with permission from Ref. 27)*

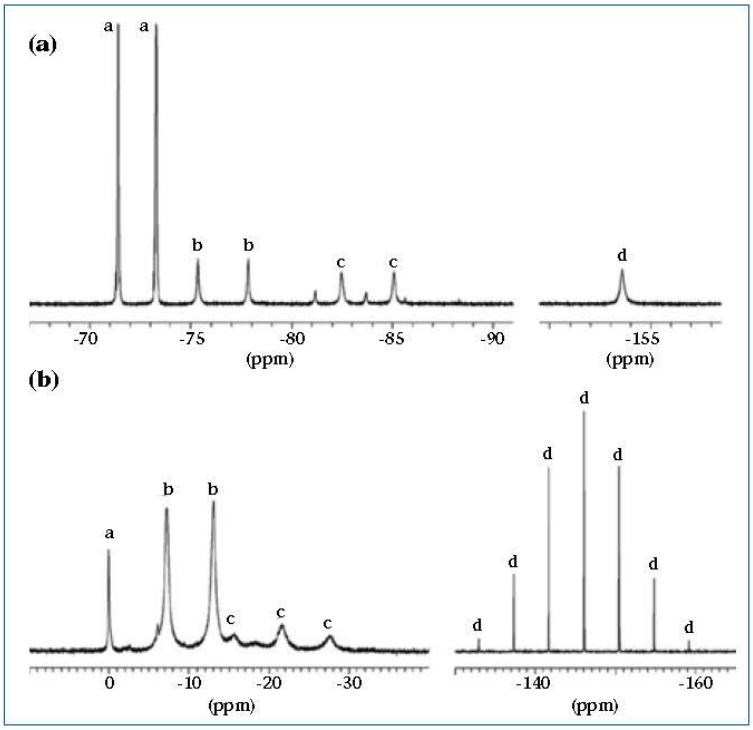

Fig. 2. *Typical ^{19}F and ^{31}P NMR spectra of the $LiPF_6$-containing solutions and of the products of $LiPF_6$ hydrolysis. (a) Signals a, b, c, and d are assigned to PF_6^-, PO_2F^{2-}, $PO_2F_2^-$, and HF, respectively. (b) Signals a, b, c, and d belong to $H_2PO_4^-$, PO_2F^{2-}, $PO_2F_2^-$, and PF_6^-, respectively. (Reprinted with permission from Ref. 28, license number 2713681279312)*

a fast spinning frequency does not allow averaging the interaction. Therefore, a very broad and unresolved signal is typically seen for lithium ions within the structure of the host matrix (Fig. 3). This signal is usually shifted due to the strong Fermi-contact interaction and according to the distribution of transition metals carrying localized unpaired electrons.[22,40,41] Much narrower signals, superimposed to the bulk signal, were observed by Tucker *et al.*[25] and Ménétrier *et al.*[42] between 0 and 1 ppm. This narrow signal can be assigned to Li present outside the active material in a surface layer. No departure of the isotropic resonance from the diamagnetic chemical shift range is observed in this case, indicating that the detected surface layer, composed of diamagnetic lithium-containing species, is not chemically bonded with the bulk active material, and therefore it is presumed to be predominantly physisorbed. NMR is a quantitative technique and thus all lithium nuclei in the sample are detected using ^{6,7}Li NMR. However, since the quantity of lithium in surface species is much smaller than the quantity of lithium within the bulk of host material, it becomes difficult to obtain accurate information on "surface" lithium from the complete spectrum.

Exerting through space, with a $1/r^3$ dependence on the distance, this strong dipolar interaction is a very efficient relaxation mechanism for the NMR magnetization. Based on the extremely fast relaxation observed for lithium in the bulk material compared to that of lithium in diamagnetic secondary phase(s), a single pulse with a long pre-acquisition delay suppresses the broad signal from bulk lithium making the signal assigned to surface lithium much more pronounced and easier to analyze. The weaker interaction felt by Li in the interphase allows resolving the NMR signal into spinning sidebands even at high field. Since the size of the dipolar coupling depends on the gyromagnetic ratio, g_N, larger dipolar couplings are seen for nuclei with larger values of g_N. Thus, ^{7}Li with its much larger gyromagnetic ratio than ^{6}Li ($g_{7Li}/g_{6Li} = 2.6$) results in MAS spectra with much larger spinning sideband manifolds and easier to interpret.

Using first this method in a study of the so-called interphase layer present at the surface of $Li(Ni_{1-y-z}Co_yAl_z)O_2$, Ménétrier *et al.*[42] mentioned the influence on the lineshape of MAS NMR spectra of the strong through-space dipolar interaction between the electron spins of the paramagnetic material and lithium nuclei in the surface layer, resulting in broadening of the sidebands manifold over a wide frequency range. In that case, this discrimination method in ^{7}Li NMR, along with ^{1}H NMR was used to understand the evolution of the nature of the surface layer upon hydration of the material. In particular, results indicated the presence of protons intercalated in the material, which amount increases upon hydration, thus releasing lithium ions that form the growing layer. More recently, this method proved appropriate and straightforward to probe the surface of electrode materials as ^{7}Li and ^{19}F MAS NMR analyses revealed unambiguously the presence of fluorine as a LiF "coating" on the surface of the $Li(Ni_{0.425}Mn_{0.425}Co_{0.15})O_2$ particles, rejecting the formation of fluorine-substituted $Li_{1.1}(Ni_{0.425}Mn_{0.425}Co_{0.15})_{0.9}O_{1.8}F_{0.2}$ materials[43,44] claimed to be obtained by several authors based on changes in cell parameters observed using X-ray diffraction.[45-47]

Following this precursor work, a ^{7}Li MAS NMR study of physisorbed surface layers on $LiNi_{1/2}Mn_{1/2}O_2$ has been performed[42,48] on a series of samples obtained by mixing the material with lithium carbonate or from contact of the material with ambient atmosphere, as well as with electrolyte. The progressive narrowing of the sidebands manifold of MAS NMR spectra reflects the decreasing intimacy or increasing distance of surface lithium with bulk material (Fig. 4) and therefore can yield extremely useful information complementary to the chemical information obtained from XPS or FTIR.

However, when considering such a signal, it appears that it cannot be considered as a single lithium site but it is rather a superposition of resonances corresponding to a distribution of lithium ions. They are ranging from locations close to the surface of the bulk material, on the inside of a secondary phase dispersed on the bulk material grains, to locations on the outside of this surface phase. Then the observed signal should evolve according to two parameters: the thickness of the surface phase and its intimacy with the bulk.

Spin-lattice (T_1) relaxation time measurements can be used as a probe of surface layers, allowing the discrimination of interphases from different origins. The b and T_1 values obtained using a stretched exponential[48] can describe the growth of a layer on the surface of the grains of active material and an evolution of the intimacy between the surface layer and the active material. For instance, T_1 increases and b decreases as the thickness increases, reflecting the decreasing influence of the paramagnetic phase on the relaxation time with the distance and the subsequent wider distribution of T_1 values, respectively. This method

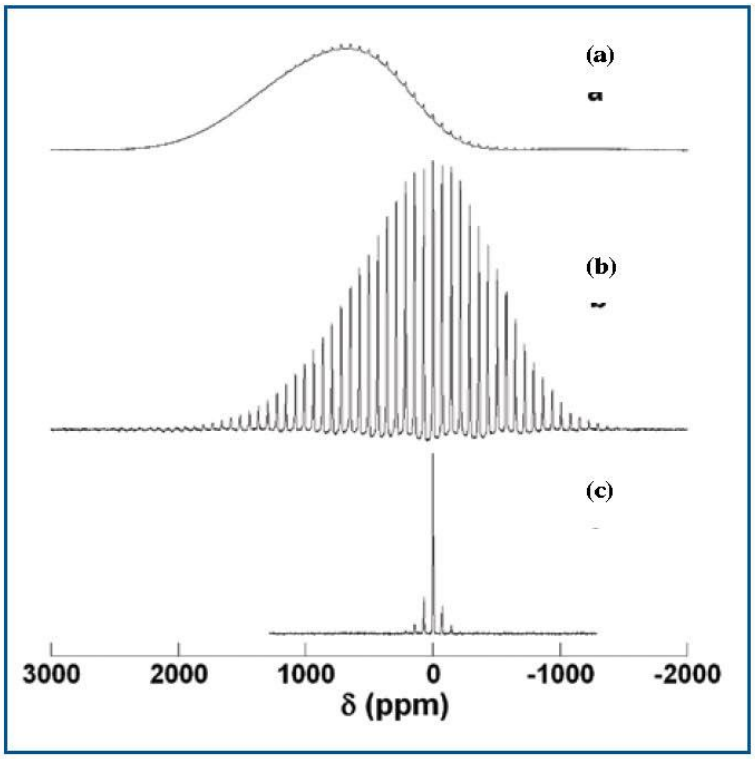

Fig. 3. *^{7}Li MAS NMR spectra for $LiNi_{1/2}Mn_{1/2}O_2$ stored in ambient atmosphere for two months acquired (a) with a Hahn-echo pulse sequence, (b) with a single pulse sequence, and (c) Li_2CO_3 as a reference. (Reprinted with permission from Ref. 48)*

(continued on next page)

(continued from previous page)

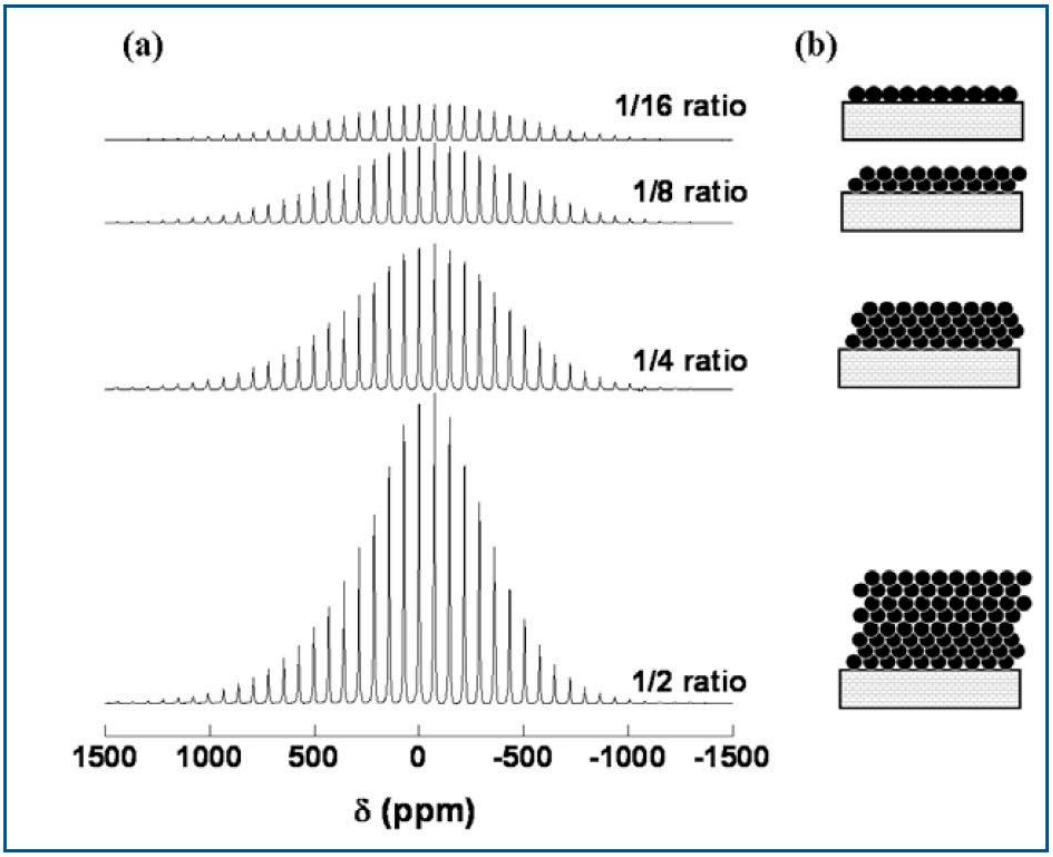

FIG. 4. *(a) ^{7}Li MAS NMR spectra for $LiNi_{1/2}Mn_{1/2}O_2$ ball-milled with various $Li_2CO_3/LiNi_{1/2}Mn_{1/2}O_2$ weight ratios. The ratios are indicated in the figure. (b) schemes showing the amount of lithium species on the surface of active material. The white rectangles represent an idealized section of the surface of one particle of active material and the black disks represent particles or aggregates of diamagnetic lithium-containing species. (Reproduced by permission of The Royal Society of Chemistry)*

of characterization using NMR measurements seems promising but has been applied so far only on samples obtained by mixing paramagnetic electrode material and known amount of diamagnetic lithiated species or by soaking the material in electrolyte. It would require further development.

The formation and the growth of surface species coming from reaction with $LiPF_6$ electrolyte have been subsequently followed by combining analyses of spectra lineshapes and integrated intensities in ^{7}Li MAS NMR in the case of $LiNi_{1/2}Mn_{1/2}O_2$ and $LiFePO_4$, two materials amongst promising candidates for positive electrodes for lithium batteries. Concerning the layered nickel manganese oxide, the reaction with electrolyte is extremely fast during the first moments of exposure and slows down for longer exposure times, evolving like a passivation reaction (Fig. 5a). Nevertheless, integrated NMR intensities are not proportional to specific surfaces of materials. Moreover, the clear overall decrease of the spectra line shapes for longer contact times suggests that the additional species have a weaker interaction with the paramagnetic bulk of active material (Fig. 5b). The slow NMR evolution observed after the initial important increase can be assigned to the stacking of lithium containing species on the top of the initial deposits, instead of further covering of material surface by decomposition products. The formation of discrete deposits instead of an homogenous layer was proven by TEM experiments (Fig. 5c) confirming the ability of NMR experiment to provide topological information about the electrode/electrolyte interphase. ^{7}Li NMR combined with ^{1}H NMR[42] and XPS[49,50] experiments on soaked samples displaying initial surface Li_2CO_3 showed that these species react with the electrolyte, yielding fluorinated products such as Li_xPF_y, LiF, and $Li_xPO_yF_z$ for short contact times. Only for a longer exposure to electrolyte appear organic products coming from the electrolyte solvents decomposition.

Similar ^{7}Li MAS NMR experiments on $LiFePO_4$ samples[51] permitted also to observe the growth of an interphase, the reaction being significantly aggravated in the case of the non-carbon coated material in spite of the smaller grain size and the higher specific surface area of the carbon coated $LiFePO_4$. These results demonstrated the clear influence of the carbon coating as a protection against parasitic reaction with the electrolyte. The interphase grows continuously on olivine particles as no passivation state is reached after one month of contact with the electrolyte contrasting with the behavior of $LiNi_{1/2}Mn_{1/2}O_2$. In addition, the integrated intensity of the corresponding ^{7}Li NMR signal being much lower, it allowed confirming that the two materials display a completely different surface chemistry, not only in terms of chemical nature of the reaction products, as shown in previous XPS and

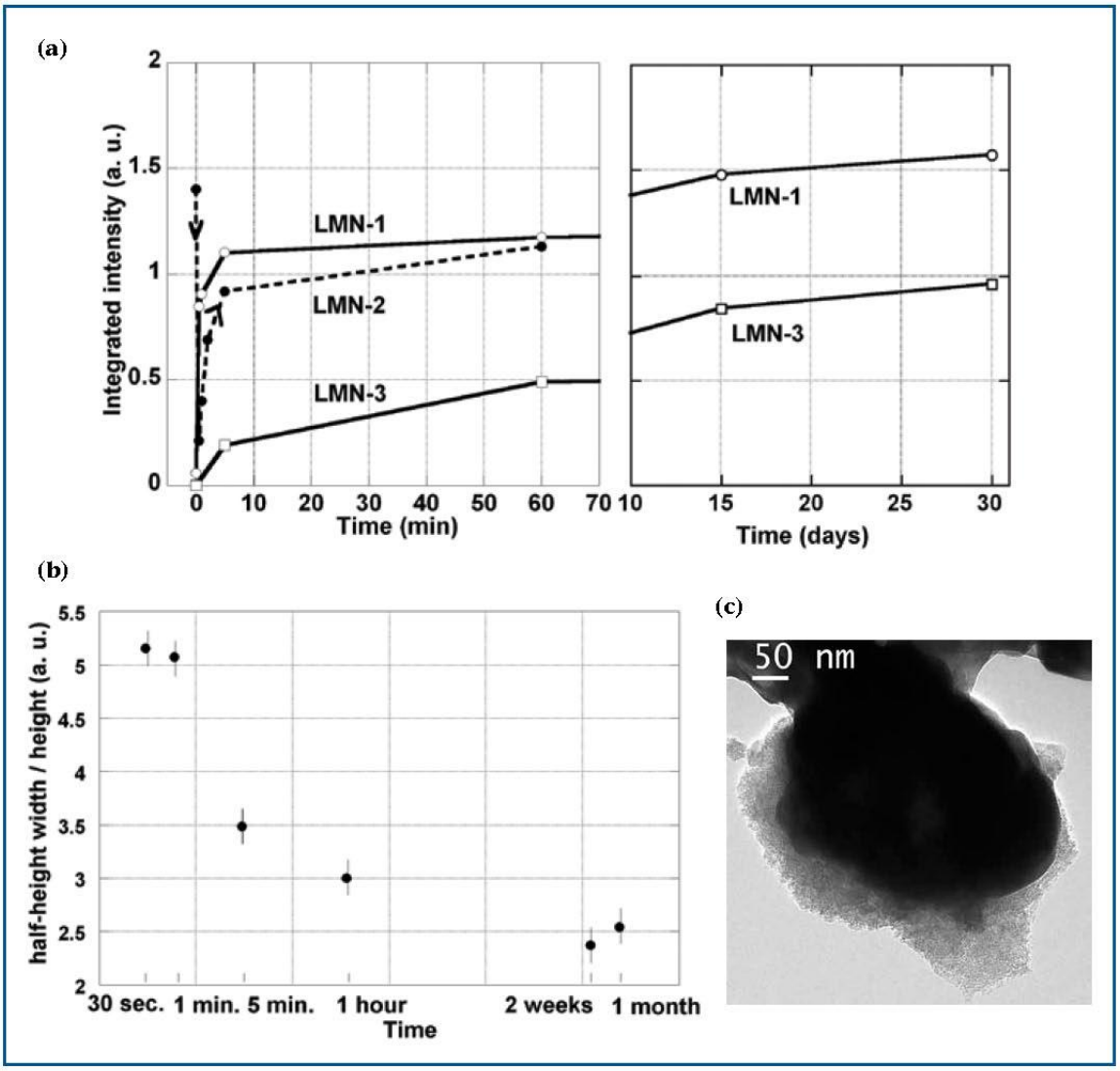

Fig. 5. *(a) Evolution of the normalized integrated intensities of ^{7}Li MAS NMR spectra, for different $LiNi_{1/2}Mn_{1/2}O_2$ samples soaked in $LiPF_6$ (EC/DMC 1M) electrolyte for various amounts of time. LMN-1 and LNM-3 were stored in argon and exhibit specific surfaces of 8 m²/g and 4 m²/g, respectively. LMN-2 was stored in air and displays a pristine Li_2CO_3 interphase. (b) Half-height width of ^{7}Li NMR spectra normalized to the height for LMN-1 soaked in $LiPF_6$ (EC/DMC 1M) electrolyte for various amounts of time. Estimated errors are reported as vertical bars. (c) TEM pictures for LMN-1 after 2 weeks of contact with the electrolyte.*

FTIR studies,[7,14-18] but also in terms of the surface reactivity towards electrolyte. This result combined with EIS confirmed the very limited role of the interphase on the electrochemical performances of $LiFePO_4$ electrodes as opposed to the behavior of most oxides.

These first steps in the characterization of the electrode/electrolyte interface using MAS NMR spectroscopy suggest that a systematic investigation using the NMR characterization should allow some further understanding of the surface layer present on the pristine positive electrode materials of Li-ion batteries, as well as of the SEI formed during battery operation.^{7}Li MAS NMR permitted to follow the evolution of the interphase along the electrochemical cycling of $LiNi_{1/2}Mn_{1/2}O_2$.[52,53] The good correlation between the evolution of surface phenomena probed by NMR and bulk properties showed in particular the influence of surface species on the electrochemical behavior. In particular, for air-stored $LiNi_{1/2}Mn_{1/2}O_2$ the overall electrochemical behavior, which depends normally on bulk properties, is here strongly driven by the evolution of surface phenomena. On the other hand, for $LiNi_{0.5}Mn_{0.5}O_2$ protected from air contact, the low amount of surface species and its progressive removal along the continuous decrease of electrochemical performances suggested that the interphase is needed to some extend to protect the electrode from degradation. Semi-quantitative ^{7}Li NMR experiments performed upon cycling

(continued on next page)

indicated the formation of lithiated interphase species in reduction and their partial removal in oxidation, indicating a dynamic character of the interphase upon cycling. Limitations of the method resides in the small chemical shift range of Li and XPS experiments were required to gather complementary chemical information about the composition of interphase species. In order to achieve further characterization of interphase species, ^{19}F and ^{31}P MAS NMR is currently under progress as the wider chemical shift range enables to separated different fluorinated and/or phosphored species such as LiF and fluorophosphates ($LiPF_6$, Li_xPF_z, RPO_yF_z).

Conclusions

^{7}Li NMR is a powerful tool to study the surface layer on Li-ion battery electrode materials, especially coupled with techniques giving chemical information such as XPS or FTIR. The use of other nuclei such as ^{19}F or ^{31}P as probes of elements contained in the interphase is another straightforward way to gather additional insight on the evolution of the chemical composition of inorganic products of electrolyte decomposition. Concerning the organic part of the interphase, the use of ^{13}C NMR has proved also to be of great interest to understand the decomposition or reaction pathway of organic solvents even though the need of isotopic enrichment and the sensitivity of ^{13}C NMR to the presence of paramagnetic centers complicate the detection.

In the case of materials containing transition metals with unpaired electrons, in addition to the chemical composition and quantification, it is possible to extract physical or topological information from electron-nucleus dipolar interaction. Especially in the case of ^{7}Li NMR, the advantage of this method lies in the efficient separation of surface signal from paramagnetic bulk signal, allowing the extraction of surface information including intimacy between bulk material and surface phase.

The detection and observation of electrode/electrolyte interphase using NMR technique is now applied to a wide range of cathode and anode materials for lithium-ion batteries and is becoming an efficient characterization tool in this research area. More investigations are necessary however to further explore the possibilities of this new interface characterization technique.

Although the technique is being developed for interface characterisation of Li-ion battery materials, it is clear MAS NMR is applicable to surface or interface characterization in many systems in which surfaces and/or interfaces are of premier importance such as for instance other electrochemical systems (Ni-MH batteries, supercapacitors, fuel cells) as well as in photovoltaic and catalysis domains.

About the Authors

Nicolas Dupré received his PhD in 2001 from Université Pierre et Marie Curie-Paris VI working under the direction of Prof. Michel Quarton. Dupré was appointed as a postdoctoral associate at SUNY Stony Brook in 2002, where he worked with Prof. Clare P. Grey. Dupré has been working as a CNRS researcher in the Institut des Matériaux Jean Rouxel (IMN) in Nantes, France since 2005. His current research interests are focused on the study of the behavior of materials for lithium batteries, including electrode/electrolyte interface using solid-state NMR. He may be reached at nicolas.dupre@cnrs-imn.fr.

Marine Cuisinier received her master's degree in 2008 in materials science from the Universities of Rennes 1, France and Turin, Italy in the frame of the MaMaSELF Erasmus Mundus program. She is a now a PhD student in the Institut des Matériaux Jean Rouxel (IMN) in Nantes. Her current focus is on electrode/electrolyte interface studies in lithium batteries. She may be reached at marine.cuisinier@cnrs-imn.fr.

Dominique Guyomard obtained his PhD in 1985 in materials science and electrochemistry. From 1990 to 1992, he was a visiting scientist under the supervision of Prof. J. M. Tarascon in Bellcore (U.S.), working on the carbon/spinel manganese oxide Li-ion project. He is now Director of Research at CNRS and the head of the Electrochemical Energy Storage and Transformation Department (EEST) of IMN, with about 30 researchers, gathering the activities on Li batteries, on moderate and high temperature fuels cells, and on calculations and simulations and advanced spectroscopies. His expertise deals with basic and applied solid state electrochemistry, and materials and surface science, applied to the fields of Li-ion & Li metal polymer batteries. More specifically, his research is focused on the conception of new materials for electrode applications, on the use of innovative synthesis techniques, and on the characterization of electrode materials for better understanding of reaction mechanism. He may be reached dominique.guyomard@cnrs-imn.fr.

References

1. J. M. Tarascon and M. Armand, *Nature*, **414**, 359 (2001).
2. A. S. Arico, P. Bruce, B. Scrosati, J. M. Tarascon, and W.Van Schalkwijk, *Nature Materials*, **4**, 366 (2005).
3. D. Aurbach, B. Markovsky, I. Weissman, E. Levi, and Y. Ein-Eli, *Electrochim. Acta*, **45**, 67 (1999).
4. R. Yazami, *Electrochim. Acta*, **45**, 87 (1999).
5. B. Markovsky, A. Rodkin, Y. S. Cohen, O. Palchik, E. Levi, D. Aurbach, H.-J. Kim, and M. Schmidt, *J. Power Sources*, **119-121**, 504 (2003).
6. L. Larush, E. Zinigrad, Y. Goffer, and D. Aurbach, Langmuir, **23**, 12910 (2007).
7. D. Aurbach, B. Markovsky, G. Salitra, E. Markevich, Y. Talyossef, M. Koltypin, L. Nazar, B. Ellis, and D. Kovacheva, *J. Power Sources*, **165**, 491 (2007).
8. D. Aurbach, Y. Talyosef, B. Markovsky, E. Markevich, E. Zinigrad, L. Asraf, J. S. Gnanaraj, and H. J. Kim, *Electrochim. Acta*, **50**, 247 (2004).
9. D; Aurbach, B. Markovsky, A. Rodkin, E. Levi, Y. S. Cohen, H. J. Kim, and M. Schmidt, *Electrochim. Acta*, **47**, 4291 (2002).
10. D. Aurbach, Y. Gofer, and J. Langzam, *J. Electrochem. Soc.*, **136**, 3198 (1989).
11. G. G. Amatucci, C. N. Schmutz, A. Blyr, C. Sigala, A. S. Gozdz, D. Larcher, and J. M. Tarascon, *J. Power Sources*, **69**, 11 (1997).
12. D. Aurbach, M. D. Levi, E. Levi, H. Teller, B. Markovsky, G. Salitra, U. Heider, and L. Heider, *J. Electrochem. Soc.*, **145**, 3024 (1998).
13. E. Ericksson, PhD Thesis, Uppsala University, **2001**.
14. T. Matsushita, K. Dokko, and K. Kanamura, *J. Electrochem. Soc.*, **152**, A2229 (2005).
15. H. Ota, T. Akai, H. Namita, S. Yamaguchi, and M. Nomura, *J. Power Sources*, **119-121**, 567 (2003).
16. B. J. Neudecker, R. A. Zuhr, B. S. Kwak, J. B. Bates, and J. D. Robertson, *J. Electrochem. Soc.*, **145**, 4148 (1998).
17. J. C. Dupin, D. Gonbeau, H. Benqlilou-Moudden, P. Vinatier, and A. Levasseur, *Thin Solid Films*, **384**, 23 (2001).
18. K. Edström, T. Gustafsson, and J. O. Thomas, *Electrochim. Acta*, **50**, 397 (2004).
19. M. Letellier, F. Chevallier, C. Clinard, E. Frackowiak, J. N. Rouzaud, F. Beguin, M. Morcrette, and J. M. Tarascon, *J. Chem. Phys.*, **118**, 6038 (2003).
20. M. Letellier, F. Chevallier, and M. Morcrette, *Carbon*, **45**, 1025 (2007).

21. B. Key, R. Bhattacharyya, M. Morcrette, V. Seznec, J. M. Tarascon, and C. P. Grey, *J. Am. Chem. Soc.*, **131**, 9239 (2009).
22. C. P. Grey and N. Dupré, *Chem. Rev.*, **104**, 4493 (2004).
23. M. C. Smart, B. V. Ratnakumar, S. Surampudi, Y. Wang, X. Zhang, S. G. Greenbaum, A. Hightower, C. C. Ahn, and B. Fultz, *J. Electrochem. Soc.*, **146**, 3963 (1999).
24. Y. Wang, X. Guo, S. Greenbaum, J. Liu, and K. Amine, *Electrochem. Solid-State Lett.*, **4**, A68 (2001).
25. M. C.Tucker, A. Braun, U. Bergmann, H. Wang, P. Glatzel, J. A. Reimer, and E. J. Cairns, *Interfaces, Phenomena and Nanostructures in lithium Batteries Workshop*, (Eds: A. landgrebe and R.J. Klinger), *Electrochem. Soc. Proc. Series*, **2001**.
26. Y. Oumellal, N. Delpuech, D. Mazouzi, N. Dupre, J. Gaubicher, P. Moreau, P. Soudan, B. Lestriez, and D. Guyomard, *J. Mat. Chem.*, **21**, 6201 (2011).
27. B. Meyer, N. Leifer, S. Sakamoto, S. Greenbaum, and C. P. Grey, *Electrochem. Solid-State Lett.*, **8**, A145 (2005).
28. A. V. Plakhotnyk, L. Ernst, and R. Schmutzler, *J. Fluorine Chem.*, **126**, 27 (2005).
29. Y. Matsuo, R. Kostecki, and F. McLarnon, *J. Electrochem. Soc.*, **148**, A687 (2001).
30. D. Ostrovskii, F. Ronci, B. Scrosati, and P. Jacobsson, *J. Power Sources*, **103**, 10 (2001).
31. T. Eriksson, A. M. Andersson, C. Gejke, T. Gustafsson, and J. O. Thomas, *Langmuir*, **18**, 3609 (2002).
32. M. Herstedt, M. Stjerndahl, A. Nyten, T. Gustafsson, H. Rensmo, H. Siegbahn, N. Ravet, M. Armand, J. O. Thomas, and K. Edstrom, *Electrochem. Solid-State Lett.*, **6**, A202 (2003).
33. S. W. Song, G. V. Zhuang, and P. N. Ross Jr., *J. Electrochem. Soc.*, **151**, A1162 (2004).
34. N. Leifer, M. C. Smart, G. K. S. Prakash, L. Gonzalez, L. Sanchez, K. A. Smith, P. Bhalla, C. P. Grey, S. And G. Greenbaum, *J. Electrochem. Soc.*, **158**, A471 (2011).
35. I. Nicotera, G. D. McLachlan, G. D. Bennett, I. Plitz, F. Badway, G. G. Amatucci, and S. G. Greenbaum, *Electrochem. Solid-State Lett.*, **10**, A5 (2007).
36. D. Carlier, M. Ménétrier, and C. Delmas, *J. Mater. Chem.*, **11**, 594 (2001).
37. D. Carlier, M. Ménétrier, C. P. Grey, C. Delmas, and G. Ceder, *Phys. Rev. B*, **67**, 174103 (2003).
38. C. Chazel, M. Menetrier, D. Carlier, L. Croguennec, and C. Delmas, *Chem. Mat.*, **19**, 4166 (2007).
39. D. Carlier, M. Menetrier, and C. Delmas, *J. Phys. Chem. C*, **114**, 4749 (2010).
40. W. S. Yoon, Y. Paik, X. Q. Yang, M. Balasubramanian, J. McBreen, and C.P. Grey, *Electrochem. Solid-State Lett.*, **5**, A263 (2002).
41. W. S. Yoon, S. Iannopollo, C. P. Grey, D. Carlier, J. Gorman, J. Reed, and G. Ceder, *Electrochem. Solid-State Lett.*, **7**, A167 (2004).
42. M. Ménétrier, C. Vaysse, L. Croguennec, C. Delmas, C. Jordy, F. Bonhomme, and P. Biensan, *Electrochem. Solid-State Lett.*, **7**, A140 (2004).
43. M. Ménétrier, J. Bains, L. Croguennec, A. Flambard, E. Bekaert, C. Jordy, P. Biensan, and C. Delmas, *J. Solid State Chem.*, **181**, 3303 (2008).
44. L. Croguennec, J. Bains, M. Ménétrier, A. Flambard, E. Bekaert, C. Jordy, Ph. Biensan, and C. Delmas, *J. Electrochem. Soc.*, **156**, A349 (2009).
45. G. H. Kim, J. H. Kim, S. T. Myung, C. S. Yoon, and Y.-K Sun, *J. Electrochem Soc.*, **152**, A1707 (2005).
46. S. U. Woo, B. C. Park, C. S. Yoon, S. T. Myung, J. Prakash, and Y. K. Sun, *J. Electrochem. Soc.*, **154**, A649 (2007).
47. S. H. Kang and K. Amine, *J. Power Sources*, **146**, 654 (2005).
48. N. Dupré, J-F. Martin, D. Guyomard, A. Yamada, and R. Kanno, *J. Mat. Chem.*, **18**, 4266 (2008).
49. N. Dupré, J-F. Martin, D. Guyomard, A. Yamada, and R. Kanno, *J. Power Sources*, **189**, 557 (2008).
50. N. Dupré, J-F. Martin, J. Oliveri, P. Soudan, D. Guyomard, A. Yamada, and R. Kanno, *J. Electrochem. Soc.*, **156**, C180 (2009).
51. N. Dupré, J-F. Martin, J. Degryse, V. Fernandez, P. Soudan, and D. Guyomard, *J. Power Sources*, **195**, 7415 (2010).
52. N. Dupré, J.-F. Martin, J. Oliveri, D. Guyomard, A. Yamada, and R. Kanno *Electrochem. Comm.*, **10**, 1897 (2008).
53. N. Dupré, J-F. Martin, J. Oliveri, P. Soudan, D. Guyomard, A. Yamada, and R. Kanno, *J. Power Sources*, **196**, 4791 (2011).

CHAPTER 2. SPECIFICITY OF THE STUDY: INTERPHASE CHARACTERIZATION BY MAS NMR AND EELS

This chapter aims at introducing the analytical techniques employed in this thesis to study interphases in Li-ion batteries. The originality of this work lies above all in the use of MAS NMR and EELS to investigate inhomogeneous surface layers made of diamagnetic species in interaction with paramagnetic electrode materials, hence justifying a special treatment in these pages.

The first section introduces solid state NMR and the particular case of paramagnetic electrode materials is treated here, based on an article from Grey *et al.* [1]. NMR applied to electrode/electrolyte interface in lithium batteries using NMR is then presented more specifically and the technical aspects of this approach pioneered by Ménétrier *et al.* [2] and developed in our group [3-8] is summarized. Follows complementary methodology implemented in this thesis to perform absolute quantification of interphasial species using ^{7}Li, ^{19}F and ^{31}P NMR [**paper IV**].

A second section is focused on EELS, and aims not only at introducing this analytical technique but also, and maybe most importantly, at discussing the challenges related to the investigation of inhomogeneous, air/beam sensitive interphases on composite electrodes by TEM.

Finally, in a third section, a "case study" published in *Solid-State NMR* is presented, reporting both high field multinuclear NMR and EELS quantification of electrode/electrode interphases for the first time [**paper IV**].

I- CHARACTERIZATION OF ELECTRODE/ELECTROLYTE INTERFACE IN LITHIUM BATTERIES USING NMR

I.1. NMR applied to paramagnetic materials [ref. 1 and ref. herein]

Typically, MAS NMR spectra discussed in this work are composed of an envelope comprising an isotropic resonance and spinning sidebands (ssb). The chemical shift range for diamagnetic species is rather small in the case of lithium, which usually impedes resolved resonances for distinct diamagnetic lithium local environments. In compounds containing paramagnetic ions (i.e., $Fe^{2/3+}$, Mn^{4+} and $Ni^{2/4+}$ for the compounds studied inhere) on the contrary, significant hyperfine shifts are observed, resulting from the transfer of localized unpaired electron spin density from these paramagnets to the lithium (or phosphorus) nuclei, through overlapping orbitals, by Fermi contact interactions. The spinning sidebands arise from the partial averaging by MAS of the large dipolar interaction between the Li nuclei spin and the magnetic moments of the paramagnetic centers (i.e. their electronic spins). The ascendancy of such nuclear-electron hyperfine interactions on the NMR spectra gives access to physical and chemical information such as local electronic and crystallographic structures. Such approach has recently been made even more powerful since contact shift mechanisms have been addressed using theoretical calculations [9-11].

I.1.1. Origin of hyperfine coupling

Paramagnetic ions, carrying an electronic spin *S*, are associated to magnetic moments μ_e that align in the presence of a B_0 static field, conventionally defined parallel to the *z*-direction. S_z represents the spin component in this direction. Since the lifetime of an ion in a particular electronic state (T_{1e}) is very short compared to the relatively long time scale probed by NMR, nuclear spins can only couple with a time-averaged local field $\langle S_z \rangle$. This value, necessarily nonzero due to the difference in population of the different states of a magnetic field, is proportional to the net magnetic moment of an ensemble, which is the quantity measured in a magnetic susceptibility measurement:

$$\langle S_z \rangle = -\frac{B_0}{\mu_0 g N_0 \mu_B} \chi_M \qquad \text{(Eq. II-1)}$$

where μ_0 is the permeability, *g* the Landé-factor of the electron, μ_B the Bohr magneton, N_0 Avogadro's number, and χ_M the molar magnetic susceptibility. The magnitude of the

nucleus-electron interaction can be quantified via a hyperfine coupling constant, A/h (in Hz), and NMR experiments are only possible for ions with such short T_{1e} that:

$$\left|A/h\right| \langle\langle 1/T_{1e} \qquad \text{(Eq. II-2)}$$

In the case $1/T_{1e}$ is similar in magnitude to A/h, considerable broadening of the NMR signal can occur, preventing the acquisition of high-resolution NMR spectra. In particular, large hyperfine constants (up to hundreds of MHz) can be observed when the nuclear and electronic spins are carried by the same atom and in these conditions, high-resolution NMR spectra are not observed. This is not the case for lithium ions present in intercalation compounds, as Li is usually separated by two or more bonds from the paramagnet and besides, involved in mostly ionic bonds, reducing the size of *A*.

The nuclear spins can interact with the time-averaged magnetic moments via either through-bond (Fermi-contact) or through-space (dipolar) interactions.

I.1.2. Fermi-contact interaction

The Fermi contact is a measure of spin density of unpaired electrons that is transferred from the paramagnet (transition metal ion) to the observed nucleus (lithium). In the regime defined by Eq. II-2, the NMR shift (δ) induced by the Fermi-contact interaction is directly proportional to $\langle Sz \rangle$.

$$\delta = \frac{\Delta\omega}{\omega_0} = -\frac{Ac}{\omega_0 h}\langle S_z \rangle \qquad \text{(Eq. II-3)}$$

The direction and magnitude of the shift are determined by the sign and magnitude of the hyperfine constant A_c/h, which depends on the electron spin (i.e., unpaired electron) density at the nucleus, $\rho(r=0)$.

$$A_c/h = g\mu_B\gamma_N\rho(r=0)\mu_0/3S \qquad \text{(Eq. II-4)}$$

γ_N is the gyromagnetic ratio of the investigated NMR isotope, and ω_0 its Larmor frequency (in radians). Thus, the ^{6}Li/^{7}Li hyperfine shifts observed can be much larger for transition-metal based materials compared to diamagnetic materials (0-5 ppm).

$\rho(r=0)$ depends on the connectivity between the orbitals on the paramagnetic center and the orbitals on the NMR nucleus. Only the electron density transferred to the s orbitals needs to be considered. Electron density may be transferred either directly from the paramagnet or indirectly via a transferred hyperfine interaction to the *s* orbitals, involving a

third atom such as oxygen atom intervening in the connection between the lithium atom and the paramagnet. In this latter case, the signal contains information regarding the chemical bonds involved (additivity of hyperfine shifts, dependency according to the number of electrons or according to the coordination angles)

I.1.3. Electron-nucleus dipolar interaction

The dipolar interaction is the same interaction that occurs between two or more nuclear moments and is caused by the local magnetic fields of the nuclear or electronic spins that are felt at the nearby nuclear spin observed. When the dipolar interaction involves coupling to electrons or paramagnetic ions, the nuclear spins can only couple to the time-averaged magnetic moment. The electron-nucleus dipolar interaction, like the Chemical Shift Anisotropy (CSA), scales with the field and at high field (typically above 500 MHz), even a relatively fast spinning frequency does not allow averaging the interaction and resolve the spectrum into isotropic resonance and spinning sidebands. Therefore, a very broad signal is seen for lithium ions within the structure of the host matrix.

The spinning sidebands manifold contains information concerning the magnitude of the interaction and the relative orientation of the spins (see the following section for further details). The Hamiltonian for this interaction, H_{en}, can be represented by:

$$\boldsymbol{H}_{en} = \frac{\boldsymbol{\mu}_0}{4\boldsymbol{\pi}} \overline{\boldsymbol{\mu}_e} \tilde{\boldsymbol{D}}_{en} \boldsymbol{\mu}_N \quad \text{(Eq. II-5)}$$

where $\overline{\mu_e}$ is the magnetic moment of the electrons averaged on time or temperature (i.e., $-g\mu_B\langle S_z\rangle$) thus depending on the static magnetic field B_0 applied. If this latter is too strong, the electron-nuclear is dramatically increased and prevents the analysis. $\tilde{D}_{en}$ is the dipolar coupling tensor between the unpaired electron and nucleus, which is defined by its matrix elements as follows:

$$D_{ij} = \frac{1}{r^3}(\delta_{ij} - 3e_i e_j) \qquad \text{(Eq. II-6)}$$

It depends on both the distance between the nuclear and electronic spins, *r*, and the orientation of the interatomic vector (paramagnetic electron – studied nucleus) with respect to the static magnetic field, B_0. δ_{ij} is the Kronecker delta (δ_{ij} =1 for $i = j$ and 0 for $i \neq j$), e_i and e_j are the *x, y, z* components of a unit vector pointing from the nuclear spin (lithium) to the electron spin of the paramagnetic ion unpaired electron.

This dipolar interaction is also expected to exist between a paramagnetic material and a diamagnetic material in strong intimacy. This property is exploited in this thesis to investigate lithiated surface species (Li_2CO_3, LiOH, organic compounds…) in the interphase on paramagnetic positive electrode materials. Notably, in the case of a secondary diamagnetic phase lying on the surface of the paramagnetic phase, the distance parameter will play an obvious role. On the other side, the term dealing with orientation of the interatomic vector (paramagnetic nucleus – studied nucleus) is difficult to estimate considering the inherent disorder of the active material / interphase system. In a first approach, it seems reasonable to consider a predominance of the influence of the distance parameter and to consider an overall macroscopic distribution of the interphase on the surface of the active material leading to a similar averaged contribution of orientation of the paramagnetic nucleus – studied nucleus vector.

I.2. Qualitative interface characterization using ^{7}Li MAS NMR

I.2.1 Selective NMR detection of interface species on paramagnetic materials

As explained in the previous section, under a high magnetic field (typically at 11.8 T in our case) a very broad signal is seen for lithium ions within the structure of the host matrix of insertion materials. This signal is usually shifted due to the strong Fermi-contact interaction and according to the distribution of transition metals carrying localized unpaired electrons around the intercalated lithium [1, 12, 13]. As observed on electrode materials after reaction with a surrounding media (e. g. atmosphere or electrolyte), lithium-containing diamagnetic interphasial species exhibit much narrower signals between 0 and 1 ppm, superimposed to the bulk signal [2, 14].

In the aim at investigating interphasial Li, the idea pioneered by Ménétrier *et al*. [2] consists in playing with the electron-nucleus dipolar interaction. Exerting through space, with a $1/r^3$ dependence on the distance (see Eq. II-5 and II-6), this strong dipolar interaction is a very efficient relaxation mechanism for the NMR magnetization.

Based on the extremely fast relaxation observed for lithium in the bulk material compared to that of lithium in diamagnetic interphasial phase(s), a single pulse with a long preacquisition delay (**Fig. II-1**) suppresses the broad signal from bulk lithium which makes the signal assigned to surface lithium much more pronounced and easier to analyze. The use of a long preacquisition delay can be considered as a low pass filter on the linewidth,

suppressing the decayed broad component at the cost of a baseline correction procedure. In this work, only spectra acquired under these conditions, and therefore displaying only the lithium signal corresponding to the surface layer, will be discussed.

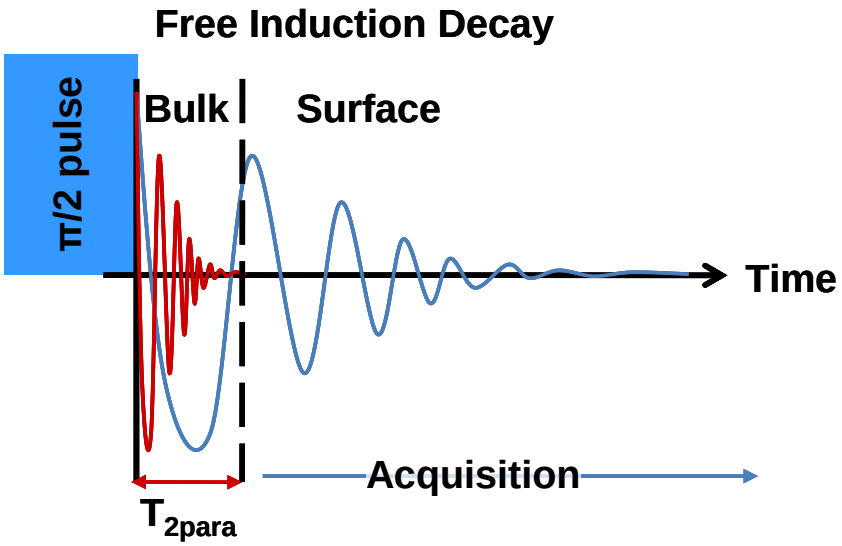

Figure II-1. Schematic view of free induction decays corresponding to lithium in a paramagnetic phase, exhibiting a fast decay, and that corresponding to lithium in a surface diamagnetic phase, exhibiting a longer decay. Waiting after the former has completely disappeared allows recording only the signal arising from "surface lithium".

I.2.2. Qualitative estimation of the electrode / interphase interaction

In previous works, it has been shown that the ssb manifold width can be correlated to strength of the electron-nucleus dipolar interaction between lithium in the interphase and paramagnetic electrode grains underneath through the characteristic T_1^* spin-lattice relaxation time [2, 3].

T_1 measurements, carried out as described earlier, were not fitted using an ideal exponential law but rather a stretched exponential (Eq. II-7), to consider the complex processes observed experimentally.

$$I(t) = I_0\left[1 - \exp\left[-(t/T_1^*)\beta\right]\right] \qquad \text{(Eq. II-7)}$$

The β and T_1^* values obtained can describe the growth of a layer on the surface of the grains of active material and an evolution of the intimacy between the surface layer and the active material, as extensively discussed in ref [3]. For instance, T_1^* increases and β decreases as the thickness increases, reflecting the decreasing influence of the paramagnetic phase on the relaxation time with the distance and the subsequent wider distribution of T_1 values, respectively.

On experimental spectra (**Fig. II-2**), the progressive narrowing of the sidebands manifold of MAS NMR spectra can thus reflect whether the decreasing "average" intimacy or increasing "average" distance of surface lithium with bulk material. In both cases, such a surface signal cannot be considered as a single lithium site but rather as a superposition of resonances corresponding to a distribution of lithium ions. They are ranging from locations close to the surface of the bulk material, to locations on the outside of the interphase. Then the observed signal width should evolve according to two parameters: the intimacy of the surface phase with the bulk powder and its thickness. This method of characterization using T_1 measurements or the ssb manifold width seems promising but has been applied so far only on samples obtained by mixing paramagnetic electrode material and known amount of diamagnetic lithiated species or by soaking the material in electrolyte [3]. Although it would require further development, the electronic spin *S* carried by paramagnetic electrode materials varies with the state of charge (SOC), making difficult the comparison of spectra recorded after cycling unless considering fully (des)intercalated states.

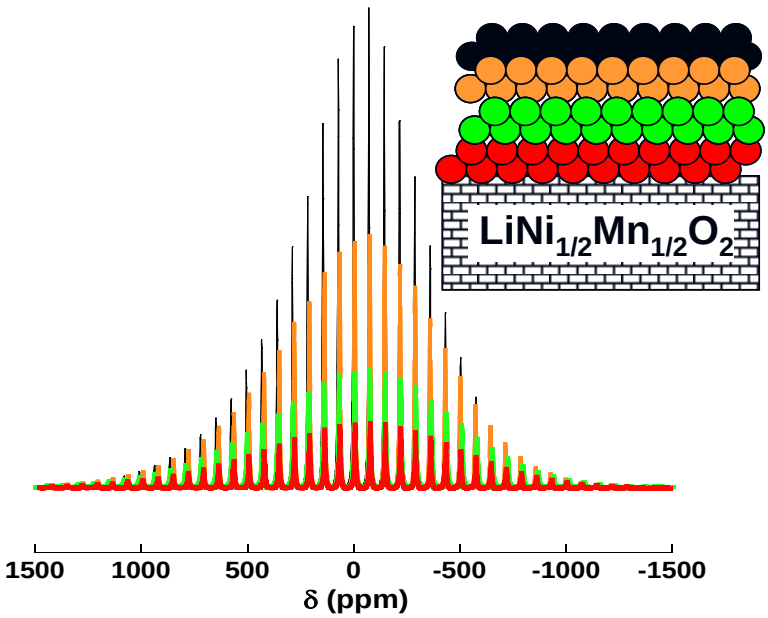

Figure II-2. ^{7}Li MAS NMR spectra for $LiNi_{1/2}Mn_{1/2}O_2$ ball-milled with various Li_2CO_3 / $LiNi_{1/2}Mn_{1/2}O_2$ weight ratios. Insert: scheme attributing the NMR intensity to layers of diamagnetic lithium-containing species interacting with a paramagnetic electrode material.

In a further attempt to correlate the material/interphase interaction with the dipolar interaction and its influence on the relaxation times of NMR resonances, the electrode / interphase intimacy (i.e. the strength of the electron-nucleus dipolar interaction) is tentatively discussed through the transverse relaxation time, T_2. As a matter of fact, proper T_2

measurements, are extremely time consuming, as are T_1 ones. Nevertheless, T_{2r} (where the ***r*** index stands for ***residual***) can be estimated from the signal linewidth [15-16], avoiding additional NMR experiments. In paramagnetic systems, the linewidth can be written as a function of the hyperfine coupling constant A/ħ, the spin-lattice relaxation time of electrons (T_{1e}) to which the nucleus is coupled and transverse relaxation arising from other effects ($T_{2a,b}$):

$$FWHM = \frac{1}{T_{2r}} = \frac{1}{T_{2a,b}} + \frac{(A/\hbar)^2 T_{1e}}{8} \qquad \text{(Eq. II-8)}$$

The term of Eq. II-8 governed by effects other than those induced by the presence of paramagnetic centers is significantly smaller than the paramagnetic contribution [17] and it appears that T_{2r} can be mostly associated with the unpaired electron spin density sitting on the metal center (T_{1e} and $A/\hbar$ terms) and is therefore depending on the metal electronic spin (i.e. the SOC). Thus, the comparison of NMR signals linewidth (or the T_{2r}) between samples recovered at the same SOC provides an easy estimation of the evolution of electrode / interphase intimacy.

In order to achieve further characterization of interphase species, ^{19}F and ^{31}P MAS NMR have been developed in this thesis to obtain complementary chemical information. In these two cases, the wider chemical shift range enables to assign spinning sidebands manifolds to the different fluorinated and/or phosphored species such as LiF and fluorophosphates ($LiPF_6$, Li_xPF_z, RPO_yF_z). As part of this work, the use of ^{7}Li, ^{19}F and ^{31}P MAS NMR, was made quantitative through the implementation of the empirical calibration method presented hereunder.

I.3. ^{7}Li, ^{19}F and ^{31}P MAS NMR quantification method [paper IV]

I.3.1.Description

The spin-counting approach, initially developed for the strongly dipolar-coupled proton networks, is typically used to directly count the number of chemically bonded (through the scalar coupling) or spatially close (through the spin–spin dipolar interaction) neighbours and to estimate the number of nuclei involved in finite size clusters [18, 19]. This approach consists in the use of a solid echo (90°x-τ_{dip}-90°y) sequence prior to a MQ preparation period. This solid echo provides a convenient way to select out isolated, strongly coupled spins by setting evolution times τ_{dip} much longer than the effective T_1 of the weakly coupled multispin

system. Nevertheless, in the case of paramagnetic materials dominated by electron-nucleus dipolar interactions several orders of magnitude stronger than nucleus-nucleus dipolar interaction, this method becomes non-trivial. The fast decay of the magnetization, in particular, prevents the use of long selective τ_{dip}. Moreover, our point is to quantify surface species deposits with size that cannot be compared with those of small clusters (see section 3) rather than to estimate the size of possible clusters. The species on the surface of the electrode active material and resulting from electrolyte decomposition can be present under the form of layer, discrete deposits without any fixed size or shape and contain in general several organic and inorganic species [20]. Therefore, we rather opted for a more direct and straightforward method, through NMR calibration – or titration – curves using several series of mixtures of $LiNi_{1/2}Mn_{1/2}O_2$ (LMN) with known precise amounts of diamagnetic lithium-, fluorine-, and/or phosphorus-containing species namely $LiPF_6$ and LiF with natural abundance (92.5 % for ^{7}Li, 100% for ^{19}F and ^{31}P). These two model compounds were chosen because they are the most likely to be found on the surface of the electrode material. Other fluorophosphates, such as PF_5, POF_3 or $Li_xPO_yF_z$ displaying ^{19}F resonances close to that of $LiPF_6$ [21], have been identified as intermediate or final products of the decomposition of the electrolyte but have never been obtained pure and separately.

The interest of this simple method lies above all in the possibility to compare directly the amount of Li, F and P nuclei deduced from intensities integrated from ^{7}Li, ^{19}F and ^{31}P MAS NMR spectra respectively, enabling to estimate the amounts of the various species contained in the interphases and comprising at least one of these elements. **Figure II-3** displays the results of ^{7}Li, ^{19}F and ^{31}P NMR signals quantification, and the equations resulting from the experimental data fitting. Please note that the experimental data points used to draw the calibration curves and the corresponding equations were obtained only from $LiNi_{1/2}Mn_{1/2}O_2$ mixed with $LiPF_6$ or LiF. Data points obtained in the case $LiNi_{0.4}Mn_{1.6}O_4$, $LiFePO_4$ and silicon were added later on the graphic in order to validate the calibration curves for the quantification of ^{7}Li, ^{19}F and ^{31}P nuclei involved in the interphase for other types of electrode materials.

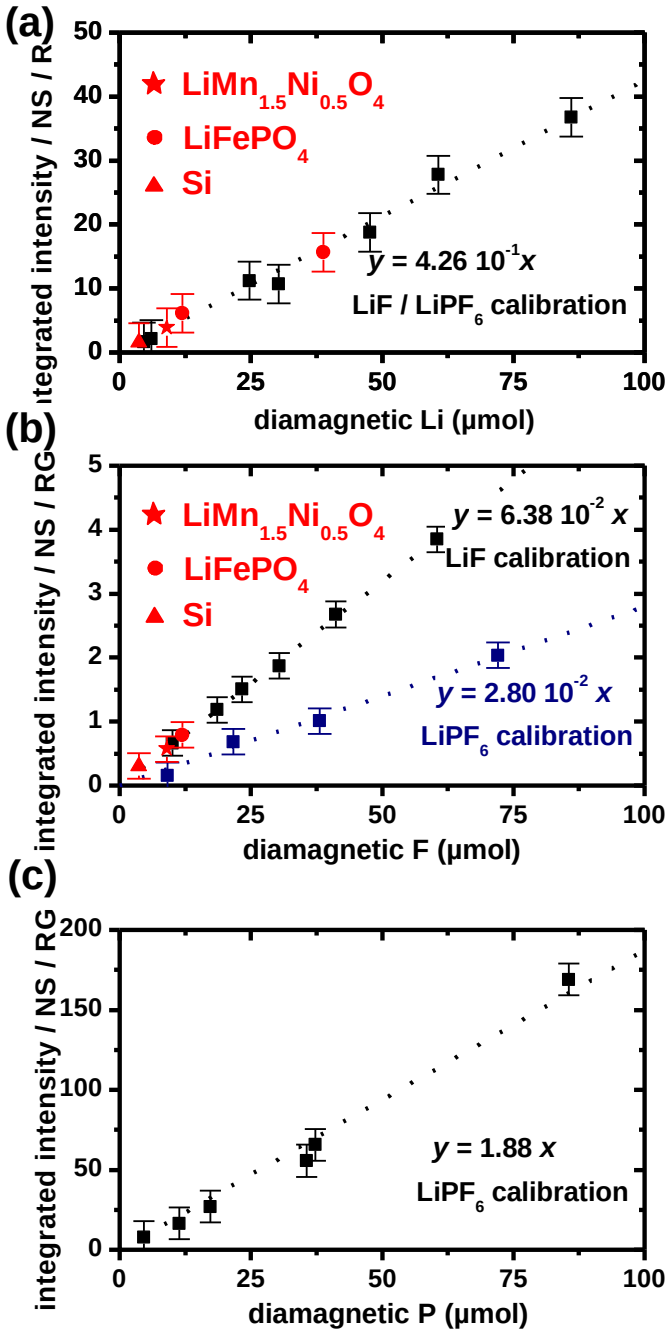

Figure II-3. ^{7}Li (a), ^{19}F (b) and ^{31}P (c) NMR signal calibration curves employed in this study and obtained from mixing various diamagnetic compounds with $LiMn_{0.5}Ni_{0.5}O_2$. Extra data points in red from other electrode materials - $LiFePO_4$ (dots), $LiMn_{1.5}Ni_{0.5}O_4$ (stars) and Si (triangles) - show a good match with linear fitting curves.

I.3.2. Case of fluorine

While ^{7}Li NMR calibration curve, obtained from single pulse experiments, includes both points obtained from LMN-LiF and LMN-$LiPF_6$ mixtures, demonstrating the straightforward applicability of such quantification method to any diamagnetic lithiated

species, ^{19}F NMR intensities integrated from LMN-LiF and LMN-$LiPF_6$ spectra after a Hahn echo clearly display different intensity losses. Spin-spin relaxation breaks the phase coherence created by the initial 90° pulse and causes the transverse magnetization to decay at T_2^{*-1} rate. This dephasing, as a consequence of the fluctuating magnetic field, is not refocused by the 180° pulse.

The NMR intensity of each resonance on the echo spectrum will then depend on the value of its T_2^*. Echo spectra obtained for samples containing species with significantly different T_2^* are usually not quantitative and the relative amount of these species cannot be directly deduced. A large difference in T_2^* between LiF mixed with LMN 1w% ($2.2.10^{-4}$ s) and $LiPF_6$ mixed with LMN 1w% ($0.97.10^{-4}$ s) was measured by Spin-echo measurement. Nonetheless, the integrated intensities of the corresponding NMR signals vary linearly with the known amounts of LiF and fluorophosphates, respectively. Thus, two calibration curves with very distinct slopes are obtained, enabling to quantify LiF and fluorophosphates, respectively. As illustrated by the two distinct correlation coefficients determined for ^{19}F MAS NMR calibration, multiple factors affect the NMR experiment sensitivity.

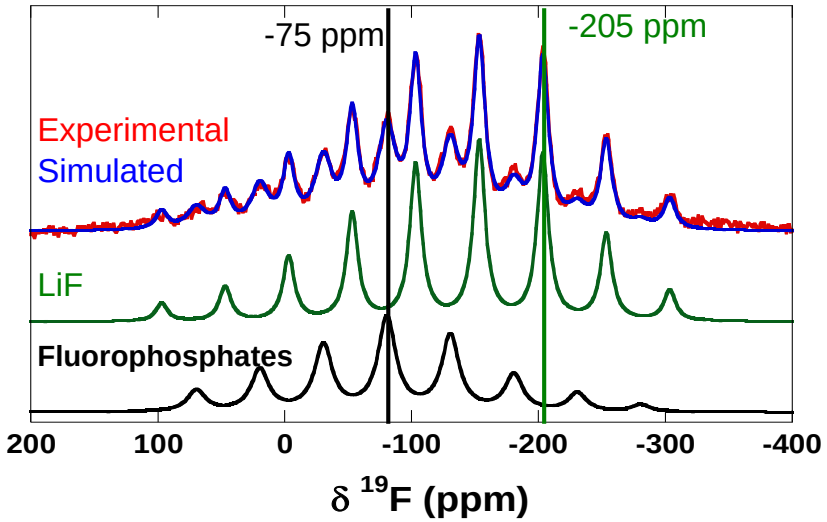

Figure II-4. Example of ^{19}F MAS NMR spectrum and its simulated decomposition in Dmfit software [18]. Only the MAS frequency is constrained.

When analyzing spectra of stored or cycled samples containing these species, the two obtained calibration curves enable the distinct quantitative detection of LiF vs. fluorophosphates (**Fig. II-3b**). The large chemical shift difference (-204 ppm and -70 ppm for LiF and $LiPF_6$, respectively [21]) combined to an appropriate MAS frequency (23.5 kHz or 27 kHz) enables to decompose experimental ^{19}F MAS NMR spectra into different sets of spinning sidebands, assigned to LiF and fluorophosphates ($LiPF_6$, Li_xPF_z, RPO_yF_z) as shown

on **Figure II-4**. In spite of its dependence on the experimental set-up and acquisition parameters, the interest of this purely empirical method is its easy implementation by the operator.

I.3.3. Use of NMR quantification for electrode/electrolyte interface studies

When recording the MAS NMR spectra of $LiNi_{1/2}Mn_{1/2}O_2$ positive electrode materials after storage or cycling in electrolyte, the intensities integrated from each set of spinning side-bands can therefore be converted into a molar amount of lithium, fluorine (in LiF or fluorophosphates) or phosphorus using the corresponding calibration coefficient and reported to µmol of surface nuclei per g or m² of active material. This latter unit ($mmol.m^{-2}$) would require normalizing the results taking into account their specific surface area, as determined by the BET method for instance. Although there is no clear evidence whether the BET surface area corresponds to the electrochemical surface area in the battery, it appears extremely convenient to compare the surface reactivity of different electrode materials [22] or materials obtained through different synthetic routes [6].

It should also be noted that these calibration curves could match very well with extra points resulting from the mix of diamagnetic matter with other paramagnetic compounds such as $LiFePO_4$ and spinel $LiNi_{0.5}Mn_{1.5}O_4$ as shown in **Figure II-3** (red extra points) regardless the dipolar interaction / bulk paramagnetism due to the different transition metals contained in the electrode material or their different oxidation states. The dominant effect of the strong electron-nucleus dipolar interaction is to distribute the intensity over a narrow or broad frequency span depending on the distance/intimacy between surface species and paramagnetic electrode material [3]. This implies that the correlation coefficients obtained remain valid to study different electrode/electrolyte interphases, in the charged and uncharged states. This is confirmed by experiments performed on silicon (in this case, the absence of unpair localized electrons leads to a typical quadripolar ^{7}Li lineshape) since the integrated intensities deduced from experimental data fit well the calibration curves (**Fig. II-3**).

I.4. Concluding remarks

In the case of electrode materials containing transition metals with unpaired electrons, in addition to the chemical composition (obtained from chemical shift), the predominance of the distance dependent electron-nucleus dipolar interaction make it is possible to extract physical or topological information regarding the interphase. Especially in the case of ^{7}Li

NMR, the advantage of this method over other surface analytical techniques lies clearly in the efficient separation of surface signal from paramagnetic bulk signal, allowing the extraction of surface information including intimacy between bulk material and surface phase.

In addition to this qualitative information, the implementation of empirical calibration of ^{7}Li, ^{19}F and ^{31}P MAS NMR spectra, carried out on the $LiMn_{1/2}Ni_{1/2}O_2$, has proven its ability to monitor quantitatively interphasial species on different active materials and will also be roped in all along this thesis.

As represented in **Figure II-5** and extensively discussed later on, NMR allows probing selectively the whole interphase but hardly can differentiate interphasial species whereas more classical XPS probes a small area of the sample (0.7mm×0.3mm) that can include surface contamination and/or bare electrode material. Although the sketches drawn in Figure II-5 are not scaled, it has to be added that contrary to NMR, the XPS analysis is limited by the penetration depth of the X-rays (5-10 nm in our case). Despite these drawbacks, XPS gives valuable chemical information, detecting not only elements but almost any functional group in the interphase (**see Appendix 1**). The combination of both techniques leads us to the characterization of electrolyte decomposition products in the interphase of positive electrodes, which is both qualitative and quantitative.

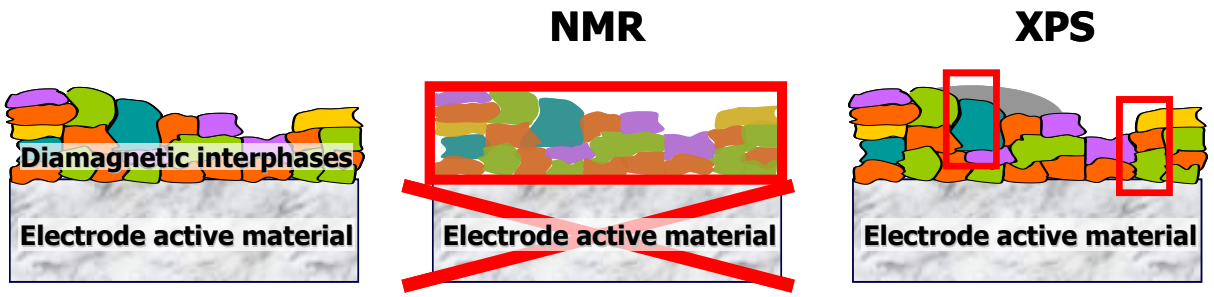

Figure II-5. Schematic illustration of XPS and NMR complementarity in the investigation of interphasial species.

II- INTRODUCTION TO EELS APPLIED TO ELECTRODE MATERIALS AND ELECTRODE / ELECTROLYTE INTERPHASES

Electron energy loss spectroscopy (EELS) in a transmission electron microscope (TEM) has proven a powerful tool for nanoscale characterization. In the field of lithium battery electrode materials, it is noteworthy that all proposed insertion mechanisms for lithium in $LiFePO_4$ are based on EELS or HRTEM observations [23-25]. Recent investigations of overlithiated layered oxides also make profit of EELS to highlight surface structure modifications upon lithium extraction [26, 27]. Similarly to NMR, most of reported studies deal with the local investigation of active bulk materials although examples exist of TEM/EELS characterization of the SEI layer formed on graphite electrodes [28, 29].

In the frame of this work, not only did we use TEM to illustratively probe the interphase of positive electrode materials, but we also considered EELS as a complement to NMR to perform quantitative elemental analysis, taking profit of the spatial resolution to highlight chemical inhomogeneities within the interphase depth.

II.1. Theoretical considerations

II.1.1. Principle of detection

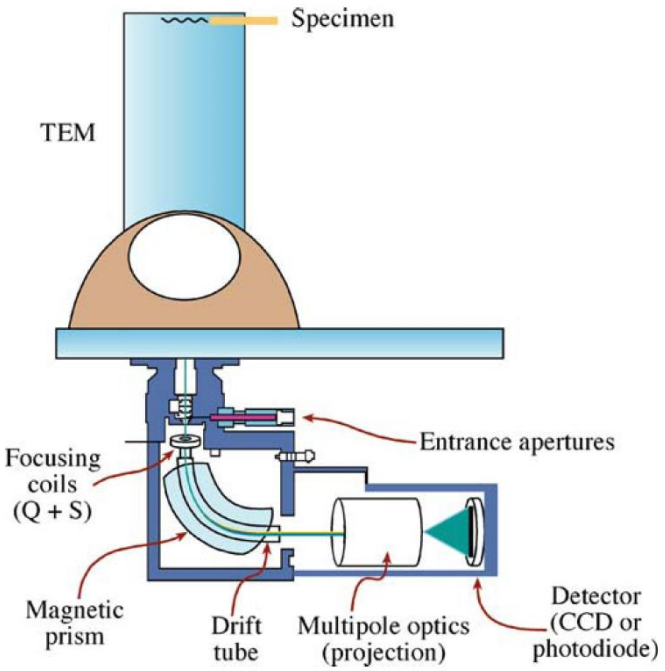

Figure II-6. Scheme of an EELS spectrometer equipped with a CCD detector

When, in a TEM, high-energy electrons are transmitted through a thin specimen there is a probability of both inelastic and elastic scattering. In the EELS spectrometer, the transmitted electrons are separated by a magnetic field according to their kinetic energy and an energy loss spectrum is detected on a charge-coupled device (CCD) camera, showing the scattered intensity as a function of the decrease in kinetic energy of the fast electrons (**Fig. II-6**). The excitation spectrum of the material can be therefore deduced from an EELS spectrum.

II.1.2. Interactions giving rise to EELS spectrum

A typical spectrum, obtained from a sample of $LiNi_{1/2}Mn_{1/2}O_2$, is shown in **Figure II-7.** The EELS spectrum can be divided into two regions that contain information about the sample: the low-loss region (from 0 to approximately 50 eV) and the core-loss region (50 eV and above). These two regions are actually acquired separately, as attested by the break in the energy loss axis, due to the large scale difference of the corresponding interactions.

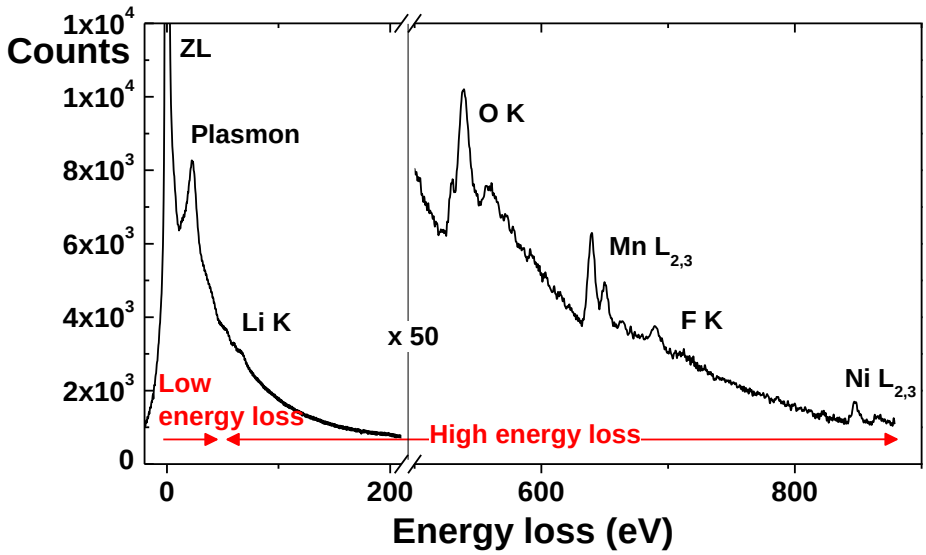

Figure II-7. EEL spectra taken at the interface of $LiNi_{1/2}Mn_{1/2}O_2$.

In the low-loss region the predominant feature is the zero-loss peak (ZLP) containing no useful analytical information in itself. Indeed, the ZLP contains all primary electrons that did not undergo a noticeable energy loss during the transmission through the sample. Nonetheless, the width of the ZLP being mainly attributed to the energy spread of the electron gun, its FWHM is commonly accepted as a measure of the energy resolution of the spectrometer (around 1.8 eV for a typical dispersion of 0.3 eV/channel in our experiments). The low-loss spectrum exhibits a number of different excitations such as plasmons (collective

excitation of the valence electrons), interband transitions (excitations of electrons from the occupied valence states up to unoccupied conduction states), intra-band transitions, excitons, relativistic loss and low-lying core state excitations [30]. As a result, this region of the EELS spectrum can be tricky to interpret and generally requires reference materials and/or DFT calculations. The information accessed from this range of the EELS spectrum comprise the local variation of density of valence electrons, the relative thickness of the probed area and also the real and imaginary parts of the local dielectric function from which the local optical indexes (absorption and refraction) can be deduced.

The core-loss region is dominated by a smoothly decaying background and element-specific core excitations. These core excitations are caused by the excitation of an atomic core-state of an atom in the sample to an unoccupied higher-lying state of the crystal or even a free electron state. The energy position of these core-state excitations is determined by the difference in core-state energy and the energy of the first free-state and enables a sensitive discrimination between different elements. Therefore EELS spectra can directly be used for qualitative analysis of the local chemical composition and also for quantitative analysis after removal of the background as detailed in the following.

At the excitation edge, and approx. 50 eV above this edge, important intensity variations are observed and referred to ELNES (Energy Loss Near Edge Structure). These fine structures correspond to electronic transitions from the core state level up to the unoccupied states and therefore are sensitive to changes of bonding and oxidation state in solids. Hence, ELNES enables analysis of the chemical bonding and oxidation state of a particular compound with high spatial resolution. A practical method of phase identification is to use ELNES as a finger print by comparing the fine-structures recorded from an unknown phase with those measured from reference materials of known structure and stoichiometry.

In this work, to investigate the interphase grown at the surface of active material grains and track the possible fine surface structure changes within the grains, we focused our attention on the core-loss region of the EELS spectrum. However, for each core-loss analyzed, a low-loss spectrum was also recorded on the same area of the sample to correct the former from multiple scattering. This phenomenon occurs when an electron looses energy to more than one excitation process when interacting with the sample and results in a blurring of the experimental spectrum with a redistribution of counts to higher energy as shown in **Figure II-8**. Removal of multiple scattering is of primary importance to study the shape of the

excitation edge (ELNES) and allows for comparison spectra taken from different samples or from different regions of the same sample.

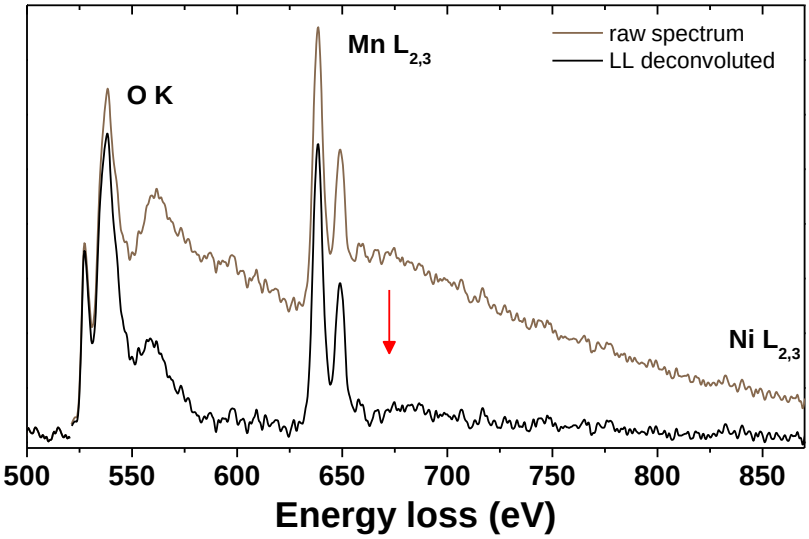

Figure II-8. Core loss EEL spectra of $LiNi_{1/2}Mn_{1/2}O_2$ after deconvolution by the ZL and background subtraction, before and after deconvolution by the low loss spectrum.

II.1.3 Quantitative elemental analysis

Elemental quantification is based on the analysis of the core edges. First of all, it is necessary to extract the edge signal from the superimposed spectral background (usually by modeling the preedge background with an inverse power law and extrapolating it into the edge region of the spectrum).

Consider two elements *A* and *B* detected in the EELS spectrum, the integrated intensity I_A, characteristic inner-shell signal of A, is proportional to $N_A \sigma_A I_0$ where I_0 is the intensity of incident beam, N_A the number of A atoms exposed to the incident beam and σ_A the cross-section per atom for ionizing an inner-shell electron *A*. In most microanalytical problems we are more interested in relative numbers of atoms *A* and *B* rather than their absolute numbers. The atomic ratio is simply given by:

$$\frac{N_A}{N_B} = \frac{I_A}{I_B} \cdot \frac{\sigma_B}{\sigma_A} \qquad \text{(Eq. II-9)}$$

Because it is experimentally difficult to integrate the core edge signal over all energy losses we choose a given energy range $I_A(\Delta E)$ and $I_B(\Delta E)$ measured over a ΔE-large energy window above each edge as shown in **Figure II-9**. Since the inelastically scattered electrons are collected inside semiangle β, usually greater than the probe convergence semiangle α.; the cross-sections are partially integrated in energy and angle, over ΔE and β,

respectively. The atomic ratio, as calculated by the quantification tool of Digital Micrograph software (Gatan) for instance, is therefore given by:

$$\frac{N_A}{N_B} = \frac{I_A(\Delta E)}{I_B(\Delta E)} \frac{\sigma_B(\beta,\Delta E)}{\sigma_A(\beta,\Delta E)} \quad \text{(Eq. II-10)}$$

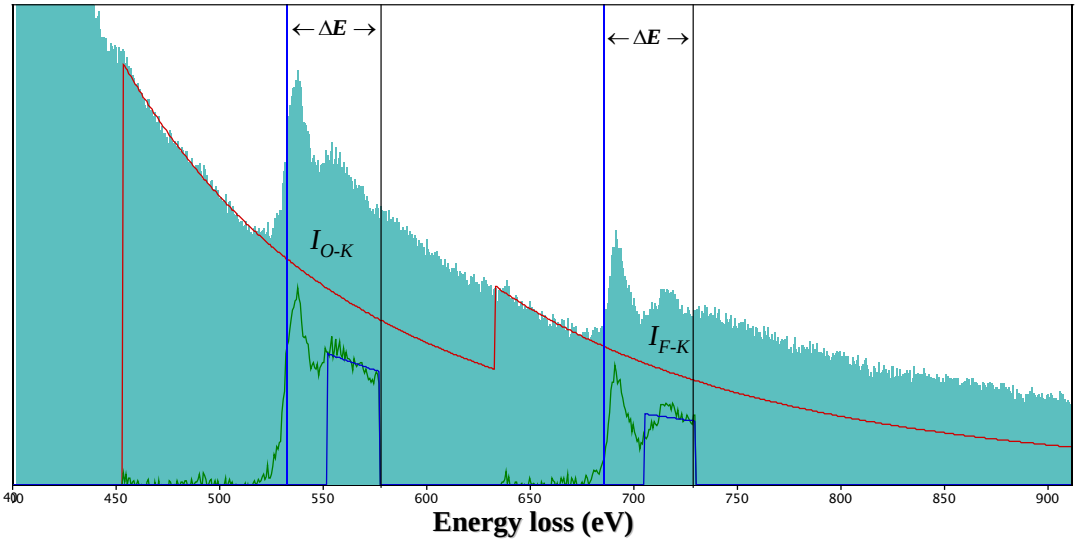

Figure II-9. Principle of EELS quantitative elemental analysis

The precision and accuracy of such analyses are influenced by several factors, and most importantly by the atomic model considered to calculate ionization cross-sections which is known to work poorly in the case of edges with high quantum numbers (M, N, etc.) [31]. In the present work, repeated quantification performed on bulk $LiNi_{1/2}Mn_{1/2}O_2$ however proved satisfying in the estimation of O/Mn/Ni ratio based on the integration of O-K, Mn-$L_{2,3}$ and Ni-$L_{2,3}$ edges; and a precision of 10% and 20% is assumed here, in the case of L and M edges, respectively.

II.2. Practical considerations

This subsection has been devised as an answer to TEM detractors as well as an advice to prospective users. Each characterization technique has its *DOs* and *DON'Ts*, the latter being particularly numerous in the case of TEM.

As a local imaging and analytical tool, TEM/EELS provide a unique standpoint to observe topological and chemical inhomogeneities within a sample, down to a 1.5 nm resolution in the best cases. The price to pay for such spatially resolved studies consists in repeated experiments, as the only way to ensure the results representativeness. Although this precaution is common to any experimental technique, it is of primary importance for microscopy, where results are strongly dependant on the experimenter "free will". Several

critical factors must be also taken into account when performing TEM analyses in the field of lithium battery electrode materials in order to preserve the sample integrity. A non exhaustive list of such precautions is presented here.

II.2.1. General precautions

Lithium being an extremely light element, its evaporation under the electron beam is well known [32]. This phenomenon can easily be underestimated, as it often occurs with no optically obvious degradation of the grain. Besides, the thinner the sample, the easier electron beam can reduce transition metal cations [33]. The grains surface is therefore more susceptible to observe beam induced artificial fine structure changes. For instance, the intensity of the pre-peak on O-K edge observed at 77 K in **Figure II-10** is characteristic of the oxygen environment in $LiNi_{1/2}Mn_{1/2}O_2$ and the Mn L_3/L_2 ratio corresponds to Mn(IV). In comparison, the spectral features observed at room temperature indicate an evolution of oxygen environment together with manganese reduction. This risk of material alteration can be avoided by limiting sample irradiation (in our case by using accelerating voltage as low as 100 kV and probe size larger than 10 nm) but also by lowering the experimental temperature down to 77 K with liquid nitrogen.

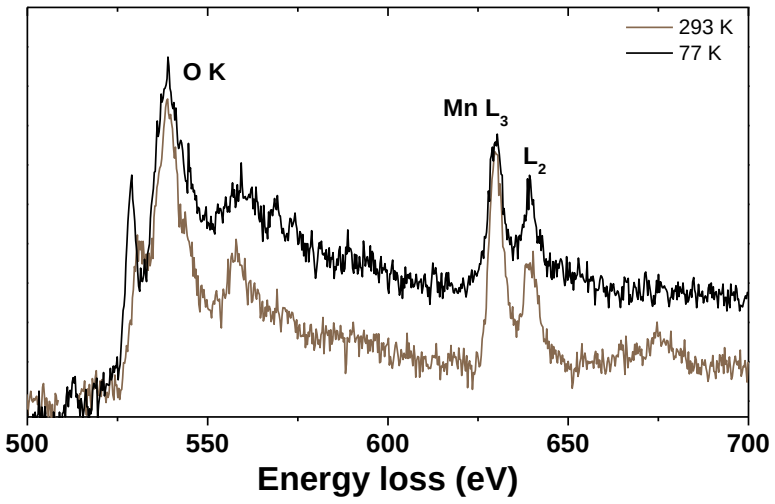

Figure II-10. O-K and Mn-$L_{3,2}$ edges measured at the surface of a $LiNi_{1/2}Mn_{1/2}O_2$ particle at room and liquid nitrogen temperature.

Other microscope settings, such as the condenser and objective lenses are more or less dictated by the necessities in terms of convergence and collection angles, respectively. Prolonged beam exposure would necessarily result in lithium evaporation but considering our experimental setup, the combination of these three precautions proved conclusive to record satisfying spectra.

Air-sensitive electrode materials (such as Li_xSi alloys [34, 35]) involve one more experimental challenge, which can be settled with the help of an air-tight specimen holder allowing transferring samples from the glovebox to the TEM without exposing them to ambient atmosphere. However, such device, as available in the laboratory, cannot operate at low temperature and a concession has to be made; in this work for which long acquisition times (up to 60 s) were required, room temperature measurements could not be considered and therefore air-sensitive interphasial species were briefly exposed to air (~ 5 min).

II.2.2. Precautions regarding the analysis of composite electrodes

Composite electrodes consist in well dispersed active material, conducting agent(s) and binder(s), thanks to an appropriate composition and handling of the slurry. Electrode formulation may also include a calendaring step, which enhances the electrical contacts by lowering the porosity. TEM analysis, whether it aims at investigating battery failure or interphase evolution, usually requires altering the electrode microstructure. The powder is scratched apart from the current collector so as to be deposited on a TEM grid. Thus, new surfaces are created and the network observed under the microscope cannot accurately represent the "real" architecture of the electrode. Progress in TEM preparation methods are under way, and alternative techniques, more respectful of the electrode integrity, lie in the cutting of extremely thin slices of electrode, known as sections, by focused ion beam (FIB) or ultra microtome (recently arrived in our lab).

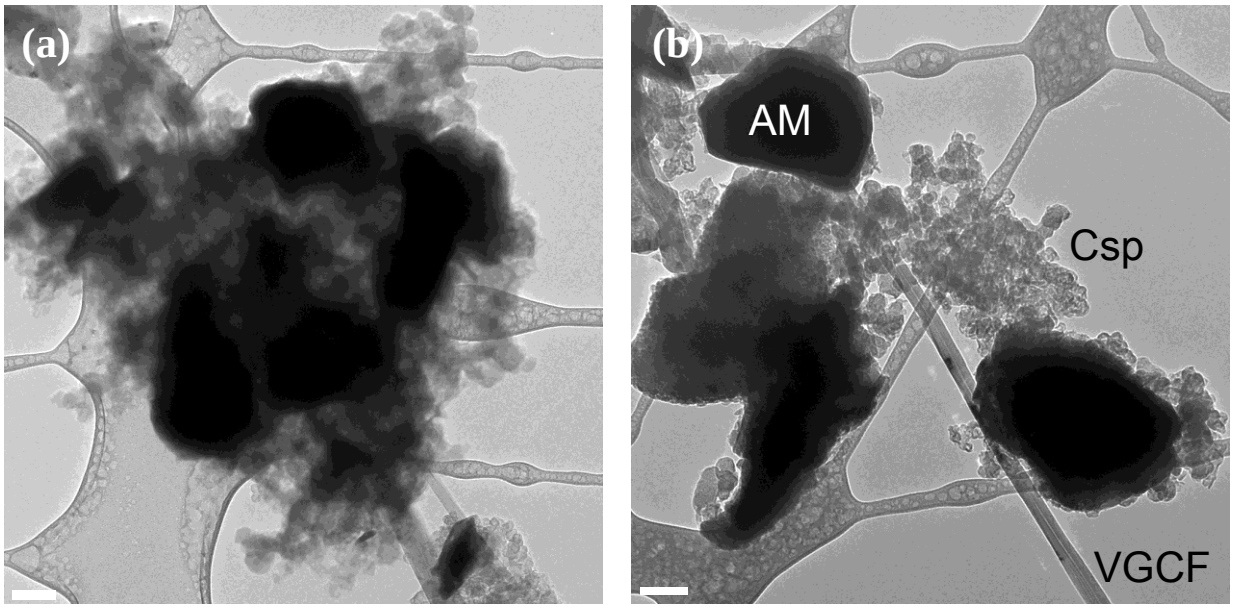

Figure II-11. Powder scratched from a working electrode after cycling, before (a) and after (b) CMC binder degradation under the electron beam. Images were taken within a minute.

Besides, lithium-containing active material is not the only beam-sensitive component and a major issue when dealing with composite electrodes lies in the binder burn out, even at 77 K (**Fig. II-11**). Not only are the remaining active material and conducting agents thus observed out of their pristine agglomeration state, but the investigation of interphasial deposits becomes even trickier, as organic species tend to depart along with the binder burn out.

For the different reasons exposed above, TEM/EELS analyses of interphasial deposits on positive electrodes were performed mostly on pure active materials, after simple contact (by soaking) with electrolyte, or after cycling the powder in a battery without any binder or conductive additive. In fact, carbon black being extremely light, a small mass percentage in the formulation results in an important volume (see **Fig. II-11b**) and further complicates interphasial studies.

II.2.3. Precautions regarding the analysis of interphases

Pioneering the chemical analysis of interphases by TEM, Naji *et al*. [29, 38] identified carbonates and LiF through the use of electron diffraction and EELS on crystalline SEI products (**Fig. II-12a**).

However, they seem to have considered the SEI as chemically homogeneous and highly stable. Experiments conducted in this thesis would rather lead to believe they observed the products of beam degradation instead of untouched SEI. Indeed, as shown in **Figure II-12b**, crystallization was typically observed under the electron beam at room temperature. The cubic morphology of the crystals could be assigned to LiF thanks to its electron diffraction pattern and recognizable Li-K edge [33]. However, under the careful analysis conditions described above, no LiF crystal could be highlighted, implying its amorphous state in the interphase.

The most critical issue faced in this thesis, common to all studies of that kind is often expressed through the question: **"to wash or not to wash?"** which arises before any surface characterization. There is indeed strong evidence that rinsing the powders/electrodes from the excess electrolyte partially (or sometimes even totally) removes the interphase [37, 38] but leaving it would imply observing/accounting for this excess electrolyte and the interphase alike. Once again, a compromise has to be made and as for the present work, electrodes have always been gently rinsed with a single drop of DMC and dried under vacuum at 90°C for 4 h. The same procedure has been used for all samples prior to any characterization in order to

ensure, failing total integrity of the interphase, the maximal reproducibility in our experiments as well as the observation of trends within series of samples.

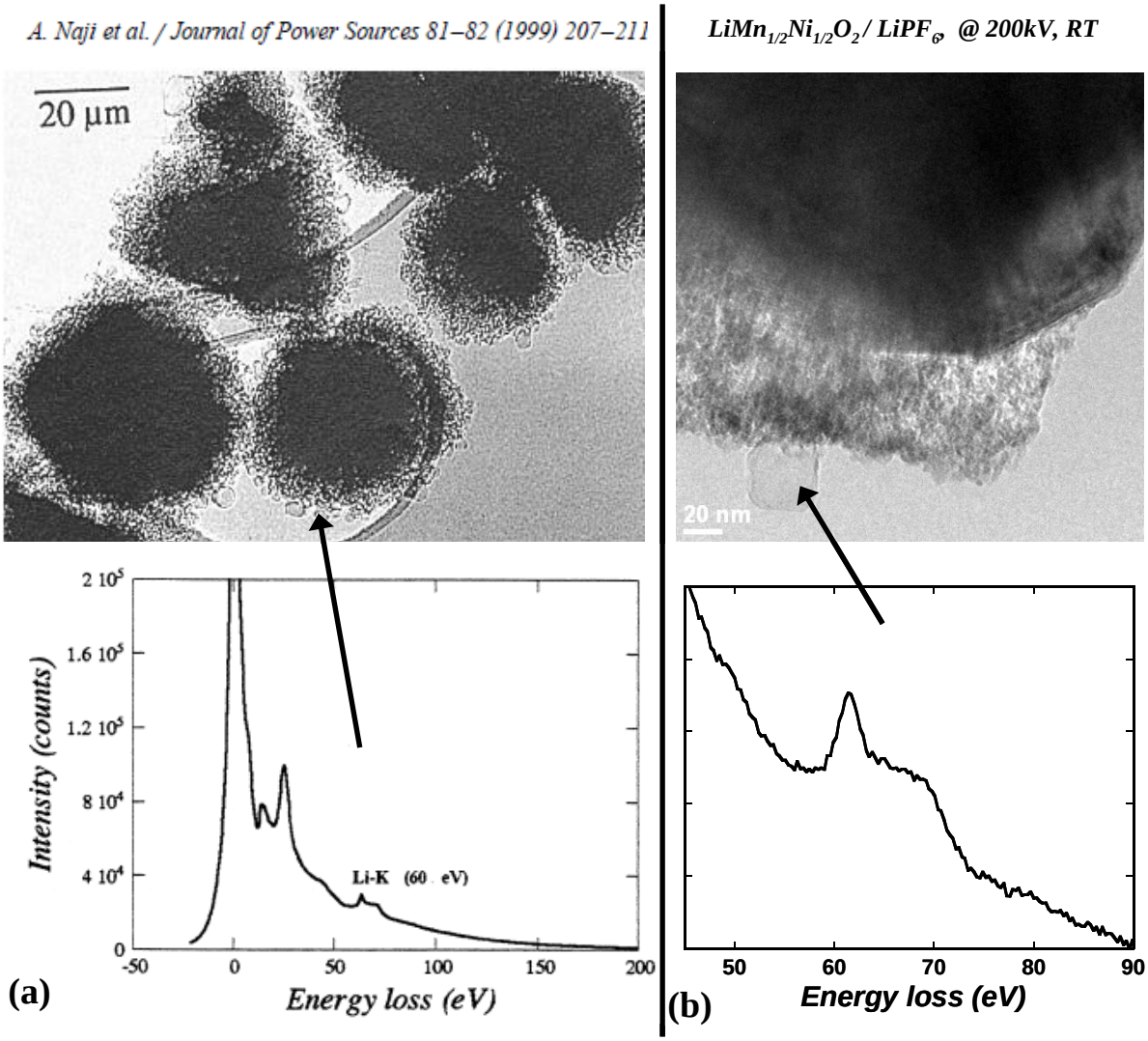

Figure II-12. TEM micrographs of beam induced crystallization of the interphase and corresponding EEL spectra identifying LiF. (a) Reproduced from ref [36], (b) experimental observation under similar conditions.

Arising from this tendency of the interphase to detach from the grains surface upon contact with solvents, it stands to reason that TEM preparation must circumvent their use to disperse sample grains. **Figure II-13** illustrates this idea of *DON'Ts vs. DOs* in TEM characterization: the same sample was prepared by sonicating the powder in ethanol, analyzed using a TEM operating at 300 kV at room temperature, leading to the complete removal of the interphase (**Fig. II-13, left**) or by dry preparation, and analyzed using a TEM operating at 100 kV at liquid nitrogen temperature, then allowing the proper observation of the interphasial deposits (**Fig. II-13, right**).

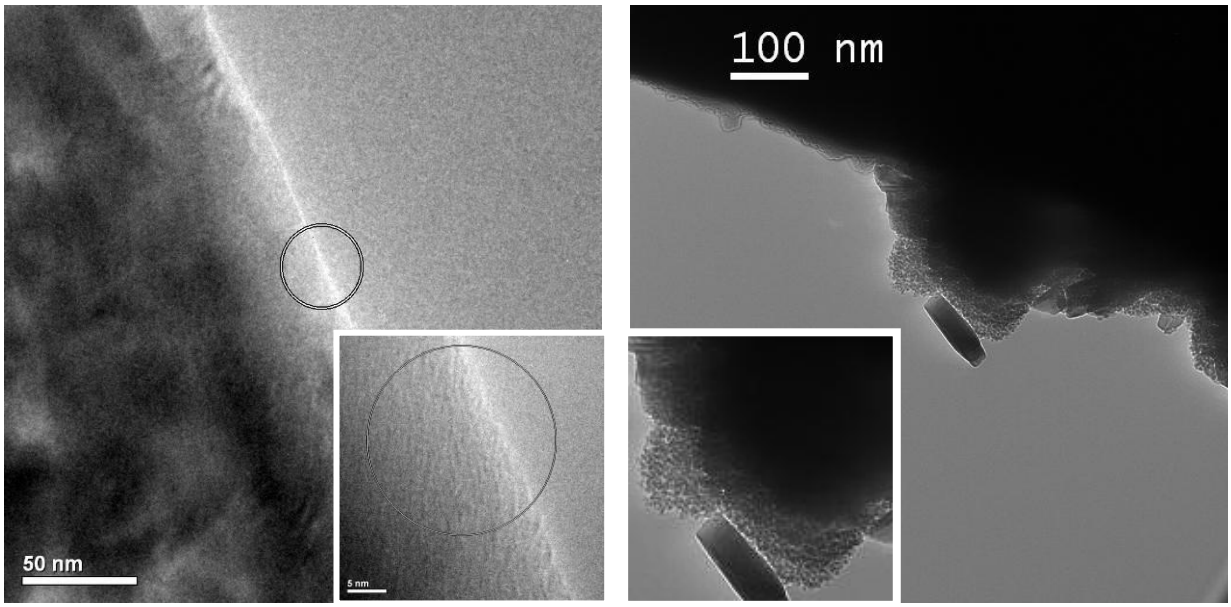

Figure II-13. Representative TEM micrographs of the same sample of $LiMn_{1.6}Ni_{0.4}O_4$ after soaking in $LiPF_6$ electrolyte prepared and analyzed under different conditions: (left) and (right) are made explicit in the text.

II.3. Concluding remarks

As further discussed in the light of experimental results, it is never possible to completely rule out the interphase alteration during the sample preparation for TEM. We believe however having taken all the possible care to avoid misleading observations, the brief air exposure should therefore be kept in mind as a source of possible oxygen overestimation.

The following table lists the main parameters typically used in our TEM/EELS experiments:

Accelerating voltage	100 kV
Resolution	1.8eV / channel
Dispersion	0.3 eV / channel
Probe size	10 nm
Exposure times	20 - 60 s (CL) 0.1 - 0.2 s (LL)
Convergence angle	1.4 mrad
Collection angle	18 mrad

Table 1. HF2000 microscope settings used in this work to characterize electrode / electrolyte interphases

III- EXEMPLE: INVESTIGATION OF THE $LiNi_{0.5}Mn_{0.5}O_2$ /ELECTROLYTE INTERPHASE

This section takes up a "case study" published in *Solid-State NMR* [**paper IV**]. Its presence in this introduction chapter is justified by the unique combination of characterization techniques developed during this thesis; namely high field multinuclear NMR and EELS quantification dedicated to electrode/electrode interphase studies. Concepts and reasoning proposed in the discussion properly characterize the philosophy of the work conducted in this thesis.

III.1. Introduction

In the present work, the nature and amount of the interphases grown upon storage at 25°C and 55°C are compared in the case of $LiNi_{1/2}Mn_{1/2}O_2$ with commonly used $LiPF_6$ EC/DMC electrolyte.

The implementation of empirical quantitative calibration for ^{7}Li, ^{19}F and ^{31}P MAS NMR has been presented in section III-3. In order to resolve ambiguities arising from XPS, this NMR-based quantification method is here combined with transmission electron microscopy (TEM) and electron energy-loss spectroscopy (EELS). We make use of the spatial resolution offered by these techniques to shed light on chemical inhomogeneities within the interphasial layer and unravel the architecture of the interphase.

III.2. Electrode/Electrolyte interphase along storage: classical characterization and related challenges

III.2.1 Experimental

Illustrating samples of $LiNi_{1/2}Mn_{1/2}O_2$ (see chapter 3, I.1, p. 82 for preparation details), LMN-25 and LMN-55, were prepared by the aging of the active material for one month in $LiPF_6$ (1M in EC:DMC, 1/1 in volume) electrolyte at 25°C and 55°C respectively. Typical amounts used for these experiments were 50 mg of LMN soaked in 0.5 mL of liquid electrolyte; to reproduce the active mass / electrolyte volume ratio of our Swagelok cells. Samples were recovered after centrifugation to eliminate the supernatant electrolyte. Samples were then rinsed with 0.5 mL of DMC, centrifuged again and dried at 90°C under vacuum for 4 hours before ex-situ analysis.

III.2.2. Microscopic observation

The scanning electron microscopy (SEM) pictures of the samples as prepared and after one month aging are displayed in **Figure II-14**. The estimated grain size is about 200 nm, and it is obvious on these pictures that the surface of aged sample is covered by a glue-like film filling the interstices between grains. Further TEM observation enables to shed light on the topological distribution of interphase grown on the $LiNi_{1/2}Mn_{1/2}O_2$ surface.

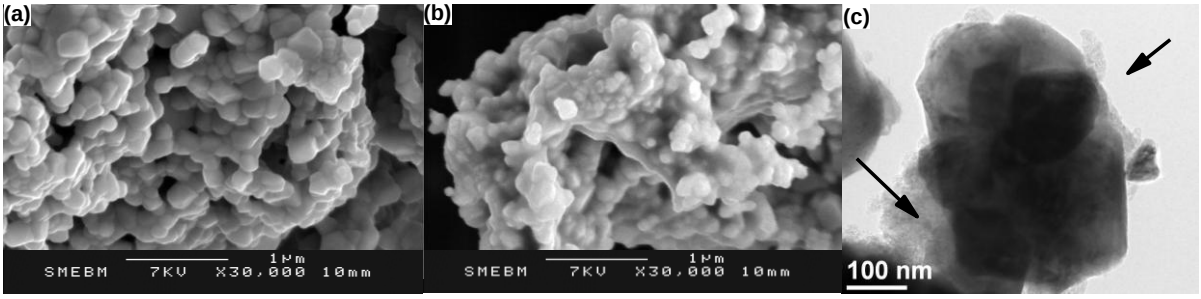

Figure II-14. SEM observation of pristine $LiNi_{1/2}Mn_{1/2}O_2$ (a) and sample LMN-55, aged for one month at 55°C in electrolyte (b), with corresponding TEM picture (c).

While part of the surface remains bare from any coverage, the porous deposit observed elsewhere exhibits an uneven thickness, from few nm to several hundreds nm. It is not possible to completely rule out the partial destruction of the surface layer during the soft manual grinding (to break particles aggregates) and prior to sample deposition on the TEM grid. Homogeneous grain covering was nevertheless, never observed. Moreover, it is not clear at this stage whether the contrast observed within the interphase is of chemical origin or due to thickness gradient.

III.2.3. Characterization using EIS and XPS

In order to probe the electrical properties of these interphases, EIS, as a useful *in situ* spectroanalytical technique, was performed on a fresh $LiNi_{1/2}Mn_{1/2}O_2$-based electrode as a reference and compared to electrodes stored in electrolyte. As shown in **Figure II-15**, pristine impedance only exhibits one semicircle at high/middle frequencies. Based on previous data [5], this resistance can be mostly attributed to charge transfer phenomena in agreement with the hypothesis of nonhomogeneous covering of the electrode, as seen in **Figure II-14c**. As explained in reference [5], although the dominating process was found to be charge transfer coupled with double layer formation, it was not possible to completely rule out the contribution of discrete deposits of interphasial matter that could hinder the charge transfer process and distort the observed semi-circle. In order to discuss the two phenomena together,

in the absence of a clear second semi-circle, we refer to the overall resistance as "interfacial" resistance. Storage for one month in electrolyte at 25° and 55°C leads to a significant increase of the OCV interfacial resistance, from 18 $\Omega.mg^{-1}$ to 22 $\Omega.mg^{-1}$ and 35 $\Omega.mg^{-1}$, respectively.

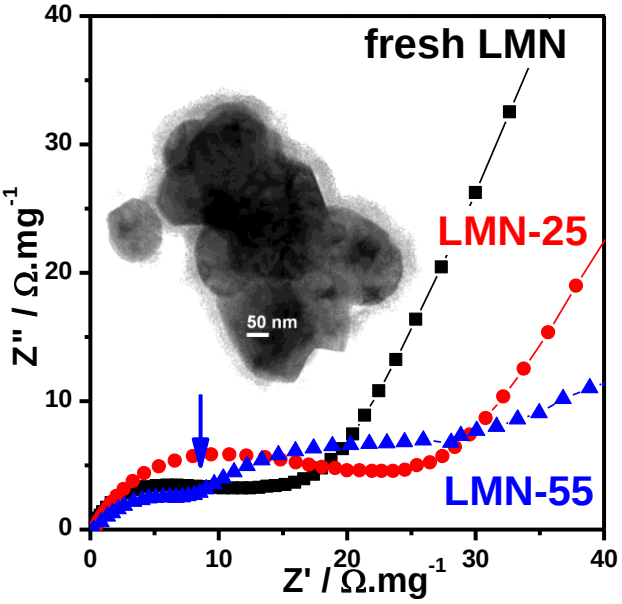

Figure II-15. Nyquist diagrams for $LiMn_{0.5}Ni_{0.5}O_2$ electrode in $LiPF_6$ 1M right after the cell assembly (black squares), after one month storage at 25°C (red dots) and 55°C (blue triangles) Insert: peculiar TEM micrograph of LMN-55 illustrating the formation of a resistive film.

After storage at 25°C in electrolyte, no evidence of a second circle is found, similarly to the pristine electrode, again in agreement with the deposition of surface species under the form of discrete agglomerates. On the contrary, the appearance of a second semicircle at high frequencies in the case of LMN-55 should imply the presence of a resistive film covering the whole surface of active material grains, in agreement with the quite homogenous surface layer remarkably observed on the TEM picture displayed in the insert of **Figure II-15**.

The chemical composition of the resistive deposits grown on LMN-25 and LMN-55 can easily be probed by XPS, which C 1s, O 1s, F 1s and P 2p core level spectra are displayed in **Figure II-16**. As previously reported [39-41], decomposition products of electrolyte salt and solvents, such as LiF, Li_xPF_z, $Li_xPO_yF_z$ and $ROCO_2Li$ can be found on the extreme surface (5-10 nm, as limited by XPS penetration depth). The elemental percentages obtained from the analysis of XPS spectra are reported in **Table II-2**.

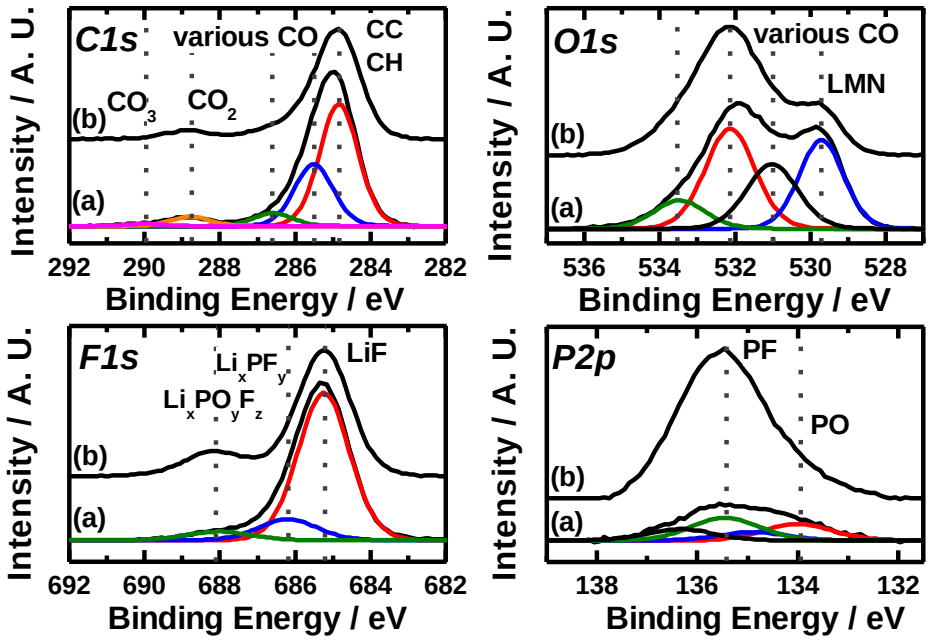

Figure II-17. XPS C 1s, O 1s, P 2p, and F 1s peaks for LMN-25 (a) and LMN-55 (b) soaked in $LiPF_6$ EC:DMC electrolyte for 1 month at 25°C and 55°C, respectively.

Element	Binding energy	Attributed species	LMN-25	LMN-55
C 1s	284.8 eV	C-C, C-H	17 %	15.5 % ↓
	285.5 eV	C-O	9 %	7 % ↓
	286.6 eV	C-O	2 %	2 %
	288.8 eV	CO_2	1.5 %	1.5%
	289.8 eV	CO_3	0.3 %	0.5 % ↑
O 1s	529.8 eV	$LiNi_{1/2}Mn_{1/2}O_2$	5 %	3.5% ↓
	531.2 eV	C-O	4 %	4 %
	532.2 eV	C-O	6.5 %	8.5% ↑
	533.6 eV	CO_3	2 %	2.5 %
L i1s	56.2 eV	Li-F, Li-O	21 %	21 %
Mn $2p_{3/2}$	642.2 eV	$LiNi_{1/2}Mn_{1/2}O_2$	1 %	0.5 % ↓
F 1s	685.3 eV	Li-F	24 %	23 %
	686.1 eV	P-F	4 %	2.5 % ↓
	688.1 eV	P-F	2 %	5.5% ↑
P 2p	134.0 eV	P-O	0.2 %	0.2%
	135.5 eV	P-F	0.3 %	2% ↑

Table II-2. Binding energies and atomic percentages deduced from quantitative XPS analyses for LMN-25 and LMN-55.

The decrease observed for the intensities of the overall Mn $2p_{3/2}$ peak and the O1s peak at 259.8 eV corresponding to the $LiMn_{0.5}Ni_{0.5}O_2$ oxide would suggest a more important covering of the material after 55°C storage, in agreement with EIS results, although no further information can be obtained on the thickness or distribution of the interphase. Regarding the contributions of interphasial species, the main constituent is obviously lithium fluorine, since fluorine under the form of LiF (at 685.3 eV) accounts for approx. 23% of the total detected nuclei.

Although the percentage of detected C slightly decreases from LMN-25 to LMN-55, this should probably not be assigned to a decreasing amount of carbonated species but rather to the evolution of fluorophosphates, whose corresponding F 1s (686-688 eV) and P2p (134-136 eV) peaks clearly increase. Since the atomic percentage of lithium is kept constant, close to that of fluorine under the form of LiF, these additional fluorophosphates are more probably found at the end of non lithiated organic compounds or polymeric chains of solvent decomposition products such as OPF_2OMe or $OPF_2(OCH_2CH_2)_nF$ [42].

III.3. Implementation of new surface analytical tools

III.3.1. Quantification of electrode/electrolyte interphases by MAS NMR

As discussed in section 1.2, the range of diamagnetic lithium chemical shifts is small in NMR, between -5 and +2 ppm; therefore it is not always possible to discriminate different diamagnetic lithium species, especially in the case of a mix spanning from inorganic carbonated / fluorinated salts to organic polymers [2, 43]. On the contrary, fluorine and phosphorus NMR offer more contrast, and enable identifying the chemical species detected on the surface of LMN-25 and LMN-55, as shown in **Figure II-18**. Hence, ^{19}F NMR shift of lithium fluoride (-204 ppm) enables not only to identify LiF as the only fluorinated species detected on LMN-25 but also to separate its contribution from that of fluorophosphates on LMN-55, at -72 ppm to -77 ppm and -84 ppm for $LiPF_6$, $R\text{-}PO_3F$ and $R\text{-}PO_2F_2$, respectively [21]. While no phosphorus is detected on LMN-25, the ^{31}P resonance observed around -20 ppm on LMN-55 can be assigned to $R\text{-}PO_2F_2$ again in agreement with liquid NMR results whereas remaining $LiPF_6$ salt would appear at -150 ppm making it easy to detect and discriminate [21].

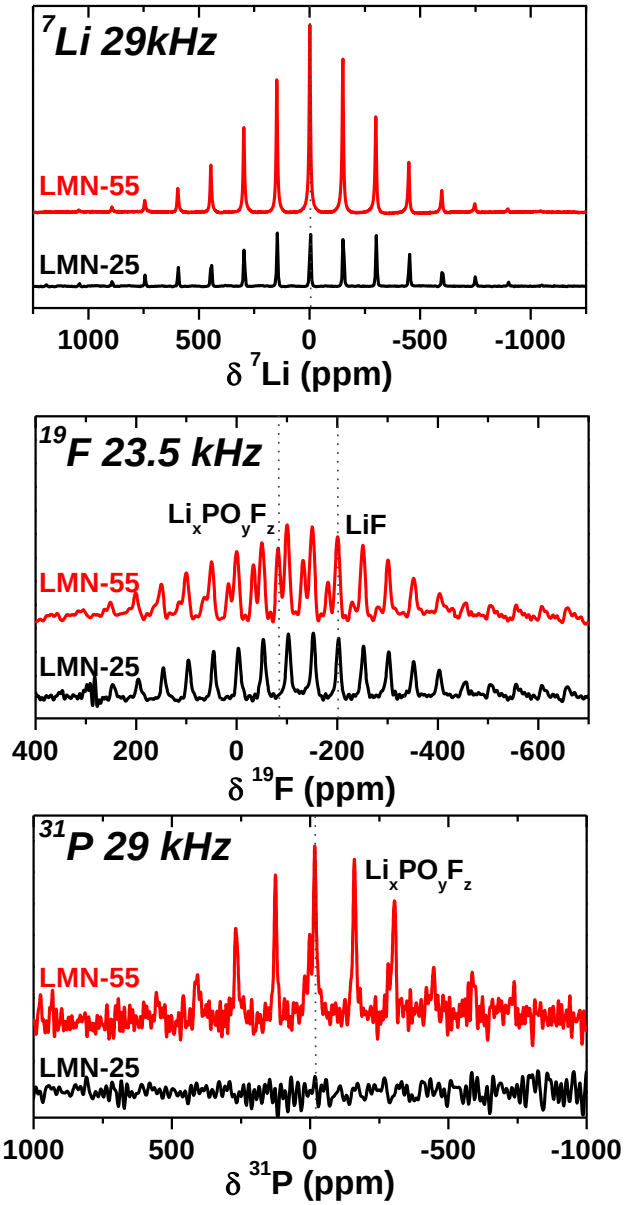

Figure II-18. ^{7}Li, ^{19}F and ^{31}P NMR normalized spectra recorded for $LiMn_{0.5}Ni_{0.5}O_2$ samples stored one month in $LiPF_6$ electrolyte at 25°C and 55°C.

As explained in chapter 2, section I-2, it has been shown that the sidebands manifold width can be linked to the strength of the electron-nucleus dipolar interaction between lithium in the interphase and paramagnetic electrode grains underneath [2, 3]. Comparing the ^{7}Li NMR spectra of LMN-25 and LMN-55, it appears that there is a factor of 4 in the full width at half height of the sidebands manifold: the fact that spectral lineshape of LMN-55 is significantly thinner suggests that additional species having a weaker interaction with the paramagnetic material are stacked on the top of initial deposits.

The interphase growth therefore not only proceeds in further covering of the surface as suggested by EIS but also in interphase thickening. In order to validate such hypothesis, we

take profit of the quantification tool described in section 1.3 to compare interphases amounts grown on $LiNi_{1/2}Mn_{1/2}O_2$ surface after aging in the electrolyte; NMR results are gathered in **Table II-3**, to be confronted with **Table II-2**. Of course, the use of a pre-acquisition delay, or a spin echo sequence, should induce some error in the quantification, but we believe that this error remains limited insofar as the calibration curves were obtained using the very same experimental settings. Besides, we do not claim having reached absolute quantification, but only approaching it closer than with any classical surface characterization technique.

	^{7}Li	^{19}F (LiF)	^{19}F (PF)	^{31}P
LMN-25	0.32 mmol/g (21%)	0.15 mmol/g (24%)	- (6%)	- (0.5%)
LMN-55	1.1 mmol/g (21%)	0.20 mmol/g (23%)	0.15 mmol/g (8%)	0.08 mmol/g (2%)

Table II-3. Quantification of ^{7}Li, ^{19}F and ^{31}P NMR spectra recorded for $LiNi_{1/2}Mn_{1/2}O_2$ samples stored one month in $LiPF_6$ electrolyte at 25°C and 55°C. Data in parenthesis are recalls from **Table II-2**.

Concerning the interphase grown on LMN-25, the fact that no fluorophosphates are detected, neither by ^{19}F nor by ^{31}P NMR implies that their signals are below the detection limit. Their detection by XPS suggests that these species, although in small amounts, are present on the external part of the interphase. Comparing the amounts of lithium and fluorine, it appears that half of the detected lithium should be found under the form lithium fluorine, therefore in the absence of measurable amounts of fluorophosphates, the second half of surface lithium could be assigned to alkylcarbonates such as CH_2CO_2Li or $ROCO_2Li$.

As probed by NMR, the difference between LMN-25 and LMN-55 in the amounts of interphasial lithiated species is particularly significant (from 0.32 $mmol.g^{-1}$ to 1.1 $mmol.g^{-1}$, i.e. +240%), compared to the evolution of lithium fluoride (from 0.15 $mmol.g^{-1}$ to 0.20 $mmol.g^{-1}$, i.e. +30%). This result might seem contradictory with estimations obtained from XPS, which sees similar atomic percentages for the total amount of Li and the amount of F in LiF in both samples. Nonetheless, since XPS only probes the extreme surface of the interphase, similar compositions might as well hide changes in the nature and/or amount of interphasial species located deeper below the penetration depth.

The detection of fluorophosphates in the interphase grown on LMN-55 by both ^{19}F and ^{31}P NMR (0.15 $mmol.g^{-1}$ and 0.08 $mmol.g^{-1}$, respectively) results in a ratio F/P ~ 2, suggesting the presence of $-PO_2F_2$ groups, whether combined with lithium or with solvent

decomposition products (OPF_2OMe, $OPF_2(OCH_2CH_2)_nF$). An interesting comparison can be made between the ratios of fluorine in LiF vs. fluorophosphates, equal to 2.9 by XPS and 1.3 by NMR techniques which are surface and bulk sensitive, respectively. This difference implies that the proportion of fluorophosphates is underestimated by XPS, meaning that these species are located in the inner part of the interphase.

III.3.2. Local investigation of electrode/electrolyte interphases using EELS

Through the use of TEM coupled with EELS, the local compositions of interphasial layers grown on $LiMn_{0.5}Ni_{0.5}O_2$ after storage in electrolyte were studied. The 500-950 eV energy loss range was used to probe O-K, Mn-$L_{2,3}$, F-K and Ni-$L_{2,3}$ edges on the same spectrum and facilitate atomic quantification. EELS spectra collected on LMN-25 and LMN-55, as well as corresponding quantification results are reported in **Figure II-19**.

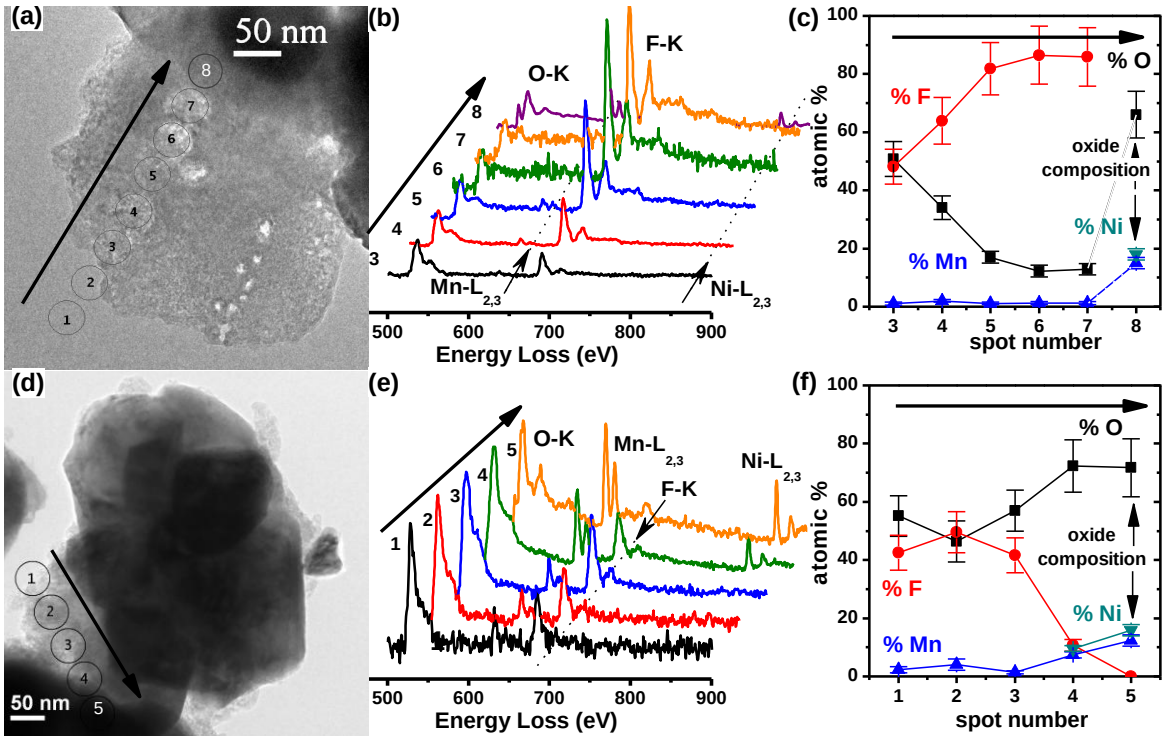

Figure II-19. EELS line scans of interphasial layer of LMN-25 and LMN-55. Spectra (b,e) and related quantification diagrams (c,f) refer to the points highlighted on the images (a,d). In these experiments, the probe size was set to 30 nm to limit beam damages.

On LMN-25, going from outside the interphase towards the electrode material, it appears that the interphase is not homogenous in composition. The F/O ratio is approx. of 1/1 on the external part of the interphase and extremely high (> 4/1) near the surface. By NMR we observed that the only fluorinated interphasial species was lithium fluorine, therefore we can infer from the atomic percentages that the inner interphase is rich in LiF while the outer

interphase comprises a mixture of less concentrated lithium fluoride with organic compounds arising from solvents decomposition. We also shed light on manganese dissolution and reprecipitation in the interphase, the Mn-L_{23} edge was indeed clearly detected far from the grain surface (**Fig. II-19b**, point 3 for instance). The cross-section for ionization of an electron in the Ni-L shell being roughly two times smaller than that of the Mn-L shell, the detection of small amounts of nickel can be tricky. ICP measurements (shown later in **Table III-2**) performed on electrolyte solutions after the storage tests highlight similar dissolution of both transition metals Therefore, the presence of few percents of manganese in the interphase might imply an equal amount of nickel, which would remain below the detection threshold.

Similar EELS line scans through the interphase grown on LMN-55 result in a different distribution of interphasial species (**Fig. II-19f**). The F/O ratio remains close to 1/1 and no LiF-rich area can be found near to the active material grain surface. The basic conclusion to these experiments is that not only there is a composition gradient within the interphase depth, but this one is strongly affected by the temperature. Higher temperature not only favors the decomposition of solvents molecules ($LiPF_6$ in EC:DMC readily decomposes at 85°C [42]) but might as well increase LiF solubility. The pristine (= inner) LiF interphase formed immediately upon soaking is therefore found partially replaced by organic lithiated compounds upon solvents degradation. The polymerization of such species results in the formation of a Li-rich film, as seen by EIS and NMR, intrinsically less resistive than the LiF-rich interphase grown at room temperature.

III.3.3 Discussion

Despite the significant increase of interphasial resistance with the storage temperature in electrolyte, there is only little difference between the compositions determined by XPS for the two stored samples. In addition, the appearance of a second semi-circle on the Nyquist plot, sign of a covering resistive surface layer, cannot be unambiguously linked to any given amount of surface species. The absolute amount of interphase cannot be determined by the XPS analysis either. Considering the spatial inhomogeneities, the limited penetration depth (max. 10 nm) does not enable to probe the whole interphase thickness although the active material remains visible on bare surface areas. In particular, such topological interphase distribution cannot be differentiated from a thin covering surface layer allowing the observation of the underlying active material. Besides, apparent proportions of chemical

species are affected by the non-linearity of penetration, sorting surface species as a function of their deepness within the interphase is not possible unless tuning the incident angle or X-ray energy [37, 44]. Therefore routine XPS also fails at clearing up the topology/architecture/distribution of the various components of the interphase.

The amount of lithium, fluorine and phosphorus contained in the interphase formed on $LiMn_{0.5}Ni_{0.5}O_2$ during storage in $LiPF_6$-based electrolyte could be quantified by MAS NMR. The oxide surface is mainly covered by LiF and lithiated organic species which can only be probed through the difference in the amounts of lithium and fluorinated species. In addition, the difference in the amount of fluorophosphates found by XPS and NMR implies that the proportion of fluorophosphates is underestimated by XPS (which penetration depth is about 5-10 nm), meaning that these species are located in the inner part of the interphase. Such considerations show that the interpretation of XPS results can be made less ambiguous in the light of more quantitative data obtained by MAS NMR. Nevertheless, non lithiated species still remain invisible to NMR, since ^{13}C MAS NMR appeared impossible to implement considering its low natural abundance and the small amounts of interphasial species per mass unit of sample.

It would be tempting to convert the molar amounts detected by NMR into an average thickness of interphase but not only this would require considering the density of close packed model compounds (such as LiF) whereas the interphase seems amorphous and porous but the complex topography revealed by TEM observation further makes any modeling in terms of thickness questionable, especially when basing this modeling on average analyses.

Moreover, the apparent disagreement between XPS and NMR emphasizes the chemical inhomogeneity within the interphase depth. These two spectroanalytical techniques both give average results; whether at the scale of the XPS probe size (0.7mm×0.3mm) or the whole sample in the case of NMR, so that no indication regarding the distribution of chemical compositions with thickness can be obtained.

The quantification of oxygenated species by EELS analyses gives a valuable information, complementary to ^{7}Li, ^{19}F and ^{31}P NMR and highlights the chemical inhomogeneity within the interphase depth. At this stage it is now clear that a multi-layered model is not more realistic that an average homogeneous mixture of interphasial species.

Despite these limitations, we believe this example (and its extrapolation to various electrode materials) demonstrates the relevance of MAS NMR to monitor quantitatively elements and in some extend the chemical species comprised in the interphases grown in a Li-ion battery. The only ambiguity regarding the quantitative results obtained from this method

would concern diamagnetic active materials for which intercalated or alloyed lithium should be carefully distinguished from interphasial species. Of course, one should always keep in mind that complementary characterization techniques such as XPS or space-resolved EELS will always be necessary to a more precise and realistic sketch of electrode/electrolyte 3D interphases. Quantification of the interphasial species by MAS NMR appears however a reliable and unequivocal way to measure the effects of any solvent, lithium salt, additive, electrode formulation etc. on the nature and amounts of interphases and interpret subsequent electrochemical behavior such as impedance evolution.

III.4. Concluding remarks

The implementation of empirical calibration of ^{7}Li, ^{19}F and ^{31}P MAS NMR spectra has proven its ability to monitor quantitatively the evolution of interphasial species on the $LiNi_{1/2}Mn_{1/2}O_2$ surface during storage. This average information obtained on the inorganic part of the interphase is to be combined with XPS to consider the contributions of purely organic species as well as space-resolved EELS to shed light on chemical inhomogeneities within the interphasial depth and unravel the architecture of the interphase. Such a combination of characterization techniques confirms the complexity of the interphasial systems and again warns against simplified homogeneous or even multi-layered models.

The most critical point of this work concerns the samples preparation procedure used prior all *ex situ* analyses. Indeed, as explained in the section II.2.3., samples were always rinsed with one drop of DMC and dried under vacuum at 90°C for 4 h. The late drying step is susceptible to decompose $LiPF_6$ (see chapter 1, section III.1.1.), should some salt remain within the sample at this point. The release of gaseous PF_5 would then artificially increase the LiF relative concentration, explaining why we always account lithium fluoride as a major component of the interphase. However, the numerous examples exposed in the next chapters indicate that:

- Samples insufficiently rinsed exhibit the characteristic NMR signature of $LiPF_6$, implying that the salt resists to the above mentioned drying process.
- Surface modification or electrochemical cycling sometime lead the observation of huge amounts of fluorophosphates that clearly differ from $LiPF_6$. In such cases, those species are not removed during the drying process.

These observations lead us to conclude that such experimental procedure does not significantly alter the nature of the interphase. Any error arising from this procedure should be reflected equally on all the samples analyzed and would not challenge interpretations based on the comparison of series of samples rather than punctual measurements.

IV. CONCLUSION

As demonstrated by an increasing number of publications, ^{7}Li NMR has emerged a powerful tool to study the surface layer on Li-ion battery electrode materials, especially coupled with techniques giving complementary chemical information such as XPS or FTIR (developed in Appendix 1). Not mentioned in the enclosed review, a recent work by Harris *et al.* demonstrated the possibility to monitor Li dynamics in the interphase by playing with $^{6/7}$Li interphase and electrolyte [45].

In the case of materials containing transition metals with unpaired electrons, in addition to the chemical composition and quantification, it is possible to extract physical or topological information from electron-nucleus dipolar interaction. Especially in the case of ^{7}Li NMR, the advantage of this method lies in the efficient separation of surface signal from paramagnetic bulk signal, allowing the extraction of surface information including intimacy between bulk material and surface phase. The analysis of the interphase signal will be further developed in the following chapters, through the monitoring of the apparent ^{7}Li transverse relaxation time (T_2) corresponding to interphasial lithium, estimated from the signal linewidth, to tentatively correlate evolutions of spin-spin relaxation time with an interphase architecture.

The use of other nuclei such as ^{19}F or ^{31}P as probes of elements contained in the interphase is another straightforward way to gather additional insight on the evolution of the chemical composition of electrolyte decomposition products. The short example reported in the present chapter highlights the relevance of multinuclear NMR investigation, especially now that the implementation of ^{7}Li, ^{19}F and ^{31}P calibration curves allows the straightforward comparison of the absolute quantities in $mmol.g^{-1}$ of these elements. The recent report from Murakami *et al.* of cross polarization between ^{7}Li and ^{19}F to probe LiF deposited on $LiCoO_2$ [46] is symptomatic of the need to unravel the chemical composition of elements detected in the interphase. Such fancy experiments can however not be efficiently extrapolated to paramagnetic electrode materials due to the long exchange times used in the NMR pulse sequence, incompatible with the short relaxation times observed for paramagnetic compounds.

Concerning the organic part of the interphase, Leifer *et al.* reported the use of ^{13}C NMR to understand the decomposition or reaction pathway of organic solvents [47]. However, the sensitivity of ^{13}C NMR to the presence of nearby paramagnetic centers totally impedes the detection in our case. Therefore, the presence of Li-containing organic interphasial species will have to be estimated from the difference between the total amount of interphasial lithium probed by ^{7}Li NMR and the amount of lithium fluoride detected by ^{19}F NMR.

From a technical point of view, the work conducted in this thesis could be improved in different ways. First of all, subtle T_1 or T_2 variations could be detected providing instrumental advance compared to results reported in ref. [3]. Further qualitative description of the electrode / interphase would require the modeling of spectral lineshape. Such simulations would have to take into account both the strong overall paramagnetism of the bulk of active material and the complexity of the system made of diamagnetic species distributed inhomogenously on the surface. In addition, the distribution of observed nuclei in the thickness of the interphase complicates even more the system to be described by the simulation. Finally, the dynamic study of interphase growth and evolution might be made possible by *in situ* static NMR. Such studies would allow avoiding the necessary dismantling / washing (or not) / scratching / drying of the electrode, justifiably believed to damage the interphase.

The use of EELS to characterize interphase in lithium batteries is far less developed, and the experimental setting used in this thesis is obviously subjected to the same critics than *ex situ* NMR studies. However, the results obtained are already beyond our initial expectations, not really thanks to the analytical method (in the sense that our setup does not allow probing samples at the scale of few nm but some tens instead) but rather thanks to the momentous chemical inhomogeneity of the observed interphases.

Access to an up-to-date microscope would considerably improve the picture of the interphase, through straightforward EELS chemical mapping for instance. The preservation of both the electrode and the overlying interphase integrity are currently under development in our group, through the use of ultra microtome to cut sections of sample including both active material and interphase. The idea consists in observing the electrode / interphase binary system in conditions as close as possible from the operating ones. In this respect, *in situ* TEM studies (introduced in **Appendix 1**) should however be considered with caution, for the necessary use of ionic liquids or solid state electrolytes, which reactivity towards active materials should notably differ from the conventional electrolyte investigated here.

To conclude, the more complex the system, the more advanced the characterization techniques need to be. In the particular field of interphase characterization in Li batteries, technological advances still offer tremendous opportunities.

REFERENCES OF CHAPTER 2

[1] C.P. Grey, N. Dupré, *Chem. Rev.*, **104(10)** (2004) 4493 and references contained herein

[2] M. Ménétrier, C. Vaysse, L. Croguennec, C. Delmas, C. Jordy, F. Bonhomme, P. Biensan, *Electrochem. And Solid State Lett*. **7(6)** (2004) A140.

[3]: N. Dupré, J-F. Martin, D. Guyomard, A. Yamada, R. Kanno, *J. of Mat. Chem.*, **18** (2008) 4266.

[4]: N. Dupré, J-F. Martin, D. Guyomard, A. Yamada, R. Kanno, *J. of Power Sources*, **189(1)** (2009) 557.

[5]: N. Dupré, J-F. Martin, J. Oliveri, P. Soudan, D. Guyomard, A. Yamada, R. Kanno, *J. of Electrochem. Soc.*, **156(5)** (2009) C180.

[6]: N. Dupré, J-F. Martin, J. Degryse, V. Fernandez, P. Soudan, D. Guyomard, *J. Power Sources*, **195(21)** (2010) 7415.

[7]: N. Dupré, J.-F. Martin, J. Oliveri, D. Guyomard, A. Yamada, R. Kanno, *Electrochem. Comm.*, **10(12)** (2008) 1897.

[8]: N. Dupré, J-F. Martin, J. Oliveri, P. Soudan, D. Guyomard, A. Yamada, R. Kanno, *J. Power Sources*, **196(10)** (2011) 4791.

[9] D. Carlier, M. Ménétrier, C.P. Grey, C. Delmas, G. Ceder, *Phys. Rev. B*, **67** (2003) 174103.

[10] J. Kim, D.S. Middlemiss, N.A. Chernova, B.Y.X. Zhu, C. Masquelier, C.P. Grey, *J. Am. Chem. Soc.*, **132** (2010) 16825.

[11] A. Castets, D. Carlier, Y. Zhang, F. Boucher, N. Marx, L. Croguennec, M. Ménétrier, *J. Phys. Chem. C*, **115** (2011) 16234.

[12] W.S. Yoon, Y. Paik, X.Q. Yang, M. Balasubramanian, J. McBreen, C.P. Grey, *Electrochem. Solid State Lett.*, **5** (2002) A263.

[13] : W.S. Yoon, S. Iannopollo, C.P. Grey, D. Carlier, J. Gorman, J. Reed, G. Ceder, *Electrochem. Solid State Lett.* **7** (2004) A167.

[14] M.C. Tucker, A. Braun, U. Bergmann, H. Wang, P. Glatzel, J.A. Reimer, E.J. Cairns, in *Interfaces, Phenomena and Nanostructures in lithium Batteries Workshop*, (Eds: A. landgrebe and R.J. Klinger), *Electrochem. Soc. Proc. Series*, (2001).

[15] T.J. Swift in NMR of Paramagnetic Materials, ed. G. N. La Mar, W. DeW. Horrocks, Jr., and R. H. Holm, Academic Press, New York, (1973) 53.

[16] L.J.M. Davis, I. Heinmaa, B.L. Ellis, L.F. Nazar, G.R. Goward, *Phys. Chem. Chem. Phys.*, **13** (2011) 5171.

[17] F.H. Kohler in Magnetism: Molecules to Materials, ed. J.S. Miller and M. Drillon, Wiley-VCH, New York, **1** (2001) 386.

[18] D. Massiot, F. Fayon, M. Capron, I. King, S. Le Calvé, B. Alonso, J.O. Durand, B. Bujoli, Z. Gan, G. Hoatson, *Magn. Reson. Chem.*, **40** (2002) 70.

[19] M. Deschamps, F. Fayon, J. Hiet, G. Ferru, M. Derieppe, N. Pellerin, D. Massiot, *Phys. Chem. Chem. Phys.*, **10** (2008) 1298.

[20] A. Würsig, H. Buqa, M. Holzapfel, F. Krumeich, P. Novak, *Electrochem. Solid-State Lett.*, **8** (2005) A34.

[21] A.V. Plakhotnyk, L. Ernst, R. Schmutzler, *J. Fluorine Chem.*, **126** (2005) 27.

[22] N. Dupré, J. Oliveri, J. Degryse, J.-F. Martin, D. Guyomard, *Ionics*, **14** (2008) 203.

[23] L. Laffont, C. Delacourt, P. Gibot, M.Y. Wu, P. Kooyman, C. Masquelier, J-M. Tarascon, *Chem. Mater.*, **18** (2006) 5520.

[24] G. Chen, X. Y. Song, T. J. Richardson, *Electrochem. Solid-State Lett.*, **9** (2006) A295.

[25] G. Brunetti, D. Robert, P. Bayle-Guillemaud, J. L. Rouvière, E. F. Rauch, J. F. Martin, J. F. Colin, F. Bertin, C. Cayron, *Chem. Mater*., **23** (2011) 4515.

[26] B. Xu, C. R. Fell, M. Chi; Y. S. Meng, *Energy & Environmental Science*, **4** (2011) 2223.

[27] L. Daniel, J.-F. Colin, L. Simonin, J.-F. Martin, A. Boulineau, S. Patoux, *"Structural Characterization of High Capacity Layered Oxides"*, Lithium Batteries Discussion #5 (2011).

[28] M. Dollé, S. Grugeon, B. Baudoin, L. Dupont, J.-M. Tarascon, *J.Power Sources*, **97-98** (2001) 104.

[29] A. Naji, P. Thomas, J. Ghanbaja, D. Billaud, *Micron*, **31** (2000) 401.

[30] M K Kinyanjui, P Axmann, M Wohlfahrt-Mehrens, P Moreau, F Boucher, U Kaiser, *J. Phys. Cond. Matter*, **22** (2010) 275501.

[31] R. F. Egerton, *Electron energy-loss spectroscopy in the electron microscope*, 2nd edition, Plenum press (1996).

[32] D. B. Williams, C. B. Carter, *Transmission electron microscopy, a textbook for materials science*, 2nd edition, Springer (2009).

[33] P. Moreau, V. Mauchamp, F. Pailloux, F. Boucher, *Applied Physics Letters*, **94** (2009) 123111.

[34] Y. Oumellal, N. Delpuech, D. Mazouzi, N. Dupré, J. Gaubicher, P. Moreau, P. Soudan, B. Lestriez, D. Guyomard, *J. Mat Chem.*, **21** (2011) 6201.

[35] J. Danet, T. Brousse, K. Rasim, D. Guyomard, P. Moreau, *Phys. Chem. Chem. Phys.*, **12** (2010) 220.

[36] A. Naji, P. Thomas, J. Ghanbaja, D. Billaud, *J. Power Sources*, **81–82** (1999) 207.

[37] S. Malmgren, H. Rensmo, T. Gustafsson, M. Gorgoi, K. Edström, *ECS Trans.*, **25** (2010) 201.

[38] Z. Wang, N. Dupre, L. Lajaunie, P. Moreau, D. Guyomard, *unpublished results*.

[39] K. Edström, T. Gustafsson, J.O. Thomas, *Electrochim. Acta*, **50** (2004) 397.

[40] A.M. Andersson, M. Herstedt, A. Bishop, K. Edström, *Electrochim. Acta*, **47** (2002)

1885.
[41] L.J. Rendeck Jr., G.S. Chottiner, D.A. Scherson, *J. Electrochem. Soc*., **149** (2002) E408.
[42] B. Ravdel, K.M. Abraham, R. Gitzendanner, J. DiCarlo, B. Lucht, C. Campion, *J. Power Sources*, **119-121** (2003) 805.
[43] B. Meyer, N. Leifer, S. Sakamoto, S. Greenbaum, C.P. Grey, *Electrochem. Solid-State Lett.*, **8** (2005) A145.
[44] M. Herstedt, M. Stjerndahl, A. Nyten, T. Gustafsson, H. Rensmo, H. Siegbahn, N. Ravet, M. Armand, J.O. Thomas, K. Edström, *Electrochem. Solid-State Lett.*, **6** (2003) A202.
[45] S. J. Harris, P. Lu, A. O'Neill, *Abstract #490*, 218th ECS Meeting, Las Vegas (2010).
[46] M. Murakami, H. Yamashige, H. Arai, Y. Uchimoto, Z. Ogumi, *Electrochem.Solid-State Lett.*, **14** (2011) A134.
[47] N. Leifer, M. C. Smart, G. K. S. Prakash, L. Gonzalez, L. Sanchez, K. A. Smith, P. Bhalla, C. P. Grey, S. Greenbaum, *J. Electrochem. Soc.*, **158** (2011) A471.

CHAPTER 3. INVESTIGATION OF $LiNi_{½}Mn_{½}O_2$ AS A MODEL COMPOUND

This third chapter condenses the different studies carried out on the $LiNi_{1/2}Mn_{1/2}O_2$ / electrolyte interphase. A brief first part is dedicated to the synthesis and characterization of the bulk material.

The second part directly follows the work of J.-F. Martin *et al.* [1-5] on the same material, extending previous studies with ^{19}F NMR and systematic quantitative monitoring of the interphase evolution. Parameters such as air exposure, temperature, formulation of the composite electrode and the use of an electrolyte additive are envisaged.

Then, in a third part, the overlithiation of this material, up to the $Li[Li_{0.2}Ni_{0.4}Mn_{0.4}]O_2$ composition, is investigated. This move accompanies a major trend in the research related to positive electrode materials towards higher potentials and higher energy densities. From a fundamental point of view, the release of "Li_2O" from the bulk along the first oxidative process [6-9] is expected to influence the interphasial processes.

Through all the examples presented in this chapter, the NMR tool is valued and its limits defined. In continuity with the case study presented in chapter 2, the $LiNi_{1/2}Mn_{1/2}O_2$ composition proposed by Ozhuku *et al.* [10] is used as a model compound. In addition to specific results obtained for one cathode / electrolyte system or another, the ambition here consists in determining general elements dictating the interphase growth and chemistry and correlating the nature and amounts of interphase species to bulk electrochemical features.

I- SYNTHESIS AND CHARACTERIZATION OF PRISTINE MATERIAL

In a previous work, Martin *et al.* investigated the influence of the synthesis route on the surface properties of $LiNi_{1/2}Mn_{1/2}O_2$ [3-5]. In particular, enhanced specific surface area proved to dramatically increase the reactivity of this material towards air and electrolyte [3]. Such highly reactive $LiNi_{1/2}Mn_{1/2}O_2$ material is used here in order to exacerbate interphasial reactions and later allow investigating the different parameters susceptible to impact on the surface properties and subsequent bulk electrochemistry [4, 5].

I.1. Synthesis by a combustion method

The layered $LiNi_{1/2}Mn_{1/2}O_2$ used in this work was prepared in the laboratory by the combustion method reported by Gopukumar *et al.* [11]. This sol gel synthesis uses lithium, manganese and nickel nitrate precursors ($LiNO_3$, $Mn(NO_3)_2$, $4H_2O$ and $Ni(NO_3)_2$, $6H_2O$) in aqueous solution. The gel obtained at 80°C through the addition of glycine (NH_2CH_2COOH) is then placed at 180°C to fire the organic precursor, leaving the active precursors well dispersed and finely divided. At last, the annealing of $LiNi_{0.5}Mn_{0.5}O_2$ is carried out at 850°C for 7h under pure O_2 atmosphere in a dedicated tubular quartz oven transferable to the glovebox. This compound is here referred to as LMN½.

I.2. Structural and morphological characterization

I.2.1. Structural characterization by XRD

The XRD pattern of pristine LMN½ is displayed in **Figure III-1**, and shows a perfect matching with the $\boldsymbol{R\bar{3}m}$ space group characteristic of the AMO_2 layered oxides (A = Li, Na and M = Fe, Mn, Co, Ni). The lattice parameters deduced from Rietveld refinement, as well as atomic positions and occupancies are reported in **Table III-1**. In full agreement with the literature (2.89 Å and 14.30 Å, for *a* and *c* respectively in ref. [12]), a typical Li/Ni exchange on the 3a and 3b sites is observed due to the close ionic radius of Li^+ and Ni^{2+} [12]. Moreover, crystallite size is estimated to 66(2) nm from the analysis of peaks width.

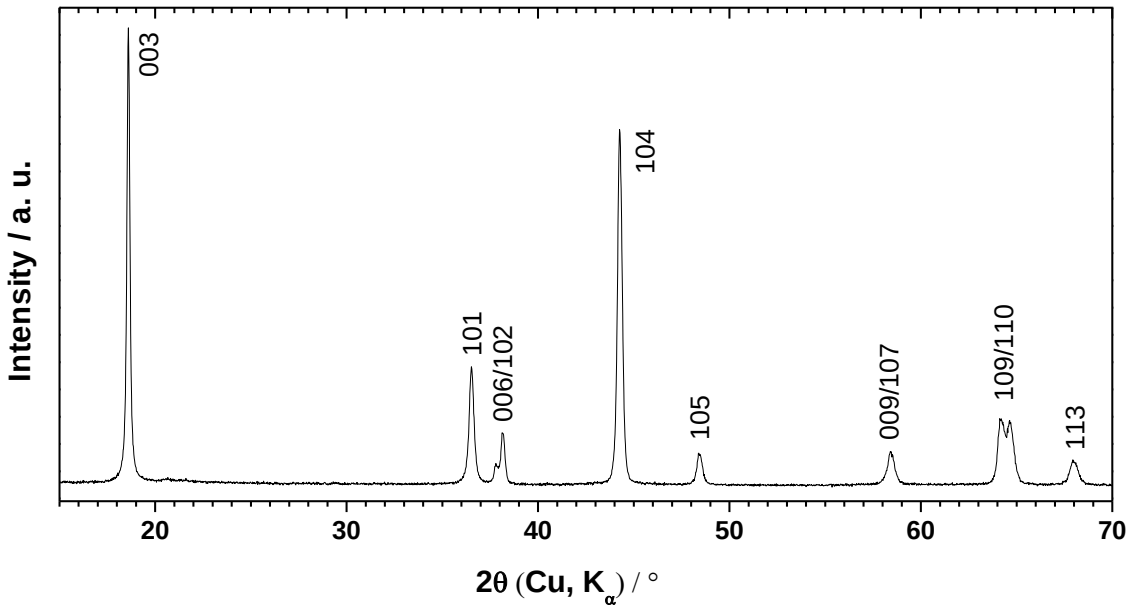

Figure III-1. XRD pattern recorded for pristine LMN½.

$LiNi_{1/2}Mn_{1/2}O_2$ Space group $\boldsymbol{R\bar{3}m}$

Lattice parameters		a_{hex} (Å) =	2.89123(3)	c_{hex} (Å)	14.3181(2)
Site		x	y	z	Occupancy
Li	3a	0	0	0	0.905(1)
Ni	3a	0	0	0	0.095(1)
Li	3b	0	0	0.5	0.095(1)
Ni	3b	0	0	0.5	0.405(1)
Mn	3b	0	0	0.5	0.5
O	6c	0	0	0.2420(2)	2
		R_{wp}	12.1 %	R_{bragg}	4.45 %

Table III-1. Lattice parameters and selected results from the Rietveld refinement of XRD pattern presented in Figure III-1

I.2.2. Morphological characterization by SEM

Scanning and transmission electron micrographs of LMN½ are shown in **Figure III-2**. Primary particles exhibit rather narrow size dispersion around 150 nm, in agreement with a specific surface area of 8 $m^2.g^{-1}$, as determined by the BET method. These small particles are agglomerated in irregular microscopic secondary particles, which easily break upon sonication. Hence, preliminary characterization highlights the important surface developed by

the $LiNi_{1/2}Mn_{1/2}O_2$ material prepared. This specificity is fundamental for the present work, and will be exploited in the different studies developed hereafter.

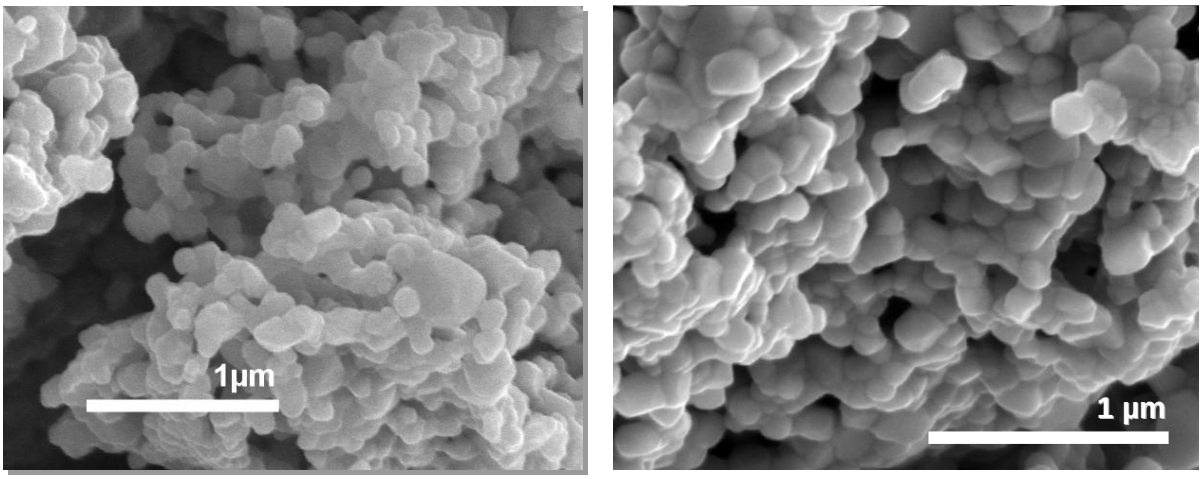

Figure III-2. SEM observations of pristine $LiNi_{1/2}Mn_{1/2}O_2$ samples .

I.3. Electrochemical characterization

I.3.1. Electrodes formulation and benchmarking

The typical benchmarking employed here consists in the magnetic stirring of active material powder, Ketjenblack carbon and carboxymethyl cellulose (wt% 80/10/10) in water. After deposition on an aluminum disk with a typical loading of 20 mg (AM).cm^{-2}, this slurry is let to dry at room temperature overnight, calendered under 2 tons and then dried under vacuum at 100°C for 4h before being used as positive electrode.

I.3.2. Electrochemical signature of $LiNi_{0.5}Mn_{0.5}O_2$

Lithium extraction from LMN½ occurs through a monophasic reaction, characterized by a smooth slope between 3.8 V and 4.5 V vs. Li^+/Li^0, as shown in **Figure III-3**. In the absence of any remarkable electrochemical signature, the significant irreversible capacity observed during the first cycle cannot be straightforwardly correlated to oxidative side reactions. However, cycling experiments performed with a lower cut off potential (4.3 V) show that if the initial irreversible charge capacity can be reduced, it is also at the cost of the reversible capacity. Hence, the intercalation and interphasial phenomena cannot be separated. On the contrary, higher cut off potential (4.8 V) only results in further electrolyte oxidation [10].

Moreover, no evidence of an additional 4.3 V process related to the decrease in the interlayer mixing of Li and Ni can be observed on the corresponding incremental capacity curve, as reported in [12].

The last comment rising from the observation of **Figure III-3** would obviously be to point out the relatively low specific capacities obtained from our $LiNi_{1/2}Mn_{1/2}O_2$-based electrodes compared to standard literature data (up to 200 $mA.h.g^{-1}$ in ref [10, 13]). The explanation lies both in the excessive electrode loading (20 $mg.cm^{-2}$) facilitating subsequent analyses as well as in the chosen synthetic route leading deliberately to a high specific surface area (8 $m^2.g^{-1}$) in order to exacerbate surface reactivity.

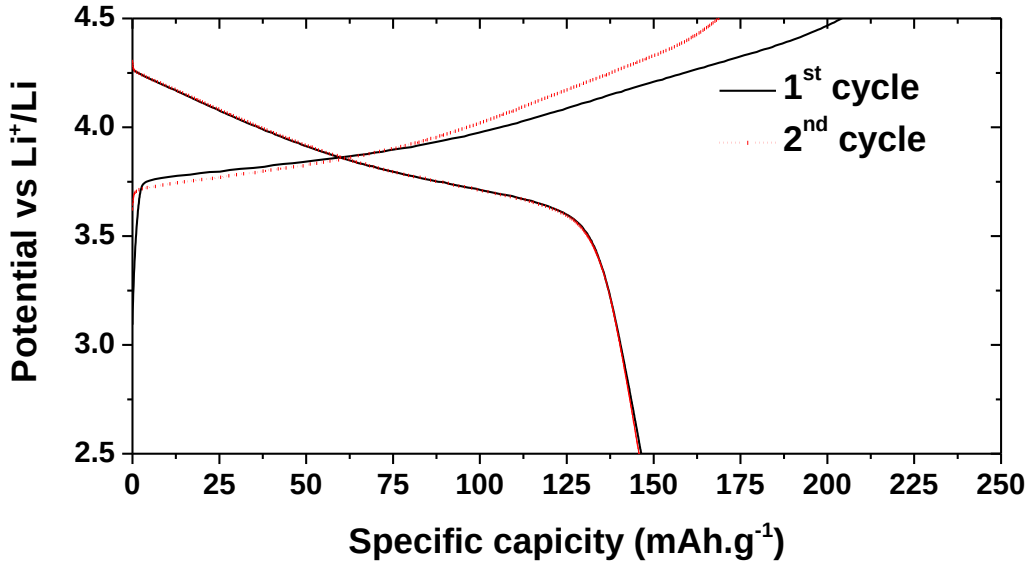

Figure III-3. First (black solid lines) and second (red dotted lines) electrochemical cycles of argon-stored LMN½ at a C/20 rate in conventional $LiPF_6$ 1M in EC:DMC electrolyte.

I.4. Concluding remarks

Although the $LiNi_{1/2}Mn_{1/2}O_2$ material synthesized here does not exhibit optimized electrochemical performance, it meets several criteria essential to this work. First, as already mentioned, the high specific surface area is expected to exacerbate surface reactivity, hence facilitating the detection of electrolyte decomposition products. Secondly, the use of a dedicated tubular quartz oven transferable to the glovebox allows working with a pristine active material that is never exposed to air. The following section makes a good use of this experimental facility, comparing the surface reactivity of such intact material compared to an air exposed one.

II- EXTERNAL PARAMETERS INFLUENCING THE INTERPHASIAL BEHAVIOR

To date, there have been several reports of electrode / electrolyte interphase formation on cathode materials, and recent evidence from electrochemical impedance [15-19], FTIR and XPS [20-23] showing that passivating films or species coming from the decomposition of the electrolyte are being formed on the cathode as a function of cycling and aging conditions. However, the experimental conditions of formation, growth and modification as well as the intimacy of the interactions between the surface layer and the surface of active material is still unclear [20, 24-27]. In particular, the beneficial or hindering role played by the interphase(s) on the interfacial charge transfer is yet to be addressed. Attempts to answer these issues are not a straightforward task due to experimental complications including the low amount of surface species that forms and the high sensitivity of the interphase towards ambient atmosphere.

This section has been devised as an outlook of the opportunities offered by solid state NMR [2-5, 28-30] to monitor the impact of external physico-chemical parameters on the nature and amount of interphase. Parameters such as air exposure, temperature, formulation of the composite electrode and the use of an electrolyte additive are investigated in the following. In each case, the changes induced at the scale of the electrode surface are tentatively correlated to bulk electrochemical properties.

II.1. Background: effect of air exposed surface

In this sub-section are summarized results obtained during the PhD thesis of Jean-Frédéric Martin (2008) [1] on the influence of air exposure on the interphasial reactivity upon contact with electrolyte or electrochemical cycling.

II.1.1. Interphase growth upon storage monitored by NMR [3]

The evolution of the ^{7}Li NMR integrated intensities for LMN½ powder samples soaked in conventional $LiPF_6$ in EC:DMC (1:1) electrolyte for various amounts of time is reported in **Figure III-4**. Blue and red curves correspond to LMN½ material prepared by the combustion method presented here and subsequently stored in air or argon, respectively.

LMN½ material prepared by the standard coprecipitation method [10, 12] and displaying a lower specific surface area is also shown here (green curve).

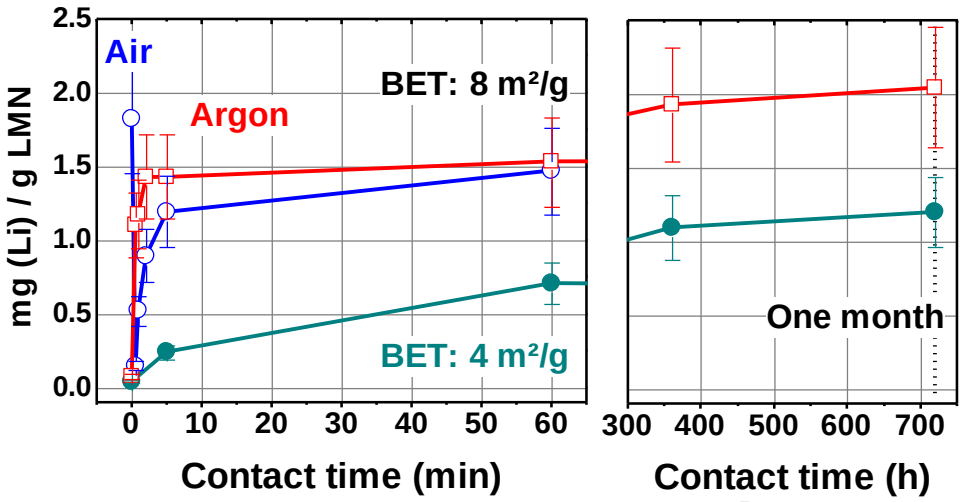

Figure III-4. Evolution of the normalized integrated intensities of ^{7}Li MAS NMR spectra, for LMN½ samples soaked in $LiPF_6$ (1 M EC/DMC) electrolyte for various durations.

^{7}Li MAS NMR performed on as synthesized LMN½ samples (**Fig. III-4**, t = 0) indicates the presence of Li_2CO_3 for the material stored in air (blue curve), consistent with previous study [2] and confirmed by XPS and IR results displaying the characteristic binding [20, 31], stretching and bending energies of Li_2CO_3 [17, 32, 33]. By comparison, LMN½ samples stored in argon (red and green curves) did not give any measurable ^{7}Li NMR signal prior the exposition to electrolyte.

In the case of the LMN½ displaying a pristine Li_2CO_3 interphase, a global decrease in the integrated intensity is first observed after 30 s of contact. This important decrease of initial NMR signal intensity, followed by a passivation-like evolution, supports results obtained by Koltypin *et al.* [34], demonstrating the reaction of Li_2CO_3 additive with electrolyte impurities (see Eq. I-6d for instance) . In our case, the Li_2CO_3 on the surface would react with HF traces, at least partially, leaving the surface of LMN½ bare and free to react with the electrolyte, in a very similar way to the sample with no initial Li_2CO_3 on its surface.

For all the samples, the drastic increase of the signal intensity after the first minutes of contact indicates that the reaction with the electrolyte is extremely fast. If air- and argon-stored materials display similar evolution on the long term, the specific surface area exposed to electrolyte seems to have a more significant influence on the overall amount of surface lithiated species. Nevertheless, the integrated NMR intensity is not proportional to the specific surface, suggesting a nonhomogeneous covering of the surface of the grains of active material, as confirmed by TEM and EIS measurements. Of course, there is no clear evidence

whether the BET surface area corresponds to the electrochemical surface area in the battery. As an approximation, it appears however extremely convenient to compare the surface reactivity of different electrode materials subjected to similar treatments.

In addition to ^{7}Li NMR, XPS experiments on soaked samples displaying initial surface Li_2CO_3 showed that these species further react with the electrolyte, leaving an interphase comprised of fluorinated products such as Li_xPF_y, LiF, and $Li_xPO_yF_z$ for short contact times, similarly to the unexposed material. For a longer exposure to electrolyte, organic products, detected by XPS coming from the decomposition of the electrolyte solvents appear. Combined NMR and XPS studies allow getting a time-resolved evolution of the interphase formation upon soaking, indicating a more complex mechanism than a strict surface passivation.

II.1.2. Interphase evolution upon cycling monitored by NMR [4, 5]

The formation and the evolution of lithium-containing interphasial species and the interfacial charge transfer resistance have been carefully monitored upon cycling, by coupling *ex situ* ^{7}Li MAS NMR and *in situ* electrochemical impedance spectroscopy (EIS), as presented in **Figure III-5** comparing the cases of air and argon storage. In these previous studies, classical electrode formulation based on PVDF binder was used. For both samples, impedance diagrams exhibit a single semi-circle, mostly attributed to charge transfer processes [3-5], allowing the extraction of interfacial resistance, labeled R_{ct}.

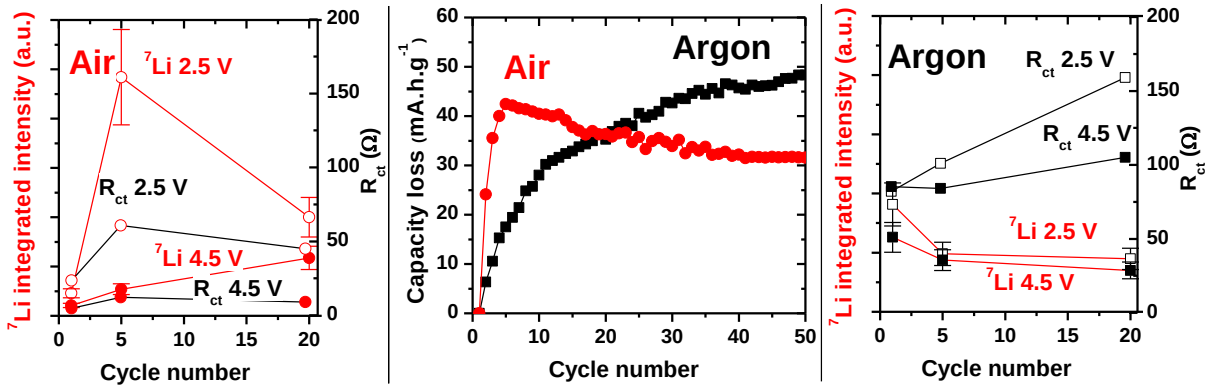

Figure III-5. Center: discharge capacity loss measured for Li//$LiPF_6$// $LMN_{1/2}$ cells at a C/20 rate in the case of prior air and argon storage. ^{7}Li integrated intensities and charge transfer resistance fitted from EIS measurements carried out after a 5h rest at the end of charge and discharge (3 electrodes) for air-stored (left) and argon-store (right) $LMN_{1/2}$

The specific capacity curves as a function of the cycle number obtained at C/20 rate (for the sake of consistency the attending figures, the capacity loss is plotted in **Figure III-5**,

center), exhibits a fast and important decay along the 5 first cycles before reaching stabilization, with only a slight continuous increase of the specific capacity for the following cycles. Considering such difference in the electrochemical behavior of air- and argon-stored $LiNi_{1/2}Mn_{1/2}O_2$ materials, the influence of Li_2CO_3 formed upon air exposure has been further investigated.

Concerning the sample stored in air (i.e. containing Li_2CO_3 native surface layer), an important increase in the amount of interphasial lithium is observed during the first electrochemical cycles along with an increase of the charge transfer resistance. After reaching a maximum at the 5^{th} cycle, both integrated intensity of the NMR signal and charge transfer resistance decrease, indicating a strong correlation between these two different surface characteristics, obtained from *ex situ* and *in situ* experiments, respectively.

Hence, the evolution of surface species, as probed by NMR and EIS, follow the same variation as electrochemical parameters related to the bulk of active material, such as the capacity loss from the initial discharge (**Fig. III-5, center**). The correlation between the electrode cycling performance and amount of interphasial lithiated species may thus be depicted as a steric restriction caused by the presence of a too important amount of interphasial species, hindering accessibility to the active material.

Such control of the overall electrochemical behavior by surface phenomena completely differ from the case of $LiNi_{1/2}Mn_{1/2}O_2$ stored in argon. In the absence of Li_2CO_3, no stabilization of the specific discharge capacity is observed but a continuous decrease along the 30 first cycles. As shown in **Figure III-5 (right)**, this bulk electrochemical behavior however may also be explained by the evolution of the interphase. Instead of a maximum, and important variations between the end of charge and discharge, the amount of interphasial lithium species detected by NMR decreases continuously and remains extremely low, so that the growth of a blocking interphase made of lithiated species coming from the decomposition of electrolyte cannot be hold responsible for the decreasing electrochemical performance. The significant increase of charge transfer resistance between the 1^{st} and 20^{th} cycles has therefore to be assigned to another aging mechanism such as the composite electrode breakdown (i.e. loss of percolation) or the material fatigue (i.e. irreversible phase transformation or dissolution). Hence, low amounts of interphasial lithiated species do not necessarily result in good electrochemical performance, and a protective role of the interphase against the degradations caused by positive electrode / electrolyte interactions might be considered, similarly to the role played by the SEI on graphitic anodes.

II.1.3. Discussion

The examples presented here highlight the complexity of the electrode / electrolyte interactions. The detrimental impact of too high amounts of interphase is revealed, as is the no less detrimental impact of too low amounts of interphase (or certain species contained in the interphase). Noteworthy, the studies summarized herein before only depict the evolution of lithiated species in the interphase. Complementary XPS analyses (see ref. [3-5]) suggest that the distribution of this overall Li content, between fluorinated products such as LiF, Li_xPF_y, or $Li_xPO_yF_z$ and organic products, evolves with contact time or cycling. The antagonist evolution of fluorinated and organic species detected by XPS however poses the problem of the supposed screening of fluorinated interphasial species by organic/polymeric ones (see **Fig. III-8** and the associated discussion). Hence, the first objective of the present work consisted in implementing ^{19}F and ^{31}P MAS NMR, as described in chapter 2, in order to benefit from the complementarity of XPS and NMR (see **Fig. II-5**) and clarify the interphase chemistry and evolution.

As demonstrated here, the presence of this deposit made of salt and solvents decomposition products can be beneficial to the overall electrochemical behavior at a certain extend. The difficulty therefore lies in controlling the growth and chemistry of this interphase, with the help of electrolyte additives for instance [35, 36].

Nonetheless, it appears that multiple changes may take place unsuspectingly at the electrode surface, even upon storage in air, as seen here with the formation of surface Li_2CO_3, or in chapter 4 with the surface oxidation of $LiFePO_4$ in air.

II.2. Reinvestigation of the $LiNi_{1/2}Mn_{1/2}O_2$ / $LiPF_6$ electrolyte interphase in the light of ^{19}F and ^{31}P MAS NMR

With the development of new analytical tools, previous studies were completed or redone, for the former electrode formulation using a PVDF binder did not allow the proper investigation of interphasial fluorinated species, as illustrated by **Figure III-6**.

On these ^{19}F MAS NMR spectra recorded from cycled electrodes of LMN½, it appears clearly that the amount of interphasial fluorinated species, here highlighted by LiF rising at -205 ppm, is to remain negligible compared to the 10wt% of PVDF present in the composite electrodes. Hence the following experiments shown here make use of the formulation described in section 1.3 using CMC.

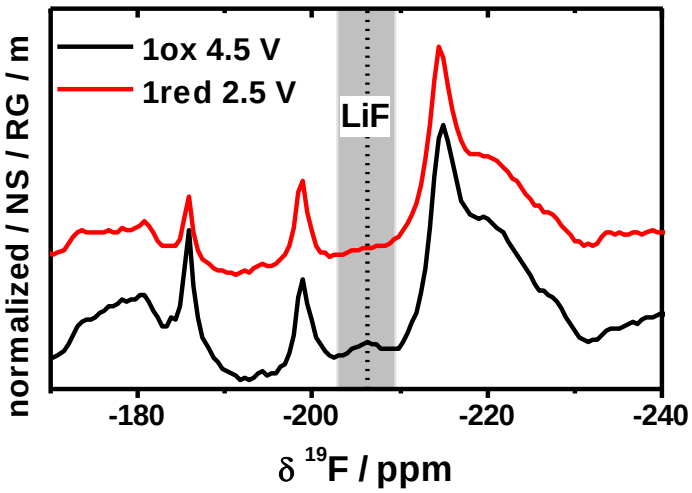

Figure III-6. ^{19}F MAS NMR spectra of PVDF-based electrodes of LMN½ at the end of first charge (black) and (discharge). Only the signal denoted by the grey area is assigned to the interphase while the other peaks are spinning sidebands from PVDF signals.

II.2.1. Interphase growth upon contact with electrolyte at room temperature

Figure III-7 displays the amounts of interphasial lithium and fluorine detected after different contact times of air-stored LMN½ powders with electrolyte. The evolution observed for lithiated species in **Figure III-4** is confirmed, with an important decrease of initial NMR signal intensity assigned to pristine Li_2CO_3 dissolution, followed by a first sharp and then smooth increase, describing a passivation-like evolution. The novelty brought by this experiment lies in the comparative evolution of fluorinated species and lithiated species.

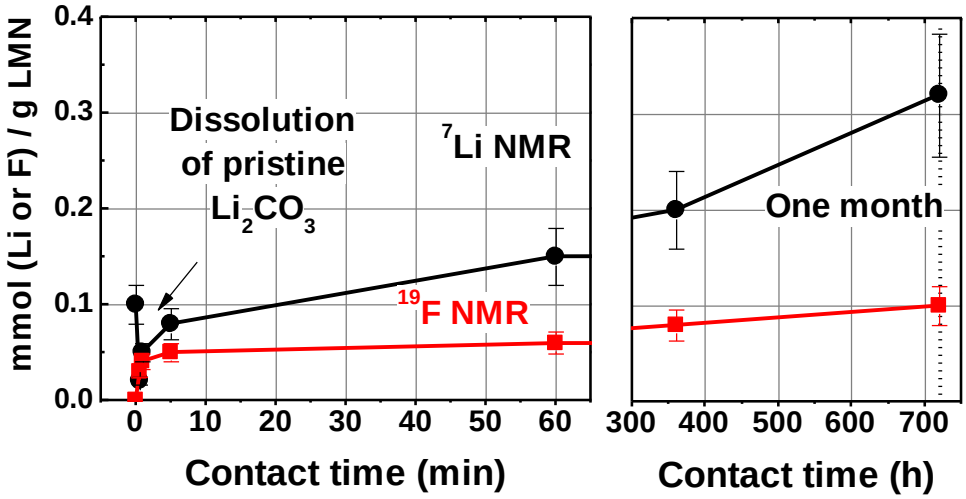

Figure III-7. Evolution of the normalized integrated intensities of ^{7}Li and ^{19}F MAS NMR spectra, for air-stored LMN½ soaked in conventional $LiPF_6$ 1M in EC:DMC electrolyte for various durations.

A passivation-like evolution can also be observed insofar half of the amount of fluorine detected after one month contact was already formed after 5 minutes. Although spectra are not shown here (see spectra in Appendix 2, **Fig. AII-1**), it should be noted that all the intensity integrated from ^{19}F MAS NMR spectra can be attributed to lithium fluoride. This fact has a double implication when it comes to cross "bulk" NMR with "surface" XPS results, displayed in **Figure III-8**.

First, considering fluorinated species detected by XPS (**Fig. III-8, left**), it appears that the amount of fluorophosphates rising at 688 eV is clearly overestimated compared to lithium fluoride, since these species are not even detectable by NMR. Fluorophosphates should therefore be pictured at the extreme surface of the interphase, contrary to LiF. Thus, the different fluorinated species (LiF and Li_xPF_x, $Li_xPO_yF_z$ or RPO_yF_z) probably precipitate in the interphase through different mechanisms (see degradation reactions in Chapter 1, Eq. I-4 to I-6) and under different conditions.

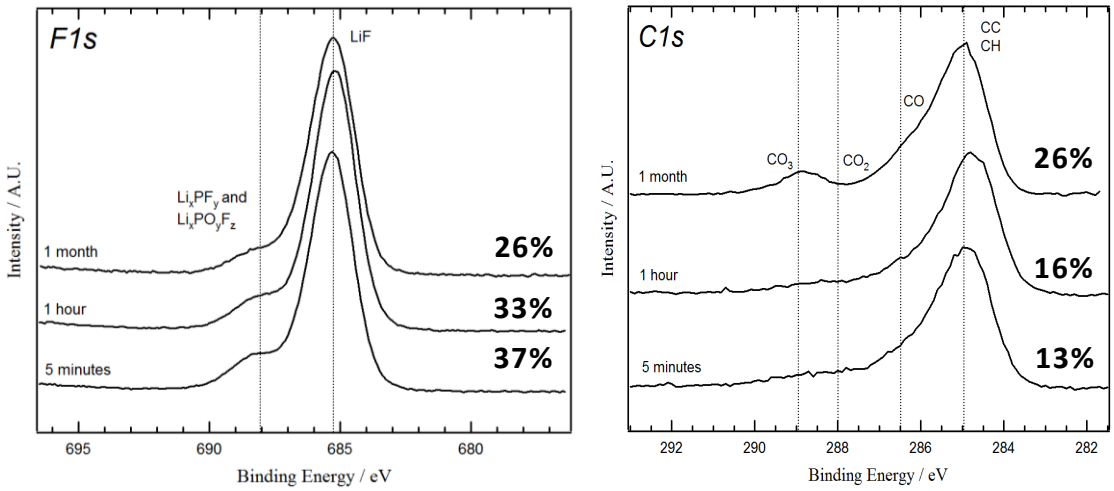

Figure III-8. XPS *F 1s* and *C 1s* core spectra measured after a different contact times with $LiPF_6$ in EC:DMC electrolyte. Figures on the right correspond to elemental percentages. [1]

Secondly, if most of the fluorine amount is found under the form of LiF by NMR, it implies that an equal atomic or molar amount of lithium can be attributed to LiF and therefore the difference between the lithium and fluorine amounts should be assigned to fluorine-free interphasial species, i.e. lithium alkylcarbonates or other lithiated organic species. Hence, the compared evolutions of lithium and fluorine amounts along storage in electrolyte indicate the rapid precipitation of LiF on the LMN½ surface, followed by a progressive deposition of organic species. This conclusion, drawn by quantitative bulk NMR, allows clarifying the relative decrease of fluorine elemental percentage detected by XPS, which is in fact the

artificial result of the increasing amount of organic species covering fluorinated salts, as sketched in **Figure III-9**.

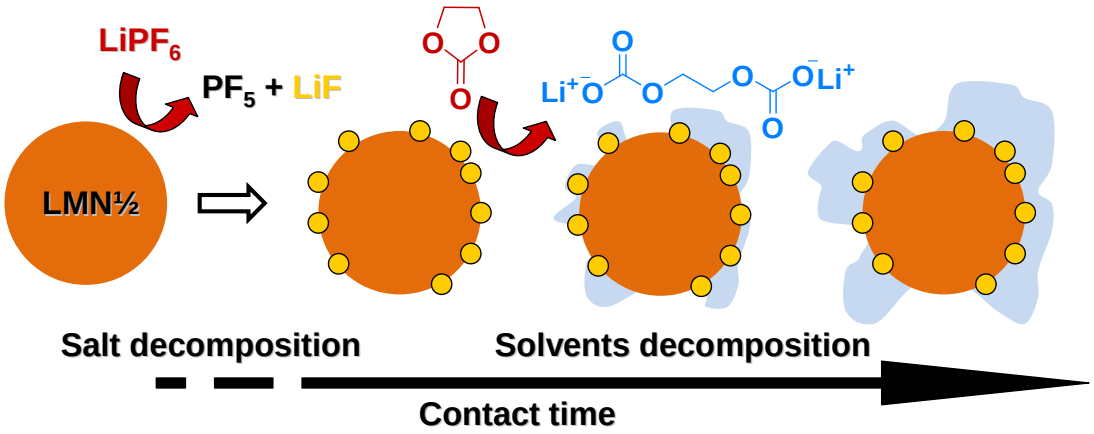

Figure III-9. Overview of the impact of the contact time of LMN ½ with conventional $LiPF_6$ 1M in EC:DMC (1:1) electrolyte on the chemistry of the interphase observed.

II.2.2. Interphase evolution upon cycling

The interphasial behavior of argon-stored LMN½ is here monitored along electrochemical cycling. Electrochemical data reported in **Figure III-10** do not significantly differ from previous studies (see **Fig. III-5**).

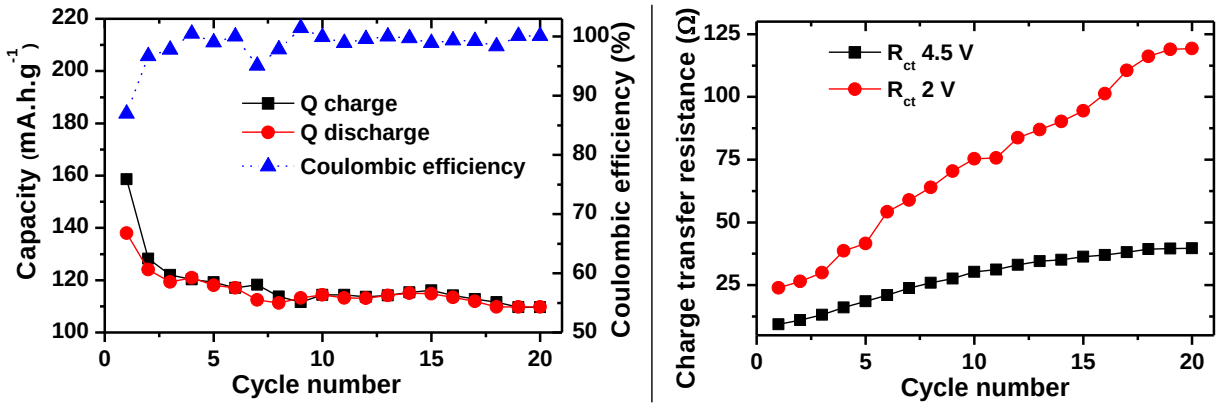

Figure III-10. Electrochemical data gathered from Li//$LiPF_6$//$LiNi_{1/2}Mn_{1/2}O_2$ cells at a C/20 rate. Left: specific charge (black squares), discharge (red dots) capacities and the resulting coulombic efficiency (blue triangles). Right: Charge transfer resistance fitted from EIS measurements carried out after a 5h rest at the end of charge (black squares) and discharge (red dots) in a 3 electrodes cell.

An important discharge capacity loss along the first cycles is observed before approaching stabilization around 110 $mA.h.g^{-1}$ at the 7^{th} cycle. However, the charge transfer resistance estimated from EIS measurements (**Fig. III-10, right**) keeps increasing

significantly after this stage, suggesting that no surface passivation is reached at the scale of this 20 cycles-long experiment. Except for the first cycle, the coulombic efficiency of the half-cell (i.e. how much of the quantity of electricity used to charge is usable during discharge) remains close to 100 %, suggesting that the electrochemical formation of the positive electrode / electrolyte interphase is limited to the initial charge process.

Although high resolution ^{31}P NMR was dismissed due to excessive duration of spectra acquisition (≥15h), the absence of remaining $LiPF_6$ could be attested (see Appendix 2, **Fig. AII-2**). ^{7}Li and ^{19}F MAS NMR spectra recorded at the end of the 1st, 5th and 20th charges and discharges are displayed in **Figure III-11**.

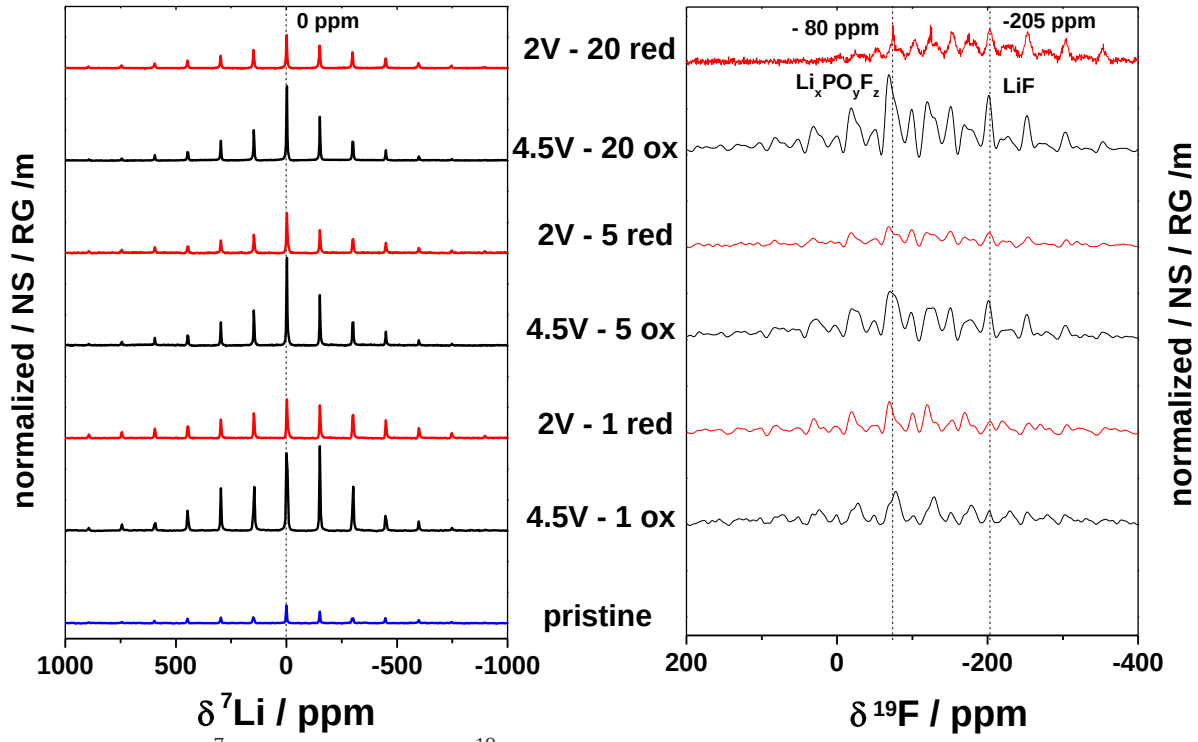

Figure III-11. ^{7}Li (29 kHz) and ^{19}F (23.5 kHz) MAS NMR spectra of LMN½ after stabilization at the end of the 1st, 5th and 20th charges and discharges. Dotted lines denote the position of isotropic shifts.

Regarding the amount of interphasial lithiated species (**Fig. III-12**), a maximum Li content is reached at the end of the first charge after which the amount of surface Li stabilizes around 0.2 $mmol.g^{-1}$, in agreement with results previously obtained (**Fig. III-5, right**). Therefore, NMR shows that the interphase growth seems not to consume any lithium, at the exception of the first cycle, during which the Li consumption in the interphase can hence be correlated to the irreversible consumption of electrons, as highlighted by the poor coulombic efficiency.

Concerning fluorinated species, LMN½ interphase exhibits an accumulation of LiF which stabilizes around 0.2 mmol.g^{-1}, while fluorophosphates fluctuate with a tendency to accumulation, up to 1.0 mmol(F).g^{-1}.

Based on the reasoning described in the previous section, it appears that the interphase composition evolves upon cycling. Whereas the initial interphase (1st charge) comprises lithiated fluorophosphates or organic species, for the 0.25 mmol(Li).g^{-1} difference between the total amount of lithium probed by ^{7}Li NMR and the amount of LiF probed by ^{19}F NMR. The interphase probed from the 5th cycle on is then composed of a mixture of LiF and non lithiated species.

T_2 variations are necessarily dictated by the state of charge (SOC); in the present case the paramagnetic behavior of the active material changes from an average S=3/2 at the reduced state (Mn(IV): d^4 and Ni(II): d^8) to S=2 at the oxidized state (Mn(IV): d^4 and Ni(IV): HS d^6). Hence, a stronger nuclear electron dipolar interaction is expected in the reduced state, resulting in a shorter T_2 value, all other parameters considered unchanged (interphase thickness, and intimacy with the active material).

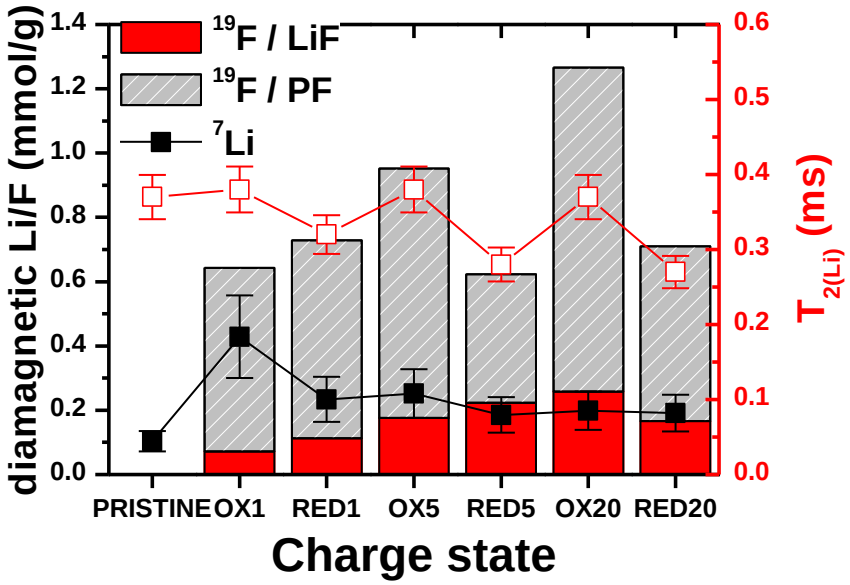

Figure III-12. ^{7}Li and ^{19}F NMR interphase quantification performed on LMN½ at the end of 1st, 5th and 20th charge and discharge at a C/20 rate. Red open squares correspond to $T_{2r(Li)}$ estimated from the spectral linewidth for a MAS rate of 29 kHz (see chapter 2, section 1.2.2).

Besides, the relative decrease of $T_{2r(Li)}$ between the 1st and the successive reduced states might be explained in the light of the chemical evolution of the interphase. Indeed, only at the 1st discharge might some lithium still be present under the form of Li alkylcarbonates.

Thus, the picture of interphase architecture given in chapter 2 (section 3.3, **Fig. II-19**), comprising an inner LiF rich interphase and an outer organic rich interphase seems to work properly here. The departure of lithium alkyl-carbonates, distant from the grain surface (i.e. having a long T_2) between the 1st and 5th cycles, leaves an interphase comparatively poorer in lithium, but in which lithiated species (identified under the exclusive form of LiF) are in close contact with the paramagnetic centers.

Important amounts of fluorophosphates might as well be accompanied by Li-free alkylcarbonates invisible to our experiments. Supporting XPS analyses, performed at the end of 1st charge and 20th discharge, are reported in **Figure III-13**.

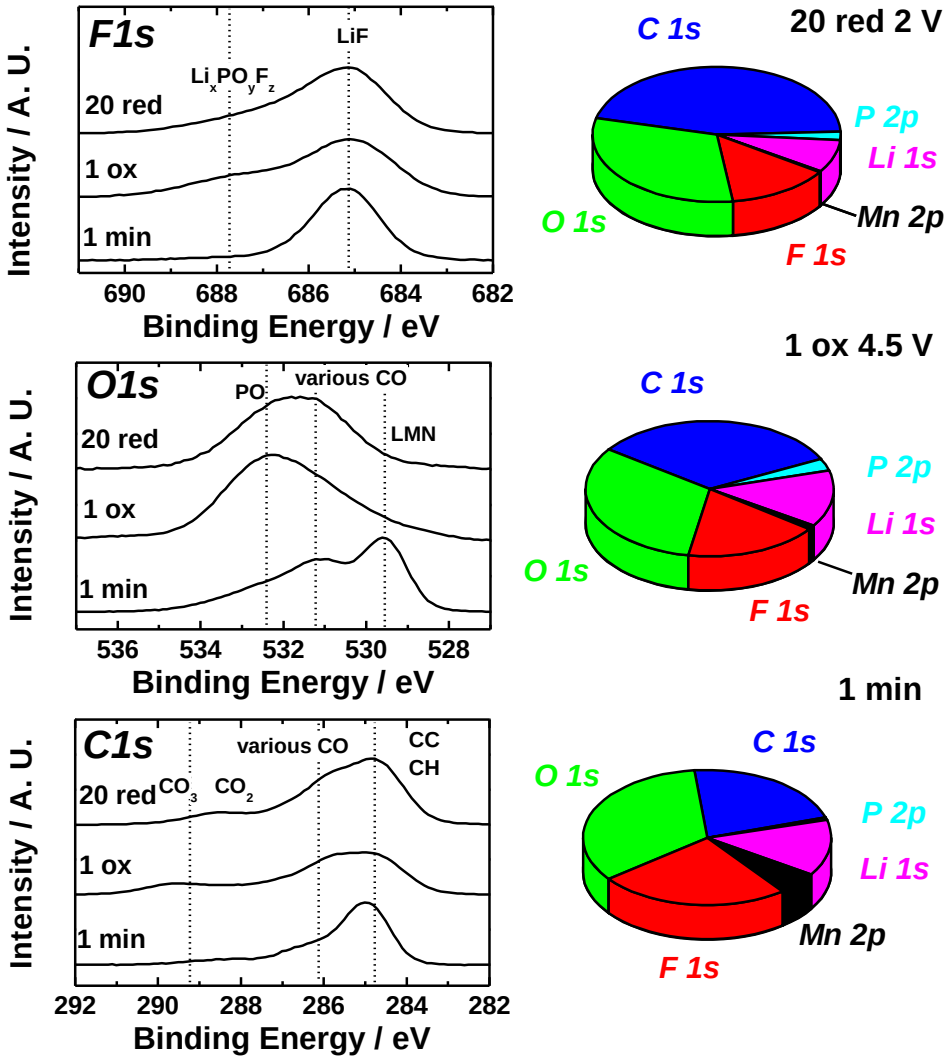

Figure III-13. Left: XPS *F 1s*, *O 1s* and *C 1s* core spectra measured after a brief contact with electrolyte (1 min) and at the end of the 1st charge and 20th discharge. Right: XPS elemental quantification diagrams for the three samples. The carbon percentage does not take the contribution at 284.8 eV of Ketjenblack carbon.

From XPS analyses, it appears that the interphase evolves along cycling towards a more organic composition, with the contribution of carboneous species increasing from 30 % to 43 % between the 1st charge and 20th discharge, respectively. The fact that the percentage of detected manganese decreases between the 1st charge and 20th discharge indicate a more important surface covering. This covering should be mostly attributed to non lithiated species such as alkyl-carbonates or POE-type polymers [37-39], since the contributions of fluorinated or lithiated species also significantly decrease by screening effect from covering species in the same time.

II.2.3. Discussion

The reinvestigation of the $LiNi_{1/2}Mn_{1/2}O_2$ / $LiPF_6$ 1M in EC:DMC electrolyte interphase has been made possible by the implementation of new NMR analytical tools, namely the extension to ^{19}F and ^{31}P nuclei, and the introduction of NMR calibration curves allowing the quantification of the integrated intensities.

By these means, the evolution of interphase chemistry upon contact with electrolyte can be monitored, indicating that the observed accumulation of lithiated species is solely to be assigned to Li-alkylcarbonates. At room temperature, salt decomposition occurring in the very first minutes of contact only leads to the precipitation of LiF, which amount remains stable for extended contact time. The apparent decrease observed by XPS can therefore be attributed to the screening effect originating from topping Li-alkylcarbonates.

The qualitative and quantitative evolution of interphase upon electrochemical cycling can easily be carried out by MAS NMR. Contrary to XPS or EELS (see chapter 2, **Fig II-11**), the presence of conductive additive(s) or binder(s) in composite electrodes does not impede or restrict the analysis, providing the use of non fluorinated binder(s).

In the present example, the extension of NMR to ^{19}F enables infirming the hypothesis previously expressed that the interphase grown on argon-stored $LiNi_{1/2}Mn_{1/2}O_2$ was not covering enough to passivate the electrode surface. Indeed, it appears that the low and decreasing abundance of lithiated species detected by ^{7}Li NMR does not depict properly the overall evolution of the interphase upon extended cycling. On the contrary, the same interphase probed by ^{19}F NMR is found to comprise a mix of resistive LiF with non lithiated species, whose accumulation can reasonably hamper the charge transfer at the interface (even if not covering totally the surface of the active material), as represented in **Figure III-14**.

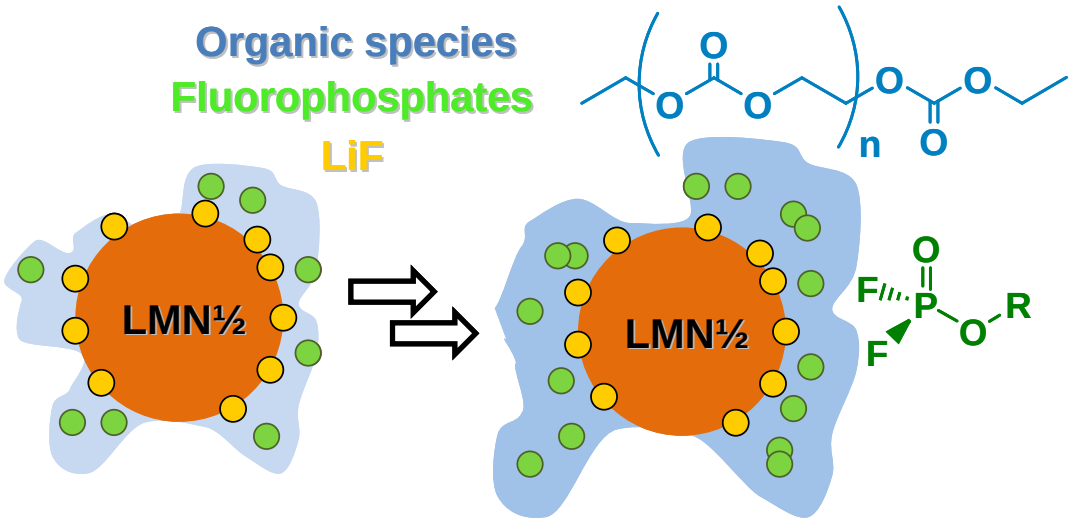

Figure III-14. Overview of the interphasial behavior of Ar-stored LMN ½ along cycling in conventional $LiPF_6$ 1M in EC:DMC (1:1) electrolyte. Cycling promotes the precipitation of non lithiated fluorophosphates and polymeric species, hence diminishing the conductivity of the interphase.

Although it is still unclear which part of the interphase is probed by XPS, the complementarity of this technique with NMR is undeniable. Not only does it provide fine chemical characterization, but it also gives access to the non lithiated organic part of the interphase, invisible to our NMR experiments. Thus, the accumulation of alkyl carbonates in the interphase can be evinced. The increase of charge transfer resistance and decrease of specific discharge capacity can therefore be correlated to the growth of a Li-poor interphase, unfavorable to the overall electrochemical behavior.

II.3. Effect of electrode formulation

The monitoring of the interphase evolution upon cycling by ^{19}F NMR requiring the use of non fluorinated binder(s), the choice of this inactive component remains limited. However, the influence of the polymer(s) used for its mechanical properties, and its dispersion in the composite electrode is expected to be significant, for its capability (or not) to form a protective film on the active material surface [40, 41]. This short section only gives a foretaste of the impact of electrode formulation on the interphasial behavior, opening the door to its systematic investigation.

II.3.1. Introduction

The second formulation tested during this work for $LiNi_{1/2}Mn_{1/2}O_2$ was optimized for $LiNi_{1/3}Mn_{1/3}Co_{1/3}O_2$ in power applications [42, 43]. Two different conductive agents are blended, namely carbon black particles and carbon fibers (VGCF). The binder used is still carboxymethyl cellulose (CMC), and a surfactant (TX100) is added in order to improve the carbons dispersion in water. The last and key ingredient is ethylene carbonate (EC), which aims at adjusting the slurry viscosity and maintaining an important porosity in the composite electrode. Indeed, its dissolution allows a subsequent improved impregnation of the composite electrode by the electrolyte [43]. The overall electrode composition consists in a 85/10/5 mixture of LMN ½/Carbons/Binder.

II.3.2. Electrochemical characterization

The power performance and cyclability of LMN ½ with this electrode formulation was investigated, as displayed in **Figure III-15**. The initial discharge capacity observed is particularly high, close to the value reported by Ozhuku *et al.* in ref. [10]. However, the capacity decay during the first ten cycles is also extremely sharp, after which it stabilizes around 100 $mAh.g^{-1}$, i.e. lower than batteries prepared with the previous formulation. The erratic evolution of the coulombic efficiency as a function of cycle number suggests a complex interphasial building process for the second formulation.

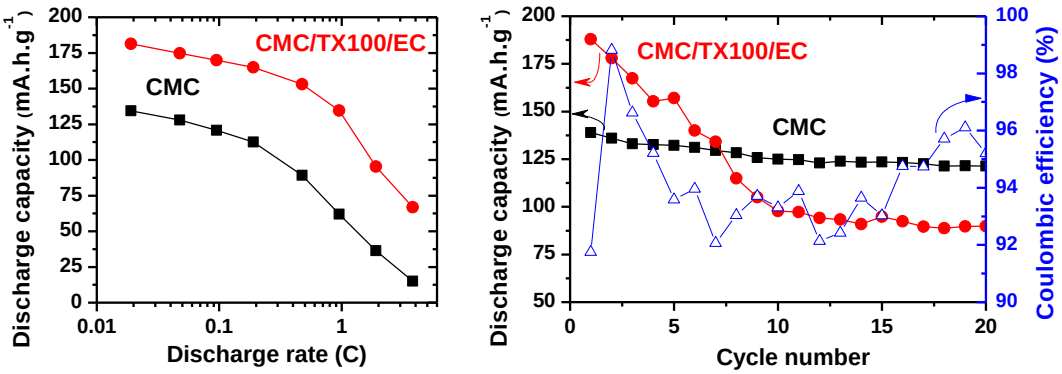

Figure III-15. Compared (left) power capabilities measured by cumulative discharges and (right) specific discharge capacities the previously used CMC formulation (black squares), and the CMC/TX100/EC formulation (red dots). The coulombic efficiency is given on the right scale for the second formulation (blue triangles).

II.3.3. Interphase characterization by NMR

The difference observed in terms of electrochemical behavior can only find its origin in the electrode formulation. Aiming at clarifying the interphasial processes induced by this change at the level of the composite electrode, ^{7}Li and ^{19}F NMR measurements were carried out. Quantification results and $T_{2r(Li)}$ estimated from the spectral linewidth are reported here in **Figure III-16** (see spectra in Appendix 2, **Fig. AII-3**).

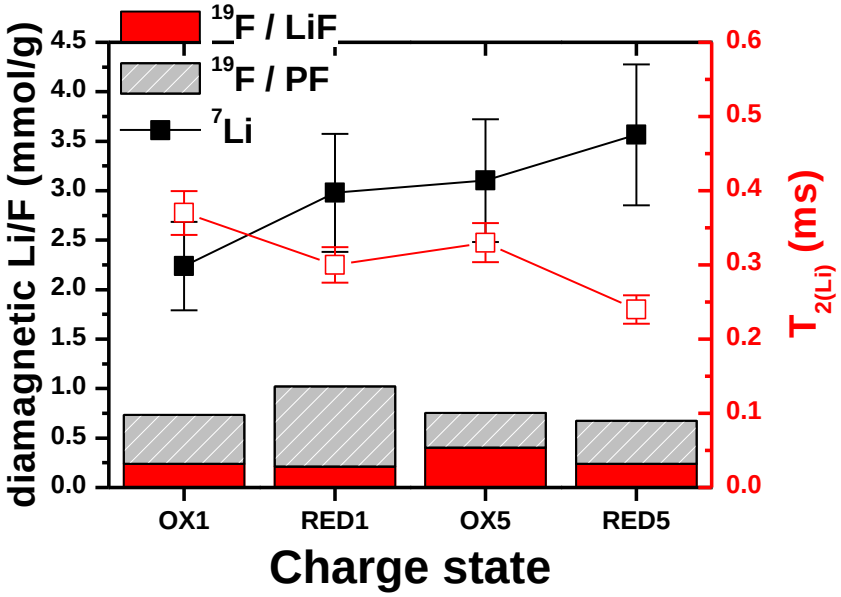

Figure III-16. ^{7}Li and ^{19}F NMR interphase quantification performed on LMN½ at the end of 1st and 5th charge and discharge at a C/20 rate **when using the CMC/TX100/EC formulation**. $T_{2(Li)}$ are estimated from the spectral linewidth for a MAS rate of 29 kHz.

By comparison with previous results reported in **Figure III-12**, the amounts of interphasial lithium detected here are one order of magnitude higher. The amount of fluorinated species is also more important, but remains at the same scale. Hence, the dramatic capacity decay may be attributed to an exacerbated accumulation of non fluorinated interphasial species containing Li at the electrode surface.

Such increase in the amount of interphasial Li would be expected to be accompanied by an increase of $T_{2r(Li)}$, as a sign of an increasingly weaker intimacy between the bulk and the interphase as the growth of this latter pushes additional lithiated species further from the grain surface [2, 3]. On the contrary, the relative $T_{2r(Li)}$ decrease observed at both the oxidized and reduced states might be the result of two distinct processes: first, the inability to charge the material up to the level of the initial cycle would induce an overall decrease of the average electronic spin carried by transition metals in the bulk material and thus a $T_{2r(Li)}$ decrease.

Second, a gradual increase of the intimacy of interphasial lithiated species with the active material can be considered if the accumulation of interphase proceeds in an increasing surface covering rather than the stacking of additional surface species on the top of the existing interphase. However, such considerations should be taken with caution since the capacity decay necessarily impacts the $T_{2r(Li)}$ and as mentioned previously. In future work, the trend observed here could be for instance reconsidered in the light of cycling experiments at lower rate or finished with a floating at 4.5 V or 2.0 V until the complete charge or discharge, respectively.

II.3.4. Discussion

Although the present study has not been carried out very far, the difference in electrochemical behavior between the two formulations can be explained in the light of the interphase characterization. In the case of the CMC/TX100/EC based formulation, NMR data indicate the exacerbated deposition of interphasial lithiated organic or polymeric species as sketched in **Figure III-17** and, from a more qualitative point of view, suggest a more important covering of the electrode surface. As a result, electrochemical reactions are found hampered to a considerable extent and impedance measurements should enable highlighting the possible formation of a resistive film.

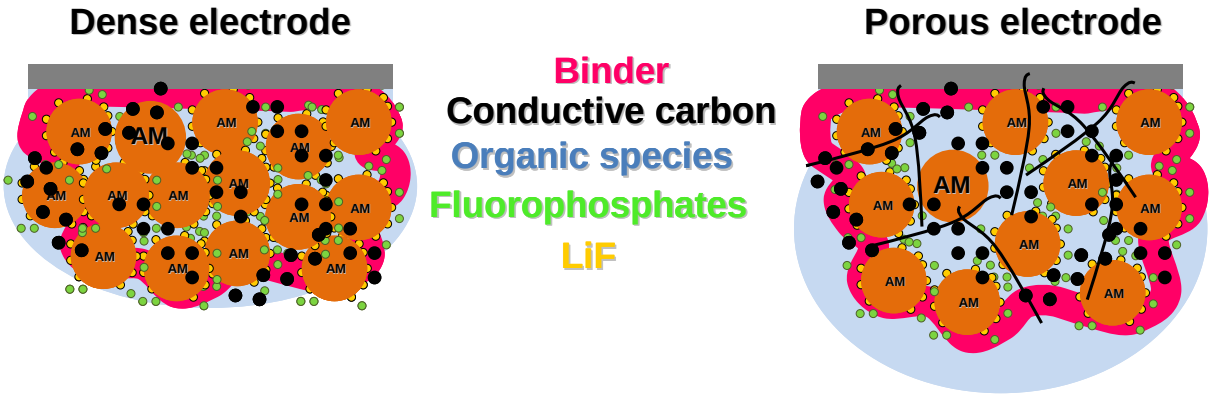

Figure III-17. Overview of the impact an electrode formulation leading to a higher porosity. The dissolution of EC upon contact with conventional $LiPF_6$ 1M in EC:DMC (1:1) electrolyte leaves room for lithiated organic species. Such important amounts of interphase, although extremely rich in Li, result in fast capacity decay.

Such reactivity towards electrolyte may find its origin in the electrode formulation. Indeed, ethylene carbonate has been identified as a pore former and the resulting improved impregnation of the electrode by the electrolyte (attested by the improved initial capacity and power performance) might be accounted responsible for the aggravation of solvents

decomposition. Maybe ethylene carbonate is degraded at the electrode surface even before the contact with electrolyte, throughout the electrode film drying. The reason why this formulation worked well for micrometric $LiNi_{1/3}Mn_{1/3}Co_{1/3}O_2$ active particles and does not in the case of our nanometric $LiNi_{1/2}Mn_{1/2}O_2$ further points out the critical role played by the surface developed by the active material. Hence, this short study highlights the importance of tailoring the electrode formulation not only as a function of the active material chemistry, but also to its morphology, in order to limit the extent of detrimental interphasial processes. Such considerations should be kept in mind when dealing with nanometric alloys or conversion materials.

II.4. Effect of LiBOB as an additive [paper IV]

The highlight of transition metals in the $LiNi_{1/2}Mn_{1/2}O_2$ / $LiPF_6$ 1M in EC:DMC electrolyte interphase by EELS (see chapter 2, **Fig. II-19**) set us on an electrolyte additive susceptible to limit manganese and nickel dissolution.

II.4.1. Introduction

While the detrimental impact of $LiPF_6$ hydrolysis reaction products is undisputed, alternatives to $LiPF_6$ salt in commercial batteries have not yet emerged due to the multiple requirements to be satisfied in terms of ionic conductivity and thermal stability. Lithium bis(oxalate)borate (LiBOB) has been reported as a promising candidate as electrolyte salt or additive for lithium-ion batteries leading to improved cycling performance and limited thermal reactivity [44-46]. Although cathodic interphasial mechanisms driven by the presence of LiBOB remain unclear [46], the reductive polymerization of the BOB^- anion around 1.7 V forming a protective film, is believed to effectively protect both negative and positive electrodes [47, 48]. The significant benefits of LiBOB-based electrolytes for lithium-ion batteries are however counterbalanced by a dramatic increase of the interfacial impedance resulting from interphase thickening, which in the end critically limits the power capability [49].

This section is devoted to the investigation of the effect of LiBOB as an additive both in terms of interphase amount, probed by quantitative surface NMR, and impact on the cyclability of $LiNi_{1/2}Mn_{1/2}O_2$. Here we make use of MAS NMR to clarify the interphasial processes associated to the presence of LiBOB in a mixed electrolyte: 0.9M $LiPF_6$, 0.1M LiBOB in EC:DMC (1:1).

II.4.2. Effect of LiBOB upon storage in electrolyte

Soaking experiments were carried out at 25°C and 55°C and the dissolution rates of $LiNi_{1/2}Mn_{1/2}O_2$ in standard and modified electrolytes were compared by ICP. Results are gathered in **Table III-2** with ^{7}Li, ^{19}F and ^{31}P NMR analyses performed on the recovered powders. Although lower amounts of Mn are detected in solution, it seems that the presence of LiBOB does not have any major impact on the dissolution of LMN½ in the electrolyte. Neither is the interphase composition significantly modified, at least from what NMR can probe.

These preliminary experiments indicate that if the presence of LiBOB is susceptible to modify the positive electrode interphase chemistry, it requires to be electrochemically activated by cycling, similarly to reported reductive polymerization mechanisms [47, 48, 50]**.**

	$LiPF_6$ 25°C	***$LiPF_6$ + LiBOB 25°C***	***$LiPF_6$ 55°C***	***$LiPF_6$ + LiBOB 55°C***
Mn in solution	1.5 mg.L^{-1}	0.9 mg.L^{-1}	16 mg.L^{-1}	11 mg.L^{-1}
Ni in solution	2.2 mg.L^{-1}	2.4 mg.L^{-1}	28 mg.L^{-1}	25 mg.L^{-1}
Interphasial Li	0.32 mmol.g^{-1}	0.38 mmol.g^{-1}	1.1 mmol.g^{-1}	1.27 mmol.g^{-1}
Interphasial F	0.15 mmol.g^{-1}	0.12 mmol.g^{-1}	0.21 mmol.g^{-1}	0.10 mmol.g^{-1}
Interphasial P	-	-	0.08 mmol.g^{-1}	0.08 mmol.g^{-1}

Table III-2. Amounts of Mn and Ni (± 10%) detected by ICP in standard and modified electrolytes after one month storage of LMN ½ powders at 25°C and 55°C. Amounts of interphasial species (± 20%) are deduced from integrated intensities of ^{7}Li, ^{19}F and ^{31}P NMR spectra.

II.4.3. Electrochemical characterization

Specific charge and discharge capacities obtained from LMN½-based electrodes cycled in the LiBOB containing electrolyte are plotted in **Figure III-18**, together with the charge transfer resistance measured in parallel by EIS in a 3 electrodes cell at the end of charge and discharge.

To allow for comparison with **Figure III-10**, the experimental conditions were kept constant with the exception of the investigated lithium salts. Although both electrolytes result in comparable discharge capacities, the coulombic efficiencies of the two series of cells differ significantly. LiBOB-based electrolyte does not only exhibit higher initial irreversible capacity (65 mA.h.g^{-1} vs. 20 mA.h.g^{-1} in the case of standard $LiPF_6$) but also shows a

persistently poor coulombic efficiency that one would expect accompanied by an increase of the cell impedance. However, as displayed in **Figure III-18** (right), LiBOB-modified electrolyte shows a fairly stable interfacial resistance (+25% over 20 cycles) compared to pure $LiPF_6$, for which the charge transfer resistance at the cathode increases by a factor of three to five by the same time. Such apparently inconsistent electrochemical features are discussed in the following in the light of surface analyses.

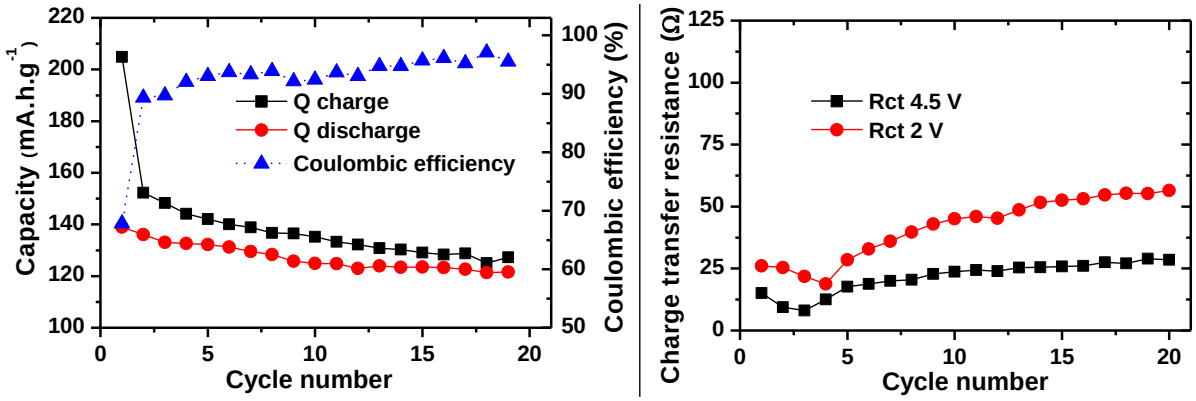

Figure III-18. Electrochemical data gathered from **Li//$LiPF_6$ + LiBOB//LMN½** cells at a C/20 rate. Left: specific charge (black squares), discharge (red dots) capacities and the resulting coulombic efficiency (blue triangles). Right: Charge transfer resistance fitted from EIS measurements carried out after a 5h rest at the end of charge (black squares) and discharge (red dots) in a 3 electrodes cell.

II.4.4. ^{7}Li and ^{19}F MAS NMR and XPS characterization

The evolution of the interphase along cycling was monitored by MAS NMR, as reported in **Figure III-19** (see spectra in Appendix 2, **Fig. AII-4**).

First of all, the evolutions of lithiated interphasial species differ significantly from what is observed with the conventional electrolyte. Whereas the amount of surface Li stabilizes around 0.2 $mmol.g^{-1}$ in the case of standard $LiPF_6$ in EC:DMC electrolyte (**Fig. III-12**), LiBOB-modified electrolyte exhibits a progressive increase of lithiated species with a marked potential dependence, the amounts being always more important in reduction compared to previous charged state. Noteworthy, this potential dependence is similar to the case where Li_2CO_3 is initially present at the electrode surface (**Fig. III-5, left,** [4, 5]), suggesting the modification of the interphasial chemistry. At the end of the 20^{th} discharge, there is approx. 0.6 $mmol(Li).g^{-1}$ of active material, i.e. three times more than in the case of pure $LiPF_6$. Such accumulation of lithiated species differs from the interphasial behavior previously observed in the conventional electrolyte. Indeed in the presence of LiBOB, the

persistently poor coulombic efficiency suggests that the interphase growth proceeds via an electrochemical mechanism all along cycling at the expense of the lithium metal electrode or electrolyte consumption.

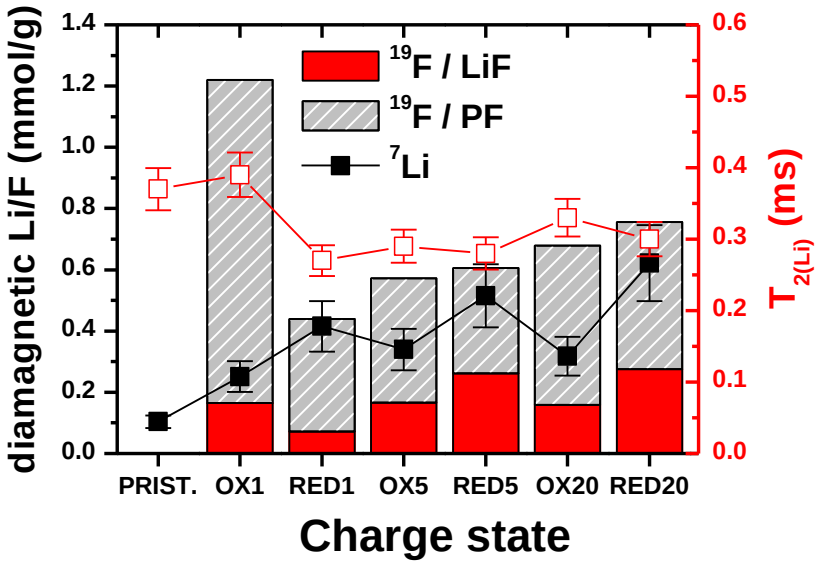

Figure III-19. ^{7}Li and ^{19}F NMR interphase quantification performed on LMN½ at the end of 1st, 5th and 20th charge and discharge at a C/20 rate **in the LiBOB modified electrolyte**. Red open squares correspond to $T_{2r(Li)}$ estimated from the spectral linewidth.

The modification of interphasial chemistry in the presence of LiBOB also seems to result in the aggravated precipitation of fluorophosphates during the 1st charge. Most of these fluorophosphates subsequently depart in the electrolyte along the next reduction process, and are not observed for the following oxidized states, suggesting the initial fluorophosphates detected may differ from those present later on. Indeed, from the 1st reduction on, LiBOB-modified interphase shows a rather stable "breathing" of LiF (0.15 and 0.25 mmol.g^{-1} at the end of charge and discharge, respectively) and a slow accumulation of fluorophosphates up to 0.6 mmol(F).g^{-1}.

The absence of correlation between the variation of lithiated and fluorinated species may imply that a significant proportion of lithiated species correspond to Li-alkylcarbonates rather than Li-containing fluorophosphates.

Compared to standard electrolyte, LiBOB-modified interphase contains lithium not only under the form of LiF (20-50%), but also some Li-rich alkylcarbonates (and fluorophosphates whose lithiation can hardly be evaluated but not totally ruled out). Supporting XPS analyses, performed at the end of 1st charge and 20th discharge, are reported in **Figure III-20**. Unfortunately, the presence of boron in the interphase cannot be

investigated by XPS, for the B 1s and P 2s core signals arising at close binding energies (187 and 191 eV, respectively).

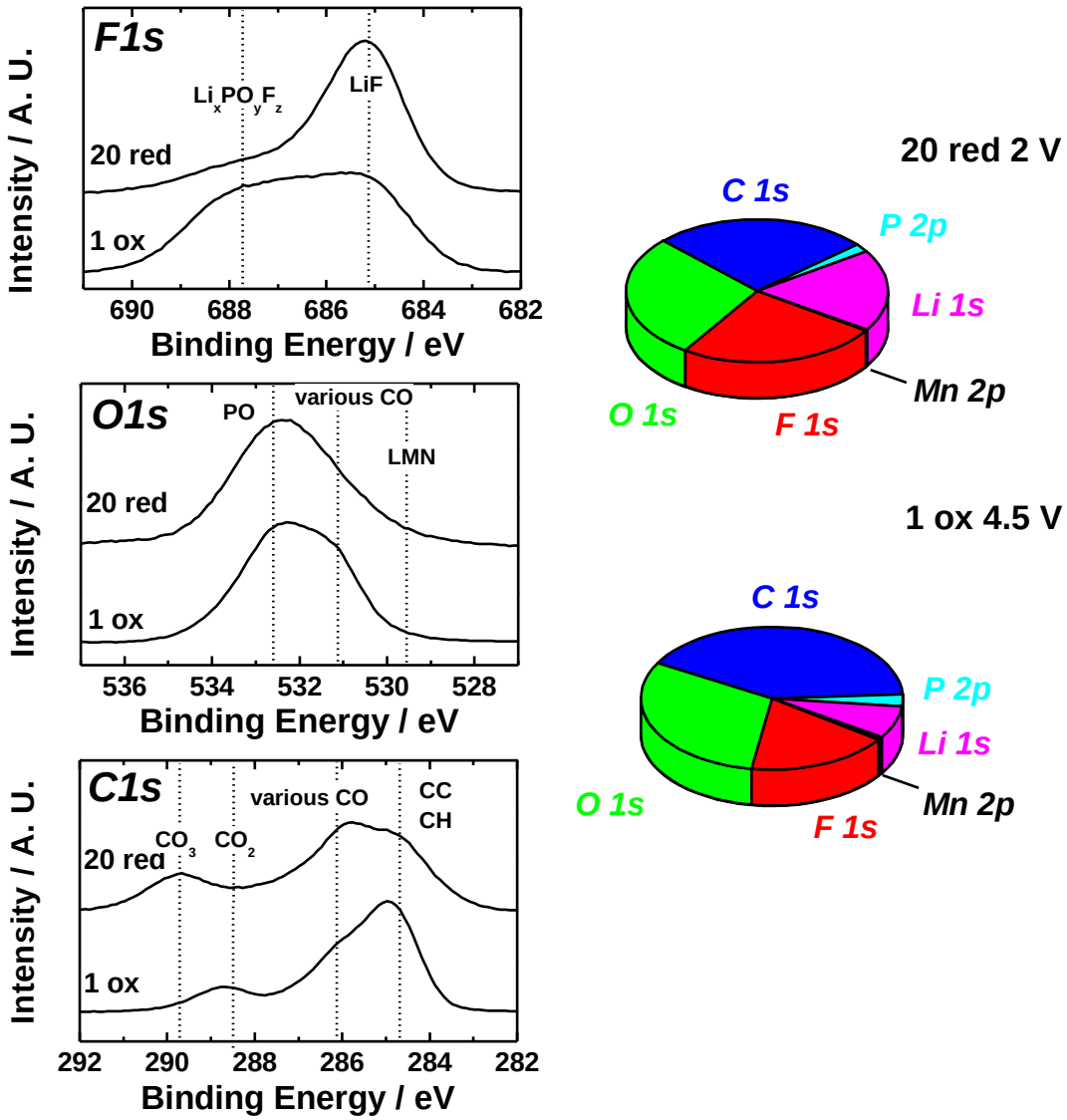

Figure III-20. Left: XPS *F 1s*, *O 1s* and *C 1s* core spectra measured at the end of the 1st charge and 20th discharge using **LiBOB-modified electrolyte**. Right: XPS elemental quantification diagrams for the two samples. The carbon percentage does not take into account the contribution at 284.8 eV from Ketjenblack carbon.

Remarkably, the interphase present at the end of the 1st charge is found rich in fluorophosphates (in agreement with NMR results) as well as carboxylate and oxalate groups, arising from BOB^- anions [51], which form the major part of the interphase. The percentage represented by lithium at this stage is as small as 7 %, in agreement with "bulk" NMR. At the end of the 20th discharge, not only has the contribution of Mn decreased from 0.7 to 0.3 % indicating further covering of the surface, but the Li percentage has more than doubled, up to

19%. In addition to an accumulation of lithiated species, as probed by NMR, XPS highlights a significant change in the chemical distribution of the interphase.

If any polymeric film is formed, it does not seem to passivate the surface since the contribution of salt decomposition products progressively increases along the following cycles. Cathodic interphasial mechanisms related to the presence of LiBOB are unclear [46]. The polymerization of BOB^- anions has been reported to occur upon reduction around 1.7 V vs Li^+/Li^0 [46, 52], and can therefore be ruled out here. Besides, the low coulombic efficiency (< 70 % at the 1st and <95% on the following cycles) would suggest chemical interphasial processes in discharge and electrochemical ones in charge. However, the absence of marked electrochemical signature related to the presence of LiBOB does not allow explaining such observation, as pointed out in ref [46].

While the T_{2r} characteristic dependency in SOC is still observed, it is weakly marked, probably due to the opposite effects of SOC and Li accumulation in reduction. However, the important decrease of $T_{2r(Li)}$ between the pristine interphase and the one observed at the end of the 1st discharge, in spite of a Li amount multiplied by a factor of 4, suggests a radical modification of the distribution of lithiated species in the interphase at the electrode surface. Hence, the interphase present from the 1st reduction on appears in greater intimacy with the active material, suggesting a more important coverage of the surface rather than a thickening of the preexisting interphase upon cycling.

II.4.5. Discussion

In the light of NMR surface analyses, it appears that the use of LiBOB-modified electrolyte results in a Li-enriched interphase rather than a thicker one. At the scale of the present experiments, the formation of this interphase implies lithium consumption all along the cycling, and is expected to result in poor coulombic efficiency, in agreement with electrochemical results. Apparently inconsistent electrochemical features (poor coulombic efficiency and stable impedance) could be discussed in the light of the accumulation of "good" (i.e. conducting) interphase. Indeed, based on the charge transfer resistance values, this interphase is found intrinsically less resistive (or less blocking) than the standard $LiPF_6$-based interphase, comprised of a mix of resistive LiF with non lithiated species, whose accumulation is expected to hamper the charge transfer at the interface. In comparison, Li-rich interphase sketched in **Figure III-21** acts more as a solid electrolyte interphase (SEI), hence paving the way toward the tailoring of a desirable interphase. Tuning the LiBOB concentration to optimize the nature and amounts of interphasial species appears necessary.

Indeed, if the concentration of LiBOB used in this study was set deliberately high to allow the observation of significant effects, literature reports the addition of 2 wt% of LiBOB to $LiPF_6$ as sufficient to form a stable SEI film [46].

Thus, the successful use of LiBOB as an additive may rely on its complete consumption during the first cycle, in opposition with the 20 cycles (or more) necessary to consume the 0.1 M used in the present study. As an example, using our LiBOB-modified electrolyte, the amount of surface lithium found at the end of the first full cycle (0.5 $mmol.g^{-1}$) corresponds roughly to the consumption of 2% of the lithium available in the electrolyte salt to form the interphase on the sole positive electrode. Similar investigation, run at the same time on both electrodes would enable to correlate directly capacity losses to interphasial processes, which might also be extremely precious for post mortem diagnosis.

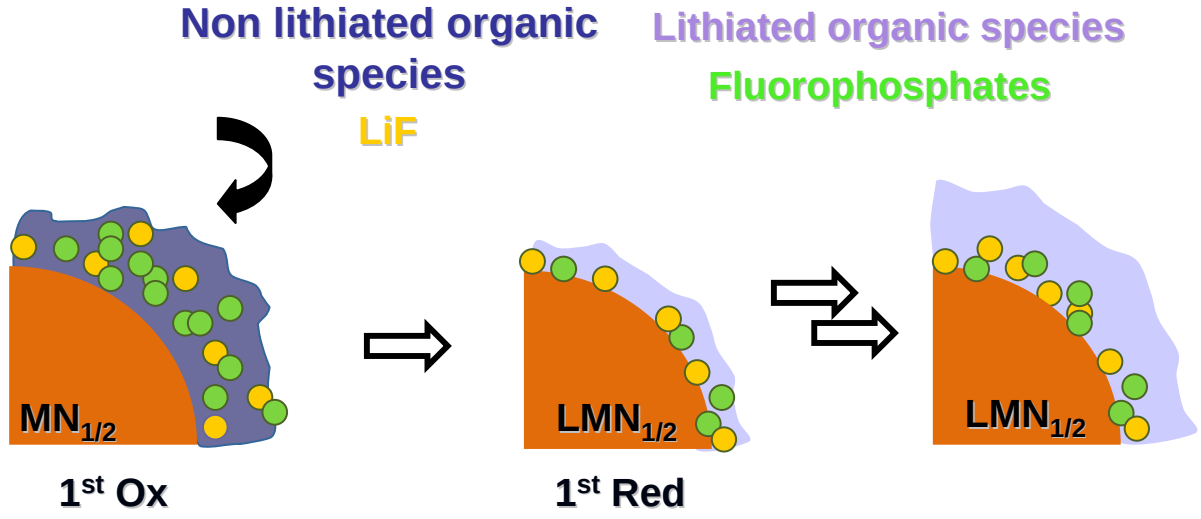

Figure III-21. Interphase observed on LMN ½ in the presence of 10 wt% of LiBOB in $LiPF_6$, EC:DMC electrolyte. While the initial interphase is poor in lithiated species others than LiF, it evolves upon cycling towards a "desirable" composition through an accumulation of Li-alkylcarbonates.

II.5. Concluding remarks

Keeping in mind its limitations, the use of MAS NMR quantification method offers wide perspectives in the field of interphases within electrochemical devices, as shown through the various examples developed here.

The presence of pristine Li_2CO_3 does not intervene in interphasial processes as a protective or resistive layer, but rather as an additive, whose influence differs between the

first 5 cycles that see Li consumption in the interphase at the cost of the bulk electrochemical capacity, and the subsequent cycles for which interphase and electrochemical performance have stabilized. Obviously, this particular behavior must also depend on the amount of native Li_2CO_3 on the surface and a whole range of electrochemical behaviors can be expected. The comparison with Li_2CO_3-free and LiBOB containing systems shows that a Li-rich interphase is to be preferred to the F-rich interphase observed for argon-stored material, even if the growth of this latter proceeds without Li consumption. Hence, a desirable positive electrode / electrolyte interphase should be conceived similarly to the SEI on graphitic anodes: rich in conductive lithiated species to ensure a good diffusion, homogeneous to allow surface passivation but the thinnest possible to limit the extent of lithium sacrifice. In this respect, results obtained on the formulation leading to an enhanced porosity demonstrate that in spite of a favorable chemistry, the upper limit in terms of quantity (thickness) can easily be reached.

Such optimization study, applied to LiBOB or to any other artificial SEI forming agent (additive, coating etc.) requires unequivocal and reliable spectroanalytical tools. We demonstrate here the strength of MAS NMR in such applications. Although carried out *ex situ*, the analyses shown here prove to correlate properly with *in situ* EIS and bulk electrochemical performance, thus validating the method to monitor interphase evolution. The observation of $T_{2(Li)}$, unreported so far, seems delicate but encouraging to describe qualitatively the electrode / interphase interaction. Estimated values should however be substituted by proper T_2 experimental determinations, providing more accurate and richer qualitative description in terms of interphase architecture for instance**.**

III- ELECTRODE MATERIAL MODIFICATIONS INFLUENCING THE INTERPHASIAL BEHAVIOR

The study of $LiNi_{1/2}Mn_{1/2}O_2$ has been extended to overlithiated layered oxides, and the composition $Li[Li_{0.2}Ni_{0.4}Mn_{0.4}]O_2$, was selected owing to its position in the $LiNiO_2$-$LiMnO_2$-$LiMn_2O_3$ ternary system (see chapter 1, **Fig. I-3, right**) making it the Li-richest compound for which the Li_2O net loss during the initial high potential plateau would result in the composition of our model compound $LiNi_{1/2}Mn_{1/2}O_2$. The differences between the two chosen materials, in terms of interphase chemistry and electrochemical performance, therefore only lie in the initial particular charge process.

Indeed, previous HRTEM studies report the formation of cracks and nanosize domains after the initial charge, the former being ascribed to oxygen loss [7, 53, 54]. However, no oxygen was observed in ref [7] by *ex situ* mass spectrometry measurements on the gases evolved from the battery, the oxygen presumably reacting with the electrolyte.

III.1. Synthesis and characterization of $Li_{1.2}Ni_{0.4}Mn_{0.4}O_2$

Aiming at comparing the surface reactivity of this Li-rich layered oxide (labeled hereafter LMN⅓) to that of the model compound LMN½ investigated so far, synthesis conditions were first kept as close as possible. However, excessive electrochemical polarization did not allow the proper study of this material, and a slight optimization of synthesis conditions had to be made.

III.1.1. Synthesis by a combustion method

The combustion synthetic route described in section 1.1 is used here. Precursors are introduced in stoichiometric amounts in solution with glycine and the resulting gel is fired at 180 °C. The annealing of $Li_{1.2}Ni_{0.4}Mn_{0.4}O_2$ is carried out at 900 °C for 62 h under air and ends with a quenching by liquid nitrogen.

III.1.2. Structural and morphological characterization

A typical XRD diagram of LMN⅓ is displayed in **Figure III-22**. All reflections can be assigned to the desired phase, described here in the $\boldsymbol{R\bar{3}m}$ space group. In agreement with the literature, small diffraction peaks observed around 20° reveal the presence of the

superstructure characteristic of Li_2MnO_3 [6-10]. The lattice parameters deduced from Rietveld refinement, as well as atomic positions and occupancies are reported in **Table III-3**. Moreover, crystallite size is estimated to 97(2) nm from the analysis of peaks width.

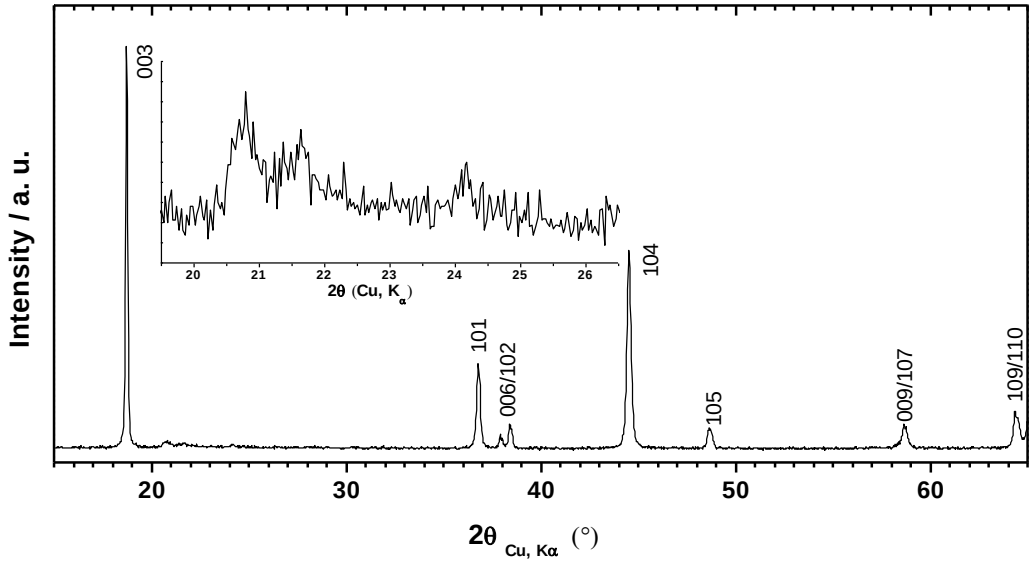

Figure III-22. XRD pattern recorded for $Li_{1.2}Ni_{0.4}Mn_{0.4}O_2$.

$LiNi_{1/2}Mn_{1/2}O_2$		Space group $R\bar{3}m$			
Lattice parameters		a_{hex} (Å) =	2.8766(6)	c_{hex} (Å)	14.2807(8)
Site		x	y	z	Occupancy
Li	3a	0	0	0	1.000(1)
Ni	3a	0	0	0	0.000(1)
Li	3b	0	0	0.5	0.216(1)
Ni	3b	0	0	0.5	0.400(1)
Mn	3b	0	0	0.5	0.4
O	6c	0	0	0.2444(5)	2
		R_{wp}	18.2 %	R_{bragg}	9.18 %

Table III-3. Lattice parameters and selected results from the Rietveld refinement of XRD pattern presented in Figure III-22

Scanning electron micrographs of LMN⅓ are shown in **Figure III-23**. As seen on SEM images, particles display an irregular shape and grain boundaries are not well defined, indicating a strong agglomeration that resists to sonication. Primary particles exhibit rather narrow size dispersion around 1 µm, in agreement with a specific surface area of 0.9 $m^2.g^{-1}$, as determined by the BET method. The discrepancy observed between the particle size and the

coherent length determined by XRD Rietveld refinement suggests that the synthesized LMN⅓ material is polycrystalline.

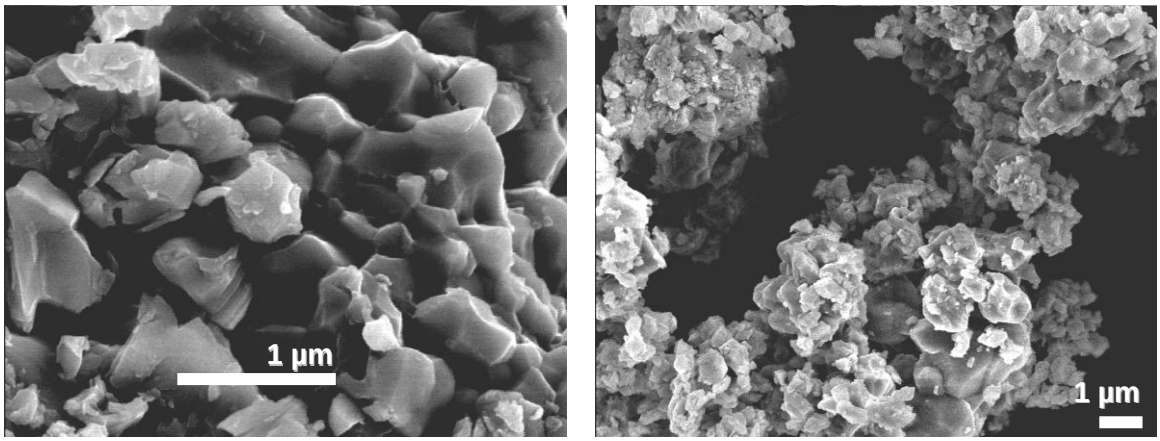

Figure III-23. SEM observations of pristine LMN⅓

III.1.3. Electrochemical characterization

The interest of investigating $Li_{1.2}Ni_{0.4}Mn_{0.4}O_2$ lies in the initial irreversible delithiation above 4.6 V, reported as an electrochemical activation step for these layered oxides [8]. As shown from the incremental capacity curves in **Figure III-24 (left)**, a significant irreversible oxidation peak accounting for approximately 0.3 Li per formula unit at the first cycle is indeed observed in the high potential range (4.6 – 5.0 V).

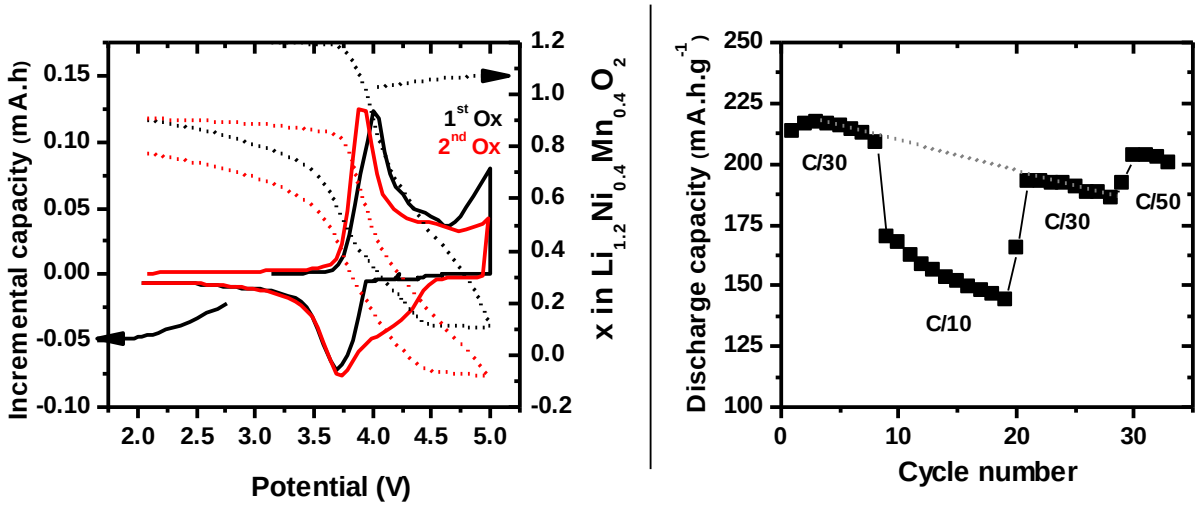

Figure III-24. Incremental capacity observed in a potentiodynamic mode between 2.0 and 5.0 V (5 $mV.h^{-1}$ steps with a C/100 current cut-off limit) for the 1st and 2nd cycles (left) and cyclability of **LMN⅓** at different galvanostatic rates between 2.0 and 4.8 V (right)

This value is far from a good agreement with the theoretical departure of 0.8 Li expected for this composition (Eq. III-2), as recalled in the equations below. However, the

overall theoretical capacity is almost reached, thanks to the important capacity observed in the 3.7-4.5V V region (Eq. III-1). During the subsequent discharge, 0.8 Li are reinserted in the material, as expected by Eq. III-3.

$$Li_{1.2}Ni(III)_{0.4}Mn(IV)_{0.4}O_2 - 0.4\ Li \rightarrow Li_{0.8}Ni(IV)_{0.4}Mn(IV)_{0.4}O_2 \quad \text{(Eq. III-1)}$$

$$Li_{0.8}Ni(IV)_{0.4}Mn(IV)_{0.4}O_2 - 0.4\ Li_2O \rightarrow Ni(IV)_{0.4}Mn(IV)_{0.4}O_{1.6} \quad \text{(Eq. III-2)}$$

$$Ni(IV)_{0.4}Mn(IV)_{0.4}O_{1.6} + 0.8\ Li \rightarrow Li_{0.8}Ni(II)_{0.4}Mn(IV)_{0.4}O_{1.6} \quad \text{(Eq. III-3)}$$

Galvanostatic cycling experiments (**Fig. III-24, right**) highlight the kinetic limitations faced with this material through the important capacity drop when accelerating the rate from C/30 to C/10. Besides, the initial performance cannot be recovered when slowing the rate down to its initial value, or even further down to a C/50 rate, indicating the irreversible degradation of the electrode upon "high" current densities. These experiments however do not allow ascribing the origin of this electrode aging to an intrinsic modification of the active material or to the damage of the composite electrode. Both explanations could intervene, insofar literature reports indicate the appearance of cracks in Li-rich layered oxides upon the irreversible delithiation [7, 53, 54], which could maybe also set mechanical stress to the electrode framework.

Hence, although the synthesized material exhibits a poor power capability, the irreversible delithiation, supposedly attributed to the departure of Li_2O can be observed. In this case, the resulting material composition should be that of the model compound LMN½, and the practical capacity obtained from the Li-rich derivative at C/30 (around 200 $mAh.g^{-1}$) is significantly improved compared to that of LMN½ cycled at comparable regime (around 120 $mAh.g^{-1}$, see **Fig. III-10**), for the overlithiated starting composition allows a higher utilization rate of the material.

III.2. Effect of overlithiation on the electrode / electrolyte interactions

Before considering the impact of the possible Li_2O release in the electrolyte on the interphasial processes upon cycling, the investigation of pristine $Li_{1.2}Ni_{0.4}Mn_{0.4}O_2$ surface reactivity towards electrolyte is necessary. Indeed, the material morphology, especially the surface developed that can be exposed to electrolyte, clearly differs from that of LMN½ reported in section 1.2.2. A lower specific surface area is here expected to limit the extent of electrolyte decomposition. Nonetheless, the overlithiation, being balanced by the increase of

nickel valence from (+II) to (+III), might result in the increase of surface nucleophilic character, as observed for $LiNi(III)O_2$ and thus, in an exacerbated reactivity [55, 56].

III.2.1. Interphase grown upon aging in $LiPF_6$ electrolyte

Soaking experiments, similar to those previously discussed in section 2.2.1 (**Fig. III-7**) are here reported in **Figure III-25**, in the case of the Li-rich LMN⅓ (see spectra in Appendix 2, **Fig. AII-5**).

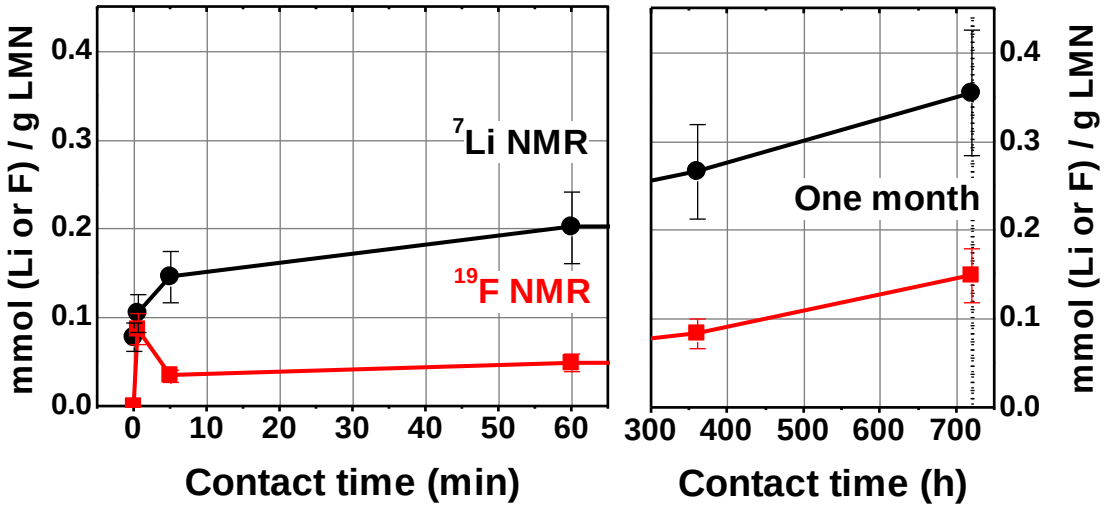

Figure III-25. Evolution of the normalized integrated intensities of ^{7}Li and ^{19}F MAS NMR spectra, for **LMN⅓** soaked in conventional $LiPF_6$ 1M in EC:DMC electrolyte for various durations.

Here again, all the ^{19}F MAS NMR intensity can be assigned to lithium fluoride (-205 ppm). Noteworthy, as reported per mass unit of active material, the amounts of interphasial species found at the surface of the Li-rich material are extremely close to previous results on the reference LMN½ material. However, the difference of surface developed by the two materials (8 $m^2.g^{-1}$ and 1 $m^2.g^{-1}$ for LMN½ and Li-rich LMN⅓, respectively) suggests that the interphase grown on this latter should therefore be eight times thicker. Similarly to the reference material, the difference in the amounts of interphasial Li and F also suggests the presence of important amounts of Li alkylcarbonates in the interphase. Nonetheless and contrary to results reported in **Figure III-10** for LMN½, the amount of fluoride under the form of LiF does not stabilize after few minutes of contact with $LiPF_6$-based electrolyte but rather follows the same trend as the amount of interphasial lithiated species.

The interphase grown upon contact with electrolyte after one month on the surface of Li-rich LMN⅓ was probed by TEM and EELS, as summarized in **Figure III-26**. Irregular interphasial aggregates are observed, with a thickness ranging from 20 to 100 nm. Noteworthy, contrary to the analysis carried out on LMN½ , no manganese could be detected in the interphase. Composition profiles such as the one shown here suggest an interphase rich in fluorinated species (identified by NMR as LiF in the experiment above). The area probed in spot #4 comprises oxygen and manganese in the proportions of LMN⅓ but also fluorine, suggesting that this area is located at the interface of the active material with an interphase only made of lithium fluoride. While the inner part of this interphase is rich in fluorine (#4 > #3 > #2 > #1), the extreme surface mostly contains oxygenated species such as alkylcarbonates.

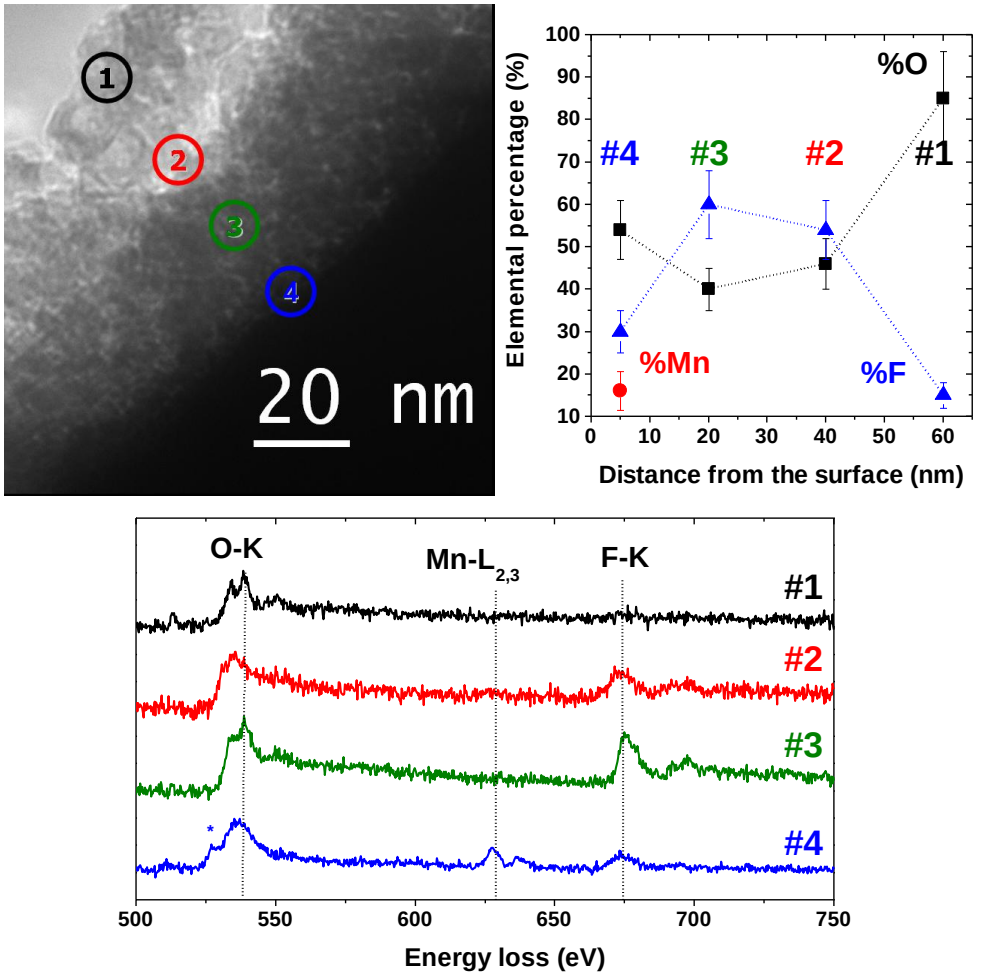

Figure III-26. TEM image of **LMN⅓** after one month soaking in conventional $LiPF_6$ 1M in EC:DMC electrolyte. Numbers denote spots subjected to EELS analysis, which results are reported together with illustrating spectra.

Hence, complementary NMR and EELS measurements indicate an important covering of the Li-rich oxide upon contact with electrolyte. Although its external part is mostly composed of alkylcarbonates, an average O/F ratio of 1 is observed by EELS. Considering that this interphase remains as rich in lithium fluoride (0.15 mmol(F).g^{-1} of LMN⅓) as that of the LMN½ reference (0.15 mmol(F) g^{-1} of LMN), a similar trend with respect to lithiated organic species can be assumed. So to say, no significant difference in chemical composition of the interphase can be noticed. The only difference lying in the surface developed by the two materials, these experiments suggest a similarly aggravated decomposition of salt and solvents in the case of the Li-rich derivative.

III.2.2. Interphase grown upon electrochemical cycling

The impact of the initial irreversible delithiation on the interphasial chemistry can be monitored by ^{7}Li and ^{19}F NMR along the two first electrochemical cycles, as illustrated by **Figure III-27** (see spectra in Appendix 2, **Fig. AII-6**).

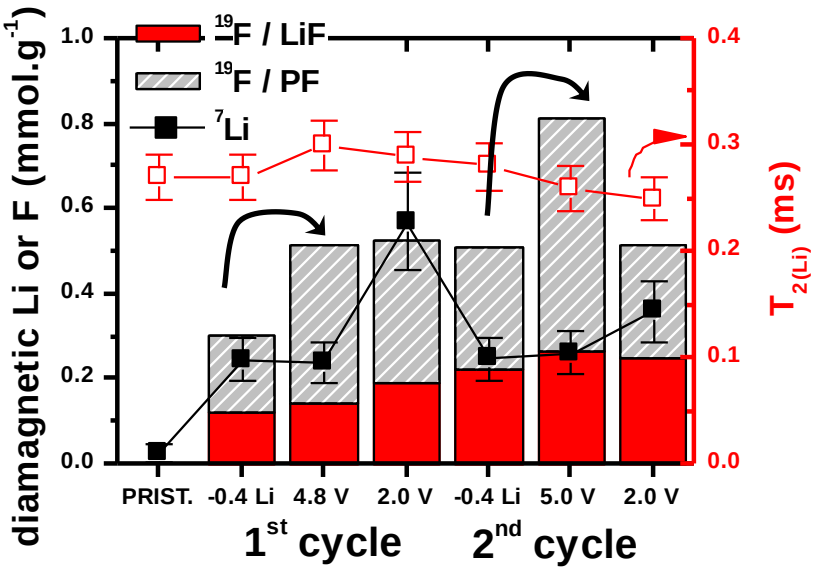

Figure III-27. ^{7}Li and ^{19}F NMR interphase quantification performed on **LMN⅓** during the two first electrochemical cycles, after the removal of 0.4 Li (see Eq. III-1), after the high potential plateau (Eq. III-2) and after Li reinsertion (Eq. III-3) at a C/50 rate in conventional $LiPF_6$ 1M in EC:DMC electrolyte. Red open squares correspond to $T_{2r(Li)}$ estimated from the spectral linewidth.

The little evolution in the amount of lithium fluoride upon cycling suggests that the pristine interphase formed by contact with electrolyte is extremely stable upon subsequent cycling. Considering the composition gradient probed by EELS in the previous section, one

can imagine that the LiF-rich inner interphase does not evolve upon cycling. In the same time, the evolution of lithiated interphasial species seems to follow the trend previously observed on the air-stored LMN½ material (see **Fig. III-5, left**), since higher Li amounts are detected at the end of discharge compared to the previous charge.

From the NMR quantification of the interphase, it appears that the irreversible "Li_2O" extraction from the material above 4.5 V only results in an important increase, highlighted by arrows on **Figure III-27**, of the amount of fluorophosphates detected by ^{19}F NMR (approx. +100%). In fact, there is no variation of the amount of interphasial lithium between the end of the electrochemical deintercalation of Li from the structure and 4.8V. On the other hand, the increase in phosphorus amount was confirmed by ^{31}P NMR measurements performed during the initial oxidation, showing not only such increase (+72 % on the integrated intensities) but also that the nature of those fluorophosphates is unchanged. Indeed the F/P ratio remains close to 1.5, in agreement with an isotropic shift arising at -17 ppm (i.e. between that of RPO_3F and RPO_2F_2) large enough to embrace both signals. Besides, most of these fluorophosphates are probably non lithiated, for the overall amount of lithium detected at high potential is very close to that of fluorine in LiF.

Hence, the irreversible delithiation at high potential should not be seen as the formation of Li_2O as a chemical entity but rather to separated Li^+ extraction and possible generation of gaseous oxygen from O^{2-} ions, as investigated by GC-MS in the literature [7, 9]. While *in situ* measurements highlight the presence of O_2 in the system [9], *ex situ* analyses suggest that in closed circuit [7], this oxygen actually reacts with electrolyte salt and solvents, leading to the direct oxidation of EC and/or DMC from the electrolyte by the highly oxidized electrode material. In-chain reactions may imply the increased precipitation of non lithiated fluorophosphates such as OPF_2OR or $OPF_2(OCH_2CH_2)_nF$.

The quite weak magnitude of the variation of the T_{2r} values, as well as the absence of correlation with the SOC, over the two first cycles is tentatively assigned to the thickness of the interphase and the stability of the inner LiF component.

In order to monitor the impact of O_2 release in the system on the electrode / electrolyte interactions, further NMR investigation of the interphase evolution upon extended cycling is presented in **Figure III-28** (see spectra in Appendix 2, **Fig. AII-7**).

The absence of evolution in the amount of lithium fluoride upon cycling is confirmed at the scale of the 20 first cycles. The amount of fluorophosphates does not exceed those observed during the two first cycles (**Fig III-27**), but rather decrease on the long term.

The variation observed in the amount and distribution of lithiated interphasial species upon cycling are comparatively much more important than that of fluorinated salts. First, the potential dependency in the amount of interphasial Li, also observed in the presence of Li_2CO_3 and LiBOB, is striking here. The absence of correlation between such variation and the amounts of fluorinated species suggests once again that the extra lithiated species formed upon discharge are probably Li alkylcarbonates and POE polymers. Besides, the progressive decrease of $T_{2(Li)}$ in this case, regardless the SOC, suggests that the global interaction between the active material and its interphase is strengthening upon cycling.

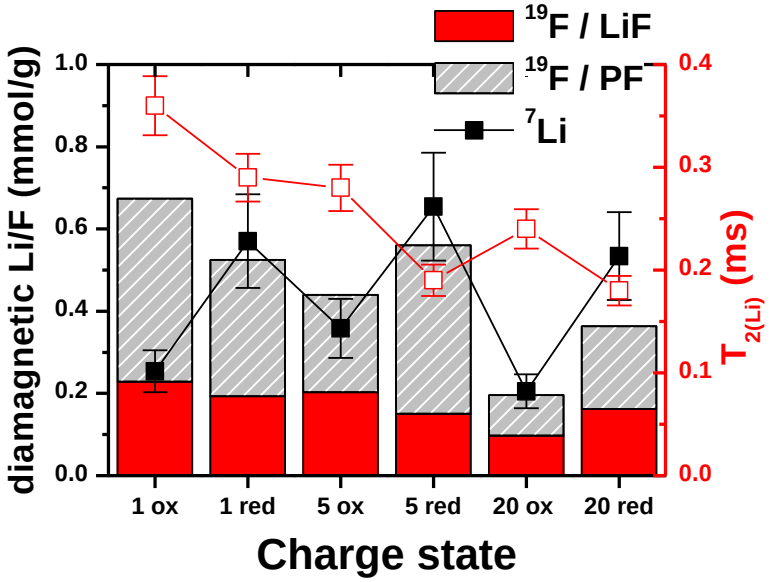

Figure III-28. ^{7}Li and ^{19}F NMR interphase quantification performed on **LMN⅓** at the end of 1st, 5th and 20th charge and discharge at a C/30 rate between 2.0 and 4.6 V in conventional $LiPF_6$ 1M in EC:DMC electrolyte. Only the first charge was prolonged up to 4.8 V. Red open squares correspond to $T_{2r(Li)}$ estimated from the spectral linewidth.

The result of such interphase evolution can be observed *in situ* through EIS measurements, as shown in **Figure III-29**. Similarly to the reference material, only one semi-circle is observed on the Nyquist plots, which can therefore be assigned to the interfacial charge transfer and double layer capacitance [3-5]. In the absence of interphase accumulation (to be confirmed by XPS able to probe non lithiated organic species) susceptible to hamper the charge transfer at the electrode surface, the gradual increase of the charge transfer resistance can be attributed to the electrode breakdown, e.g. the loss of percolation within the electrode. Contrary to the LMN½ reference, no sign of impedance stabilization appears at the term of the 20 first cycles, suggesting a long-lasting aging of the electrode / electrolyte interface.

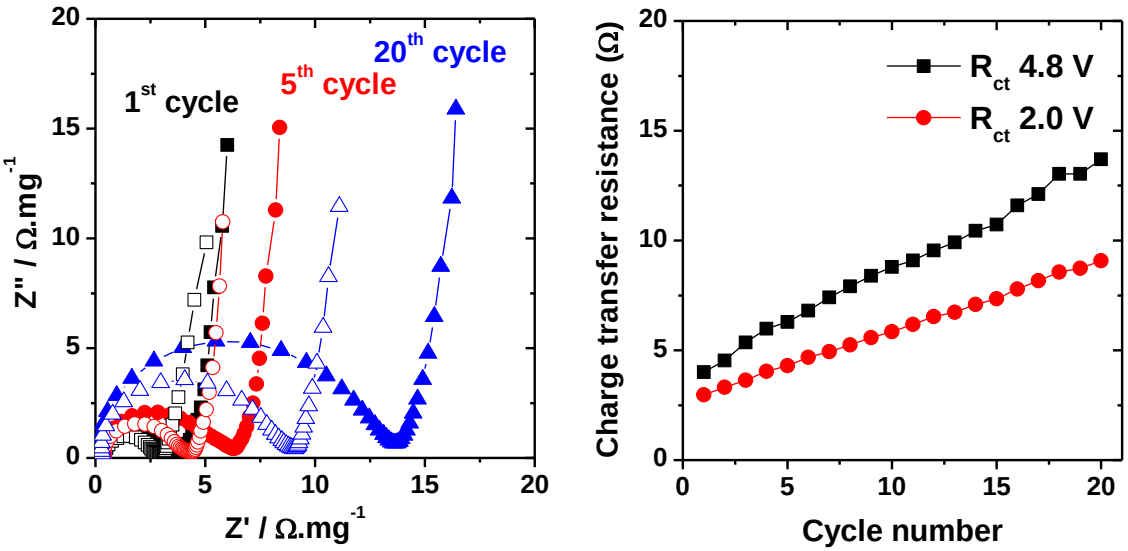

Figure III-29. Left: Nyquist plots of EIS performed in a 3 electrodes cell on **LMN⅓** at the end of 1st, 5th and 20th charges (closed symbols) and discharges (open symbols) at a C/30 rate between 2.0 and 4.8 V. Right: Charge transfer resistance fitted from EIS measurements carried out at the end of charge (black squares) and discharge (red dots).

III.2.3. Discussion

Considering that the $T_{2r(Li)}$ decrease along an extended cycling is neither correlated to the SOC, nor anymore to the detected amounts of interphasial species, a possible explanation would consist in the active material decrepitation, mentioned above as a possible origin to the capacity decay. In the hypothesis of cracks propagating from the grain surface, new surface would be created. It is reasonable to expect these bare surfaces exposed to electrolyte to react preferentially and interphasial species would precipitate on this free surface rather than stack on existing ones. This progressive redistribution of interphasial species along the successive dissolution/precipitation processes might then explain the overall increase of interphase/material intimacy and hence, global decrease in $T_{2r(Li)}$. However, the reason why this phenomenon would not be accompanied by an overall increase in the amounts of lithiated and fluorinated species per mass unit of active material is still unclear.

To conclude, in the case of the $Li_{1.2}Ni_{0.4}Mn_{0.4}O_2$ starting material compared to $LiNi_{1/2}Mn_{1/2}O_2$ presenting a pristine Li_2CO_3 interphase, it seems that all interphasial features are exacerbated: while fluorinated species are formed by direct contact with electrolyte or along the 1st electrochemical cycle and then do not undergo substantial modifications upon repeated cycles, lithiated species exhibit a strong potential dependency not related to the SOC. The amounts of surface Li and F detected per mass unit being similar for a specific surface

area 8 times lower, the interphase should necessarily be thicker and/or more covering. Nonetheless, the amount of surface Li_2CO_3 formed on $Li_{1.2}Ni_{0.4}Mn_{0.4}O_2$ during the synthesis and storage under air is negligible (**Fig. III-25**) and cannot be hold responsible for such reactivity towards electrolyte.

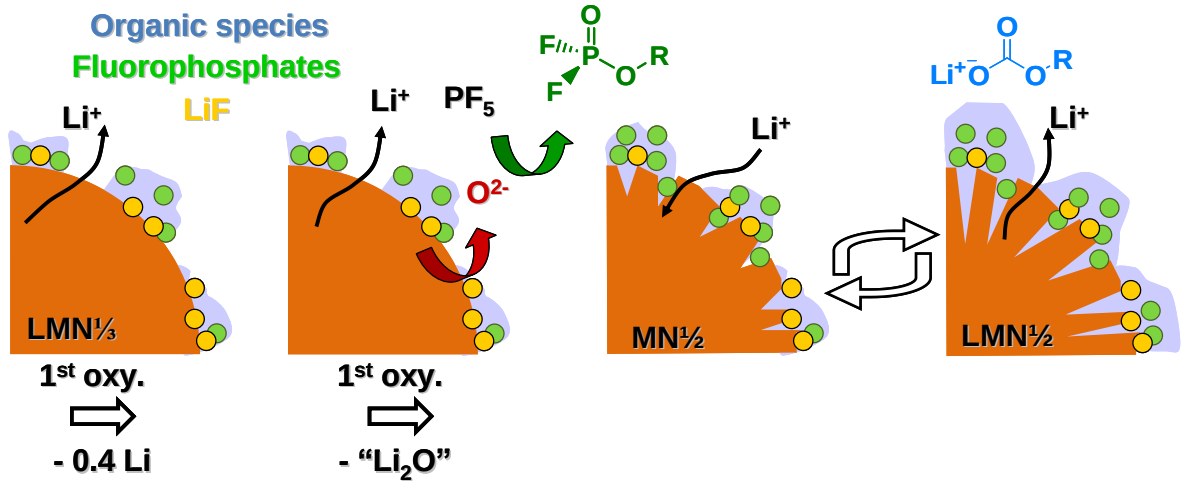

Figure III-30. Overview from left to right of the deintercalation of Li ions up to 4.5V and the subsequent net loss of "Li_2O" between 4.5 and 4.8V, leading to the reaction of oxygen with conventional $LiPF_6$ 1M in EC:DMC (1:1) and the formation of cracks in the material upon subsequent cycling.

Thus, several interphasial mechanisms should be considered: first, enhanced surface nucleophily might aggravate salt and solvents decomposition upon contact and then the release of oxygen from the active material might dictate the interphasial chemistry, as sketched in **Figure III-30**. In the same way, Li_2CO_3 or LiBOB could be considered as oxygen sources, leading to an overall similar interphase evolution upon cycling.

III.3. Use of coatings: effect of a heterochemical surface layer

In the following, the modification of reactivity towards electrolyte of $Li_{1.2}Ni_{0.4}Mn_{0.4}O_2$ is evaluated subsequently to surface modification by the deposition of an Al_2O_3 buffer layer as described below. In the literature, this type of coating has indeed been reported to decrease the initial irreversible capacity and improve the cyclability of Li-rich layered oxides [57, 58].

In this work, the Al_2O_3 layer is deposited through the precipitation of $Al(OH)_3$ from $Al(NO_3)_3$,$9H_2O$ and NH_4OH on the active material, followed by a post annealing of 4 h at

300°C under air [57]. The resulting Al_2O_3 layer is assumed to represent 3wt % of the total composite material, referred to as AlO/LMN⅓.

III.3.1. Characterization of aluminum oxide coated $Li_{1.2}Ni_{0.4}Mn_{0.4}O_2$ material

XRD shows that the bulk structure is not modified by the chemical and thermal treatments necessary to deposit the Al_2O_3 coating, as shown from the pattern in **Figure III-31**. Rietveld refinement indicates neither a modification of the lattice parameters, nor of the cationic distribution. No additional diffraction peaks are observed and the heterochemical coating is thus present under a nanocristalline or amorphous form. Characterization at the local scale by ^{27}Al MAS NMR (Appendix 2, **Fig. AII-8**) indicates that most of the aluminum corresponds to Al_2O_3. However, a minor contribution around 80 ppm can be attributed to a tetragonal environment, suggesting a side reaction during the thermal treatment. Cationic exchange should be considered here, in the light of previously reported works [59, 60].

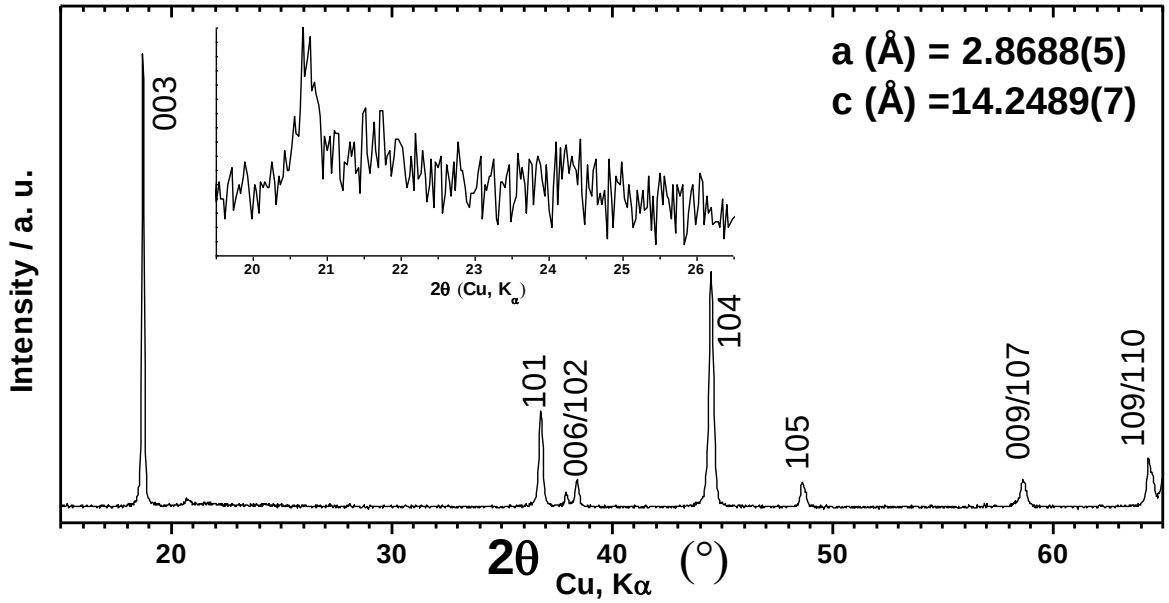

Figure III-31. XRD pattern recorded for as prepared **AlO/LMN⅓.**

SEM images (**Fig. III-32, left**) show that the nanometric particles of LMN⅓ are now aggregated in large microscopic secondary particles (~ 10 µm), exhibiting a rather continuous surface. Such observation suggests the presence of an extremely thick coating at the scale of the secondary particles (> 50 nm), but does not allow certifying the penetration of aluminum oxide within these aggregates. Complementary TEM characterization at the scale of primary particles (**Fig. III-32, right**) highlights the inhomogeneity of the deposited coating, which is observed under the form of small amorphous aggregates, exhibiting a thickness ranging from 0 to 30 nm. The doubling observed in the BET specific surface area, from 0.9 to 1.7 $m^2.g^{-1}$,

should be attributed to the presence of these irregular deposits of Al_2O_3 and indicates that the presence of a thick layer of coating at the surface of secondary particles does not reduce the surface developed by the material.

Considering the previous investigation of $Li_{1.2}Ni_{0.4}Mn_{0.4}O_2$ / electrolyte interactions, a rather poor electrochemical behavior is expected for this material, since the distribution of the coating on the active material is not satisfying: bare surfaces should still be subjected to reactions with the electrolyte as previously described. An improvement of the electrochemical performances subsequently to the coating treatment is not expected.

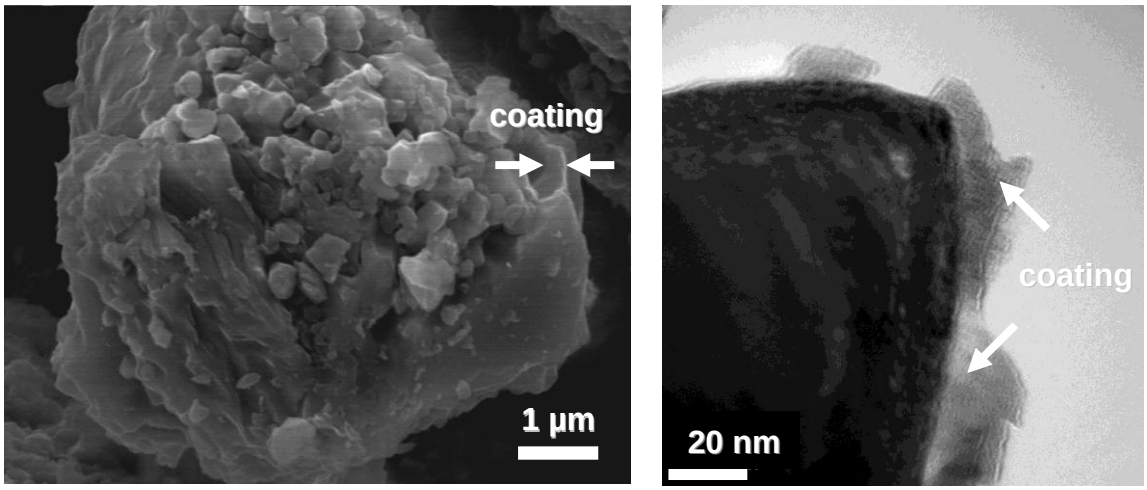

Figure III-32. SEM observation of an **AlO/LMN⅓** secondary particle (left) and TEM picture of the surface of a primary particle (right).

The detrimental impact of Al_2O_3 on the power performance of LMN⅓ (**Fig. III-33, left**) is visible at all cycling rate. The difference between discharge capacities observed for bare LMN⅓ and AlO/LMN⅓ does not vary significantly as a function of the discharge rate. This result suggests rather a disconnection (or insulation) of active material particles from the percolating network, possibly by thick resistive aggregates.

Noteworthy, such power test based on cumulative discharges supports the damage brought to these Li-rich oxides by high current densities since the C/50 capacities reached here are significantly lower than those measured under constant current (**Fig. III-33, right**). On this second plot, the evolution of the discharge capacity vs. cycle number for the coated material exhibits the same trend than the bare material, consistent with a behavior dictated by either bulk material or accessible bare surface exposed to electrolyte. The capacity decay along the first 5 cycles is however, more pronounced and cannot be explained straightforwardly based only on bulk structural and morphological evolution and then, has to be seen as a consequence of the surface treatment.

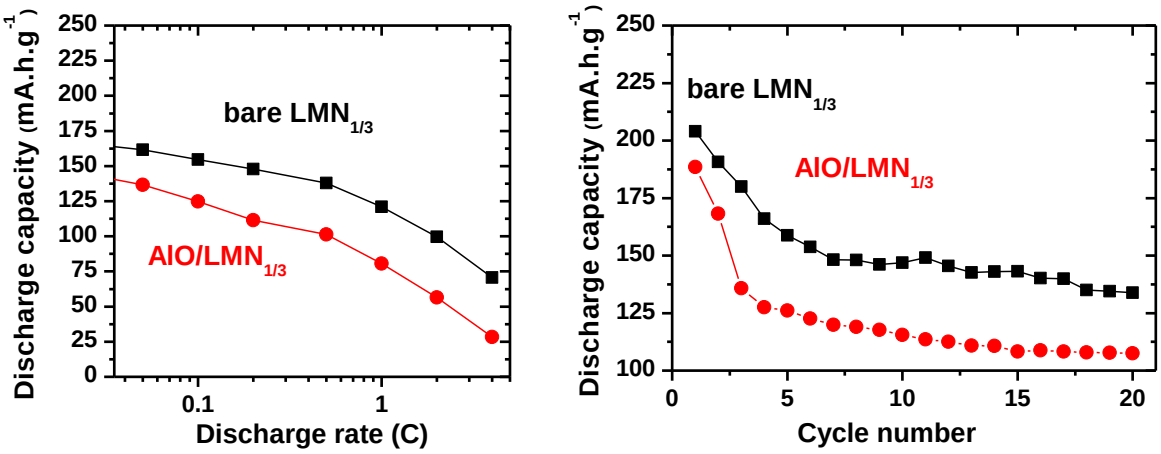

Figure III-33. (Left) Compared power performance and (Right) cyclability of **bare and AlO/LMN⅓** measured between 2.0 and 4.6 V at a C/50 rate, after an initial charge up to 4.8 V.

III.3.2. Interphase grown upon aging in $LiPF_6$ electrolyte

In order to evaluate possible change in the reactivity towards electrolyte, soaking experiments, similar to those carried out on the bare material (**Fig. III-25**) are here reported in **Figure III-34** in the case of the Al_2O_3 coated LMN⅓ (see spectra in Appendix 2, **Fig. AII-9**).

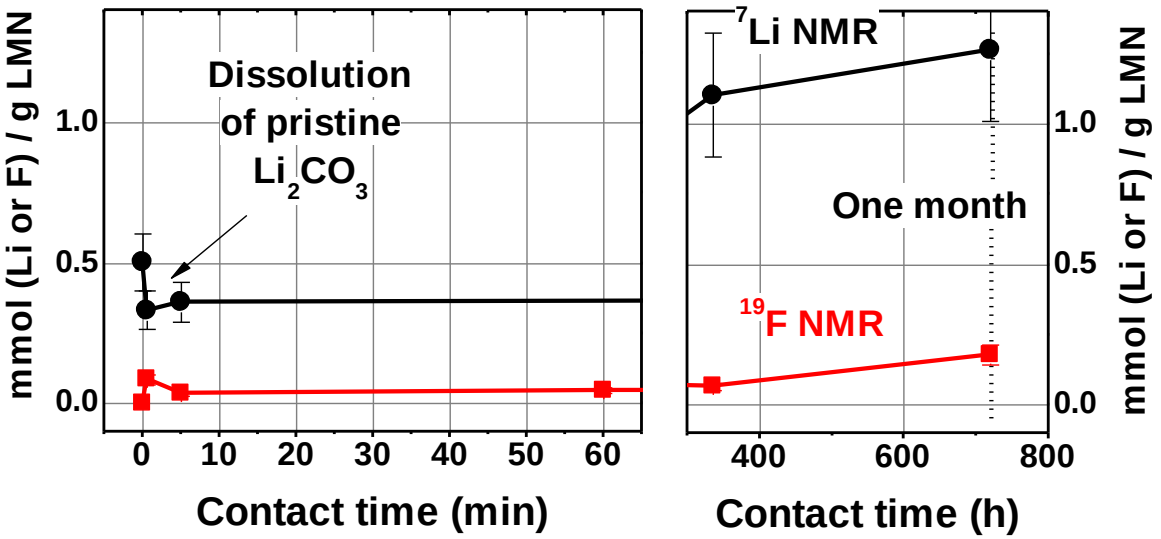

Figure III-34. Evolution of the normalized integrated intensities of ^{7}Li and ^{19}F MAS NMR spectra, for **AlO/LMN⅓** soaked in conventional $LiPF_6$ 1M in EC:DMC electrolyte for various durations.

Attention should be paid to the scale used in **Figure III-34**, in comparison with **Figure III-25.** Indeed, if comparable amounts of fluorine are detected on the surface of

AlO/LMN⅓, the amount of lithiated species is roughly multiplied by a factor of 3. In particular, the pristine Li_2CO_3-rich interphase (detected by IR measurements) is 5 times more important than on bare $Li_{1.2}Ni_{0.4}Mn_{0.4}O_2$, suggesting the extraction of lithium from the bulk in the presence of aluminum oxide during the thermal treatment in air. It should also be noted that the gellification of the electrolyte solution in contact with AlO/LMN⅓ was observed for the longest experiment (one month), indicating a completely modified interphasial chemistry in the presence of Al_2O_3. Besides, the ^{19}F NMR intensity does not only correspond to LiF, as observed so far for simple contact experiments, but also to RPO_2F_2 type fluorophosphates (see spectra in Appendix 2, **Fig. AII-9**), which amount is found not only for short contact times but also significantly increased after gellification.

In an attempt to further describe the interphase grown upon contact with electrolyte after one month, the recovered AlO/LMN⅓ powder was probed by TEM and EELS, as seen in **Figure III-35**.

After such extended contact with electrolyte, no bare surface can be observed, in contrast with previous analyses performed on LMN⅓ or LMN½ materials. Considering the detection of the F-K edge on all the EELS spectra, it seems that the Al_2O_3 coating cannot be observed alone, and is always intimately mixed or impregnated with fluorinated interphasial species. Similarly to the interphase grown on bare materials, the fluorine concentration is still found more important when probing the inner part close to the active material compared to the extreme surface, suggesting the preferential deposition of fluorinated salts upon immediate contact with the material.

An additional difference from interphase observed on bare LMN⅓ lies in the detection of 5% of manganese at any location in the interphase of AlO/LMN⅓. The changes displayed from the bulk oxide (see **Fig. III-35, #4**) in the L_3/L_2 ratio and in the fine structure of oxygen indicate a chemical modification of manganese valence and environment, which would require further investigation to specify the mechanism of manganese dissolution and subsequent trapping/ reaction within the interphase.

To summarize, after one month soaking in conventional $LiPF_6$ 1M in EC:DMC electrolyte, Al_2O_3 coated $Li_{1.2}Ni_{0.4}Mn_{0.4}O_2$ show signs of dissolution, contrary to the bare material. The constant presence of manganese in the whole interphase thickness supports the aggravated reactivity towards electrolyte measured by ^7Li NMR. A dramatic increase in the amount of interphasial lithiated species, uncorrelated to a variation in the amount of fluorinated species, suggest the exacerbation of solvents decomposition upon contact with electrolyte in the presence of Al_2O_3.

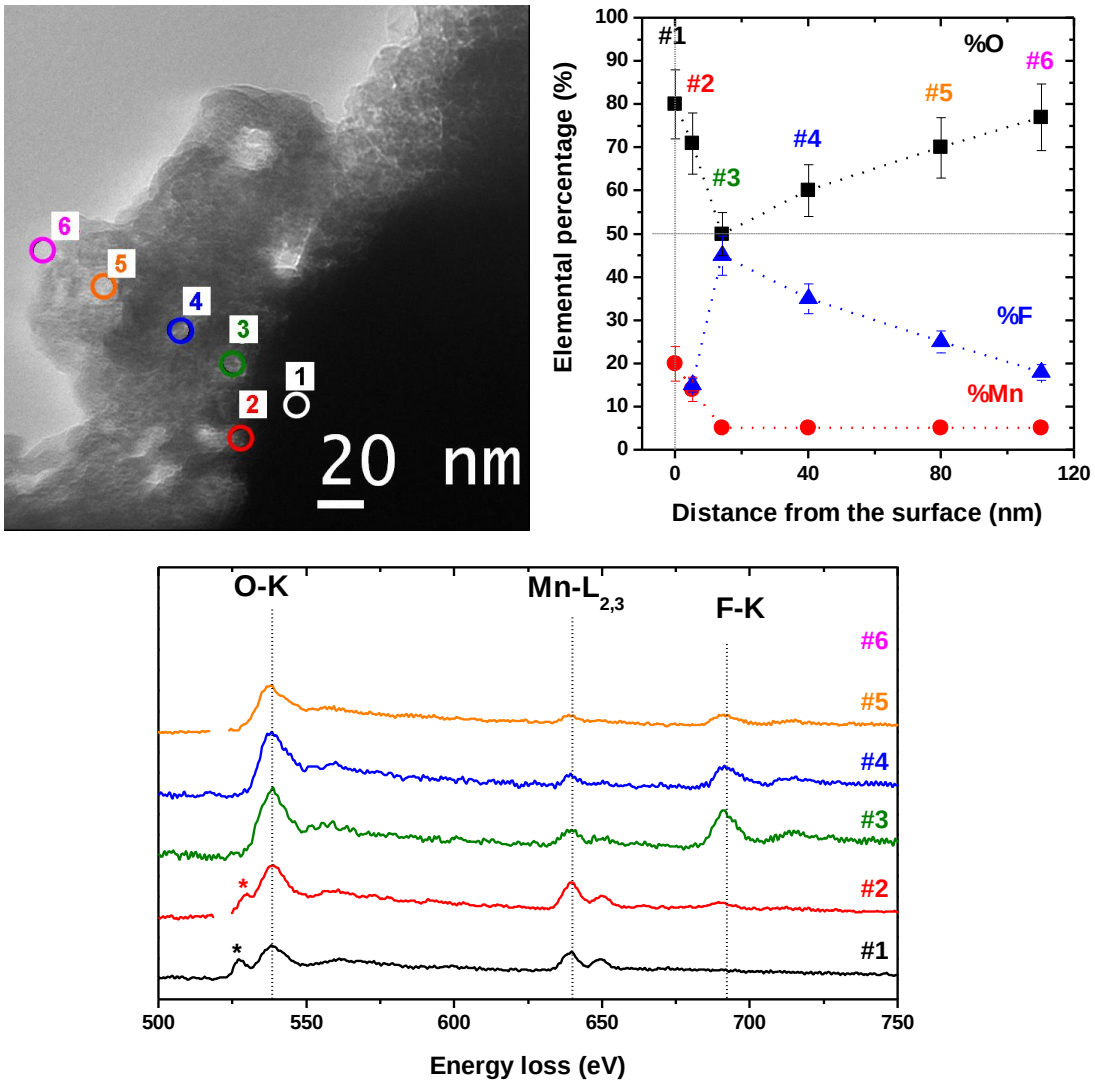

Figure III-35. TEM image of **AlO/LMN⅓** after one month soaking in $LiPF_6$ / EC:DMC electrolyte. Numbers denote spots subjected to EELS analysis, which results are reported together with illustrating spectra.

III.3.3. Interphase evolution upon electrochemical cycling

The interphasial behavior of AlO/LMN⅓ is here investigated upon electrochemical cycling at a C/50 rate between 2.0 V and 4.6 V, after an initial charge up to 4.8 V. *In situ* EIS measurements shown in **Figure III-36** shed light on the impedance rise caused by the presence of Al_2O_3.

Although possibly multiple charge transfers at the active material / Al_2O_3 / electrolyte interfaces cannot be resolved due to close characteristic frequencies, the corresponding loop clearly exhibit a flattening compared to what is observed for the bare material. Besides, the

additivity of charge transfer resistance implies that an approximately 5 Ω resistance is added here, which should be attributed to the presence of Al_2O_3.

As intuited from the observation of SEM images, too thick resistive layer proves to impede Li diffusion, in agreement with the lower discharge capacity reached by the coated material, suggesting the insulation of active material particles from the percolating network. Apart from this, the evolution of the impedance measured for the coated positive electrode / electrolyte follows that of the bare material. Even the slope of R_{ct} vs. cycle number, characterizing the aging kinetics of the interphase upon cycling, remains close to that of bare LMN⅓.

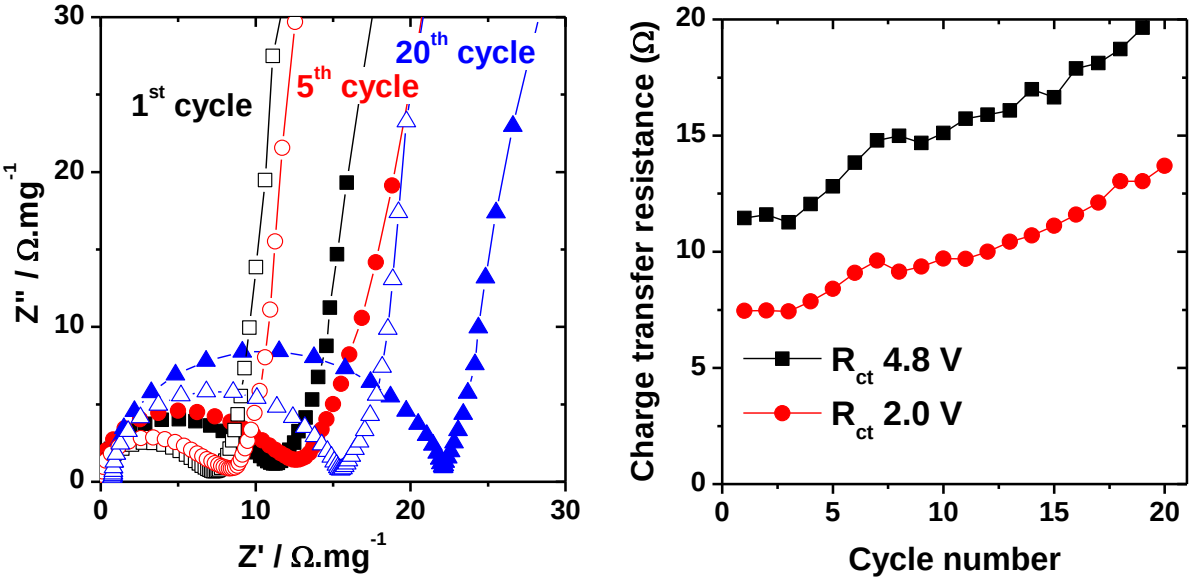

Figure III-36. Left: Nyquist plots of EIS performed in a 3 electrodes cell on **AlO/LMN⅓** after a 5h rest at the end of 1st, 5th and 20th charges (closed symbols) and discharges (open symbols) at a C/30 rate between 2.0 and 4.8 V. Right: Charge transfer resistance fitted from EIS measurements carried out at the end of charge (black squares) and discharge (red dots).

Interphase characterization was carried out by ^7Li and ^{19}F MAS NMR upon cycling. The resulting quantification diagram is reported in **Figure III-37** below (see Appendix 2, **Fig. AII-10** for raw spectra). First of all, it should be noted that the point corresponding here to the 20th reduced state is considered aberrant, for its deviation from the rest of the series, both in terms of the amount of lithium detected and $T_{2r(Li)}$. It is believed that this sample, which could not be reproduced due to a lack of time, has undergone a too strong washing. Besides, the fact that the amounts of fluorinated species detected match properly with that of previous points confirms the proposed interphase model consisting in an inner part rich in salt decomposition

products comprised in and further capped by (Li)-alkylcarbonates. The removal of these surface lithiated species by washing should indeed result in a decrease in the amount of interphasial Li only, together with a decrease of $T_{2r(Li)}$. Indeed, the removal of Li-alkylcarbonates, located far from the paramagnetic active material, leaves only the remaining LiF, close to the surface of active material, containing lithium nuclei in strong interaction with paramagnetic centers [2].

Following the trend observed upon simple contact with the electrolyte, Al_2O_3 coated material exhibits upon electrochemical cycling an interphase extremely rich in fluorine-free lithiated species. The potential dependency of these species seems exacerbated here, with a factor of 5 between the amounts of interphasial lithium detected at the end of discharge and charge, except for the first charge. Again, the fluorinated species do not seem to undergo substantial variations upon cycling and the evolutions of LiF and fluorophosphates on one hand and Li-alkylcarbonates and lithiated organic species on the other hand are clearly different and cannot be correlated.

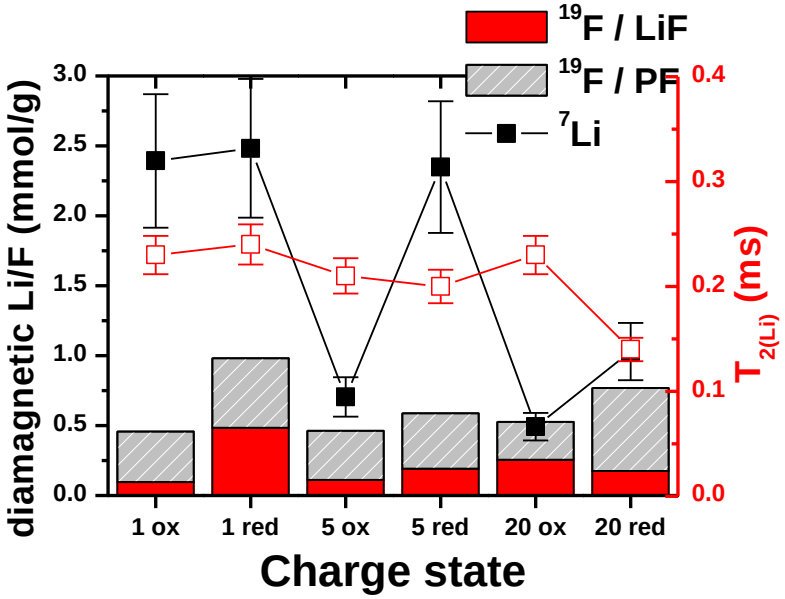

Figure III-37. ^{7}Li and ^{19}F NMR interphase quantification performed on **AlO/LMN⅓** at the end of 1st, 5th and 20th charge and discharge at a C/30 rate between 2.0 and 4.6 V in conventional $LiPF_6$ 1M in EC:DMC electrolyte. Only the first charge was prolonged up to 4.8 V. Red open squares correspond to $T_{2r(Li)}$ estimated from the spectral linewidth.

No significant variations of $T_{2r(Li)}$ could be observed along the electrochemical cycling even for drastic changes in lithium amount in the interphase. The presence of manganese in the whole thickness of interphase, detected after simple contact with the electrolyte, is expected to influence strongly the relaxation time of lithium ions contained in both

surrounding organic and inorganic species, thus, masking at least partially the influence of the bulk electrode.

III.3.4. Discussion

The momentous amounts of lithiated interphasial species detected on Al_2O_3 coated $Li_{1.2}Ni_{0.4}Mn_{0.4}O_2$ might result from the combination of two factors: first, the important amount of lithium extracted from the bulk during the thermal treatment and storage in air (**Fig. III-34**), exacerbating surface reactions with electrolyte previously observed in the case of $LiNi_{1/2}Mn_{1/2}O_2$ in the presence of Li_2CO_3 (section 2.1.1) and then, the increased surface nucleophily of the Li-rich $Li_{1.2}Ni_{0.4}Mn_{0.4}O_2$, as observed for $LiNi(III)O_2$ [55, 56], found to intensify the degradation of the electrolyte salt and solvents (section 3.2.2).

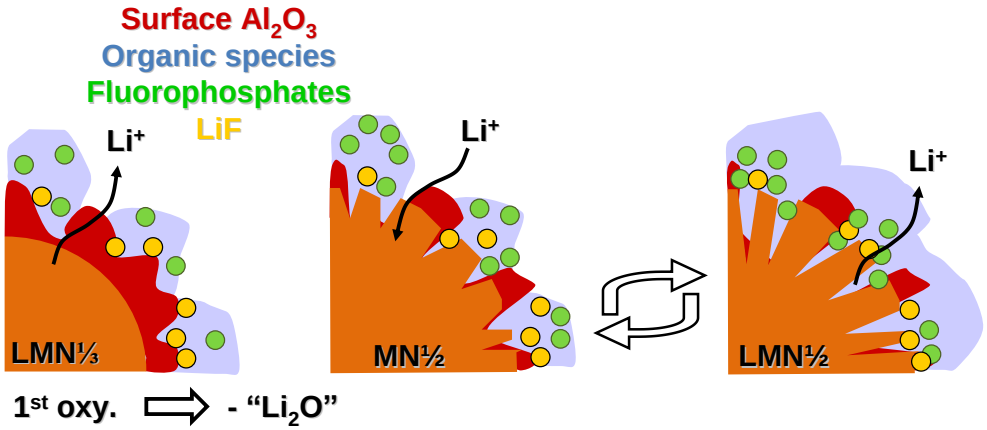

Figure III-38. Overview from left to right of the impact of the Al_2O_3 coating on the interphasial behavior of the lithium rich LMN⅓ upon cycling in conventional $LiPF_6$ 1M in EC:DMC (1:1). Compared to bare LMN⅓ material, the presence of Al_2O_3 results in the aggravated precipitation of lithiated organic species.

The sharp capacity decay observed on the first cycles for the Al_2O_3 coated material compared to bare $Li_{1.2}Ni_{0.4}Mn_{0.4}O_2$ (**Fig. III-33, right**) could be investigated in details with the help of NMR combined to XPS along the two first electrochemical cycles, in order to clarify the interphasial processes specific to the coated material. These interphasial processes as well as the bulk behavior of the material might also be influenced by the modifications of the extreme surface of active material after the likely incorporation of Al in the structure, as evidenced in the case of Al_2O_3-coated $LiCoO_2$ [59, 60]. At this point, it is only possible to correlate the increase of interfacial resistance to an aggravated precipitation of Li-alkylcarbonates in the presence of Al_2O_3, as schematically represented in **Figure III-38**. The capacity decay can thus be explained by the resultant increase of half-cell polarization.

III.4. Concluding remarks on Li-rich oxides and their surface reactivity

Regarding Li-rich layered oxides, represented by the $Li_{1.2}Ni_{0.4}Mn_{0.4}O_2$ material synthesized in this work, it appears that the initial step of electrochemical oxidation, leading to oxygen extraction above 4.5V, might be considered as the possible source of oxygenated species, leading to comparable interphasial processes observed in the presence of carbonates, oxalates (see the case of LiBOB additive) or gaseous oxygen.

Such type of reactivity towards electrolyte is found significantly amplified in the presence of an Al_2O_3 coating in the absence of bulk modifications, confirming the absence of Li_2O as a chemical entity susceptible to govern the interphasial chemistry. Therefore the irreversible extraction of lithium from the bulk should not be hold responsible for the chemistry and quantity of interphase, which is maybe only driven by chemical reactions bringing oxygenated species into play. As a matter of fact, literature reports the use of double layer coating (inner $AlPO_4$ or $CoPO_4$ and outer Al_2O_3) to limit the growth of undesired interphasial layers thanks to the retention of a higher number of oxide ion vacancies in the layered lattice after the first charge [61].

However, the use of an overlithiated starting composition allows access to higher discharge capacities and efforts should be pursued in this direction. The low power capability of these materials, and the poor capacity retention observed here might be explained both by the bulk mechanical damage caused during the irreversible extraction of "Li_2O"[54], and by the exacerbation of electrolyte decomposition by contact with the Ni(III)-rich material surface, as observed in the case of $LiNiO_2$ [55, 56].

Starting from this assessment, several research directions can be envisaged. General comments are discussed in the general conclusion but regarding surface nucleophily, a straightforward improvement in the control of the interphase growth may be found in the synthesis of core-shell active composites. Indeed, Amine *et al.* reported the preparation of overlithiated layered oxides, comprised of intermediate local compositions between a $LiNiO_2$ core and a Li_2MnO_3 shell [62]. The control of interphase growth induced by the formation of cracks may be implemented by tuning the morphology and aggregation of primary particles, once again through the synthesis of adapted composites [62]. Hence, the present study would be best applied to high performance materials, in order to confirm and clarify the interphasial behaviors observed here.

IV- CONCLUSION

All along this chapter dedicated to $LiNi_{1/2}Mn_{1/2}O_2$ material, a typical interphasial behavior was observed in the presence of surface carbonates, oxalates or gaseous oxygen: fluorinated salts, and lithium fluoride more particularly are formed upon simple contact with the active surface. In a second time, Li-alkylcarbonates undergo a precipitation / dissolution dynamic process at low / high potentials, respectively.

This archetypal interphasial behavior however totally differs from that of the material stored in Ar and never exposed to atmospheric pollution. Hence, the surface reactivity of $LiNi_{1/2}Mn_{1/2}O_2$ seems dictated by oxygenated surface species. The absence of discernable redox activity associated to such interphasial processes might suggest the corresponding degradation mechanisms imply organic oxygenated radicals rather than free electrons. This hypothesis remains of course to be confirmed by in situ electrolyte studies [63]. This idea is particularly appealing since it matches well with the observation of coulombic efficiency close to 100%, at the exception of the first cycle.

In spite of the departure of most of the lithiated interphasial species during the subsequent charge, a net accumulation is still observed, resulting both in lithium consumption from the available reservoir (it can be electrolyte since it happens through a chemical process) and in the increase of interfacial resistance.

If the correlation between such interphasial behavior and oxygenated surface species could be confirmed, an adapted treatment could be considered to prevent the precipitation of too important amounts of Li-alkylcarbonates, based on the use of oxygen solubilizer additives, such as those under investigation for Li-air applications [64, 65].

Nonetheless, the interphasial behavior of $LiNi_{1/2}Mn_{1/2}O_2$ free from Li_2CO_3 native layer shows that Li-alkylcarbonates should be the main interphasial component, by opposition with undesirable lithium fluorine which is intrinsically resistive for instance. The surface chemistry should therefore be tailored in order to prevent the salt decomposition by simple contact with the active surface, which could be achieved with $LiPF_6$ stabilizer additives. In this regard, the use of excess LiF in a chemical equilibrium principle (see Eq. I-4), mentioned in ref. [66] for reducing the LiF concentration in the SEI, proved experimentally to intensify by a factor of 10 the precipitation of Li-alkylcarbonates on $Li_{1.2}Ni_{0.4}Mn_{0.4}O_2$. Such a study, not developed in this manuscript, would be worth pursuing by tuning the LiF concentration, or consider other $LiPF_6$ stabilizers.

Finally, although not successful as positive electrodes, the layered nickel and manganese oxides synthesized for this work fulfilled perfectly their role as model compounds to test the NMR tool through the investigation of various physico-chemical parameters susceptible to influence the interphase.

The feedback on these experiments is encouraging, especially when considering the interphase topology highlighted by TEM (with thickness ranging from 0 to 10^2 nm) that make the XPS analysis questionable. Combined ^{7}Li and ^{19}F NMR studies are comparatively more robust, and often enable to correlate bulk electrochemical features to interphasial chemistry and evolution. Even when the interphase growth cannot be hold responsible for the poor electrochemical behavior, the physical aging of the active material or composite electrode can be envisaged more unequivocally.

REFERENCES OF CHAPTER 3

[1] Jean – Frédéric Martin, *Evolution de la surface de matériaux d'électrode positive pour accumulateurs au lithium au cours du vieillissement et du cyclage électrochimique*, PhD thesis from the University of Nantes, (2008).

[2] N. Dupré, J-F. Martin, D. Guyomard, A. Yamada, R. Kanno, *J. Mat. Chem.*, **18** (2008) 4266.

[3] N. Dupré, J-F. Martin, D. Guyomard, A. Yamada, R. Kanno, *J. Electrochem. Soc.*, **156** (2009) C180.

[4] N. Dupré, J-F. Martin, J. Oliveri, D. Guyomard, A. Yamada, R. Kanno, *Electrochem. Com.*, **10** (2008) 1897.

[5] N. Dupré, J-F. Martin, J. Oliveri, P. Soudan, A. Yamada, R. Kanno, D. Guyomard, *J. Power Sources*, **196** (2011) 4791.

[6] Z. Lu, D.D. MacNeil, J. R. Dahn, *Electrochem. Solid-State Lett.*, **4** (2001) A191.

[7] C. P. Grey, W. S. Yoon, J. Reed, G. Ceder, *Electrochem. Solid State Lett*., **7** (2004) A290.

[8] M. M. Thackeray, S.-H. Kang, C. S. Johnson, J. T. Vaughey, R. Benedek, S. A. Hackney, *J. Mater. Chem.*, **17** (2007) 3112.

[9] A. R. Armstrong, M. Holzapfel, P. Novak, C. S. Johnson, S. H. Kang, M. M. Thackeray, P.G. Bruce, *J. Am. Chem. Soc.*, **128** (2006) 8694.

[10] Y. Makimura, T. Ohzuku, *J. Power Sources*, **156** (2003) 119.

[11] S. Gopukumar, K.Y. Chung, K.B. Kim, *Electrochim. Acta*, **49** (2004) 803.

[12] Z. Lu, L. Y. Beaulieu, R. A. Donaberger, C. L. Thomas, J. R. Dahn, *J. Electrochem. Soc.*, **149** (2002) A778.

[13] N. Yabuuchi, S. Kumar, H.-H. Li, Y.-T. Kim, S.-H. Yang, *J. Electrochem. Soc*. **154** (2007) A566.

[14] Y. K. Sun, C. S. Yoon, Y. S. Lee, *Electrochim. Acta*, **48** (2003) 2589.

[15] K. Amine, M. J. Hammond, J. Liu, C. Chen, D. W. Dees, A. N. Jansen, G. L. Henriksen, abstract 332, the 10th International Meeting on Lithium Batteries, Como, Italy, May 28 June 2, 2000.

[16] E. Peled, *J. Electrochem. Soc.*, **126** (1979) 2047.

[17] D. Aurbach, B. Markovsky, M. D. Levi, E. Levi, A. Schechter, M. Moshkovich, Y. Cohen, *J. Power Sources,* **81-82** (1999) 95.

[18] S. S. Zhang, K. Xu, T. R. Jow, *Electrochem. and Solid-State Lett.*, **5** (2002) A92.

[19] D. Aurbach, B. Markovsky, G. Salitra, E. Markevitch, Y. Talyossef, M. Koltypin, L. Nazar, B. Ellis, D Kovacheva,. *J. Power Sources*, **165** (2007) 491.

[20] K. Edström, T. Gustafsson, J.O. Thomas, *Electrochim. Acta*, **50** (2004) 397.

[21] Y. Sundarayya, S. K. C. Kumara, C. S. Sunandana, *Mat. Res. Bul.*, **42** (2007) 1942.

[22] D. Aurbach, M. D. Levi, E. Levi, H. Teller, B. Markovsky, G. Salitra, U. Heider, L. Heider, *J. Electrochem. Soc.*, **145** (1998) 3024.

[23] T. Eriksson, *Comprehensive Summaries **651**, Faculty of Science and Technology*, Uppsala.

[24] T. Matsushita, K. Dokko, K. Kanamura, *J. Electrochem. Soc.*, **152** (2005) A2229.

[25] H. Ota, T. Akai, H. Namita, S. Yamaguchi, M. Nomura, *J. Power Sources*, **119-121** (2003) 567.

[26] B. J. Neudecker, R. A. Zuhr, B. S. Kwak, J. B. Bates, J. D. Robertson, *J. Electrochem. Soc.*, **145** (1998) 4148.

[27] J.C. Dupin, D. Gonbeau, H. Benqlilou-Moudden, Ph. Vinatier, A. Levasseur, *Thin Solid Films*, **384** (2001) 23.

[28] M. Ménétrier, C. Vaysse, L. Croguennec, C. Delmas, C. Jordy, F. Bonhomme, P. Biensan, *Electrochem. Solid State Lett.*, **7** (2004) A140.

[29] B. Meyer, N. Leifer, S. Sakamoto, S. Greenbaum, C. P. Grey, *Electrochem. Solid-State Lett.*, **8** (2005) A145.

[30] M. Murakami, H. Yamashige, H. Arai, Y. Uchimoto, Z. Ogumi, *Electrochem.Solid-State Lett.*, **14** (2011) A134.

[31]W. Li, B. L. Lucht, *J. Electrochem. Soc.*, **153** (2006) A1617.

[32] T. Nohma, H. Kurokawa, M. Uehara, M. Takahashi, K. Nishio and T. Saito, *J. Power Sources*, **54** (1995) 522.

[33] S. W. Song, G. V. Zhuang , P. N. R. Jr., *J. Electrochem. Soc.*, **151** (2004) A1162.

[34] M. Koltypin, D. Aurbach, L. Nazar, B. Ellis, *Electrochem. Solid State Lett.*, **10** (2007) A40.

[35] S. A. Zhang, *J. Power Sources*, **162** (2006) 1379.

[36] K. Xu, A. v. Cresce, *J. Mater. Chem.*, **21** (2011) 9849.

[37] A. M. Andersson, M. Herstedt, A. Bishop, K. Edström, *Electrochim. Acta*, **47** (2002) 1885.

[38] G. Zhuang, Y. Chen, *Langmuir*, **15** (1999) 1470.

[39] L. J. Rendeck, G. S. Chottiner, *J. Electrochem. Soc.*, **149** (2002) E408.

[40] D. Mazouzi, B. Lestriez; L. Roue, D. Guyomard. *Electrochem. Sol State Lett*. 12 (2009) A215.

[41] V. Sivasankaran, C. Marino, M. Chamas et al. *J. Mater. Chem.*, **21** (2011) 5076.

[42] P. Mongondry, B. Lestriez*, K. Ahmed Seid, P. Moreau, J. Gaubicher, D. Guyomard and G. A. Nazri, *unpublished results*.

[43] E. Ligneel, B. Lestriez, A.Hudhomme, D. Guyomard, *J. Electrochem. Soc.*, **154** (2007) A235.

[44] U. Wietelmann,W. Bonrath, T. Netscher, H. Noth, J.-C. Panitz, M. Wohlfahrt-Mehrens, *Chem.-Eur. J*. **10** (2004) 2451.

[45] J. Jiang, J. R. Dahn, *Electrochem. Solid-State Lett*. **6** (2003) A180.

[46] C. Taubert, M. Fleischhammer, M. Wohlfahrt-Mehrens, U. Wietelmann, T. Buhrmester, *J.Electrochem.Soc.*,**157** (2010) A721.

[47] K.Xu, S. S. Zhang, T. R. Jow, W. Xu, C. A. Angell, *Electrochem. Solid-State Lett*., **5** (2002) A26.

[48] Z. Chen, W. Q. Lu, J. Liu, K. Amine, *Electrochim. Acta*, **51** (2006) 3322.

[49] K. Xu, S. Zhang, U. Lee, J. L. Allen, T. R. Jow, *J. Power Sources*, **146** (2005) 79.

[50] J.C. Panitz, U. Wietelmann, M. Wachtler, S. Strobele, M. Wohlfahrt-Mehrens, *J. Power Sources*, **153** (2006) 396.

[51] K. Xu, S. Zhang, T. R. Jow, *Electrochem. Sol.-State Lett.*, **6** (2003) A144.

[52] K. Xu, S. S. Zhang, B. A. Poese, T. R. Jow, *Electrochem. Sol.-State Lett.*, **5** (2002) A259.

[53] B. Xu, C. R. Fell, M. Chi; Y. S. Meng, *Energy & Environmental Science*, **4** (2011) 2223.

[54] L. Daniel, J.-F. Colin, L. Simonin, J.-F. Martin, A. Boulineau, S. Patoux, *"Structural Characterization of High Capacity Layered Oxides"*, Lithium Batteries Discussion #5 (2011).

[55] D. Aurbach, K. Gamolsky, B. Markovsky, G. Salitra, Y. Gofer, U. Heider, R. Oesten, M. Schmidt, *J. Electrochem. Soc.*, **147** (2000) 1322.

[56] H. S. Liu, Z. R. Zhang, Z. L. Gong, and Y. Yang, *Electrochem. Solid-State Lett*., **7** (2004) A190.

[57] Y. Wu , A. Manthiram, Solid State Ionics, **180** (2009) 50.

[58] J. Liu, A. Manthiram, J. Electrochem. Soc., **156** (2009) A66.

[59] L. Dahéron, R. Dedryvère, H. Martinez, D. Flahaut, M.Ménétrier, C. Delmas, D. Gonbeau, *Chem. Mater.*, **21** (2009) 5607.

[60] S. Verdier, L. El Ouatani, R. Dedryvère, F. Bonhomme, P. Biensan, D. Gonbeau, *J. Electrochem. Soc.*, **154** (2007) A1088.

[61] Q. Y. Wang, J. Liu, A. Vadivel Murugan, A. Manthiram, *J. Mater. Chem.*, **19** (2009) 4965.

[62] Y. K. Sun, S. T. Myung, B. C. Park, J. Prakash, I. Belharouak, K. Amine, *Nat. Mater.*, **8** (2009) 320.

[63] F. Alamgira, C. Petersburga, R. Daniela, C. Jayeb, D. Fischer, Abstract #289, 218th ECS Meeting, Las Vegas (2010).

[64] D. Shanmukaraj, S. Grugeon, G. Gachot, S. Laruelle, D. Mathiron, J.-M. Tarascon, M. Armand, *JACS*, **132** (2010) 3055.

[65] Y. Wang, Yufei, D. Zheng, X. Q. Yang, D. Y. Qu, *Energy & Environmental Science*, **4** (2011) 3697.

[66] O. Hiroi, K. Hamano, Y. Yoshida, S. Yoshioka, H. Shiota, J. Aragane, S. Aihara, D. Takemura, T. Nishimura, M. Kise, H. Urushibata, H. Adachi, U.S. Patent 6,305,540 (2001).

CHAPTER 4. INVESTIGATION OF $LiFePO_4$

Very few studies deal with interphase evolution of $LiFePO_4$ electrode material upon its operation in a lithium battery as it was considered as chemically inert upon immersion in electrolyte. Concerning species formed on the surface of grains of active material, Herstedt *et al.* [1] did not observe any organic product such as polycarbonates, polymers or Li alkyl carbonates usually found in the case of oxides. Only products from decomposition of the $LiPF_6$ electrolyte (e.g. LiF, Li_xPF_y and $Li_xPO_yF_z$ compounds) were detected after cycling and no correlation with the electrochemical performance could be made.

This chapter covers multiple parameters susceptible to influence the interphasial behavior of $LiFePO_4$ but before all, a first section is devoted to the synthesis and characterization of the pristine materials used in this thesis.

In a second section, the intrinsic interphasial behavior of $LiFePO_4$ is investigated, at the scale of the first electrochemical cycle, and also along subsequent repeated cycles. The fundamental questions at the origin of this work concern the interphase architecture and dynamics.

$LiFePO_4$ being anisotropic in all its physico-chemical properties, the third section is focused on the possible lattice plane dependence of the surface reactivity towards electrolyte.

The fourth and last section is a long story, recounting the aging process undergone by $LiFePO_4$ upon its exposure to atmospheric oxidative species along storage. From the structural and electrochemical characterization of air-aged materials, reaction mechanisms are proposed. From then on, the impact of such aging on the interphasial chemistry is highlighted and likely appropriate treatments are carried out.

These various examples illustrate the possibility to correlate the nature and evolution of the $LiFePO_4$ / electrolyte interphase, as probed by NMR spectroscopy, to the material surface chemistry, and finally elucidate the overall electrochemical performance evolution.

I- SYNTHESIS AND CHARACTERIZATION OF PRISTINE MATERIALS

It has to be noted that all $LiFePO_4$ samples investigated in this work were synthesized in the laboratory to ensure their maximal quality, in terms of crystallinity and limited presence of Fe(III) impurities or inactive phases. This section demonstrates the relevance of such choice through different indicators: the achievement of pure phases, with the lowest possible ferric content (< 6 %), which deliver electrochemical capacities (> 155 $mA.h.g^{-1}$) extremely close to the theoretical one.

I.1. Solid state syntheses

I.1.1. Bare $LiFePO_4$

The $LiFePO_4$ material is synthesized via the solid-state method developed by Yamada *et al.* and described in previous papers [2, 3]. Stoichiometric amounts of precursors, namely lithium carbonate Li_2CO_3, iron acetate $FeC_2O_4 \cdot 2H_2O$, and diamonium hydrogenophosphate $(NH_4)_2HPO_4$, are first ball milled in acetone at 240 rpm for 6 h. The annealing is then carried out at 700°C for 6 h under Ar/H_2 atmosphere, after setting a careful vacuum of the furnace to avoid iron oxidation. The pristine bare $LiFePO_4$ material is here referred as LFP-noC.

I.1.2. $LiFePO_4$ - C composite

As also developed by Yamada *et al.* [2, 3], a $LiFePO_4$-C composite can be obtained by adding 10 wt% of a conducting carbon, such as Ketjenblack, to $LiFePO_4$ precursors. The amount of carbon, although important, enables the use of such composite in a battery without any further conducting agent. The mixing is performed by dry ball milling at 240 rpm for 24 h, and the annealing temperature can be lowered to 600°C. The composite $LiFePO_4$-C material is here referred as LFP-C.

I.1.3. Carbon coated $LiFePO_4$

Carbon can also be attached to the material through the post annealing of $LiFePO_4$ with a carbon precursor. This method, developed by Ravet *et al.* [4], offers the advantage to keep a microstructure close to bare material together with the possibility to easily tune the coating. Two sources of carbon, namely sucrose and cellulose acetate, are considered in this work and introduced to account for 4 wt% of the final product. Post annealing is performed at

700°C for 3 h under Ar/H_2 atmosphere. Coated $LiFePO_4$ materials are here referred as S/LFP and CA/LFP.

I.2. Structural characterization

I.2.1. Structural characterization by XRD

Figure IV-1 displays the experimental XRD patterns recorded for the different $LiFePO_4$ materials synthesized.

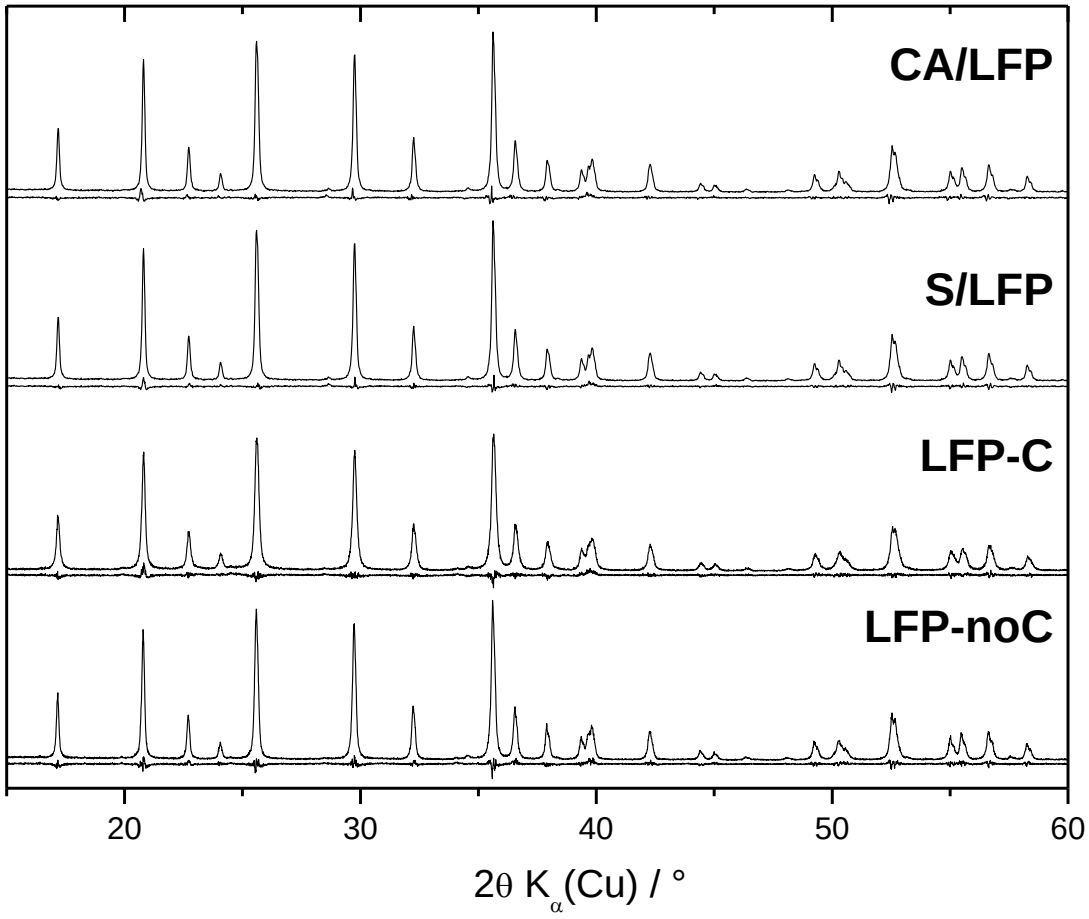

Figure IV-1. XRD patterns of as synthesized LFP-noC, LFP-C, S/LFP and CA/LFP. For the sake of clarity, results of Rietveld refinements only appear via the differential patterns.

As seen in **Figure IV-1**, in each case, the diffraction peaks are in full agreement with the $LiFePO_4$ olivine structure indexed in the orthorhombic *Pnma* space group and no evidence of impurity phases could be observed. The broadening of diffraction peaks for sample LFP-C is characteristic of smaller crystallites, as confirmed by the Rietveld refinement of experimental diagrams using TOPAS software presented in **Table IV-1**. Cell volumes inferior to 291.5 $Å^3$ suggest no significant Li/Fe exchange between the 4a and 4c sites [5].

		LFP-noC	*LFP-C*	*S/LFP*	*CA/LFP*
R-Values	Rwp (%)	10.36	10.51	7.49	8.84
	R_{Bragg} (%)	2.469	2.790	1.489	3.029
Cell Volume	($Å^3$)	291.340(8)	291.11(2)	291.399(9)	291.339(5)
Crystallite Size	(nm)	94.7(4)	56.9(5)	102.8(6)	99.1(3)
Lattice parameters	a (Å)	10.3303(2)	10.3260(4)	10.3302(2)	10.3308(7)
	b (Å)	6.0086(8)	6.0071(2)	6.0082(1)	6.0089(5)
	c (Å)	4.6937(8)	4.6931(2)	4.6950(1)	4.6932(4)
Fe on Li 4a site	%	0.8(1)	0.6(1)	0.9(1)	0.8(1)

Table IV-1. Lattice parameters and selected results from the Rietveld refinement of XRD patterns presented in Figure 1

Special attention has to be given to crystallite sizes, which differentiate samples from one another. The presence of carbon in LFP-C precursors is known to limit particles growth [6], which results in shorter coherence domains, while post annealed S/LFP and CA/LFP see the size of their coherence domains increase compared to bare LFP-noC, by 9.5% and 4.6% respectively. At the exception of such little crystal growth, the deposition of carbon coating on LFP-noC does not induce any bulk modification.

I.2.1. Structural characterization by Mössbauer spectroscopy

The Mössbauer spectra recorded for the different $LiFePO_4$ pristine materials are shown in **Figure IV-2**. The major component of the Mössbauer spectra (≥ 95 %) stands for high spin Fe(II) in an oxygen octahedral environment. The associated parameters are well defined and correspond to the $LiFePO_4$ olivine environment (IS = 1.22 mms^{-1}, QS = 2.95 mms^{-1}, $\Gamma < 0.3$ mms^{-1}) [2]. The Mössbauer characteristics for residual Fe(III) (IS = 0.4 mms^{-1}, QS = 0.9 mms^{-1}, $\Gamma > 0.6$ mms^{-1}) are in full accordance with previous results [7, 8]. Such Mössbauer parameters and broad peaks deviating from Lorentzian profile indicate a highly disordered octahedral phosphate environment close to that of Fe(III) in mineral olivine [9] and can be a sign of a defective or amorphous phase [7], which presence seems unavoidable unless taking drastic storage and handling precautions [8, 10], as further discussed in section 4. The decrease in the Fe(III) content from LFP-noC to samples S/LFP and CA/LFP, from 5 % to 3 % can be explained by a carboreduction process taking place during the post annealing.

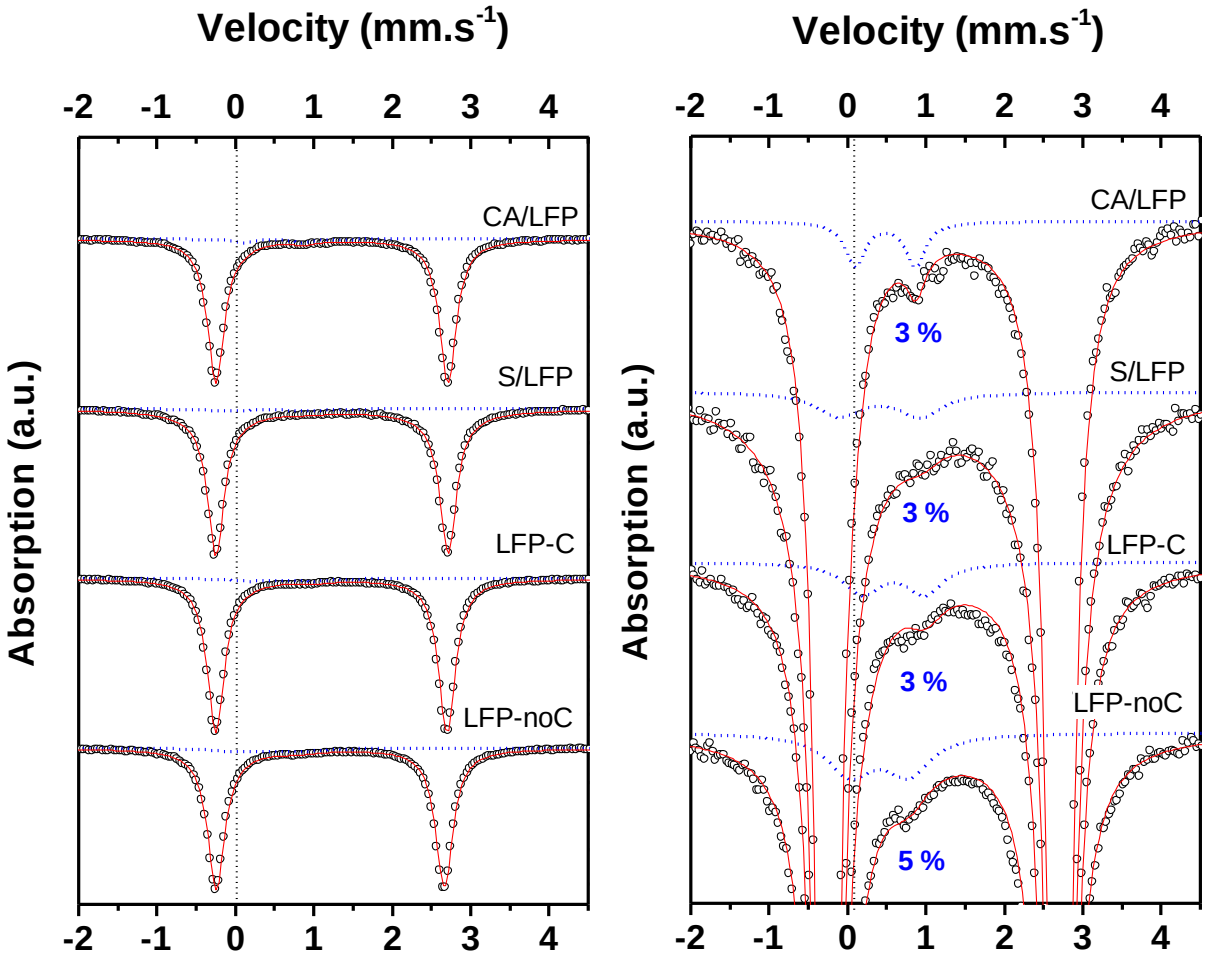

Figure IV-2. Mössbauer spectra of as synthesized LFP-noC, LFP-C, S/LFP and CA/LFP. On the right, a zoom on the peaks base highlights the presence of a small Fe(III) doublet, which relative intensity is given in blue for each sample. In the following, percentages fitted from Mössbauer spectra will always be given with a precision of 1%.

I.3. Morphological characterization

I.3.1. Particles size determination

SEM observations, as shown in **Figure IV-3**, indicate a rather narrow dispersion of the particles size for all samples. Materials exhibit porous aggregates of few microns, and the carbon particles are extremely well dispersed in the case of LFP-C. Specific surface area measurements by the BET method give 22 $m^2.g^{-1}$, 64 $m^2.g^{-1}$, 19 $m^2.g^{-1}$ and 25 $m^2.g^{-1}$, for samples LFP-noc, LFP-C, S/LFP and CA/LFP, respectively. The value for LFP-noC is quite different from the 14 $m^2.g^{-1}$ expected from 120 nm large spheric particles and highlights the trace presence of carbon residues from the oxalate precursor. In agreement, ICP evaluated the carbon content in this material at 1.6 wt%.

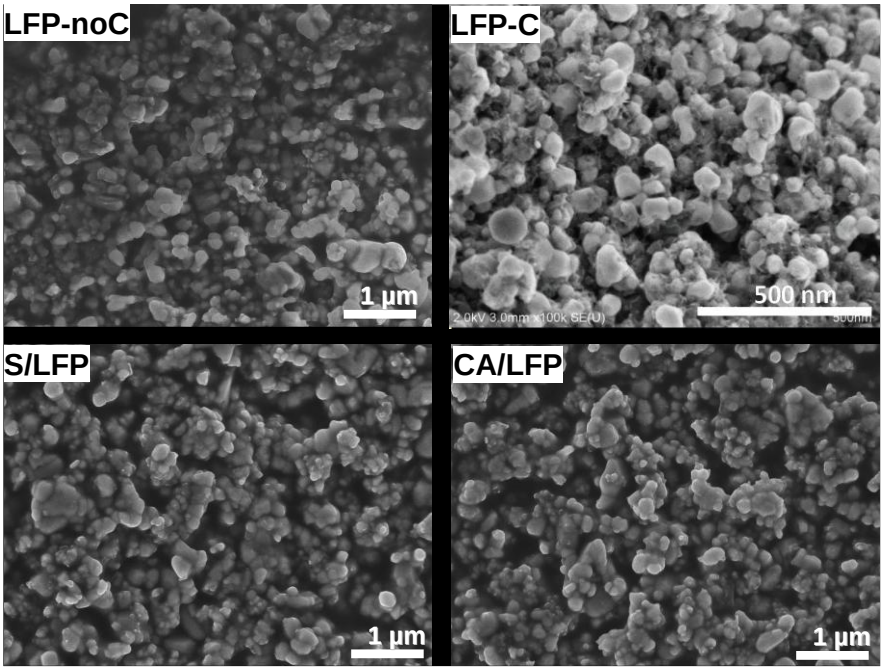

Figure IV-3. Scanning electron micrographs of as synthesized LFP-noC, LFP-C, S/LFP and CA/LFP.

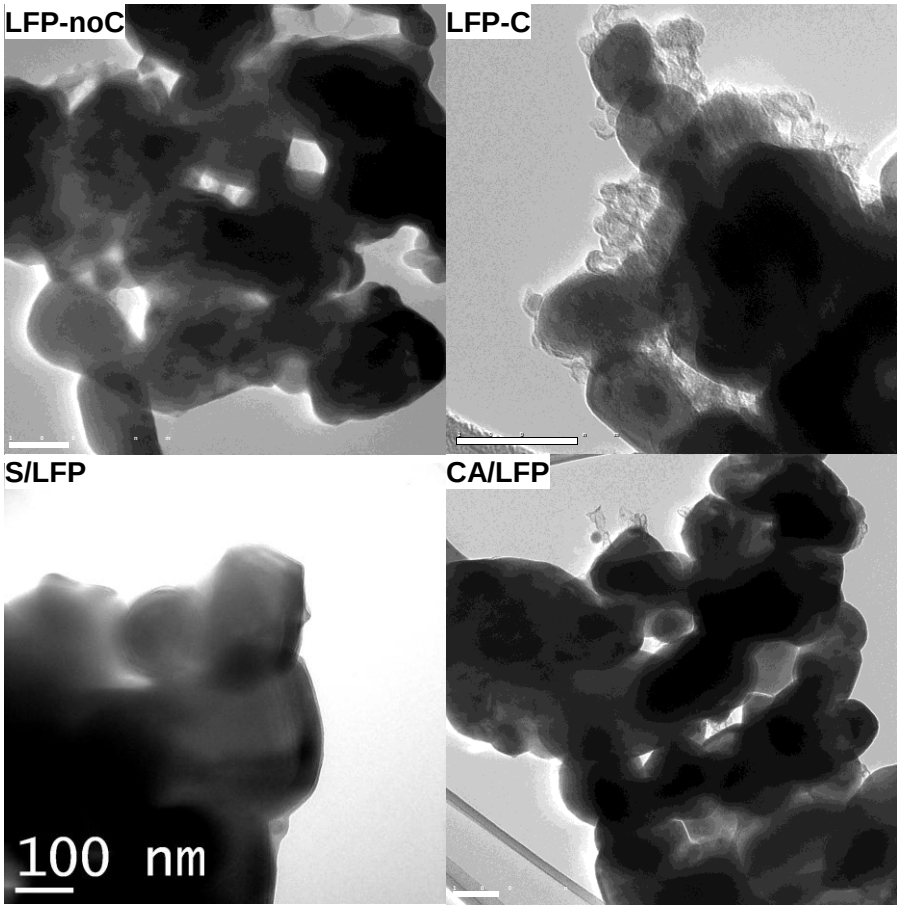

Figure IV-4. Transmission electron micrographs of as synthesized LFP-noC, LFP-C, S/LFP and CA/LFP.

The huge specific surface area given for LFP-C can be pictured as 35 $m^2.g^{-1}$ coming from the 10 wt% of Ketjenblack carbon while the remaining 29 $m^2.g^{-1}$ correspond well with the value expected for 60 nm large spheric particles.

In addition, particle size estimated from coherence domains lengths (**Table IV-1**) are confirmed by TEM (**Figure IV-4**): 60-80 nm for LFP-C and 100-200 nm in the case of LFP-noC, S/LFP and CA/LFP. Atomic planes can be observed at high resolution up to the grains surface suggesting a good crystallinity.

I.3.2. Coating characterization by TEM/EELS

TEM also highlights the distribution of carbon in the different samples and high resolution images are displayed in **Figure IV-5**. LFP-C clearly exhibits well distinct carbon balls at the surface and in the interstices of LFP aggregates. However, bare surface can also be observed. On the contrary, coated materials exhibit at least a 2 nm-thick carbon layer that covers the whole surface, even if thicker deposits are also found within the aggregates.

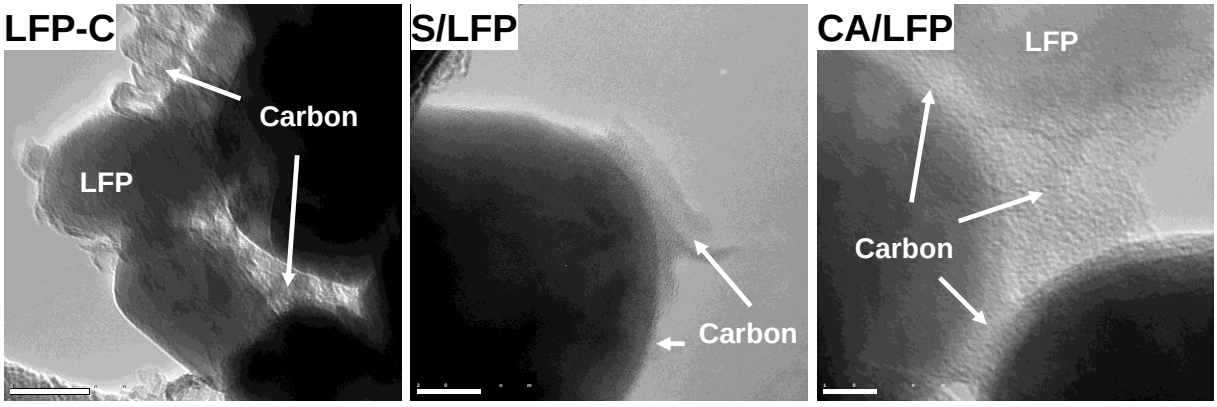

Figure IV-5. TEM images detailing carbon distribution in LFP-C, S/LFP and CA/LFP.

In order to further characterize the carbon coating, and possibly differentiate samples S/LFP and CA/LFP, EELS analyses were performed both on free surfaces and aggregate interstitial spaces filled by carbon. Characteristic C-K edges observed on these two samples are displayed in **Figure IV-6**.

A careful analysis of the C-K edge, as summarized hereunder in **Table IV-2**, can provide valuable information regarding the hybridization of carbon in the coating, indicating its conducting properties. Hence the presence of a sharp π* peak at 285 eV suggests a principally sp^2 hybridization for carbon in the two coatings. The width of this peak indicates the degree of crystallinity and the sp^2/sp^3 ratio can be deduced by comparing the intensity of the π* peak with the rest of the spectrum (π+σ), taking graphite as the reference for pure sp^2 hybridization [11-14]. As observed on the spectra labeled CA-1 and S-1, additional intensity

is sometimes detected between the π* and the π+σ, either as a distinct peak or a shoulder around 286 eV. This spectral feature is assigned in the literature to the presence of C-H and C=O bands [15], and indicates an incomplete carbonization of the organic precursor during the post annealing, detrimental to the electronic conductivity.

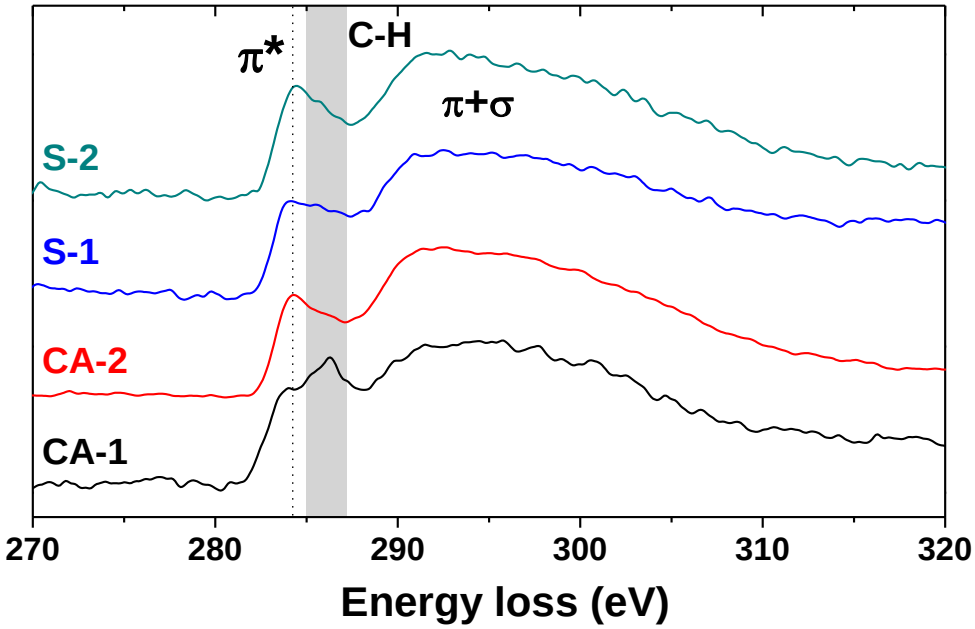

Figure IV-6. EELS C-K edges measured at the surface of S/LFP and CA/LFP. The gray band highlights the presence of C-H and C=O bands in the π* domain.

Based on localized EELS analyses (probe size set to 10 nm) averaged in **Table IV-2**, it appears that the carbon referred as S/LFP and CA/LFP exhibits roughly similar crystallinity and sp^2/sp^3 ratio. However, data gathered on S/LFP sample show a significantly broader dispersion, and average values differ between the thin layer present at the particles surface and larger carbon aggregates. These observations suggest a more pronounced inhomogeneity of the electronic conductivity at the nanoscale for this sample.

		π * peak width (eV)	R= π*/(π+σ) intensity %	% sp^2
S/LFP	C - Layer	2.4 (4)	9.6 (15)	74 (10)
	C - Aggregates	2.8 (4)	10.7 (12)	81 (7)
CA/LFP	C- Layer	2.7 (2)	11.6 (4)	87 (3)
	C - Aggregates	2.7 (3)	11.7 (3)	87 (2)
Graphite		1.8 (1)	14.0 (1)	100

Table IV-2. Results of averaged EELS analyses on the coating of S/LFP and CA/LFP

I.4. Electrochemical characterization

I.4.1. Electrode formulation

Previous work by Porcher *et al.* demonstrated the stability of $LiFePO_4$ in water [16, 17], opening the door for CMC-based aqueous formulation. They actually obtained good power performance with such composite electrodes [17], comparable to PVDF-based formulation using NMP as a solvent. In this work, a composition 80/10/10 (AM/CMC/KB) is used for LFP-noC, while the carbon content is adjusted for S/LFP and CA/LFP to reach similar composition. Electrodes are pressed under two tons.cm^{-2} and cycled again Li in $LiPF_6$, 1M (EC:DMC).

I.4.2. Electrochemical signature of $LiFePO_4$

Lithium extraction from LFP occurs through a biphasic reaction, characterized by a voltage plateau around 3.5 V vs. Li^+/Li^0, as shown in **Figure IV-7**.

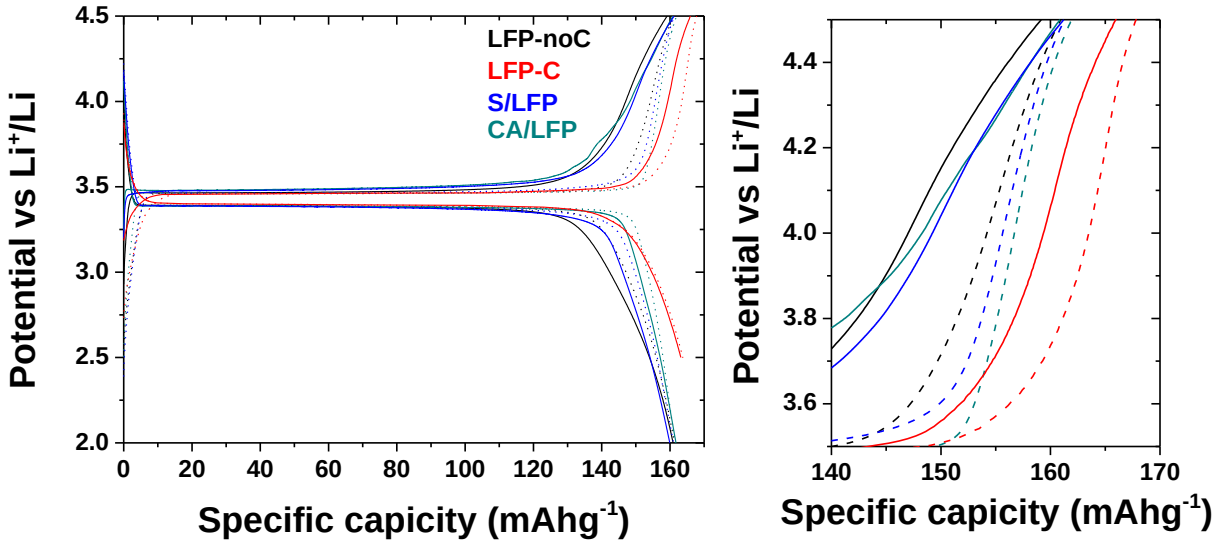

Figure IV-7. First (solid lines) and second (dash lines) electrochemical cycles of LFP-noC, LFP-C, S/LFP and CA/LFP at a C/20 rate in $LiPF_6$ EC:DMC.

Galvanostatic cycling at a rate as low as C/20 shows that all $LiFePO_4$ materials can deliver discharge capacity very close to the theoretical value of 172 mAh.g^{-1} [18]. An important result lies in the capacity measured at the end of the first charge, since this value represents the maximal capacity accessible in a Li-ion cell, in the absence of a Li infinite reservoir. As shown in **Figure IV-7** (right) this value, correlated to the amount of Fe(II) detected by Mössbauer spectroscopy, ranges from 159 mAh.g^{-1} to 161 mAh.g^{-1}, 162 mAh.g^{-1} and 166 mAh.g^{-1} for LFP-noC, S/LFP, CA/LFP and LFP-C, respectively. This small

difference in the charge capacity however fades from the second cycle, supporting a small initial Li deficiency instead of Li/Fe antisites.

I.4.3. Power performance and cyclability

As shown in **Figure IV-7**, all materials exhibit similar electrochemical behavior at low rate. However, it is widely known that small particle size as well as the presence of well dispersed carbon significantly improves the power capability of $LiFePO_4$ [2-4]. This statement is illustrated in **Figure IV-8 (left)**, where the LFP-C composite material clearly outperforms the other LFP materials at moderate and high rate. Contrary to the second coating CA/LFP, and as predicted by their EELS analysis, the carbon coating labeled S/LFP does not show any improvement in terms of power capability. This coating however significantly improves the long term cyclability compared to LFP-noC (**Fig. IV-8**, **right**).

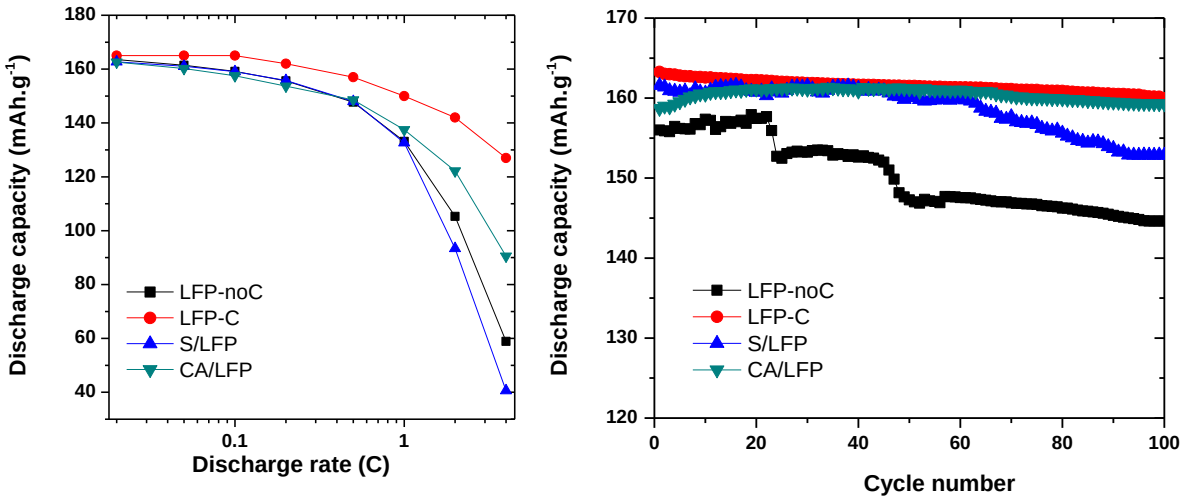

Figure IV-8. Power capability (measured by cumulative discharges) and cyclability of LFP-noC, LFP-C, S/LFP and CA/LFP at C/10.

Regarding this experiment, it appears reasonable to believe that the battery failure in the case of LFP-noC, which lost 6% of its intial capacity after 100 cycles, can be assigned to a breakdown of the composite electrode, coming from the loss of electrical contact and/or the loss of active material. Such failure mode is not observed for any of the coated materials, nor the composite LFP-C. The best performance is obtained with LFP-C and CA/LFP, which still deliver 159 $mAh.g^{-1}$ after 100 cycles.

I.5. Concluding remarks

Although the LFP-C composite exhibits excellent cycling properties, the inhomogeneous presence of carbon balls at the surface makes interphasial studies much more delicate. In the light of these preliminary experiments, the investigation of $LiFePO_4$ has been pursued using the bare material LFP-noC, so as to investigate the intrinsic surface reactivity of $LiFePO_4$. When clearly stated in the following, the carbon coated material labeled CA/LFP is used instead. Indeed, the influence of carbon on the surface reactivity is considered hereafter as a possible way to limit the electrolyte degradation (section 3.2) but also to limit the aging induced by air exposure (section 4.4).

II- INTRINSIC INTERPHASIAL BEHAVIOR OF LiFePO4

The first electrochemical cycle is investigated in order to understand the processes of reversible formation and dissolution of interphase components as a function of potential. Sophisticated spectroscopic analyses then allow correlating the interphase dynamics with the distribution of chemical species within the interphase depth. The irreversible accumulation after a longer cycling is also highlighted.

II.1. Illustration of interphase dynamics

N.B. In order to get rid of the binder contributions on ^{1}H MAS NMR and XPS spectra, a binder-free formulation (90:10) was used in this specific study. Although not meticulously compared, it seems that these binder-free electrodes exhibit a significantly higher amount of interphase per mass unit of active material, suggesting the role of CMC as a protective layer.

II.1.1. Interphase evolution upon voltage variations monitored by XPS [J.-F. Martin, 2008]

The results obtained along the first electrochemical cycle of $LiFePO_4$ (sample LFP-noC) are displayed in **Table IV-3** and **Figure IV-9**. Samples were recovered after a two hours constant voltage step, except for the batteries stopped at 3.5 V for which the capacity was limited at x = 0.5 Li. The species detected on the surface of the active material are similar to those found on samples soaked or stored in the electrolyte [19] with fluctuations depending on the potential of the sample (see Appendix 1, **Table AI-1** for peaks assignment).

Several CO environments are observed between 285.5 and 289.1 eV on the C1s spectra as well as on the O1s spectra at 533.5 eV, with a contribution at 531.5 eV, overlapping with phosphates. These signals, assigned to PEO-type polymers are observed along the first oxidation and first reduction above 3.5V. They tend to disappear during the second oxidation, from 2V to 3.5V.

Fluorine contribution under the form of LiF (685 eV), Li_xPF_y and $Li_xPO_yF_z$ (688 eV) increases clearly at the end of the first discharge at 2.0V. The corresponding percentage decreases slowly during the subsequent oxidation but remains higher than its level during the first cycle. The opposite evolutions of organic compounds and inorganic fluorinated species can suggest that the two different types of interphase are covering each other although it is not possible to determine which one is closer to the active material and which one constitutes the external part of the interphase.

Binding Energy		***4.5V ox1***	***4.1V red1***	***3.5V red1***	***2.7V red1***	***2V red1***	***2.7V ox2***	***3.5V ox2***	***4.1V ox2***	***4.5V ox2***
C sp^2	284.6 eV	46%	41%	40%	39%	36%	37%	32%	36%	43%
CC-**C**H	285.5 eV	2%	8.5%	10.5%	10%	4.5%	4%	12%	7%	5.5%
CO	286.5 eV	4.5%	4.5%	4.5%	4.5%	2.5%	2.5%	1.5%	4.5%	4.5%
CO	287.7 eV	1.5%	1.5%	1.5%	1.5%	1%	0.5%	0.5%	2%	1.5%
CO_2	289.1 eV	2%	3.5%	4%	4%	1.5%	1%	0.5%	3%	4%
P**O**$_4$	531.5 eV	31.5%	27.5%	25.5%	24%	29%	29%	33%	26%	23.5%
C**O**-OH	533.5 eV	1%	3.5%	4%	5%	2.5%	3.5%	1%	5%	3.5%
Li**F**	685.1 eV	3%	3%	2%	3%	8.5%	7%	6.5%	4%	5.5%
Li_xPO_y**F**$_z$	687.6 eV	2%	1.5%	1%	1.5%	6%	4%	2.5%	5%	3%
PO_4	133.4 eV	3.5%	3%	4%	4.5%	5%	5%	6%	4%	3.5%
PO	135.7 eV	0%	0%	0%	0.5%	0%	1.5%	0.5%	1%	0.5%
PF	137 eV	0%	0%	0%	0%	0.5%	0%	0%	0%	0%
Fe(II)	709.9 eV	0%	0%	1.5%	2%	4%	3.5%	2%	0%	0%
Fe(III)	712.0 eV	3%	3%	1.5%	0.5%	0%	1.5%	2%	2.5%	2%

Table IV-3. Quantitative evolution of elemental percentages obtained from the analysis of XPS spectra for $LiFePO_4$ during the first electrochemical cycle (C/10) in $LiPF_6$ 1M EC:DMC (1:1). Binding energies are constrained at ± 0,2 eV. Concerning the iron signal, binding energies corresponding to Fe $2p_{3/2}$ peaks are given in the table but the quantification has been performed on the Fe $2p_{1/2}$ peaks due to the possible overlapping with a fluorine satellite [20].

The covering of the active material can be monitored with the parallel evolutions of the P 2p signal corresponding to the phosphate group (133.4 eV) and Fe 2p. As a general trend, it seems from the evolution of visible iron that the interphase is thicker for high potentials. The antagonist evolutions of visible iron and surface fluorinated species from the one hand, and organic surface species from the other hand, suggest that the organic interphase is mostly covering both the active material and the inorganic part of the interphase. These results are summarized in the **Figure IV-9** and highlight the change in the composition of the interphase along potential variation encountered by the material during the cycling.

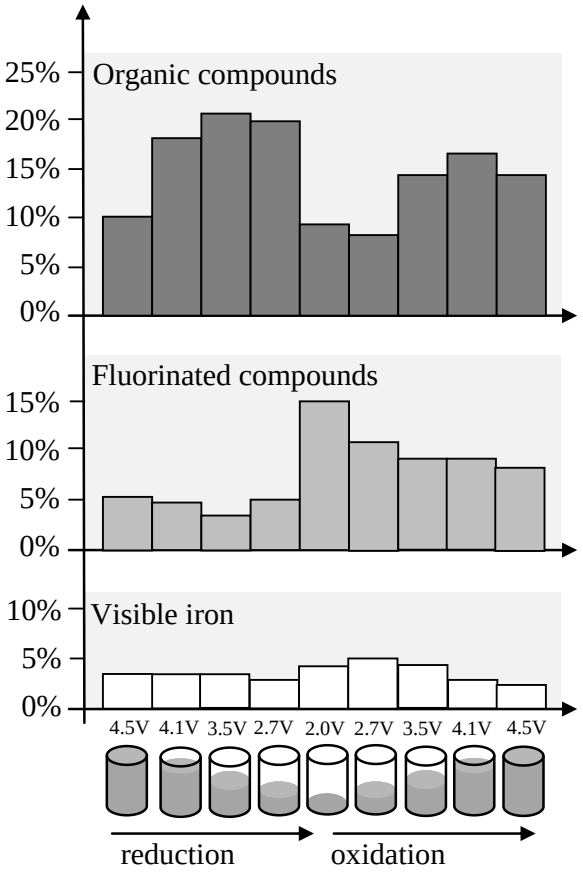

Figure IV-9. Evolution of the amount of carbonaceous, fluorinated species and iron along the first discharge and second charge, as probed by XPS. The carbon percentage does not include the contribution at 284.6 eV of Ketjenblack carbon.

II.1.2. Illustration of interphase evolution upon voltage variations by NMR

In order to follow the quantitative evolution of surface species, MAS NMR has been performed on the same samples, corresponding to different step (voltage-composition) along the first electrochemical cycle. The corresponding ^{7}Li spectra, as well as the resulting quantification of interphasial lithium, are reported in **Figure IV-10**.

The interphase appears richer in diamagnetic lithium at high potential, after the oxidation process compared to samples stabilized at 2.7 V and below. As a matter of fact, the ^{7}Li NMR signal almost disappears for low potentials. However, lithium containing species are detected by XPS for low potential. Three possible hypotheses would allow explaining this apparent inconsistency by NMR failure to detect the interphase:

First, the intimacy between the paramagnetic active material and the lithiated interphase, and then the nucleus-electron dipolar interaction being extremely strong, a broadening of the NMR signal beyond MAS resolution could partially mask the corresponding resonances in the reduced state. Indeed, Julien *et al.* [21] showed that the

magnetic susceptibility of $LiFePO_4$ is larger than that of $FePO_4$. Even if the difference between their respective values is small, it appears to impact significantly on both the shape of the spinning sidebands manifold, and the residual linewidth. Discussion concerning the material/interphase intimacy based on these spectral features [22] then becomes relatively delicate unless considering samples recovered at the same state of charge (SOC). However, in the hypothetic case of a nucleus-electron dipolar interaction strong enough to impede MAS resolution for part of lithium ions in the interphase and resulting in a loss of the corresponding signal, the ^7Li NMR signal of remaining detected lithium is expected to display a very wide sidebands manifold. This does not seem to be the case here, for samples recovered at low potential and showing a weak integrated intensity only display a couple of spinning sidebands, even for long scans accumulation.

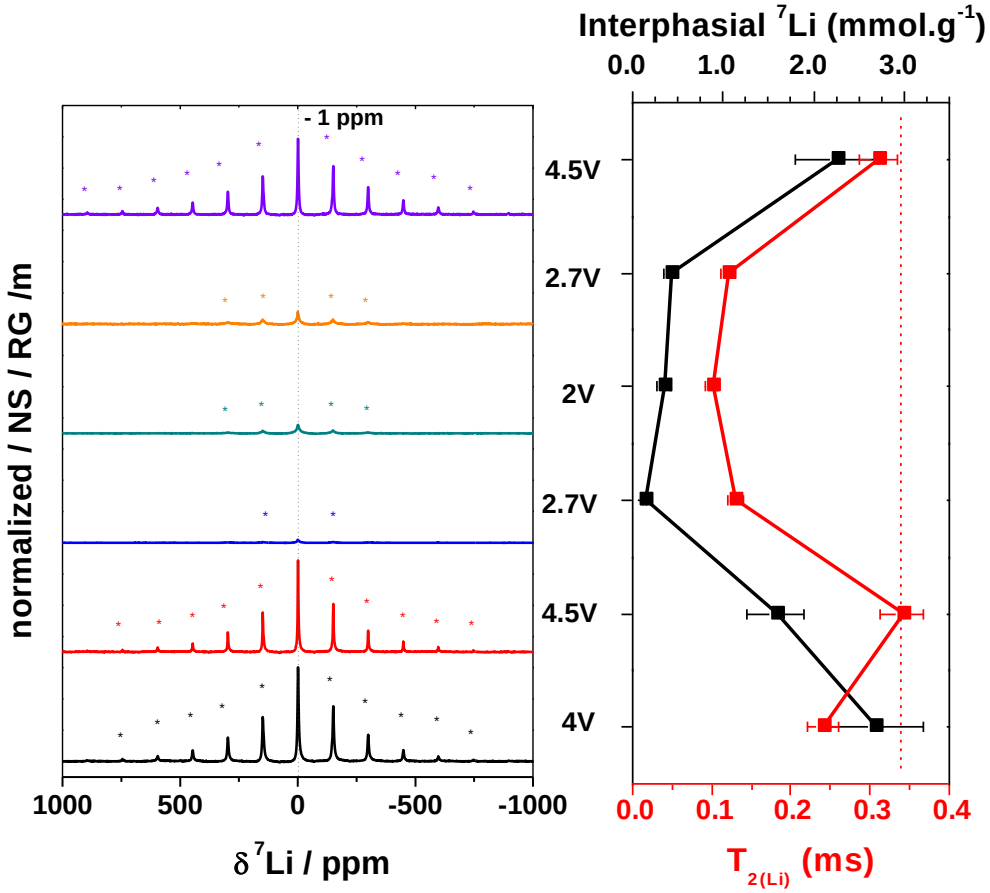

Figure IV-10. Normalized ^7Li NMR spectra for $LiFePO_4$ along the first electrochemical cycle at a C/20 regime in $LiPF_6$ EC:DMC (MAS = 29 kHz). Asterisks denote spinning sidebands. The amounts of interphasial lithium deduced from integrated intensities, as well as T_{2r}s estimated by the signal width are reported on the right.

Moreover, regarding the integrated intensity, the experiments carried out on different paramagnetic and diamagnetic electrode materials indicated that it was apparently not affected

by the strength of dipolar interaction; interphasial species were detected equally on the surface of $LiFePO_4$ and Silicon (see chapter 2, **Fig. II-3**). Besides, although T_{2r}s reported in **Figure IV-10** show significant evolution with SOC, the linewidth remains reasonable and provides sufficient resolution for the NMR signal. Hence the difference in strength of the nuclear-electronic dipolar interaction should not impede the detection of interphasial diamagnetic species at the surface of $LiFePO_4$ compared to $FePO_4$ and the simple quantification tool used here remains valid to shed light on XPS results

Second, the NMR signal fading could also be a consequence of the dissolution of iron in the electrolyte, some of it being trapped in the interphase, leading to a close mixing with the interphasial species. However in this case, the electron-nuclear dipolar interaction would then remain extremely strong upon further cycling, independently from the SOC. As a result, T_{2r} should remain short after iron dissolution rather than recover its value from the previous oxidation due to proximity of Fe(III).

This second hypothesis can therefore also be ruled out, leading us to the third hypothesis that the lithium containing species detected by NMR, in simultaneity with the organic species detected by XPS, undergo a process of dissolution at low potentials and precipitation at high potentials. Finally $T_{2r(Li)}$ evolution is the result of both SOC variations and the evolving distribution of lithiated species within the interphase, as highlighted in the following section. The fact that the amount of lithium detected by XPS does not decrease along this dissolution process can be explained by the extreme surface sensitivity of the technique: in spite of the dissolution of a major part of interphase present at high potential, the lithiated species remaining at low potential can still account for similar elemental percentage at the scale of the 5 nm probed.

^{1}H MAS NMR analysis after a Hahn echo allows confirming the correlation between the surface organic species and the lithium signal detected by ^{7}Li MAS NMR. As seen in **Figure IV-11 (left)**, the detected protons can be separated into two kinds of contributions. A first signal, centered at -4 ppm, gives rise to the spinning side bands denoted by the asterisks. The variation of detected protons interacting with the active material follows the evolution observed previously for lithium, with an extremely broad sidebands manifold at high voltage. Meanwhile, most of the intensity detected, rising in the central part of the spectrum and including a possible residual signal from the probe, does not exhibit any sideband. This second contribution, very difficult to estimate, is therefore accounted as purely diamagnetic,

with no interaction with the paramagnetic active material and has not been considered further in the present work.

^{19}F MAS NMR maybe provides more unambiguous information, insofar as LiF signal at -204 ppm can clearly be separated from that of fluorophosphates arising around -77 ppm and -85 ppm for R-PO_3F and R-PO_2F_2, respectively (**Figure IV-11, right**) [23]. Rather than the net decrease observed in the amount of lithiated or protonated species, the electrochemical reduction is mostly accompanied by a significant broadening of the ^{19}F NMR signals. The different variations observed on ^{7}Li and ^{19}F signals (see **Figure IV-13**) suggest that ^{7}Li NMR mainly probes the evolution of non fluorinated species.

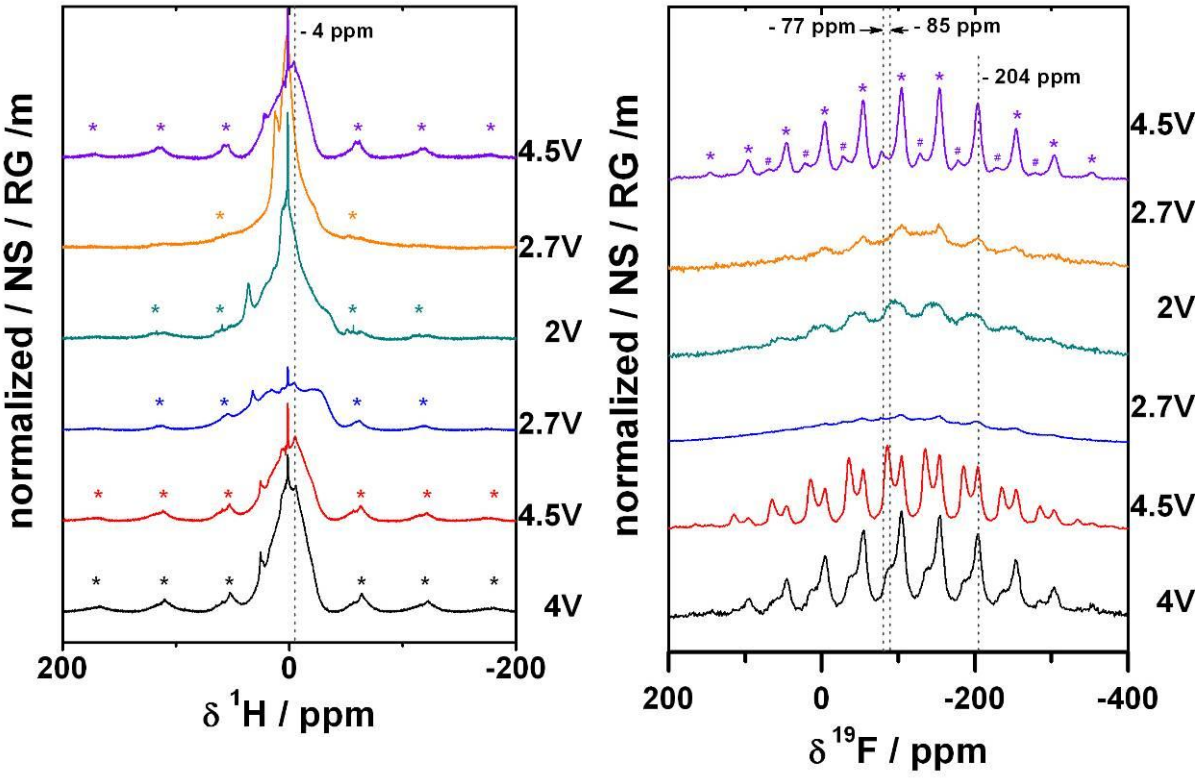

Figure IV-11. ^{1}H (29 kHz) and ^{19}F (23.5 kHz) MAS NMR normalized spectra for $LiFePO_4$ along the first electrochemical cycle at a C/20 regime in $LiPF_6$ / EC:DMC. Asterisks denote spinning sidebands.

In the case of ^{19}F MAS NMR, the amount of fluorine nuclei involved in the interphase does not vary significantly upon potential variation and only a line broadening due to the change of the oxidation state of iron altering the nucleus-electron dipolar interaction, is observed. Due to this signal broadening, it is not possible, as this stage, to completely rule out the presence of remaining $LiPF_6$, which signal would arise at -70 ppm. To this aim, ^{31}P MAS NMR, performed at the end of charge and discharge, completes the multinuclear investigation (**Fig. IV-12**). If the very low sensitivity of this latter experiment unfortunately results in a

significant uncertainty from a quantitative point of view, the qualitative assignment of NMR shifts is straightforward. Should excess electrolyte salt be present in our samples, the corresponding isotropic ^{31}P NMR signal for $LiPF_6$ would be observed at -145 ppm, far away from that of R-PO_3F and R-PO_2F_2, at -10 ppm and -22 ppm, respectively [23]. The experimental observation of a broad signal centered around -17.5 ppm can therefore be assigned to a mixture of these two types of fluorophosphates.

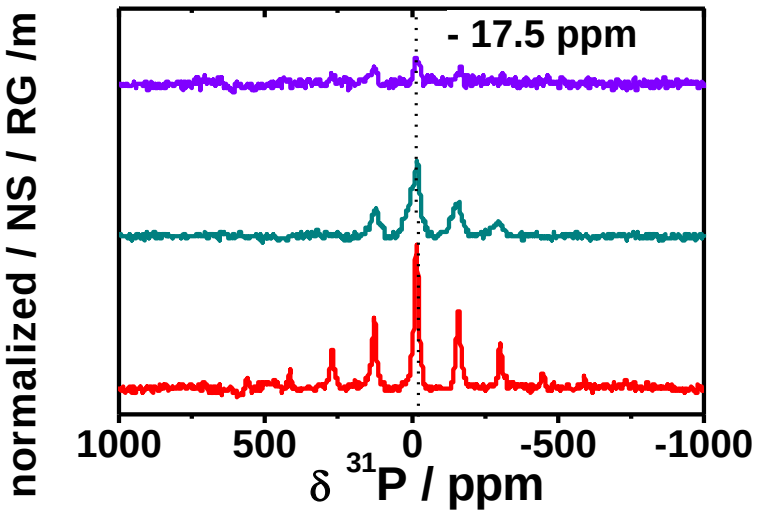

Figure IV-12. ^{31}P MAS NMR normalized spectra for $LiFePO_4$ at the end of charge and discharge at a C/20 regime in $LiPF_6$ / EC:DMC.

Aiming at summarizing all the experimental results discussed above, **Figure IV-13** contains the NMR quantifications obtained along the first electrochemical cycle. ^{31}P MAS NMR results are here reported in the light of the detected amounts of fluorine in fluorophosphates. This comparison confirms that those species correspond rather to R-PO_2F_2 or a mixture with R-PO_3F, as suggested by the assignments made from the NMR shifts.

Finally, it appears that the evolution of interphase species observed by NMR upon potential variations mostly concerns “fluorine-free” lithiated species such as Li-alkyl carbonates. This conclusion is in full agreement with XPS results, and with the idea of a dynamic organic interphase mostly covering both the active material and the inorganic part of the interphase. Free from the detrimental screening effect faced with XPS, NMR indicates that inner inorganic species such as LiF and fluorophosphates do not undergo substantial change upon voltage variation.

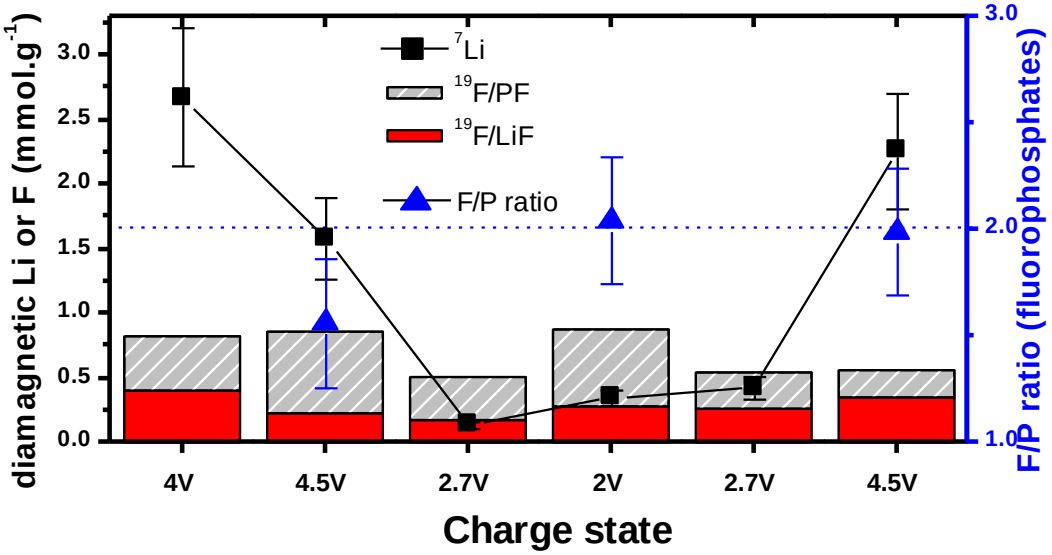

Figure IV-13. NMR quantification results for $LiFePO_4$ along the first electrochemical cycle at a C/20 regime in $LiPF_6$ / EC:DMC.

Based on purely average spectroanalytical techniques, this study comes up with a 3D, dynamic model of the $LiFePO_4$ / electrolyte interphase, which we propose now to establish with the help of depth sensitive analyses.

II.2. Unraveling of interphase architecture

In order to rebuild the interphase architecture along electrochemical cycling, $LiFePO_4$ epitaxial films offering ideal 2D interfaces are here investigated through the use of non-destructive depth profiling by angular resolved X-ray Photoelectron Spectroscopy (XPS). The preparation of *a*-oriented $LiFePO_4$ epitaxial thin films, deposited by PLD on $SrTiO_3$ substrates, was carried out in the Department of Electronic Chemistry of the Tokyo Institute of Technology, headed by Pr. R. Kanno. Under the supervision of Dr. M. Hirayama, a first batch of samples was prepared in the frame of a one month student exchange, with the help of K. Suzuki and S. Taminato. A second batch was later prepared by K. Suzuki and M. Komo. Details regarding the synthesis conditions can be found in ref. [24].

II.2.1. Thin films characterization

First is displayed in **Figure IV-14** a summary of the structural and morphological data gathered on pristine films, from X-ray diffraction, reflectivity (XRR) and TEM analyses. The (100) orientation of the film is confirmed by out of plane XRD measurement (**Fig. IV-14d**) and XRR highlights a roughness inferior to 1 nm for the 20 nm thick LFP layer

(**Fig. IV-14c**). In addition, a surface pollution film is detected, and assigned to Li_2CO_3 for its 2.1 $g.cm^{-3}$ density.

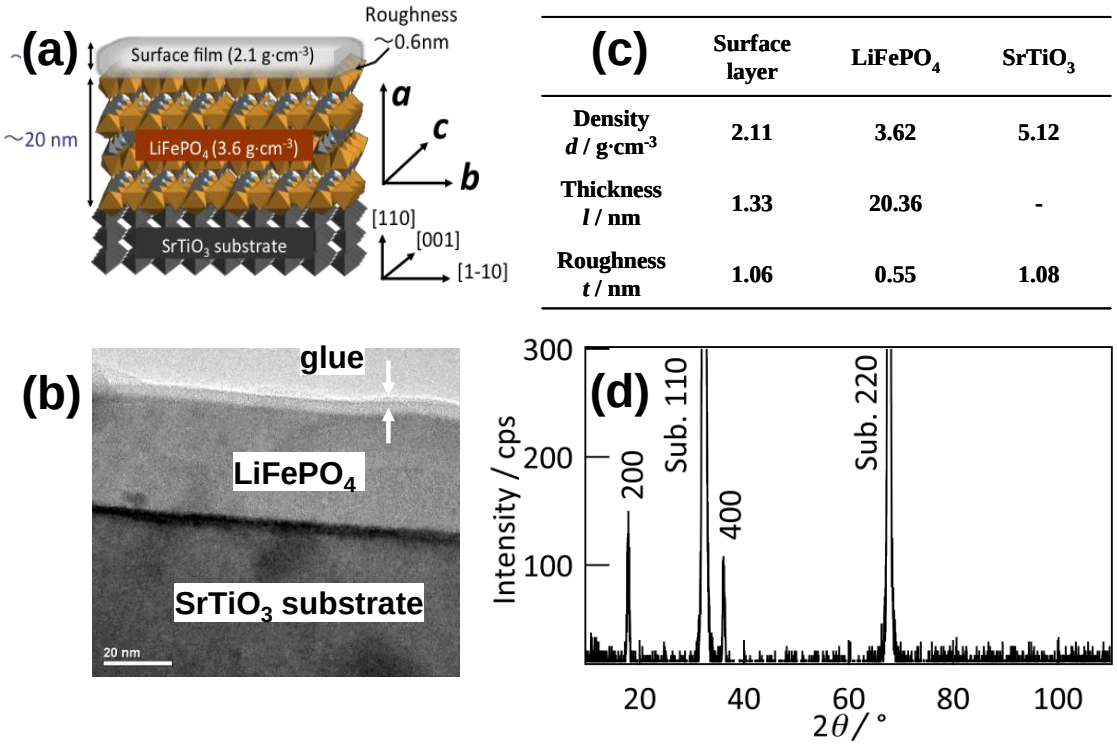

(c)	Surface layer	$LiFePO_4$	$SrTiO_3$
Density d / g·cm^{-3}	**2.11**	**3.62**	**5.12**
Thickness l / nm	**1.33**	**20.36**	**-**
Roughness t / nm	**1.06**	**0.55**	**1.08**

Figure IV-14. (a) Schematic and (b)TEM picture of $LiFePO_4$ epitaxial thin films with *a*-plane orientation. (c) Parameters obtained by refining X-ray reflectivity data for as-grown (100) $LiFePO_4$ film and (d) Out-of-plane XRD pattern for $LiFePO_4$ deposited on $SrTiO_3$ (110) substrate. Reprinted from ref. [24]

II.2.2. Quantitative elemental analyses by XPS

For the acute precision of the qualitative information obtained, XPS is the technique of choice to probe fine chemical changes within interphasial layers. The extremely low roughness of these epitaxial $LiFePO_4$ thin films allowed us considering their surface as purely 2D and subjecting them, in the lab, to angular resolved XPS experiments after cycling (see **Appendix 1**). In **Table IV-4** are reported the elemental percentages obtained from the analysis of XPS spectra at $\theta = 0°$ and $\theta = 60°$ for an as-synthesized pristine film as well as at the end of the first charge and discharge.

The cross-reading of these results might appear delicate but in a first approach, a comparison of the three samples measured at $\theta = 0°$ suggests that since C *1s* contribution at 284.6 eV significantly decreased from 11% for air exposed pristine film to 3% or less for cycled films, carbon contamination could be avoided during the transfer of samples from the glovebox to the analysis chamber. The pristine sample is only covered by a small amount of

carbonates, while the interphase present on cycled films is rich in fluorinated species and PEO-type polymers. The nature of these species is found unchanged, and the signal assignment proposed in the previous section still applies. Moreover, the predominance of inorganic species at the end of discharge compared to the previous charge is observed on the thin films similarly to powder samples. In comparison with powder samples, the high elemental percentages corresponding to bulk $LiFePO_4$ suggest a significantly lower coverage of the thin films.

Binding Energy		***Pristine*** $\theta = 0°$	***Pristine*** $\theta = 60°$	***4.5 V*** $\theta = 0°$	***4.5 V*** $\theta = 60°$	***2.5 V*** $\theta = 0°$	***2.5 V*** $\theta = 60°$
C sp^2	284.6 eV	11.4 %	20.2 %	1.6 %	5.0 %	3.1 %	11.1 %
CC-**C**H	285.5 eV	10.8 %	16.4 %	2.6 %	6.4 %	3.5 %	6.2 %
CO	286.5 eV	1.4 %	2.0 %	1.1 %	1.6 %	1.8 %	1.8 %
CO	287.7 eV	1.1 %	1.8%	0.9 %	1.2 %	0.6 %	0.8 %
O**C**O_2	289.1 eV	1.3 %	1.2 %	0.3 %	0.5 %	0.6 %	1.0 %
P**O**$_4$	531.5 eV	54.0 %	42.8 %	57.2 %	54.0 %	48.9 %	42.6 %
C**O**-OH	533.5 eV	2.5 %	3.4 %	4.4 %	5.3 %	5.9 %	6.3 %
Li**F**	685.1 eV	0.7 %	0.6 %	7.4 %	7.1 %	13.5 %	14.2 %
Li_xPO_y**F**$_z$	687.6 eV	0.1 %	0.2 %	3.3 %	5.3 %	4.7 %	5.6 %
PO_4	133.4 eV	10.6 %	6.0 %	12.3 %	6. 1 %	9.7 %	3.9 %
PO-**P**F	135.7 eV	3.6 %	2.6 %	5.2 %	3.8 %	3.5 %	2.7 %
Fe(II)	709.9 eV	2.1 %	1.6 %	1.6 %	0.9 %	2.1 %	2.2 %
Fe(III)	712.0 eV	2.0 %	1.7 %	2.1 %	0.9 %	2.2 %	1.7 %

Table IV-4. Quantitative evolution of elemental percentages obtained from the analysis of XPS spectra for $LiFePO_4$ thin films, as prepared and after cycling in $LiPF_6$, EC:DMC electrolyte, as a function of the incident angle.

II.2.3. Estimation of interphase thickness by XPS

The estimation of interphase thickness ***d***, is here based on the angular dependence of the Fe *2p½* XPS signal at 723 eV (see Appendix 1, **Fig. AI-1**). As represented in **Figure IV-15**, the slope of $\ln[C(\theta)]$ vs. $1/\cos(\theta)$ corresponds to $-d/\lambda$ where λ is the inelastic mean-free-path of an electron in the surface layer. Taking into account an Al K_α X-Ray source and a dense LiF layer results in λ = 22 Å, to be compared with λ = 26 Å calculated for polyethylene for instance. The value used in the following estimation is the LiF one, found as a reasonable average between the inelastic mean free paths of various interphasial

components (see Appendix 1, **Fig. AI-2**). Such approximation results in a 30 % error on the thickness values deduced from angular XPS measurements.

The ***d*** values obtained by this method for the interphase thickness (**Fig. IV-15**) seem small in comparison with the value measured by XRR for the pristine sample (1.3 nm). Considering the high incertitude on the λ value, the absolute values given in **Figure IV-15** should not be considered meaningful, but can reasonably be compared. Thus, they highlight the potential dependency of the interphase thickness, for the decrease of the *Fe 2p* signal intensity with $1/\cos(\theta)$ is clearly more marked for the sample recovered at the end of charge. As a result, the interphase probed at 4.5 V is estimated almost 6 times thicker than the one measured at 2.5V.

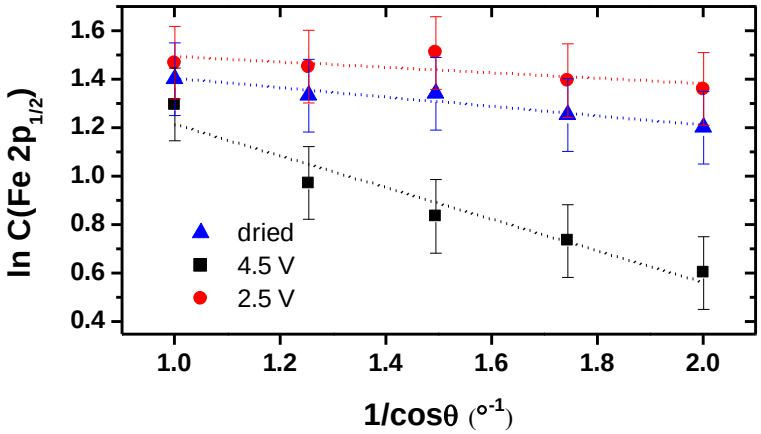

	d (nm)
Pristine	0.44
1st ox. 4.5 V	1.4
1st red 2.5 V	0.25

Figure IV-15. Angular dependency of the Fe $2p_{½}$ XPS signal measured for pristine (blue triangles), charged (black squares) and discharged (red dots) $LiFePO_4$ thin films. Linear fit gives a $-d/\lambda$ slope, from which d values are extracted, considering an average $\lambda = 22$ Å for the interphase.

II.2.4. Composition gradient within the interphase depth by XPS

The second analytical tool introduced here is the "surface exaltation coefficient", k_A, comparing the evolution of each XPS signal along angle variation, reported to a reference, played by Fe *2p* signal(see Appendix 1):

$$k_A = \ln\left[\frac{C(\theta = 60°)_A / C(\theta = 60°)_{ref}}{C(\theta = 0°)_A / C(\theta = 0°)_{ref}}\right] \quad \text{(Eq. IV-1)}$$

Figure IV-16 (left) illustrates the relevance of this indicator through the simple example of F *1s* spectra recorded at the end of charge. The intensity measured at 685 eV increases slightly with the angle, indicating that LiF is (predictably) capping $LiFePO_4$ and thus located in the interphase with $k_{LiF} \sim 0.14$. As a matter of comparison, the evolution of the intensity

corresponding to fluorophosphates at 688 eV results in $k_{PF} \sim 0.37$. This fact does not imply that fluorophosphates are more abundant that LiF in the extreme surface (elemental percentage is roughly ¾ of that of LiF for $\theta = 60°$) but rather that fluorophosphates are found more abundant in the extreme surface compared to the average interphase composition measured at $\theta = 0°$.

As illustrated in **Figure IV-16 (right)**, it appears that data obtained at the end of charge and discharge qualitatively differ only from the higher k_{CO_2} and k_{CO} values at 4.5V, suggesting first that the alkyl-carbonates present in interphase at high potential are preferentially located at the extreme surface. Although less marked, this tendency is also observed at low potential, where the interphase was found thinner, suggesting the dissolution of the "carbonate-rich" outer interphase. These observations strongly recall the XPS/NMR results obtained on powder samples along the first cycle.

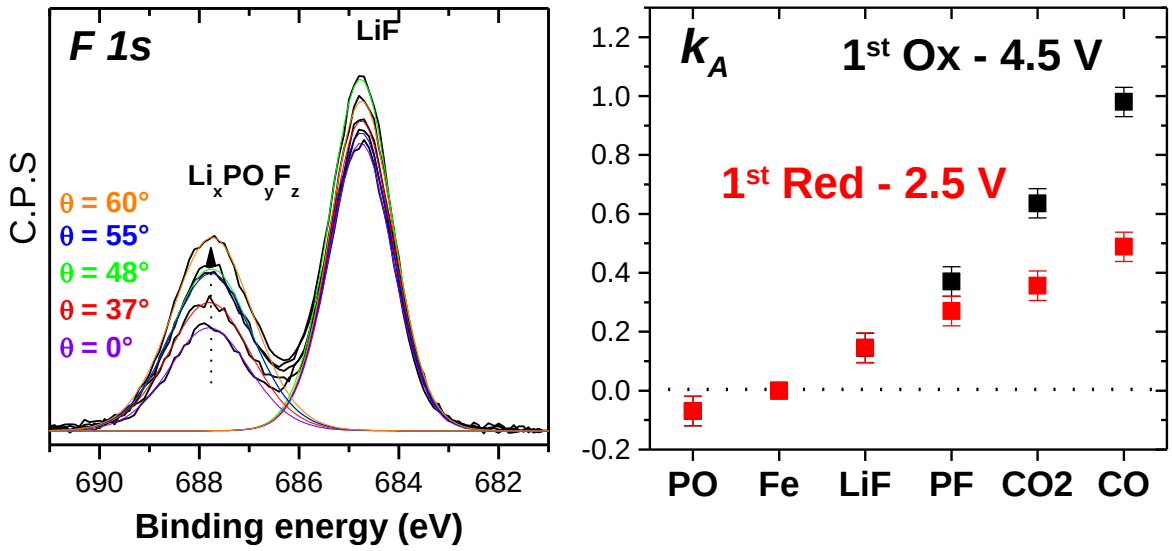

Figure IV-16. (Left) F 1s core spectra measured for the charged $LiFePO_4$ thin film along angular variation, illustrating the relative evolution of LiF and $Li_xPO_yF_z$ components when decreasing the penetration depth. (Right) k_A values extracted from XPS analyses on the charged and discharged $LiFePO_4$ thin films (see Eq. IV-1)

It would be tempting to see in the sorting of k_A values the stacking order of a multilayered interphase. Building an interphase model would however require considering not only $\theta = \{0°; 60°\}$ analysis conditions, but the whole angular domain. Besides, the chemical inhomogeneity of the interphase and the close mixing of interphasial species within the whole depth prevent the use of a multilayered model. Any attempt to draw a depth profile for each detected XPS signal would therefore necessarily be abusive. Radiation damages should also

be considered in such experiments requiring about 24 hours of acquisition per sample. Nonetheless, we believe that the preliminary data gathered in this study provide a good starting point for further qualitative investigation of interphases deposited on epitaxial thin films.

II.2.5. EELS depth profiling of powder $LiFePO_4$ / electrolyte interphase

To illustrate the inhomogeneities of the interphase topology and chemistry, EELS analysis was performed on a powder sample of bare $LiFePO_4$, soaked in the electrolyte for 5 minutes. **Figure IV-17** displays the EELS spectra recorded on the 500-800 eV energy range at different locations in the interphase, together with the corresponding quantification results. Sample preparation and analytical conditions are described in chapter 2 and **Table II-1**.

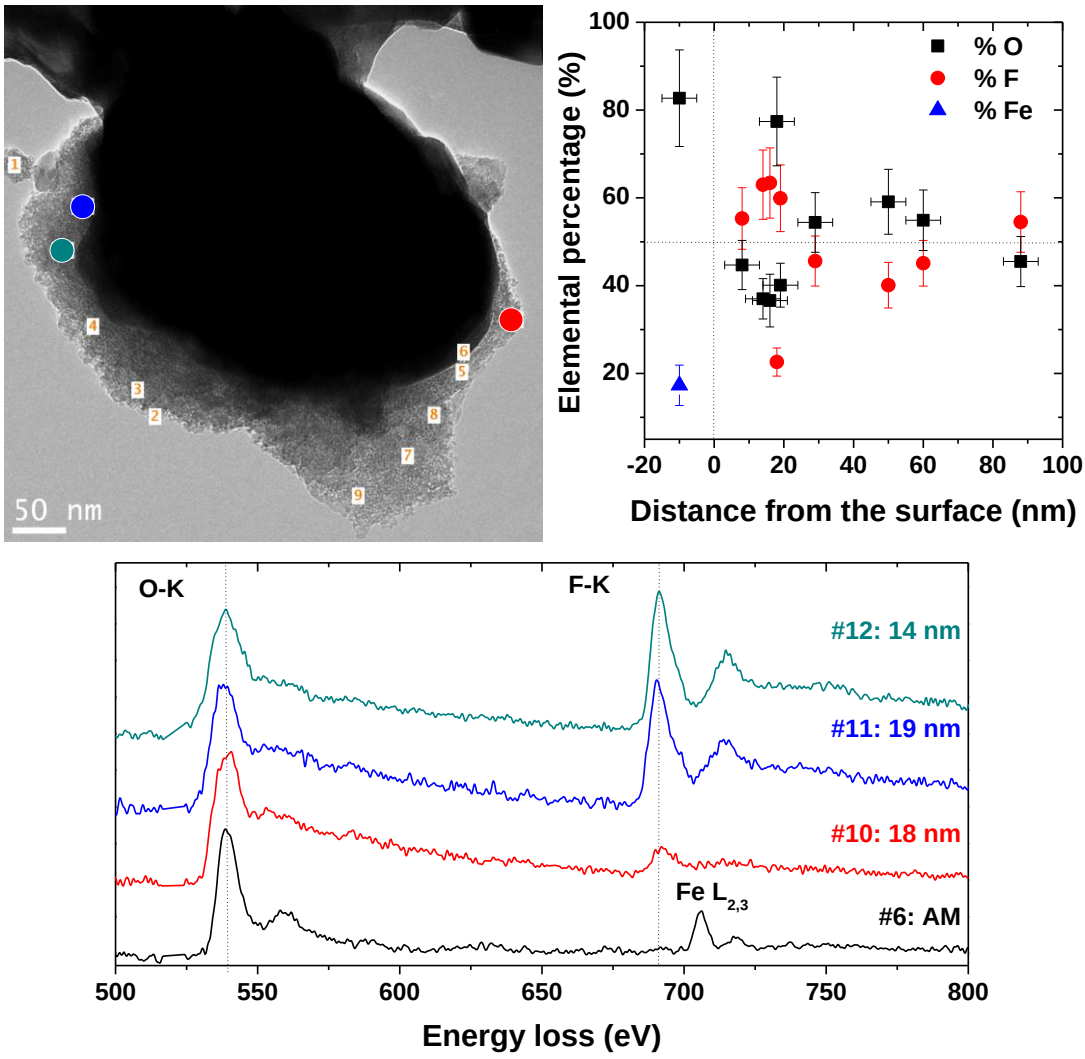

Figure IV-17. TEM image of a LFP-noC aggregate after 5 min soaking in $LiPF_6$ / EC:DMC electrolyte. Numbers denote spots subjected to EELS analysis, which results are reported opposite, together with illustrating spectra measured at similar distances from the surface.

Although only subjected to a simple contact with the electrolyte, the study of the interphase grown on this powder LFP-noC sample sheds light on two decisive points. First of all, the deposit exhibits an irregular thickness, ranging from 0 to 100 nm. Any layered conception of the interphase should thus be avoided. In addition, the statistical analysis of its composition *vs.* depth highlights a significant chemical inhomogeneity, even between positions equidistant from the grain surface. At any point, the interphase comprises a mixture of fluorinated species (identified by NMR as LiF) and Li-alkylcarbonates. Even if trends regarding the preferential stacking order of interphasial species can be drawn from analyses such as NMR and XPS (offering no spatial resolution) or averaging EELS results, it is clear that the positive electrode / electrolyte interphase is neither a homogeneous, nor a strictly multilayered deposit. Hence the model considered hereafter for the $LiFePO_4$ / electrolyte interphase is the Solid Polymer electrolyte Layer (SPL), as defined in Appendix 1, section I.3.1.

II.3. Illustration of interphase aging along cycling

If the interphases formed during first electrochemical cycle of a Li-ion battery play a significant role on the battery performance, a second critical point is to ensure the passivation of both reactive electrode surfaces in order to limit (or ideally to stop) lithium consumption in the interphases and the resulting capacity fading along prolonged cycling. Hence, the following experiments focus on the twenty first electrochemical cycles of the Li // $LiPF_6$, EC:DMC // LFP-noC system.

II.3.1. Electrochemical characterization

Electrochemical impedance spectroscopy (EIS) measurements (from 200 kHz to 50 mHz) were performed at the end of the 1^{st}, 5^{th} and 20^{th} cycles, after a 5 h rest, as shown from the Nyquist diagrams in **Figure IV-18**.

The flat shape of the EIS diagram is in full accordance with a SPL model of the interphase (see **Table AI-3**). As previously demonstrated, most of the impedance can be assigned to charge transfer phenomena [19]. The fact that no distinct semi-circle can be observed at high frequencies further suggests that the interphase grown on $LiFePO_4$ does not behave like a strictly resistive film or that it is not covering homogeneously the surface. Noteworthy, the impedance measured along cycling hardly increases, and the characteristic frequency sees no evolution either, indicating that no interphasial phenomenon impeding the

charge transfer appears. Hence, the evolution of the $LiFePO_4$ / electrolyte interphase along cycling, if any, does not induce any conductivity limitation to the system.

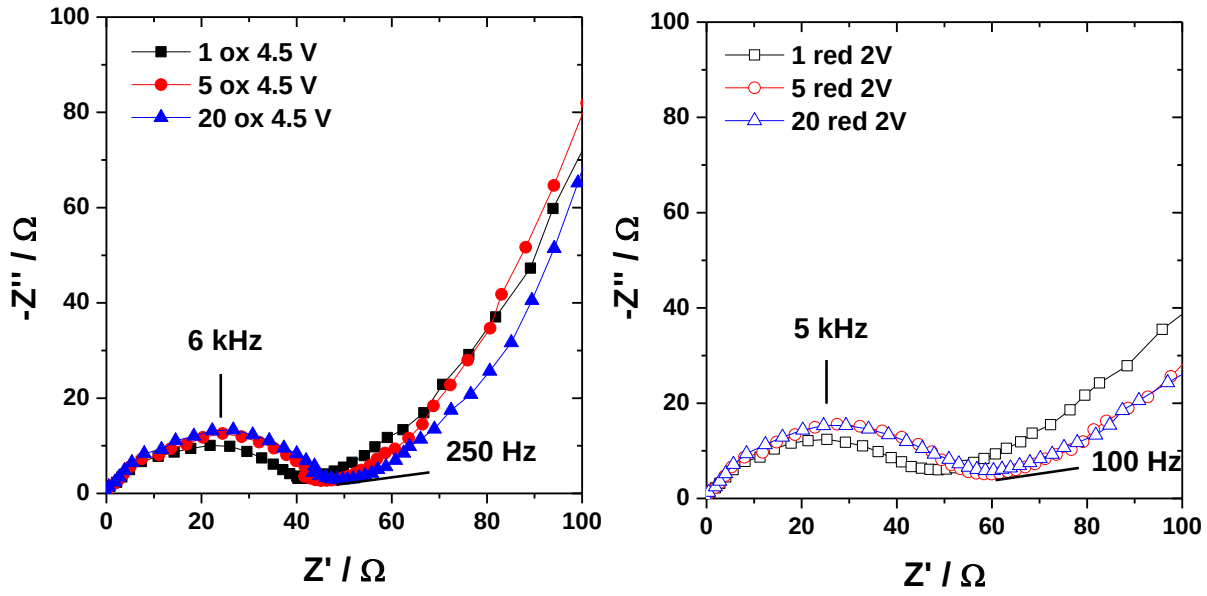

Figure IV-18. Nyquist plots of EIS performed on LFP-noC at the end of the 1st, 5th and 20th charges (closed symbols, left) and discharges (open symbols, right) at a C/20 rate.

II.2.2. Irreversible interphase accumulation probed by NMR

Similar cycling experiments were stopped at the end of the 1st, 5th and 20th charges and discharges in order to analyse the nature and amount of interphasial species deposited on LFP-noC electrodes. The ^{7}Li NMR spectra are presented in **Figure IV-19** together with the resulting quantification plot.

The interphase dynamics revealed during the first electrochemical cycle is confirmed by these additional experiments. Indeed, the process of dissolution at low potentials and precipitation at high potentials of lithiated species appears reversible, although a slight accumulation is observed between the 1st, 5th and 20th charges and discharges.

Considering points taken at the same SOC, T_{2r} increase along cycling suggests the weakening of the nuclear-electronic dipolar interaction, hence an average weakening of the electrode / interphase intimacy. As explained in ref. [22], this observation can imply either a thicker interphase or a more loosely attached one. The increase observed in the amounts of interphasial lithium supports the first hypothesis, while the repeated dissolution/precipitation process allows explaining the second. Both are probably intervening here.

Results from ^{19}F MAS NMR appear in **Figure IV-20**, under the form of a quantification diagram. At the scale of the twenty first cycles, it appears that the amounts of

fluorinated species also evolve along cycling. Considering the close mixing of interphasial species revealed by EELS, it does not seem unlikely that the dissolution of the SPL organic matrix would result in the detachment of less soluble inorganic species upon discharge. During the subsequent charge, those fluorinated salts occur to be trapped again in the reformed SPL.

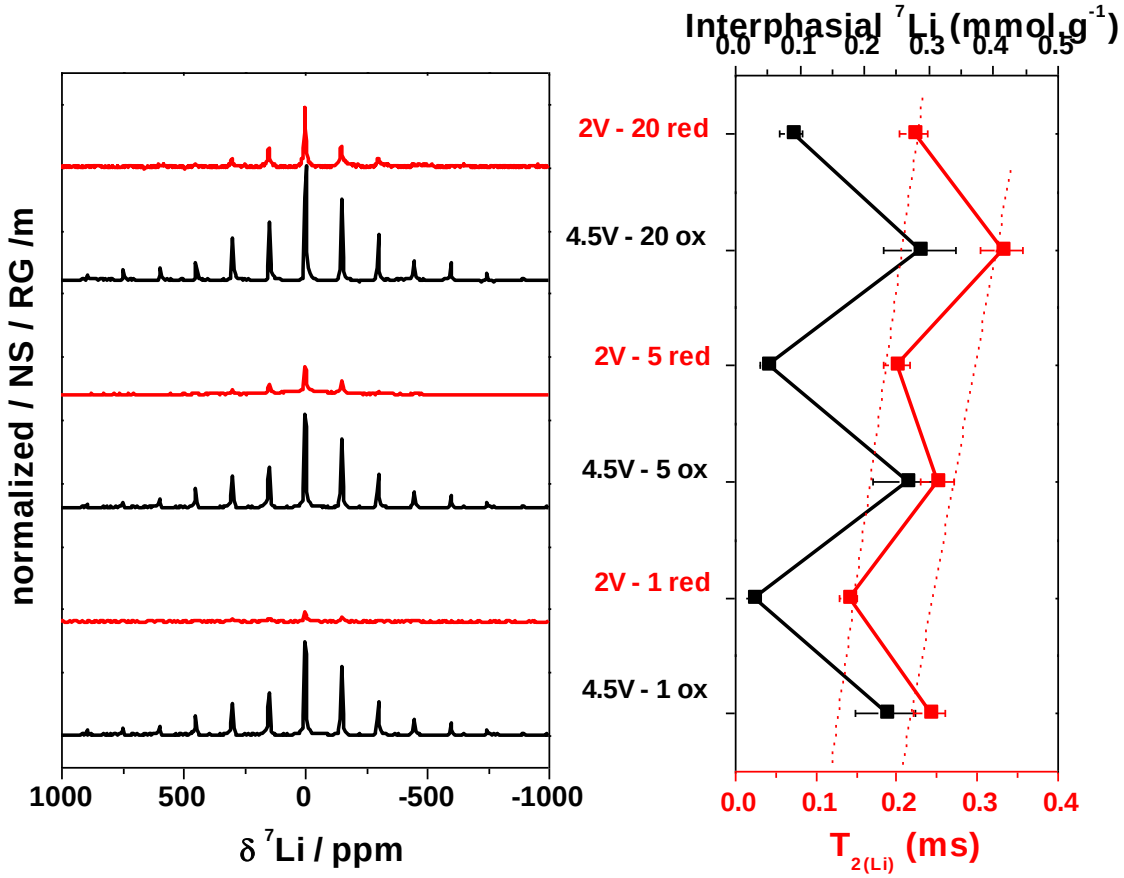

Figure IV-19. Normalized ^{7}Li NMR spectra for LFP-noC at the end of the 1st, 5th and 20th charges and discharges at a C/20 rate in $LiPF_6$ EC:DMC. Amounts of interphasial lithium deduced from integrated intensities, as well as T_{2r}s estimated from the signal width are reported on the right.

The accumulation observed between the 1st, 5th and 20th charges and discharges of LiF and fluorophosphates in the $LiFePO_4$ / electrolyte interphase may seem inconsistent with the unchanging impedance. However, these combined results support the conception of an interphase in decreasing intimacy with the active material. Preventing the blocking of the electrode surface by salt decomposition products, the repeated dissolution/precipitation process of the organic component of the interphase is therefore significantly beneficial to the electrochemical performance of the positive electrode, insofar as the interphasial processes do not bring any limitations to the system.

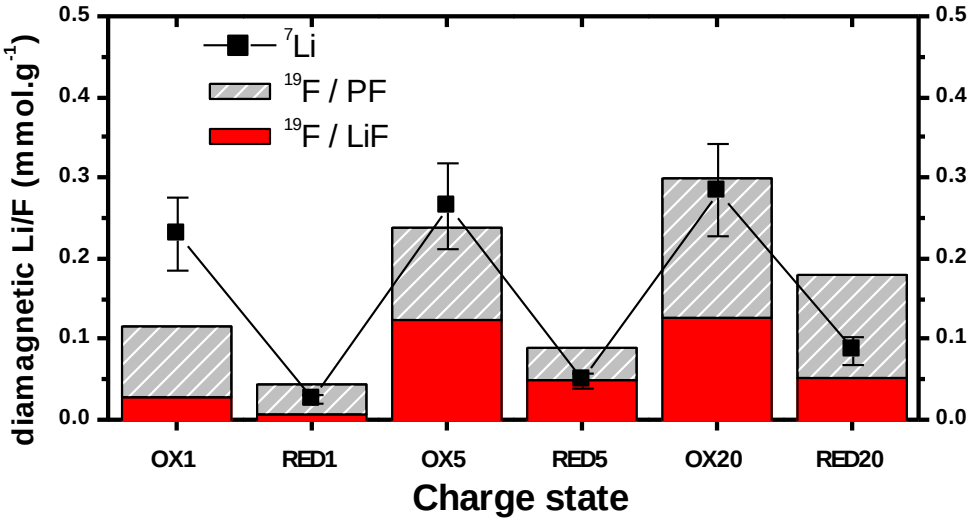

Figure IV-20. NMR quantification results for LFP-noC at the end of the 1st, 5th and 20th charges and discharges at a C/20 rate in $LiPF_6$ EC:DMC.

II.4. Concluding remarks

Widely considered as chemically inert toward the electrolyte, $LiFePO_4$ actually exhibits a complex, dynamic interaction with classical $LiPF_6$ / EC:DMC solution. As tentatively represented in **Figure IV-21**, the present section highlighted that:

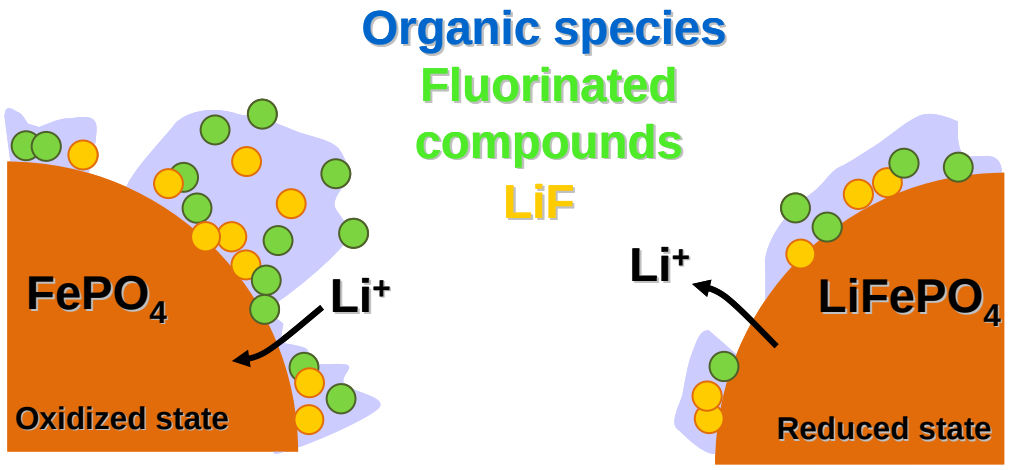

Figure IV-21. Schematic view of the interphase pictured on $LiFePO_4$ at the charged and discharged states along cycling in conventional $LiPF_6$ 1M in EC:DMC (1:1) electrolyte. The higher amount of lithiated organic species does not seem to hamper the interfacial charge transfer, for additional interphasial species tend to stack on the top of the preexisting interphase.

- Solvents are degraded on $LiFePO_4$ surface at high potentials, and their decomposition products form a SPL type interphase that subsequently dissolves at lower potentials.
- Less voltage-sensitive salt decomposition products such as LiF, Li_xPF_y and $Li_xPO_yF_z$ compounds are trapped in this SPL. Although a significant amount departs along the organic matrix dissolution, the interphase observed at low potential is therefore richer in fluorinated compounds.
- The net accumulation of interphasial species is balanced by a looser attachment of this SPL-type interphase to $LiFePO_4$ surface, and maybe also by the emphasis of topological inhomogeneities resulting in an enhanced SPL porosity. New interphasial species are therefore believed to stack on the top of the existing interphase rather than further cover the active material surface, hence preventing the blocking of charge transfer between the electrolyte and the active material.

Nevertheless, the benefit of such interphase dynamics should not eclipse the overall accumulation of lithiated decomposition products at the positive electrode surface. The experiments conducted here do not allow identifying the source of those lithiated species; further analyses performed in a Li-ion configuration would be necessary to discriminate a "cross-talk" between the negative and the positive electrode interphases from detrimental faradic lithium consumption. The answer to this last question would enable for instance choosing appropriate additive(s), either to facilitate the shuttle of interphasial species between the two electrodes or to strictly passivate $LiFePO_4$ surface.

III- CHARACTERIZATION AND CONTROL OF THE LATTICE PLANE DEPENDANCE OF SURFACE REACTIVITY

$LiFePO_4$ stands now as a choice cathode material for high-power rechargeable lithium-ion batteries, but much of its transport properties remain to be understood. The orthorhombic olivine structure of $LiFePO_4$ has a space group of *Pnma* and is rather anisotropic in many of its properties [25]. Considering the disparity of $LiFePO_4$ surfaces towards electrochemical reactions expected from first principle calculations [26, 27], we synthesize here highly oriented particles and investigate the influence of crystallographic orientation on the formation of the surface species at the electrode / electrolyte interface in an attempt to determine surface reactivity from its crystallographic and/or chemical characteristics and finally correlate this reactivity with bulk electrochemistry.

III.1. Background

III.1.1. Illustration of reactivity anisotropy by first principle calculations

Given the one dimensional Li diffusion path along the [010] direction, Richardson *et al.* suggested that the use of thin, unagglomerated particles with large (010) surface area would increase the active area and ease both charge transfer and diffusion of Li ions [28]. Several theoretical studies further focused on $LiFePO_4$ surfaces properties [26, 27]. Thus, a summary of the conclusions drawn by first principle calculations that are relevant to our present work is presented hereunder.

Reprinted from ref. [26] is the Wulff shape for $LiFePO_4$ shown in **Figure IV-22**. Its construction is based on the calculated surface energies; the lower in energy a surface is, the more the contribution of the facet is important to the Wulff shape. In fact, the (010) surface exhibits a surface energy significantly lower than the others and its predominance in subsequent calculated growth morphologies is therefore considerable [27]. This explains why hydrothermal syntheses, as shown in the next sub-section, easily result in plate-like particles favoring large (010) surfaces.

Moreover, as also reprinted from ref. [26] in **Figure IV-22**, the redox potential for the (010) surface is 2.95 V vs. Li^+/Li^0, also significantly lower than the calculated bulk value of 3.55 V. Hence, it is expected that for a well-faceted $LiFePO_4$ particle, Li will be first extracted from the (010) surface upon charging and inserted last upon discharging.

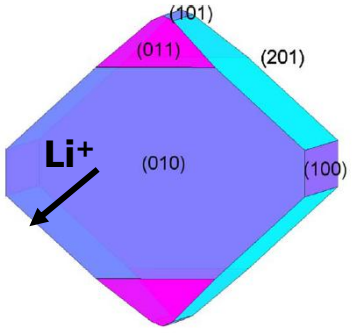

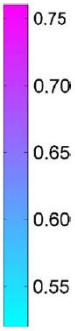

PHYSICAL REVIEW B **76**, 165435 (2007)

TABLE V. Calculated redox potentials for the extraction of Li from five surfaces of $LiFePO_4$ as well as the bulk potential.

Orientation	(100)	(010)	(101)	(011)	(201)	bulk
Voltage (V)	3.84	**2.95**	3.25	3.79	3.76	3.55

Figure IV-22. Selected results from ref [26] highlighting the distinctiveness of $LiFePO_4$ (010) surface from an energetic point of view. Left: Wulff shape. Right: calculated redox potentials.

The authors emphasize the benefice of maximizing this particular surface for improved rate capability as the [0 1 0] direction is the most facile pathway for lithium ion conduction in $LiFePO_4$. They conclude with: *"any clearing of the (010) surface upon charge and discharge should facilitate Li motion across the surface layer [and propagation into the bulk]"*. Hence, the present study aims at evaluating the possible blocking of the (010) surface by the electrode / electrolyte interphase.

III.1.2. Hydrothermal synthesis of plate-like $LiFePO_4$ particles

The synthesis employed here is the one established by Dokko *et al.* [29]. Iron precursor used is $Fe(NH_4)_2(SO_4)_2 \cdot 6H_2O$, together with LiOH as the lithium precursor, and a mixture of $(NH_4)_2HPO_4$ and H_3PO_4 used not only as the phosphorus sources but also to set the appropriate pH. Thermal treatment is carried out at 180°C, for 5h and 12h, resulting in nm-large isotropic beans (refered as LFP-iso) and µm-large *b*-oriented platelets (labeled LFP b-plates), respectively. The orientation of LFP b-plates was confirmed by electronic diffraction and **Figure IV-23** displays typical micrographs observed for these two samples, together with their BET specific surface area.

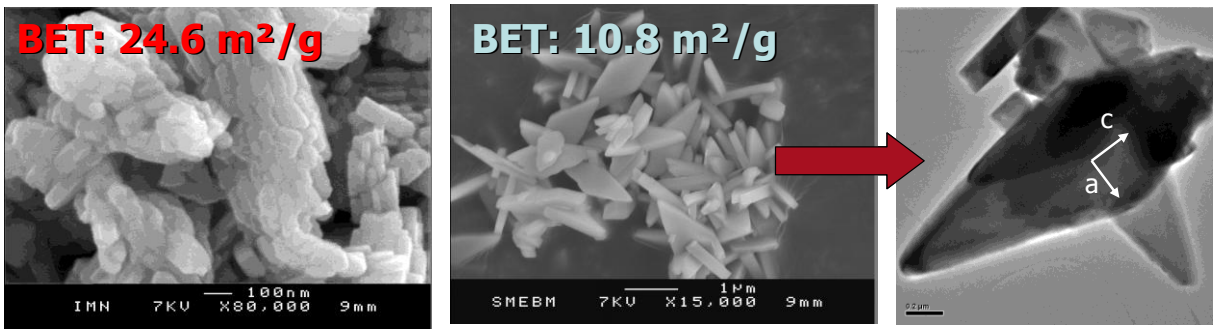

Figure IV-23. SEM images of LFP-iso and LFP b-plates, with attending TE micrograph.

LFP-iso particles are about 100 nm large, in agreement with a specific surface area of 24.6 $m^2.g^{-1}$. Although these values are close to those measured in the case of the solid state synthesis referred as LFP-noC, the aggregations of primary particles significantly differ for the two materials. LFP-iso particles are indeed closely packed at the scale of micrometric lozenge-shaped aggregates, which strongly suggest the ulterior formation of LFP b-plates upon longer thermal treatment. These LFP b-plates exhibit a 2µm length by a 0.5-1.0 µm width and an average 0.2 µm thickness. The specific surface area is therefore significantly reduced to 10.8 $m^2.g^{-1}$, of which an approximate calculation, using a lozenge-based particle volume, indicates that roughly 55% corresponds to (010) surfaces.

III.1.3. Structural characterization by XRD and Mössbauer

As seen in **Figure IV-24**, no impurity phase can be observed on the XRD patterns of hydrothermally prepared $LiFePO_4$ materials. By comparison with LFP-noC, the width of diffraction peaks indicates that LFP b-plates are made of larger crystallites (<L>= 221(8) nm). On the contrary, broaden diffraction peaks for LFP-iso suggest a lower degree of crystallinity (<L>= 58(15) nm), caused by the low temperature and short duration of thermal treatment.

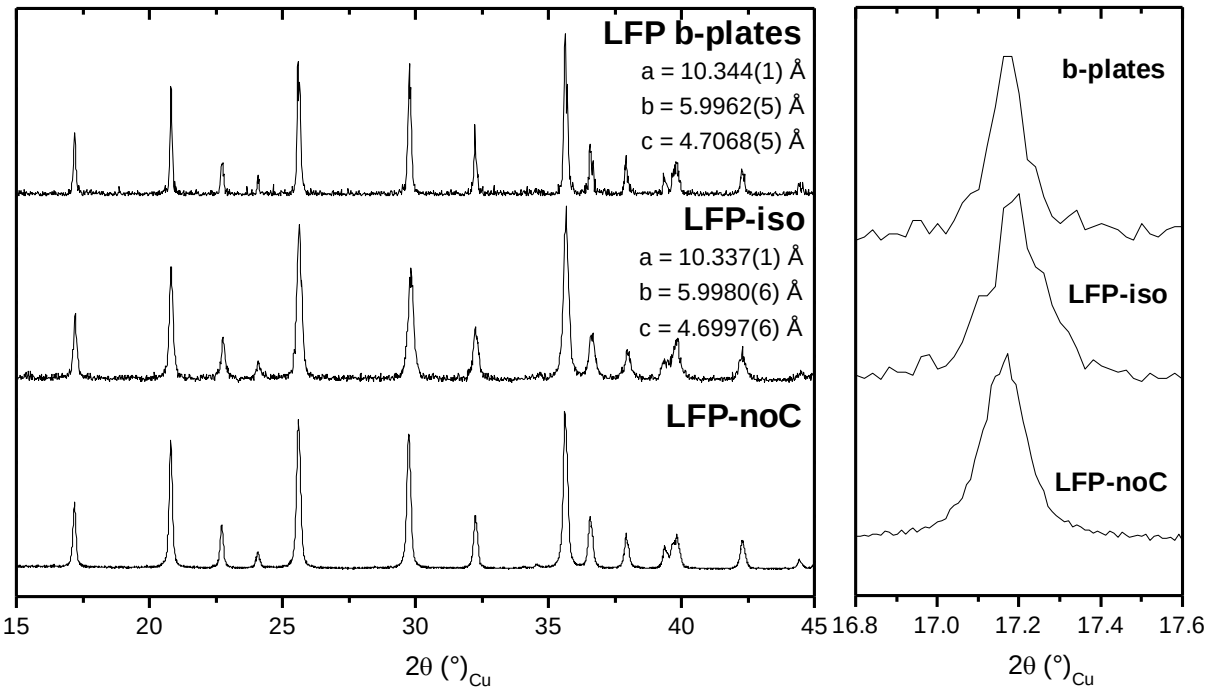

Figure IV-24. Normalized XRD patterns of as synthesized LFP-iso and LFP b-plates. The diagram of LFP-noC serves here as a reference.

Mössbauer spectroscopy was performed on hydrothermal LFP-iso and LFP b-plates samples, indicating that these materials contain 9 % and 8 % of Fe(III), respectively.

Similarly to samples prepared via a solid state route, hyperfine parameters suggest an octahedral phosphate environment for this Fe(III). Hydrothermal materials however exhibit a higher amount of Fe(III) defects, identified by XRD as Li/Fe antisites, estimated at 2.4(7) % and 7.0(4) % for LFP-iso and LFP b-plates, respectively.

III.1.4. Electrochemical characterization

Standard electrochemical tests were carried out on hydrothermal LFP-iso and LFP b-plates materials, as illustrated by **Figure IV-25**. The poor performance of LFP b-plates, attributed to the large particle size, even in the [010] direction, could be improved by a carbon coating. Based on previous results (**Fig. IV-8**) the cellulose acetate precursor was selected.

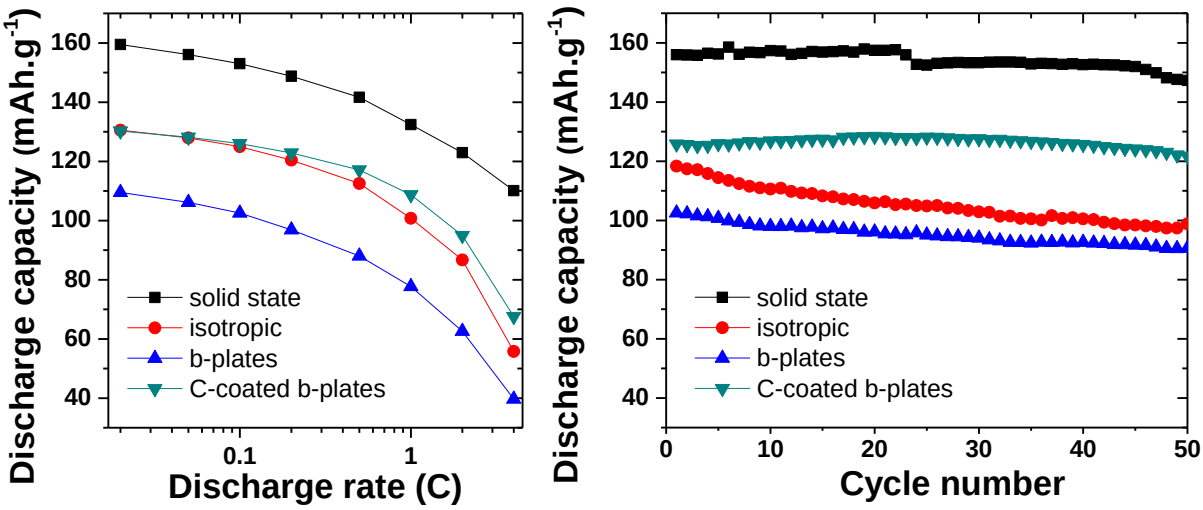

Figure IV-25. Power capability measured by cumulative discharges and cyclability of LFP-noC, LFP-iso, LFP b-plates and C/LFP b-plates at C/10.

The materials prepared by a hydrothermal route are clearly outperformed by the sample prepared by high temperature solid state synthesis, both in terms of practical capacity and power capability. Regarding the power behavior of LFP b-plates, expected to be enhanced by the low (010) surface energy and the accessibility of Li channels, it appears that the detrimental thickness (~ 200 nm) balances these favorable energetic considerations. The low discharge capacity delivered by both hydrothermal materials might be assigned to their poor crystallinity, and structural defects such as Fe / Li exchange [30]. Their cyclability is however satisfying, especially for the b-oriented material. Although the power behavior of C-coated LFP b-plates is not improved, the discharge capacity accessible at C/50 is increased by almost 20%. This improvement is therefore mostly assigned to cationic rearrangement during the post annealing at 700°C rather than the presence of carbon at the platelets surface.

EIS measurements, as displayed at the end of the first charge in **Figure IV-26** further highlight a difficult charge transfer at the interface of both hydrothermal materials.

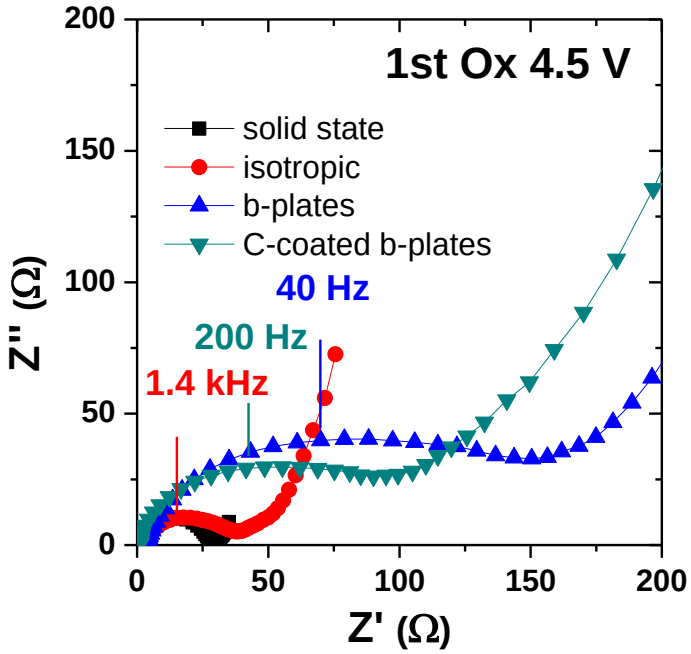

Figure IV-26. Nyquist plot of EIS performed on LFP-noC, LFP-iso, LFP b-plates and C/LFP b-plates at the end of the 1st charge at a C/20 rate.

The micrometric dimensions of these particles are certainly detrimental to electrical contacts within the electrode and with the current collector, but if this were to be the limiting contribution to the electrical properties, the carbon coating should overcome this drawback, and increasing the calandering pressure should also have beneficial impact, which is not the case here. Hence, the clear and significant impedance increase observed for bare and carbon coated oriented particles may rather highlight the influence of preferential orientation and of the exposed surface. Flat EIS loop being associated with charge transfer resistance and the SPL, it seems to indicate that (010) surface is more likely to be blocked by the interphase deposition, at least from kinetics point of view. Thus, even if (010) surface may favor the electrochemical insertion/deinsertion process in $LiFePO_4$. It seems that parasitic interphasial reactions might also be exacerbated by the enhanced exposure of this particular surface.

III.2. Effect of crystalline orientation on the reactivity towards electrolyte

In order to isolate the influence of crystalline orientation from that of surface chemistry, previous work carried out on LFP-noC (section 2.3) could not be taken as a direct

reference. Hence the following NMR study has been conducted on both hydrothermally prepared LFP-iso and LFP b-plates. Similarly to the above mentioned study, experiments focus on the twenty first electrochemical cycles of the Li // $LiPF_6$, EC:DMC // LFP system.

N.B. For the important difference in the surface developed by these two materials, quantification results are reported in surface rather than mass units. Although the specific surface area as determined by the BET is known to differ significantly from the electrochemical surface, this value was used to normalize integrated intensities.

III.2.1. Illustration of increased reactivity of (010) electroactive surface by NMR

Figure IV-27 shows the ^{7}Li NMR spectra measured at the end of the 1st, 5th and 20th charges and discharges for hydrothermal LFP b-plates. The attending quantification diagram also contains the results of similar experiments conducted on LFP-iso, and **Figure IV-28** gathers data obtained by complementary ^{19}F NMR experiments.

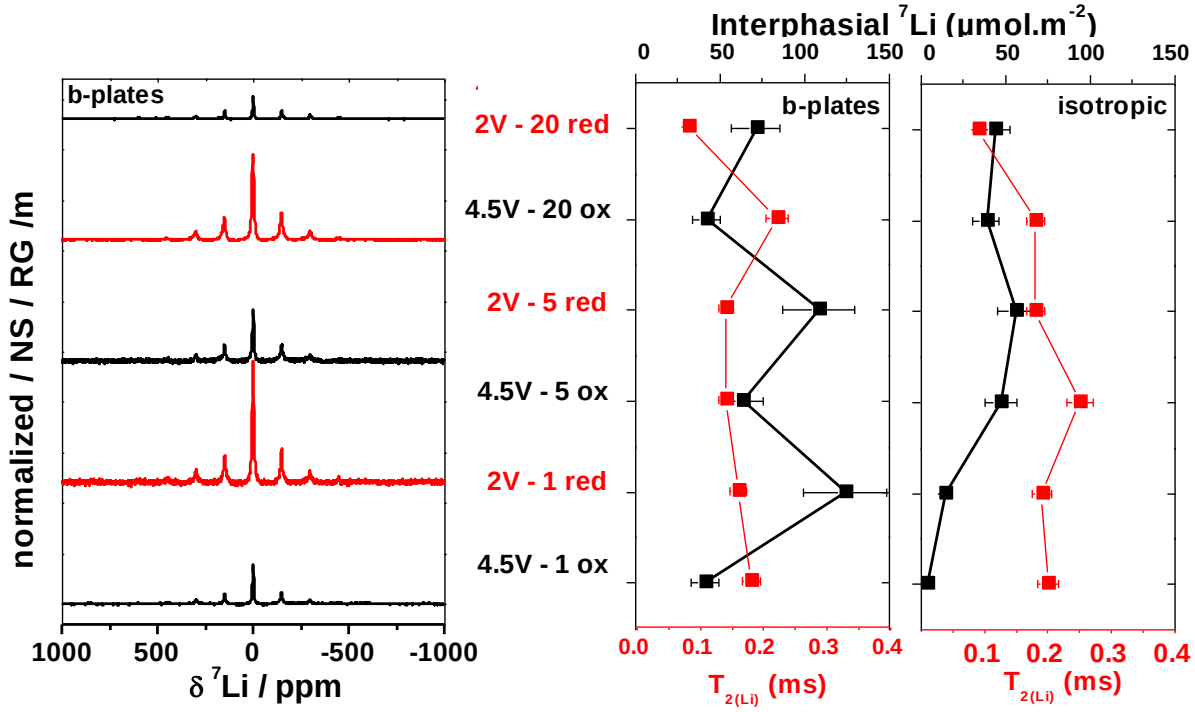

Figure IV-27. Normalized ^{7}Li NMR spectra for LFP b-plates at the end of the 1st, 5th and 20th charges and discharges at a C/20 rate in $LiPF_6$ EC:DMC. The amounts of interphasial lithium deduced from integrated intensities, as well as T_{2r}s estimated by the signal width are reported on the right. Comparison is made with sample LFP-iso.

Concerning the different evolutions of both lithium amount and T_{2r}s observed for LFP-iso particles obtained through hydrothermal method compared with solid state route (LFP-

noC), although a general accumulation is observed alike, no real influence of the potential could be noticed here. Moreover, similar result is observed for ^{19}F NMR. Possibly, the different surface chemistries between the two materials govern different chemical reactions at the interface. An additional hypothesis that can be brought forward to explain this discrepancy is linked with the aggregation / shape of the secondary particles (**Fig. IV-23**). The high degree of aggregation of the hydrothermal LFP-iso particles leads us to expect an inside porosity difficult to access and most probably easy to block.

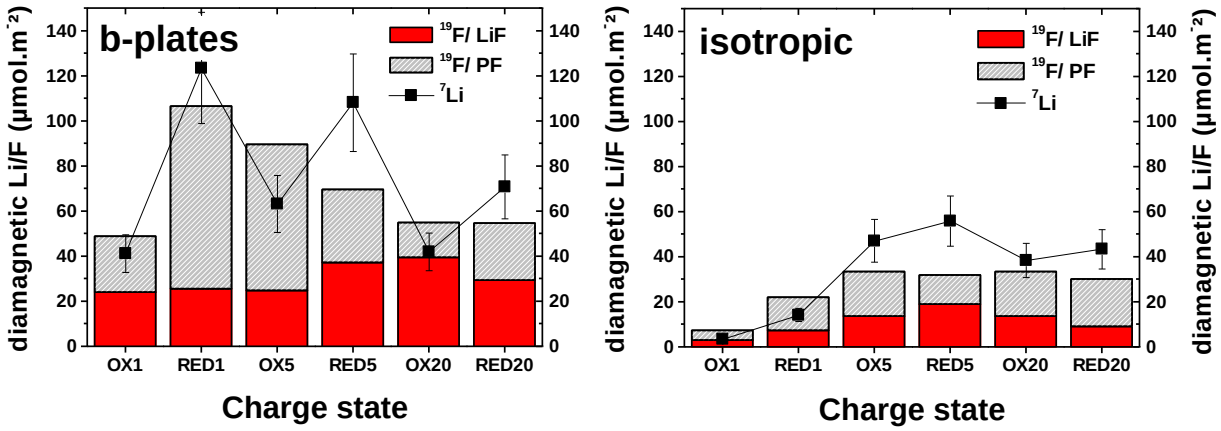

Figure IV-28. NMR quantification results for LFP-iso and LFP b-plates at the end of the 1st, 5th and 20th charges and discharges at a C/20 rate in $LiPF_6$ EC:DMC electrolyte.

The slight monotonous increase in lithium amount together with a slight monotonous decrease of T_{2r}s suggest for this material a further covering of the surface rather than the stacking process observed on LFP-noC, in the case of a dissolution/precipitation of interphasial species. With an important part of their surface as inside porosity, it seems reasonable to consider that part of the insoluble fluorinated salts, which would normally depart upon dissolution of the organic matrix, stay trapped within the porosity of the aggregates (see sketch in **Fig. IV-29**). Hence, these LFP-iso aggregated particles would be less sensitive to the process of dissolution / precipitation of the SPL as a function of the potential. Another possibility is that structural defects could be present near the surface (since Li/Fe antisites are observed by XRD for hydrothermally prepared samples [30]). If these defects were to be persistent, the surface of these materials would be constantly richer in Fe(II) and no (or less) variation in T_{2r} would be observed as a function of the potential. Similar T_{2r} evolution is observed for LFP b-plates, and can be explained using the same argument.

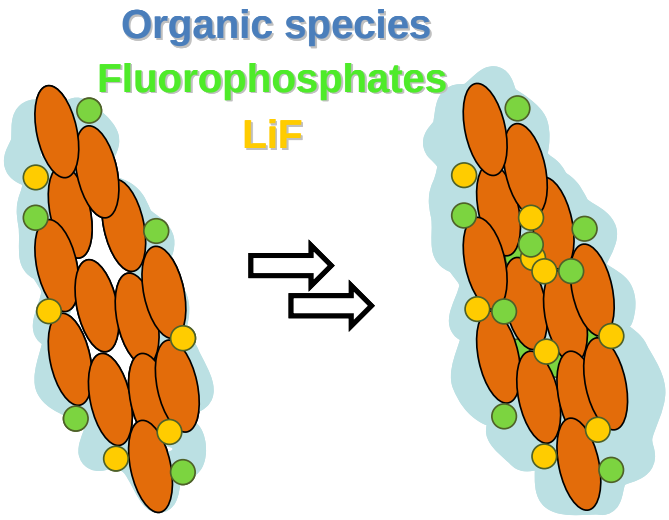

Figure IV-29. Overview of hydrothermal LFP-iso reactivity towards conventional $LiPF_6$ 1M in EC:DMC (1:1) electrolyte. Trapping of interphasial compounds within the porosity results in surface passivation by the 5th cycle.

Concerning the b-plates, as opposed to the isotropic particles, the variation of lithium amount is much more pronounced along potential variation and the amount of LiF (from ^{19}F), although it does not seem to vary significantly, is one order of magnitude higher. As observed during soaking experiments in electrolyte (not shown here), the reactivity of the (010) face is such that it is immediately saturated with salt decomposition products by simple contact. Hence, the amounts of LiF measured by NMR along the 5 first cycles are similar to what was detected after 3 min or 3 days of LFP b-plates immersion into $LiPF_6$, EC:DMC solution.

At the scale of an extending cycling of the LFP-noC material, the variations of fluorinated compounds follow the same trend that lithiated species. The deviation from this model for LFP b-plates suggests that the organic species probed in this case and in the case of solid state LFP-noC are different. The variations in the lithium amount with the potential (i.e. important for reduced and small for oxidized state) are in fact opposed to those of LFP-noC but resemble what is observed for $LiNi_{1/2}Mn_{1/2}O_2$ oxide (chapter 3), suggesting that the surface of LFP b-plates is sufficiently deep and covered not to govern anymore the interphasial chemistry.

As a result, the variation observed for the amount of lithium depicts rather processes occurring at the interface between interphase and electrolyte (i.e. the outer area of the interphase). The overall decrease in the amount of interphasial lithium suggests the dissolution of lithiated organic species and fluorophosphates while the inner part, made of lithium fluoride formed upon simple contact with the electrolyte is not subject to significant variations.

III.2.2. Effect of carbon coating on the (010) surface reactivity

The influence of the carbon coating deposited on the LFP-b plates on the surface reactivity was investigated by NMR spectroscopy, as summarized in **Figure IV-30**. From a qualitative point of view, the intrinsic T_{2r} dependence vs. SOC is recovered for CA/LFP b-plates, supporting the hypothesis of cationic rearrangement during the high temperature treatment necessary to carbonize the coating.

The amounts of interphasial species are here normalized by the specific surface area of bare LFP b-plates (10.8 $m^2.g^{-1}$) rather than the net specific surface area measured after the coating deposition (18.6 $m^2.g^{-1}$). By doing so, results gathered in **Figure IV-28** (for bare LFP b-plates) and **Figure IV-30** (for CA/LFP b-plates) can be compared more easily and it appears that the absolute amount of fluorinated species is not significantly decreased by the presence of a carbon layer. Although variations in the amount of interphasial lithium are less pronounced, it is reasonable to conclude that the surface reactivity of C-coated b-plates towards electrolyte is still dictated by the exacerbated reactivity of the (010) surface, as attested by the impedance measurements (**Fig. IV-26**).

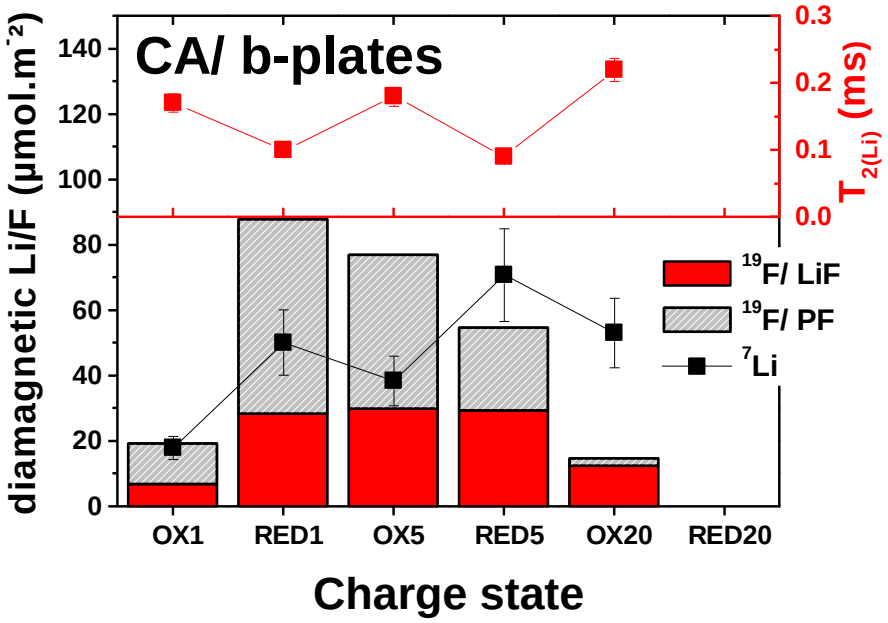

Figure IV-30. NMR quantification results for C-coated/LFP b-plates at the end of the 1st, 5th and 20th charges and discharges at a C/20 rate in $LiPF_6$ EC:DMC electrolyte, as well as T_{2r}s estimated by the signal width.

III.3. Concluding remarks on crystalline orientation and its consequences

The synthesis of $LiFePO_4$ materials by a hydrothermal route must result in a significant amount of structural defects, namely Li/Fe antisites, which limit the electrochemical performance in terms of accessible capacity. The subsequent high temperature annealing performed to deposit a carbon coating on highly oriented b-plates, displaying about 50% of (010) surfaces, proves efficient to reduce the amount of such structural defects.

Then, free from their detrimental impact on the electrochemical performance, it appears however that the exacerbated exposition of the (010) surfaces leads to an aggravated reactivity towards electrolyte. Thus, the interphasial chemistry on (010) oriented materials is found governed by the increased precipitation of inorganic salt decomposition products at the electrode surface upon simple contact rather than by the intrinsic reactivity of $LiFePO_4$ (leading to the precipitation / dissolution process described in section 1.3). The half-cell impedance measured for bare and carbon coated LFP b-plates shows that this morphology, and the surface reactivity implied, might not be suitable for a battery application. Indeed, the benefice of maximizing this particular surface for improved rate capability is completely opposed by the surface blocking with interphasial species, as sketched in **Figure IV-31**.

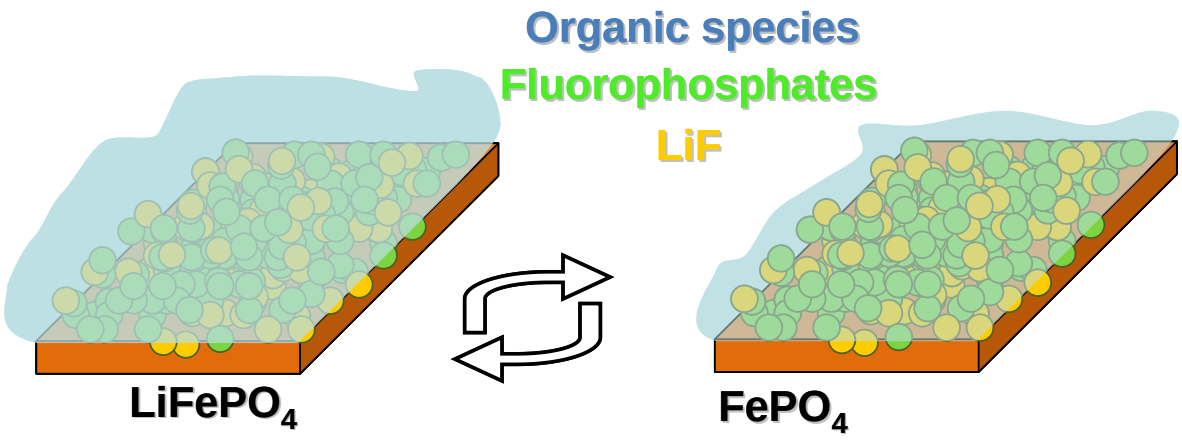

Figure IV-31. Overview of the impact of the orientation on $LiFePO_4$ reactivity towards electrolyte. Surface blocking upon immediate contact with conventional $LiPF_6$ 1M in EC:DMC (1:1) electrolyte result in the evolution of interphase upon cycling regardless (Li)$FePO_4$ surface reactivity.

IV- CHARACTERIZATION AND CONTROL OF SURFACE AGING ALONG AIR EXPOSURE AND ITS REPERCUSSIONS ON THE ELECTROCHEMISTRY

The first step to a better understanding of electrode / electrolyte interactions is the accurate knowledge of the surface of pristine material(s). As presented in the introductive chapter, the covering of active particles surface by Li_2CO_3 has been reported on various air-exposed materials such as $LiNiO_2$, [30-32] $LiMn_2O_4$, [32, 33] and Li_2FeSiO_4, [34] for example. In the case of $LiFePO_4$, Herstedt *et al.* suggested by the use of PES that, although Li is present at the surface of pristine olivine, it is not under the form of Li_2CO_3 [1].

Besides, the reduction of the particle size is now understood as a key point to optimize $LiFePO_4$ materials response in terms of capacity and rate capability [1-3, 35, 36]. Lowering the particle size increases the importance of surface chemistry, including possible parasitic side reactions [36, 37]. This aspect, in addition to the intrinsic wider solid-solution domains of nanoparticles [1, 10, 35, 37], becomes crucial when the size drops under 100 nm. Facilitated adsorption of atmospheric species, especially for high surface area nanoparticles, and the subsequent reactivity of olivine itself to oxygen and moisture could explain some electrochemical results. For instance, degradation of the electrochemical performance of $LiFePO_4$ was revealed after air exposure for a few weeks and up to one year at ambient temperature [38].

In that context, this study aims at shedding light on the alteration of olivine in atmosphere and monitoring the structural and chemical changes occurring along storage. As a conclusion of these studies, reported in ref. [8] and papers **I**, **II** and **III**, a scheme of the most probable aging scenario is proposed. Then, electrochemical experiments and interphasial studies point the consequences of these modifications on $LiFePO_4$ batteries performance. Finally, two practical means to control $LiFePO_4$ surface aging, namely carbon coating and the use of a dedicated additive, are demonstrated.

IV.1. Structural modifications induced by moderate air exposure [J.-F. Martin, 2008, ref. 8, paper II]

IV. 1.1. Illustration of lithium extraction in the $Li_{1-x}FePO_4$ solid solution domain

XRD was carried out to investigate the effect of different atmosphere exposure conditions. No evidence of cationic exchange could be found by Rietveld refinement as no increase of *a* and *b* lattice parameters values has been observed [5]. **Figure IV-32**

demonstrates the linear relative dependence of *a* and *b* lattice constants following Vegard's law, in the hypothesis of a solid solution between stoichiometric $LiFePO_4$ (prepared with no contact with air), and $Li_{0.82}FePO_4$ (a = 10.2987 Å and b = 5.9921 Å) [10].

$$b = 0.9205 + 0.4942\ a \qquad \text{(Eq. IV-2)}$$

These results show that some lithium is certainly extracted when $LiFePO_4$ is put in contact with atmosphere. Values for x in $Li_{1-x}FePO_4$ can be calculated from Eq. IV-2, which gives for instance 4.1% of missing lithium after ambient air exposure for 10 days at 120°C.

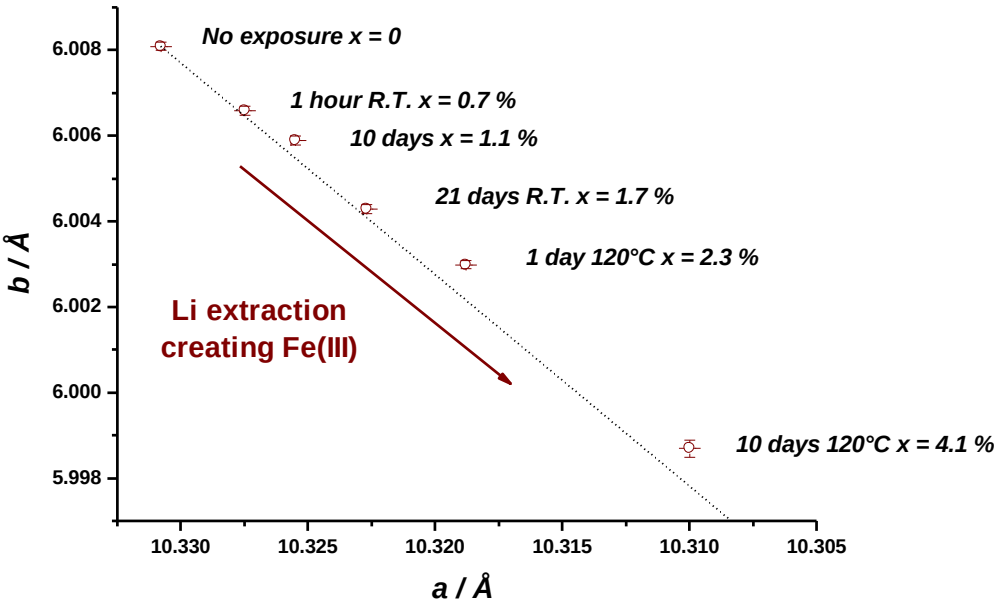

Figure IV-32. Lattice constant changes for $Li_{1-x}FePO_4$ after different air contact experiments following Vegard's law (black dot line). Duration and temperature of the aging experiments are given together with the resulting *x* values in $Li_{1-x}FePO_4$.

Furthermore, lithium extraction from olivine could be observed by the use of high field ^{7}Li MAS NMR experiments, performed in the same conditions employed for interphase studies. The amounts of diamagnetic lithium calculated from integrated intensities are plotted in **Figure IV-33** as a function of x values calculated using the above mentioned Vegard's law (Eq. IV-2). For each analyzed sample, it appears that approximately one tenth of the expected diamagnetic lithium can be detected by NMR. The fact that the corresponding $T_{2r(Li)}$ goes increasing with the amount of lithium supposedly extracted from $LiFePO_4$ can be explained by iron gradual oxidation in the close environment of the extracted lithium. The variation of $T_{2r(Li)}$ as a function of the extracted Li , and therefore Fe(III) formation, suggests that the extracted Li is not only sensitive to the oxidation state of the iron in the immediate vicinity but can feel the overall change of oxidation state of a wider volume range of the sample. The

important $T_{2r(Li)}$ variation suggests that this extracted lithium remains in very strong interaction with the bulk, hence justifying the detection of a small fraction of this diamagnetic lithium. The rest of extracted Li probably displaying a shorter T_{2r} would be truncated by the long pre-acquisition delay used in these experiments.

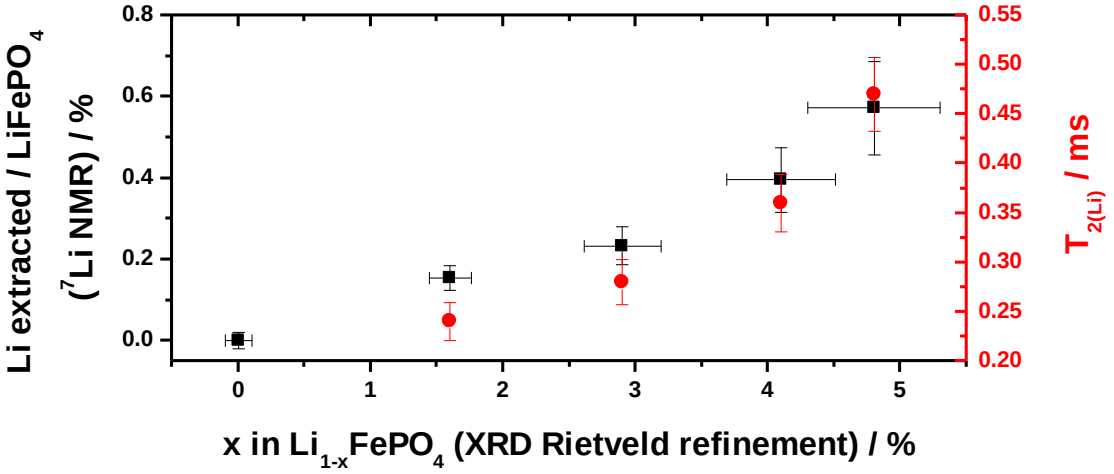

Figure IV-33. ^{7}Li NMR quantification results vs. x values in $Li_{1-x}FePO_4$ determined by XRD.

IV.1.2. Illustration of material oxidation by Mössbauer spectroscopy

Mössbauer analyses were carried out by Alain Wattiaux in ICMCB, to observe possible Fe(III)-containing phases (Fig**. IV-34**). In this regard, Mössbauer spectroscopy is much more sensitive than XRD for detecting different valence states, as it is a direct scrutiny of atomic information and does not rely on the long-range coherent interaction.

Figure IV-34 shows a comparison of four LFP-C samples: before exposure, after 10 days exposure at room temperature, after 24 h and after 10 days exposure at 120°C. The iron is mainly under Fe(II) form (IS = 1.24 $mm.s^{-1}$ and QS = 2.96 $mm.s^{-1}$) in all cases, but a subsignal of Fe(III) is found for samples having experienced ambient air exposure (IS = 0.40 $mm.s^{-1}$ and QS = 0.90 $mm.s^{-1}$). This trivalent doublet can be evaluated to 6, 11 and 35% of the total iron content, respectively. Hyperfine parameters can be assigned to a ferric phosphate environment such as in the reported lithium deficient $Li_{1-x}FePO_4$ [8-10], highly defective $Li_xFe_yPO_4$ [39], $FePO_4$, $2H_2O$ [40], or $FePO_4$, H_2O [41].

The significant difference between the calculated quantity of lithium missing in the triphylite phase and the amount of Fe(III) visible via Mössbauer is attributed to the presence of an amorphous ferric phosphate phase. To support this hypothesis, subsequent Rietveld refinement made quantitative by the addition of an internal reference of crystallized Si prior aging [42], indicate that 15 wt% of the sample air-aged for 10 days at 120°C is amorphous, highly disordered or nano-crystallized.

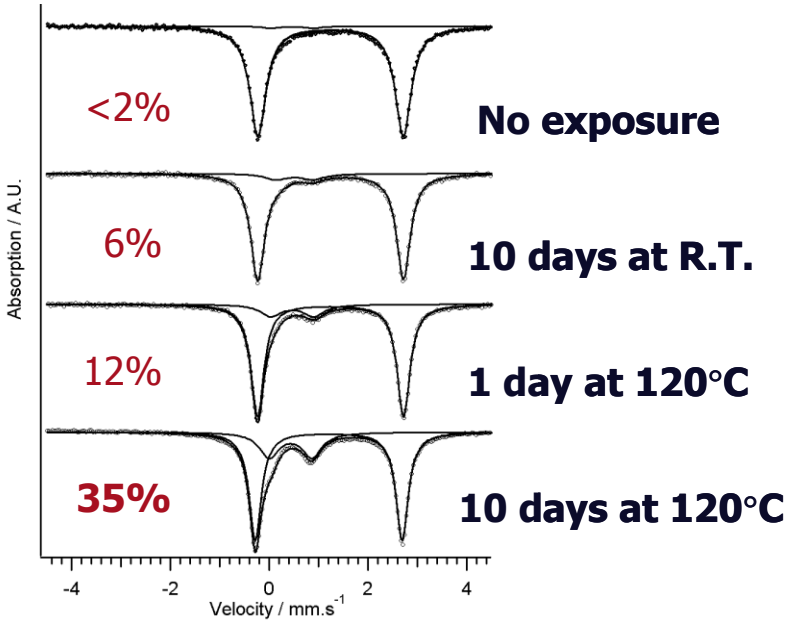

Figure IV-34. Mössbauer spectra of studied samples after different air contact experiments (same as in **Fig. IV-32**). The figures indicate the amount of Fe(III)-containing phase.

IV.1.3. Proposed aging mechanism

In the TGA experiment displayed in **Figure IV-35**, a pristine LFP-C sample has been exposed at 120°C for 24 hours first in dry oxygen and then in the presence of 1% of relative humidity. Hence, it was clearly demonstrated that although reaction with O_2 is possible, the main cause of the alteration of $LiFePO_4$ is the reaction involving humidity contained in the atmosphere.

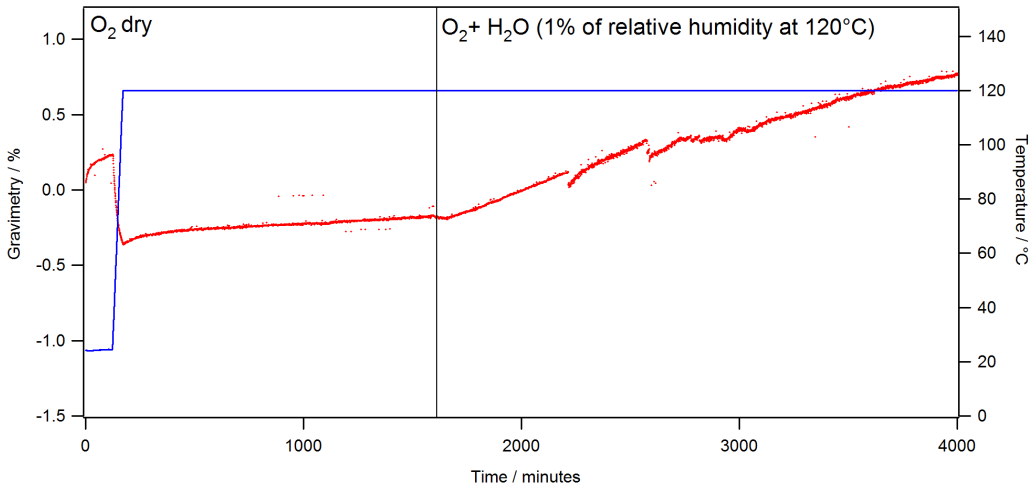

Figure IV-35. TGA curve of an atmosphere preserved LFP–C sample during a 24 h 120°C stage in dry O_2 followed by a stage in a 1% of relative humidity atmosphere.

Considering a role of both oxygen and water, it seems then reasonable to propose the two possible following "corrosion" mechanisms:

$$LiFe^{II}PO_4 + x/2\ H_2O + x/4\ O_2 \rightarrow Li_{1-x}Fe^{II}_{1-x}Fe^{III}_{x}PO_4 + x\ LiOH \quad \text{(Eq. IV-3)}$$

$$LiFe^{II}PO_4 + 1/2\ H_2O + 1/4\ O_2 \rightarrow LiFe^{III}PO_4(OH) \quad \text{(Eq. IV-4)}$$

The first reaction describes lithium extraction from the olivine phase, as probed by XRD and ^{7}Li NMR, and described in ref. [8, 43]. The second reaction was proposed by mineralogists for hydrated and hydroxylated iron phosphates, as pointed out by Fransolet *et al.* [44] in the case of olivine that leads to the formation of tavorite $LiFePO_4(OH)$. Not only does this reaction allows iron oxidation in a significantly higher extent than in the $Li_{1-x}Fe^{II}_{1-x}Fe^{III}_{x}PO_4$ solid solution domain (Eq. IV-3) but it also supports the mass uptake observed in **Figure IV-35** under moisture exposure. The absence of crystalline tavorite in air exposed samples is investigated further in section 4.2.

In addition, the Fe(III)/Fe(II) ratio determined by XPS in paper **II** is found to be significantly higher when determined by this extreme surface sensitive technique (~ 80 %), compared to Mössbauer spectroscopy (~ 35 %). Considering the surface nature of the Fe(III)-rich phase, a core-shell schematic view is deduced at the scale of a particle, which Fe(II)-rich core is made of $Li_{1-x}FePO_4$ triphylite. This view is in agreement with an aging process initiated by the exposure of the grain surface to an oxidative moist atmosphere. **Figure IV-36** summarizes the possible overall structural and chemical changes undergone by $LiFePO_4$ upon air exposure:

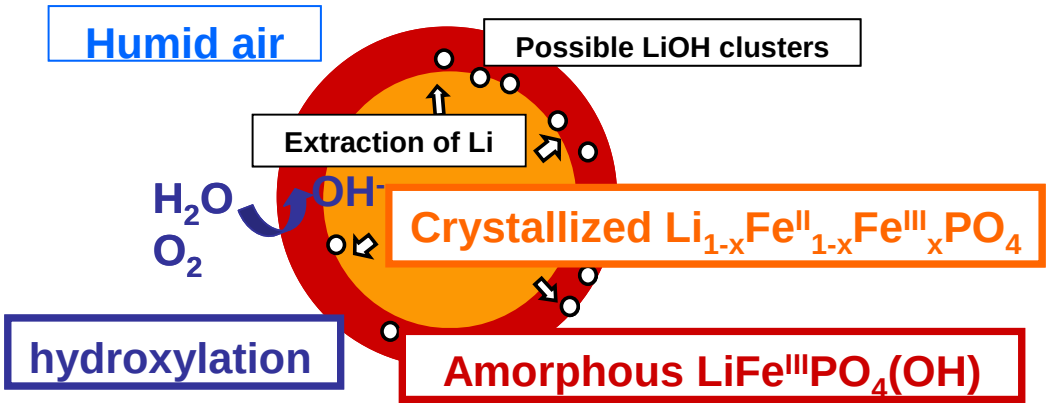

Figure IV-36. Overview of the consequences of atmosphere exposure of $LiFePO_4$ at 120°C.

IV.2. Structural modifications induced by moisture exposure [paper III]

In order to investigate the nature of the side-phase(s) appearing after exposure of $LiFePO_4$, our strategy consisted in increasing the amount of side-phases by accelerated aging, such as hot air exposure up to 120°C, or moisture saturated air exposure prolonged up to 80 days, thus allowing their proper study.

IV.2.1. Illustration of amorphisation followed by tavorite crystallization by XRD

The aging process under moisture saturated air can be monitored by XRD thanks to an internal reference, as shown in **Figure IV-37**. During the early stage ($t \leq 2$ days, **Fig. IV-37a**), the moisture exposure only results, with lithium extraction, in a decreasing content of crystalline olivine, similarly to what was observed for the sample air-aged for 10 days at 120°C. Up to 24 wt% of the total material is quantified as X-ray amorphous (i.e. highly disordered or nano-crystallized), thanks to a TiO_2 anatase internal reference.

In a second step, new diffraction peaks appear (**Fig. IV-37c**), assigned to tavorite $LiFePO_4(OH)$. Long term moisture exposure actually leads to the full transformation of olivine into tavorite (**Fig. IV-37b**). The structural incorporation of hydroxyls or water molecules was corroborated in paper **I** by coupled TGA and mass spectrometry even before the appearance of crystalline tavorite.

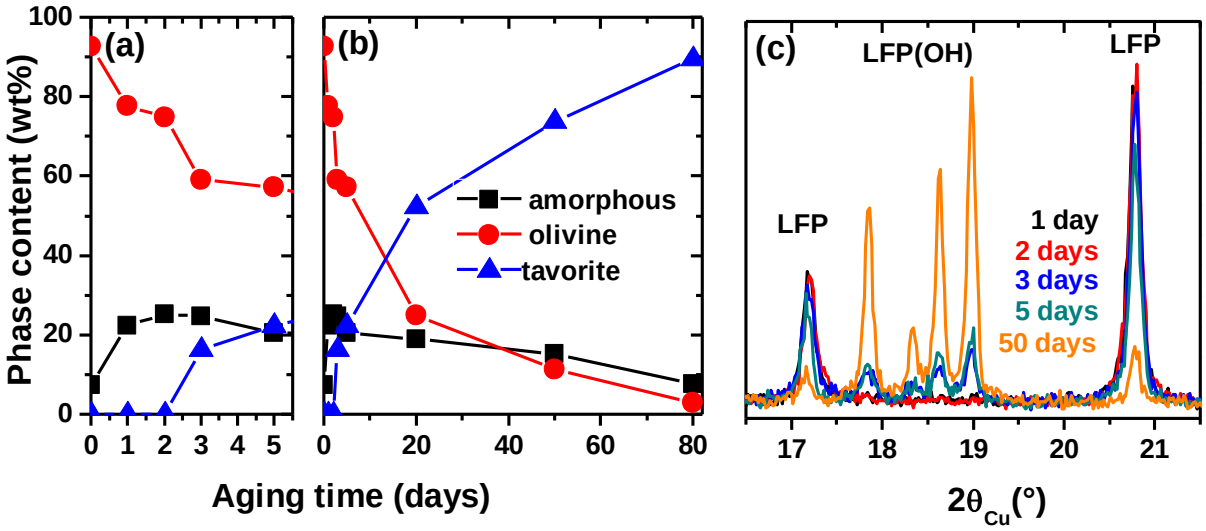

Figure IV-37. XRD phase quantification using TiO_2 anatase along aging in moisture saturated air at 120°C for different LFP-noC samples vs. time (a, b) and illustrative XRD patterns, normalized thanks to the internal TiO_2 reference (c).

IV.2.2. Illustration of material oxidation by Mössbauer spectroscopy

Although there is no straight resemblance between the two crystalline structures of triphylite (*Pnma* spacegroup) and tavorite (*P-1* spacegroup [45]), long term moisture exposure actually results in the full transformation of triphylite into tavorite. To explain how this phase transformation is possible, we plotted in **Figure IV-38 (left)** the XRD phase quantification for a whole series of samples versus the Fe(III) content determined by Mössbauer. It allows putting into perspective the results described so far. Monitoring the aging on this Fe(III)-based scale seemed actually more consistent than a time scale, as it can embrace samples aged at different temperatures or under different atmospheres.

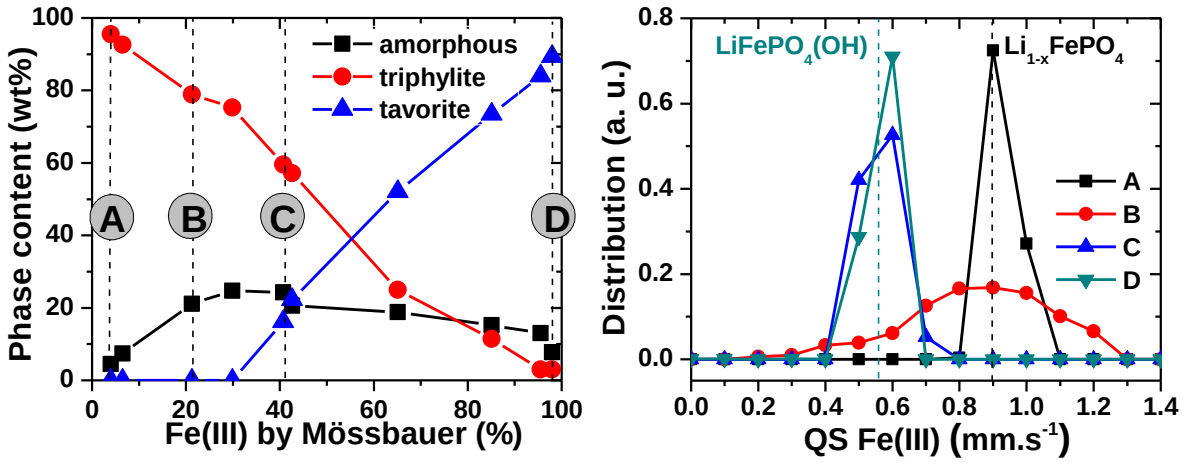

Figure IV-38. XRD phase quantification using TiO_2 anatase along aging at 120°C in ambient or moisture saturated air for ten different $LiFePO_4$ samples vs. Fe(III) percentages determined by Mössbauer (left), corresponding quadrupolar splitting (QS) distribution of the Fe(III) component of four selected samples (right).

In the light of the ten samples displayed on **Figure IV-38 (left)**, it appears clearly that the amorphous content should always be accounted as purely ferric, in order to match quantitatively the Fe(III) content determined by Mössbauer with the phases refined by XRD. The fact that olivine is the only ferrous species is in agreement with the corresponding hyperfine parameters (IS = 1.220 $mm.s^{-1}$ and QS = 2.95 $mm.s^{-1}$) as well as the FWHM around 0.2 $mm.s^{-1}$ characterizing a discrete (i.e. ordered) environment around Fe(II).

As followed by Mössbauer spectroscopy, the growth of the amorphous and tavorite phases, at the expense of triphylite, results in iron oxidation from Fe(II) to Fe(III).

The fact that the amount of amorphous matter decreases significantly from the appearance of crystalline tavorite raises the question of the role of the disordered ferric phosphate in the transformation from triphylite to tavorite. Considering the very different

structures of triphylite and tavorite, both the nature and local structure of the amorphous phase remain unclear. A detailed characterization at the local scale becomes then necessary to understand the aging mechanism.

IV.2.3. Further local scale characterization by Mössbauer, NMR and EELS

Among air-aging LFP materials displayed in **Figure IV-38 (left)**, samples B (30 days under ambient atmosphere), C and D (3 and 80 days under moisture saturated atmosphere, respectively) were subsequently characterized at the local scale.

The quadrupolar splitting (QS) related to ferric ions is described in **Figure IV-38 (right)** under the form of QS distribution rather than discrete hyperfine parameters, which is consistent with a structural disorder, even at a local scale. The two end members A and D exhibit a rather sharp QS distribution around the value characteristic of a discrete $Li_{1-x}FePO_4$ (IS=0.457mm.s^{-1} and QS=0.82 mm.s^{-1}) and $LiFePO_4(OH)$ (IS=0.404 mm.s^{-1} and QS=0.56 mm.s^{-1} [41]) environment, respectively. It is therefore possible to follow qualitatively the evolution of local environment along air aging, in addition to long range characterization by XRD.

Interestingly, these Mössbauer measurements lead to two observations: first, the amorphous phase contained in sample C (IS=0.406 mm.s^{-1} and QS=0.57 mm.s^{-1}) is different from the one in sample B (IS=0.432 mm.s^{-1} and QS=0.89 mm.s^{-1}). Therefore, the local environment of ferric ions within the amorphous phase evolves upon aging from a "triphylite-like" (sample A) to a "tavorite-like" environment (sample D), as shown by the QS distributions. While in sample B, only a minor contribution can be ascribed to a "tavorite-like" local environment, sample C containing both an important amount of amorphous phase and crystalline tavorite exhibits a 100% "tavorite-like" QS distribution. This fact may imply that the amorphous phase in sample C is then composed of tavorite disordered at the X-ray scale, while the iron local environment is already well defined at the scale of its first neighbors.

To confirm this hypothesis, as well as the existence of intermediate local structures, ^{6}Li MAS NMR measurements were performed at 200 MHz on ^{6}Li enriched samples aged in similar conditions as samples A, B, C and D. Bulk spectra displayed in **Figure IV-39** are therefore labeled A', B', C' and D' since the exact aging could not be reproduced, and correspond to samples containing 6%, 31%, 63% and 95% of Fe(III), respectively.

In accordance with the literature, isotropic NMR shift characteristic of triphylite (A') rises at -20 ppm [39, 46, 47] and that of tavorite (D') at 220 ppm [48]. On air aged samples B' and C', the NMR signal is distributed within these boundaries, and additional peaks can be fitted at 90 ppm (B') and 205 ppm (C'), both exhibiting large spinning sidebands manifolds and thus corresponding to paramagnetic Li environments. These new peaks result either from cations disorder and/or Li sitting at the interphase $LiFePO_4$ / $LiFePO_4(OH)$ [46]. In any of these two hypotheses, they can be assigned to "triphylite-like" and "tavorite-like" environments, respectively.

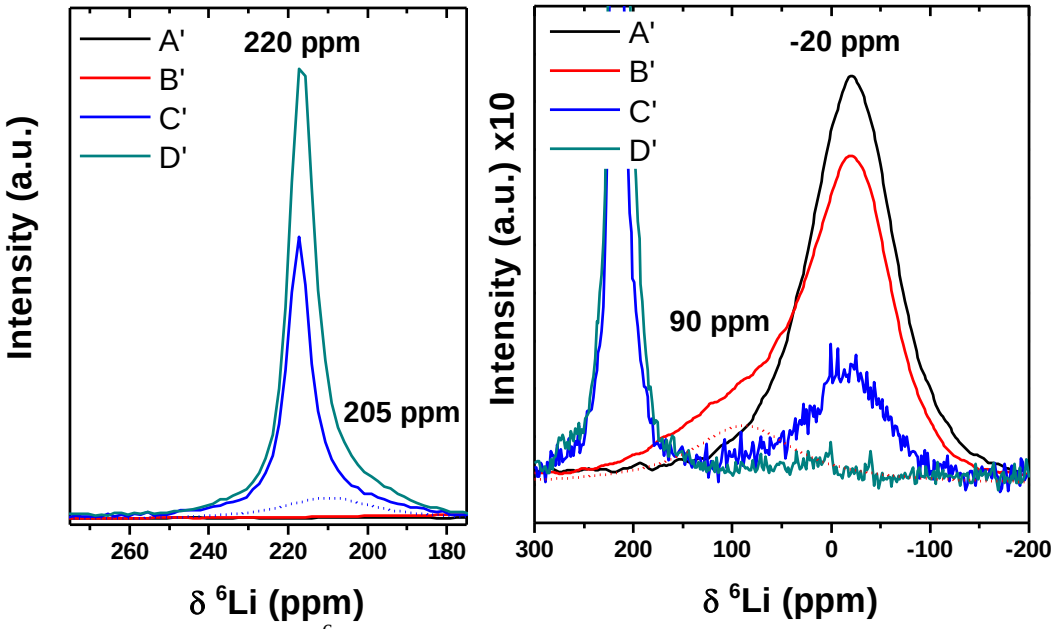

Figure IV-39. Central area of ^{6}Li MAS NMR (30 kHz) spectra of pristine (A') and air-aged ^{6}LFP-noC B', C' and D'. Dot lines denote fitted contributions of peaks assigned to the amorphous phase.

Regarding the new peak rising at 90 ppm in sample B', it has to be noted that considerable paramagnetic shift from pristine $LiFePO_4$ up to 65 ppm has been previously reported in the case of Li/Fe antisites [39, 46]. In the Fe 4c configuration, lithium is surrounded by 7 Fe(II) rather than 6, and although the additivity of Fermi-contact interaction accounts for the Li-shift increase, it should not cause any significant broadening of the linewidth compared to the major peak corresponding to lithium in the Li 4a site (-20 ppm), as both belong to the same phase. However, compared to its "parent peak" at -20 ppm, this new peak in sample B' is not only shifted further (at 90 ppm) but also deconvolutes with a significant broadening (+ 50%), supporting the hypothesis of NMR shift distribution (i.e. high Li disorder). This disorder felt by lithium ions is in full agreement with the disorder observed by Mössbauer around Fe(III) in sample B, revealed by the extremely broad QS distribution of

the corresponding doublet. Moreover, the integration of ^{6}Li NMR spectrum indicates that the signal centered at 90 ppm accounts for 28% of the total intensity, in full agreement with the 31% of Fe(III) detected by Mössbauer in this sample. In spite of its significant width and small isotropic shift, this NMR peak should therefore be attributed to lithium in a ferric phosphate environment, which is, at this stage of the air-aging, highly disordered even at the local scale.

In the case of sample C', the new peak observed at 205 ppm exhibits not only a smaller NMR shift compared to its parent peak at 220 ppm but also a much more pronounced broadening (+ 300%) that can be assigned both to a high disorder at the local scale and to a weaker paramagnetism induced by the vicinity of Fe(II) (S=2). While Mössbauer spectroscopy detects 37% of Fe(II), NMR integrated intensities are distributed as follows: 35 % of pure olivine and 45% of pure tavorite (similarly to XRD Rietveld refinement) while the 16% of "tavorite-like" and 5% of "olivine-like" environments correspond roughly to the 19 wt% of X-ray amorphous content detected by XRD. In order to balance the valence observed by Mössbauer, the X-rays amorphous content should again be accounted as purely ferric. Thus, the combination of XRD, Mössbauer and ^{6}Li NMR converge to demonstrate the amorphous ferric phosphate phase evolves from a 100% "olivine-like" environment for lithium in sample B' to a 75 % "tavorite-like" environment in sample C'.

The results presented here suggest that the amorphous phase is an intermediate between triphylite and tavorite. Therefore we believe that the insertion of hydroxyl groups into the bulk is only made possible by the presence of the amorphous phase acting like a buffer at the phase upfront. This disordered phosphate can accommodate hydroxylation up to a certain level, while evolving from an olivine-like to a tavorite-like local environment before recrystallizing in the form of tavorite under moisture saturation. However, XRD, NMR and Mössbauer spectroscopies being macroscopic analytical techniques, microscopic characterization was necessary in order to confirm this hypothetic aging mechanism.

We called upon electron energy loss spectroscopy (EELS) to investigate locally oxygen and iron environments at the scale of a single particle. In particular, this technique gives easily access to iron oxidation states. **Figure IV-40** shows the EELS core spectra of different $LiFePO_4$ samples along aging, including the end members $LiFePO_4$ (A) and $LiFePO_4(OH)$ (D), which can be taken as the reference spectra of Fe(II) and Fe(III), respectively. Similarly to spectra collected by Laffont *et al.* on Li_xFePO_4 samples, the

noticeable differences between the two end members are the following [49]: The Fe-$L_{2,3}$ edges show a 1.8 eV chemical shift at the maximum of the Fe-L_3 line with changing Fe valence state, from Fe(II) to Fe(III). In addition, a clear pre-peak *A* exists on the O-K edge of phosphates containing octahedral Fe(III). This characteristic pre-peak, which is lacking in the case of Fe(II) bonded to oxygen, can then be used as an indicator of iron valence state in our aged LFP materials [50]. For each sample, an isolated particle was selected, and spectra were taken at different locations, from grain surface to the core, until no transmission was offered.

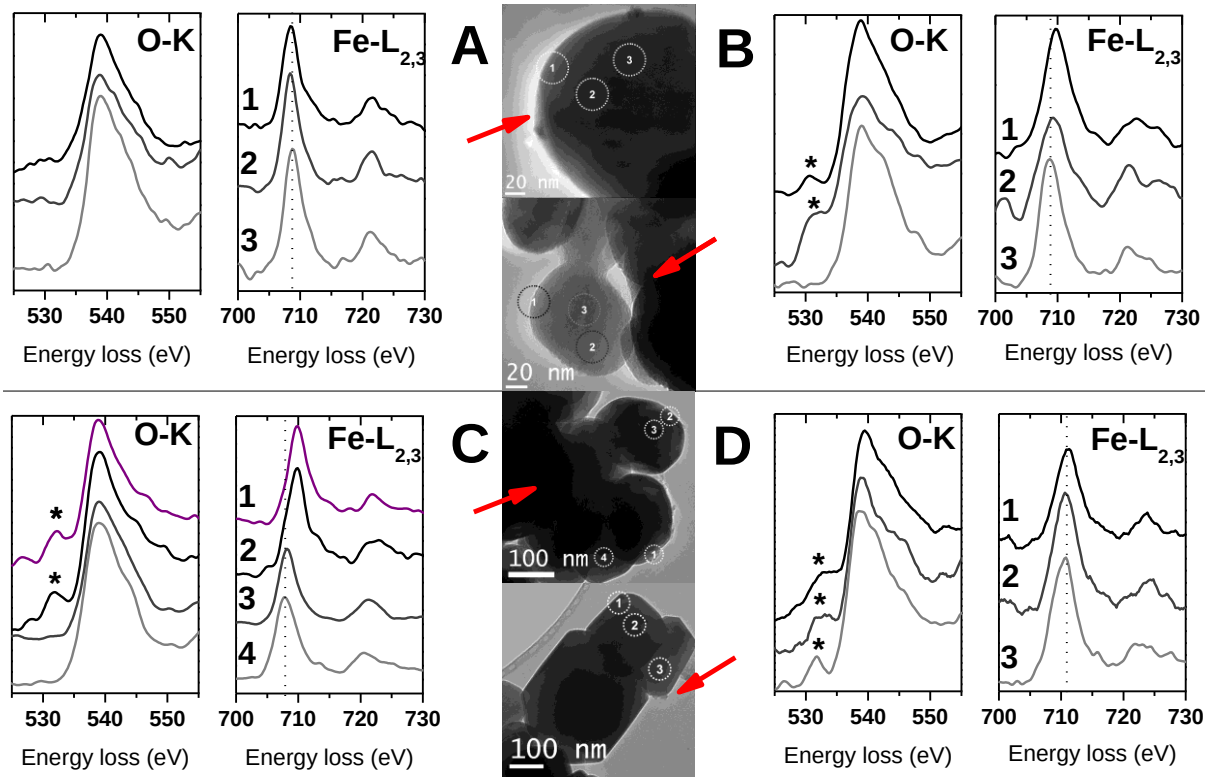

Figure IV-40. EELS core spectra of different LFP-noC along aging and associated TEM images. Circles represent the areas analyzed (diameter of the probe 25 nm)

For aged samples B and C, containing a significant amount of both Fe(II) and Fe(III), EELS gives an undeniable piece of evidence that LFP oxidation is initiated at the grain surface. In fact, the core spectra measured at the grain surface of samples B and C exhibit both the *A* pre-peak on O-K edge (highlighted by an asterisk) and the chemical shift of the Fe-L_3 line toward higher energy losses characterizing a Fe(III) environment while the particle core remains intact, i.e. Fe(II)-rich (**Fig. IV-40b** and **IV-40c**).

Thus, the results of microscopic analyses confirm that prolonged exposure to atmosphere induces moisture driven $LiFePO_4$ oxidation from the surface toward the core of

active material nanoparticles, to form an X-ray amorphous ferric phosphate before the crystallization at a microscopic scale of tavorite $LiFePO_4(OH)$.

IV.2.4. Proposed aging mechanism

Based on structural data, the transformation of triphylite into tavorite should result in approx. 20% volume expansion due to hydroxyls incorporation, and TEM imaging actually displays increasing particles size upon aging, from 100 nm to 150 to 200 nm, and finally to 1-10 µm for samples A, B, C and D respectively. And yet, the average Lorentzian crystallite size determined by XRD for the tavorite phase in sample D is about 195 nm, meaning those large plate-like particles are polycrystalline.

In the present section, an in-depth long range and local scale structural investigation of a series of LFP-noC samples having undergone a stay at 120°C under ambient or humid atmosphere has been carried out to shed light on the successive steps of the degradation process occurring at moderate temperature (below 150°C) from a quantitative point of view. The growth of a disordered ferric phosphate phase has been observed directly for the first time and the combination of quantitative X-ray diffraction and Mössbauer, NMR and EELS spectroscopies prove clearly an aging mechanism going from the surface of particles toward a slightly deintercalated core. As sketched in **Figure IV-41**, olivine consumption is accompanied by particles growth due to volume expansion, consistent with OH group incorporation, followed by merging upon recrystallization under the form of large platelets of tavorite.

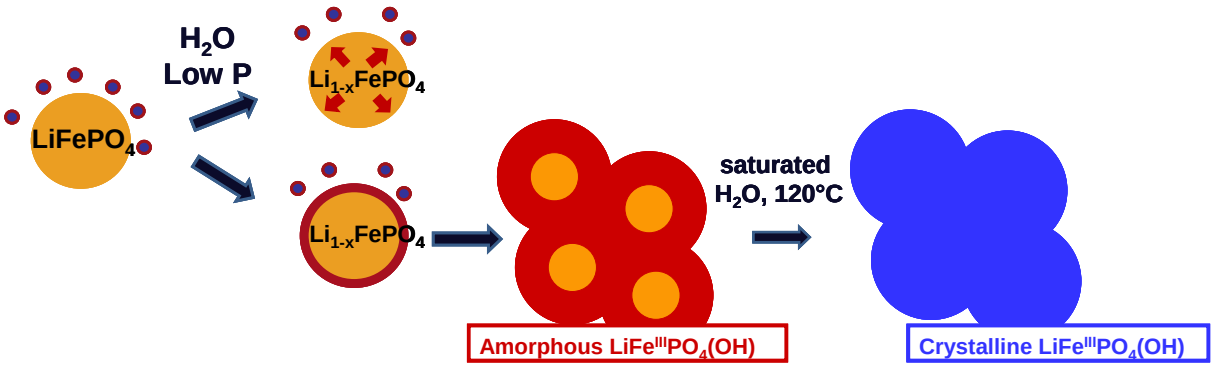

Figure IV-41. Overview of the consequences of moisture exposure of $LiFePO_4$ at 120 ◦C.

IV.3. Influence of air aging on the electrochemical behavior of $LiFePO_4$

From a practical point of view, the oxidation of iron resulting from air storage of $LiFePO_4$ powders leads directly to a decrease of the accessible electrochemical capacity in a Li-ion configuration. Nevertheless, the net loss of electroactive material and the influence of a ferric phosphate layer enclosing particles of healthy $LiFePO_4$ on the intercalation process are still unknown/poorly understood. Therefore, a detailed characterization of the electrochemical behaviour of air-aged samples is necessary to understand the consequences of an uncontrolled storage of $LiFePO_4$ on the expected electrochemical performance.

*IV.3.1. Prediction of $LiFePO_4$ specific capacity by aging monitoring [paper **III**]*

It was demonstrated in paper **I** that it was possible to reduce aged $LiFePO_4$ materials by a simple annealing under inert atmosphere. Indeed, coupled TGA-MS experiments showed the quantitative removal of structural hydroxyls from the amorphous ferric phase around 450°C, similarly to crystalline tavorite, through the following carboreduction reaction:

$$\boldsymbol{Li_xFePO_4(OH)_x + \tfrac{x}{4}C \rightarrow Li_xFePO_4 + \tfrac{x}{2}H_2O + \tfrac{x}{4}CO_2} \quad (\boldsymbol{Eq.IV-5})$$

At this stage, the $Li_xFePO_4(OH)_x$ formula used for the amorphous phase takes into account the complete iron oxidation and a possible incomplete incorporation of hydroxyls. The following experiments highlight the possibility to experimentally determine the x value. TGA curves of aged LFP-noC samples under inert atmosphere (**Fig. IV-42, left**) typically comprise two distinct steps: an exothermic weight loss below 150°C corresponding to the removal of adsorbed water (also observed for pristine material) and an endothermic loss between 150°C and 600°C assigned to the dehydroxylation of the ferric phosphates. From the value of the second weight loss and the weight distribution of phases determined by XRD (**Fig. IV-38, left**), it is possible to estimate the amount of hydroxyls present in the amorphous phase $Li_xFePO_4(OH)_x$. The theoretical formula, deduced from Eq. IV-5 is the following:

$$\boldsymbol{x = \frac{M_{FP}.\left(\frac{\Delta M}{M}\right)_{am}}{20.w_{am} - M_{LiOH}.\left(\frac{\Delta M}{M}\right)_{am}}} \quad (\boldsymbol{Eq.IV-6}) \qquad \boldsymbol{with} \quad \boldsymbol{\left(\frac{\Delta M}{M}\right)_{am} = \left(\frac{\Delta M}{M}\right)_{endo} - \frac{20.w_{Tav}}{M_{Tav}}}$$

$$\boldsymbol{M_{am} = M_{FP} + x.M_{LiOH}}$$

$$\boldsymbol{20 = M(\tfrac{1}{2}H_2O + \tfrac{1}{4}CO_2)}$$

where M_{FP}, M_{LiOH} and M_{Tav} are respectively the molecular weight of $FePO_4$, LiOH and $LiFePO_4(OH)$; w_{am} and w_{Tav} the massic ratio of amorphous and tavorite deduced from XRD

refinement; $(\Delta M/M)_{endo}$ the endothermic weight loss associated to the carboreduction reaction (Eq. IV-5 and **Fig. IV-42, left**) and $(\Delta M/M)_{am}$ the weight loss corrected from the reduction of crystalline tavorite, thus associated to the amorphous phase. The implementation of such a method to monitor the aging is however not straightforward, due to the necessary use of an external reference to perform Rietveld refinement in addition to the TGA measurement.

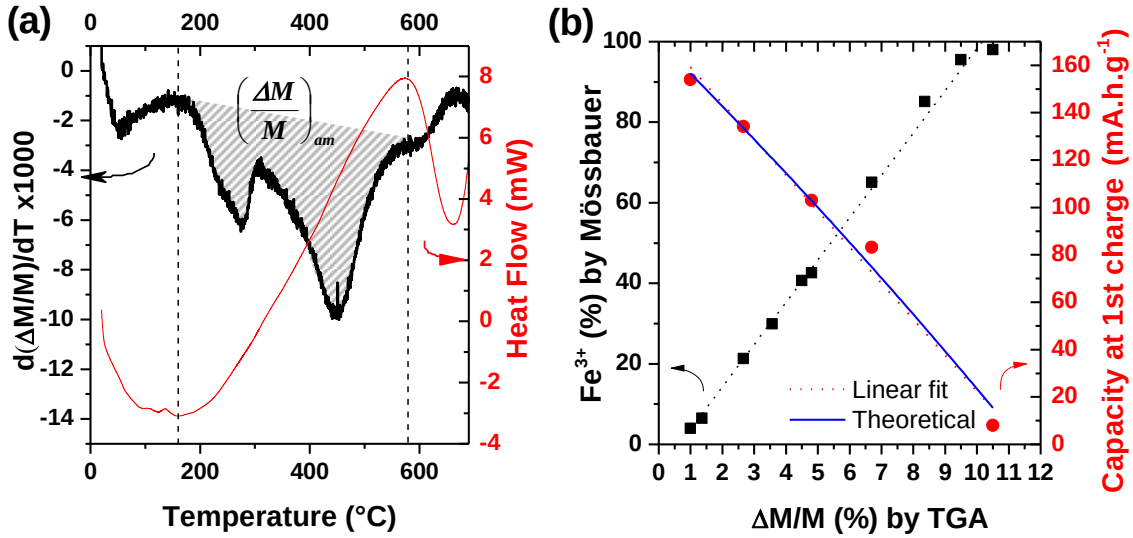

Figure IV-42. (left) DTG-DSC curves of sample B under argon atmosphere and (right) experimental correlation between the endothermic weight loss observed and the amount of ferric ions in our aged $LiFePO_4$ samples (black) as well as the practical capacity obtained during the first charge (red).

Considering the observed correlation between the weight loss observed by TGA and the proportion of Fe(III), as displayed on **Figure IV-42 (right)**, one can expect to finally predict empirically the maximal capacity of a $LiFePO_4$ sample in a Li-ion cell. Thus, aiming at correlating directly experimental results from TGA to electrochemistry, a whole series of aged samples have been examined (**Fig. IV-42, right**). First, it appears that the weight loss assigned to dehydroxylation varies linearly with the Fe(III) content, implying a constant (OH)/Fe(III) ratio along aging, that should necessarily be equal to one to match the tavorite nominal formula $LiFePO_4(OH)$. Rigorously, the resolution of Eq. IV-6 confirms this trend and gives for example x_B=1.11 and x_C=0.95 in the cases of samples B and C respectively. These results confirm Mössbauer measurements suggesting that the amorphous matter may be made of tavorite-like environments at the local scale which is also in agreement with its electrochemical signature discussed in previous section.

Moreover, as explained earlier, the Fe(III) content dictates the maximal capacity in a Li-ion configuration. Consequently, a direct relation is expected between the weight loss and the first electrochemical charge capacity. Experimental data gathered in **Figure IV-42 (right)** confirmed this hypothesis. It is therefore possible to predict the capacity of $LiFePO_4$ materials subjected to air exposure by a simple TGA experiment through the empiric formula deduced from a linear fitting (Eq. IV-7):

$$C_{Li-ion}^{\exp} = 172 - 14.5.\left(\frac{\Delta M}{M}\right)_{endo} mA.h.g^{-1} \quad (Eq.IV-7) \qquad C_{Li-ion}^{th} = 172.(1-x)\, mA.h.g^{-1} \quad (Eq.IV-8)$$

This is in good agreement with the theoretical weight loss implied by Eq. IV-5 and plotted in blue on **Figure IV-42** (Eq. IV-8). The main limitation of this method lies however in the necessary presence of small amount of carbon to perform the reduction reaction. The recovery of triphylite from fully oxidized tavorite requires 1.7 wt% of carbon that can be attributed to synthesis residues alone (1.6 wt% by ICP on LFP-noC) but one additional possible source of carbon could involve carbon known to be present on the surface from atmospheric pollution. The major working hypothesis stands in considering stoichiometric $LiFePO_4$ material prior aging, free of Li_3PO_4 impurities for example, which can be the case in Li-excess LFP samples [51]. Any unconsidered inactive weight would induce a discrepancy from the theoretical weight loss. Nonetheless, the prediction method should not only be valid for bare $LiFePO_4$, but might also be easily adapted to impure products, coated materials or composites (papers **I** and **II**), by applying the corresponding weight correction.

*IV.3.2. Electrochemical signature of the ferric phase formed upon aging (paper **III**)*

Figure IV-43 shows the incremental capacities obtained in potentiodynamic mode from the selected $LiFePO_4$ aged samples (A-D), shedding light on the nature and amount of ferric species capable of intercalating lithium. As highlighted from **Figure IV-43 (left)**, capacity can be partially recovered at the tail of the 3.5V plateau characteristic of $LiFePO_4$ during the first discharge in the case of samples B and C. This reduction peak is necessarily linked with the reintercalation of lithium in the $Li_{1-x}FePO_4$ solid-solution formed during the first stage of aging. The capacity observed at this potential (10 $mAh.g^{-1}$ and 5 $mAh.g^{-1}$ from sample B and C, respectively) matches the theoretical value calculated from XRD refinement (7 $mAh.g^{-1}$ and 7 $mAh.g^{-1}$, respectively); considering the experimental error.

As described in ref. [8] and papers **I**, **II**, and **III**, air aging results in the appearance of new redox processes around 2.7 V assigned to the amorphous phosphate. Sample B is here

particularly meaningful as it does not contain any crystalline tavorite. The incremental capacity obtained on this potential region can be decomposed in two perfectly reversible redox peaks, accounting for 18 mAh.g^{-1} and one irreversible reduction peak, at 2.75 V, accounting for 14 mAh.g^{-1}.

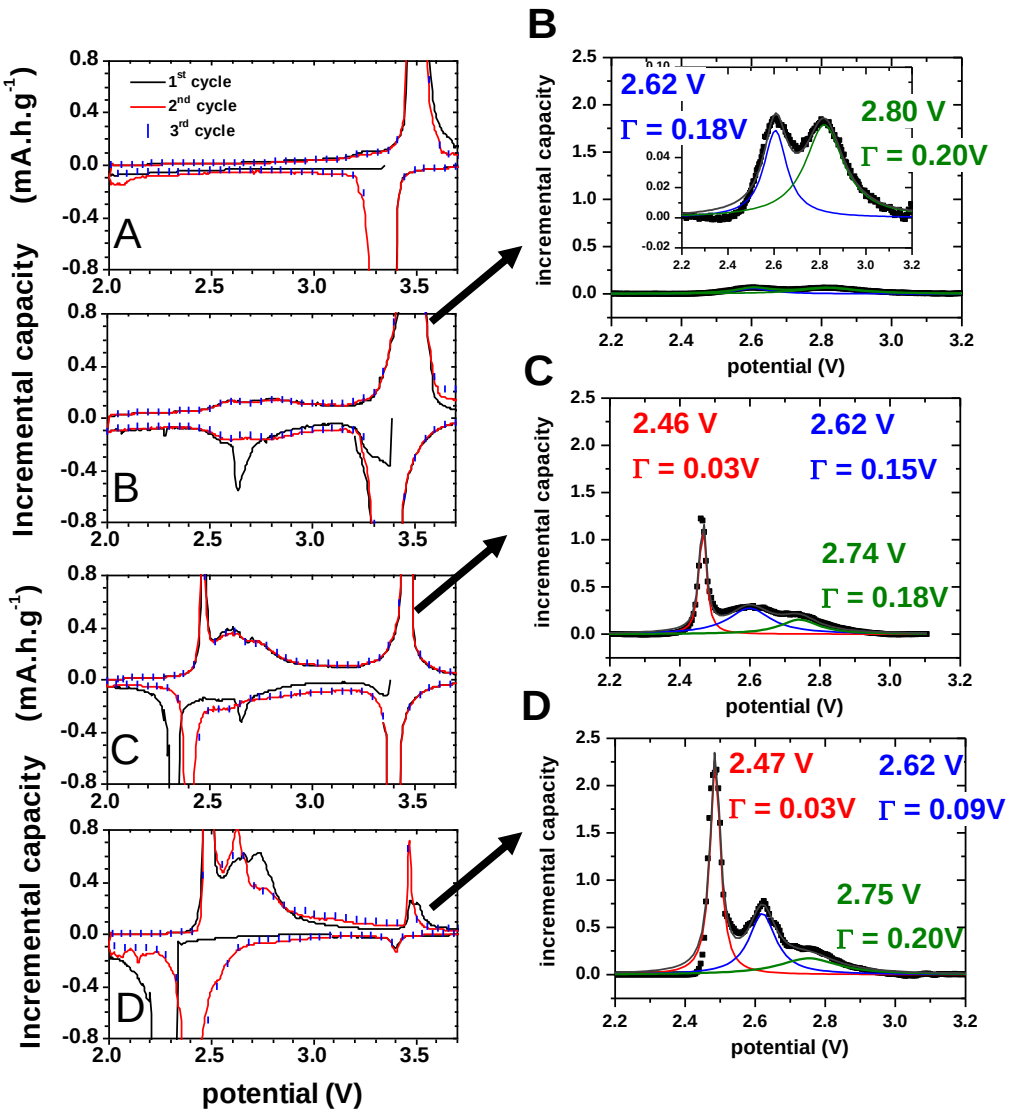

Figure IV-43. (Left) incremental capacity curves of different $LiFePO_4$ along the first (black), second (red) and third (blue dots + symbols) cycles starting in discharge. (Right) curves fitting using pseudo-Voigt functions, the Γ values stands for their FWHM. Example of the 2nd charge recorded on sample B, C and D.

The reversible redox processes are comparable in potential to previously reported $FePO_4,2H_2O$ from Wang *et al.* [40], or highly defective $Li_xFe_yPO_4$ samples from Hamelet *et al.* [39]. The characteristic redox peaks of tavorite can actually be observed around 2.4V on the incremental capacity curves of samples C and D. The biphasic insertion of lithium to form a $Li_{1+x}FePO_4(OH)$ phase with x ~ 0.6 is shifted from 2.35 V on the first discharge to 2.5 V on

the following cycles. Such electrochemical characteristics (incomplete lithium insertion and activation cycle) were also observed by Marx *et al.* on pure tavorite [41].

Structural disorder might be responsible for a broadening of incremental capacity peaks characterizing the lithium (de)insertion reactions, as a slight change of bond lengths and angles around the transition metal ion can affect its redox potential through inductive effect. Therefore, the gradual sharpening of tavorite characteristic peaks from sample B to D (plotted for the 2^{nd} oxidation in **Figure IV-43, right**), together with an increase of the corresponding integrated capacity along aging, suggest tavorite crystallization in agreement with the conclusions drawn from Mössbauer and NMR spectroscopies (**Fig. IV-38** and **IV-39**). In addition, similar measurements on aged samples containing between 10 and 22 wt% of amorphous phase have shown that the intensity of these reversible redox peaks varies rather linearly with the amorphous content and accounts for approximately 85 mA.h per gram of amorphous phase, which is close to the capacity obtained from sample D under similar cycling conditions.

The irreversible reduction peak is similar to a feature observed by Zaghib *et al.* after they exposed LFP materials to water or humid atmosphere that they assigned to the lithiation of iron oxide [52]. Nevertheless, this hypothesis can here be rejected as the potential does not match properly (2.15V), and no Fe_2O_3 was detected in our samples, neither by Mössbauer nor by SQUID. Through *in situ* Mössbauer experiments (**Fig. IV-44**), a careful analysis of x *vs.* time slops suggests first that aged $LiFePO_4$ is partially reduced upon simple immersion in the electrolyte and then, that the irreversible capacity might not be correlated to a change in the overall oxidation state of iron in the cathode material, since the effective oxidation rate (probed by Mössbauer) is inferior to that estimated from the integrated amount of current (given by electrochemistry). Such discrepancy between the intercalation rates obtained by Mössbauer and electrochemistry cannot be observed upon the subsequent charge, highlighting the particularity of the initial discharge process.

As a matter of fact, e*x situ* measurements, offering a better resolution of the Mössbauer spectra, were performed after stabilizing the potential at 3.0 V before and after the first reduction (points are represented in **Figure IV-44 b,c**) and support these observations. This parasitic reaction might imply either soluble iron-containing species (not probed by Mössbauer spectroscopy) or interphasial species. In the hypothesis of iron dissolution, a decrease in the total absorption should be observed at this stage, but it does not seem to be the case here. Thus, the hypothesis of parasitic interphasial reaction appears more plausible. In addition, such irreversible reduction peak cannot be seen on the incremental capacity curve of

tavorite (**Fig. IV-43**, sample D), suggesting that the corresponding reaction only occurs at the interface between the amorphous phase and electrolyte.

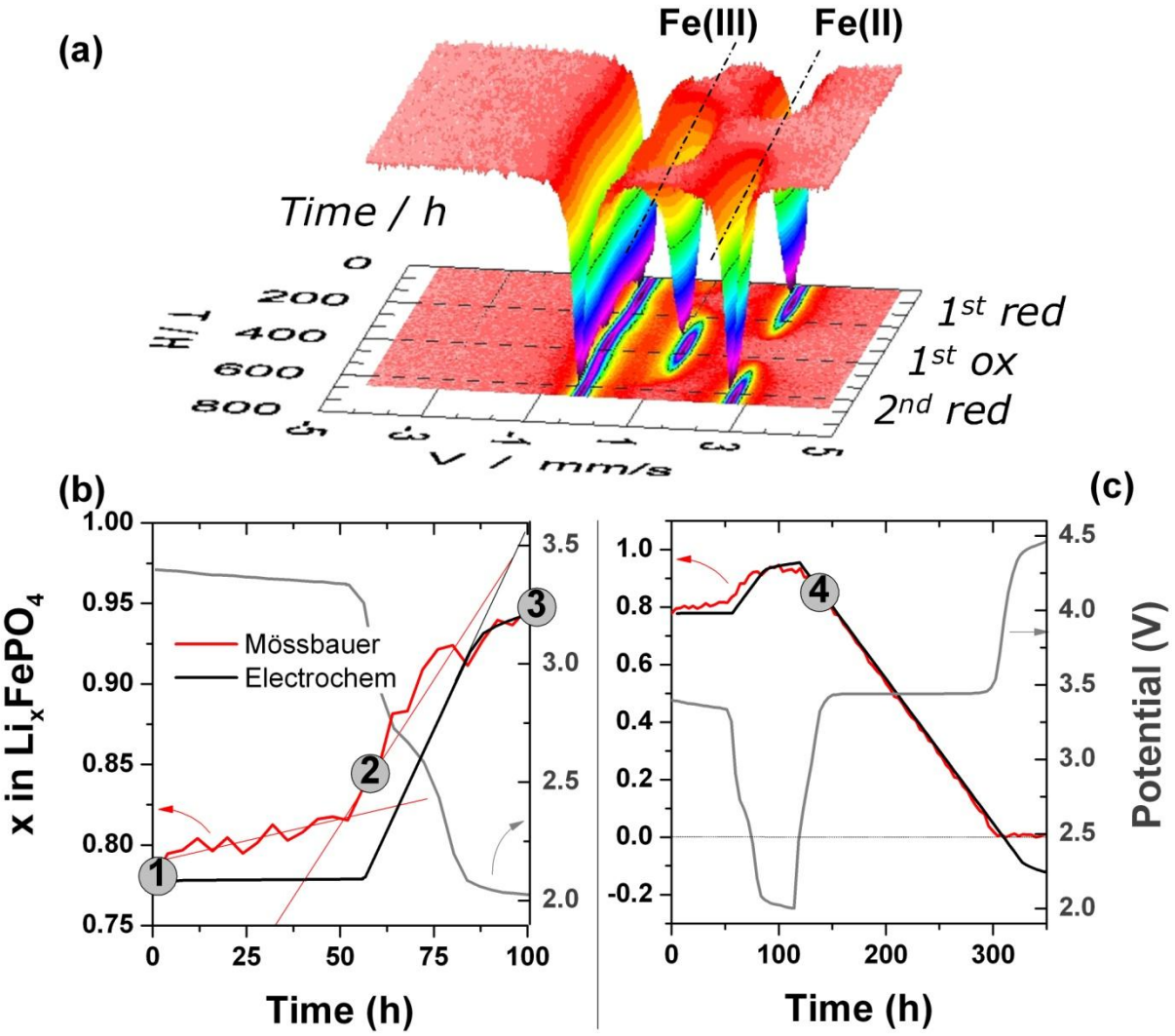

Figure IV-44. *Operando* Mössbauer measurements carried out on air-aged LFP-noC (sample B) in a GITT mode (C/50 for one hour followed by a three hours relaxation). (a) Experimental time resolved spectra recorded every four hours. (b,c) Time resolved electrochemical response to a C/50 current: intercalation rates calculated by electrochemistry (black) and Mössbauer (red) are plotted on the left axes. While the potential (grey line) is plotted on the right scale. Fig. b zooms on the initial discharge. Numbers (1-4) denote extra *ex situ* analyses performed.

The key point regarding the electrochemical behavior of aged samples is not only that air exposure, even to a limited extent, leads directly to a practical capacity loss in a Li-ion configuration. In addition, the formed ferric species exhibit a complex electrochemical activity, including a significant irreversible reaction with electrolyte.

IV.3.3. Long term cyclability of air aged LFP materials

The cyclability of air-aged $LiFePO_4$ materials was evaluated and the corresponding specific discharge capacities obtained at a C/10 regime are displayed in **Figure IV-45** for samples A and B. The specific capacity observed for pristine LFP-noC material (A) has already been discussed in section 1.4, it serves here as a reference. Concerning aged sample B, it appears clearly that the initial capacity (145 $mAh.g^{-1}$) cannot be maintained over more than few cycles and fades rapidly (-30 % after 20 cycles, -50 % after 100 cycles).

At this point, it is not clear whether the poor electrochemical capacity retention of the air-aged sample can be explained by iron dissolution, growth of an insulating interphase and/or loss of electrical contact within the electrode.

In the case of pristine $LiFePO_4$ upon storage in $LiPF_6$ based electrolytes, Koltypin *et al.* observed a decrease of the performance along an increase of the electrode resistance that they attributed to an Fe dissolution at elevated temperature [53]. In the present work, ICP measurements carried out after a one month long soaking experiment at 55°C demonstrated a three times more important dissolution with 1.4 $g(Fe).L^{-1}$ in the case of air-aged $LiFePO_4$ compared to pristine material LFP-noC (0.5 $g(Fe).L^{-1}$) while room temperature storage resulted for both samples in lesser olivine dissolution (~ 0.04 $g(Fe).L^{-1}$). Thus, $LiFePO_4$ reactivity towards electrolyte is found significantly exacerbated by prior air exposure, especially at higher temperature. The role of hydroxyls chemisorbed or incorporated in the bulk surface (susceptible to react with $LiPF_6$ to form highly corrosive HF) should be decisive in the interphasial chemistry.

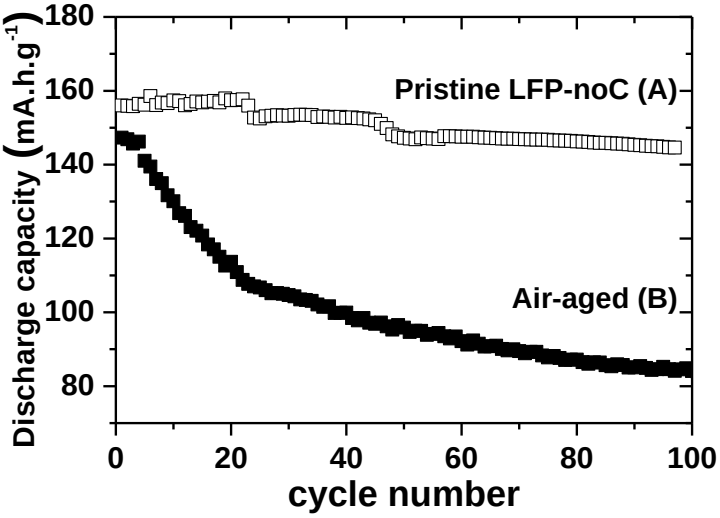

Figure IV-45. Compared cyclability of pristine and air-aged (sample B) LFP-noC at C/10.

Also attesting a poor cyclability, EIS experiments performed on air-aged sample (B) over 20 galvanostatic cycles (**Fig. IV-46**) show severe differences with the impedance stability observed for pristine $LiFePO_4$ (**Fig. IV-18**).

The frequency characterizing the flat pseudo capacitance associated with charge transfer resistance and the SPL significantly decreases along cycling, while its resistance increases from 15 to 40 Ω (20 to 60 Ω) at the end of charge (discharge) between the first and 20th cycles. This observation implies a continuous surface blocking for the air-aged $LiFePO_4$ sample. Moreover, the appearance of a high frequency semi-circle at the 18th cycle (that remains visible on the subsequent cycles) indicates that the interphase then acts as a resistive film. The fact that the additional high frequency loop remains visible on the subsequent cycles and that the impedance is then stabilized suggests an effective passivation of the electrode surface at this stage. Hence, this stabilization of the interphase might allow explaining the break observed in the decreasing specific capacity of sample B in **Figure IV-45**.

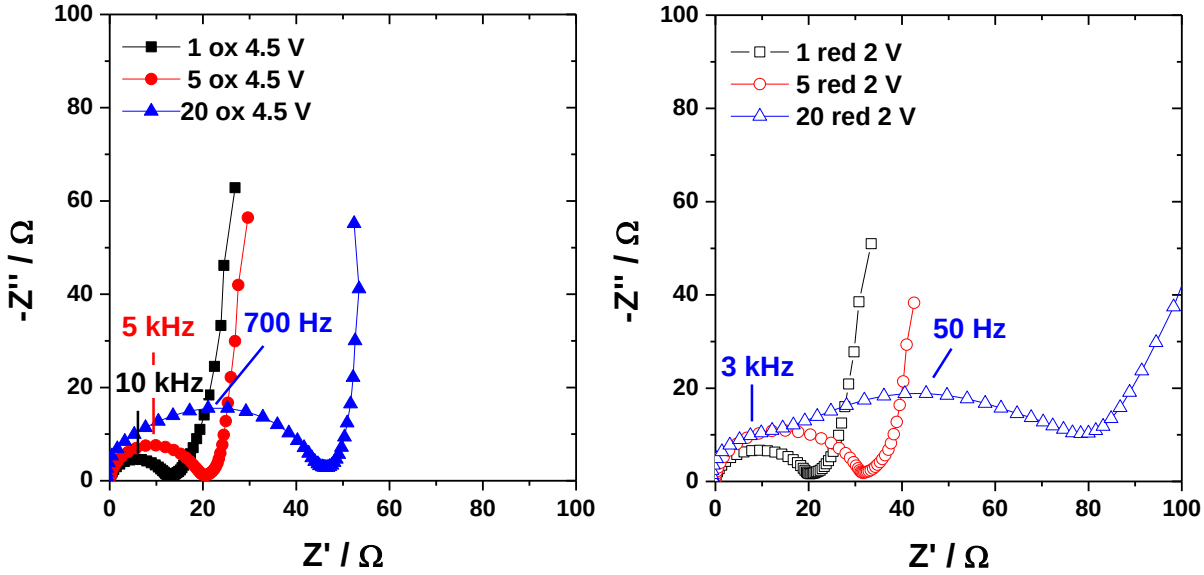

Figure IV-46. Nyquist plots of EIS performed on air aged LFP-noC (sample B) at the end of the 1st, 5th and 20th charges (closed symbols, left) and discharges (open symbols, right) at a C/20 rate. N.B. For this particular experiment, impedance stabilization is observed at the 18th cycle (± 2 cycles when repeating experiments).

IV.3.4. Effect of air aging on the reactivity towards electrolyte, a NMR study

The difference in surface reactivity towards electrolyte has been investigated by NMR and **Figure IV-47** shows the ^{7}Li NMR spectra measured at the end of the 1st, 5th and 20th charges and discharges for air-aged LFP-noC material (sample B).

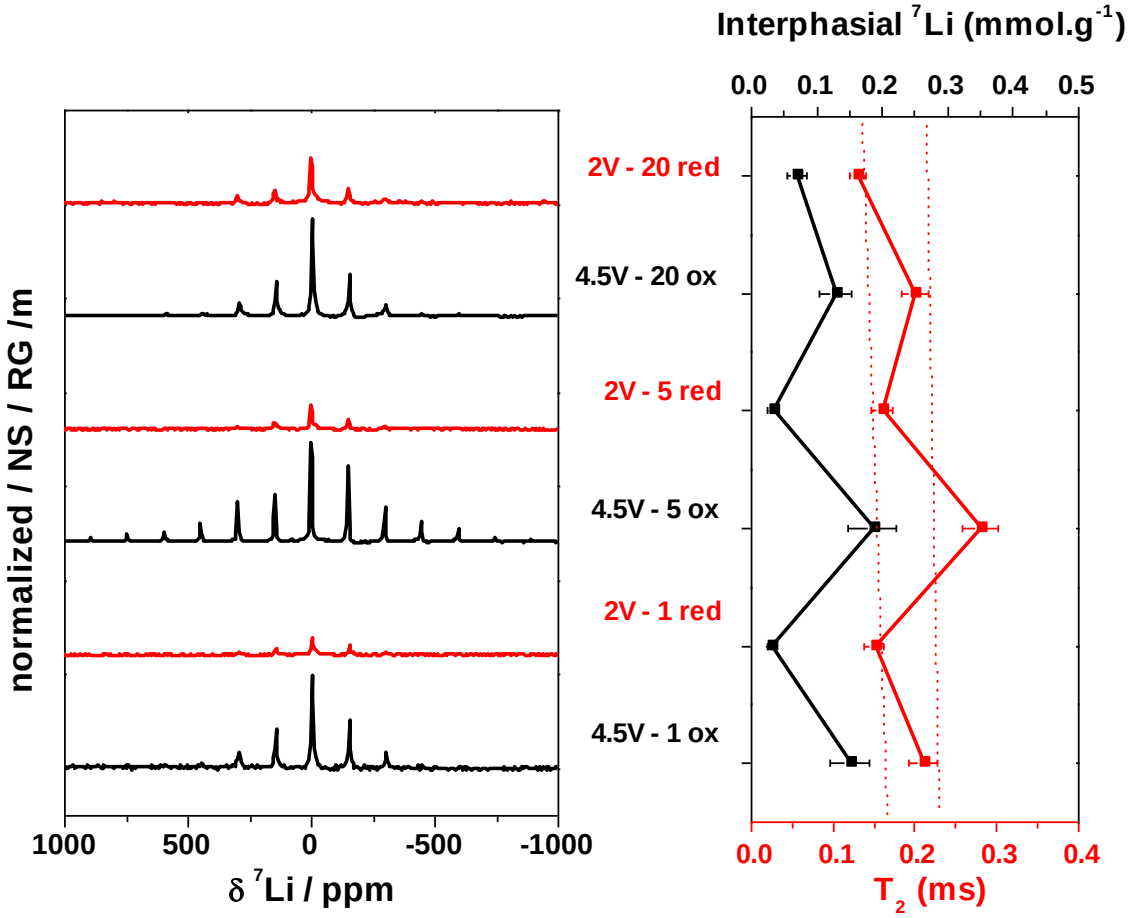

Figure IV-47. Results from ^{7}Li NMR performed on air-aged LFP-noC (sample B) at the end of the 1st, 5th and 20th charges and discharges at a C/20 rate in $LiPF_6$ EC:DMC.

The potential dependency observed for the amount of interphasial lithium on pristine LFP-noC (**Fig. IV-19**) is retained, although the variations between the end of charge and discharge are less pronounced in the case of the air-aged sample. The lesser evolution in the amount of lithium detected by NMR suggests that no interphase accumulation occurs at the electrode surface along cycling. Besides, if the precipitation/dissolution process of the SPL is maintained, the intimacy of the interphase with Fe paramagnetic centers is not weakened by repeated cycles. Indeed T_{2r}s variations are also limited, which could be explained by the presence of Fe dissolved from the active material and reprecipitated in the interphase, confirmed in this case by EELS analysis.

The quantification diagram, containing complementary ^{19}F NMR experiments, is shown in **Figure IV-48** and should be compared with **Figure IV-20**, reporting the results obtained for a pristine sample.

The evolution of fluorinated compounds follows that of lithiated species. Rather than an overall accumulation of interphasial species between the first and 20th cycle that would explain the growth of a resistive film as observed by EIS, NMR highlights the almost perfect reversibility of the interphase precipitation/dissolution process.

Compared to the SPL model considered at the surface of pristine LFP-noC, the interphase observed on air-aged $LiFePO_4$ is significantly richer in salt decomposition products such as LiF and fluorophosphates. In particular, attention should be paid to the amount of Li in LiF in the oxidized state, accounting for 50 to 90 % of the total detected interphasial lithium, while the high voltage SPL on LFP-noC only contains 20 to 50 % of lithium under the form of lithium fluoride. Hence, the interphase of air-aged LFP-noC can be seen as a mixture of highly resistive LiF and non lithiated fluorophosphates or polymeric species, these latter being invisible to our NMR experiments.

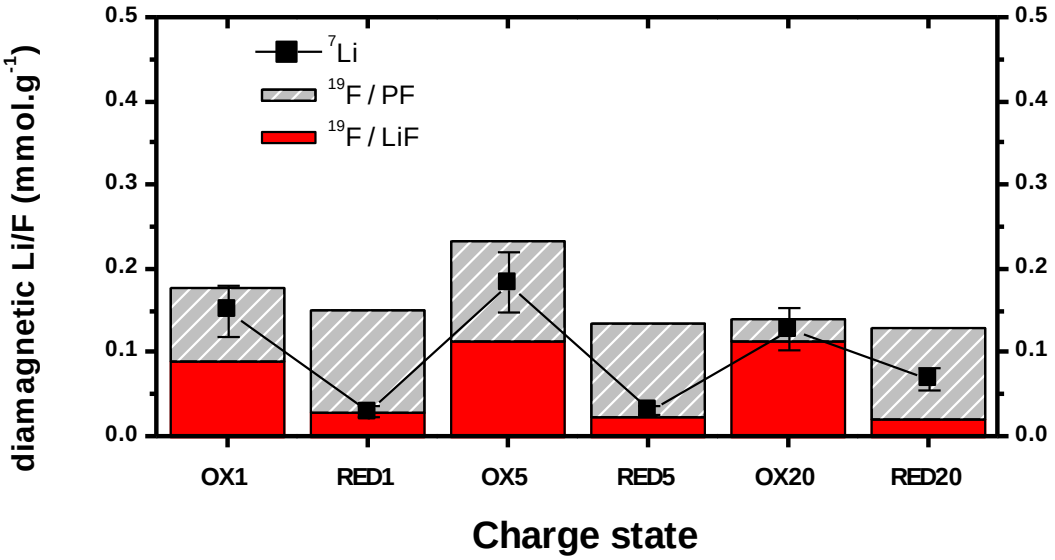

Figure IV-48. NMR quantification results for air-aged LFP-noC (sample B) at the end of the 1st, 5th and 20th charges and discharges at a C/20 rate in $LiPF_6$ EC:DMC.

Considering the aggravated Fe dissolution observed for the air-aged material, a plausible hypothesis regarding the interphasial processes is that chemisorbed/incorporated water or hydroxyl groups would favor the dissolution of the $LiFePO_4$ upon contact with the electrolyte or cycling. This dissolution would be accompanied by the departure of the present interphase and a new interphase would then form on a newly exposed surface.

IV.3.5. Concluding remarks

The degradation of both the active material and the electrolyte would thus last until the full consumption of the aqueous species, or unless a passivation film is formed, which seems

to happen here around the 20th cycle. The poor electrochemical performance of air-aged $LiFePO_4$ material is therefore considered as the result of reaction of aqueous species chemisorbed/incorporated upon air exposure with $LiPF_6$ to form HF:

- The produced HF can subsequently attack the active material, then driving the dissolution of $LiFePO_4$ or rather surface $LiFePO_4(OH)$, as represented in **Figure IV-49**.
- HF can also react with interphasial species, especially lithiated organic or polymeric species, to form (among others) an important amount of highly resistive LiF (see the decomposition reactions in chapter 1, Eq. I-6).

Consequently, electrode surface passivation occurs due/thanks to the presence of a mostly inorganic interphase, probably denser than the SPL observed on pristine $LiFePO_4$, acting as an effective barrier from further acidic attacks.

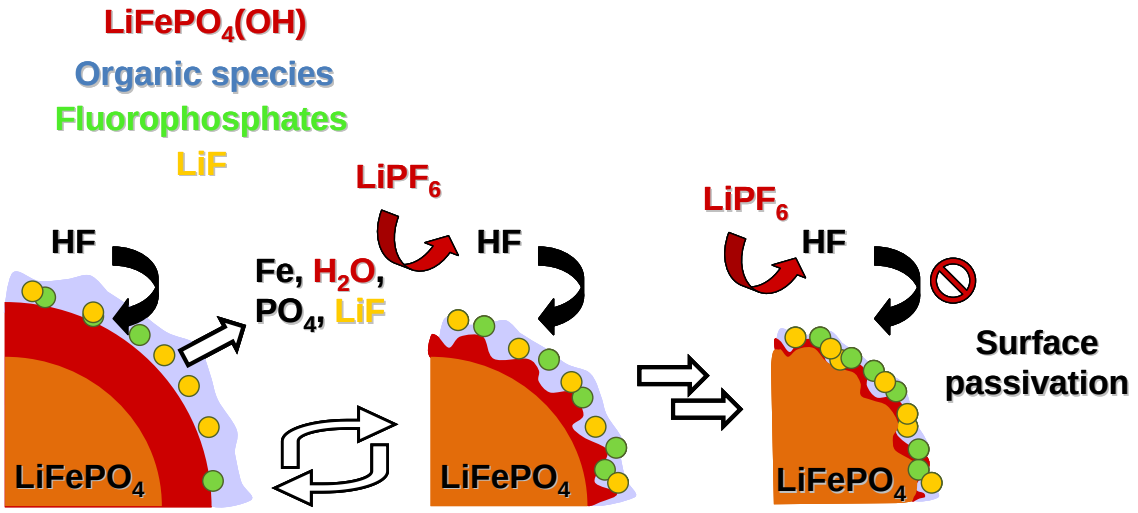

Figure IV-49. Proposed failure mode of air-aged on $LiFePO_4$ exhibiting a $LiFePO_4(OH)$-rich surface along cycling in conventional $LiPF_6$ 1M in EC:DMC (1:1) electrolyte. Material dissolution may be driven by the generation of fluorhydric acid and be stopped by surface passivation with interphase growth.

IV.4. Control of air aging through the use of carbon coating

The degradation of the electrochemical performance of $LiFePO_4$ upon air exposure could be assigned to a corrosion-type aging mechanism, implying both atmospheric oxygen and moisture. Therefore, a trivial protection from this detrimental reaction is here considered through the use of a carbon coating. Not only is the presence of a conducting carbon layer expected to improve the electrical properties of the material but carbon being hydrophobic, it

is also aimed at impeding the chemisorption and incorporation of hydroxyl group in the underlying $LiFePO_4$ surface.

IV.4.1. Illustration of material protection by Mössbauer spectroscopy

The protection offered by a carbon coating is evaluated via a simple comparative aging test between the material labeled CA/LFP prepared from the carbonization of cellulose acetate and bare $LiFePO_4$ (LFP-noC). After one month storage at 120°C, Mössbauer spectroscopy (**Fig. IV-50, left**) indicates that coated material could effectively be shielded against the atmospheric oxidative species. The resulting samples are subsequently tested in battery and only the coated material showed excellent cyclability, as attested by **Figure IV-50 (right)**.

In spite of its experimental demonstration, the protection mechanism of the carbon layer remains unclear. In fact, the other carbon coating envisaged (S/LFP, prepared from a sucrose precursor) proves almost ineffective towards air induced $LiFePO_4$ oxidation, and similar aging test resulted in 18 % of Fe(III). The difference in the hydrophobic properties of the two coatings allows explaining such different reactivity. Indeed, the EELS analysis carried out on materials S/LFP and CA/LFP highlighted an incomplete carbonization of the organic precursors in both cases (**Fig. IV-6**). The important inhomogeneity observed for S/LFP may imply however the presence of residual polar domains at the particles surface, which would favor water adsorption rather than repel it. On the contrary, organic residues are well distributed in the carbon layer present in CA/LFP, forming a barrier sufficiently hydrophobic.

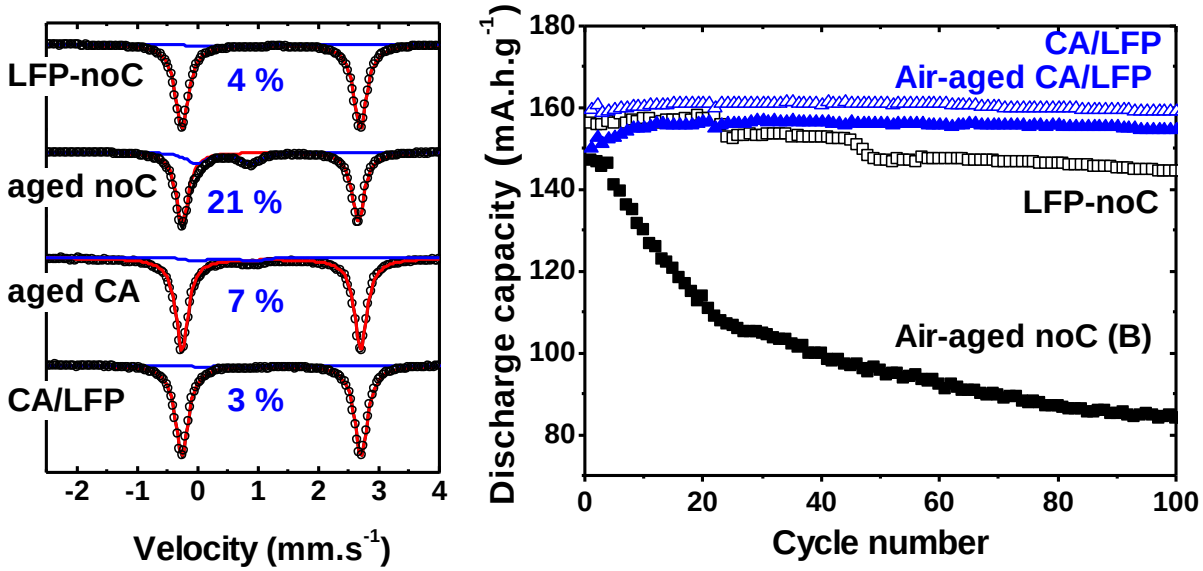

Figure IV-50. Mössbauer spectra and cyclability of pristine (open symbols) and air-aged (closed symbols) CA/LFP (blue) compared to bare (black) LFP-noC at C/10.

IV.4.2 Effect of carbon coating on the reactivity towards electrolyte

Proven to influence surface reactivity of $LiFePO_4$ against air exposure, the above mentioned carbon coating must afterward be investigated as a parameter susceptible to modify the reactivity towards electrolyte. **Figure IV-51** displays the EIS Nyquist plots recorded along the 20 first electrochemical cycles for the CA/LFP material.

The initial values for CA/LFP are similar to those measured for LFP-noC in section 1.3. Surprisingly however, the impedance of this carbon-coated material shows a dramatic increase of the loop associated to the charge transfer resistance and double layer capacitance between the first and 20th cycle. Low frequency processes are not affected, and no additional semi-circle indicating the formation of a resistive film can be observed.

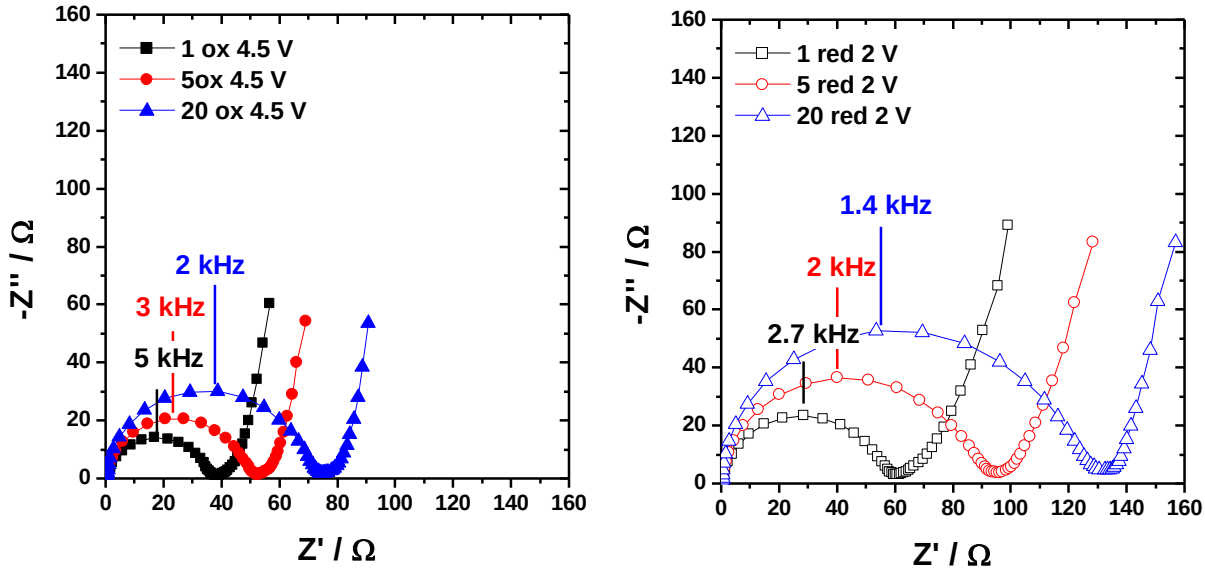

Figure IV-51. Nyquist plots of EIS performed on **pristine CA/LFP** at the end of the 1st, 5th and 20th charges (closed symbols, left) and discharges (open symbols, right) at a C/20 rate.

^{7}Li NMR experiments shown in **Figure IV-52** support this hypothesis. Indeed, while the amount of interphasial lithium notably increases between the first and 20th charge, the corresponding $T_{2r(Li)}$ slightly decreases, indicating a stronger intimacy between the paramagnetic electrode material and its interphase.

Apart from this difference, the potential dependant precipitation / dissolution process is retained, indicating that $LiFePO_4$ surface still governs the interphasial chemistry. To understand how CA/LFP material is capable of delivering a constant discharge capacity in spite of the significant increase of charge transfer resistance, complementary ^{19}F NMR measurements were carried out. As shown in **Figure IV-53**, the accumulation of interphasial lithiated species at the surface of CA/LFP is not accompanied by any accumulation of

fluorinated salt decomposition products. Besides, the gradual decrease of $T_{2r(Li)}$ suggests an increased intimacy of the interphase with the paramagnetic active material. Compared to bare $LiFePO_4$ (LFP-noC), the increase of impedance along cycling for the coated material may thus be assigned to a gradual covering of the electrode surface by interphasial species rather than their stacking on the top of each others.

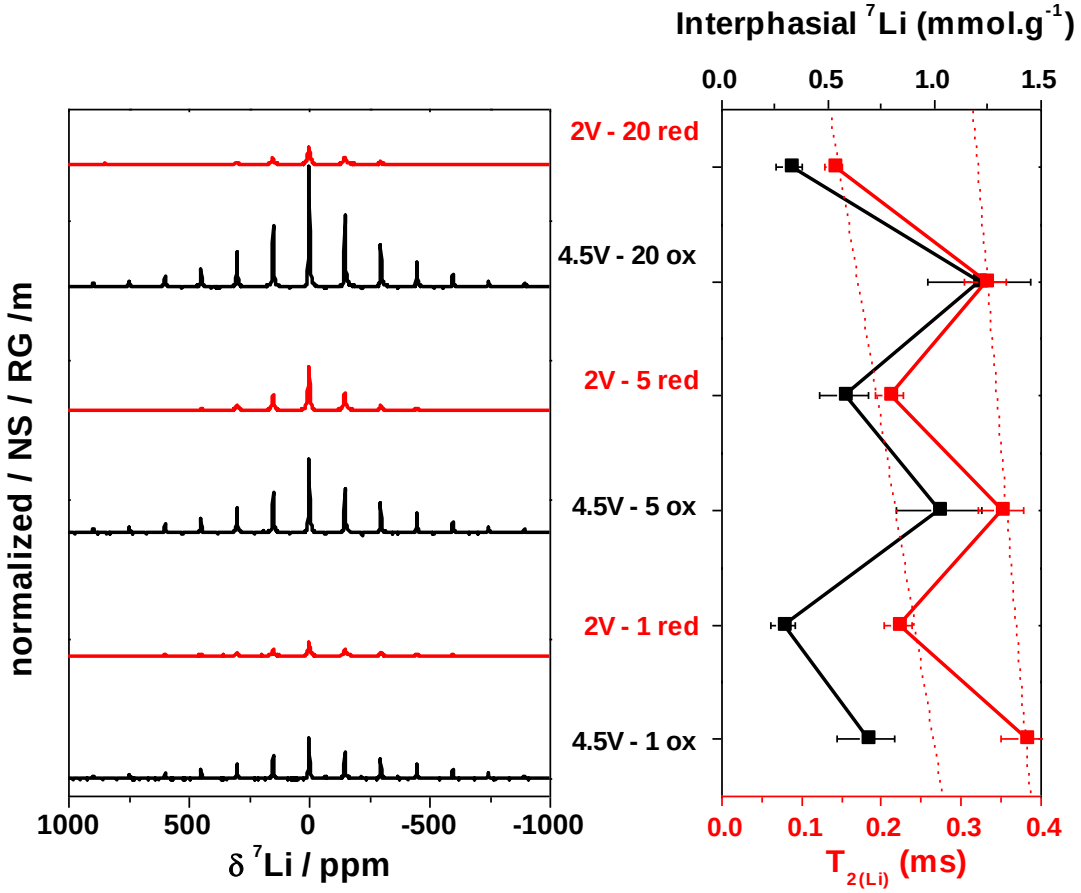

Figure IV-52. Results from ^{7}Li NMR performed on **pristine CA/LFP** at the end of the 1st, 5th and 20th charges and discharges at a C/20 rate in $LiPF_6$ EC:DMC.

While the amount of LiF exhibits almost no evolution, the amount of fluorophosphates remains significantly lower than the amount of interphasial lithium. Thus, the SPL covering CA/LFP at high voltage must be extremely rich in lithium under the form of organic / polymeric species that dissolve during the subsequent discharge rather than insoluble inorganic salts. Although the charger transfer at the interface is affected, lithium can travel through this Li-rich interphase, and therefore no effect on the discharge capacity is observed.

The absence of evolution in the amount of LiF suggests that contrary to solvents decomposition, the salt decomposition is not aggravated in the case of CA/LFP. These combined observations might be explained by the material surface chemistry. In fact, the

material surface has been made hydrophobic by the presence of the coating, and a lower amount of adsorbed water impurities is expected for CA/LFP compared to bare LFP-noC. Hence, the increase of contact surface with the deposition of the carbon layer (BET specific surface area increases from 21 $m^2.g^{-1}$ to 25 $m^2.g^{-1}$) does not favor parasitic reactions with $LiPF_6$. On the contrary, the decomposition of electrolyte solvents (that we proved catalyzed by the $FePO_4$ surface) is aggravated during charge by the increase of contact surface induced by carbon porosity.

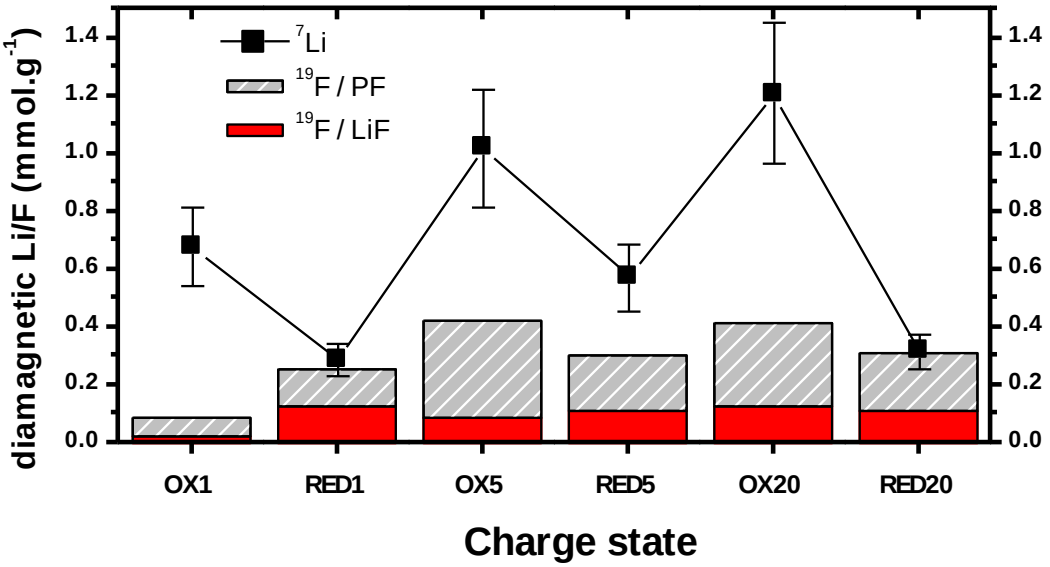

Figure IV-53. NMR quantification results for **pristine CA/LFP** at the end of the 1st, 5th and 20th charges and discharges at a C/20 rate in $LiPF_6$ EC:DMC.

IV.4.3 Concluding remarks

The effect of carbon coating on the surface reactivity of $LiFePO_4$ is not only complex but also ambivalent. Air-aging could be prevented, and both the power capability and the cyclability improved. However, the accumulation of organic lithiated species and the probable Li consumption that results were exacerbated by the presence of the carbon coating (see **Fig. IV-54**); similarly to bare $LiFePO_4$ material, this study would then need to be completed with tests in full cells. Maybe more importantly, it is commonly agreed that slow rates favor electrolyte decomposition and it would be worth investigating the effect of charge/discharge rate on the interphasial processes using carbon coated materials.

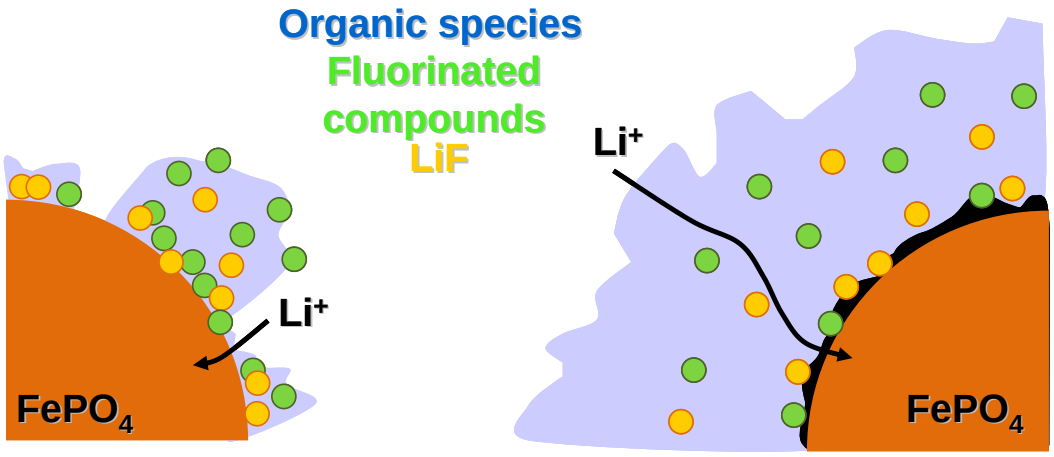

Figure IV-54. Overview of the impact of a carbon coating on $LiFePO_4$ reactivity towards conventional $LiPF_6$ 1M in EC:DMC (1:1) electrolyte. Interphasial processes implying solvents decomposition are exacerbated, resulting in a considerable Li-rich interphase.

IV.5. Control of air aging through the use of electrolyte additive

In the previous section, the detrimental effect of air aging on the electrochemical performance of $LiFePO_4$ was confronted with the help of a preventive treatment. Having identified the reaction of surface aqueous species with $LiPF_6$ as the origin of battery failure, another route can be considered so as to enable the cycling of air-aged $LiFePO_4$ materials nevertheless. This curative treatment relies on an electrolyte additive, the *N*,*N*-diethylamino trimethylsilane, which is capable of scavenging both H_2O and HF via breaking "N–Si" bond as below [54, 55]:

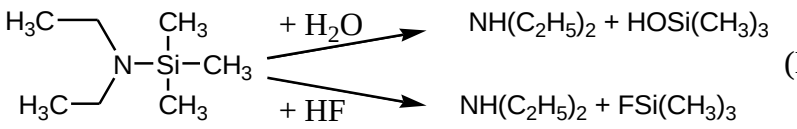

(Eq. IV-9)

This additive was added to $LiPF_6$ 1M in EC:DMC (1:1) up to 1 wt% and the present section aims at evaluating its effect on the cyclability of the air-aged $LiFePO_4$ material labeled B containing 21% of Fe(III), i.e. about 0.2 M of hydroxyls (based on the formula [0.79 $LiFePO_4$ - 0.21 $LiFePO_4(OH)$]).

IV.5.1. Improvement of the electrochemical performance by the use of an H_2O scavenger

As seen from **Figure IV-55**, the air-aged $LiFePO_4$ material can be cycled with no capacity fading over 20 cycles thanks to the addition of the H_2O scavenger in the electrolyte. Although its mechanism of action is still unclear, electrochemical characterization may

provide some insights. Along galvanostatic cycling (**Fig. IV-55, left**), the coulombic efficiency points out a significant irreversible capacity at the end of the first oxidation, while the electrochemical signature obtained in a potentiodynamic mode (**Fig. IV-55, right**) exhibits at this stage an additional oxidation peak with a potential onset around 3.8 V. This peak is not observed during the cycling neither of a pristine LFP-noC sample in the modified electrolyte, nor of an air-aged sample in conventional electrolyte. Although it cannot be characteristic of the reactions displayed in Eq. IV-9 (for the absence of involved electron), this additional oxidation peak seems specific to the action of the additive with the air-aged LFP-noC sample. Further experiments on LFP-noC samples air-aged to various extents should enable confirming (or not) such preliminary results.

In addition, the incremental capacity curve highlights a significant irreversible charge capacity above 4.4 V, also observed when cycling a pristine LFP-noC electrode in the modified electrolyte. It is not clear at this stage if the corresponding electrochemical process either plays a role in stabilizing the electrochemical performance or unnecessarily consumes current and maybe also lithium. This phenomenon is amplified in the case of pristine LFP-noC suggesting that it may correspond to the oxidation of the excess additive present in the electrolyte. In this latter case, a lower cut-off potential should circumvent such possible drawback.

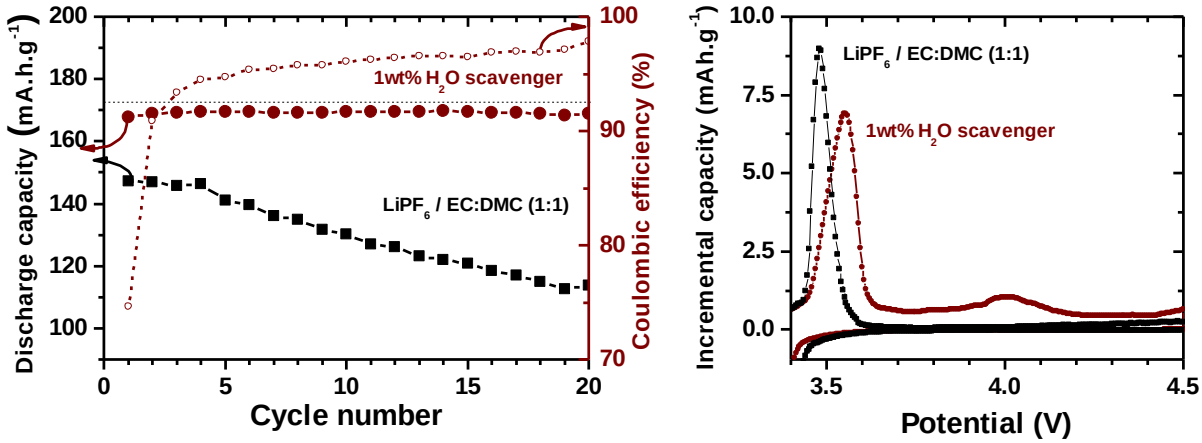

Figure IV-55. Left: Compared cyclability of air-aged LFP-noC (sample B) at C/20 using standard and modified electrolytes (closed symbols). The coulombic efficiency (small open symbols) is given for the electrolyte containing the H_2O scavenger additive. Right: Compared incremental capacity curves along the first charge.

An additional question concerns the abnormally high discharge capacity observed in the presence of the additive (166 $mAh.g^{-1}$) for this air-aged material. Based on the performance known for the $LiFePO_4$ and $LiFePO_4(OH)$ phases (see **Fig. IV-43** and associated

discussion) a specific capacity higher than 157 mAh.g^{-1} was not expected. In addition, the presence of the additive certainly induces kinetic limitations to the system, visible on the apparent potential shift of the redox peaks, the onset potential of the electrochemical reaction being similar to that of pristine LFP-noC. Although power capability of the modified electrolyte remains to be evaluated, it should be noted that impedance diagrams (**Fig. IV-56**) do not exhibit any marked increase of the electrolyte resistance.

The outstanding cyclability of air-aged $LiFePO_4$ in the presence of the H_2O scavenger is accompanied by the remarkable stability of the impedance measured at the end of charge and discharge (**Fig. IV-56**), compared to the standard electrolyte (**Fig. IV-46**). First of all, the addition of 1wt% of *N*,*N*-diethylamino trimethylsilane proves not to play on the electrolyte resistance, which is essential for a practical application. The charge transfer resistance measured at the end of charge and discharge is extremely similar to that of LFP-noC, and therefore it seems that the additive allows maintaining the electrochemical performance of pristine $LiFePO_4$.

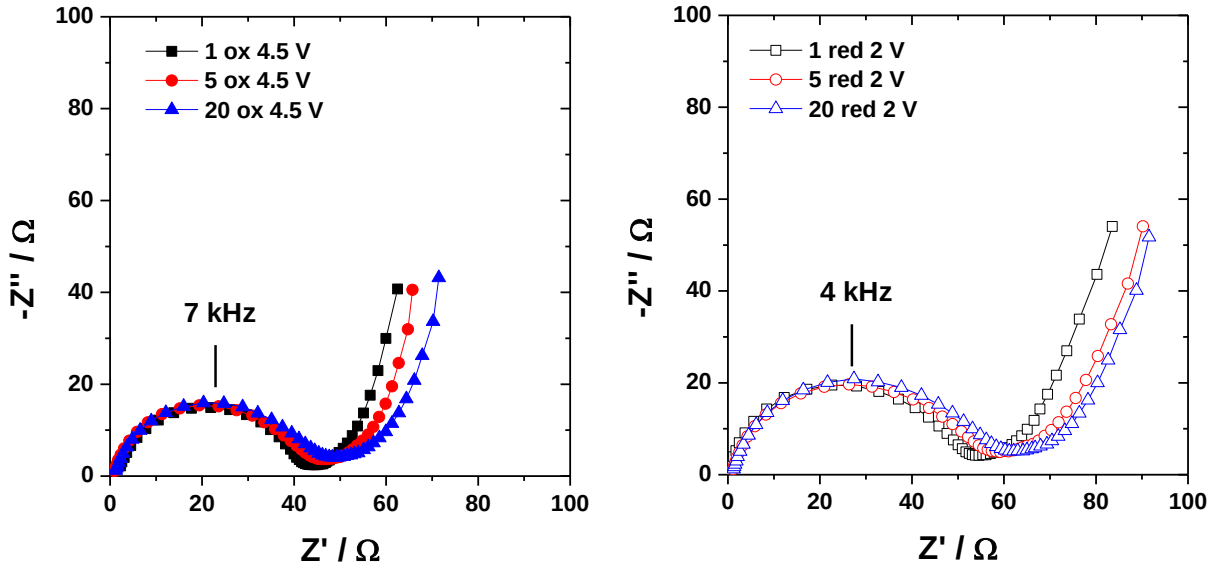

Figure IV-56. Nyquist plots of EIS performed on **air aged LFP-noC** (sample B) at the end of the 1st, 5th and 20th charges (closed symbols, left) and discharges (open symbols, right) at a C/20 rate **using the modified electrolyte**.

IV.5.2 Effect of an H_2O scavenger on the reactivity towards electrolyte

The additive was first subjected to the test of iron dissolution upon air-aged $LiFePO_4$ soaking in the standard $LiPF_6$ 1M in EC:DMC and modified electrolytes at 55°C. Pristine LFP-noC was used as control samples. After one week, the supernatants were separated for ICP analyses, currently underway.

We expect, as suggested by Koltypin *et al.* [53], that the dissolution of $LiFePO_4$ in $LiPF_6$ based electrolyte can be limited by the presence of an H_2O scavenger. Upon reaction with acidic impurities, the breaking of the "N-Si" bond of the *N*,*N*-diethylamino trimethylsilane (Eq. IV-9) produces colored organic species that could, in the near future, be titrated by liquid NMR or UV spectroscopies. For what it is worth, the amplification of such reaction for the air-aged LFP-noC sample seems visible at the naked eye.

NMR spectroscopy was used to probe the evolution of interphasial species at the surface of air-aged LFP-noC in the presence of the selected additive (**Fig. IV-57**).

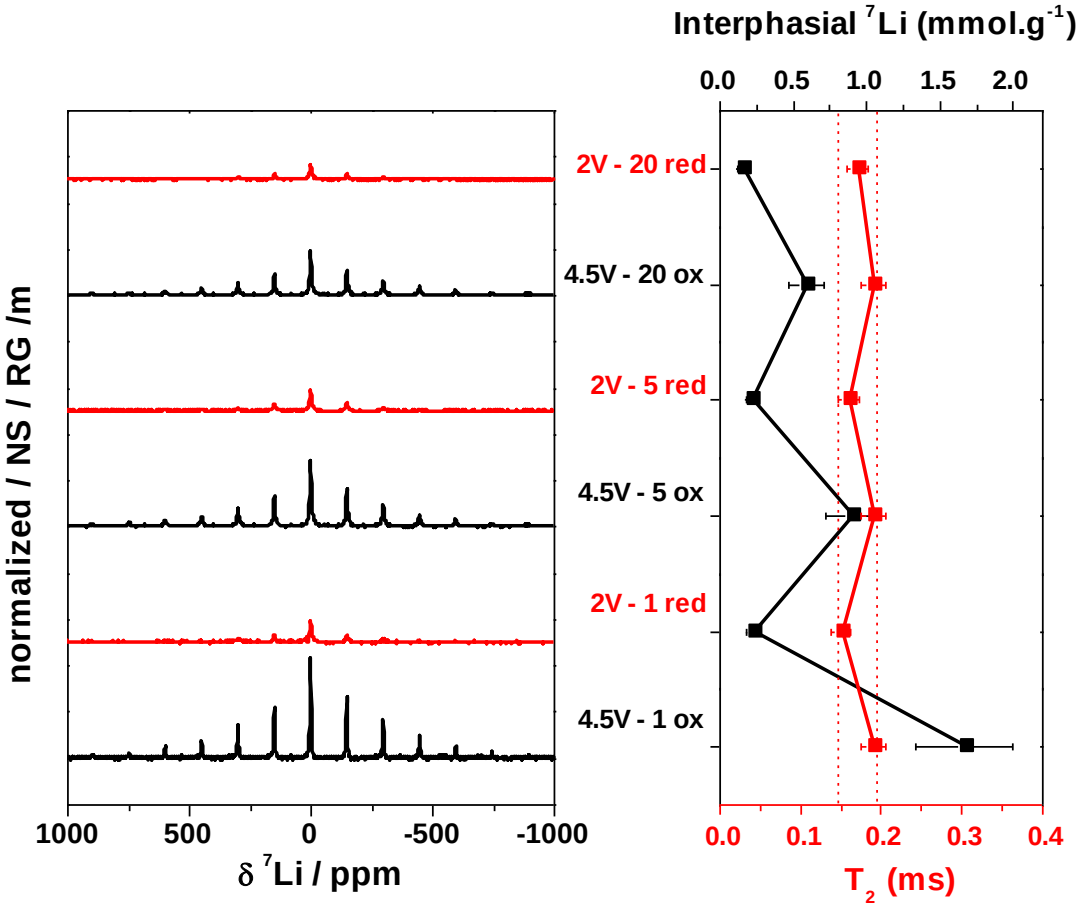

Figure IV-57. Results from ^{7}Li NMR performed on **air-aged $LiFePO_4$** at the end of the 1st, 5th and 20th charges and discharges at a C/20 rate in **modified** $LiPF_6$ EC:DMC.

^{7}Li NMR results, presented in **Figure IV-57**, suggest that the irreversible electrochemical process observed during the first charge results in the deposition of an important amount of lithiated species at the positive electrode / electrolyte interface. Indeed, the 1.5 mmol(Li).g^{-1} observed at this point should be compared to 0.25 mmol(Li).g^{-1} and 0.15 mmol(Li).g^{-1} detected at the end of the first charge in standard electrolyte in the case of

pristine and air-aged LFP-noC, respectively. The origin of such important amount of lithiated interphasial species at the end of the first charge probably lies in the two irreversible oxidation peaks highlighted in **Figure IV-55 (right)**.

However, contrary to pristine LFP-noC in standard $LiPF_6$ based electrolyte, no gradual accumulation is observed and the tendency rather describes the departure of pristine lithiated species and the stabilization of the interphase. In this configuration, T_{2r} is only slightly dependant on the SOC and also exhibits a stable behavior along cycling. These favorable characteristics of the interphase are however balanced by the absolute amount of interphasial lithium, which remains two times more abundant than what was found on pristine LFP-noC in standard $LiPF_6$ based electrolyte.

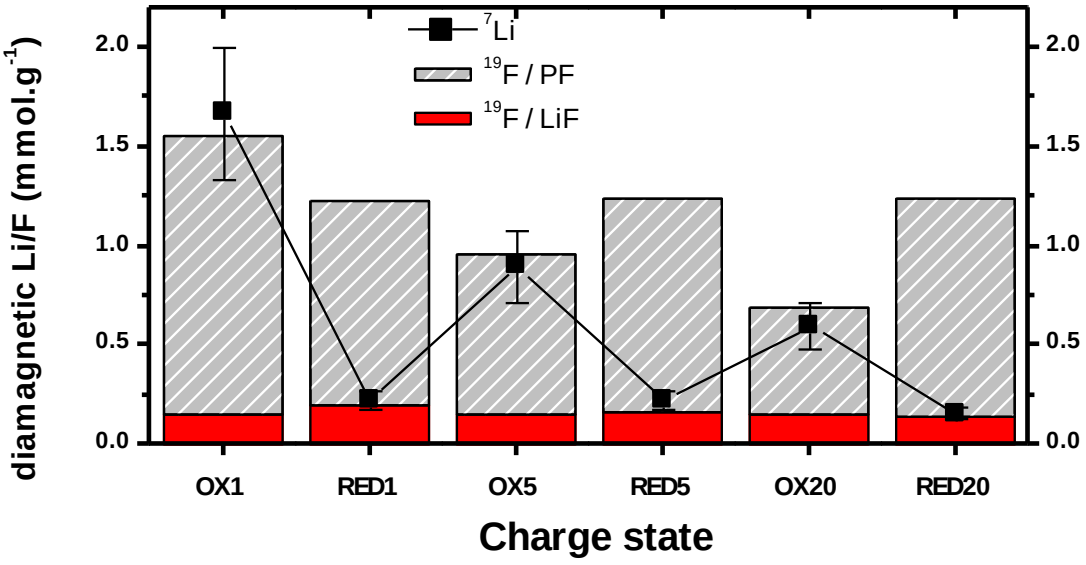

Figure 58. NMR quantification results for **air-aged $LiFePO_4$** at the end of the 1st, 5th and 20th charges and discharges at a C/20 rate in **modified** $LiPF_6$ EC:DMC.

The evolution of fluorinated species, as monitored by ^{19}F NMR (**Fig. IV-58**), is also unique compared to pristine (**Fig. IV-20**) or air-aged LFP-noC (**Fig. IV-48**) in standard $LiPF_6$ based electrolyte. While the amount of detected lithium fluoride is kept constant and in the same order of magnitude than materials cycled in standard electrolyte, fluorophosphates detected at the end of the first charge do not seem to depart either with lithiated species during the subsequent discharge. Those fluorophosphates remain extremely numerous in the presence of the additive in spite of strong variations in the amount of lithium, suggesting that those fluorophosphates are non lithiated.

The increasing coulombic efficiency, at the scale of the 20 first cycles might be explained by the availability of a lithium reservoir in the positive electrode / electrolyte interphase. Indeed, whereas the initial deposition of the interphase up to 1.6 mmol(Li).g^{-1} is

made at the expense of 25% of the initial charge capacity, the precipitation of 0.7 mmol(Li).g^{-1} at the end of the 5th charge only costs 5 % of the coulombic efficiency. Accordingly, from the 2nd cycle on, new interphasial processes must involve the Li-interphasial species initially formed via chemical reactions, rather than consume additional electrons. More prolonged cycling experiment should enable shedding light on the electrochemical behavior after the full consumption of this reservoir. Nonetheless, it seems that the interphase is governed by the additive chemistry. A similar study on pristine LFP-noC should allow separating the effect of this H_2O scavenger from that of the hydroxylated ferric phosphate phase.

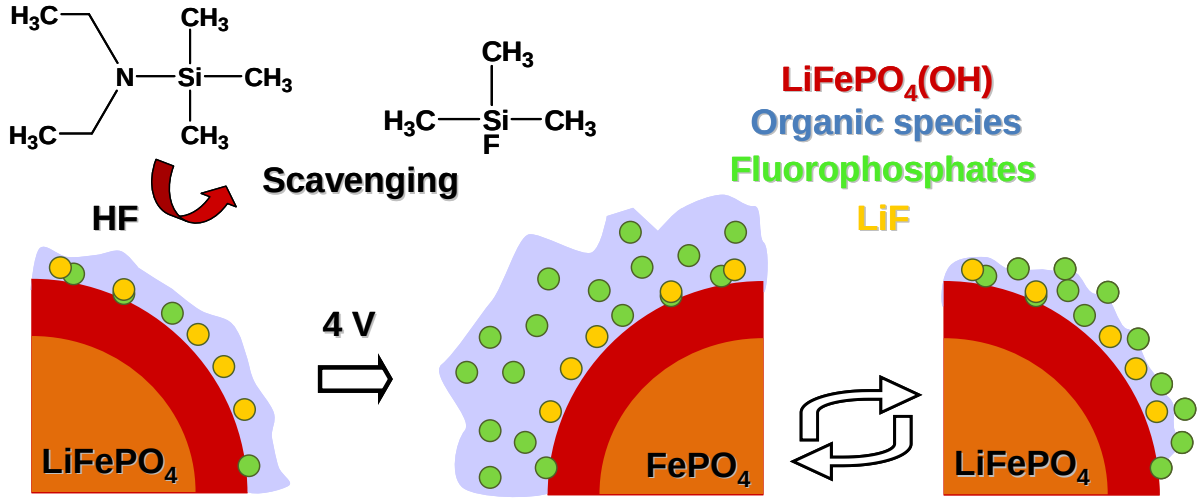

Figure IV-59. Overview of the impact of 1 wt% of *N*,*N*-diethylamino trimethylsilane on air-aged $LiFePO_4$ reactivity towards $LiPF_6$ 1M in EC:DMC (1:1) electrolyte. Acidic impurities being scavenged, the dissolution of the active material seems prevented. Interphasial side reactions upon charge result in the deposition of large amounts of fluorophosphates.

IV.6. Concluding remarks on air exposure and its consequences

Although widely considered as inert toward air exposure, $LiFePO_4$ exhibits certain reactivity towards atmospheric oxidizing species, namely oxygen and moisture. Its aging can become significant along storage at moderate temperature or in possibly moist atmospheres in some parts of the world.

Based on an exhaustive structural and electrochemical investigation, this section proposes two possible "corrosion" mechanisms considering a role for both oxygen and water. In a first stage, air exposure results in lithium extraction from $LiFePO_4$, in the limit of the $Li_{1-x}FePO_4$ solid solution domain [8]. This reaction has little influence in a Li half-cell but reduces the practical capacity accessible in a Li-ion battery. The second corrosion mechanism

observed leads to the incorporation of hydroxyls in the bulk surface, under the form of an amorphous $LiFePO_4(OH)$ phase [papers **II** and **III**]. Following this reaction which further reduces the capacity accessible in a Li-ion configuration, iron oxidation can be much more severe compared to the first mechanism. But more critically, the presence of aqueous species in the material, which cannot be expelled unless performing a thermal treatment at 600°C under inert atmosphere [paper **I**], dramatically modify the material reactivity towards electrolyte.

In fact, the vulnerability of $LiFePO_4$ against acidic impurities [53] is not only confirmed here, but proves considerably aggravated after air aging. The work conducted here demonstrates that in such a case, the electrode / electrolyte interactions are dominated by the dissolution of the active material and the reaction of incorporated hydroxyls with the electrolyte salt.

Having elucidated the failure mechanism of air-aged $LiFePO_4$, practical means to limit surface aging or its detrimental impact on the reactivity towards electrolyte are demonstrated. The preventive treatment considered calls on the deposit of a carbon coating, which effectively circumvents iron oxidation in the limits of the $Li_{1-x}FePO_4$ solid solution. Although increased solvent decomposition is observed at high potentials (4.5 V) compared to the bare material, a lower cut off potential should be enough to limit this drawback. The curative treatment presented here, still under investigation, relies on an additive capable of scavenging acidic impurities, either released from the active material (structural OH) or further formed upon reaction with the electrolyte salt (HF). In this case, the interphasial chemistry is found governed by the additive, and further experiments such as long term cycling are required to shed light on the possible side effects. Nonetheless, the dissolution of $LiFePO_4$ in $LiPF_6$ based electrolyte might be successfully contained, and outstanding electrochemical performance can be obtained, even from severely air-aged materials.

Finally, the achievement of reproducible good cyclability can be obtained from $LiFePO_4$, in spite of significant exposure to hot or humid air, based on sufficient knowledge of the reaction mechanisms unraveled in this study.

V- CONCLUSION

This chapter dedicated to $LiFePO_4$ has covered all the questions arising from various discussions which are:

Is it possible to experimentally highlight the architecture and homogeneity of the interphase?

The answer is affirmative, and the development of analytical tools such as environmental XPS and TEM should provide an even more unequivocal piece of evidence. In the present chapter, both routes (i.e. local investigation by EELS and XPS depth profiling) are shyly explored and prove extremely encouraging. Description of the interphase often errs either on the side of simplicity or abstraction. In this regard, epitaxial thin films provide the most exciting device, for their chemical nature is that of the investigated active material (by contrast with noble metals often used as "models") and their 2D morphology considerably simplifies the analysis and the resulting model as well (by comparison with composite electrodes using powder samples, but also carbons and binders…).

Hence, the most realistic model of the $LiFePO_4$ / electrolyte interphase is one of the most complex, i.e. a rough solid polymer electrolyte interphase encompassing a mixing of inorganic species.

How dynamic is the $LiFePO_4$ / electrolyte interphase upon cycling?

The interphase observed on all the investigated $LiFePO_4$ materials, unless the salt decomposition blocks the active surface, exhibit the same general behavior upon potential variations, i.e. the precipitation of a Li-rich SPL above 4.0 V, dragging fluorophosphates into the interphase; and their dissolution upon the subsequent discharge, releasing most of the trapped fluorinated salts. In addition to this dynamic process, a gradual accumulation of interphasial species is however observed in all cases. This archetypal interphasial behavior is however to be nuanced in the light of possible structural defects, as shown in the case of hydrothermal $LiFePO_4$ materials prepared in this work.

Are $LiFePO_4$ (010) electroactive surfaces more catalytic towards the electrolyte decomposition?

Most probably, yes. Although this study would be best enhanced with the investigation of epitaxial thin films offering each a different crystallographic surface, the work conducted

here on hydrothermally prepared (010) platelets seems to indicate a considerably amplified salt and solvents decomposition at their contact.

Moreover, such experimental approach of the interphase formation mechanisms on specific crystalline surfaces could be more easily coupled to theoretical studies modeling the adsorption of surface species on active surfaces, as developed elsewhere [56, 57]. In this respect, the tailoring of particles morphology for improved rate capabilities would be considerably more relevant.

To which extent does the surface aging induced by air and/or moisture exposure influence the $LiFePO_4$ / electrolyte interphasial processes?

The corrosion mechanisms highlighted in this work propose the growth of an X-ray amorphous $LiFePO_4(OH)$ phase at the surface of the material upon air and/or moisture exposure. The interphase chemistry seems then driven by the dissolution of this phase, due to acidic impurities, unavoidable in $LiPF_6$-based electrolytes. The impact of such dissolution on the electrochemical performance of Li-ion batteries using $LiFePO_4$ is critical: not only the performance of the positive electrode is found significantly diminished, as observed in the present chapter, but the poisoning of the negative counter electrode by migrating iron species has to be considered as well. In this regard, examples from the literature show that the consequences of transition metal deposition on the negative electrode may be even more detrimental to the system than the net loss of Li storage capacity in the positive [58].

The exhaustive bulk and surface characterization along the $LiFePO_4$ surface aging proved essential to select the adapted additive, and such approach should be favored against a trial and error method.

REFERENCES OF CHAPTER 4

[1] M. Herstedt, M. Stjerndahl, A. Nyten, T. Gustafsson, H. Rensmo, H. Siegbahn, N. Ravet, M. Armand, J. O. Thomas and K. Edstrom, *Electrochem. Solid-State Lett.*, **6** (2003) A202.

[2] A. Yamada, S. C. Chung, K. Hinokuma, *J. Electrochem. Soc.*, **148** (2001) A224.

[3] A. Yamada, H. Koizumi, N. Sonoyama, R. Kanno, *Electrochem. Solid-State Lett*., **8** (2005) A409.

[4] M. Armand, M. Gauthier,J. F. Magnan, N. Ravet, World Patent WO 02/27823 A1 (2002).

[5] S.F. Yang, Y.N. Song, P.Y. Zavalij, M.S. Whittingham, *Electrochem. Commun.*, 4 (2002) 239.

[6] J.-K. Kim, J.-W. Choi, G. Cheruvally, J.-U. Kim, J.-H. Ahn, G.-B. Cho, K.-W. Kim, H.-J. Ahn, *Mat. Lett.*, **61** (2007) 3822.

[7] M. Maccario, L. Croguennec, A. Wattiaux, E. Suard, F. Le Cras, C. Delmas, *Solid State Ionics*, **179** (2008) 2020.

[8] J.F. Martin, A. Yamada, G. Kobayashi, S.I. Nishimura, R. Kanno, D. Guyomard, N. Dupré, *Electrochem. Solid State Lett*., **11** (2008) A12.

[9] F. Hatert, P. Schmid-Beurmann, *Fe^{2+} oxidation in triphylite $LiFePO_4$: possible formation of Ferrisicklerite and Heterosite*, in: European Conference on Mineralogy, E. Schweizerbart Science Publishers (2005).

[10] G. Kobayashi, S. Nishimura, M. Park, R. Kanno, M. Yashima, T. Ida, A. Yamada, *Adv. Funct. Mater.*, **19** (2009) 395.

[11] S.D Berger, D.R McKenzie, P. J. Martin, *Phil. Mag. Lett.*, **57** (1988) 285.

[12] J.J Cuomo and J.P Doyle, J. Bruley, J. C. Liu, *Appl. Phys. Lett.*, **58** (1991) 466.

[13] P.J Fallon and V.S Veerasamy, C.A. Davis, J. Robertson, G. Amaratunga, W. Milne, J. Koskinen, *Phys. Rev. B*, **48** (1993) 4777.

[14] J Bruley and D.B Williams, J. J. Cuomo, *J. Microscopy—Oxford*, **180** (1995) 22.

[15] J. Bruley, P. Madarson, J.C. Liu, *Nuclear Instruments and Methods in Physics Research B*, **45** (1990) 618421.

[16] W. Porcher, B. Lestriez, S. Jouanneau, D. Guyomard, *J. Electrochem. Soc.*, **156** (2009) A133.

[17] W. Porcher, B. Lestriez, S. Jouanneau, D. Guyomard, *J. Power Sources*, **195** (2010) 2835.

[18] A. K. Padhi, K. S. Najundaswamy, J. B. Goodenough, *J. Electrochem. Soc*., **144** (1997) 1188.

[19] N. Dupré, J-F. Martin, J. Degryse, V. Fernandez, P. Soudan, D. Guyomard *J. Power Sources*, **195** (2010) 7415.

[20] M. Scrocco, *Phys. Rev. B*, **32** (1985) 1306.

[21] A. Ait-Salah, J. Dodd, A. Mauger, R. Yazami, F. Gendron, and C. M. Julien, *Z. Anorg. Allg. Chem.*, **632** (2006) 1598.

[22] N. Dupré, J-F. Martin, D. Guyomard, A. Yamada, R. Kanno, *J. Mater. Chem.*, **18** (2008) 4266.

[23] A.V. Plakhotnyk, L. Ernst, R. Schmutzler, *J. Fluorine Chem.*, **126** (2005) 27.

[24] M. Hirayama, M. Yonemura, K. Suzuki, N.Torikai, H. Smith, E. Watkinsand, J. Majewski, R. Kanno, *Electrochemistry (Tokyo, Japan)*, **5** (2010) 413.

[25] G. Liang, K. Park, J. Li, R. E. Benson, D. Vaknin, J. T. Markert, M. C. Croft, *Phys. Rev. B*, **77** (2008) 064414.

[26] L. Wang, F. Zhou, Y. S. Meng, G. Ceder, *Phys. Rev. B*, **76** (2007) 165435.

[27] C. A. J. Fisher, M. S. Islam, *J. Mater. Chem.*, **12** (2008) 1209.

[28] G. Chen, X. Y. Song, T. J. Richardson, *Electrochem. Solid-State Lett.*, **9** (2006) A295.

[29] K. Kanamura, S. Koizumi K. Dokko, *J. Mater. Sci.*, **43** (2008) 2138.

[30] J. Chen, M. J. Vacchio, S. Wang, N. Chernova, P. Y. Zavalij, M. S. Whittingham, *Solid State Ionics*, **178** (2008) 1676.

[30] D. Aurbach, B. Markovsky, M. D. Levi, E. Levi, A. Schechter, M. Moshkovich, and Y. Cohen, *J. Power Sources*, **81-82** (1999) 95.

[31] M. Menetrier, C. Vaysse, L. Croguennec, C. Delmas, C. Jordy, F. Bonhomme, P. Biensan, *Electrochem. Solid-State Lett.*, 7 (2004) A140.

[32] D. Aurbach, *J. Power Sources*, **89** (2000) 206.

[33] D. Aurbach, K. Gamolsky, B. Markovsky, G. Salitra, Y. Gofer, U. Heider, R. Oesten, M. Shmidt, *J. Electrochem. Soc.*, 147 (2000) 1322.

[34] A. Nyten, M. Stjerndahl, H. Rensmo, H. Siegbahn, M. Armand, T. Gustafsson, K. Edström, J. O. Thomas, *J. Mater. Chem.*, **16** (2006) 3483.

[35] N. Meethong, H.Y.S. Huang, S.A. Speakman, W.C. Carter, Y.M. Chiang, *Adv. Funct. Mater.*, 17 (2007) 1115.

[36] A. Yamada, H. Koizumi, S.-I. Nishimura, N. Sonoyama, R. Kanno, M. Yonemura, T. Nakamura, Y. Kobayashi, *Nat. Mater.*, **5** (2006) 357.

[37] Y.-H. Rho, L.F. Nazar, L. Perry, D. Ryan, *J. Electrochem. Soc.*, **154** (2007) A283.

[38] N. Ravet, C. Michot, G. Nuspl, G. Liang, M. Gauthier, *Proceedings of the 210th ECS Meeting Cancun*, Mexico (2006)

[39] S. Hamelet, P. Gibot, M. Casas-Cabanas, D. Bonnin, C.P. Grey, J. Cabana, J.B. Leriche, J. Rodriguez-Carvajal, M. Courty, S. Levasseur, C. Masquelier, *J. Mater. Chem.*, **19** (2009) 3979.

[40] X. Wang, X. Yang, H. Zheng, Z. Zhang, *J. Crystal Growth*, **274** (2005) 214.
[41] N. Marx, L. Croguennec, D. Carlier, A. Wattiaux, F. Le Cras, E. Suard, C. Delmas, *Dalton Trans.*, **39** (2010) 5108.
[42] T. Suzuki-Muresan, P. Deniard, E. Gautron, V. Petricek, S. Jobic, B. Grambow, *J. Applied Crystallography*, **43** (2010) 1092.
[43] Jean – Frédéric Martin, *Evolution de la surface de matériaux d'électrode positive pour accumulateurs au lithium au cours du vieillissement et du cyclage électrochimique*, PhD thesis from the University of Nantes, (2008).
[44] P. Keller, A.M. Fransolet, F. Fontan, *Contrib. Mineral. Petrol*,. **92** (1986) 502.
[45] O.V. Yabukovitch, *Geochem. Int.*, 1997, **35**, 630.
[46] L. J. M. Davis, I. Heinmaa, B. L. Ellis, L. F. Nazar, G. R. Goward, *Phys. Chem. Chem. Phys.*, **13** (2011) 5171.
[47] J. Cabana, J. Shirakawa, G. Chen, T. J. Richardson, C. P. Grey, *Chem. Mater.*, **22** (2010) 1249.
[48] A. Castets, D. Carlier, F. Boucher, Y. Zhang, N. Marx, L. Croguennec, M. Ménétrier, *J. Phys. Chem. C*, **115** (2011) 16234.
[49] L. Laffont, C. Delacourt, P. Gibot, M. Y. Wu, P. Kooyman, C. Masquelier, J. M. Tarascon, *Chem. Mater.*, **18** (2006) 5520.
[50] S. Hamelet, M. Casas-Cabanas, L. Dupont, C. Davoisne, J. M. Tarascon, C. Masquelier, *Chem. Mater.*, **23** (2011) 32.
[51] P. Axmann, C. Stinner, M. Wohlfahrt-Mehrens, A. Mauger, F. Gendron, C. M. Julien, *Chem. Mater.*, **21** (2009) 1636.
[52] K. Zaghib, M. Dontigny, P. Charest, J.F. Labrecque, A. Guerfi, M. Kopec, A. Mauger, F. Gendron, C.M. Julien, *J. Power Sources*, **185** (2008) 698.
[53] M. Koltypin, D. Aurbach, L. Nazar, B. Ellis, *J. Power Sources*, **174** (2007) 1241.
[54] K. Takechi, T. Shiga, U.S. Patent 6 235 431 (2001).
[55] S.A. Zhang, *J. Power Sources*, **162** (2006) 1379.
[56] K. Persson, L. Wang, C. Dassonville, M. Kocher, G. Ceder, Abstract #487, 218th ECS Meeting, Las Vegas (2010).
[57] Nathalie Andreu, *Réactivité de surface d'un matériau type d'électrode positive pour batterie lithium-ion : $LiCoO_2$*, PhD thesis from the University of Pau, (2011).
[58] I. Belharouak, K. Amine, Abstract #482, 218th ECS Meeting, Las Vegas (2010).

CONCLUSION

As mentioned in the introduction, this thesis directly takes over the work carried out by Jean Frédéric Martin (thesis defended in November 2008). It seems obvious to assess the work conducted here in the light of the prospects envisaged then. From this point of view, the surface evolution of bare $LiNi_{½}Mn_{½}O_2$ and $LiFePO_4$ along aging and electrochemical cycling in conventional $LiPF_6$ 1M in EC:DMC electrolyte were to be compared with results obtained via the use of electrolyte additives or surface modifications by physical coating or molecular grafting. Such surface modifications were to be evaluated in terms of interphase modification and their impact on the electrochemical performance. Studies reported here highlight the complexity of such approach, not for any particular experimental obstacle, but rather for the essential importance of prior characterization of the electrode / electrolyte interphase. So to say, blind surface modification is not worth investigating, all the less when powerful surface characterization techniques allow identifying interface aging and failure mechanisms.

The objectives of this work were double, as indicated in the title **"Characterization and control of positive electrode / electrolyte interphase in lithium batteries"**. The first element ("characterization") has been developed in various directions, the most fruitful being MAS NMR. The initial approach, based only on ^{7}Li NMR could be expanded to ^{19}F and ^{31}P nuclei, in order to shed light on the inorganic interphasial species. The implementation of empirical NMR calibration curves is the result of a long questioning, on what the physics behind the experiment allows, and what it does not. This tentative research is barely highlighted in the manuscript, but the set up of such convenient-but-robust experimental tool has not been straightforward. Of course it remains questionable, as it should be, but even more than specific results on specific electrode material / electrolyte couples, the spectroscopic methods presented here are of importance. For instance, they are now used in our group to monitor the interphase evolution on silicon and conversion negative electrodes.

The methodology implemented for TEM/EELS analyses could also be successfully applied by co-workers for the characterization of 5 V spinels upon aging in electrolyte. The analysis of cycled materials could not be reported here, for a lack of time and the additional challenges posed by the presence of the inactive electrode components. Such experiments are still under way, and represent a unique way to depict interphasial deposits, complementary to NMR or XPS results.

The highlight of bare surfaces and up to 200 nm thick interphases by TEM, again questionable due to the indirectness of the analysis, seriously poses the question of the

representativeness of what is probed by XPS. Clearly, this issue has not been solved here but XPS stands as an incredibly powerful technique for clarifying the interphase chemistry, complementary to "bulk" NMR analyses. However, we seized the opportunity offered by Pr. Kanno to play with epitaxial thin films of $LiFePO_4$ and launched into angular resolved XPS analyses. Although meticulous models exist to reconstruct depth profiles in the case of multilayered assemblies, we restricted ourselves to qualitative conclusions and "trends", as a first approach. Yet, epitaxial thin films offer tremendous opportunities to investigate the formation and evolution of interphases, by XPS but also by TEM or *in situ* EQCM or ellipsometry for instance. We leave such exciting work to competent people.

The second element ("control") has been considered late in the thesis in the light of previous results, once sufficient basis was gathered on bare "model" compounds. Transition metal dissolution from $LiNi_{½}Mn_{½}O_2$, highlighted by EELS, has been addressed through the use of an additive or heterochemical coatings susceptible to prevent such phenomenon. The surface aging of $LiFePO_4$ has been limited through the use of a carbon coating, and its detrimental impact on the interphasial chemistry solved via the use of an appropriate electrolyte additive. These different treatments met some success, but always proved to induce unexpected side reactions. Thus, the moral of all this work would be to "*think global"*. Electrochemical systems are complex, and the reactivity between their different components not always predictable. However, the present thesis, and most reports on interphase control, would gain by considering not only the identified aging or failure mechanism and the appropriate handling of one component. A broad and long-term vision of the possible interactions induced by the addition of one more component into such complex systems is, in fact, crucial.

There is a general consensus on what a "good" or "desirable" interphase should be, which is basically conductive to Li^+ ions. From the various studies reported here, lithiated organic species such as Li-alkylcarbonates should be favored at the expense of non lithiated polymers or lithium fluoride, clearly proved to impede satisfying charge transfer at the positive electrode / electrolyte interface.

Future works should try to combine *ex situ* analyses such as those presented here, with *in situ* monitoring of liquid electrolyte, probing short lived species, and gas evolution in the battery upon cycling. This latter could be done by GC-MS for instance, providing insights on intermediate interphasial reactions. To help elucidating degradation mechanisms, organic chemists are definitely needed. Of course, such multidisciplinary approach is laborious, but definitely smarter, and in the end probably cheaper than repeated trials-and-error processes.

APPENDIX 1. METHODS

This chapter aims at introducing the analytical techniques employed in this thesis to study interphases in Li-ion batteries.

The first section quickly goes through more usual surface sensitive analytical techniques, discussing their contribution, their limits, and the prospects opened up in the field of interphase characterization by recent technological advances. The second section, reviewing the dominant interactions that govern NMR spectra serves as a theoretical introduction to the technique. Finally, the third section describes the electrochemical cycling tests using in this work.

I- SURFACE SENSITIVE ANALYTICAL TECHNIQUES AND THEIR DEVELOPMENT

The development of surface sensitive analytical techniques in recent years, *in situ* spectroanalytical techniques in particular, has opened the door for efficient and detailed studies of the correlation between surface chemistry, morphology, 3D structure, and the electroanalytical response and performance of electrodes and electrolyte systems for advanced Li batteries.

I-1. Vibrational spectroscopies

In order to identify surface species and discuss their formation mechanism, the determination of their specific chemical nature such as the presence of particular functional groups is of primary importance. Fourier transform infrared spectroscopy (FTIR) is one of the early characterization methods to obtain such information, especially effective in the case of organic compounds. In particular, attenuated total reflectance (ATR) technique enables to analyze thin filmy materials on solid plate for FTIR [1].

Using FTIR, Aurbach and coworkers basically paved the way for the chemical characterization of the SEI, as well as interphases on positive electrode materials, by identifying the nature of interphasial species that are generated by electrolyte degradation on the electrodes surface [1-4]. Once depreciated for more powerful analytical techniques such as XPS (see below), vibrational spectroscopies enjoy a renewed interest with the development of dedicated electrochemical cells allowing *in situ* ATR or Raman observation of interfacial phenomena [5-7]. By this mean, Kostecki *et al.* proved able to monitor the FTIR band intensity characteristic of alkyl-carbonates vs. SOC for instance [7]. Providing the setting of an exhaustive spectral database correlated to electrochemical performance, those techniques could provide excellent diagnostics.

Although vibrational spectroscopies give access to extremely precise chemical compositions, neither the architecture of interphases nor their interactions with the electrode materials can be investigated.

I-2. X-ray Photoelectron spectroscopy

X-ray photoelectron spectroscopy (XPS) is another useful tool to study the surface chemistry of battery materials [8-12]. This technique is based on the analysis of the kinetic energy E_k of photoelectrons ejected following to the sample irradiation by soft X-rays (usually Al K_α or Mg K_α) with a specific photon energy, hv; from a given state of binding energy E_B. Conservation of the total energy results in the following relation:

$$hv - E_k = E_B \qquad \text{(Eq. 1)}$$

The binding energy E_B, characteristic of the orbital from which the electron is ejected, can therefore be deduced as the difference between the photon energy (that we know) and the kinetic energy (that we measure). On a XPS spectrum, photoelectrons are counted depending on their binding energies, unique to each element, which can therefore be used to determine the elemental composition of a sample.

I-2.1. Chemical characterization of interphases

The intensity of each XPS peak depends on several factors as follows:

$$I \propto \sigma . \int N(z) . \exp(-z / \lambda . \cos(\theta)) . dz \qquad \text{(Eq. 2)}$$

Where σ is the cross-section per atom for ionizing an inner-shell electron, $N(z)$ the concentration of the element at a given depth z, λ the inelastic mean-free-path of an electron and θ the angle defined between the incident beam and the sample surface normal. The atomic fraction C_A of an element A is therefore given by:

$$C_A = \frac{I_A / f_A}{\sum_i I_i / f_i} \qquad \text{(Eq. 3)}$$

where I_i is the integrated intensity of a given spectral peak and f_i the sensitivity factor associated. The small escape depth $\lambda . \cos(\theta)$ of the ejected photoelectrons (<5 nm) provides excellent surface sensitivity and makes XPS a technique of choice for the chemical characterization of interphases, which from a global point of view would only represent a tiny fraction of the probed sample.

In addition to quantitative elemental analysis, chemical information of the surface elements can be obtained by studying the variations in elemental binding energies. These chemical shifts can indeed be seen as the effect of the variations of the electron density of the valence orbitals (induced by chemical environment and oxidation state) on the initial atomic

energy and on the final energy resulting from the photoelectron emission. Chemical analysis is thus performed by decomposing core-shell elemental spectra into various components centered on specific binding energies depending on the existing bonds. A library of binding energies reported for interphasial species can be found in **Table AI-1**. As a result, the chemical composition of the extreme surface can be described very precisely.

Although this technique is particularly powerful for this type of studies, the use of polymers like PVDF as mechanical strengtheners in the composite electrodes masks a number of interesting XPS signals, especially on *C 1s* and *F 1s* core spectra. Encouraged by the work of Lestriez *et al.* on aqueous based electrode formulation [13-15], we decided during this thesis to change for carboxymethylcellulose (CMC) binder to avoid such handicap during XPS and NMR analyses. Besides this very pragmatic argument, this idea was of course to accompany the turn toward more environmental friendly electrode formulation taken by our group.

Unfortunately, elemental or chemical quantification using XPS appears relatively tricky due to the rapid intensity decay with the depth probed. From Eq. 2, it is easily noticed that chemical inhomogeneities along **z** critically influence the quantification results. The mean compositions obtained are thus severely affected by the so-called screening effect of surface species, overestimated compared to those they overlap. A realistic quantification therefore requires a basic knowledge of the interphase architecture.

I-2.2. Depth profiling

In the domain of thin films, it is often possible to describe the architectures of stacked layers by XPS thanks to ion etching, highlighting multi-layered geometries (e.g. layers thickness and stacking order). Although encouraging in earlier studies focused on Li-ion batteries, it is now commonly agreed that Ar^+ sputtering on interphases dramatically modifies their composition, due to preferential evaporation and/or redeposit of extraneous species [16]. Hence, non-destructive depth profiling using photoelectron spectroscopy (PES) is rather performed by varying the beam wavelength in order to tune the penetration depth $\lambda.\cos(\theta)$. For a given chemical bond (e.g. $\boldsymbol{E_B}$), $\boldsymbol{E_k}$ varies with $\boldsymbol{h\nu}$ according to ***Eq. 1***; the harder the X-rays (i.e. the smaller the source wavelength), the longer the escape depth, and the deeper the sample is analyzed. This type of study is nowadays increasingly reported [19-21], thanks to technical developments as well as the accessibility of tunable synchrotron radiation.

C 1s	*Binding energy*	*References*
C-Li bonds	282.5 eV	[22]
C-C bonds (graphite)	284 eV	[23, 24]
C-C bonds (MCMB)	284.2 eV	[25]
C-C bonds (HOPG)	284.3 - 284.4 eV	[25]
C-C bonds (polyolefin)	284.6 eV	[22]
C-C bonds (amorphous carbon)	285 eV	[23]
C-H bonds (Hydrocarbon/polymeric contamination)	284.8 - 285 eV	[24-30]
C-C bonds ($EtOCO_2Li$)	285.3 eV	[28]
C-O bonds (C-O-H or C-O-C bonds)	285.5 eV	[22]
C-O bonds (ethereal linkage)	286-288 eV	[22, 24, 31]
C-O bonds ($EtOCO_2Li$)	286.4 eV	[28]
C-O bonds ($MeOCO_2Li$)	286.7 eV	[28]
C-O bonds ($ROCO_2Li$/PEO oligomers)	286 - 288 eV	[22, 23, 27-29, 31]
C-O bonds (ROLi)	286.5 – 287.5 eV	[24, 26, 31]
C-O bonds (LiOCOR)	288 eV	[26]
CO2 bonds	289.0-289.3 eV	[26, 27]
CO3 bonds ($ROCO_2Li$ / Li_2CO_3)	288 - 291 eV	[22-33]
CF2 bonds (PVDF)	291 - 291.2 eV	[29]
CF3 bonds	293 - 293.7 eV	[29]

O 1s	*Binding energy*	*References*
Li-O bonds (Li_2O)	528-529 eV	[26, 30, 31]
Li-O-C bonds (ROLi)	528 eV	[31]
C-O bonds (ethereal linkage)	531 - 533 eV	[24, 31]
C=O bonds	531.5 eV	[22]
Li-O-H bonds (LiOH)	531.6 - 532 eV	[25, 30]
CO3 bonds (Li_2CO_3)	531.5 - 533 eV	[23, 25-28, 30, 31]
C-C bonds ($ROCO_2Li$)	531.8 eV	[28]
C-O bonds ($ROCO_2Li$)	531.8 - 532.5 eV	[23, 24, 28]
Li-O-C bonds ($LiOCH_3$)	532.3 eV	[26]
C-O bonds (C-O-H)	532.5 eV	[22]
P-O bonds (P_2O_5)	533 eV	[23]
CO3 bonds ($ROCO_2Li$)	533.3 - 534 eV	[23, 24, 27, 28]
C-O bonds (PEO oligomers)	533-533.5 eV	[23, 27]

Li 1s	*Binding energy*	*References*
Li-O bonds (Li_2O)	53.7 - 55 eV	[26, 31, 32]
Li-O-H bonds (LiOH)	54.7 - 55.6 eV	[25]
Li-O bonds (Li_2CO_3)	54.7 - 55.6 eV	[25, 23, 26, 28]
Li-O bonds ($ROCO_2Li$)	55 eV	[23]
Li-O bonds ($EtOCO_2Li$)	55.5 eV	[28]
Li-O bonds ($MeOCO_2Li$)	55.5 eV	[28]
Li-F bonds (LiF)	55.6-56.5 eV	[25, 26, 31, 32]
Li-P bonds ($LiPF_6$)	58.2 eV	[29, 33]

F 1s	*Binding energy*	*References*
Li-F bonds (LiF)	685-686.2 eV	[22, 24-27, 29-31]
P-F bonds ($LiPF_6$)	686.5 - 687.9 eV	[24, 27, 29, 33]
P-F bonds (Li_xPF_y)	687 eV	[23]
C-F bonds (PVDF)	687.5 - 688 eV	[24]
P-F bonds ($Li_xPO_yF_z$)	688 eV	[24]

P 2p	*Binding energy*	*References*
P-O bonds ($Li_xPO_yF_z$ or PO_4 ending PEO)	134.2 eV	[27]
P-O bonds (P_2O_5)	135 eV	[23]
P-F bonds ($L_{ix}PF_y$)	137 eV	[23]
P-F bonds ($LiPF_6$)	136.5 - 138.2 eV	[27, 29, 33]

Table AI-1. Binding energies characteristic of elements found in interphasial species.

In this thesis, we implemented XPS depth profiling by varying the second accessible parameter, i.e. the incident angle, using a Kratos Ultra Axis spectrometer equipped with a Al K_α monochromator, as illustrated in **Figure AI-1**. Contrary to energy resolved depth profiling, this second method requires an extremely flat surface, and cannot be applied to powder samples. Thin films exhibiting a roughness < 1 nm were used, thanks to our collaboration with Pr. Kanno's group in Tokyo Tech.

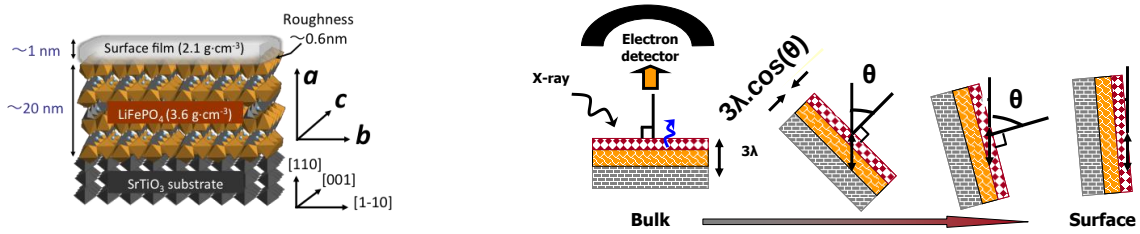

Figure AI-1. (a) $LiFePO_4$ thin film model and (b) Principle of an angular resolved XPS experiment, the 3λ.cos(θ) approximation for the penetration depth remains valid for $\theta \leq 60°$

Considering the chemical inhomogeneity of the interphase, as very simple model is used here, considering a surface layer homogeneous in thickness ($\boldsymbol{d}$) and an average composition ($\boldsymbol{\lambda}$).The angular dependence of an XPS signal of the substrate (here our active material) can be written as follow:

$$\boldsymbol{C}(\boldsymbol{\theta}) = \boldsymbol{C}_0.\exp(-\boldsymbol{d}/\boldsymbol{\lambda}.\cos(\boldsymbol{\theta})) \qquad \text{(Eq. 5)}$$

where $\boldsymbol{d}$ is the thickness of the covering layer and $\boldsymbol{\lambda}.\cos(\boldsymbol{\theta})$ the penetration depth of the X-ray within this surface layer. After selecting a necessary average $\boldsymbol{\lambda}$ value (see **Fig. AI-2**), the surface layer thickness $\boldsymbol{d}$ can be determined by fitting linearly $\ln[\boldsymbol{C}(\boldsymbol{\theta})]$ vs. $1/\cos(\boldsymbol{\theta})$.

Besides, the precision on $\boldsymbol{\theta}$ varies with the chosen experimental settings but ranges typically from 5 to 10°. As a result, this calculation is extremely rough, and values determined by this way were carefully confronted to those obtained through X-Ray Reflectivity (XRR) measurements.

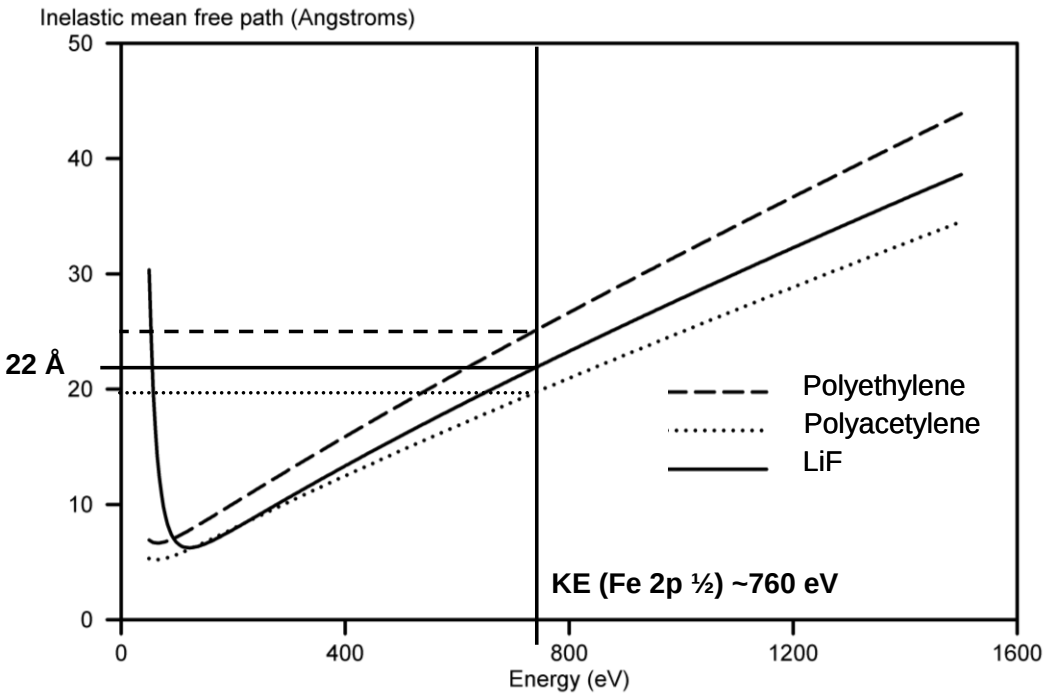

Figure AI-2. Simulated inelastic mean free paths for LiF, polyethylene and polyacetylene, illustrating the error maid assuming an average λ value within the interphase.

Nonetheless, from a qualitative point of view, angular resolved XPS analyses can provide significant insight on the interphase architecture by estimating the exaltation of XPS signal from surface species, compared to bulk species. At this aim, we introduce here for a chemical species ***A*** detected, a k_A factor calculated as follows:

$$k_A = \ln\left[\frac{C(\theta = 60°)_A / C(\theta = 60°)_{ref}}{C(\theta = 0°)_A / C(\theta = 0°)_{ref}}\right] \qquad \text{(Eq. 6)}$$

where $C(\theta = x°)_i$ is the concentration determined for the XPS signal of ***i*** measured for an angle θ defined as above. The notation ***ref*** refers to a given XPS signal chosen as the reference of the interphase profile, typically arising from a species present in bulk active material, such as the *M 2p* for a transition metal cathode, expected to mark out the interface.

- $k_A \leq 0 \Leftrightarrow A$ is located in the bulk; its relative detection decreases along surface enhanced measurement.
- $k_A \geq 0 \Leftrightarrow A$ is located in the interphase; its relative detection increases along surface enhanced measurement. The larger k_A, the larger the difference between surface ($\theta = 60°$) and average ($\theta = 0°$) concentration of ***A***.

Sorting the detected species along increasing k_i values therefore provides a good assumption of the stacking order of chemical species within the interphase, from the bulk active material

toward the outside. Such experiments were conducted on $LiFePO_4$ thin films, and therefore are described and commented further in Chapter 4.

Vibrational spectroscopies and XPS roughly give access to the same information: the interphase chemistry. While the decomposition of a FTIR spectrum into specific and quantitative components reveals more complicated than XPS, its depth-dependant response and the resulting screening effect works against the latter. Therefore, chemical characterization performed by XPS will always be considered qualitatively in this work, and elemental quantification discussed in the light of more unequivocal techniques.

I-3. Electrochemical spectroscopies

I-3.1 Electrochemical impedance spectroscopy (EIS)

EIS is probably the most affordable tool for the *in situ* monitoring and diagnosis of interfacial reactions.

An electric dipole is characterized by its complex impedance $\boldsymbol{Z}$ defined by Ohm's law that correlate the current $\boldsymbol{I}$ that goes through to the potential $\boldsymbol{U}$ measured between its limits:

$$\boldsymbol{E} = \boldsymbol{Z}.\boldsymbol{I} \qquad \text{(Eq. 7)}$$

where $\boldsymbol{U}$, $\boldsymbol{Z}$ and $\boldsymbol{I}$ are complex numbers. Complex impedance $\boldsymbol{Z}$ can be written under the form $\boldsymbol{Z=Z'+ j.Z''}$ where $\boldsymbol{Z'}$ and $\boldsymbol{Z''}$ are its real and imaginary part, respectively. An EIS measurement consists in applying a sinusoidal voltage $\boldsymbol{E_0.cos(\omega t)}$ and analyzing the resulting intensity $\boldsymbol{I_0.cos(\omega t+\Phi)}$, i.e. the amplitude $\boldsymbol{I_0}$ and the change in phase $\boldsymbol{\Phi}$ compared to the applied voltage. Then,

$$\boldsymbol{Z} = |\boldsymbol{Z}|.(\cos\boldsymbol{\Phi} + \boldsymbol{j}\sin\boldsymbol{\Phi}) = \left|\frac{\boldsymbol{E}_0}{\boldsymbol{I}_0}\right|.(\cos\boldsymbol{\Phi} + \boldsymbol{j}\sin\boldsymbol{\Phi}) \qquad \text{(Eq. 8)}$$

And thus,

$$\boldsymbol{Z}' = \left|\frac{\boldsymbol{E}_0}{\boldsymbol{I}_0}\right|.\cos\boldsymbol{\Phi} \qquad \text{and} \qquad \boldsymbol{Z}'' = \left|\frac{\boldsymbol{E}_0}{\boldsymbol{I}_0}\right|.\sin\boldsymbol{\Phi} \qquad \text{(Eq. 9)}$$

$\boldsymbol{I_0}$ and $\boldsymbol{\Phi}$ depending on the frequence ω, the characterization of electric properties requires multiple measurements over a wide ω range. For each frequency the [$\boldsymbol{Z}$'; $\boldsymbol{Z}$''] couple can be reported on the so-called Nyquist plot ($\boldsymbol{Z}$'' vs. $\boldsymbol{Z}$') which is characteristic of the system. The amplitude $\boldsymbol{E_0}$ of the sinusoidal voltage should always be carefully set to ensure both a linear response of the system (the smaller $\boldsymbol{E_0}/\boldsymbol{E}$, the better, see Eq. 7) and a satisfying signal to noise ratio (the larger $\boldsymbol{I_0}/\boldsymbol{I}$, the better). In the present work, impedance measurements were

performed using E_0 = 10 mV, at the open circuit voltage (OCV) or at the end of charge and discharge, after a 5 h relaxation step.

Early researchers proposed that the electrical properties of the electrode / electrolyte interface result from a combination of charge transfer resistance coupled with interfacial double layer capacitance, interphase resistance to Li^+ migration coupled with film capacitance, Li^+ diffusion in electrodes, etc [34, 35]. On impedance diagrams, the various time constants influencing the Li interfacial electrical properties can be separated and eventually assigned to one of those specific interfacial processes. Moreover, using a 3 electrodes-cell, EIS allows distinguishing the contributions from each electrode and analyzing the sources of battery impedance or identify battery failure. The analysis is usually based on the modeling and fitting of experimental results with appropriate equivalent-circuit analogs.

To depict interfacial phenomena, equivalent-circuits comprising for instance a single resistance or a resistance and a capacitance in parallel are commonly used, to model the electrolyte resistance (R_{el}, see **Fig. AI-3a**) or a charge transfer resistance (R_{ct}) coupled with a double layer capacitance (C_{dl}), respectively. In the second case, the impedance of the positive electrode (Z_p) is given by $1/Z_p = 1/R_{ct} + jC_{dl}\omega$ and thus:

$$Zp = \frac{R_{ct}}{1 + R_{ct}^{\,2} C_{dl}^{\,2} \omega^2} - j \frac{R_{ct}^{\,2} C_{dl} \omega}{1 + R_{ct}^{\,2} C_{dl}^{\,2} \omega^2} \qquad \text{(Eq. 10)}$$

Noteworthy, this equation describes a semi-circle of diameter R_{ct} in the Nyquist plot (see **Fig. AI-3b**). Similarly, each interphase model can be translated into an equivalent-circuit using a series of analogs which can be confronted to experimental data by mathematical fitting.

- The typical Solid Electrolyte Interphase (SEI) model consists in a homogeneous layer comprised of inorganic compounds which properties are close to that of a solid electrolyte. The presence of such layer is depicted by a resistance (R_{SEI}) and capacitance (C_{SEI}) in parallel added in series to the impedance characterizing the electrolyte (R_{el}) and electrode (Z_p), giving rise to two semi-circles in the Nyquist plot, as shown in **Figure AI-4c** [34].
- The Polymer Electrolyte Interphase (PEI) model can be seen as a compact mixing of polymeric species with inorganic compounds [36]. The layer exhibits the properties of a polymer electrolyte. Although the corresponding equivalent circuit is more complex (**Fig. AI-3d**), the resulting Nyquist diagram remains close to that of the SEI.

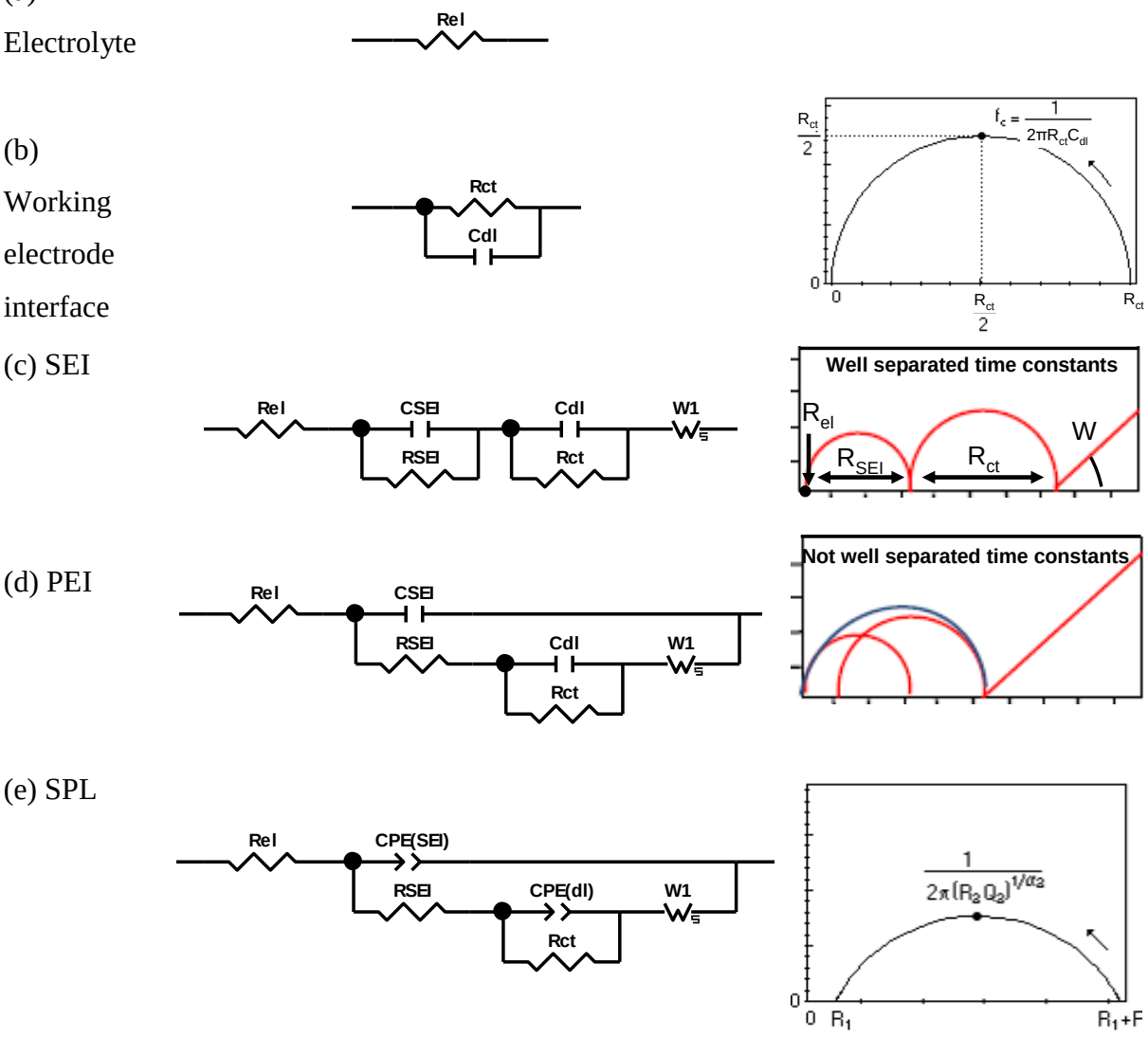

Figure AI-3. Equivalent circuits typically used in EIS to model the electrode / electrolyte interface.

- In the Solid Polymer Electrolyte (SPL) model, the interphase can be considered as a mixing of solid inorganic species dispersed in a polymer electrolyte matrix and the equivalent circuit is identical to that of the PEI [37, 38]. However in this case, the time constants characterizing the different processes might be too close to result in well separated semi-circles. A single flat loop is then observed, which distortion from the semi-circle can be seen as a dispersion of time constants for a sole process.

  In that case, a Constant Phase Element (CPE) can also be used instead of pure capacitance (**Fig. AI-3e**). Its impedance, $1/\boldsymbol{Z}_{\boldsymbol{CPE}}(\boldsymbol{\omega}) = \boldsymbol{C}(\boldsymbol{j\omega})^{\boldsymbol{p}}$, introduces a resistive component to the capacitance trough the parameter $\boldsymbol{p}$ and defines the

phase angle $\beta : \beta = \frac{p\pi}{2}$ with $0 \leq p \leq 1$ so as to convey the dispersion of time constants observed for experimental systems [39].

- Last, the Compact Stratified Layer (CSL) describes the interphase as the superimposition of different SEI [40, 41]. The equivalent circuit is therefore based on the addition of different R_{SEI} // C_{SEI} in series. Depending on their characteristic time constants, those SEI units might not be well resolved, also giving rise to a flat loop.

As intuited by the observation of **Figure AI-3**, it was demonstrated that excellent matching of an experimental diagram could be reached by several different equivalent circuit analogs, even though each of these electrical models depicts different surface physics and chemistry [42]. Therefore, conclusions drawn from EIS are always strongly dependant on the chosen analogs model, and efforts are being made to rather develop physical models based on diffusion equations, that would provide a more realistic view of the interphase through meaningful fitting parameters [43].

I-3.2 Electrochemical quartz crystal microbalance (EQCM)

EQCM has been widely used for the study of electrochemical systems, and several comprehensive reviews of the application of this technique to Li-ion electrochemistry have already appeared in the literature [44, 45]. The technique uses the piezoelectric properties of a thin quartz crystal placed between two electrodes (one being the working electrode) to measure changes in the attached surface mass. Its application to monitor surface film formation in Li-ion batteries was thought to enable access to fine details such as the order of deposition of surface species and their exact molar mass, the rates of dissolution of solution species and the selectivity of the electrodes at different potentials. An early report from Aurbach's group [46] suggests the precipitation of LiF and $Li_xPO_yF_z$ at low potential and carbonates at high potential on a lithium metal electrode in a $LiPF_6$/PC solution. However, due to its non specificity (EQCM only provides the mass accumulated on electrode per mole of electrons aka mpe), the interpretation of EQCM data for these systems depends on identification of the surface species formed using spectroscopic techniques. Besides, electrolyte decomposition products might be partially dissolved into solution and/or electrolyte molecules adsorbed on electrode before the electrochemical reactions take place.

This complexity of surface reactions explains why the use of EQCM actually remained rather anecdotic.

Though the common disadvantage of all electroanalytical techniques is the ambiguousness of the response measured, they balance adequately with powerful spectroscopies such as XPS and NMR requiring the battery to be dismantled and the interphase to be perturbed from its operating state. The trend regarding the development of analytical techniques in the field of Li-ion batteries is actually to overcome both drawbacks by adapting experimental setups to seek operando acquisition. In addition to above mentioned studies making use of in situ FTIR or Raman spectroscopies, the following section is dedicated to exploratory works demonstrating the feasibility of more exotic in situ surface characterization, opening doors for direct observation of interphase formation and evolution.

I-4. Emerging techniques

I-4.1 Neutron depth profiling (NDP) [47-48]

NDP is a nuclear analytical technique that bombards a planar sample with thermal neutrons. The absorption of a neutron by ^{6}Li atom results in an alpha and triton particle emission, as shown here: $^{6}Li + n \rightarrow \alpha + {}^{3}H$. The emitted alpha and triton particles exit the sample having lost energy due to the interactions they experienced with the other electrons and nuclei in the sample. The energy loss can be scaled per length unit of the path that it travelled through the sample, and allows determining a depth profile of the light isotope within the sample and *in situ* studying the Li-concentration inside the battery upon (dis)charging.

I-4.2. In situ Transmission Electronic Microscopy (TEM) [49-51]

In contrast to the composite electrodes/electrolyte interfaces in conventional lithium ion batteries, where quantitative interface characterization is extremely difficult; Meng *et al*. have developed a novel *in situ* instrumental system to probe dynamic phenomena in an all solid-state nano-battery prepared using focused ion beam (FIB). Although the *operando* observation of a thin film battery in a TEM equipped with spectroanalytical tools such as Electron Energy Loss Spectroscopy (EELS) remains a major challenge, it is realistic to foresee the real-space observation of the extraction and insertion behaviors of Li ions in electrode materials and their interphases using spectrum-imaging.

From a broader point of view, the use of ionic liquid electrolytes together with the development of environmental TEM or XPS equipped with differential pressure pumps, is certainly offering tremendous opportunities to measure samples in conditions always closer to their operating state.

I-5. Concluding remarks

A variety of spectroanalytical techniques enables the investigation of interphases in a Li-ion battery. From a technical point of view, each of them possesses its own challenges and rewards but none can reach alone a wide angle 3D chemical mapping of such particular phases. However, there is no reason to pick up a single technique and satisfy with a blurred and/or truncated picture.

The determining role of the interphases on the safety and life time of Li-ion batteries requires their accurate qualitative and quantitative characterization. However, the review of classical surface characterization methods highlights important missing information: the amount of interphase species, that we propose to probe thanks to NMR spectroscopy.

The philosophy behind the present work consists in crossing spectroanalytical results obtained from different techniques (namely XPS, EIS, NMR and EELS) and assembling into a multiple spectral database correlated to electrochemical performance.

II – INTRODUCTION TO NMR

II-1. Fundamental interactions with external magnetic field

Basically, nuclear magnetic resonance (NMR) spectroscopy detects re-emitted electromagnetic radiation from magnetic nuclei placed in a magnetic field. However, only isotopes that exhibit a nonzero spin $\boldsymbol{I}$ are observable. Since they are electrically charged, they also have an intrinsic magnetic moment $\boldsymbol{\mu}$, caused by transitions between nuclear spin levels at the origin of the NMR phenomenon. μ is given by:

$$\boldsymbol{\mu} = \gamma.\hbar.\boldsymbol{I} \qquad \text{(Eq. 11)}$$

γ_N is the gyromagnetic ratio of the investigated NMR isotope, and $\hbar$ the reduced Planck constant. Nuclei can therefore be treated as small magnetic dipoles susceptible to interact with an applied external magnetic field.

In the absence of external field, all nuclear spin states are degenerate, (i.e. there is no energy difference between them). Hence the population of these states will be approximately equal at thermal equilibrium. On the contrary, when placed in an external static magnetic field $\boldsymbol{B_0}$, the nuclear spins align either with or against the magnetic field. The so-called Zeeman interaction between the nuclear magnetic moment $\boldsymbol{\mu}$ and $\boldsymbol{B_0}$ has a total energy $\boldsymbol{E}$ given by: $\boldsymbol{E} = -\boldsymbol{\mu}.\boldsymbol{B}_0$. The individual Zeeman energy corresponding to the $2\boldsymbol{I}$+1 nuclear spin states is:

$$\boldsymbol{E}_{\boldsymbol{m}} = -\boldsymbol{m}.\gamma.\hbar.\boldsymbol{B}_0 \qquad \text{(Eq. 12)}$$

with $\boldsymbol{m}$ the magnetic quantum number ($\boldsymbol{m}$= 1, I-1…, -I). As a result the different nuclear spin states have different energies in a non-zero magnetic field and the energy difference between the two adjacent states is:

$$\Delta\boldsymbol{E} = \gamma.\hbar.\boldsymbol{B}_0 \quad \text{(Eq. 13)}$$

As shown by Eq. 13, the energy difference absorbed by each nucleus is proportional to γ_N. Hence for NMR experiment purpose, the larger the gyromagnetic ratio, the more sensitive the nucleus.

A NMR experiment usually involves the sequential application of two magnetic fields. As explained above, the permanent external magnetic field $\boldsymbol{B_0}$ results in the alignment (polarization) of the magnetic nuclear spins. At the equilibrium, the macroscopic magnetization $\boldsymbol{M_0}$ is thus parallel to $\boldsymbol{B_0}$.

The perturbation from the equilibrium is then performed by employing a radio frequency (RF) magnetic field $\boldsymbol{B_1}$. As shown in **Figure AI-4**, the magnetization $\boldsymbol{M}$ responds by a precession around $\boldsymbol{B_0}$ called the Larmor precession. Resonant absorption by nuclear spins will occur when a RF pulse of the correct perturbing frequency (e.g., equaling the Larmor precession rate ν_L) is being applied to match ΔE. The signal will be maximal when $\boldsymbol{M}$ is located in the transverse plane (the xOy plane perpendicular to $\boldsymbol{B_0}$) for a $\pi/2$ pulse duration.

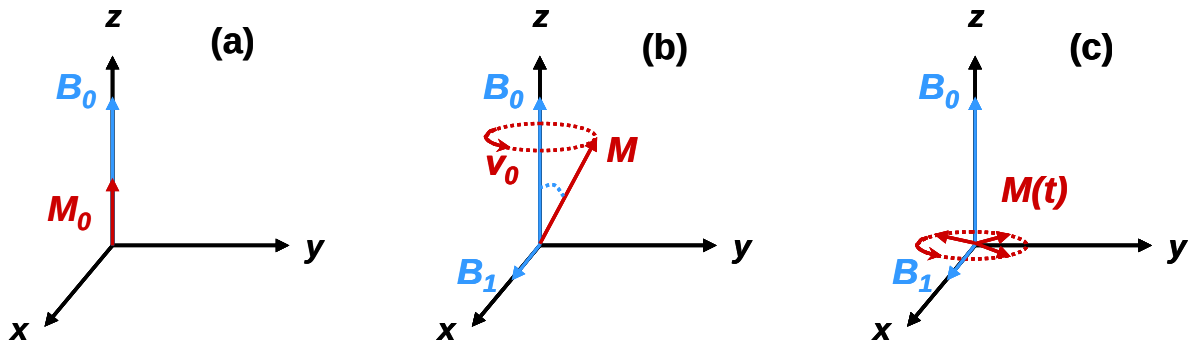

Figure AI-4. Evolution of magnetization before (a) and during the application of the RF pulse (b). For a a $\pi/2$ pulse duration, the magnetization is transferred in the transverse xOy.

Transitions between adjacent states are then allowed and the resulting time-dependant relaxations of the magnetic nuclear spins are the phenomena that are exploited in NMR spectroscopy. The relaxation phenomena can be distinguished via two distinct relaxation times:

- T_2, the transverse (or spin-spin) relaxation time, defines the lifetime of the signal in the transverse plane (xOy plane). The time dependant signal of the return to equilibrium in this plan is recorded in the reception/emission coil and is known as the Free Induction Decay (FID). Applying a Fourrier transform to the FID results in the NMR spectrum. The evolution of the FID (and thus the NMR spectrum) depends on the interactions present in the solid, as developed in the following section.
- T_1, the longitudinal (or spin-lattice) relaxation time, represents the lifetime of the process that returns the magnetization to the Boltzman equilibrium along the z axis. The relaxation mechanisms observed in the solid exhibit distinct amplitude ranges (from 10^1 to 10^9 Hz) and therefore significantly influence the T_1. The interval between 2 transients should be long enough ($D_1 \approx$ 3- 5 T_1) to recover the $\boldsymbol{M_0}$ magnetization. This condition is necessary to ensure an accurate quantitative integration of NMR spectra. At this aim, experimental spin-lattice relaxation times (T_1) were measured by saturation

recovery method under MAS conditions and the recycle times were accordingly in the 0.5-720s. To do so, 400 scans were recorded for each of the 10 data points and enough signal could be observed for the last point, after 10 rotor periods. The negligible change in intensity observed for the last data points ensured us that saturation was reached and that enough points were recorded to deduce an accurate T_1 value.

II.2. Internal interactions and magic angle spinning

Depending on the electronic cloud surrounding the probed nucleus, several kinds of nuclear spin interactions are met in solid state NMR, as listed in **Table AI-2**. The magnitude of Zeeman interaction is such that all others might appear as perturbations.

Interaction	Cause	Amplitude (Hz)	Information	Field dependency
Zeeman	Interaction with B_0 magnetic field	10^7 -10^9	Nucleus selection	$\propto \boldsymbol{B}_0$
Chemical Shift	Local field modification by electrons	10 - 10^4	First neighbors, coordination	$\propto \boldsymbol{B}_0$
Dipolar spin-spin coupling	Spin-spin interaction through space	10^4 - 10^5	Distances	Independent
Dipolar nuclear-electron spin coupling	Paramagnetic nuclear-spin interaction through space	10^7 -10^8	Distances	$\propto \boldsymbol{B}_0$
Quadrupolar coupling	Quadrupolar moment and electric field gradient interaction	10^6 - 10^9	Geometry	1^{st} order: independent 2^{nd} order: $\propto -1/\boldsymbol{B}_0$
Indirect J coupling	Spin-spin interaction through bonds	10 - 10^3	Bonds, distances	Independent

Table AI-2. Interactions present in the solid giving rise to NMR spectra.

- Chemical shielding is the result of currents induced at the nucleus by the application of an external field: a local magnetic field specific to the chemical environment is created. Its anisotropy gives rise to orientation dependent frequency shifts.
- The dipolar interaction results from the interaction of one nuclear spin with the local magnetic field generated by another nuclear spin. Chemical shift and dipolar interactions are considered as first order perturbation of the Zeeman interaction.

- Indirect J coupling describes the interaction of nuclear spins through chemical bonds. Its preponderant term is the Fermi contact, which describes the electronic orbitals overlapping of coupled nuclei.
- The quadrupolar interaction observed for $I > 1/2$ can be extremely important and unlike all of the other anisotropic NMR interactions, can be written as a sum of first and second order interactions.

All these interactions are anisotropic. In solution, molecules reorient quickly so that nuclear spins feel a time average of the spatial part of the Hamiltonians. Hence NMR spectra consist of a series of very sharp transitions. In the case of powders, in which crystallites are randomly oriented vs. B_0, first order interactions containing $(3\cos^2\theta - 1)$ terms cannot be averaged.

To enhance the spectral resolution, Magic Angle Spinning (MAS) technique introduces an artificial spinning motion of the sample at the magic angle (54.74°) with respect to B_0 in order to average the term $3\cos^2\theta - 1$ to zero, providing a MAS frequency greater than the magnitude of the anisotropic interaction. Values reported in Table X for chemical shift and dipolar interactions show that it is hardly possible experimentally and these interactions are therefore only reduced. In the place of very broad static solid state NMR spectra exhibiting the full effects of anisotropic interactions, a manifold of spinning sidebands (separated by the MAS rate in Hz) becomes visible.

In this work, ^{7}Li, ^{19}F and ^{31}P NMR experiments were carried out at room temperature on a Bruker Avance-500 spectrometer (B_0 = 11.8T, Larmor frequencies $\nu_0(^{7}\text{Li})$ = 194 MHz, $\nu_0(^{19}\text{F})$ = 470 MHz, $\nu_0(^{31}\text{P})$ = 202 MHz). MAS spectra were obtained by using a Bruker MAS probe with a cylindrical 2.5 mm o.d. zirconia rotor. Spinning frequencies of 23.5 kHz and 29 kHz were utilized for ^{19}F and ^{7}Li / ^{31}P MAS NMR experiments, respectively.

III – ELECTROCHEMICAL TESTS

This section devises the experimental setup and cycling protocols used in this thesis. **Figure AI-5** below shows the different constituents required to assemble a Swagelok®-type cell. These cells are known to suffer from a lower hermeticity compared to button-type cells at the scale of months or years, they are very easy to disassemble in the glovebox and enable the recovery of cycled electrodes.

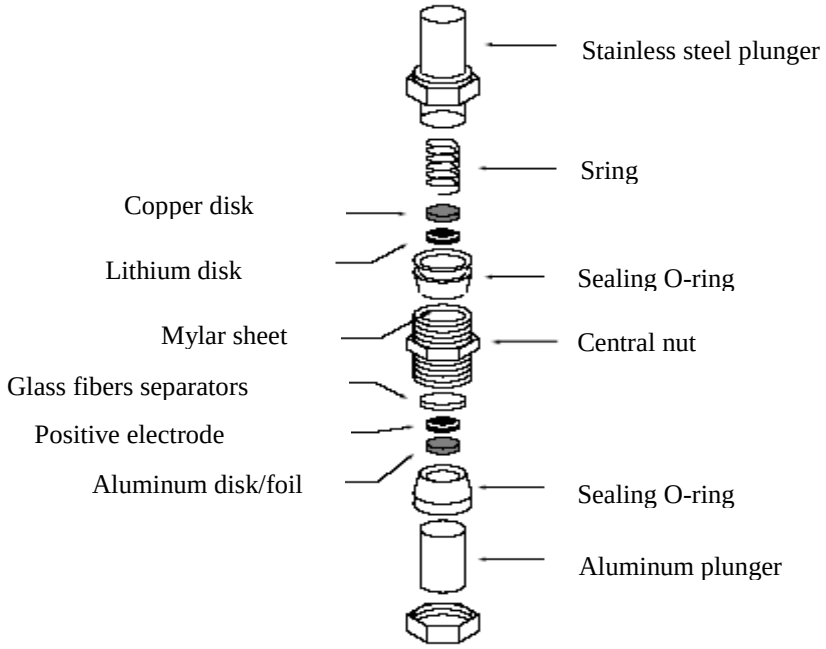

Fig. AI-5. Swagelok®-type cell used in this thesis

III-1. Definitions of the electrochemical dimensions used in this work

Parameters characterizing the Li intercalation reactions in an electrode material are defined as follows:

- The intercalation rate x can be determined from the amount of current Q_e involved in the Faraday law: $Q_e = \int_{t_{initial}}^{t_{final}} Idt = x\frac{m}{M}F$ $(Eq.14)$

  where F is the Faraday constant, m and M the mass and the molecular weight of the active material, respectively.

- The specific capacity, expressed in $Ah.kg^{-1}$ or $mAh.g^{-1}$, corresponds to the total amount of current available when the battery is fully (dis)charged from (up to) $\boldsymbol{x}$ Li:

$$\boldsymbol{Q} = \boldsymbol{x}\frac{\boldsymbol{F}}{3600}\frac{1000}{\boldsymbol{M}} \qquad (\boldsymbol{Eq}.15)$$

- Currents are often expressed as a C-rate in order to normalize against battery capacity. A C-rate is a measure of the rate at which a battery is discharged relative to its maximum capacity (in our cases, for $\boldsymbol{x}$ = 1). A 1C rate means that the discharge current will theoretically discharge the entire battery in 1 hour.

III-2. Typical electrodes formulation and benchmarking used in this work

The benchmarking employed here consists in the magnetic stirring of active material powder, Ketjenblack carbon and carboxymethyl cellulose (wt% 80/10/10) in water. After deposition on an aluminum disk with a typical loading of 20 mg (AM).cm^{-2}, this slurry is let to dry at room temperature overnight, pressed under 2 tons.cm^{-1} and then dried under vacuum at 100°C for 4h before being used as positive electrode.

III-3. Typical electrochemical tests used in this work

Electrochemical cycling tests were carried out on Macpile, MPG2 and VMP3 Biologic multichannel galvanostats/potentiostats.

- Galvanostatic cycling was used most of the time. Since the rate and potential lower and upper limits may vary, they are made explicit in the text. 30 minutes-long rests are always programmed at the end of charge and discharge, except for the last sweep during which a 2 hours-long potential floating is applied.
- Power capability was evaluated using the cumulative discharges method. The two first cycles were performed at a C/20 or C/50 rate, and then the discharge profile consisted in applying a 4C current down to the cut off voltage, followed by a 30 min rest and then decreasing the discharge rate at 2C, 1C, C/2, C/5, C/10, C/20 and finally C/50. The power capacity for a given rate was then estimated by the sum of the discharge capacities obtained at higher and given rates.
- Potentiodynamic Cycling with Galvanostatic Acceleration (PCGA) was used to examine the electrochemical signature of the investigated materials. In this mode, the successive 5 mV steps of potential are applied, without going through an open circuit period, every

times the reduction (oxidation) current has reached a predefined value which is considered as negligible compared to the capacity of the system (set to C/1000). One gets in this way a set of quasi-equilibrium incremental capacities values, at periodic potential intervals corresponding to the potential step amplitude. When reported as ΔQ vs. the potential, the result of such an experiment is the incremental capacity voltammogram, obtained with the resolution of the potential step amplitude [52].

REFERENCES OF APPENDIX 1

[1] D. Aurbach, Y. Ein-Eli, O. Chusid, Y. Carmeli, H. Yamin. *J. Electorchem. Soc.*, **141** (1994), 603.

[2] Y. Ein-Eli, B. Markovsky, D. Aurbach, Y. Carmeli, H. Yamin, S. Luski. *Electrochim. Acta*, **39** (1994) 2559.

[3] D. Aurbach, A. Zaban, A. Shechter, Y. Ein-Eli, E. Zinigrad, B. Markovsky. *J. Electrochem. Soc*, **142** (1995) 2882.

[4] D. Aurbach, B. Markovsky, A. Shechter, Y. Ein-Eli, H. Cohen. *J. Electrochem. Soc.*, **143** (1996) 3809.

[5] G. Zhuang, K. Wang, G. Chottiner, R. Barbour, Y. Luo, I.T. Bae, D. Tryk, D.A. Scherson. *J. Power Sources*, **54** (1995) 20.

[6]Y. Ikezawa, T. Ariga. *Electrochim. Acta*, **52** (2007) 2710.

[7] R. Kostecki, "Interfacial processes – Diagnostics", http://batt.lbl.gov/battfiles/BattReview2011/es085_kostecki_2011_o.pdf

[8] T. Eriksson, *Comprehensive Summaries **651**, Faculty of Science and Technology*, Uppsala.

[9] D. Aurbach, B. Markvsky, I. Weissman, E. Levi, Y. Ein-Eli, *Electrochim. Acta* **45** (1999) 67.

[10] D. Bar-Tow, E. Peled, L. Bustein, *J. Electrochem. Soc*. **146** (1999) 824.

[11] H. Ota, T. Sato, H. Suzuki, T. Usami, *J. Power Sources*, **97–98** (2001) 107.

[12] S. Leroy, *Etude d'interfaces électrode/électrolyte dans les batteries au lithium. Approche par XPS et AFM*, Thesis in University of Pau (2006).

[13] Porcher W.; Moreau P.; Lestriez B.; et al. *Electrochem. And Solid State Lett*. **11** (2008) A4

[14] Mazouzi D.; Lestriez B.; Roue L.; et al. . *Electrochem. And Solid State Lett*. **12** (2009) A215.

[15] Sivasankaran V.; Marino C.; Chamas M.; et al. *J. Mater. Chem*., **21** (2011) 5076.

[16] Edstrom, K, Herstedt, M, Abraham, DP, *J. Power Sources*, **153** (2006) 380.

[17] M.P. Seah, W.A. Dench, *Surf. Interface Anal.*, **1** (1979) 2.

[18] Anna Andersson, *Comprehensive Summaries **656**, Faculty of Science and Technology*, Uppsala

[19] M. Herstedt, M. Stjerndahl, A. Nyten, T. Gustafsson, H. Rensmo, H. Siegbahn, N. Ravet, M. Armand, J. O. Thomas, K. Edstrom, *Electrochem. Solid-State Lett.*, **6** (2003) A202.

[20] S. Malmgren, H. Rensmo, T. Gustafsson, M. Gorgoi, K. Edström, *ECS Transactions*, **25** (2010) 201.

[21] L. Castro, R. Dedryvere, M. El Khalifi, P.- E. Lippens, J. Breger, C. Tessier, D Gonbeau *Lithium Battery Discussions #5* (2011).

[22] V. Eshkenazi, E. Peled, L. Burstein, D. Golodnitsky, *Solid State Ionics*, **170** (2004) 83.

[23] K. Edström, T. Gustafsson, J. O. Thomas, *Electrochim. Acta*, **50** (2004) 397.

[24] S.H. Kang, D.P. Abraham, A. Xiao, B. L. Lucht, *J. Power Sources*, **175** (2008). 526

[25] K. Kanamura, H. Tamura, Z. I. Takehara, *J. Electroanal. Chem.*, **333** (1992) 127.

[26] A. Nyten, M. Stjerndahl, H. Rensmo, H. Siegbahn, M. Armand, T. Gustafsson, K. Edstrom, J. O. Thomas, *J. Mat. Chem.*, **16** (2006) 3483.

[27] R. Dedryère, S. Laruelle, S. Grugeon, L. Gireaud, J. M. Tarascon, D. Gonbeau, *J. Electrochem. Soc.*, **152** (2005) A689.

[28] R. Dedryère, L. Gireaud, S. Grugeon, S. Laruelle, J. M. Tarascon, D. Gonbeau, *J. Phys. Chem. B*, **109** (2005). 15868

[29] S. Leroy, H. Martinez, R. Dedryère, D. Lemordant, D. Gonbeau, *App. Surf. Sci.*, **253** (2007). 4895

[30] I. Ismail, A. Noda, A. Nishimoto, M. Watanabe, *Electrochim. Acta*, **46** (2001) 1595.

[31] D. Aurbach, I. Weissman, A. Schechter, *Langmuir*, **12** (1996). 3991

[32] S. Shiraishi, K. Kanamura, Z. I. Takehara, *Langmuir*, **13** (1997). 3542

[33] R. Dedryère, S. Leroy, H. Martinez, F. Blanchard, D. Lemordant, D. Gonbeau, *J. Phys. Chem. B*, **110** (2006).

[34] E. Peled, *J. Electrochem. Soc.*, **126** (1979) 2047.

[35] D. Aurbach, B. Markovsky, M.D. Levi, E. Levi, A. Schechter, M. Moshkovich, Y. Cohen, *J. Power Sources* **81–82** (1999) 95.

[36] D. Ostrovskii, F. Ronci, B. Scrosati, P. Jacobsson, *J. Power Sources*, **103** (2001) 10.

[37] T. Eriksson, *Comprehensive Summaries* **651**, Faculty of Science and Technology, Uppsala.

[38] F. Croce, B. Scrosati, *J. Power Sources*, **43** (1993) 9.

[39] J. R. MacDonald, *Impedance Spectroscopy*, Wiley, New York, 1987.

[40] A. Zaban, E. Zinigrad, D. Aurbach, *J. Phys. Chem*. **100** (1996) 3089.

[41] E. Peled, 0. Golodnitsky, G. Ardel, *J. Electrochem. Soc.*, **144** (1997) L208.

[42] Orazem, M. E.; Agarwal, P.; Garcia Rubio, L. H. *J. Electroanal. Chem*. **378** (1994) 51.

[43] C. Pascot, P. Guillemet, R. Dugas, Y. Scudeller, T. Brousse, *«Analyse des phénomènes de transfert dans les supercondensateurs électrochimiques de puissance »*, Ecole Energie Recherche (2004).

[44] K. Shimazu, S. Ye, Y. Sato, K. Uosaki, *J. Electroanal Chem.*, **375** (1994) 409.

[45] S. Bruckenstein, M. Shay, *J. Electroanal. Chem.*, **180** (1985) 131.

[46] D. Aurbach, A. Zaban, *J. Electroanal. Chem.*, **393** (1995) 43.

[47] S. Whitney, S. R. Biegalski, Y. H. Huang, J. B. Goodenough, *J. Electrochem. Soc.*, **156** (2009) A886.

[48] P.H.L. Notten, *Lithium Battery Discussions #5 (2011)*

[49] J. Kikkawa, T. Akita, M. Tabuchi, M. Shikano, K. Tatsumi, M. Kohyama, *Electrochem. Sol.-State Lett.*, **11** (2008) A183.

[50] J. P. Sullivana, A. Subramaniana, J. Huanga, M. J. Shawa, N. Hudaka, Y. Zhanb, J. Loub, *Abstract #504*, 218th ECS Meeting, Las Vegas (2010).

[51] Meng, Y. S.; McGilvray, T.; Yang, M. C.; Gostovic, D.; Wang, F.; Zeng, D.; Zhu, Y. and Graetz, J. Interface 2011, in print

[52] Biologic, "*Electrochemistry - Application note n°2*", http://www.bio-logic.info/potentiostat/notes/Application%20note%202.pdf

APPENDIX 2. SUPPORTING NMR SPECTRA

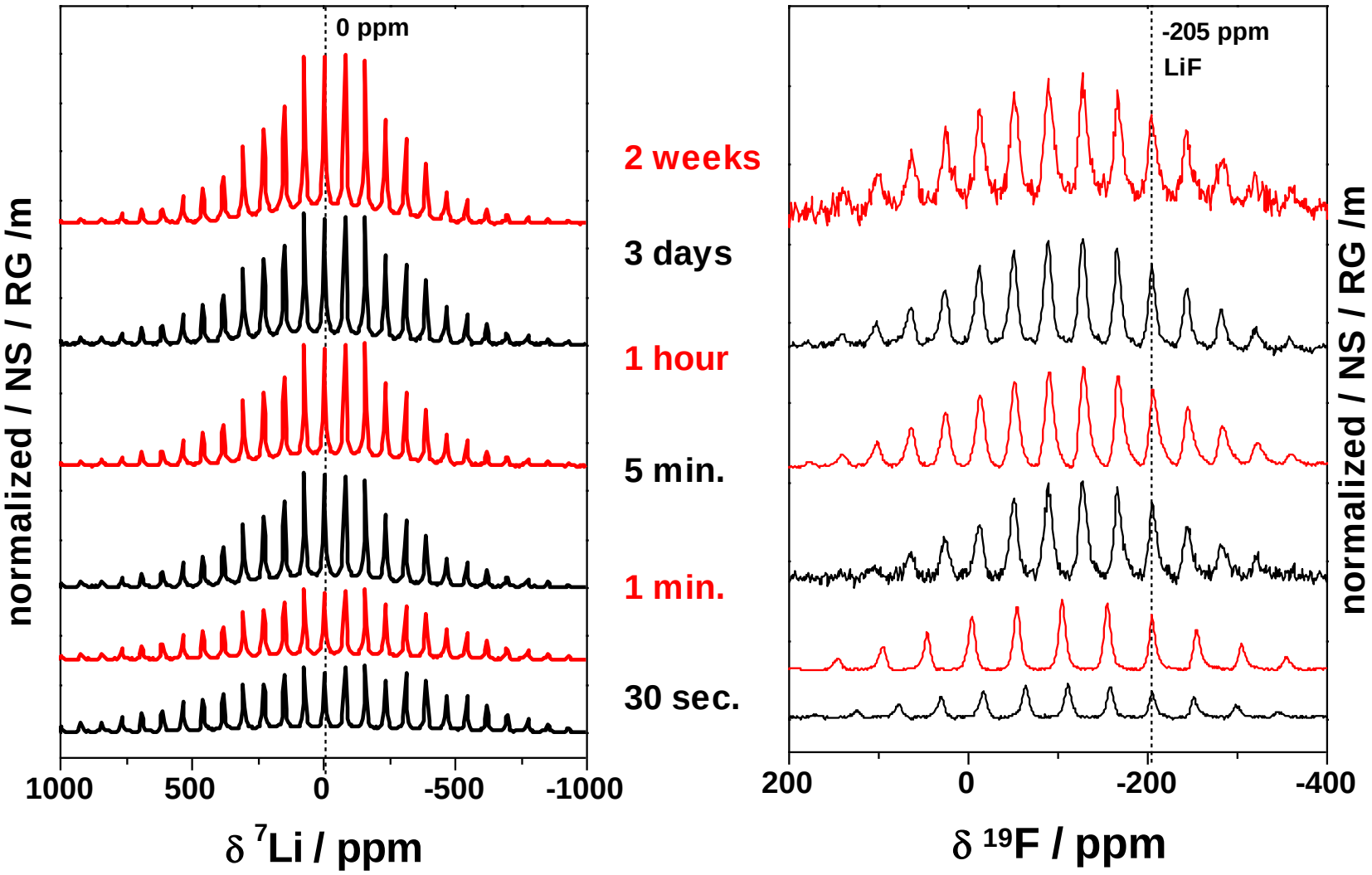

Figure AII-1. ^{7}Li (20 kHz) and ^{19}F (23.5 kHz) MAS NMR spectra of LMN½ soaked in conventional $LiPF_6$ in EC:DMC electrolyte for various durations. Dotted lines denote the position of isotropic shifts.

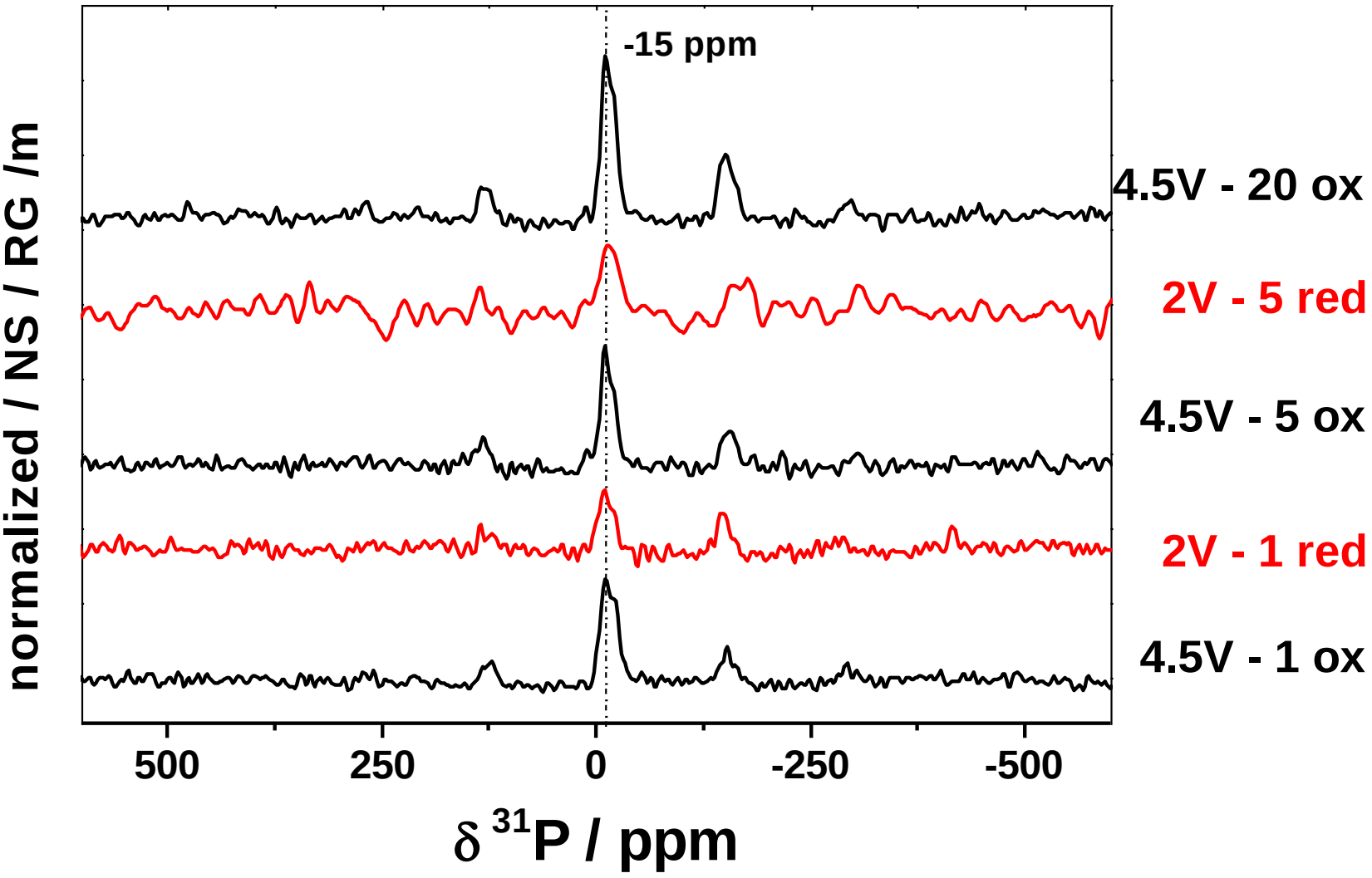

Figure AII-2. ^{31}P (29 kHz) MAS NMR spectra of LMN½ after stabilization at the end of the 1st, 5th and 20th charges and discharges in the conventional $LiPF_6$ 1M in Ec:DMC electrolyte.

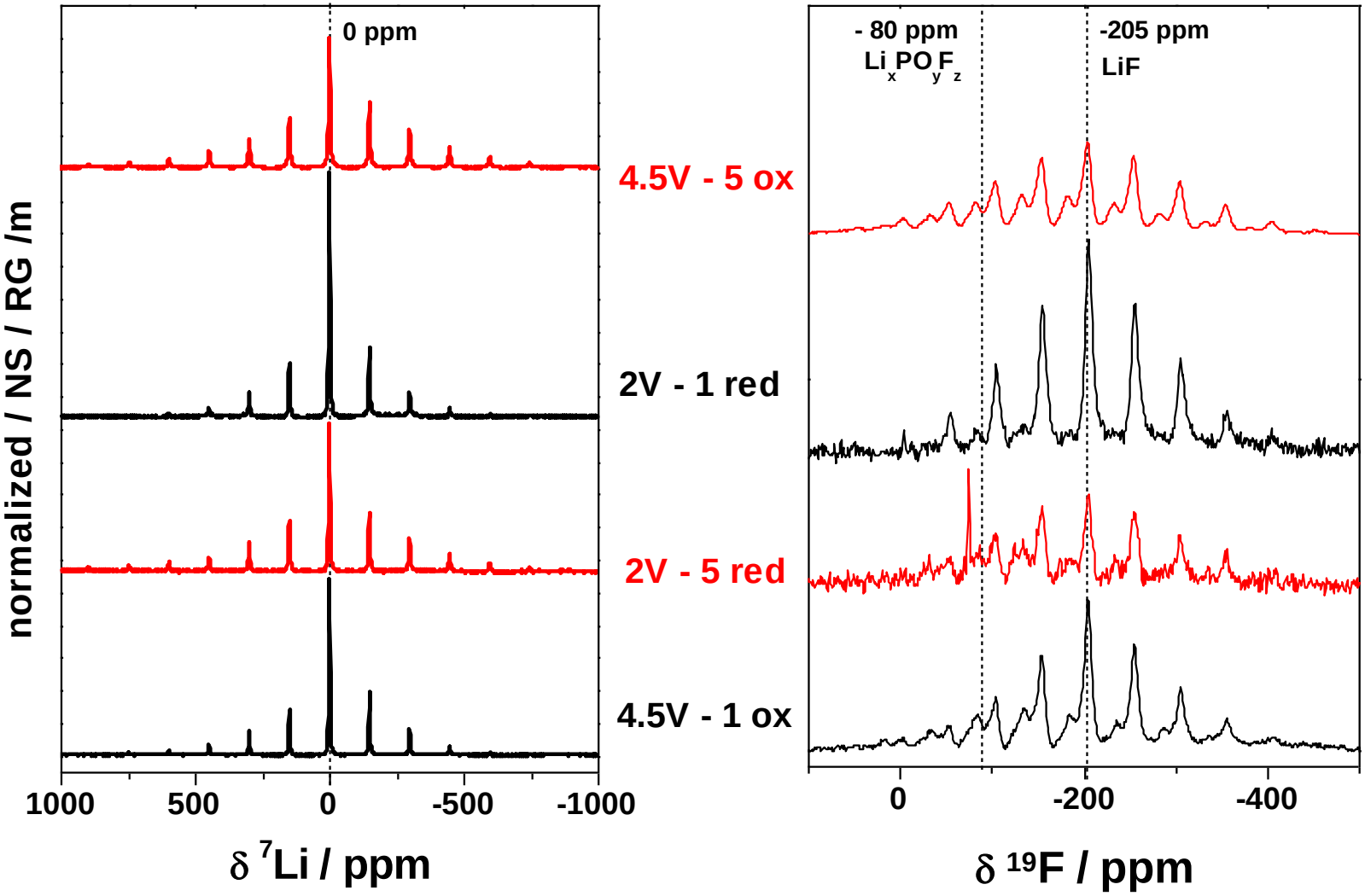

Figure AII-3. ^{7}Li (29 kHz) and ^{19}F (23.5 kHz) MAS NMR spectra of LMN½ after stabilization at the end of the 1st and 5th charges and discharges in conventional $LiPF_6$ in EC:DMC electrolyte when using the CMC/TX100/EC-based formulation. Dotted lines denote the position of isotropic shifts.

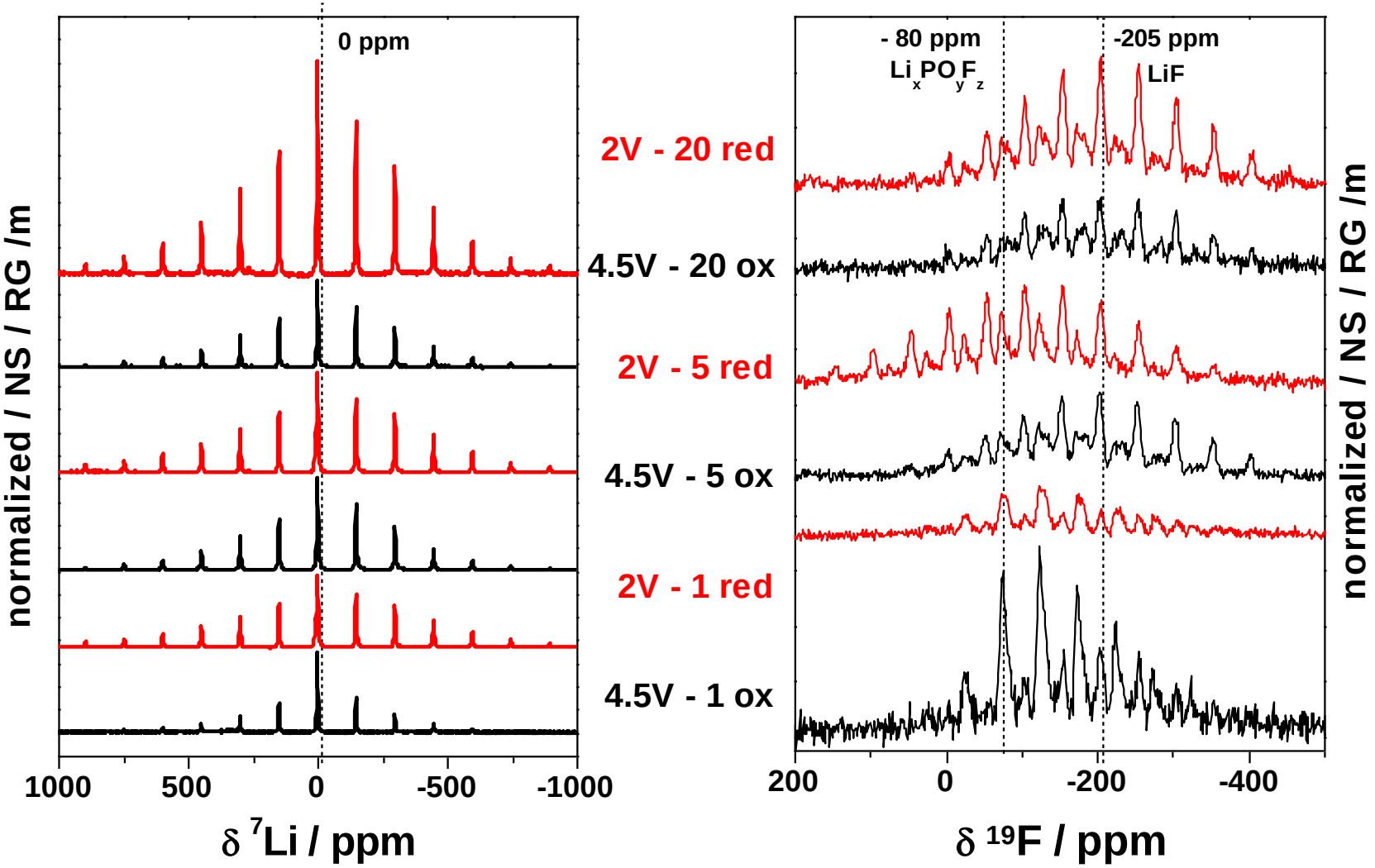

Figure AII-4. ^{7}Li (29 kHz) and ^{19}F (23.5 kHz) MAS NMR spectra of LMN½ after stabilization at the end of the 1st, 5th and 20th charges and discharges in the LiBOB modified electrolyte. Dotted lines denote the position of isotropic shifts.

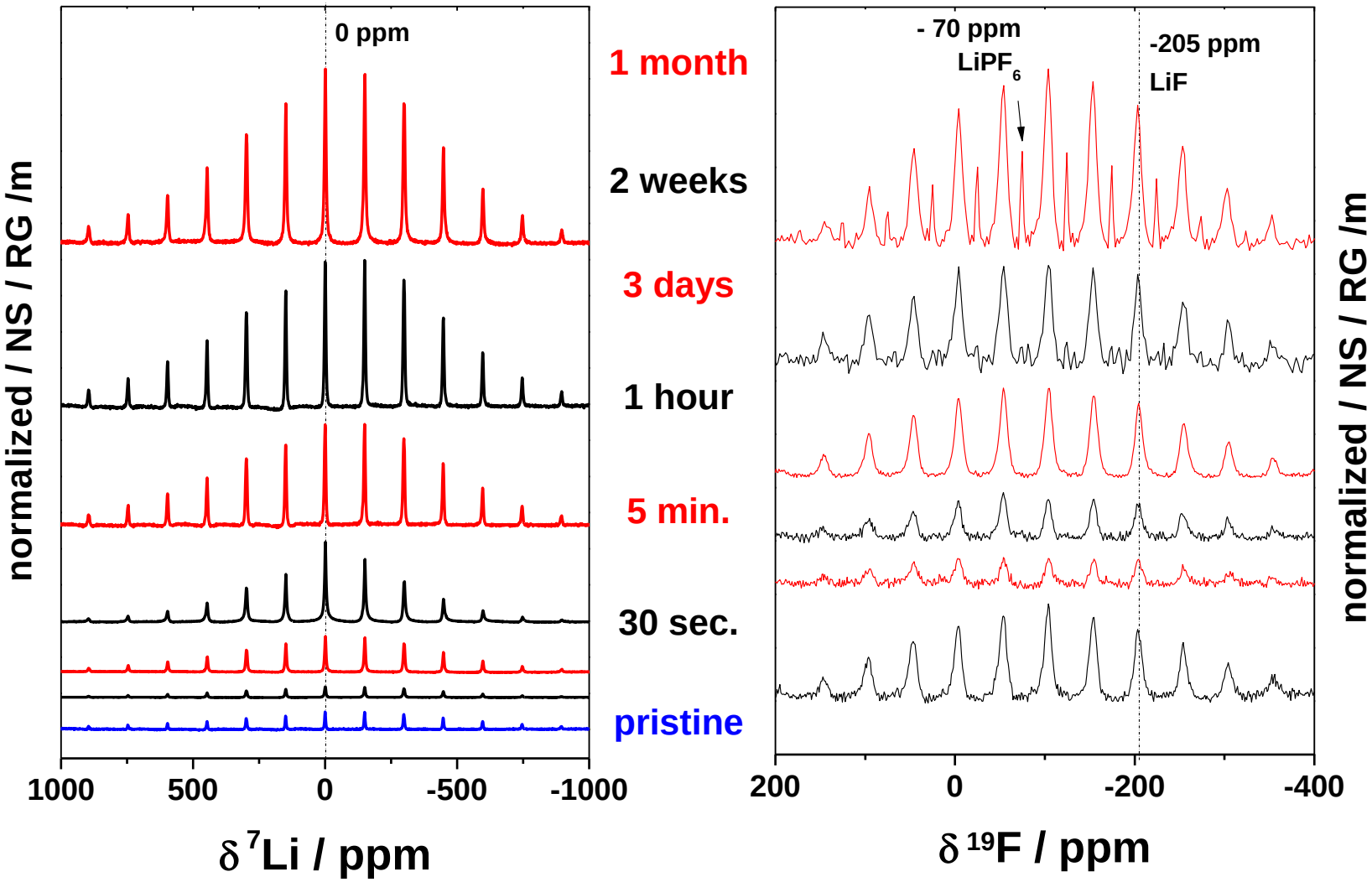

Figure AII-5. ^{7}Li (29 kHz) and ^{19}F (23.5 kHz) MAS NMR spectra of LMN⅓ soaked in conventional $LiPF_6$ in EC:DMC electrolyte for various durations. Dotted lines denote the position of isotropic shifts.

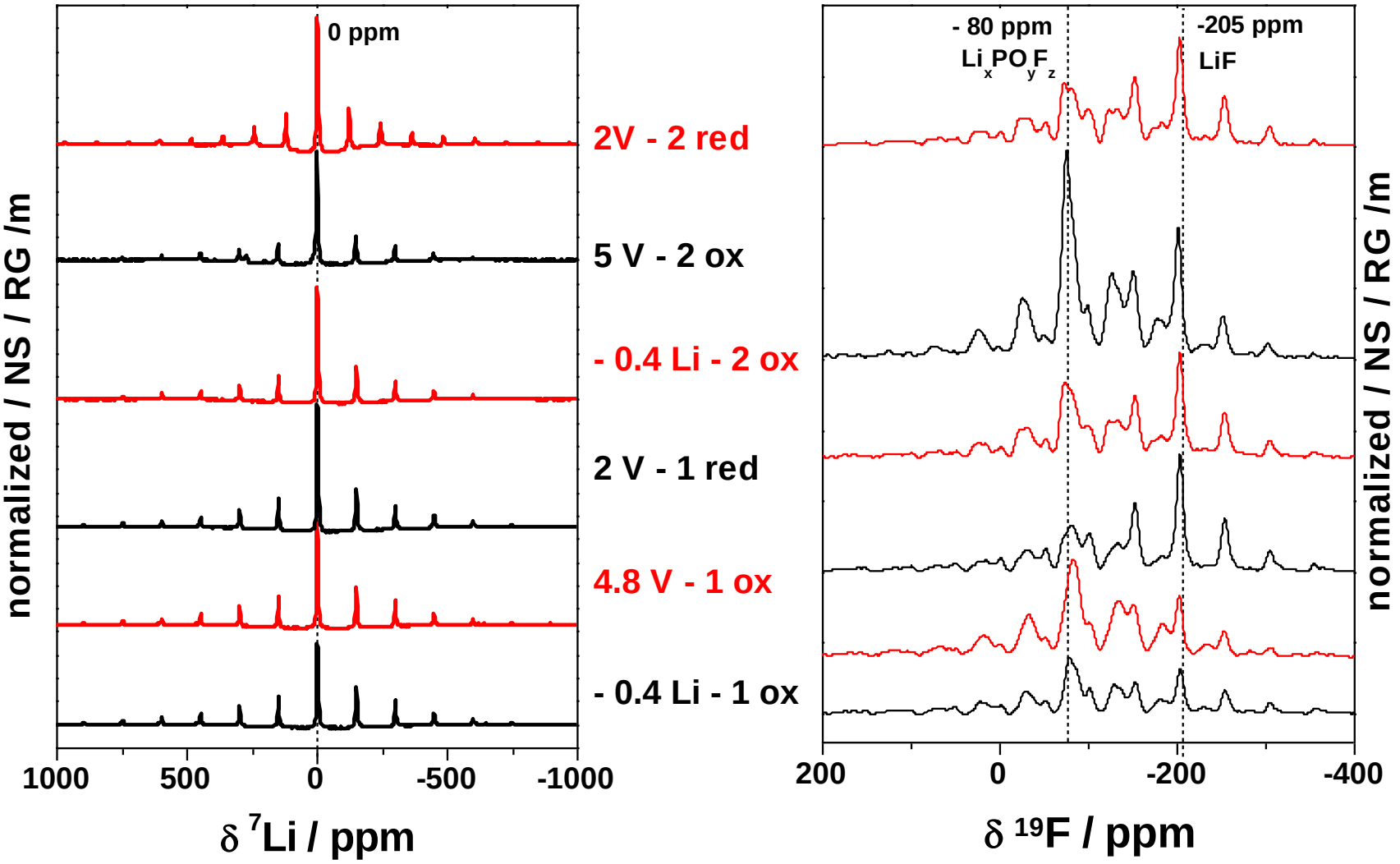

Figure AII-6. ^{7}Li (29 kHz) and ^{19}F (23.5 kHz) MAS NMR spectra of LMN⅓ along the two first electrochemical cycles in conventional $LiPF_6$ in EC:DMC electrolyte. Dotted lines denote the position of isotropic shifts.

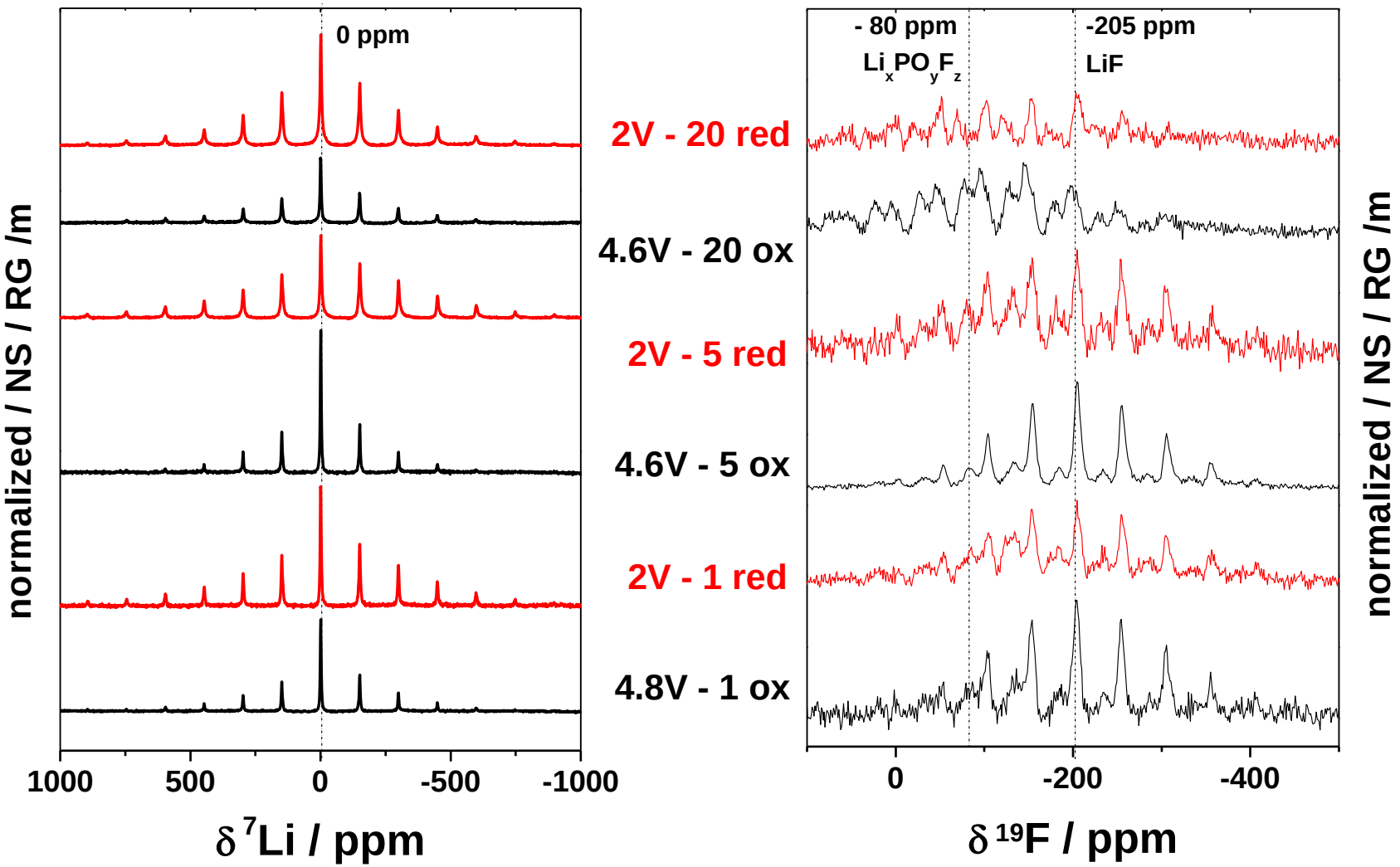

Figure AII-7. ^{7}Li (29 kHz) and ^{19}F (23.5 kHz) MAS NMR spectra of LMN⅓ after stabilization at the end of the 1st, 5th and 20th charges and discharges in conventional $LiPF_6$ in EC:DMC electrolyte. Dotted lines denote the position of isotropic shifts.

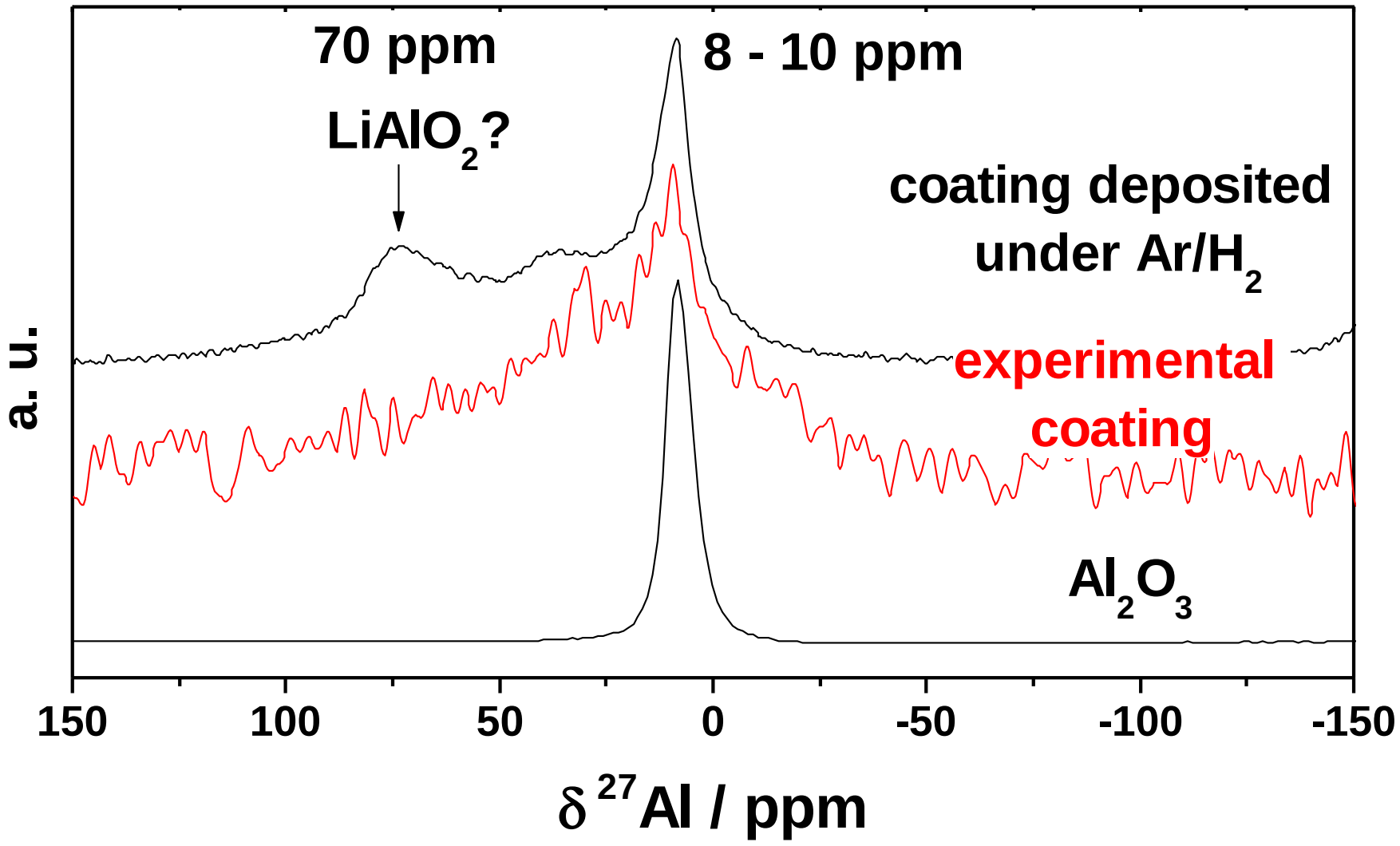

Figure AII-8. ^{27}Al MAS (29 kHz) NMR spectra of an Al_2O_3 reference and of AlO/LMN⅓ (red). A post annealing carried out under reductive atmosphere instead of air exacerbates the intensity of aluminated side phases.

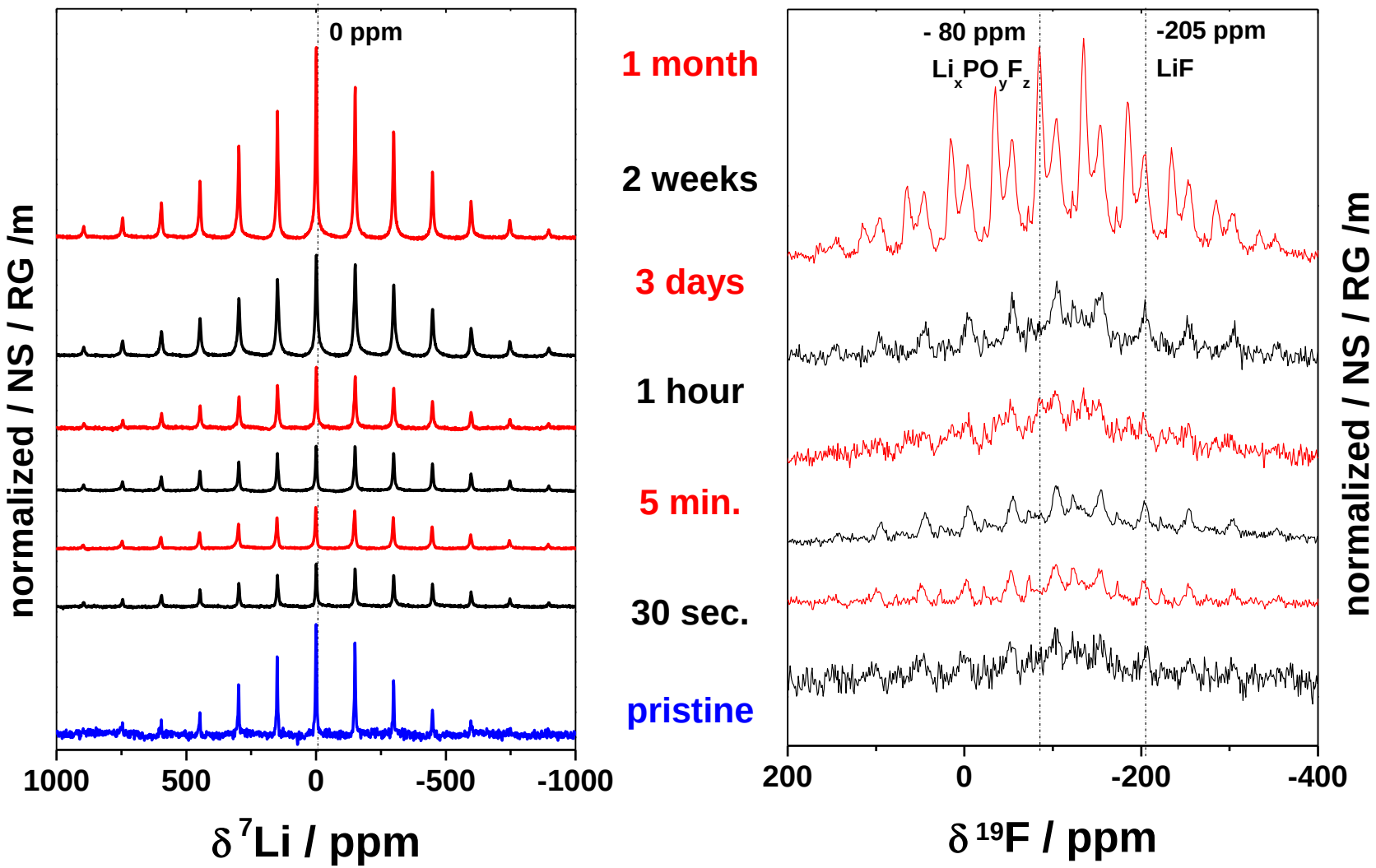

Figure AII-9. ^{7}Li (29 kHz) and ^{19}F (23.5 kHz) MAS NMR spectra of AlO/LMN⅓ soaked in conventional $LiPF_6$ in EC:DMC electrolyte for various durations. Dotted lines denote the position of isotropic shifts.

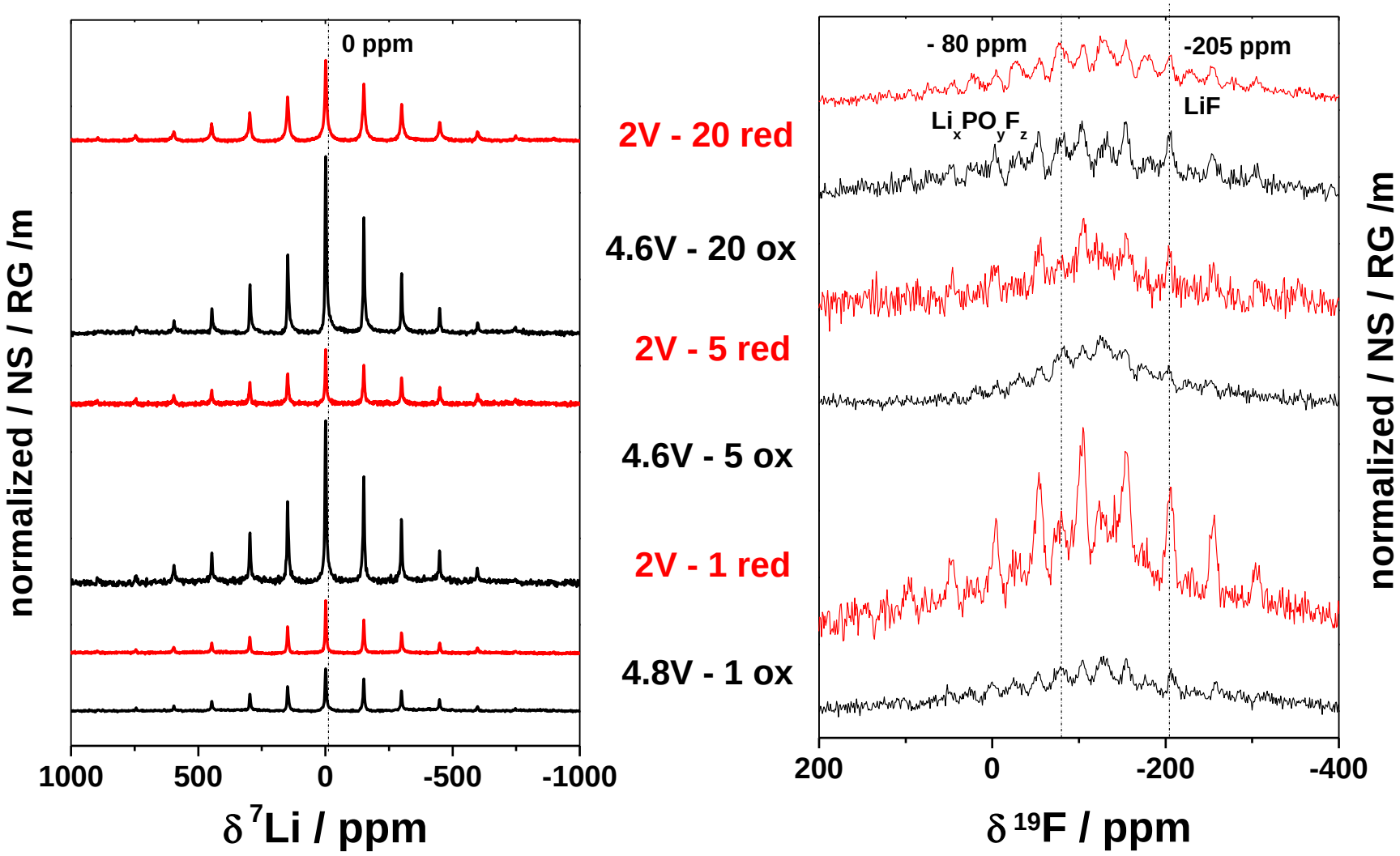

Figure AII-10. ^{7}Li (29 kHz) and ^{19}F (23.5 kHz) MAS NMR spectra of AlO/LMN⅓ after stabilization at the end of the 1st, 5th and 20th charges and discharges. Dotted lines denote the position of isotropic shifts.

RÉSUMÉ EN FRANÇAIS : INTRODUCTION

Les besoins en systèmes avancés de stockage de l'énergie n'ont cessé de croître de façon significative au cours des dix dernières années et resteront sans aucun doute l'un des défis majeurs du XXI^{ème} siècle. Les ordinateurs et téléphones portables, les magnétoscopes audio et/ou, les appareils-photo, ainsi qu'une multitude d'autres appareils électroniques portatifs (PEDs), sont toujours plus présents dans nos vies. Ainsi, ces appareils se développant rapidement, ils requièrent une puissance et donc une consommation énergétique toujours plus importante. Tandis que nous consommons puis jetons en masse, surgit, d'une manière presque schizophrénique, une prise de conscience collective des limites de nos ressources naturelles et des problèmes de pollution environnementale nous incitant à remplacer les voitures à essence par les véhicules électriques hybrides (VEH) à faible émission de CO_2, voire des véhicules électriques (VE) sans émission. Cette transition, encouragée par la crise économique actuelle et la nécessité pour les Etats de trouver des sources innovantes de croissance, repose également sur la disponibilité de systèmes appropriés de stockage de l'énergie. L'essor des technologies liées aux sources d'énergies renouvelables mais néanmoins intermittentes comme le photovoltaïque (PV) et l'éolien pourrait être judicieusement exploité, à condition que ces technologies soient intégrées dans un réseau intelligent et combinées à des solutions de stockage stationnaire de l'énergie ainsi produite. Ainsi, les attentes toujours croissantes envers des dispositifs de stockage de l'énergie portent généralement sur deux critères importants, la densité d'énergie (Wh / kg ou Wh / L) et / ou la densité de puissance (W / kg ou W / L), qui caractérisent respectivement la quantité d'énergie stockée par unité de poids ou de volume et la rapidité avec laquelle l'énergie peut être délivrée. Parmi les dispositifs électrochimiques capables de répondre à ces besoins, nous comptons les supercondensateurs, les piles à combustible et les batteries. A l'heure actuelle, les supercondensateurs présentent la plus haute densité de puissance, mais une densité d'énergie plutôt faible et une importante auto-décharge. D'autre part, les piles à combustible ont la plus forte densité d'énergie (à condition que le réservoir soit grand par rapport à la pile à combustible). Cependant, les différentes technologies de piles à combustible souffrent toutes d'une efficacité médiocre (<60%) et d'autres désavantages comme le coût, la durée de vie et la sécurité limitent leur utilisation à des marchés de niche. Alliant une haute densité d'énergie avec une puissance intermédiaire, les batteries représentent actuellement le dispositif de stockage de l'énergie le plus populaire.

Depuis que Sony Corporation a rendu publique la première cellule Li-ion commerciale en 1991, les accumulateurs lithium-ion ont supplanté les anciennes technologies de batteries rechargeables tels que les systèmes acide/plomb, nickel/cadmium, et nickel/métal-hydrure sur plusieurs segments de marché. Surpassant ses concurrents tant en termes de densité d'énergie gravimétrique et volumétrique, les accumulateurs Li-ion offrent également les avantages supplémentaires d'une tension de fonctionnement élevée (~ 3.5V), une longue durée de vie en cyclage (> 1000 cycles), un faible taux d'autodécharge, et ne présentent pas d'effet mémoire [1-2]. Au cours des dix dernières années, la capacité des accumulateurs Li-ion a augmenté d'un facteur deux, pour atteindre des valeurs supérieures à 600 Wh / L et 250Wh/kg [3]. Grace aux récentes améliorations en termes de densité de puissance, les accumulateurs Li-ion constituent maintenant la meilleure solution technologique pour les applications portatives à haute puissance telles que l'outillage électrique. En conséquence, les accumulateurs Li-ion dominent désormais le marché des accumulateurs portables, représentant environ 75% des ventes mondiales de piles et accumulateurs portables. Le marché mondial des accumulateurs Li-ion, extrêmement dynamique, a crû jusqu'à atteindre 3,3 milliards d'unités vendues en 2008 avec un taux de croissance annuel de 20%, seulement légèrement ralenti depuis en raison la crise économique [3-4].

Concernant le secteur des transports, nécessitant une capacité élevée ainsi qu'une forte puissance, les batteries nickel/métal-hydrure dominent dans les VEH actuellement commercialisés, notamment grâce au succès de la Toyota Prius. Toutefois, depuis 2010, la nouvelle génération de véhicules hybrides comme la Nissan Leaf et la Chevrolet Volt de GM utilise la technologie Li-ion, démontrant que les obstacles tels que la sécurité, le coût, la durée de vie et la puissance ont su être surmontés. De fait, le marché des accumulateurs Li-ion dans les applications VEH devrait croître considérablement et dépasser les nickel/métal-hydrures dans un avenir proche [4].

Dans un monde produisant annuellement plus d'un milliard de téléphones portables, près de 300 millions de lecteurs MP3 ainsi que 50 millions de voitures individuelles (dont 10% pourraient être des VEH / VE d'ici 10 ans), l'enjeu ne porte pas seulement sur la façon de satisfaire une telle demande en termes de production de cellules Li-ion, mais aussi sur la façon de limiter l'impact environnemental de ces batteries, depuis l'extraction de matériaux pour la production des cellules jusqu'à leur élimination et leur recyclage. La technologie Li-ion jouera, à coup sûr, un rôle important dans un quelconque avenir énergique, que notre responsabilité en tant que scientifiques est de rendre plus raisonné et plus durable.

Parmi les défis restant dans ce domaine de recherche, la nécessité de contrôler les interfaces entre les différents composants de la batterie est devenue particulièrement évidente [5]. En effet, la couche de passivation entre l'électrode négative et l'électrolyte d'une batterie Li-ion (ou S.E.I. pour Solid Electrolyte Interphase) est reconnue pour impacter sur le comportement global de l'accumulateur au niveau de la perte irréversible de capacité, de la cinétique de transfert de charge, et des propriétés de stockage [6].

Des réactions parasites et la croissance d'une couche de passivation ont également été mises en évidence à la surface de différents matériaux d'électrode positive et ont été identifiées comme étant d'une importance capitale car elles peuvent conduire à une dégradation des performances de la batterie lors du vieillissement et du cyclage [7]. Si l'existence de réactions de surface à l'interface entre l'électrode positive et électrolyte a été clairement démontrée, les conditions expérimentales de formation, de croissance et de vieillissement de l'interphase, ainsi que son influence ultérieure sur les performances électrochimiques, demeurent floues. En particulier, les propriétés physico-chimiques et structurales de la couche interphasiale à l'électrode positive sont encore mal connues, et ce domaine de recherche, plus récent, est donc du plus grand intérêt [8, 9].

Cette thèse s'inscrit dans ce cadre précis et décrit la caractérisation ainsi que diverses tentatives pour contrôler les processus interfaciaux se produisant sur les matériaux d'électrode positive $LiNi_{1/2}Mn_{1/2}O_2$, $Li_{1.2}Ni_{0.4}Mn_{0.4}O_2$ et $LiFePO_4$ au cours de leur stockage et de leur cyclage électrochimique.

Le premier chapitre est donc consacré à la description des matériaux actifs pour accumulateurs Li-ion, ainsi que les principaux processus interphasiaux - basés sur la décomposition de l'électrolyte - pouvant conduire à la défaillance d'un accumulateur.

Dans la mesure où ce travail repose sur l'utilisation poussée de la RMN hétéro-nucléaire à haut champ pour en extraire des informations sur l'interphase électrode / électrolyte présente sur des matériaux actifs paramagnétiques, le second chapitre s'attache à décrire le développement d'outils spectroscopiques adaptés, à savoir la RMN MAS (^{7}Li, ^{19}F et ^{31}P) et l'EELS, pour décrire quantitativement l'interphase et clarifier son architecture.

Le troisième chapitre regroupe diverses études réalisées sur l'interphase $LiNi_{1/2}Mn_{1/2}O_2$ / électrolyte. Différents types de modifications de surface sont envisagés et des paramètres tels que l'exposition de l'air, la température, la formulation de l'électrode composite, l'ajout d'un additif dans l'électrolyte mais aussi la surlithiation du matériau initial, sous la forme de $Li_{1.2}Ni_{0.4}Mn_{0.4}O_2$, sont étudiés.

Le quatrième et dernier chapitre traite des différents paramètres susceptibles d'influencer le comportement interphasial de $LiFePO_4$ comme la présence favorisée d'une orientation cristalline particulière ou le processus de vieillissement encouru lors de l'exposition aux espèces oxydantes de l'atmosphère.

Dans chaque cas, ce travail tente d'une part de corréler la nature et l'évolution de l'interphase électrode / électrolyte, sondée par spectroscopie RMN (mais aussi XPS et EELS), à la chimie de surface du matériau, et d'autre part d'élucider le lien entre l'évolution des performances électrochimiques et celle de la surface.

CHAPITRE 1 : CONTEXTE DE L'ÉTUDE

I. Fonctionnement d'un accumulateur Li-ion

Une batterie consiste en l'assemblage de deux électrodes, une cathode et une anode, séparées par une couche poreuse qui est à la fois un conducteur ionique et un isolant électronique. Lors de la décharge, le courant est généré par la conversion de l'énergie chimique des matériaux actifs d'électrode en énergie électrique, via des réactions d'oxydo-réduction. Pour une batterie rechargeable, les termes anode et cathode désignent tour à tour l'une ou l'autre des électrodes lorsque la cellule passe de l'état de décharge à celui de charge. Aussi pour éviter toute confusion, les termes électrode positive et électrode négative sont généralement privilégiés, et leur utilisation sera systématique dans cette thèse.

Une cellule Li-ion commerciale comme celle lancée par Sony en 1991 repose sur un oxyde métallique de lithium tel que $LiCoO_2$ à l'électrode positive et un carbone graphitique comme électrode négative. Les deux électrodes sont immergées dans un électrolyte liquide non aqueux contenant un sel de lithium dissous tels que $LiPF_6$.

Pendant la décharge, l'oxydation de l'électrode négative libère des ions Li^+ qui diffusent au travers de l'électrolyte vers l'électrode positive, comme schématisé dans la **Figure I-1**. Cette réaction est équilibrée par un flux d'électrons dans le circuit externe de l'accumulateur générant ainsi le courant. Pendant la charge, le processus inverse se produit sous l'impact d'un générateur externe.

II. Matériaux d'électrode positive

Parmi les matériaux étudiés se dressent deux familles de composés d'intérêt, de par leur chimie de surface différente, à savoir les oxydes lamellaires et des phosphates de métaux de transition, parmi lesquelles nous avons sélectionnés nos composés modèles: $LiNi_{1/2}Mn_{1/2}O_2$ et $LiFePO_4$.

II.1. les oxydes lamellaires $LiMO_2$ et leurs dérivés surlithiés

Dans cette thèse, nous avons fait le choix de travailler sur le diagramme ternaire $LiNiO_2$-$LiMnO_2$-$LiMn_2O_3$ (voir **Fig. I-3, droite**) et axé notre étude sur le composé $LiNi_{1/2}Mn_{1/2}O_2$, proposé par Ohzuku et Makimura [41]. Ces derniers rapportent une capacité

réversible de l'ordre de 200 $mAhg^{-1}$ entre 2.5 et 4.5 V par rapport au couple Li^+/Li^0 avec une excellente rétention de capacité, bien que de telles performances n'aient pu être reproduites avec ce matériau. $LiNi_{1/2}Mn_{1/2}O_2$ présente par ailleurs une propension moindre à la surchauffe thermique, une stabilité thermique plus élevée que $LiCoO_2$ ou $LiNiO_2$, ainsi qu'une plus grande stabilité à l'état chargé [41, 42].

La substitution cationique utilisant un excès de Li pour remplir partiellement les couches de métaux de transition a conduit à la découverte de matériaux à haute densité d'énergie, membres de la solution solide existant entre $LiMn_2O_3$ et $LiMO_2$ (M = Ni, Mn, Co). Ces composés sont des candidats prometteurs d'électrode positive car ils offrent une capacité pratique beaucoup plus élevée (> 250 $mAh.g^{-1}$) et une sécurité accrue à un moindre coût [35, 36]. Les capacités importantes observées trouvent leur origine dans la particularité de cette famille de matériaux de subir un processus d'activation électrochimique lors de la première charge. Lors du processus initial de charge, la capacité provient de l'oxydation du Ni(III) en Ni(IV) jusqu'à 4.4 V. Au-delà, un plateau apparait et les capacités élevées enregistrées dans cette région de potentiel ont été attribuées à une perte irréversible d'oxygène du réseau crystallin, accompagnée d'une extraction de Li, considérée comme une étape d'activation électrochimique [37, 38].

Aussi cette étude a été étendue de $LiNi_{1/2}Mn_{1/2}O_2$ aux oxydes lamellaires surlithiés, et la composition $Li[Li_{0.2}Ni_{0.4}Mn_{0.4}]O_2$, a été retenue en raison de sa position particulière dans le diagramme ternaire $LiNiO_2$-$LiMnO_2$-$LiMn_2O_3$ qui en fait le composé le plus riche en Li pour un rapport Ni/Mn identique à $LiNi_{1/2}Mn_{1/2}O_2$. Ainsi, bien que cette composition particulière ne présente ni la capacité théorique (**Fig. I-3, droite**), ni la capacité pratique la plus elevée [37], la perte nette de Li_2O provenant de $Li_{1.2}Ni_{0.4}Mn_{0.4}O_2$ sur le plateau initial à haut potentiel résulterait en $Li_{0.8}Ni_{0.4}Mn_{0.4}O_{1.6}$ correspondant au composé modèle $LiNi_{1/2}Mn_{1/2}O_2$. Les différences entre les deux matériaux choisis, en termes de chimie de l'interphase et de performances électrochimiques, ne peuvent donc résider que dans le processus initial de charge, spécifique aux composés surlithiés. Ce travail fait l'objet du chapitre 3.

II.2 L'olivine $LiFePO_4$

Depuis les travaux précurseurs de Padhi *et al.* [46, 47] et Ravet *et al.* [48] dans les années 90, les composés de type olivine $LiMPO_4$ (avec M = Fe, Mn, Co, Ni) (Fig. I-4, gauche) ont fait l'objet d'une attention massive de la communauté scientifique. Littéralement, plus d'un millier d'articles sur ce sujet ont été publiés depuis.

Les points forts de $LiFePO_4$ pour les accumulateurs Li-ion sont ses excellentes durée de vie, stabilité thermique et structurale de la phase délithiée $FePO_4$ et le faible coût des précurseurs nécessaires à sa synthèse. Ayant réussi à surmonter sa faible conductivité électronique (~ 10^{-9} $S.cm^{-1}$ à 298 K) soit par dépôt d'un revêtement carboné [48, 49] soit par la réduction de la taille des particules [50-52], la capacité pratique de $LiFePO_4$ est maintenant proche de la valeur théorique de 172 $mAh.g^{-1}$ et de récentes études ont démontré la possibilité d'augmenter considérablement la densité de puissance [53].

III. Phénomènes de surface au sein d'un accumulateur Lithium-ion: vieillissement des différentes composantes

La durée de vie étant l'un des points clés du cahier des charges pour un accumulateur au lithium, l'étude de son vieillissement au cours de son stockage ou cyclage apparait d'une importance primordiale. Comme illustré dans la section suivante, les interfaces électrode / électrolyte, sites légitimes des réactions électrochimiques, peuvent également être le point de départ des altérations les plus importantes d'un dispositif électrochimique au cours de son vieillissement. Un examen des phénomènes de surface liés au vieillissement de chaque composant permet ainsi de faire la lumière sur les principales causes de la dégradation des performances d'un accumulateur.

III.1. Décomposition d'électrolytes à base de carbonates

Les mécanismes de dégradation multi-étapes d'électrolytes carbonate sont complexes, mais bien documentés [85-87]. Deux mécanismes de réduction possibles pour l'EC sont par exemple, montrés dans l'équation I-1. La réduction mettant en jeu un électron conduit à la formation de l'éthylène dicarbonate de lithium (LEDC), un semicarbonate considéré comme un des ingrédients clé de la SEI. Les autres solvants carbonatés conduisent ainsi à la formation de composés similaires, généralement abrégés par la notation $ROCO_2Li$. Si la réduction se poursuit, du Li_2CO_3 est alors formé.

La plupart des sels de lithium utilisés sont très hygroscopiques. Cela s'avère être extrêmement dommageable pour l'accumulateur dans le cas de $LiPF_6$, qui est facilement hydrolysé pour former l'acide fluorhydrique, HF [75, 88, 89] comme représenté dans l'équation I-5.

Ainsi, la décomposition de $LiPF_6$ 1M dans EC: DMC (1:1) après 3 semaines à 85 ° C conduit à la précipitation de LiF, $Li_xPO_yF_z$, mais aussi de fluorophosphates organiques tels

que $OPF_2(OCH_2CH_2)_nF$ et OPF_2OMe, et autres composés organiques (ROLi , $ROCO_2Li$, de polycarbonates, PEO, etc) [59].

III.2. Chimie de surface des électrodes positives et les interactions entre positive et électrolyte

Tous les matériaux d'électrode positive pour accumulateur Li-ion actuellement à l'étude sont sujets à des réactions parasites avec les solutions d'électrolyte [81, 82, 95, 96]. Parce qu'ils constituent la composante principale de l'électrode limitante - en termes de coût, de performance et de durée de vie - les matériaux de d'électrode positive méritent une attention particulière. Les mécanismes de vieillissement observés à l'interface électrode positive / électrolyte comprennent principalement:

- Des modifications de structure en surface des matériaux d'électrode, telles que la dissolution des métaux de transition (en particulier dans le cas de manganates [97-99]) ou la libération d'oxygène, conduisant à l'empoisonnement de la SEI à l'électrode négative et la formation de phases électrochimiquement inactives. Des résultats tirés de la littérature sont ainsi résumés dans le **Tableau I-1**.
- Le remplacement de l'interphase initiale de Li_2CO_3, formé sur les positives de type $LiMO_2$ lors du contact à l'air, par des produits de décomposition du sel, des Li-alkyl carbonates et des polycarbonates par attaque nucléophile ou oxydation des molécules de solvant [97, 100, 101].

Un certain nombre d'observations générales peut être tiré de cette revue de la littérature concernant les phénomènes de surface sur des matériaux d'électrode positive. Les oxydes ($LiCoO_2$, $LiNiO_2$, $LiMn_2O_4$) présentent généralement une interphase originelle faite de carbonate de lithium qui se forme facilement à l'air. Alors que l'olivine $LiFePO_4$ semble être épargnée par un tel phénomène, Li_2FeSiO_4 est également recouvert par Li_2CO_3. Lors du contact avec l'électrolyte, les réactions interphasiales dépendent fortement du couple matériau / électrolyte. Au cours du cyclage dans un électrolyte à base de $LiPF_6$, les électrodes positives sont recouvertes par LiF qui est fortement résistif, des fluorophosphates tels que Li_xPF_y ou $Li_xPO_yF_z$, mais aussi des espèces organiques et des polymères résultant de la décomposition des solvants à base de carbonates au dessus de 4.5 V. Concernant la dépendance en potentiel des phénomènes de surface, plusieurs études insistent sur la «dynamique» de l'interphase, les Li^+ «piégés» dans l'interphase étant plus ou moins mobiles selon les espèces chimiques. Par ailleurs les performances électrochimiques semblent fortement corrélées à l'interphase observée, cette dernière étant directement régie par des paramètres tels que la température ou la présence d'impuretés dues à l'humidité. Si le dépôt de produits de décomposition de

l'électrolyte est le processus interphasial dominant, la dissolution des matériaux actifs ($LiFePO_4$, $LiMn_2O_4$) dans l'électrolyte a également prouvée et joue très certainement un rôle sur l'orientation des réactions interphasiales. Des exemples portant sur l'usage d'additifs, rapportés dans le **Tableau I-3**, mettent en évidence la possibilité de jouer sur ces réactions.

IV. Conclusion

Le vieillissement des électrodes et de l'électrolyte sont bien souvent interdépendants et si une abondante littérature décrit l'évolution d'une surface d'électrode face à l'électrolyte lors du stockage et du cyclage, rares sont les études corrélant l'évolution de cette surface d'électrode aux performances électrochimiques globales. Cependant, les résultats spectroscopiques recueillis d'après ces nombreux travaux offrent une excellente base de données, qui sera exploitée dans les chapitres suivants.

Au contraire, les études s'intéressant à la cyclabilité à long terme ou à l'impact du stockage sur les performances des cellules complètes donnent souvent l'image d'une boîte noire, qui décrit la défaillance de l'accumulateur par une augmentation de l'impédance et / ou par une perte de capacité et l'attribue à la variation de tel ou tel paramètre physico-chimique. Ainsi, l'approche choisie dans ce travail va plutôt consister à essayer d'analyser en premier lieu l'impact de ces paramètres externes sur l'interphase électrode positive / électrolyte en termes de quantité et de qualité des espèces formées, avant de corréler le comportement interphasial aux performances électrochimiques.

Par ailleurs, la modification de surface constitue une tendance majeure de la chimie des batteries au lithium, et nous nous attacherons ici à comprendre plus clairement l'impact de la chimie de surface sur les processus interphasiaux résultants et à établir des corrélations avec les performances globales de l'accumulateur, lorsque cela est possible.

Une telle corrélation de l'évolution de la surface d'électrode avec les performances électrochimiques nécessite à la fois une connaissance précise de la chimie des composants de la batterie et des réactions parasites susceptibles de survenir à leurs interfaces respectives.

CHAPITRE 2. SPECIFICITÉ DE L'ÉTUDE: CARACTÉRISATION D'INTERPHASE PAR RMN MAS ET EELS

Ce chapitre vise à introduire les techniques d'analyse employées dans cette thèse pour étudier les interphases au sein d'accumulateurs Li-ion. L'originalité de ce travail réside notamment dans l'utilisation de la RMN MAS et l'EELS pour analyser des couches de surface inhomogènes, constituées d'espèces diamagnétiques en interaction avec des matériaux d'électrode paramagnétiques. La non trivialité de ces méthodes justifie leur description détaillée dans ce chapitre.

I. Caractérisation par RMN d'interphases électrode / électrolyte dans les batteries au lithium

I.1 Détection sélective par RMN MAS du ^{7}Li d'espèces interphasiales sur les matériaux paramagnétiques

Sous un champ magnétique externe élevé (11.8 T dans notre cas) un signal très large est observé pour les ions lithium au sein de la structure hôte des matériaux d'insertion. Ce signal est généralement décalé en raison de la forte interaction de type Fermi-contact et dépend fortement de la distribution locale des métaux de transition portant des électrons non appariés autour du lithium intercalé [1, 12, 13]. Après réaction avec un milieu environnant (par exemple l'atmosphère ou l'électrolyte), des espèces diamagnétiques interphasiales contenant du lithium sont observées et sont caractérisées par des signaux beaucoup plus étroits entre 0 et 1 ppm, superposés au signal du bulk [2, 14].

Dans le but d'étudier le Li interphasial, l'idée proposée par Ménétrier *et al.* [2] consiste à jouer avec l'interaction dipolaire électron-noyau. S'exerçant dans l'espace, avec une dépendance en $1/r^3$ où r est la distance entre le centre paramagnétique et le noyau sondé (voir Eq. II-5 et II-6), cette forte interaction dipolaire est un mécanisme de relaxation de l'aimantation RMN très efficace.

En se basant sur la décroissance extrêmement rapide de la FID observée pour le lithium dans le matériau par rapport à celle du lithium interphasial diamagnétique, une impulsion suivie d'un long délai de pré-acquisition (**Fig. II-1**) supprime le signal large provenant du lithium intercalé, ce qui rend le signal attribué au lithium de surface de

beaucoup plus prononcé et plus facile à analyser. Dans ce travail, seuls des spectres obtenus dans ces conditions, et donc présentant uniquement le signal de lithium correspondant à la couche de surface, seront discutés.

I.2. Estimation qualitative de l'interaction électrode / interphase

Dans des travaux antérieurs, il a été démontré que la largeur de l'enveloppe du signal RMN peut être corrélée à la force de l'interaction dipolaire électron-noyau entre le lithium dans l'interphase et les grains de matériau paramagnétique au travers du temps de relaxation spin-réseau T_1* [2, 3]. Ainsi une augmentation de T_1* reflète la décroissance de l'influence de la phase paramagnétique sur le temps de relaxation du signal RMN du lithium diamagnétique lorsque la distance entre les deux augmente.

Sur les spectres expérimentaux (**Fig. II-2**), le l'affinement progressif de l'enveloppe des bornes de rotation peut donc refléter une baisse de l'intimité «moyenne» ou l'augmentation "moyenne" de la distance des lithium de surface avec le matériau paramagnétique. Dans les deux cas, un tel signal de surface ne peut pas être attribué à un unique environnement du lithium, mais plutôt à une superposition de résonances correspondant à une distribution des noyaux de lithium dans l'épaisseur de l'interphase. Leurs environnements possibles vont d'emplacements proches de la surface du matériau actif jusqu'à l'extrême surface de l'interphase. Ainsi la largeur du signal observé doit évoluer en fonction de deux paramètres: l'épaisseur de la phase de surface et son intimité avec la grains de matériau actif.

I.3. Méthode de quantification de la RMN MAS du ^{7}Li, ^{19}F et ^{31}P [article IV]

Afin d'atteindre une caractérisation plus poussée des espèces présentes dans l'interphase, la RMN MAS du ^{19}F et ^{31}P ont été développées au cours de cette thèse pour obtenir des informations chimiques complémentaires. Dans ces deux cas, la plus large gamme de déplacement chimique permet d'attribuer les différentes résonances observées à un type d'espèces tel que le LiF ou les fluorophosphates ($LiPF_6$, Li_xPF_z, RPO_yF_z). Dans le cadre de ce travail, l'utilisation de ^{7}Li, ^{19}F et ^{31}P RMN MAS, a été rendue quantitative par la mise en œuvre d'une méthode empirique d'étalonnage présentée ci-dessous.

Nous avons ainsi opté pour une méthode directe et simple, grâce à l'étalonnage - ou calibration – des spectres RMN en utilisant plusieurs séries de mélanges de $LiNi_{1/2}Mn_{1/2}O_2$ (LMN) avec des quantités connues et précises d'espèces diamagnétiques lithiées, fluorées, et /

ou phosphorées à savoir $LiPF_6$ et LiF en abondance naturelle (92,5% pour ^{7}Li, 100% pour les ^{19}F et ^{31}P). Ces deux composés modèles ont été choisis car ils sont les plus susceptibles d'être trouvés en surface du matériau d'électrode.

L'intérêt de cette méthode simple réside avant tout dans la possibilité de comparer directement les quantités de noyaux Li, F et P déduites à partir des intensités intégrées des spectres RMN MAS du ^{7}Li, ^{19}F et ^{31}P, respectivement. La **Figure II-3** présente les résultats de quantification des signaux RMN du ^{7}Li, ^{19}F et ^{31}P, ainsi que les équations résultant de la régression linéaire des données expérimentales. A noter que seuls les points de données expérimentales obtenus à partir $LiNi_{1/2}Mn_{1/2}O_2$ ont été utilisés pour tracer les courbes d'étalonnage. Les points expérimentaux obtenus dans le cas de $LiNi_{0.4}Mn_{1.6}O_4$, $LiFePO_4$ et du silicium ont été ajoutés dans un second temps sur le graphique afin de valider les courbes d'étalonnage pour la quantification des noyaux de ^{7}Li, ^{19}F et ^{31}P impliqués dans l'interphase pour d'autres types de matériaux d'électrode.

Lors de l'enregistrement des spectres RMN MAS de matériaux d'électrode positive après le stockage dans l'électrolyte ou le cyclage, les intensités intégrées de chaque peigne de bornes de rotation peuvent donc être converties en une quantité molaire de lithium, de fluor (dans LiF ou dans des fluorophosphates) ou de phosphore en utilisant le coefficient d'étalonnage correspondant et rapportées en moles d'interphase par g ou m² de matière active. Cette dernière unité (mmol.m-²), nécessite de normaliser les résultats en tenant compte de la surface développée par l'électrode, telle qu'approchée par la méthode BET par exemple. Bien qu'il n'y ait pas de preuve claire que la surface BET correspond à la surface électrochimique de l'électrode, cette hypothèse apparaît raisonnable pour comparer la réactivité de surface de matériaux d'électrode différents [22] ou des matériaux obtenus par différentes voies de synthèse [6].

Il convient également de noter que ces courbes d'étalonnage embrassent les points supplémentaires résultant du mélange de matière diamagnétique avec des composés paramagnétiques tels que $LiFePO_4$ et $LiNi_{0.5}Mn_{1.5}O_4$ comme dans la **Figure II-3** (points rouges) indépendamment de l'interaction dipolaire et du paramagnétisme des différents matériaux d'électrode. Ainsi, l'effet dominant de l'importante interaction dipolaire électron-noyau est de distribuer l'intensité RMN sur une plage de fréquences étroite ou large selon la distance / l'intimité entre les espèces de surface et matériaux d'électrode paramagnétiques [3] sans qu'une perte d'intensité soit détectée. Par conséquent, les coefficients de corrélation obtenus restent valables pour étudier différentes interphases électrodes / électrolyte, de

matériaux contenant des métaux de transition à divers degrés d'oxydation ainsi que dans les états chargés et déchargés. Ceci est d'ailleurs confirmé par les expériences réalisées sur du silicium (dans ce cas, l'absence d'électrons localisés désappariés conduit à un profil de raie typique du ^{7}Li quadripolaire) puisque les intensités intégrées déduites à partir des données expérimentales coïncident également avec les courbes d'étalonnage réalisées (**Fig. II-3**).

I.4. Remarques

Dans le cas de matériaux d'électrode contenant des métaux de transition avec des électrons non appariés, en plus de la composition chimique (obtenue à partir de déplacement chimique), la prédominance de l'interaction dipolaire électron-noyau dépendant de la distance rend possible l'extraction d'informations physiques ou topologiques concernant l'interphase. Dans le cas du ^{7}Li, l'avantage de cette méthode sur les autres techniques analytiques de surface réside clairement dans la séparation efficace du signal de surface du signal paramagnétique du matériau actif.

En plus de cette information qualitative, l'étalonnage empirique des spectres RMN MAS du ^{7}Li, ^{19}F et ^{31}P, a démontré la possibilité de suivre quantitativement l'évolution de certaines espèces interphasiales sur différents matériaux actifs et sera ainsi mis à profit tout au long de cette thèse.

II. Introduction expérimentale à l'EELS appliquée aux matériaux d'électrode et aux interphases électrode / électrolyte

Combinant l'imagerie et l'analyse locale, le couplage TEM / EELS offre un point de vue unique pour observer d'éventuelles inhomogénéités topologiques et/ou chimiques au sein d'un échantillon. De telles études résolues spatialement nécessitent la répétition des expériences de façon statistique, afin d'assurer la représentativité des résultats. Bien que cette précaution soit commune à toute technique expérimentale, celle-ci est primordiale dans le cas de la microscopie, où les résultats sont fortement dépendants du libre arbitre de l'expérimentateur. Plusieurs facteurs essentiels doivent être également pris en compte pour effectuer des analyses TEM sur des matériaux d'électrode pour accumulateur au lithium afin de préserver l'intégrité de l'échantillon. Une liste non exhaustive de ces précautions est présentée ici.

II.1. Précautions générales

Le lithium étant un élément extrêmement léger, son évaporation sous le faisceau d'électrons est bien connue [32]. Ce phénomène peut facilement être sous-estimé, car il se produit souvent sans dégradation apparente de l'échantillon (au moins à l'œil nu). Par ailleurs, plus l'échantillon est mince, plus le faisceau d'électrons est à même de réduire les cations métalliques de transition [33]. La surface des grains est donc plus susceptible de présenter d'éventuelles modifications artificielles de structure fine induites par le faisceau électronique (**Figure II-10**). Ce risque d'altération des matériaux peut être évité en limitant l'irradiation de l'échantillon (dans notre cas en utilisant une tension d'accélération de 100 kV et une taille de sonde supérieure à 10 nm) mais aussi en abaissant la température à 77 K à l'aide d'azote liquide.

Certains matériaux d'électrode sensibles à l'air (comme les alliages Li_xSi [34, 35]) représentent un défi expérimental supplémentaire, qui peut être résolu avec l'aide d'un porte-objet hermétique, l'échantillon étant alors transféré à l'abri de l'air depuis la boîte à gants. Toutefois, celui-ci ne peut pas fonctionner à basse température, nécessitant un compromis. Dans ce travail de thèse, pour lequel des temps d'acquisition long (jusqu'à 60 s) se sont avérés nécessaires, des mesures à température ambiante ne pouvaient pas être envisagées, et bien que les espèces interphasiales soient sensibles à l'air, les échantillons ont été brièvement exposés à l'atmosphère ambiante (~ 5 minutes).

II.2. Précautions concernant l'analyse d'électrodes composites

L'analyse TEM, si elle vise à élucider le mécanisme de dégradation d'une électrode ou l'évolution de l'interphase, nécessite généralement d'altérer la microstructure de l'électrode. La poudre est désolidarisée du collecteur de courant afin d'être déposée sur une grille de cuivre. Ainsi, de nouvelles surfaces sont créées et le réseau observé sous le microscope ne peut représenter à proprement parler l'architecture réelle de l'électrode. Des progrès dans les méthodes de préparation d'échantillons TEM sont en cours, et des techniques alternatives, plus respectueuses de l'intégrité des électrodes, consistent à découper des tranches extrêmement fines de l'électrode, appelées sections, par faisceau focalisé d'ions (FIB) ou ultra microtome (récemment arrivé au laboratoire).

II.3. Précautions concernant l'analyse d'interphases

Initiant l'analyse chimique d'interphases par TEM, Naji *et al.* [29, 38] ont identifié des carbonates et du LiF par l'utilisation de la diffraction électronique et de l'EELS sur des

produits cristallins de la SEI (**Fig. II-12a**). Ils semblent cependant avoir considéré la SEI comme stable et chimiquement homogène. Les expériences menées dans cette thèse portent plutôt à penser qu'ils ont observé des produits de dégradation sous le faisceau en lieu et place de la SEI. En effet, comme le montre la **Figure II-12b**, la croissance de cristaux a pu être observée sous le faisceau électronique à température ambiante. La morphologie cubique des cristaux a été attribuée à LiF à partir de sa figure de diffraction électronique et son seuil Li-K reconnaissable en EELS [33]. Toutefois, dans les conditions d'analyse précautionneuses décrites ci-dessus, aucun cristal de LiF n'a pu être mis en évidence, indiquant plutôt sa présence à l'état amorphe et sa dispersion dans l'interphase.

Le point le plus critique rencontré au cours de ce travail de thèse, et de toutes les études de ce genre peut s'exprimer à travers la question: "rincer ou ne pas rincer?" qui se pose avant toute analyse de surface. Il a en effet été montré que le rinçage des poudres ou des électrodes de l'excès d'électrolyte supprime partiellement (voire même parfois totalement) l'interphase [37, 38], mais ne pas rincer impliquerait l'observation et/ou la prise en compte de cet excès d'électrolyte et notamment du sel comme une espèce interphasiale. Ici encore, un compromis doit être trouvé et dans le cadre de cette étude, les électrodes ont toujours été délicatement rincées avec une seule goutte de DMC puis séchées sous vide à 90 ° C pendant 4 h. La même procédure a été utilisée pour tous les échantillons avant toute caractérisation spectroscopique afin d'assurer, à défaut de l'intégrité absolue de l'interphase, une reproductibilité maximale de nos analyses ainsi que l'observation de tendances à l'échelle de chaque série d'échantillons.

Découlant de cette propension de l'interphase à se détacher de la surface des grains lors du contact avec des solvants, il va de soi que la préparation des échantillons TEM doit soigneusement éviter leur utilisation. La **Figure II-13** illustre cette idée de « bonnes contre mauvaises pratiques » dans la caractérisation d'interphase par TEM: le même échantillon a été préparé par dispersion de la poudre dans l'éthanol sous ultrasons, puis a été analysé sous une tension d'accélération de 300 kV à température ambiante (**Fig. II-13, gauche**) ou préparé à sec, et analysé sous 100 kV à la température de l'azote liquide (**Fig. II-13, droite**).

II.4. Remarques

Comme illustré par les résultats expérimentaux mentionnés ci-dessus, il n'est jamais possible d'exclure totalement une altération de l'interphase lors de la préparation des échantillons pour le TEM. Nous pensons néanmoins avoir pris toutes les précautions possibles

pour éviter les observations trompeuses, et la brève exposition à l'air de nos échantillons devra donc être gardée à l'esprit comme une source possible de surestimation de l'oxygène dans l'interphase.

III. Exemple: étude de l'interphase $LiNi_{1/2}Mn_{1/2}O_2$ / électrolyte

Cette section reprend une «étude de cas» publiée dans *solid-state NMR* [article IV]. Sa présence dans ce chapitre d'introduction est justifiée par la combinaison unique des différentes techniques de caractérisation développées pendant cette thèse, à savoir la RMN hétéronucléaire à haut champ et la quantification par EELS, adaptées à l'étude d'interphases électrode / électrode. Les concepts et arguments proposés dans la discussion illustrent bien l'approche utilisée au cours de ce travail de thèse.

Malgré l'augmentation significative de la résistance interphasiale, mesurée par spectroscopie d'impédance électrochimique, avec la température de stockage de $LiNi_{1/2}Mn_{1/2}O_2$ dans l'électrolyte, les compositions déterminées par XPS pour les deux échantillons stockés à 25°C et 55°C présentent peu de différences. En outre, l'apparition d'un deuxième demi-cercle sur le diagramme de Nyquist, symptomatique du recouvrement de l'électrode par une couche de surface résistive, ne peut pas être clairement liée à une quantité donnée d'espèces de surface. Autrement dit, la quantité absolue d'interphase ne peut pas être déterminée par l'analyse XPS. Considérant les inhomogénéités spatiales, la profondeur de pénétration limitée (max. 10 nm) ne permet pas de sonder l'interphase dans toute son épaisseur (jusqu'à 100 nm par endroits), tandis que le matériau actif reste tout de même visible, de par l'existence de surfaces nues. Ainsi, le recouvrement partiel par une interphase épaisse ne peut être différencié d'un recouvrement total par une couche suffisamment mince pour permettre l'observation du matériau actif sous-jacent. En outre, les proportions apparentes des espèces chimiques sont affectées par la non-linéarité de la pénétration du faisceau X. L'analyse de routine par XPS échoue donc également à clarifier la topologie / architecture / distribution des différentes composantes de l'interphase.

Les quantités de lithium, de fluor et de phosphore contenus dans l'interphase formée sur $LiNi_{1/2}Mn_{1/2}O_2$ pendant le stockage dans un électrolyte à base de $LiPF_6$ peut être quantifiée par RMN MAS. La surface de l'oxyde est principalement recouverte par LiF et des espèces organiques lithiées dont la présence ne peut être déduite que par la différence entre les quantités de lithium total et de fluorure de lithium. En outre, la différence entre la quantité de

fluorophosphates trouvés par XPS et RMN implique que la proportion de fluorophosphates est sous-estimée par XPS, ce qui signifie que ces espèces sont situées dans la partie intérieure de l'interphase. De telles considérations montrent que l'interprétation des résultats XPS peut être rendue moins ambiguë, à la lumière de données plus quantitatives obtenues par RMN MAS. Néanmoins, les espèces organiques non lithiées restent invisibles à la RMN, dans la mesure où la RMN MAS du ^{13}C est apparue impossible à mettre en œuvre compte tenu de la faible abondance naturelle et des faibles quantités d'espèces interphasiales par unité de masse de l'échantillon.

Le désaccord apparent entre XPS et RMN souligne l'hétérogénéité chimique de l'interphase dans sa profondeur. Ces techniques donnent toutes deux des résultats spectroscopiques moyens; que ce soit à l'échelle de la taille de la sonde XPS (0.7 mm x 0.3 mm) ou à celle de l'ensemble de l'échantillon dans le cas de la RMN, bien qu'aucune indication concernant la distribution des compositions chimiques selon l'épaisseur ne puisse être obtenue.

La quantification des espèces oxygénées par des analyses EELS donne une information précieuse, complémentaire à la RMN ^{7}Li, ^{19}F et ^{31}P et met enfin en évidence l'hétérogénéité chimique sur la profondeur de l'interphase. A ce stade, il est maintenant clair qu'un modèle multi-couches n'est pas plus réaliste que celui d'un mélange homogène moyen d'espèces interphasiales.

En dépit de ces limites, nous pensons que cet exemple (et son extrapolation aux différents matériaux d'électrode) démontre la pertinence de la RMN MAS pour un suivi quantitatif et une identification de certaines espèces chimiques présentes dans les interphases au sein d'un accumulateur Li-ion. La seule ambiguïté au sujet des résultats quantitatifs obtenus par cette méthode concerne les matériaux actifs diamagnétiques pour lesquels le lithium intercalé ou présent sous forme d'alliage doit être soigneusement discriminé des espèces interphasiales. Il faut bien sûr garder à l'esprit que des techniques de caractérisation complémentaires comme l'XPS ou l'EELS seront toujours nécessaires à une représentation plus précise et plus réaliste d'interphases 3D entre électrode et électrolyte.

IV. Conclusion

Comme illustré par un nombre croissant de publications, la RMN du ^{7}Li a émergé comme un outil robuste pour étudier la couche de surface sur des matériaux d'électrode

d'accumulateur Li-ion, notamment par couplage avec des techniques donnant accès à des informations chimiques complémentaires comme l'XPS ou le FTIR (développées en annexe 1).

Dans le cas des matériaux contenant des métaux de transition avec des électrons non appariés, en sus de la composition chimique et la quantification, il est possible d'extraire des informations physiques ou topologiques via l'interaction dipolaire électron-noyau. En particulier dans le cas de la RMN du ^{7}Li, l'avantage de cette méthode réside dans la séparation efficace du signal provenant de l'interphase de celui du matériau paramagnétique. L'analyse du signal de l'interphase sera développée dans les chapitres suivants, via l'évolution du temps de relaxation spin-spin apparent (T_2) du lithium interphasial, estimé à partir de la largeur de raie du signal.

L'utilisation d'autres noyaux tels que le ^{19}F ou ^{31}P pour sonder les éléments contenus dans l'interphase est un autre moyen simple de suivre l'évolution de la composition chimique des produits de décomposition de l'électrolyte. Le court exemple rapporté dans ce 2ème chapitre illustre la pertinence de la RMN hétéronucléaire, en particulier maintenant que la mise en œuvre de courbes d'étalonnage du ^{7}Li, ^{19}F et ^{31}P permet la comparaison directe des quantités absolues en mmol.g^{-1} de ces différents éléments. Un article récent de Murakami *et al.* rapporte le recours à la polarisation croisée entre ^{7}Li et ^{19}F pour analyser le LiF déposé sur $LiCoO_2$ [46]. Ces expériences quoique pointues ne sont cependant pas extrapolables à des matériaux d'électrode paramagnétiques en raison des longs temps de contact utilisés dans la séquence de pulse RMN, incompatibles avec les temps de relaxation courts observés pour des composés paramagnétiques.

Concernant la partie organique de l'interphase, Leifer *et al.* ont présenté l'utilisation de la RMN du ^{13}C pour élucider les mécanismes de décomposition des solvants organiques [47]. Cependant dans notre cas, la sensibilité de la RMN du ^{13}C en présence de centres paramagnétiques à proximité empêche totalement la détection du signal RMN. Par conséquent, la présence d'espèces interphasiales organiques contenant du Li devra être estimée à partir de la différence entre la quantité totale de lithium interphasial mesurée par RMN du ^{7}Li et la quantité de fluorure de lithium détectée par RMN du ^{19}F.

L'utilisation de l'EELS pour caractériser les interphases dans les accumulateurs au lithium est beaucoup moins développée dans la littérature, et le protocole expérimental utilisé dans cette thèse (notamment l'étape de rinçage) est évidemment passible des mêmes critiques que les études RMN *ex situ*.

L'accès à un microscope plus performant améliorerait considérablement l'image que l'on se fait de l'interphase, grâce à une simple cartographie chimique par EELS notamment. La préservation de l'intégrité de l'électrode et celle de l'interphase la recouvrant sont actuellement en développement dans notre groupe, grâce à l'utilisation d'un ultra microtome pour découper des sections d'échantillon. L'idée consiste à observer le système binaire électrode / interphase dans des conditions aussi proches que possible de celles du fonctionnement en accumulateur. À cet égard, les études par TEM *in situ* doivent toutefois être considérées avec prudence, en raison de l'utilisation nécessaire de liquides ioniques ou électrolytes solides, dont la réactivité envers les matériaux actifs diffère significativement de l'électrolyte conventionnel étudié ici.

CHAPITRE 3. ÉTUDE DE $LiNi_{½}Mn_{½}O_2$ COMME COMPOSÉ MODÈLE

Ce troisième chapitre regroupe les différentes études menées sur l'interphase $LiNi_{1/2}Mn_{1/2}O_2$ / électrolyte. Une première partie est consacrée à la synthèse et la caractérisation des matériaux de départ.

La deuxième partie suit directement le travail de J.-F. Martin *et al.* [1-5] sur ce même matériau. L'influence de paramètres tels que l'exposition de l'air, la température, la formulation de l'électrode composite ou l'utilisation d'un additif dans électrolyte est évaluée.

Dans une troisième partie, la surlithiation de ce matériau est étudiée, jusqu'à la composition $Li[Li_{0.2}Ni_{0.4}Mn_{0.4}]O_2$. D'un point de vue fondamental, l'extraction de "Li_2O" du matériau au cours du premier processus d'oxydation [6-9] est en effet susceptible d'influencer les processus interphasiaux.

II. Paramètres externes influençant le comportement interphasial

II.1. Contexte: influence de l'exposition à l'air

Sont résumés dans cette sous-section les résultats obtenus au cours de la thèse de Jean-Frédéric Martin (2008) [1] concernant l'influence de l'exposition à l'air sur la réactivité interphasiale lors du contact avec l'électrolyte ou du cyclage électrochimique.

II.2. Commentaire des résultats obtenus par Jean-Frédéric Martin (thèse 2008)

Les exemples présentés ici montrent la complexité des interactions entre électrode et électrolyte. L'effet néfaste d'une quantité trop élevée d'interphase est mis en évidence, de même que l'impact non moins négatif d'une quantité trop faible d'espèces lithiées dans l'interphase. Des analyses XPS complémentaires (voir réf. [3-5]) suggèrent que la distribution de la quantité totale de Li, entre produits fluorés tels que LiF, Li_xPF_y ou $Li_xPO_yF_z$ et produits organiques, évolue avec le temps de contact mais également au cours du cyclage. L'évolution antagoniste des espèces organiques et espèces fluorées détectées par XPS pose cependant le problème du recouvrement supposé des espèces interphasiales fluorées par les espèces organiques / polymériques (voir **Fig. III-8** et la discussion associée). Ainsi, le premier objectif de ce travail de thèse a consisté à mettre en œuvre la RMN MAS du ^{19}F et ^{31}P, telle que

décrite dans le chapitre 2, afin de bénéficier de la complémentarité de l'XPS et de la RMN (voir **Fig. II-5**) et de clarifier la chimie et l'évolution de l'interphase.

Comme démontré ici, la présence de ce dépôt constitué des produits de décomposition du sel et des solvants peut, dans une certaine mesure, bénéficier au comportement électrochimique. Toute la difficulté réside donc dans le contrôle de la croissance et de la chimie de cette interphase, à l'aide d'additifs dans l'électrolyte par exemple [35, 36].

II.3. Nouvelle étude de l'interphase $LiNi_{1/2}Mn_{1/2}O_2$ / électrolyte à l'aide de la RMN MAS du ^{19}F et ^{31}P.

Un nouvel examen de l'interphase $LiNi_{1/2}Mn_{1/2}O_2$ / électrolyte ($LiPF_6$ 1M dans EC: DMC) a été rendu possible par la mise en œuvre de nouveaux outils analytiques en RMN, à savoir l'extension aux noyaux ^{19}F et ^{31}P, et l'introduction de courbes de calibration RMN permettant la quantification absolue des intensités intégrées.

Par ces moyens, l'évolution de la chimie de l'interphase lors du contact avec l'électrolyte peut être surveillée sans équivoque, indiquant que l'accumulation observée d'espèces lithiées est seulement due aux alkylcarbonates de lithium. A température ambiante, la décomposition du sel survenant dès les premières minutes de contact ne mène qu'à la précipitation de LiF, dont la quantité reste stable même au cours d'un contact prolongé. La diminution apparente observée par XPS peut donc être attribuée à l'effet d'écran dû au recouvrement par les alkylcarbonates de lithium.

L'évolution qualitative et quantitative de l'interphase sur cyclage électrochimique peut être facilement réalisée par RMN MAS. Contrairement à l'XPS ou l'EELS (voir chapitre 2, **Figure II-11**), la présence d'additifs conducteur(s) ou de liant(s) dans les électrodes composites n'entrave ou ne restreint aucunement l'analyse, à condition d'utiliser un liant non fluoré.

Dans le présent exemple, l'extension de la RMN au ^{19}F permet d'infirmer l'hypothèse exprimée précédemment selon laquelle l'interphase formée en surface du $LiNi_{1/2}Mn_{1/2}O_2$ stocké sous argon n'était pas assez importante pour passiver la surface de l'électrode. En effet, il semble que la faible abondance et la diminution des espèces lithiées détectées par RMN du ^{7}Li ne représente pas correctement l'évolution globale de l'interphase au cours d'un cyclage prolongé. Au contraire, l'interphase telle que sondée par RMN du ^{19}F est constituée d'un mélange de LiF résistif avec des espèces non lithiées, dont l'accumulation peut raisonnablement entraver le transfert de charge à l'interface (bien que ne couvrant pas totalement la surface du matériau actif), comme représenté sur la **Figure III-14**.

Bien que l'on ignore encore quelle partie de l'interphase est sondée par XPS, la complémentarité de cette technique avec la RMN est indéniable. Non seulement l'XPS procure une caractérisation chimique fine, mais elle donne également accès à la composante organique non lithiée de l'interphase, invisible dans nos expériences de RMN. Ainsi, l'accumulation d'alkylcarbonates dans l'interphase peut être mise en évidence. L'augmentation de la résistance de transfert de charge et la diminution de la capacité spécifique de décharge peuvent donc être corrélées à la croissance d'une interphase pauvre en Li, défavorable au comportement électrochimique global.

II.4. Effet de LiBOB comme additif [article IV]

Alors que l'impact négatif des produits d'hydrolyse de $LiPF_6$ est incontesté, des alternatives au sel $LiPF_6$ dans les batteries commerciales peinent à émerger en raison des multiples exigences à satisfaire notamment en termes de conductivité ionique et de stabilité thermique. Le bi(oxalate) borate de lithium (LiBOB) a été repéré comme un candidat prometteur comme sel d'électrolyte ou additif pour batteries lithium-ion, conduisant à des performances améliorées en cyclage et à une réactivité thermique limitée [44-46]. Bien que les mécanismes interphasiaux cathodiques en présence de LiBOB restent confus [46], la polymérisation réductrice de l'anion BOB^- autour de 1.7 V forme un film protecteur, protégeant efficacement les deux électrodes positive et négative [47, 48]. Les avantages importants des électrolytes à base de LiBOB sont toutefois contrebalancés par une augmentation importante de l'impédance interfaciale résultant de l'épaississement de l'interphase, qui finit par limiter la capacité en puissance de manière critique [49].

À la lumière des analyses de surface par RMN, il apparait que l'utilisation de l'électrolyte modifié au LiBOB résulte en une interphase enrichie en lithium plutôt qu'en une interphase plus épaisse. Aux vues des résultats actuels, la formation de cette interphase implique la consommation de lithium tout au long du cyclage, et devrait aboutir à des rendements faradiques faibles, en accord avec les résultats électrochimiques. Des caractéristiques électrochimiques apparemment incompatibles (faible rendement faradique et l'impédance stable) peuvent s'expliquer à la lumière de l'accumulation de «bonne» d'interphase (c'est-à-dire conductrice). En effet, en se fondant sur les valeurs de résistance de transfert de charge, cette interphase apparait intrinsèquement moins résistive (ou moins bloquante) que l'interphase formée uniquement à partir de $LiPF_6$, composée d'un mélange de LiF résistif et d'espèces non lithiées, dont l'accumulation entrave le transfert de charge à

l'interface. Par comparaison, une interphase riche en Li, esquissée dans la **Figure III-21** agit davantage comme un électrolyte solide (SEI), ouvrant ainsi la voie vers l'ajustement d'une interphase appropriée. Ajuster la concentration en LiBOB semble cependant nécessaire pour optimiser la nature et les quantités d'espèces interphasiales. En effet, si la concentration en LiBOB utilisée dans cette étude a été volontairement accrue pour permettre l'observation d'effets significatifs, la littérature indique que l'addition de LiBOB à hauteur de 2% en masse dans $LiPF_6$ est suffisante pour former un film stable de SEI [46].

Ainsi, le succès de LiBOB comme additif s'appuie probablement sur sa consommation totale durant le premier cycle, en opposition avec les 20 cycles (ou plus) nécessaires pour consommer les 0,1 M utilisés dans la présente étude. Ainsi, en utilisant notre électrolyte modifié au LiBOB, la quantité de lithium de surface mesurée à la fin du premier cycle (0,5 $mmol.g^{-1}$) correspond approximativement à la consommation de 2% du lithium disponible dans le sel d'électrolyte pour former l'interphase sur la seule électrode positive. Une étude similaire, portant simultanément sur les deux électrodes permettrait de corréler directement la perte de capacité aux processus interphasiaux, ce qui s'avèrerait extrêmement précieux dans le cadre de diagnostics post mortem.

II.5. Remarques

Gardant à l'esprit ses limites, l'utilisation de la méthode de quantification par RMN MAS offre de nombreuses perspectives dans le domaine des interphases dans les dispositifs électrochimiques, comme le montrent les différents exemples développés ici.

La présence initiale de Li_2CO_3 ne semble pas intervenir dans les processus interphasiaux comme une couche protectrice ou résistive, mais plutôt comme un additif, dont l'influence diffère entre les cinq premiers cycles qui voient une consommation Li dans l'interphase aux dépens de la capacité électrochimique, et les cycles ultérieurs pour lesquels interphase et performances électrochimiques semblent stabilisés. Évidemment, ce comportement particulier doit aussi dépendre de la quantité de Li_2CO_3 natif à la surface et toute une variété de comportements électrochimiques intermédiaires peut être attendue. La comparaison avec des systèmes dépourvus de Li_2CO_3 ou contenant du LiBOB montre qu'une interphase riche en Li est préférable à l'interphase riche en fluor observée dans le cas du matériau stocké sous argon, quand bien même la croissance de cette dernière procède sans consommation de Li. Ainsi, une interphase électrode positive / électrolyte souhaitable doit être conçue de manière similaire à la SEI sur les négatives de graphite: riche en espèces

lithiées conductrices pour assurer une bonne diffusion, homogène pour permettre la passivation de la surface, mais la plus mince possible afin de limiter l'ampleur du sacrifice en lithium. À cet égard, les résultats obtenus sur la formulation conduisant à une porosité accrue démontrent que, en dépit d'une chimie favorable, la limite supérieure en termes de quantité (ou épaisseur) d'interphase peut facilement être atteinte.

Une telle étude d'optimisation, appliquée au LiBOB ou à tout autre agent formant de la SEI (additif, revêtement etc) exige des outils spectro-analytiques fiables et sans équivoque. Nous démontrons ici la pertinence de la RMN MAS pour de telles applications. Bien que réalisée *ex situ*, les analyses présentées ici semblent être convenablement corrélées avec l'EIS *in situ* et les performances électrochimiques globales, validant ainsi la méthode de suivi de l'évolution de l'interphase. L'observation du $T_{2(Li)}$, inédite jusqu'ici, semble complexe mais encourageante pour décrire qualitativement l'interaction entre électrode et interphase. Les valeurs estimées devraient toutefois être remplacées par la détermination expérimentale du T_2 réel, offrant une description qualitative plus précise et plus riche.

III. Modifications intrinsèques du matériau d'électrode susceptibles d'influencer le comportement interphasial

L'étude de $LiNi_{1/2}Mn_{1/2}O_2$ a été étendue aux oxydes lamellaires surlithiés, et la composition $Li[Li_{0.2}Ni_{0.4}Mn_{0.4}]O_2$, a été choisie en raison de sa position dans le diagramme ternaire $LiNiO_2$-$LiMnO_2$-$LiMn_2O_3$ (voir chapitre 1 , **Fig. I-3, droite**) qui en fait le composé le plus riche en Li dont la perte nette de Li_2O au cours du plateau initial à haut potentiel conduirait à la composition du composé modèle $LiNi_{1/2}Mn_{1/2}O_2$. Les différences entre les deux matériaux choisis, en termes de chimie de l'interphase et performances électrochimiques, doivent donc résider dans le processus singulier de charge initiale.

III.1 Observations faites sur le matériau $Li_{1.2}Ni_{0.4}Mn_{0.4}O_2$ de départ

Considérant que la diminution du $T_{2(Li)}$ au cours d'un cyclage prolongé n'est corrélée ni à l'état de charge (SOC), ni à des quantités d'espèces interphasiales détectées plus importantes, une explication possible consisterait en la décrépitation du matériau actif, mentionnée comme une origine possible de la perte de capacité. Dans l'hypothèse de fissures se propageant à la surface du grain, de nouvelles surfaces seraient créées. Il est raisonnable de s'attendre à ce que ces surfaces nues nouvellement exposées à l'électrolyte réagissent de façon préférentielle. Ainsi, les espèces interphasiales précipiteraient sur ces surfaces libres plutôt

que sur l'interphase existante. Cette redistribution progressive des espèces interphasiales au cours des processus successifs de dissolution / précipitation pourrait alors expliquer l'augmentation globale de l'intimité entre interphase et matériau et donc, la diminution globale du $T_{2(Li)}$. Néanmoins, la raison pour laquelle ce phénomène ne serait pas accompagné d'une augmentation globale de la quantité d'espèces lithiées et fluorées par unité de masse de matériau actif n'est pas encore élucidée.

Pour conclure, dans le cas du matériau $Li_{1.2}Ni_{0.4}Mn_{0.4}O_2$ par rapport au $LiNi_{1/2}Mn_{1/2}O_2$ de départ, il semble que toutes les réactions interphasiales soient exacerbées: alors que les espèces fluorées sont formées par contact direct avec l'électrolyte ou au cours du 1er cycle électrochimique et ne subissent ensuite pas de modification substantielle lors des cycles répétés, les espèces lithiées présentent une forte dépendance au potentiel. Les quantités de lithium et fluor de surface détectées par unité de masse étant similaires pour une surface spécifique 8 fois plus faible, l'interphase doit nécessairement être plus épaisse et / ou plus couvrante. Néanmoins, la quantité de Li_2CO_3 de surface formée sur $Li_{1.2}Ni_{0.4}Mn_{0.4}O_2$ lors de la synthèse et du stockage sous air est négligeable (**Fig. III-25**) et ne peut être tenue pour responsable de cette réactivité envers l'électrolyte.

Ainsi, plusieurs mécanismes interphasiaux devraient être envisagés: d'abord, une nucléophilie accrue de la surface pourrait aggraver la décomposition du sel et des solvants par simple contact et ensuite la libération d'oxygène depuis le matériau actif pourrait gouverner la chimie interphasiale, comme schématisé dans la **Figure III-30**. De la même manière Li_2CO_3 ou LiBOB pourraient être considérés comme des sources d'oxygène, conduisant à une évolution globalement similaire de l'interphase au cours du cyclage.

III.2. Utilisation d'un revêtement: effet d'une couche hétérochimique en surface

Dans la suite, la modification de la réactivité de $Li_{1.2}Ni_{0.4}Mn_{0.4}O_2$ face à l'électrolyte est évaluée suite à une modification de la surface par le dépôt d'une couche tampon d'Al_2O_3. Dans la littérature, ce type de revêtement a en effet été signalé comme diminuant la capacité irréversible initiale et améliorant la cyclabilité des oxydes lamellaires surlithiés [57, 58].

Les quantités d'espèces interphasiales lithiées détectées sur $Al_2O_3/Li_{1.2}Ni_{0.4}Mn_{0.4}O_2$ pourraient résulter de la combinaison de deux facteurs: premièrement, la quantité importante de lithium extraite du matériau lors du traitement thermique ou du stockage à l'air (**Fig. III - 34**), exacerbant les réactions de surface avec de l'électrolyte précédemment observées dans le

cas de $LiNi_{1/2}Mn_{1/2}O_2$ en présence du Li_2CO_3 (section 2.1.1) et ensuite, l'augmentation de la nucléophilie de la surface de $Li_{1.2}Ni_{0.4}Mn_{0.4}O_2$, intensifiant la dégradation du sel et des solvants de l'électrolyte (section 3.2.2).

La forte décroissance de capacité observée sur les premiers cycles en présence du revêtement de Al_2O_3 par rapport au $Li_{1.2}Ni_{0.4}Mn_{0.4}O_2$ nu (**Fig. III-33, droite**) pourrait être étudiée en détail par RMN couplée à l'XPS au cours des deux premiers cycles électrochimiques, afin de clarifier les processus interphasiaux spécifiques à l'enrobage. Ces processus interphasiaux ainsi que le comportement du matériau massif pourraient également être influencés par des modifications de l'extrême surface du matériau actif après l'incorporation probable de Al dans la structure, comme en témoigne le cas de $LiCoO_2$ après revêtement de Al_2O_3 [59, 60]. À ce stade, il est seulement possible de corréler l'augmentation de la résistance interfaciale à une précipitation aggravée d'alkylcarbonates de Li en présence d'Al_2O_3, comme représenté schématiquement dans la **Figure III-38**. La chute de capacité peut ainsi être expliquée par l'augmentation de polarisation de la demi-cellule.

III.4. Conclusions sur les oxydes surlithiés et leur réactivité de surface

En ce qui concerne les oxydes lamellaires surlithiés, illustrés dans ce travail par le matériau $Li_{1.2}Ni_{0.4}Mn_{0.4}O_2$, il apparait que l'étape initiale d'oxydation électrochimique conduisant à l'extraction d'oxygène au-dessus de 4.5V pourrait être considérée comme la source possible d'espèces oxygénées, conduisant à l'observation de processus interphasiaux comparables en présence de carbonates, d'oxalates (voir le cas du LiBOB) ou d'oxygène gazeux.

Un tel type de réactivité envers l'électrolyte se trouve considérablement amplifié en présence d'un revêtement d'Al_2O_3 malgré l'absence de modifications structurales, confirmant l'absence de Li_2O comme une entité chimique susceptible de régir la chimie interphasiale. Par conséquent, l'extraction irréversible du lithium de la structure ne peut pas être tenue pour responsable de la chimie et la quantité d'interphase, qui est peut-être seulement dictée par des réactions chimiques faisant intervenir des espèces oxygénées. De fait, la littérature rapporte l'utilisation d'une double couche de revêtement ($AlPO_4$ ou $CoPO_4$ à l'intérieur et Al_2O_3 à l'extérieure) pour limiter la croissance de couches interphasiales indésirables.

Cependant, l'utilisation d'une composition de départ surlithiée permet d'accéder à des capacités en décharge plus élevées et les efforts devraient être poursuivis dans cette direction. La faible aptitude en puissance de ces matériaux, et la mauvaise rétention de capacité

observées ici pourraient s'expliquer à la fois par les dommages mécaniques subis par le matériau lors de l'extraction irréversible de «Li_2O» [54], et par l'exacerbation de la décomposition de l'électrolyte par contact avec la surface riche en Ni(III) du matériau, comme observé dans le cas de $LiNiO_2$ [55, 56].

A partir de cette évaluation, plusieurs directions de recherche peuvent être envisagées. Les observations générales sont discutées dans la conclusion générale, mais concernant la nucléophilie de la surface, une amélioration simple dans le contrôle de la croissance d'interphase peut être apportée par la synthèse de matériaux actifs composites de type cœur-couronne. En effet, Amine *et al.* ont relaté la préparation d'oxydes lamellaires surlithiés, comprenant des compositions locales intermédiaires entre un noyau $LiNiO_2$ et une couronne Li_2MnO_3 [62]. Le contrôle de la croissance de l'interphase induite par la formation de fissures peut être mis en œuvre par l'ajustement de la morphologie de l'agrégation des particules primaires, une fois encore à travers la synthèse de matériaux composites adaptés [62]. Par conséquent, la présente étude gagnerait à être appliquée à des matériaux à haute performance, afin de confirmer et de préciser les comportements interphasiaux observés ici.

IV. Conclusion

Tout au long de ce chapitre consacré au matériau $LiNi_{1/2}Mn_{1/2}O_2$, un comportement interphasial similaire a été observé en présence de carbonates, d'oxalates ou d'oxygène gazeux à la surface: des sels fluorés, et plus particulièrement du fluorure de lithium sont formés par simple contact avec la surface active. Dans un second temps, des alkylcarbonates de lithium subissent un processus dynamique de précipitation/dissolution à haut/bas potentiel, respectivement.

Ce comportement interphasial archétypal est cependant tout à fait différent de celui d'un matériau stocké sous Ar et jamais exposé à la pollution atmosphérique. Ainsi, la réactivité de surface des $LiNi_{1/2}Mn_{1/2}O_2$ semble dictée par des espèces de surface oxygénées. L'absence d'activité rédox discernable associée à un tel processus pourrait suggérer les mécanismes interphasiaux de dégradation impliquant des radicaux organiques oxygénés plutôt que des électrons libres. Cette hypothèse reste bien sûr à confirmer par des études *in situ* portant sur l'électrolyte [63]. Cette idée est particulièrement séduisante car elle correspond bien à l'observation d'un rendement faradique proche de 100%, à l'exception du premier cycle.

En dépit du départ de la plupart des espèces lithiées interphasiales pendant la charge suivante, une accumulation notable est observée, résultant à la fois en la consommation de lithium à partir du réservoir disponible (qui peut être l'électrolyte puisqu'il s'agit d'un processus chimique) et en l'augmentation de la résistance interfaciale.

Si la corrélation entre le comportement électrochimique et les espèces interphasiales oxygénées pouvait être confirmée, un traitement adapté pourrait être envisagé pour éviter la précipitation de quantités trop importantes d'alkylcarbonates de lithium, en se basant sur l'utilisation d'additifs solubilisant l'oxygène, tels que ceux à l'étude pour des applications Li-air [64, 65].

Néanmoins, le comportement interphasial d'un $LiNi_{1/2}Mn_{1/2}O_2$ dépourvu d'une couche native de Li_2CO_3 montre que les alkylcarbonates de lithium devraient être la principale composante interphasiale, par opposition avec d'autres espèces indésirables telles que le fluorure de lithium intrinsèquement résistant. La chimie de surface devrait donc être adaptée afin d'éviter la décomposition du sel par simple contact avec la surface active, ce qui pourrait être réalisé avec des additifs stabilisateurs de $LiPF_6$. À cet égard, l'utilisation d'un excès de LiF solubilisé dans l'électrolyte, mentionné dans la réf. [66] pour réduire la concentration de LiF dans la SEI (suivant un principe d'équilibre chimique (voir Eq. I-4)), s'est avérée augmenter expérimentalement d'un facteur 10 la précipitation d'alkylcarbonates de lithium sur $Li_{1.2}Ni_{0.4}Mn_{0.4}O_2$. Une telle étude, non développée dans le manuscrit, mériterait d'être poursuivie en ajustant la concentration de LiF, ou en envisageant d'autres stabilisateurs de $LiPF_6$.

Enfin, bien que peu performants comme électrodes positives, les oxydes lamellaires de nickel et manganèse synthétisés pour ce travail ont parfaitement joué leur rôle de composés modèles pour tester l'outil RMN à travers l'étude des différents paramètres physico-chimiques susceptibles d'influencer l'interphase.

Les retours sur ces expériences sont encourageants, surtout lorsque l'on considère la topologie de l'interphase mise en évidence par TEM (soit une épaisseur allant de 0 à 10^2 nm) qui rend l'analyse XPS contestable. Les études RMN combinant ^7Li et ^{19}F apparaissent en comparaison plus robustes, et permettent dans la plupart des cas de corréler les caractéristiques électrochimiques globales à la chimie et l'évolution interphasiale. Même lorsque la croissance de l'interphase ne peut être tenue pour responsable du mauvais comportement électrochimique, le vieillissement physique du matériau actif ou de l'électrode composite peut alors être envisagé plus clairement.

CHAPITRE 4. ÉTUDE DE $LiFePO_4$

Très peu d'études s'attachent à l'influence de l'évolution de l'interphase de $LiFePO_4$ sur son fonctionnement dans un accumulateur au lithium car ce matériau était jusqu'ici considéré comme chimiquement inerte face à l'immersion dans l'électrolyte.

Ce chapitre couvre plusieurs paramètres susceptibles d'influencer le comportement interphasial de $LiFePO_4$, mais avant tout, le comportement interphasial intrinsèque de $LiFePO_4$ est étudié, à l'échelle du premier cycle électrochimique mais également au cours des cycles ultérieurs. Les questions fondamentales à l'origine de ce travail concernent principalement l'architecture et la dynamique de cette interphase.

$LiFePO_4$ étant anisotrope dans toutes ses propriétés physico-chimiques, la troisième partie est centrée sur la possible dépendance de la réactivité de surface envers l'électrolyte selon l'orientation cristalline.

La quatrième et dernière partie décrit le processus de vieillissement subi par $LiFePO_4$ lors de son exposition aux espèces oxydantes de l'atmosphère durant son stockage. A partir de la caractérisation structurale et électrochimique des matériaux vieillis à l'air, des mécanismes de réaction sont proposés. Dès lors, l'impact d'un tel vieillissement sur la chimie interphasiale est mis en lumière et des traitements potentiellement appropriés sont appliqués.

I. Synthèse et caractérisation de matériaux de départ

Bien que le composite LFP-C (contenant 10% en masse de Ketjenblack) présente des propriétés remarquables en cyclage, la présence inhomogène de particules de carbone en surface rendrait les études interphasiales beaucoup plus délicates. A la lumière de nos expériences préliminaires, l'étude du $LiFePO_4$ a été réalisée sur le matériau nu, afin d'analyser la réactivité de surface intrinsèque au LFP, ainsi que sur le matériau enrobé de carbone dénommé CA/LFP. L'influence du carbone sur la réactivité de surface est considérée ci-après comme un moyen susceptible de limiter la dégradation de l'électrolyte (partie 3.2) mais également de limiter le vieillissement induit par l'exposition à l'air (section 4.4).

II. Comportement interphasial intrinsèque de $LiFePO_4$

Le premier cycle électrochimique est étudié afin de comprendre le processus de formation réversible et la dissolution des composants de l'interphase en fonction du potentiel. Des analyses spectroscopiques sophistiquées permettent alors de corréler la dynamique de l'interphase avec la distribution des espèces chimiques dans la profondeur de celle-ci. L'accumulation irréversible après un cyclage prolongé est également soulignée.

La **Figure IV-13** reprend les quantifications RMN obtenues au cours du premier cycle électrochimique. Les résultats de RMN MAS ^{31}P sont ici rapportés en fonction des quantités de fluor observé sous forme de fluorophosphates. Cette comparaison confirme que ces espèces sont du type $R\text{-}PO_2F_2$ ou un mélange avec des $R\text{-}PO_3F$, comme suggéré par les attributions des valeurs de déplacement RMN.

Enfin, il apparait que l'évolution des espèces interphasiales observée par RMN en réponse aux variations de potentiel concerne surtout les espèces lithiées non fluorées tels que les alkylcarbonates de lithium. Cette conclusion est en accord avec les résultats d'XPS, et avec l'idée d'une interphase dynamique essentiellement organique couvrant à la fois le matériau actif et la partie inorganique de l'interphase. Affranchie de l'effet d'écran rencontré en XPS, la RMN indique que les espèces inorganiques telles que le LiF et les fluorophosphates ne subissent pas de modification substantielle en réponse aux variations de potentiel.

Basée sur des techniques spectro-analytiques statistique, cette étude aboutit néanmoins à une représentation dynamique et tridimensionnelle de l'interphase $LiFePO_4$/électrolyte, ce que nous nous proposons de mettre en évidence avec l'aide d'analyses localisées dans la partie 2.2(Fig. **IV-16** et **IV-17**).

Si les interphases formées pendant le premier cycle électrochimique d'un accumulateur Li-ion jouent un rôle significatif sur les performances de la batterie, un second point critique est de veiller à la passivation des surfaces des deux électrodes afin de limiter (ou idéalement de stopper) la consommation de lithium dans les interphases et de la perte de capacité tout au long d'un cyclage prolongé. Ainsi, les expériences suivantes se concentrent sur les 20 premiers cycles électrochimiques du système $Li//LiPF_6$, EC:DMC//LFP (bilan en **Fig. IV-20**).

Largement considéré comme chimiquement inerte envers l'électrolyte, le $LiFePO_4$ présente en réalité une interaction dynamique complexe avec les solutions d'électrolyte classiques à base de $LiPF_6$ dans EC:DMC. Comme représenté dans la figure **IV-21**, les conclusions suivantes peuvent être proposées:

- Les solvants sont dégradés en surface de $LiFePO_4$ à haut potentiel, et leurs produits de décomposition se présentent sous forme d'une interphase de type SPL qui se dissout par la suite aux bas potentiels.
- Moins sensibles au potentiel, les produits de décomposition du sel tels que LiF, Li_xPF_y ou $Li_xPO_yF_z$ sont piégés dans cette SPL. Bien qu'une quantité importante des ces composés quitte l'interphase au cours de la dissolution de la matrice organique, l'interphase observée à bas potentiel est donc plus riche en composés fluorés.
- L'accumulation globale d'espèces interphasiales est contrebalancée par un moindre attachement de cette interphase de type SPL à la surface de $LiFePO_4$, et peut-être aussi par l'accentuation des inhomogénéités topologiques résultant en une porosité accrue de la SPL. Les nouvelles espèces interphasiales se déposeraient donc par dessus l'interphase existante plutôt que de couvrir de nouvelles surfaces du matériau actif, évitant ainsi le blocage du transfert de charge entre l'électrolyte et le matériau actif.

Néanmoins, le bénéfice de cette dynamique de l'interphase ne doit pas éclipser l'accumulation globale de produits de décomposition lithiés à la surface de l'électrode positive. Les expériences menées ici ne permettent cependant pas d'identifier la source de ces espèces lithiées; et d'autres analyses effectuées dans une configuration Li-ion seraient nécessaires pour distinguer un échange entre les interphases depuis l'électrode négative jusqu'à la positive d'une consommation faradique préjudiciable de lithium. La réponse à cette dernière question permettrait, par exemple de choisir un(des) additif approprié(s), soit pour faciliter la navette d'espèces interphasiales entre les deux électrodes ou pour passiver strictement la surface de $LiFePO_4$.

III. Caractérisation et contrôle de la dépendance de la réactivité de surface en fonction de l'orientation cristalline

$LiFePO_4$ apparait désormais comme un matériau de cathode de choix pour des applications de lithium-ion à haute puissance, mais beaucoup de ses propriétés de transport restent à comprendre. La structure olivine orthorhombique du $LiFePO_4$ cristallise dans le groupe d'espace *Pnma* et présente une forte anisotropie pour plusieurs de ses propriétés [25]. Compte tenu de la disparité des surfaces de $LiFePO_4$ attendue à partir de calculs *ab initio* [26, 27], nous proposons de synthétiser des particules fortement orientées et étudier l'influence de l'orientation cristallographique sur la formation des espèces de surface à l'interface électrode / électrolyte afin de déterminer la réactivité de surface à partir de son orientation cristallographiques puis de corréler cette réactivité avec le comportement en électrochimie.

III.1. Illustration de la réactivité accrue de la surface électroactive (010) par RMN

Concernant les plaquettes orientées selon *b*, par opposition aux particules isotropes, la variation de la quantité de lithium est beaucoup plus prononcée en fonction des variations de potentiel et la quantité de LiF (d'après la RMN du ^{19}F), bien qu'elle ne semble pas varier de manière significative, est plus élevée d'un ordre de grandeur. Comme observé au cours des expériences de trempage dans l'électrolyte (non présentées ici), la réactivité de la face (010) est telle que celle-ci est immédiatement saturée de produits de décomposition du sel par simple contact. Par conséquent, les quantités de LiF mesurées par RMN sur les 5 premiers cycles sont similaires à ce qui a été détecté au bout de 3 minutes ou 3 jours d'immersion dans la solution de $LiPF_6$, EC:DMC.

A l'échelle d'un cyclage prolongé du matériau isotrope préparé par voie solide, les variations des quantités de composés fluorés suivent la même tendance que les espèces lithiées. L'écart par rapport à ce modèle pour les plaquettes orientées selon *b* suggère que les espèces organiques détectées dans ce cas et dans le cas du matériau isotrope préparé par voie solide sont différentes. Les variations de la quantité de lithium avec le potentiel (importante à l'état réduit et faible à l'état oxydé) sont en fait opposées à ceux du LFP préparé par voie solide, mais ressemblent à ce qui est observé pour les oxydes $LiNi_{1/2}Mn_{1/2}O_2$ (chapitre 3), suggérant que la surface des plaquettes orientées selon *b* est recouverte d'une épaisseur suffisante pour ne plus gouverner la chimie interphasiale.

En conséquence, la variation observée pour la quantité de lithium correspond plutôt à des processus se produisant à l'interface entre l'interphase et l'électrolyte (c'est-à-dire dans la

zone externe de l'interphase). La diminution globale de la quantité de lithium interphasial suggère la dissolution des espèces organiques lithiées et des fluorophosphates tandis que la partie interne de l'interphase, faite de fluorure de lithium formée par simple contact avec l'électrolyte n'est pas soumise à des variations importantes.

III.3. Conclusions sur l'orientation cristalline et ses conséquences

La synthèse par voie hydrothermale de matériaux $LiFePO_4$ semble aboutir à une quantité importante de défauts structuraux, à savoir des antisites Li/Fe, qui limitent les performances électrochimiques en termes de capacité accessible. Le recuit ultérieur à haute température effectué pour déposer un revêtement carboné sur les plaquettes fortement orientées selon *b*, affichant environ 50% de surfaces (010), s'avère efficace pour réduire la quantité de tels défauts structuraux.

Une fois affranchi de leur impact néfaste sur les performances électrochimiques, il apparait cependant que l'exposition exacerbée des surfaces (010) conduit à une réactivité accrue envers l'électrolyte. Ainsi, la chimie interphasiale sur des matériaux orientés selon (010) se trouve régie par l'augmentation de la précipitation de produits de décomposition inorganiques du sel d'électrolyte à la surface de l'électrode par simple contact, plutôt que par la réactivité intrinsèque de $LiFePO_4$ (menant au processus de précipitation/dissolution décrit dans la section 1.3). L'impédance de demi-cellule mesurée pour des plaquettes de LFP fortement orientées selon *b* nues et enrobées de carbone montre que cette morphologie, et la réactivité de surface associée, pourrait ne pas être appropriée pour une application en batterie. En effet, le bénéfice découlant de la maximisation de cette surface particulière pour une capacité améliorée à régime elevé est totalement contrecarré par le blocage de la surface avec des espèces interphasiales, schématisé dans la **Figure IV-31**.

IV. Caractérisation et contrôle du vieillissement de la surface au cours d'une exposition à l'air et répercussions sur l'électrochimie

La première étape pour une meilleure compréhension des interactions entre électrode et électrolyte est la connaissance précise de la surface du matériau de départ.

Cette étude vise à faire la lumière sur l'altération de l'olivine à l'atmosphère et à suivre les changements structuraux et chimiques qui se produisent au cours du stockage des poudres. En conclusion de ces études, publiées dans la réf. [8] et des articles I, II et III, un schéma du scénario du vieillissement le plus probable est proposé. Ensuite, des expériences

électrochimiques et les caractérisations interphasiales associées illustrent les conséquences de ces modifications sur les performances des batteries utilisant $LiFePO_4$. Enfin, deux solutions expérimentales pour contrôler le vieillissement de surface de $LiFePO_4$, à savoir un revêtement de carbone et l'utilisation d'un additif approprié, sont présentées.

IV.1. Les modifications structurales induites par une exposition modérée à l'air

Dans l'expérience ATG présentée dans la **Figure IV-35**, un échantillon de LFP a été exposé à 120°C pendant 24 heures d'abord à l'oxygène sec puis, à l'oxygène en présence d' 1% d'humidité relative. Il est clairement montré que bien que la réaction avec O_2 est possible, la cause principale de l'altération de $LiFePO_4$ est la réaction impliquant l'humidité contenue dans l'atmosphère.

Considérant le rôle à la fois de l'oxygène et de l'eau, il semble donc raisonnable de proposer les deux mécanismes possibles de corrosion ci-dessous:

$$LiFe^{II}PO_4 + x / 2\ H_2O + x / 4\ O_2 \rightarrow Li_{1-x}Fe^{II}_{1-x}Fe^{III}_{x}PO_4 + x\ LiOH \quad \text{(Eq. IV-3)}$$

$$LiFe_{II}PO_4 + 1 / 2\ H_2O + 1 / 4\ O_2 \rightarrow LiFe^{III}PO_4\ (OH) \quad \text{(Eq. IV-4)}$$

La première réaction décrit l'extraction du lithium à partir de la phase de l'olivine, observée par DRX, et décrite dans la réf. [8]. La deuxième réaction a été proposée par des minéralogistes pour les phosphates de fer hydratés et hydroxylés, comme le soulignent Fransolet *et al.* [44] dans le cas de l'olivine qui mène à la formation de tavorite $LiFePO_4(OH)$. Non seulement cette réaction permet l'oxydation du fer dans une mesure nettement plus importante que dans le domaine de solution solide $Li_{1-x}Fe^{II}_{1-x}Fe^{III}_{x}PO_4$ (Eq. IV-3), mais elle est également en accord avec la prise de masse observée dans la **Figure IV-35** en présence d'humidité. L'absence de tavorite cristalline dans les échantillons exposés à l'air est approfondie dans la partie 4.2.

En outre, le ratio Fe(III)/Fe(II) déterminé par XPS dans l'article II apparait nettement plus élevé lorsque déterminé par cette technique sensible à la surface (~ 80%), comparativement à la spectroscopie Mössbauer (~ 35%). Considérant la nature de la surface de la phase riche en Fe(III), une vue schématique de type cœur-couronne a été déduite à l'échelle d'une particule, comprenant un noyau riche en Fe(II) fait de triphylite $Li_{1-x}FePO_4$. Cette vue est en accord avec un processus de vieillissement initié en surface du grain par exposition à une atmosphère humide oxydante. La **Figure IV-36** résume la globalité des changements structuraux et chimiques possibles subis par $LiFePO_4$ lors de l'exposition à l'air.

IV.2. Modifications structurales induites par exposition à l'humidité [article III]

Afin d'étudier la nature de la phase incidente apparaissant après une exposition à l'air de $LiFePO_4$, notre stratégie a consisté à augmenter la quantité de phases secondaires par un vieillissement accéléré, par exposition à de l'air chaud (120°C), ou à une exposition prolongée jusqu'à 80 jours à de l'air saturé en humidité.

En se basant sur les données structurelles, la transformation de la triphylite en tavorite devrait se traduire par une expansion volumique d'environ 20% due à l'incorporation de groupements hydroxyles, et l'imagerie par TEM montre effectivement une augmentation de la taille des particules lors du vieillissement, de 100 nm à 150-200 nm, et enfin à 1-10 µm. Cependant, la taille moyenne des cristallites déterminée par diffraction des rayons X pour la phase tavorite dans l'échantillon vieilli 80 jours est d'environ 195 nm, impliquant que les plaquettes microscopiques de tavorite sont polycristallines.

Dans cette partie, une étude structurale approfondie aux échelles longue distance et locale d'une série d'échantillons de LFP ayant subi un séjour à 120°C sous atmosphère ambiante ou humide a été réalisée pour faire la lumière de façon quantitative sur les étapes successives du processus de dégradation se produisant aux températures modérées (inférieures à 150°C). La croissance d'une phase de phosphate ferrique désordonné a été observée directement pour la première fois et la combinaison de méthodes quantitatives telles que la diffraction des rayons X, la spectroscopie Mössbauer, la RMN et l'EELS mettent clairement en évidence un mécanisme de vieillissement allant de la surface des particules vers un cœur légèrement désintercalé. Comme schématisé dans la **Figure IV-41**, la consommation de l'olivine est accompagnée par la croissance des particules due à l'expansion volumique, compatible avec l'incorporation de groupements OH, suivie par leur fusion lors de la recristallisation sous la forme de grandes plaquettes de tavorite.

IV.3. Influence du vieillissement de l'air sur le comportement électrochimique de $LiFePO_4$

D'un point de vue pratique, l'oxydation du fer résultant du stockage sous air des poudres de $LiFePO_4$ conduit directement à une diminution de la capacité électrochimique accessible dans une configuration Li-ion. Néanmoins, l'ampleur de la perte de matière électroactive et l'influence d'une couche de phosphate ferrique renfermant des particules de $LiFePO_4$ sur le processus d'intercalation sont encore inconnues / mal comprises. Par conséquent, une caractérisation détaillée du comportement électrochimique des échantillons

vieillis à l'air est nécessaire pour comprendre les conséquences d'un stockage inadapté de $LiFePO_4$ sur les performances électrochimiques attendues.

IV.3.1. Signature électrochimique de la phase ferrique formée lors du vieillissement

Comme décrit dans la réf. [8] et les articles I, II et III, le vieillissement à l'air conduit à l'apparition de nouveaux processus redox autour de 2.7 V attribués au phosphate amorphe. L'échantillon nommé B est ici particulièrement significatif car il ne contient pas de tavorite cristalline. La capacité supplémentaire obtenue dans cette région de potentiel peut être décomposée en deux pics redox parfaitement réversibles (voir **Fig. IV-43**), et un pic de réduction irréversible à 2.75 V (voir **Fig. IV-44**).

Le point clé concernant le comportement électrochimique des échantillons vieillis est que l'exposition à l'air, même dans une moindre mesure, mène directement à une perte de capacité spécifique dans une configuration Li-ion. En outre, les espèces ferriques formées présentent une activité électrochimique complexe, y compris une importante réaction irréversible avec l'électrolyte.

IV.3.2. Cyclabilité à long terme des matériaux LFP vieillis à l'air

La cyclabilité des matériaux LFP vieillis à l'air a été mesurée et les capacités spécifiques de décharge correspondantes, obtenues à un régime de C/10 sont affichées dans la **Figure IV-45** pour les échantillons A et B. La capacité spécifique observée pour le matériau LFP de départ (A) est discutée dans la partie 1.4, et sert ici de référence. Concernant l'échantillon vieilli B, il apparaît clairement que la capacité initiale (145 $mAh.g^{-1}$) ne peut être maintenue pendant plus de quelques cycles et décroit rapidement (-30% après 20 cycles, 50% après 100 cycles).

À ce stade, il n'est pas clair si la faible rétention de capacité électrochimique de l'échantillon vieilli à l'air peut être expliquée par la dissolution du fer, la croissance d'une interphase isolante et / ou la perte de contact électrique au sein de l'électrode.

IV.3.4. Effet du vieillissement à l'air sur la réactivité envers l'électrolyte

La différence de réactivité de surface envers l'électrolyte a été étudiée par RMN et la **Figure IV-47** montre les spectres RMN du ^{7}Li mesurés à la fin des $1^{ère}$, $5^{ème}$ $20^{ème}$ charges et décharges du matériau B vieilli à l'air.

Le diagramme de quantification, contenant les expériences complémentaires de RMN du ^{19}F, est montré dans la **Figure IV-48** et peut être comparé à la **Figure IV-20** présentant les résultats obtenus pour un échantillon de départ.

L'évolution des quantités de composés fluorés suit celle des espèces lithiées. Plutôt qu'une accumulation globale d'espèces interphasiales entre le 1er et le 20ème cycle qui pourrait expliquer la croissance d'un film résistif comme observé par impédance, la RMN met en évidence la réversibilité presque parfaite du processus de précipitation/dissolution de l'interphase.

Comparé au modèle SPL considéré à la surface du LFP non vieilli, l'interphase observée sur le $LiFePO_4$ vieilli à l'air est nettement plus riche en produits de décomposition du sel d'électrolyte tels que du LiF et des fluorophosphates. En particulier, la quantité de lithium dans LiF à l'état oxydé correspond à 50 à 90% du lithium interphasial détecté au total, alors que la SPL présente à haut potentiel sur le LFP de départ ne contenait que 20 à 50% du lithium sous forme de fluorure de lithium. Ainsi, l'interphase du LFP vieilli à l'air peut être vue comme un mélange de LiF fortement résistif et de fluorophosphates ou d'espèces polymériques non lithiées, ces dernières étant invisibles dans le cadre nos expériences RMN.

Considérant la dissolution aggravée du Fe observée pour le matériau vieilli, une hypothèse plausible concernant les processus interphasiaux serait que l'eau chimisorbée ou les groupes hydroxyles incorporés favorisent la dissolution du $LiFePO_4$ lors du contact avec l'électrolyte ou du cyclage. Cette dissolution serait accompagnée par le départ de l'interphase présente et une nouvelle interphase serait alors formée sur les surfaces nouvellement exposées.

IV.3.5. Remarques

Les dégradations à la fois du matériau actif et de l'électrolyte seraient donc susceptibles de perdurer jusqu'à la consommation complète des espèces aqueuses, à moins qu'un film de passivation ne soit formé avant, ce qui semble se produire ici autour du 20ème cycle. Les mauvaises performances électrochimiques du matériau $LiFePO_4$ vieilli à l'air peuvent donc être considérées comme le résultat de la réaction des espèces aqueuses incorporées lors de l'exposition à l'air avec $LiPF_6$ pour former du HF:

- Le HF produit peut ensuite attaquer le matériau actif, alimentant ensuite la dissolution de $LiFePO_4$ ou plutôt du $LiFePO_4(OH)$ de surface, comme représenté sur la **Figure IV-49**.

- HF peut également réagir avec les espèces interphasiales, notamment les espèces organiques ou polymères lithiés, pour former (entre autres) une quantité importante de LiF fortement résistif (voir les réactions de décomposition dans le chapitre 1, équations I-6).
- Par conséquent, la passivation de surface de l'électrode se produit en raison / grâce à la présence d'une interphase essentiellement inorganique, probablement plus dense que la SPL observée sur $LiFePO_4$ de départ, agissant comme une barrière efficace contre les attaques acides ultérieures.

IV.4. Contrôle du vieillissement à l'air par l'utilisation d'un revêtement carboné

La dégradation des performances électrochimiques de $LiFePO_4$ après exposition à l'air a pu être attribuée à un mécanisme de vieillissement de type corrosion, impliquant à la fois l'oxygène atmosphérique et l'humidité. Par conséquent, une protection triviale contre cette réaction parasite est ici considérée à travers l'utilisation d'un revêtement de carbone. Non seulement la présence d'une couche de carbone conductrice devrait permettre d'améliorer les propriétés électriques du matériau, mais le carbone étant hydrophobe, il vise également à empêcher la chimisorption et l'incorporation de groupements hydroxyles dans le $LiFePO_4$ sous-jacent.

IV.4.1. Illustration de la protection du matériel par spectroscopie Mössbauer

La protection offerte par un revêtement de carbone est évaluée ici par un simple test de vieillissement comparant le matériau noté CA/LFP préparé par carbonisation de l'acétate de cellulose et le $LiFePO_4$ nu. Après un mois de stockage à 120°C, des mesures de spectroscopie Mössbauer (**Fig. IV-50, gauche**) indiquent que matériau recouvert de carbone s'avère être efficacement protégé contre les espèces atmosphériques oxydantes. Les échantillons sont ensuite testés en batterie et le matériau recouvert de carbone montre une excellente cyclabilité, comme en témoigne la **Figure IV-50 (droite)**.

IV.4.2 Effet de la couche de carbone sur la réactivité envers l'électrolyte

Alors que la quantité de LiF ne présente presque aucune évolution, la quantité de fluorophosphates reste nettement inférieure à la quantité de lithium interphasial. Ainsi, la SPL recouvrant le matériau CA/LFP à haut potentiel se trouve être extrêmement riche en lithium sous forme d'espèces organiques / polymériques qui se dissolvent pendant la décharge

ultérieure. Bien que le transfert de charge à l'interface soit affecté, le lithium peut voyager à travers cette interphase riche en Li, et aucun effet sur la capacité en décharge n'est observé.

L'absence d'évolution de la quantité de LiF suggère que contrairement à la décomposition des solvants, la décomposition du sel n'est pas aggravée dans le cas du CA/LFP. Ces observations combinées pourraient s'expliquer par la chimie de surface du matériau. De fait, la surface du matériau a été rendue hydrophobe par la présence du revêtement carboné, et une plus faible quantité d'impuretés d'eau adsorbée est attendue pour le CA/LFP par rapport au LFP. Ainsi, l'augmentation de la surface de contact avec le dépôt de la couche de carbone (la surface spécifique BET augmente de 21 $m^2.g^{-1}$ à 25 $m^2.g^{-1}$) ne favorise pas les réactions parasites avec $LiPF_6$. Par opposition, la décomposition des solvants d'électrolyte (catalysée par la surface de $FePO_4$) est aggravée pendant la charge par l'augmentation de la surface de contact, induite par la porosité du carbone.

IV.4.3 Remarques

L'effet de la couche de carbone sur la réactivité de surface de $LiFePO_4$ est non seulement complexe mais aussi ambigüe. Le vieillissement à l'air a pu être évité, et les performances en puissance et la cyclabilité améliorées. Cependant, l'accumulation d'espèces organiques lithiées est exacerbée par la présence du revêtement carboné (voir **Fig. IV-54**); de même que le $LiFePO_4$ non enrobé, cette étude gagnerait à être complétée par des tests en cellules complètes. Plus important encore, il est communément admis que les régimes de cyclage lents favorisent la décomposition de l'électrolyte et il serait utile d'examiner l'effet du régime de charge/décharge sur les processus interphasiaux en utilisant des matériaux carbonés.

IV.6. Conclusions sur l'exposition de l'air et ses conséquences

Bien que largement considéré comme inerte à l'exposition à l'air, $LiFePO_4$ présente une réactivité non négligeable envers les espèces atmosphériques oxydantes, à savoir l'oxygène et l'humidité. Son vieillissement peut devenir important au cours d'un stockage à une température modérée ou sous des atmosphères humides telles qu'existantes dans certaines parties du monde.

En se basant sur une étude structurale et électrochimique exhaustive, cette partie propose deux mécanismes possibles de "corrosion" envisageant un rôle pour l'oxygène et l'eau. Dans une première étape, l'exposition à l'air conduit à l'extraction de lithium à partir de $LiFePO_4$, dans la limite du domaine de solution solide $Li_{1-x}FePO_4$ [8]. Cette réaction a peu

d'influence dans une demi-cellule utilisant une contre électrode de Li métal, mais réduit d'autant la capacité pratique accessible dans une configuration Li-ion. Le second mécanisme de corrosion observé conduit à l'incorporation de groupements hydroxyles à la surface du matériau, sous la forme d'une phase amorphe de $LiFePO_4(OH)$ [articles II et III]. Suite à cette réaction qui réduit encore la capacité accessible dans une cellule Li-ion, l'oxydation du fer peut être beaucoup plus sévère que dans le cadre du premier mécanisme. De façon plus critique encore, la présence d'espèces aqueuses dans le matériau, qui ne peuvent être extraites qu'en effectuant un traitement thermique à 600°C sous atmosphère inerte [article I], modifie radicalement la réactivité du matériau envers l'électrolyte.

En fait, la vulnérabilité de $LiFePO_4$ contre les impuretés acides [53] est non seulement confirmée ici, mais s'avère nettement aggravée après vieillissement à l'air. Le travail réalisé ici démontre que dans un tel cas, les interactions électrode / électrolyte sont dominées par la dissolution du matériau actif et la réaction des hydroxyles incorporés avec le sel d'électrolyte.

Ayant élucidé le mécanisme de défaillance des $LiFePO_4$ vieillis à l'air, des moyens pratiques pour limiter le vieillissement de surface ou son impact néfaste sur la réactivité envers électrolyte sont proposés. Ainsi, l'obtention reproductible d'une cyclabilité convenable a pu être démontrée, et ce malgré une forte exposition à l'air chaud ou humide, en se basant sur une connaissance suffisante des mécanismes de réaction élucidés dans cette thèse.

V. CONCLUSION

Ce chapitre consacré à $LiFePO_4$ a couvert les questions découlant de diverses discussions qui étaient:

Est-il possible de mettre en évidence expérimentalement l'architecture et l'inhomogénéité de l'interphase?

La réponse est affirmative, et le développement d'outils d'analyse tels que l'XPS et le TEM devraient fournir de nouvelles preuves sans équivoque. Dans le présent chapitre, les deux voies (étude locale par EELS et le profil dans l'épaisseur par XPS) sont timidement explorées et se révèlent toutes deux extrêmement encourageantes. Les descriptions d'interphases pêchent souvent par simplisme ou par abstraction. À cet égard, les couches minces épitaxiées constituent le dispositif le plus prometteur, par leur nature chimique

identique à celle du matériau actif étudié (par opposition avec les métaux nobles souvent utilisés comme «modèles») et par leur morphologie 2D simplifiant considérablement l'analyse (par comparaison avec des électrodes composites utilisant des échantillons sous forme de poudre, mais aussi carbones et liants ...).

Ainsi, le modèle le plus réaliste de l'interphase $LiFePO_4$/électrolyte est relativement complexe, soit grossièrement celui d'une interphase de type électrolyte polymère solide englobant un mélange hétérogène d'espèces inorganiques.

A quel point l'interphase $LiFePO_4$/électrolyte est-elle dynamique au cours du cyclage?

L'interphase observée sur tous les matériaux $LiFePO_4$ étudiés, à moins d'un blocage de la surface par des produits de décomposition du sel, présente le même comportement général en réponse aux variations de potentiel, à savoir la précipitation d'une SPL riche en Li au dessus de 4.0 V, entraînant la présence de fluorophosphates dans l'interphase, et sa dissolution lors de la décharge suivante, libérant la plupart des sels fluorés piégés. En plus de ce processus dynamique, une accumulation progressive d'espèces interphasiales est cependant observée dans tous les cas.

La surface (010) électroactive du $LiFePO_4$ est-elle plus catalytique de la décomposition de l'électrolyte?

Très probablement, oui. Bien que cette étude gagnerait à être complétée par l'étude de couches minces épitaxiées offrant chacune une surface cristallographique différente, le travail effectué ici sur plaquettes (010) préparées par voie hydrothermale semble indiquer une amplification considérable de la décomposition du sel et des solvants à leur contact.

Par ailleurs, une telle approche expérimentale des mécanismes de formation d'interphase sur des surfaces cristallines pourraient facilement être couplée à des études théoriques de modélisation de l'adsorption des espèces de surface sur les surfaces actives, telle que développées par ailleurs [56, 57].

Dans quelle mesure la surface induite par vieillissement du $LiFePO_4$ lors d'une exposition à l'air et/ou à l'humidité influence-t-elle les processus interphasiaux?

Les mécanismes de corrosion mis en évidence dans ce travail proposent la croissance une phase $LiFePO_4(OH)$ aux rayons X à la surface du matériau. La chimie interphase semble ensuite gouvernée par la dissolution de cette phase, en raison d'impuretés acides, inévitables dans les électrolytes à base de $LiPF_6$. L'impact de cette dissolution sur les performances

électrochimiques d’accumulateurs Li-ion utilisant $LiFePO_4$ est essentiel: non seulement les performances de l'électrode positive s’en trouve sensiblement diminuées, comme présenté dans ce chapitre, mais l'empoisonnement de l'électrode négative par des espèces contenant du fer et migrant depuis la positive devrait être sérieusement envisagé. À cet égard, des exemples tirés de la littérature montrent que les conséquences d’un dépôt de métaux de transition sur l'électrode négative peut être encore plus nuisible pour le système que la perte nette de capacité de stockage de Li dans la positive [58].

CONCLUSION

Comme mentionné dans l'introduction, cette thèse prend directement la suite du travail réalisé par Jean Frédéric Martin (thèse soutenue en Novembre 2008). Il semble évident d'évaluer le travail réalisé ici, à la lumière des perspectives envisagées alors. De ce point de vue, l'évolution des surfaces de $LiNi_{½}Mn_{½}O_2$ et $LiFePO_4$ au cours de leur vieillissement et cyclage électrochimiques dans un électrolyte conventionnel ($LiPF_6$ 1M dans EC:DMC) devait être comparée aux résultats obtenus par l'utilisation d'additifs de l'électrolyte ou la modification de surface par revêtement physique ou greffage moléculaire. Ces modifications de surface devaient être évaluées en termes de modifications de l'interphase et de leur impact sur les performances électrochimiques. Les études présentées ici soulignent la complexité d'une telle approche, non pas en raison d'un obstacle expérimental particulier, mais plutôt en raison de l'importance primordiale de la caractérisation préalable de l'interphase électrode/électrolyte.

Les objectifs de ce travail ont été doubles, comme indiqué dans le titre "Caractérisation et contrôle d'interphase électrode positive/électrolyte au sein d'accumulateurs au lithium". Le premier élément («caractérisation») a été développé dans diverses directions, la plus fructueuse étant la RMN MAS. L'approche initiale, basée uniquement sur la RMN du ^{7}Li a pu être étendue aux noyaux ^{19}F et ^{31}P, mettant en évidence les espèces interphasiales inorganiques. La mise en œuvre de courbes de calibration RMN empiriques est le résultat d'un long questionnement, sur ce que la physique inhérente à l'expérience RMN autorise, et ce qu'elle n'autorise pas. Cette recherche préliminaire est à peine évoquée dans le manuscrit, mais la mise en place d'un tel outil expérimental commode, mais néanmoins robuste n'a pas été simple. Bien sûr, cette approche reste discutable, comme il se doit, mais bien plus que les résultats spécifiques aux couples matériaux d'électrode/électrolyte, les méthodes spectroscopiques présentées ici sont d'une réelle importance. Par exemple, elles sont maintenant utilisées dans notre groupe pour suivre l'évolution d'interphases sur des électrodes négatives à base de silicium ou de matériaux de conversion.

La méthodologie mise en œuvre pour les analyses TEM/EELS a également pu être appliquée avec succès par des collègues pour la caractérisation du vieillissement dans l'électrolyte de spinelles fonctionnant à 5V. L'analyse de matériaux après cyclage n'a pas pu être rapportée ici par manque de temps et en raison des difficultés supplémentaires posées par

la présence des composants inactifs d'électrodes. De telles expériences sont en cours, et représentent un moyen unique pour décrire les dépôts interphasiaux, complémentaires aux résultats de RMN ou XPS.

La mise en évidence par TEM de surfaces nues et d'interphases présentant une épaisseur allant jusqu'à 200 nm d'épaisseur, pose sérieusement la question de la représentativité de ce qui est sondé par XPS. De toute évidence, cette question n'a pas été résolue ici, mais l'XPS se pose néanmoins comme une technique incroyablement puissante pour clarifier la chimie de l'interphase, complémentaire aux analyses RMN. Toutefois, nous avons saisi l'opportunité offerte par le Pr. Kanno d'étudier des films minces épitaxiés de $LiFePO_4$ et d'initier des analyses préliminaires en XPS résolues en angulaire. Bien que des modèles minutieux permettent de reconstruire des profils en profondeur dans le cas d'assemblages multicouches, nous nous sommes limités à des conclusions qualitatives, lors d'une première approche. Pourtant, les couches minces épitaxiées offrent de nombreuses possibilités pour étudier la formation et l'évolution des interphases, par XPS, mais aussi par TEM ou par EQCM ou encore par éllipsométrie *in situ* par exemple. Nous laissons ces travaux passionnants aux personnes compétentes.

Le deuxième élément («contrôle») a été considéré tardivement dans la thèse à la lumière des résultats précédents, une fois qu'une base de travail suffisante a été recueillie sur nos composés "modèles". La dissolution de métaux de transition dans le cas du $LiNi_{½}Mn_{½}O_2$, mise en évidence par EELS, a été confrontée par l'utilisation d'un additif ou d'un revêtement hétérochimique, susceptibles de limiter un tel phénomène. Le vieillissement de la surface de $LiFePO_4$ a été limité par l'utilisation d'un revêtement carboné, et son impact néfaste sur la chimie interphasiale résolu via l'utilisation d'un additif approprié. Ces différents traitements ont rencontré un certain succès, mais ont toujours induit des réactions secondaires inattendues. Les systèmes électrochimiques sont complexes, et la réactivité entre leurs différentes composantes n'est pas toujours prévisible. Ainsi, la présente thèse gagnerait à considérer non seulement les mécanismes de vieillissement ou de défaillance identifiés et le traitement approprié mais également les altérations possibles à long terme, induites par l'ajout d'une nouvelle composante dans ces systèmes complexes.

Il existe un consensus général sur ce qu'une «bonne» interphase devrait être, essentiellement conductrice aux ions Li^+. A partir des différentes études rapportées ici, les espèces organiques lithiées tels que les alkylcarbonates de lithium doivent être favorisés au

détriment des polymères non lithiés ou du fluorure de lithium, clairement identifié comme entravant le transfert de charge à l'interface électrode positive / électrolyte.

Les travaux futurs devraient essayer de combiner des analyses *ex situ* telles que celles présentés ici, avec un suivi *in situ* de l'électrolyte liquide, afin d'analyser les espèces intermédiaires à courte durée de vie, et l'évolution gazeuse dans la batterie en cours de fonctionnement. Cette dernière pourrait être sondée par GC-MS par exemple, donnant un aperçu des réactions interphasiales intermédiaires. Pour élucider les différents mécanismes de dégradation, la collaboration avec des chimistes organiciens est absolument nécessaire. Bien sûr, une telle approche multidisciplinaire est laborieuse, mais certainement plus intelligente, et au final sans doute moins onéreuse qu'une recherche basée sur une approche « essai-erreur ».

Caractérisation et contrôle de l'interface électrode / électrolyte d'électrodes positives pour accumulateurs Li-ion.

Les accumulateurs au lithium, largement développés pour l'électronique portable, sont aujourd'hui envisagés pour des applications en véhicules hybrides et électriques. Les limitations actuelles sont leur faible capacité et leur durée de vie limitée provenant entre autres de la non-maitrise de l'interface électrode positive / électrolyte.

La présente étude porte sur la caractérisation et le contrôle des processus interfaciaux relatifs aux matériaux $LiNi_{0.5}Mn_{0.5}O_2$, $Li_{1.2}Ni_{0.4}Mn_{0.4}O_2$ et $LiFePO_4$ d'électrode positive lors du stockage et du cyclage électrochimique.

La thèse s'est concentrée sur la formation et l'évolution de l'interphase formée par décomposition de l'électrolyte, en fonction de l'état de surface du matériau actif. Différents types de modifications ont été envisagés, tels qu'une modification intrinsèque par vieillissement à l'air ou par favorisation d'une orientation cristalline particulière dans le cas de l'olivine $LiFePO_4$, ou encore par la surlithiation de l'oxyde lamellaire $LiNi_{0.5}Mn_{0.5}O_2$, sous la forme $Li[Li_{0.2}Ni_{0.4}Mn_{0.4}]O_2$. D'autres types de modifications, considérées comme artificielles ou externes, reposent sur l'usage d'additifs dans l'électrolyte ou d'un dépôt hétérochimique en surface de $Li_{1.2}Ni_{0.4}Mn_{0.4}O_2$. Dans chaque cas, les espèces visibles à la surface des matériaux au cours du stockage et du cyclage sont corrélées aux performances électrochimiques des électrodes positives.

L'originalité du travail repose sur le développement d'outils spectroscopiques tels que la RMN MAS (^{7}Li, ^{19}F et ^{31}P) et l'EELS, parallèlement à l'XPS, pour quantifier les interphases de manière absolue et en décrire l'architecture.

Mots clés : Accumulateur au lithium, électrode positive, $LiFePO_4$ – phosphate de fer, $LiNi_{0.5}Mn_{0.5}O_2$ – oxide de nickel et de manganèse, interface – interphase, RMN MAS du ^{7}Li, ^{19}F et ^{31}P

Characterization and control of electrode / electrolyte interface of various cathode materials in Li-ion batteries

Lithium batteries, widely developed for portable electronics, are now being considered for applications in hybrid and electric vehicles. Their current limitations are the low capacity and limited cycle life caused notably by the uncontrolled positive electrode / electrolyte interface.

The present study reports the characterization and attempts of control of interfacial processes occurring on $LiNi_{0.5}Mn_{0.5}O_2$, $Li_{1.2}Ni_{0.4}Mn_{0.4}O_2$ and $LiFePO_4$ positive electrode materials during their storage and electrochemical cycling.

The thesis focuses on the formation and evolution of the interphase formed by decomposition of the electrolyte, depending on the surface chemistry of the active material. Different types of surface modifications have been proposed, such as intrinsic modifications upon aging in air or the promotion of a particular crystalline orientation in the case of olivine $LiFePO_4$, or by overlithiation of the $LiNi_{0.5}Mn_{0.5}O_2$ oxide lamellar, under the form of Li $[Li_{0.2}Ni_{0.4}Mn_{0.4}]O_2$. Other types of modifications, considered as artificial or external, are based on the use of additives in the electrolyte or of a heterochemical coating on the surface of $Li_{1.2}Ni_{0.4}Mn_{0.4}O_2$. In each case, species detected on the surface of materials during storage and cycling are correlated with the electrochemical performance of the positive electrodes.

The originality of the work is based primarily on the development of spectroscopic tools such as MAS NMR (^{7}Li, ^{19}F and ^{31}P) and EELS, in parallel to XPS, to quantitatively describe the interphase and unravel its architecture.

Keywords : Lithium batteries, positive electrode, $LiFePO_4$ – iron phosphate, $LiNi_{0.5}Mn_{0.5}O_2$ – nickel and manganese oxide, interface – interphase, ^{7}Li, ^{19}F and ^{31}P MAS NMR